



I. R. IRAN

ISSN: 1728-144X

e-ISSN: 1735-9244



**International Journal of Engineering**

Journal Homepage: [www.ije.ir](http://www.ije.ir)



**TRANSACTIONS B: APPLICATIONS**

Volume 35, Number 05, May 2022

*Materials and Energy Research Center*

---

# INTERNATIONAL JOURNAL OF ENGINEERING

## Transactions A: Basics

---

### DIRECTOR-IN-CHARGE

A. R. Khavandi

### EDITOR-IN-CHIEF

G. D. Najafpour

### ASSOCIATE EDITOR

A. Haerian

### EDITORIAL BOARD

- |      |  |       |   |
|------|--|-------|---|
| S.B. | Adeloju, Charles Sturt University, Wagga, Australia                            | A.    | Mahmoudi, Bu-Ali Sina University, Hamedan, Iran                         |
| K.   | Badie, Iran Telecomm. Research Center, Tehran, Iran                            | O.P.  | Malik, University of Calgary, Alberta, Canada                           |
| M.   | Balaban, Massachusetts Ins. of Technology (MIT), USA                           | G.D.  | Najafpour, Babol Noshirvani Univ. of Tech., Babol, Iran                 |
| M.   | Bodaghi, Nottingham Trent University, Nottingham, UK                           | F.    | Nateghi-A, Int. Ins. Earthquake Eng. Seis., Tehran, Iran                |
| E.   | Clausen, Univ. of Arkansas, North Carolina, USA                                | S. E. | Oh, Kangwon National University, Korea                                  |
| W.R. | Daud, University Kebangsaan Malaysia, Selangor, Malaysia                       | M.    | Osanloo, Amirkabir Univ. of Tech., Tehran, Iran                         |
| M.   | Ehsan, Sharif University of Technology, Tehran, Iran                           | M.    | Pazouki, Material and Energy Research Center, Meshkindasht, Karaj, Iran |
| J.   | Faiz, Univ. of Tehran, Tehran, Iran  | J.    | Rashed-Mohassel, Univ. of Tehran, Tehran, Iran                          |
| H.   | Farrahi, Sharif University of Technology, Tehran, Iran                         | S. K. | Sadrnezhaad, Sharif Univ. of Tech, Tehran, Iran                         |
| K.   | Firoozbakhsh, Sharif Univ. of Technology, Tehran, Iran                         | R.    | Sahraeian, Shahed University, Tehran, Iran                              |
| A.   | Haerian, Sajad Univ., Mashhad, Iran  | A.    | Shokuhfar, K. N. Toosi Univ. of Tech., Tehran, Iran                     |
| H.   | Hassanpour, Shahrood Univ. of Tech., Shahrood, Iran                            | R.    | Tavakkoli-Moghaddam, Univ. of Tehran, Tehran, Iran                      |
| W.   | Hogland, Linnaeus Univ, Kalmar Sweden  | T.    | Teng, Univ. Sains Malaysia, Gelugor, Malaysia                           |
| A.F. | Ismail, Univ. Tech. Malaysia, Skudai, Malaysia                                 | L. J. | Thibodeaux, Louisiana State Univ, Baton Rouge, U.S.A                    |
| M.   | Jain, University of Nebraska Medical Center, Omaha, USA                        | P.    | Tiong, Nanyang Technological University, Singapore                      |
| M.   | Keyanpour rad, Materials and Energy Research Center, Meshkindasht, Karaj, Iran | X.    | Wang, Deakin University, Geelong VIC 3217, Australia                    |
| A.   | Khavandi, Iran Univ. of Science and Tech., Tehran, Iran                        |       |   |

### EDITORIAL ADVISORY BOARD

- |       |  |       |  |
|-------|--|-------|--|
| S. T. | Akhavan-Niaki, Sharif Univ. of Tech., Tehran, Iran                       | A.    | Kheyroddin, Semnan Univ., Semnan, Iran                                 |
| M.    | Amidpour, K. N. Toosi Univ of Tech., Tehran, Iran                        | N.    | Latifi, Mississippi State Univ., Mississippi State, USA                |
| M.    | Azadi, Semnan university, Semnan, Iran                                   | H.    | Oraee, Sharif Univ. of Tech., Tehran, Iran                             |
| M.    | Azadi, Semnan University, Semnan, Iran                                   | S. M. | Seyed-Hosseini, Iran Univ. of Sc. & Tech., Tehran, Iran                |
| F.    | Behnamfar, Isfahan University of Technology, Isfahan                     | M. T. | Shervani-Tabar, Tabriz Univ., Tabriz, Iran                             |
| R.    | Dutta, Sharda University, India  | E.    | Shirani, Isfahan Univ. of Tech., Isfahan, Iran                         |
| M.    | Eslami, Amirkabir Univ. of Technology, Tehran, Iran                      | A.    | Siadat, Arts et Métiers, France  |
| H.    | Hamidi, K.N.Toosi Univ. of Technology, Tehran, Iran                      | C.    | Triki, Hamad Bin Khalifa Univ., Doha, Qatar                            |
| S.    | Jafarmadar, Urmia Univ., Urmia, Iran                                     | S.    | Hajati, Material and Energy Research Center, Meshkindasht, Karaj, Iran |
| S.    | Hesaraki, Material and Energy Research Center, Meshkindasht, Karaj, Iran |       |  |

### TECHNICAL STAFF

M. Khavarpour; M. Mohammadi; V. H. Bazzaz, R. Esfandiar; T. Ebadi

### DISCLAIMER

The publication of papers in International Journal of Engineering does not imply that the editorial board, reviewers or publisher accept, approve or endorse the data and conclusions of authors.

## CONTENTS

## Transactions B: Applications

<b>P. Pasha; D. Domiri-Ganji</b>	Hybrid Analysis of Micropolar Ethylene-glycol Nanofluid on Stretching Surface Mounted Triangular, Rectangular and Chamfer Fins by FEM Strategy and Optimization with RSM Method	845-854
<b>H. Bahmani; H. Khani Sanij; R. Roshani; M. M. Majidi Shad; S. H. Hosseini; M. Edalati; M. Olazar; S. A. Almasi</b>	Influence of Mixing Conditions of Modified Bitumen on Moisture Sensitivity of Asphalt Compounds	855-864
<b>R. Ansari; S. A. Banihashemi; R. Taherkhani; S. Moradi</b>	Decision Support System for Analyzing Key Performance Indicators in Construction Projects Management	865-874
<b>A. Bandani; F. Barati</b>	Stable Operation Limits in Dual Active Bridge for SuperCapacitor Applications	875-882
<b>M. Aghanezhad; R. Shafaghat; R. Alamian; S. M. A. Seyedi; M. J. Raji Asadabadi</b>	Experimental Study on Performance Assessment of Hydraulic Power Take-off System in Centipede Wave Energy Converter Considering Caspian Sea Wave Characteristics	883-899
<b>J. Skovajsa; O. Přibyl; P. Přibyl; M. Ščerba; A. Janota</b>	Evaluation of a Mobile Highway Management System at Roadwork Zones	900-907
<b>S. D. Turkane; S. K. Chouksey</b>	Partial Replacement of Conventional Material with Stabilized Soil in Flexible Pavement Design	908-916
<b>H. R. Moosaei; A. R. Zareei; N. Salemi</b>	Elevated Temperature Performance of Concrete Reinforced with Steel, Glass, and Polypropylene Fibers and Fire-proofed with Coating	917-930
<b>S. Ravikumar; S. Kothandaraman</b>	Influencing Parameters of Exterior Reinforced Concrete Beam-Column Joint Shear Strength: A Depth Review of Recent Advances	931-942
<b>M. R. Babaei; G. A. Sheikhzadeh; A. A. Abbasian Arani</b>	Numerical Investigation of Geometric Parameters Effects on Heat Transfer Enhancement in a Manifold Microchannel Heat Sink	943-953
<b>Y. Noori; A. R. Teymourtash; B. Zafarmand</b>	Use of Random Vortex Method in Simulating Non-Newtonian Fluid Flow in a T-junction for Various Reynolds Numbers and Power-law Indexes	954-966

<b>V. L. Thang; L. Cung; D. S. Nguyen</b>	An Application of Artificial Neural Network to Predict the Compressive Strength of Concrete using Fly Ash and Stone Powder Waste Products in Central Vietnam	967-976
<b>M. Karevan</b>	Understanding the Effect of Interfacial Interphase on the Elastic Response of Hollow Glass Microsphere Reinforced Microcomposites	977-987
<b>A. Jahanbakhsh; M. Hosseini; M. Jahanshahi; A. Amiri</b>	Extraction of Catechin as a Flavonoid Compound via Molecularly Imprinted Polymers	988-995
<b>M. Broghany; S. Basirjafari</b>	Optimum Design of Multi-layered Micro-perforated Panel Sound Absorbers in Combination with Porous Materials in an Arbitrary Frequency Range	996-1005
<b>H. Safarzadeh; F. Kianfar</b>	Single Machine Scheduling Problem with Batch Outsourcing	1006-1016
<b>T. J. Mohammed; K. M. Breesem</b>	Enhancement of the Shear-flexural Strength of the Rubberized Concrete Prism Beam by External Reinforcement	1017-1023
<b>N. H. Thai; N. T. Trung</b>	A Novel Curve for the Generation of the Non-circular Gear Tooth Profile	1024-1036
<b>M. Torkashvand; F. Ahmadizar; H. Farughi</b>	Distributed Production Assembly Scheduling with Hybrid Flowshop in Assembly Stage	1037-1055
<b>M. Hashemi; S. M. Marandi; M. Vahidi</b>	The Effect of Heat on the Settlement Properties of Cement-stabilized Clay Soil	1056-1063
<b>H. Zare; M. Khanalizadeh Eini; A. Esmacili</b>	Stabilization of Voltage and Current in the Distribution Networks using APF and TSC	1064-1073
<b>H. Sharifi; P. Ahmadi Moghaddam; S. Jafarmadar; A. M. Nikbakht; A. Hosainpour</b>	Fouling Performance of A Horizontal Corrugated Tube due to Air Injection	1074-1081
<b>H. Hamidi; S. H. Seyed Lotfali</b>	Analysis of Role of Cloud Computing in Providing Internet Banking Services: Case Study Bank Melli Iran	1082-1088
<b>P. Ghasem Ghanbari; M. Momeni; M. Mousivand; M. Bayat</b>	Unconfined Compressive Strength Characteristics of Treated Peat Soil with Cement and Basalt Fibre	1089-1095





# Hybrid Analysis of Micropolar Ethylene-glycol Nanofluid on Stretching Surface Mounted Triangular, Rectangular and Chamfer Fins by FEM Strategy and Optimization with RSM Method

P. Pasha<sup>\*a</sup>, D. Domiri-Ganji<sup>b</sup>

<sup>a</sup> Department of Mechanical Engineering, Mazandaran University of Science and Technology, Babol, Iran

<sup>b</sup> Department of Mechanical Engineering Noshirvani University of Technology, Babol, Iran

## PAPER INFO

### Paper history:

Received 11 October 2020

Received in revised form 26 November 2021

Accepted 09 December 2021

### Keywords:

Angular Velocity

Chamfer Fins

Finite Element Method

Nanofluid Effects

## ABSTRACT

This paper analysis heat transfer and angular velocity of micropolar ethylene-glycol nanofluid over the triangular, rectangular and chamfer fins on the stretching sheet. The innovation of this paper is to investigate parameters of nanofluid flow passing from the different fins on the stretching surface. The finite Element Method is selected for solving governing equations. The nanofluid temperature in the space of fins is warm and equal to the surface temperature. The temperature value is 30 degrees. The maximum values of nanofluid temperature exist in the last fin of surfaces. By passing the nanofluid flow from the first fins of the surface, the temperature of flow comes from 25°C to 31°C and at the ends of the surface, the temperature is high value. The maximum of ethylene glycol angular velocity occurs at  $x=0.9$  for chamfer and rectangular modes and the minimum of temperature occurs at  $x=0.8$  for 3 different fins. The angular velocity for nanofluid on the triangular and chamfer modes is 6.5% bigger than other baffles.

doi: 10.5829/ije.2022.35.05b.01

## NOMENCLATURE

H	Distance the plates (m)	Nb	Brownian motion
C	Nanofluid concentration	$T_c$	Temperature of the cold wall (K)
K	Dimensionless temperature	$\Delta T$	Temperature difference
$x, y$	Coordinates (m)	<b>Greek Symbols</b>	
$u, v$	Velocity components (m/s)	$\rho$	Density (kg/m <sup>3</sup> )
$\theta$	Dimensionless temperature	$\mu$	Dynamic viscosity (kg/m. s)
$\vartheta$	Kinematic viscosity (m <sup>2</sup> /s)	$\beta$	Thermal expansion (1/K)
$C_p$	Specific heat at constant pressure (J/kg.k)	$\alpha$	Thermal diffusivity (m <sup>2</sup> /s)
k	Thermal conductivity (W/m.k)	$\nu$	Kinematic viscosity (m <sup>2</sup> /s)
P	Modified fluid pressure	$\phi$	Dimensionless concentration
$g_y$	Gravitational acceleration (m/s <sup>2</sup> )	$\sigma$	Electrical conductivity (s/m)
$Pr$	Prandtl number ( $\nu/\alpha$ )	$B_0$	Magnetic field intensity
Nt	Thermo-phoretic parameter	$\sigma_{nf}$	Ferrofluid electric conductivity

## 1. INTRODUCTION

Thread stretching sheet with different fins at steady-state two-dimensional flow of a micropolar/classical ferro-

fluid was investigated. A ferrofluid is a form of fluid that exists in which micro particles of iron, magnetite, or cobalt. Ferrofluids are made-up of magnetic iron pieces suspended in oil, commonly kerosene, with a surfactant

\*Corresponding Author Email: [pasha.pooya@yahoo.com](mailto:pasha.pooya@yahoo.com) (P. Pasha)

to prevent oleic acid. Ferrofluids and nanofluids are used in rotary seals in computer hard drives and other rotating shaft motors [1–9]. Tãlu et al. [10] investigated the fractal geometry of internal thread surfaces manufactured by cutting tap and rolling tap. The application of fractal geometry in internal threads surface characterization to disclose fault fine structures of the internal thread geometry caused by the manufacturing process is briefly presented in this work. Zheng and Dai [11] studied a new finite element method for computing structural stochastic responses of linear problems. The method decouples the stochastic response into a sequence of deterministic responses with random variable coefficients and gives a new expansion of stochastic response. Pasha et al. [12] investigated the analytical solution of non-Newtonian second-grade fluid flow by VIM and ADM methods on a stretching sheet. This study aimed at investigating the variation of heat transfer and velocity changes of the fluid flow along the vertical line on a surface drawn from both sides. Coggon [13] have reviewed electromagnetic and electrical modeling by the finite element method. The finite element approach is based on energy minimization in the solution of physical problems; in this case, electromagnetic energy is minimized. Numerical and analytical comparison of the stability and instability of angular motion of a bar drawn by a spring by AGM method reviewed by Pasha et al. [14]. Krishna et al. [15] have researched Hall and ion slip effects on unsteady MHD free convective rotating flow through a saturated porous medium. The present study has an immediate application in understanding the drag experienced at the heated and inclined surfaces. Tripathy et al. [16] investigated the chemical reaction effect on MHD free convective surface over a moving vertical plate. In this research, the nonlinear partial differential equations were transformed into a two-point limit value problem with the help of similarity and  $t$  variables. Sarkar and Sahoo [17] studied the unsteady MHD flow on a stretchable rotating disk with heat transfer. Turner and Weidman [18] investigated Homann stagnation-point flow impinging on a biaxially stretching surface. The normal impact of the axial flow of the Homann stagnation point on a surface running perpendicularly, planar, biaxial is investigated. Application of numerical methods in micropolar fluid flow and heat transfer in permeable reviewed by Pasha et al. [19]. Thread stretching sheet with different fins at steady-state two-dimensional flow of a micropolar/classical ferro fluid was investigated [20–32]. This paper analysis heat transfer and angular velocity of micropolar ethylene-glycol nanofluid over the triangular, rectangular, and chamfer fins on the stretching sheet and investigated the magnetism effect around the different fins. The innovation of this paper is to investigate parameters of nanofluid flow passing from different positions of the fins ({rectangular, triangular and chamfer fins}- {rectangular and chamfer fins})-

triangular fins}-{ triangular and chamfer fins}) on the stretching surface. The structure of this paper is a study on the differential equations of ethylene glycol nanofluid by finite element strategy. By this strategy, the magnetic parameter, velocity, and temperature of the nanofluid were studied in separate contours. The problem of grid study is shown in Figure 1 as flowsheet.

## 2. PROBLEM DEFINITION

On a stretching sheet with ten numbers of different fins in the  $y > 0$  direction, a steady-state two-dimensional flow of a micropolar/classical ferrofluid was assumed as shown in Figure 2. In the geometry of this paper, we discussed the effect of using fins with different shapes on nanofluid heat transfer and nanofluid flow velocity. In the industry, heat transfer can be optimized and increased by using fans with different positions and at the same distance from each other. Triangular and rectangular and chamfer fins are used on the surfaces. Nanofluid flow is entered with  $25\text{ }^\circ\text{C}$  and angular velocity is entered from 1 direction and passes through the fins and surface. The surface temperature is  $30\text{ }^\circ\text{C}$  and the surface have been stretched by velocity in the X direction ( $UW(x) = ax, a > 0$ ). The velocity in the x-direction is  $2\text{ m/s}$  and the velocity in the y-direction is  $0.2\text{ m/s}$ . In this paper, the effect of the magnetic force ( $B$ ) on the surface is investigated. The finite element method is used for solving this case. The governing equation for ferrofluid was simulated as Follows. The physical properties of water and Ethylene-glycol nanofluid at  $25\text{ }^\circ\text{C}$  are summarized in Table 1.

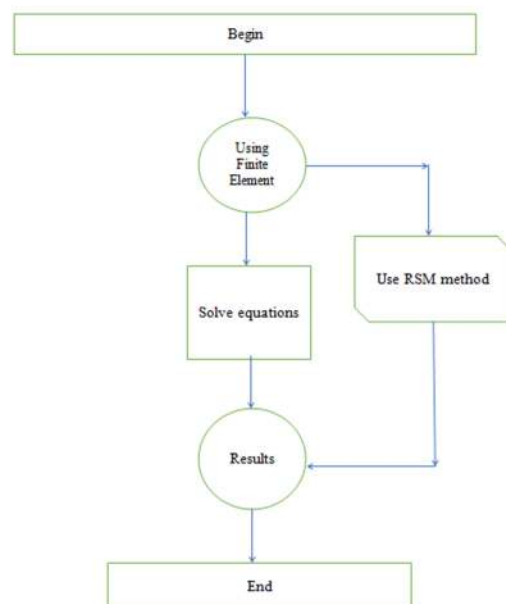


Figure 1. Grid study of the problem

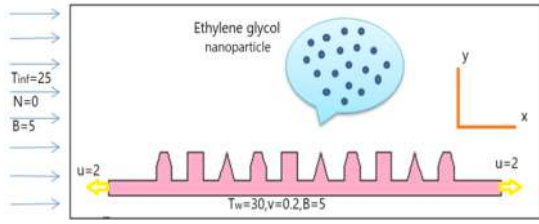


Figure 2. Schematic of different fins on the stretching sheet

TABLE 1. Properties of water and ethylene-glycol nanofluid at 25 °C [20]

	$\rho$ (kg/m <sup>3</sup> )	K (W/m.k)	C <sub>p</sub> (J/kg.k)	$\sigma$
Ethylene glycol	1111	0.252	2415	57000
H <sub>2</sub> O	997	0.613	4179	0.05

The finite element method is used to solve this case. In the below, the governing equation for ferrofluid is [27]:

$$\frac{d}{dt}(\rho_{nf}) = \nabla \cdot (\rho_{nf}v) \quad (1)$$

$$\rho_{nf} \left( \frac{dv}{dt} \right) = -\nabla p + (2\mu_{nf} + \kappa) \nabla (\nabla \cdot v) - (\mu_{nf} + \kappa) \nabla \cdot (\nabla \cdot v) + \kappa (\nabla \cdot N) + j \cdot B + \rho_{nf} g \quad (2)$$

$$\rho_{nf} j \left( \frac{dN}{dt} \right) = (\phi + \lambda + Y_{nf}) \nabla \cdot (\rho_{nf} \cdot N) - Y_{nf} \nabla \cdot (\nabla \cdot N) + \kappa (\nabla \cdot v) - 2\kappa N + \rho_{nf} I \quad (3)$$

where effective density, effective dynamic viscosity, and spin gradient viscosity are presented by Brinkman [21], Bourantas and Loukopoulos [22], respectively:

$$\rho_{nf} = (1 - \phi) \rho_f + \phi \rho_s \quad (4)$$

$$\mu_{nf} = \frac{\mu_f}{(1-\phi)^{2.5}} \quad (5)$$

$$Y_{nf} = (\mu_{nf} + \kappa/2) j \quad (6)$$

In addition, flow is incompressible in the absence of external forces. Therefore, equations will be difficult to solve.

$$\rho_{nf} \left( \frac{dv}{dt} + (v \cdot \nabla)v \right) = (\mu_{nf} + \kappa) \nabla^2 v + \kappa (\nabla \cdot N) + j \cdot B \quad (7)$$

$$\rho_{nf} j \left( \frac{dN}{dt} + (N \cdot \nabla)N \right) = Y_{nf} \cdot \nabla^2 N + \kappa (\nabla \cdot v) - 2\kappa N \quad (8)$$

and the body force proposed by hussanan et al. [23] is:

$$j \cdot B = -\sigma_{nf} B_0^2 v \quad (9)$$

The ferrofluid electric conductivity represents [24]:

$$\sigma_{nf} = \left[ 1 + \frac{3(\sigma-1)\phi}{(\sigma+2)-(\sigma-1)\phi} \right] \sigma_f \quad (10)$$

and the governing equations would be:

$$\rho_{nf} \left( u \frac{du}{dx} + v \frac{du}{dy} \right) = (\mu_{nf} + \kappa) \frac{d^2u}{dy^2} + \kappa \frac{dN}{dy} - \sigma_{nf} B_0^2 u \quad (11)$$

$$\rho_{nf} j \left( u \frac{dN}{dx} + v \frac{dN}{dy} \right) = Y_{nf} \frac{d^2N}{dy^2} - \kappa \left( 2N + \frac{du}{dy} \right) \quad (12)$$

The specific heat capacity and the effective thermal conductivities were defined by Mohyud-Din et al. [25].

$$C_{p,nf} = \frac{C_p s + (1-\phi)(\rho C_p)_f}{\rho_{nf}} \quad (13)$$

$$\frac{k_{nf}}{k_f} = \frac{k_s + 2k_f - 2\phi(k_f - k_s)}{k_s + 2k_f + \phi(k_f - k_s)} \quad (14)$$

The energy equation represented as follows:

$$u \frac{dT}{dx} + v \frac{dT}{dy} = \frac{k_{nf}}{C_p n_f} \frac{d^2T}{dy^2} - \frac{dq_r}{dy} \quad (15)$$

It is stated as according to Roseland's approximation as follows:

$$u \frac{dT}{dx} + v \frac{dT}{dy} = \frac{1}{C_p n_f} \left( k_{nf} + \frac{16\sigma^* T_\infty^3}{3k^*} \right) \frac{d^2T}{dy^2} \quad (16)$$

The boundary conditions are:

$$u = au_w(x), \quad v = v_w, \quad \text{at } y = 0, \quad u \leftrightarrow 0, \quad y \rightarrow \infty \quad (17)$$

$$N = -\delta \frac{du}{dy} \quad \text{at } y = 0, \quad N \leftrightarrow 0, \quad y \rightarrow \infty \quad (18)$$

$$T = T_w, \quad \text{at } y = 0, \quad T \leftrightarrow T_w, \quad y \rightarrow \infty \quad (19)$$

In order to familiarize ourselves with these calculations, We have defined the velocity components in the x and y directions u and v, respectively. The suction and injection are represented by the positive and negative values of the surface mass transfer velocity, v<sub>w</sub>. The angular velocity is denoted by N.  $\mu$  is dynamic viscosity, and  $\delta$  is a constant in the 0-1 range. When set to 0, the microelement is specified. If  $\delta=1/2$ , the concentration of microelements was shown to be weak. Furthermore, when the turbulent boundary layer flow is required,  $\delta=1$ . j represents microelement inertia per unit mass, where  $\delta$  is spin gradient viscosity. To solve comfortably these nonlinear differential equations, we utilized similarity variables such as:

$$\eta = y \sqrt{\frac{a}{v_f}}, \quad u = axF'(\eta), \quad v = -\sqrt{av_f}F(\eta), \quad N = ax \sqrt{\frac{a}{v_f}} G(\eta), \quad \theta(\eta) = \frac{T-T_\infty}{T_w-T_\infty} \quad (20)$$

By substituting the variables in relations (20) in to the Equations (11), (12), (16), we have:

$$\left( \frac{1}{(1-\phi)^{2.5}} + k \right) F''''(\eta) + \left( 1 - \phi + \phi \frac{\rho_s}{\rho_f} \right) F(\eta) F''(\eta) - \left( 1 - \phi + \phi \frac{\rho_s}{\rho_f} \right) F'^2(\eta) - M \left( 1 + \frac{3(\sigma-1)\phi}{\sigma+2-(\sigma-1)\phi} \right) F'(\eta) + kG'(\eta) = 0 \quad (21)$$

$$\left(\frac{1}{(1-\phi)^{2.5}} + \frac{k}{2}\right) G''(\eta) + \left(1 - \phi + \phi \frac{\rho_s}{\rho_f}\right) F(\eta) G'(\eta) - \left(1 - \phi + \phi \frac{\rho_s}{\rho_f}\right) F'(\eta) G(\eta) - k(2G(\eta) + F''(\eta)) = 0 \tag{22}$$

$$\frac{1}{Pr} \left(\frac{k_s + 2k_f - 2\phi(k_f - k_s)}{k_s + 2k_f + \phi(k_f - k_s)} + R\right) \theta''(\eta) + \left(1 - \phi + \frac{c_p s}{c_p f}\right) F(\eta) \theta'(\eta) = 0 \tag{23}$$

and here the new boundary conditions are:

$$F(\eta) = S, F'(\eta) = \alpha, G(\eta) = -\delta F''(\eta), \theta(\eta) = 1, \text{ at } \eta = 0 \tag{24}$$

$$F'(\eta) \leftrightarrow 0, G(\eta) \leftrightarrow 0, \theta(\eta) \rightarrow 0 \text{ at } \eta \rightarrow \infty \tag{25}$$

### 3. SIMULATION METHODOLOGY

**3.1. Finite Element Method (FEM)** Finite Element Method is an important numerical method that one of the practical applications for this method is Flexpde software, That is solved the nonlinear partial differential equations and ordinary differential equations. The output of the results FlexPDE is also a ‘problem-solving environment’ that executes the full range of functions required to resolve partial differential equation systems. The finite element method is a numerical method for solving partial differential equations defined based on one or two spatial variables. In this method, to solve the problem, a large system is divided into smaller and simpler parts called finite elements. This spatial discretization requires defining the object or environment of the problem as a network, or mesh.

According to Figure 3, the largest grid of mesh is around the edges, because around the baffles the fluid properties such as temperature and velocity of nanofluid flow changed.

**3.2. Validation for Methods** In this section, for validation, we compared our work with Jalili et al. [20]. The computational error in our work is very low compared to others. The maximum number of errors happened when  $\eta=1.5$  and minimum number of errors happened when  $\eta=1$ . Figure 4 shows comparison of data presentations for present study and Jalili et al. [20]. The Comparison of velocity for present work and Jalili’s work at  $K=10, \delta=0.5, \phi=0.03$  are summarized in Table 2.

### 4. RESULTS AND DISCUSSION

Figure 5 shows the nanofluid velocity is low around the space of the surface and fins. The maximum nanofluid velocity is attached to the surface of fins. The value of the maximum velocity is 2 m/s. By increasing the

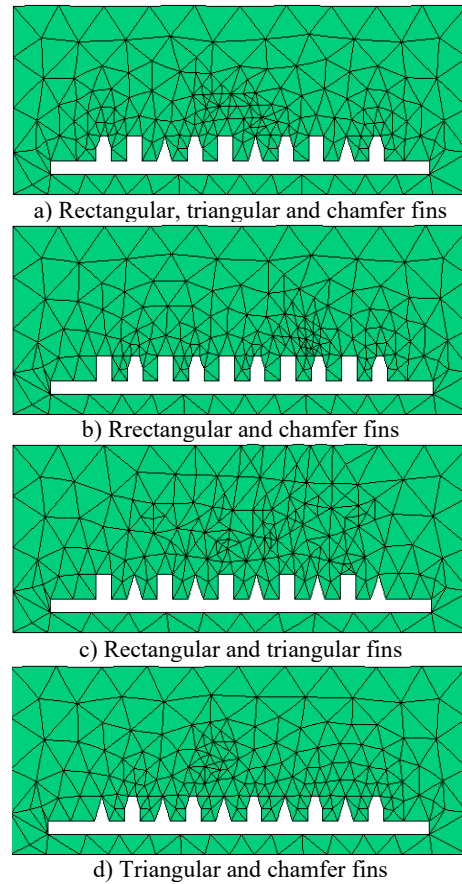


**Figure 3.** Comparison of mesh geometry for stretching surface

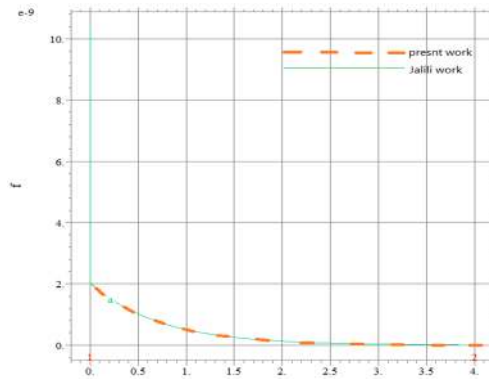


**Figure 4.** Comparison of velocity for present work and Jalili [20] at  $K=10, \delta=0.5, \phi=0.03$

**TABLE 2.** Comparison of velocity for present work and Jalili work at  $K=10, \delta=0.5, \phi=0.03$

	$\eta = 0.0$	$\eta = 1$	$\eta = 1.5$	$\eta = 2$	$\eta = 2.5$	$\eta = 4$
Present work	2	0.8	0.6	0.5	0.3	0
Jalili et al. [20]	2	0.8	0.6	0.5	0.3	0

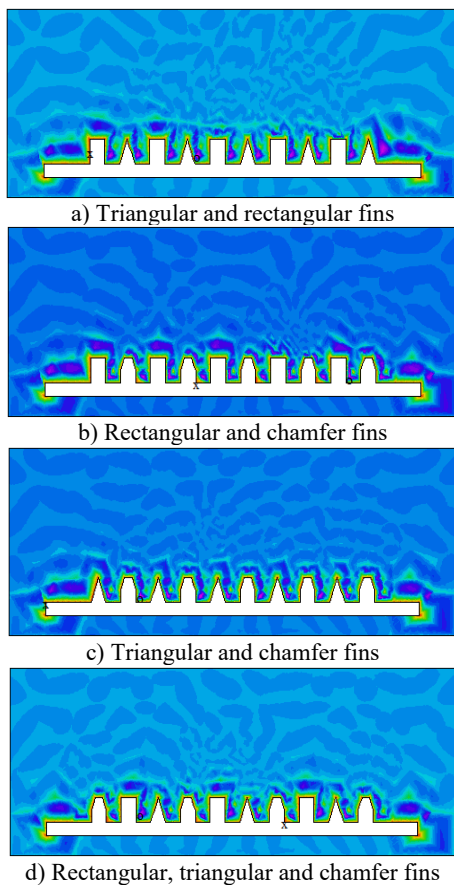


**Figure 5.** Comparison of velocity changes in the X direction in different fins for stretching surface

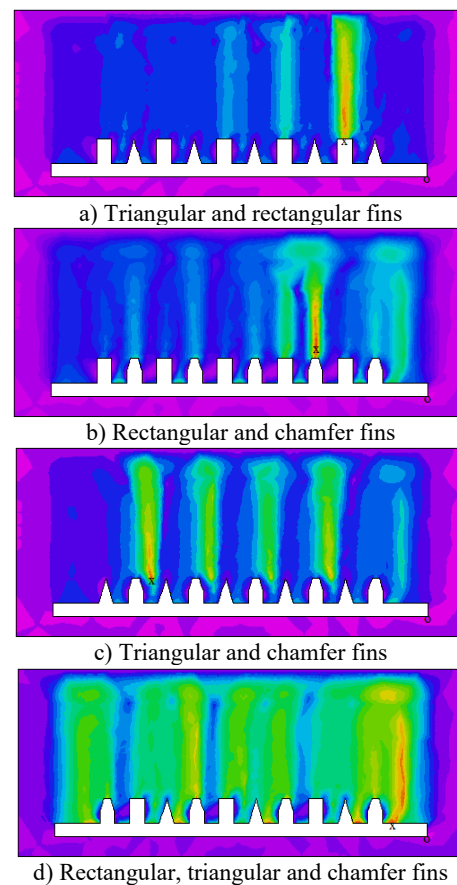


**Figure 6.** Comparison of angular velocity changes in different fins for stretching surface

distance of nanofluid from the surface, the velocity is reduced but by decreasing the distance from the surface, the velocity is increased. By comparing modes a-5 and b-5 we find that if we use a triangular blade instead of a chamber blade, we create a larger velocity gradient.

Figure 6 shows the angular velocity of nanofluid flow passing the stretching surface. On the surface, many fins exist, such as rectangular fins, triangular and chamfer fins. Under the surface, the angular velocity of nanofluid is very low but on the surface and near the fins, the angular velocity increases. In general, the angular velocities near the rectangular and chamfer fins (b-6) have an additional value than the triangular fins, because the surface of their side is larger than the triangular side. With an increase in variety of the fins (d-6) on the surface, the angular velocity of nanofluid has a maximum value.

Figure 7 shows the changes of nanofluid temperature passing the stretching surface. The nanofluid temperature in the space of fins is warm and equal to the surface temperature. The value of temperature is 30°C. The maximum values of nanofluid temperature exist in the last fin of surfaces. By passing the nanofluid flow from the first fins of the surface, the flow temperature

increased from 25 to 31°C and at the ends of the surface, the temperature is high. Due to the different positions of the fin at the top of the page, we find that if we use a chamfer blade at the top of the page, we create a larger temperature gradient than other modes.

The vectors of angular velocity for nanofluid flow are shown in Figure 8. The most dispersion of velocity (N) is shown in Figure 8d. As in the middle of the surface near the third and eighth fins, the value of angular velocity is low and at the beginning and the end, the value of velocity is high.

Figure 9 shows the changes of nanofluid flow near the rectangular and triangular and chamfer fins in the chart. The lowest value of velocity in the x-direction of nanofluid flow is in the  $x=0$  to  $x=0.1$  with  $u=0.3\text{m/s}$ . the maximum velocity in the x-direction is 2m/s. The variations in velocity all over the different fins are very high.

In the state of triangular and chamfer fins (b-10) on the surface, the maximum angular velocity exists at  $x=0.2$  near the first fins. The value of the velocity at  $x=0.2$  is 400. In the position of different fins shapes next to each other (triangular and rectangular and chamfer), most changes of angular velocity are created in the  $x=0$  to  $x=1$ .

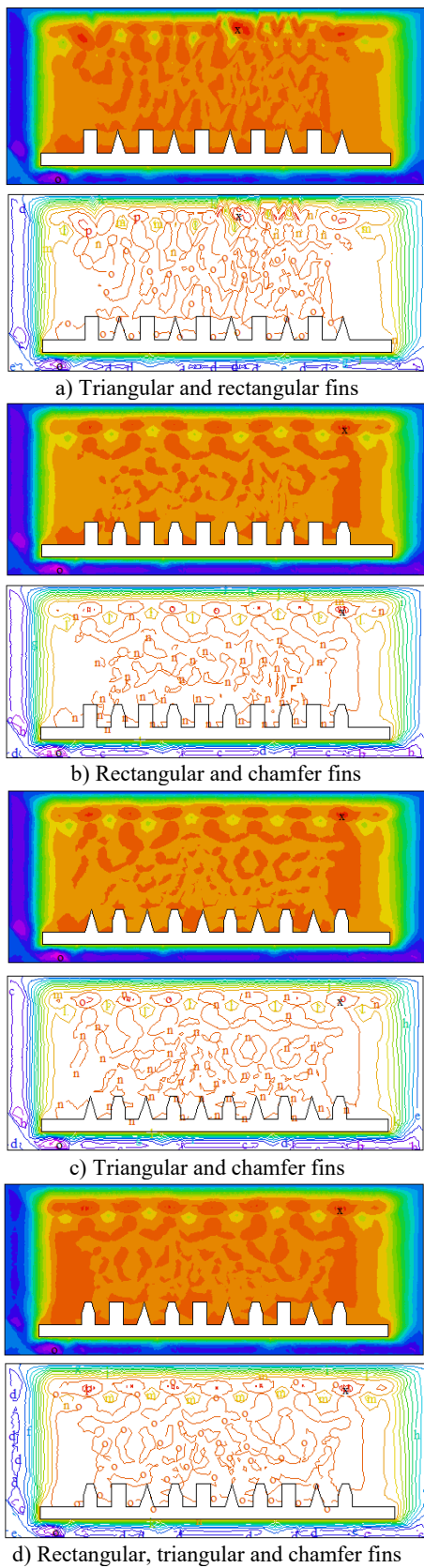
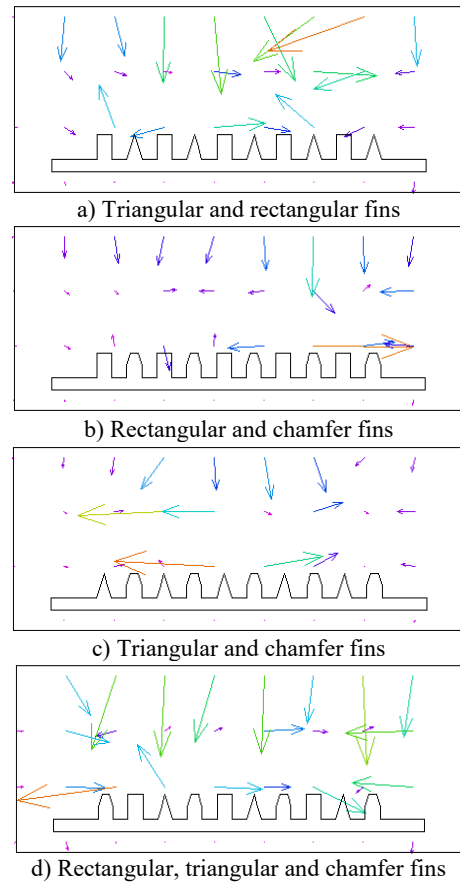


**Figure 7.** Comparison of temperature profiles for threaded stretching surface with different fins

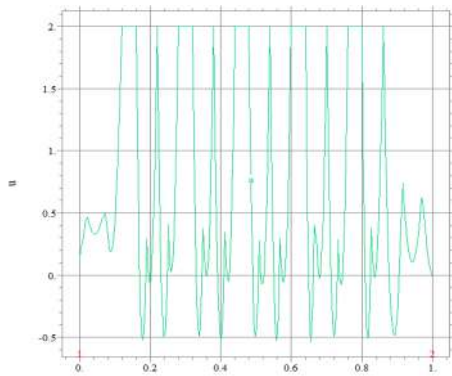
In the same case, the velocity has a variation in the modes. In the  $x=0$ , the value of angular velocity is 30 and in  $x=0.4$ , the value of velocity is  $N=150$ .

Figure 11 shows the changes of nanofluid temperature passing the stretching surfaces. The value of temperature begins from 28 to 31°C all over the different fins. The temperature of nanofluid in the  $x=0.2$  to  $x=0.8$  have a constant value ( $T=30^\circ\text{C}$ ) and no changes around the fins.

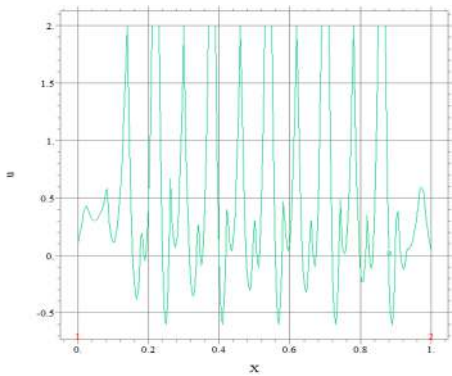
According to Table 3, the maximum ethylene glycol temperature occurs in the  $x=0.1$  for three different fins, and the minimum temperature occurs in the  $x=0$  for 3 different fins. The maximum nanofluid temperature is  $T=30.36^\circ\text{C}$  and minimum temperature is  $T=28.13^\circ\text{C}$ . The maximum temperature change exists around the 3 different (rectangular, triangular and chamfer) baffles, and the thermal boundary layer in this position is larger than in other cases. The nanofluid temperature on the 3 different fins is 4.5% bigger than chamfer and rectangular fins and 5.34% bigger than chamfer and triangular modes. Due to the different positions of the fin at the top of the page, we find that if we use a chamfer blade at the top of the page, we create a larger temperature gradient than other modes.



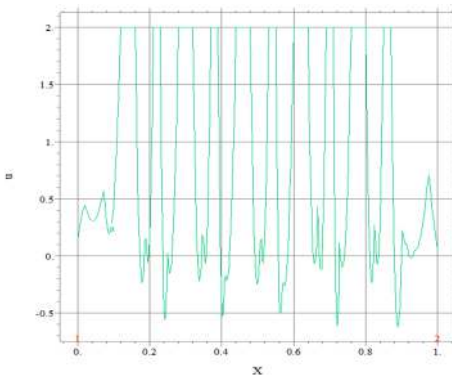
**Figure 8.** Comparison of vector grid temperature changes in different fins for stretching surface



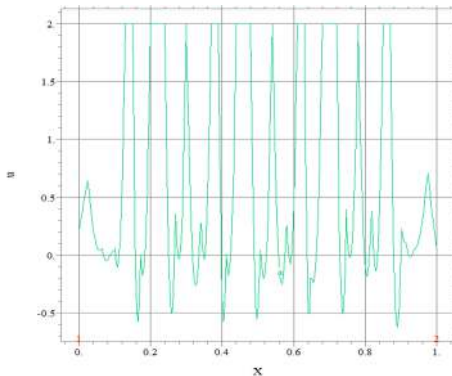
a) Triangular and rectangular fins



b) Triangular and chamfer fins

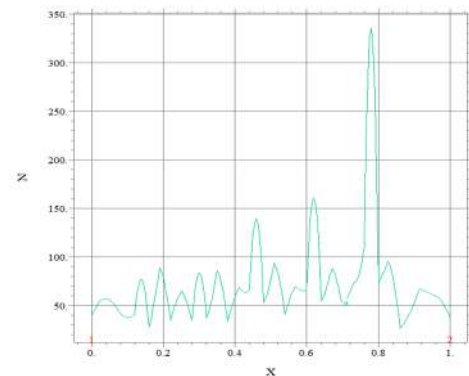


c) Rectangular and chamfer fins

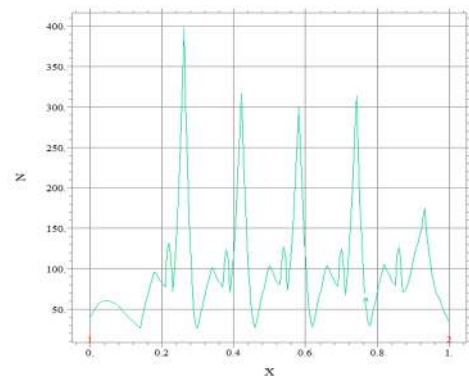


d) Rectangular, triangular and chamfer fins

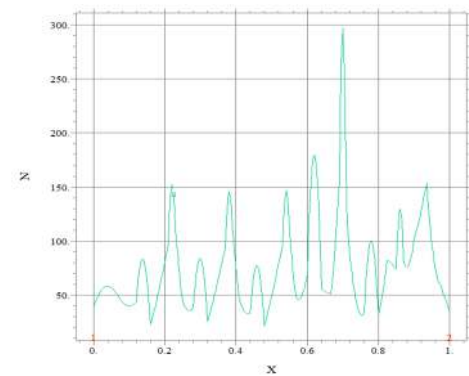
**Figure 9.** Comparison of velocity ( $u$ ) changes in in rectangular and triangular fins for threaded stretching surface



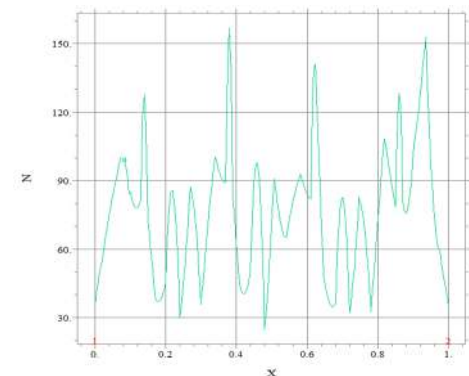
a) Triangular and rectangular fins



b) Triangular and chamfer fins

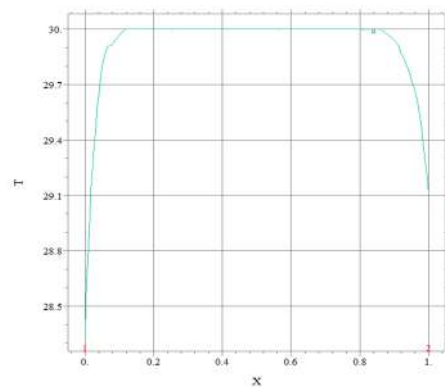


c) Rectangular and chamfer fins

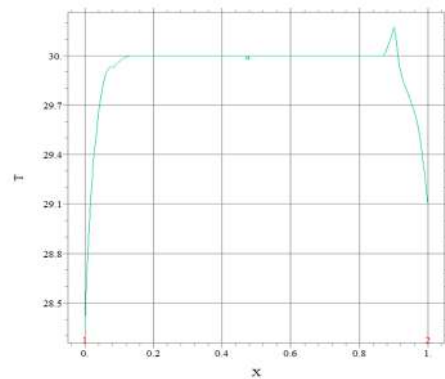


d) Rectangular, triangular and chamfer fins

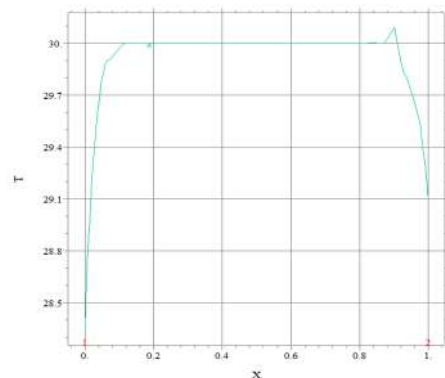
**Figure 10.** Comparison of angular velocity changes in in rectangular and triangular fins for threaded stretching surface



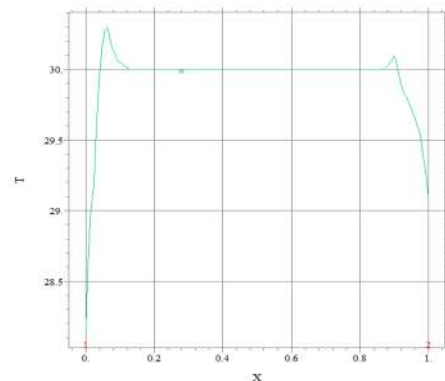
a) Triangular and rectangular fins



b) Triangular and chamfer fins



c) Rectangular and chamfer fins



d) Rectangular, triangular and chamfer fins

**Figure 11.** Comparison of temperature changes in in rectangular and triangular fins for threaded stretching surface

**TABLE 3.** Numerical comparison of temperature between different modes of fins

$\eta$	$T_3$ different fins	$T_{\text{chamfer and rectangular}}$	$T_{\text{chamfer and triangular}}$	$T_{\text{rectangular and triangular}}$
0	28.13	28.33	28.34	28.33
0.1	30.36	29.94	29.96	29.89
0.2	30.00	30.00	29.99	29.97
0.5	30.00	30.00	29.99	29.97
0.8	29.99	30.00	30.00	29.99
0.9	30.09	30.08	30.34	29.83
1	29.09	29.09	29.09	29.11

According to Table 4, the maximum of ethylene glycol velocity occurs in the  $x=0.3$  with  $T=399.98$  for chamfer and triangular modes and the minimum of temperature occurs in the  $x=0.8$  with  $T=33.34$  °C for 3 different fins. The angular velocity for nanofluid on the triangular and chamfer modes is 34.5% bigger than 3 different baffles and 58.54% bigger than chamfer and rectangular baffles. The most boundary condition for angular velocity shown around the initial baffles of the stretching sheet.

**TABLE 4.** Numerical comparison of angular velocity between different modes of fins

$\eta$	$N_3$ different fins	$N_{\text{chamfer and rectangular}}$	$N_{\text{chamfer and triangular}}$	$N_{\text{rectangular and triangular}}$
0	37.85	49.97	49.95	49.95
0.1	100.99	48.87	48.01	47.76
0.2	43.33	45.25	399.98	46.06
0.5	57.87	47.89	69.33	76.55
0.8	33.34	46.76	70.90	77.89
0.9	89.08	120.43	89.05	55.48
1	34.04	47.56	48.02	48.76

## 5. CONCLUSION

In this paper, variation of temperature and velocity in the  $x$ -direction and the angular velocity of the nanofluid flow through triangular and rectangular fins are investigated in the existence of a uniform magnetic field. The innovation of this paper is to investigate parameters of nanofluid flow passing from the different fins on the stretching surface. The finite element method is selected for solving governing equations.

- The effect of velocity changes in the  $x$ -direction around the baffles has more value than the surrounding space. The amount of flow velocity is reduced by increasing the distance from the surface in the  $y$ -

direction. General, the angular velocities near the rectangular fins and chamfer fins have an additional value than the triangular fins, because the surface of their side is larger than the triangular side. With the increasing, variation of the fins on the surface, the angular velocity of nanofluid has a maximum value.

- The temperature of nanofluid in the space of fins is warm and equal to the temperature of a surface. The value of temperature is 30°C. The maximum values of nanofluid temperature exist in the last fin of surfaces. By passing the nanofluid flow from the first fins of the surface, the temperature of flow comes from 25 to 31°C and at the ends of the surface, the temperature is high.
- The lowest value of velocity in the x -direction of nanofluid flow is in the  $x=0$  to  $x=0.1$  by  $u=0.3$ m/s. the maximum velocity in the x direction is 2m/s. changes in velocity all over the different fins are very high.
- In the state of triangular and chamfer fins together on the surface, the maximum angular velocity exists at  $x=0.2$  near the first fins. The value of velocity at  $x=0.2$  is 400. In the position of different fins shapes next to each other (triangular and rectangular and chamfer), most changes of angular velocity are created in the  $x=0$  to  $x=1$ . In the same case, the velocity has a variation the modes. In the  $x=0$ , the value of angular velocity is 30 and in  $x=0.4$ , the value of velocity is  $N=150$ . The angular velocity for nanofluid on the triangular and chamfer modes is 6.5% more than other baffles.
- The value of temperature begins from 28 to 31°C in all over the different fins. The temperature of nanofluid in the  $x=0.2$  to  $x=0.8$  have a constant value ( $T=30^\circ\text{C}$ ) and no changes around the fins.

## 6. REFERENCES

1. Atashafrooz, M., Sajjadi, H., Amiri Delouei, A., Yang, T.-F., and Yan, W.-M. "Three-dimensional analysis of entropy generation for forced convection over an inclined step with presence of solid nanoparticles and magnetic force." *Numerical Heat Transfer, Part A: Applications*, Vol. 80, No. 6, (2021), 318–335. <https://doi.org/10.1080/10407782.2021.1944579>
2. Atashafrooz, M. "Influence of radiative heat transfer on the thermal characteristics of nanofluid flow over an inclined step in the presence of an axial magnetic field." *Journal of Thermal Analysis and Calorimetry*, Vol. 139, No. 5, (2020), 3345–3360. <https://doi.org/10.1007/s10973-019-08672-0>
3. Atashafrooz, M., Sajjadi, H., and Delouei, A. A. "Interacting influences of Lorentz force and bleeding on the hydrothermal behaviors of nanofluid flow in a trapezoidal recess with the second law of thermodynamics analysis." *International Communications in Heat and Mass Transfer*, Vol. 110, (2020), 104411. <https://doi.org/10.1016/j.icheatmasstransfer.2019.104411>
4. Atashafrooz, M. "The effects of buoyancy force on mixed convection heat transfer of MHD nanofluid flow and entropy generation in an inclined duct with separation considering Brownian motion effects." *Journal of Thermal Analysis and Calorimetry*, Vol. 138, No. 5, (2019), 3109–3126. <https://doi.org/10.1007/s10973-019-08363-w>
5. Atashafrooz, M., Sheikholeslami, M., Sajjadi, H., and Amiri Delouei, A. "Interaction effects of an inclined magnetic field and nanofluid on forced convection heat transfer and flow irreversibility in a duct with an abrupt contraction." *Journal of Magnetism and Magnetic Materials*, Vol. 478, (2019), 216–226. <https://doi.org/10.1016/j.jmmm.2019.01.111>
6. Sheikholeslami, M., Sajjadi, H., Amiri Delouei, A., Atashafrooz, M., and Li, Z. "Magnetic force and radiation influences on nanofluid transportation through a permeable media considering Al<sub>2</sub>O<sub>3</sub> nanoparticles." *Journal of Thermal Analysis and Calorimetry*, Vol. 136, No. 6, (2019), 2477–2485. <https://doi.org/10.1007/s10973-018-7901-8>
7. Atashafrooz, M. "Effects of Ag-water nanofluid on hydrodynamics and thermal behaviors of three-dimensional separated step flow." *Alexandria Engineering Journal*, Vol. 57, No. 4, (2018), 4277–4285. <https://doi.org/10.1016/j.aej.2017.07.016>
8. Yamini, O. A., Kavianpour, M. R., and Movahedi, A. "Performance of Hydrodynamics Flow on Flip Buckets Spillway for Flood Control in Large Dam Reservoirs." *Journal of Human, Earth, and Future*, Vol. 1, No. 1, (2020), 39–47. <https://doi.org/10.28991/HEF-2020-01-01-05>
9. Aminoroayaie Yamini, O., Mousavi, S. H., Kavianpour, M. R., and Safari Ghaleh, R. "Hydrodynamic Performance and Cavitation Analysis in Bottom Outlets of Dam Using CFD Modelling." *Advances in Civil Engineering*, Vol. 2021, , (2021), 1–14. <https://doi.org/10.1155/2021/5529792>
10. T̄alu, Ş., Kulesza, S., Bramowicz, M., Saĝlam, H., and Kus, R. "Fractal geometry of internal thread surfaces manufactured by cutting tap and rolling tap." *Manufacturing Letters*, Vol. 23, (2020), 34–38. <https://doi.org/10.1016/j.mfglet.2019.12.001>
11. Zheng, Z., and Dai, H. "Structural stochastic responses determination via a sample-based stochastic finite element method." *Computer Methods in Applied Mechanics and Engineering*, Vol. 381, (2021), 113824. <https://doi.org/10.1016/j.cma.2021.113824>
12. Pasha, P., Nabi, H., Asadi, Z., and Domairry Ganji, D. "Analytical solution of non-Newtonian second-grade fluid flow by VIM and ADM methods on a stretching sheet." In 1st Conference on Electrical, Mechanical and Engineering Sciences, (2021), 1–17. Retrieved from <https://civilica.com/doc/1170934>
13. Coggon, J. H. "Electromagnetic and electrical modeling by the finite element method." *Geophysics*, Vol. 36, No. 1, (1971), 132–155. <https://doi.org/10.1190/1.1440151>
14. Pasha, P., Nabi, H., and Domairry Ganji, D. "Numerical and analytical comparison of the stability and instability of angular motion of a bar drawn by a spring by AGM method." In 5th National Conference on Application of Novel Technologies in Engineering Sciences, Torbat Heydarieh (2021), 1–9. Retrieved from <https://civilica.com/doc/1202840>
15. Veera Krishna, M., Ameer Ahamad, N., and Chamkha, A. J. "Hall and ion slip effects on unsteady MHD free convective rotating flow through a saturated porous medium over an exponential accelerated plate." *Alexandria Engineering Journal*, Vol. 59, No. 2, (2020), 565–577. <https://doi.org/10.1016/j.aej.2020.01.043>
16. Tripathy, R. S., Dash, G. C., Mishra, S. R., and Baag, S. "Chemical reaction effect on MHD free convective surface over a moving vertical plate through porous medium." *Alexandria Engineering Journal*, Vol. 54, No. 3, (2015), 673–679. <https://doi.org/10.1016/j.aej.2015.04.012>
17. Sarkar, G. M., and Sahoo, B. "On dual solutions of the unsteady MHD flow on a stretchable rotating disk with heat transfer and a linear temporal stability analysis." *European Journal of Mechanics - B/Fluids*, Vol. 85, (2021), 149–157. <https://doi.org/10.1016/j.euromechflu.2020.09.010>
18. Turner, M. R., and Weidman, P. "Homann stagnation-point flow

- impinging on a biaxially stretching surface." *European Journal of Mechanics - B/Fluids*, Vol. 86, (2021), 49–56. <https://doi.org/10.1016/j.euromechflu.2020.11.010>
19. Pasha, P., Mirzaei, S., and Zarinfar, M. "Application of numerical methods in micropolar fluid flow and heat transfer in permeable plates." *Alexandria Engineering Journal*, Vol. 61, No. 4, (2022), 2663–2672. <https://doi.org/10.1016/j.aej.2021.08.040>
  20. Jalili, B., Sadighi, S., Jalili, P., and Ganji, D. D. "Characteristics of ferrofluid flow over a stretching sheet with suction and injection." *Case Studies in Thermal Engineering*, Vol. 14, (2019), 100470. <https://doi.org/10.1016/j.csite.2019.100470>
  21. Brinkman, H. C. "The Viscosity of Concentrated Suspensions and Solutions." *The Journal of Chemical Physics*, Vol. 20, No. 4, (1952), 571–571. <https://doi.org/10.1063/1.1700493>
  22. Bourantas, G. C., and Loukopoulos, V. C. "MHD natural-convection flow in an inclined square enclosure filled with a micropolar-nanofluid." *International Journal of Heat and Mass Transfer*, Vol. 79, (2014), 930–944. <https://doi.org/10.1016/j.ijheatmasstransfer.2014.08.075>
  23. Hussanan, A., Ismail, Z., Khan, I., Hussein, A. G., and Shafie, S. "Unsteady boundary layer MHD free convection flow in a porous medium with constant mass diffusion and Newtonian heating." *The European Physical Journal Plus*, Vol. 129, No. 3, (2014), 46. <https://doi.org/10.1140/epjp/i2014-14046-x>
  24. Khan, U., Ahmed, N., and Mohyud-Din, S. T. "Numerical investigation for three dimensional squeezing flow of nanofluid in a rotating channel with lower stretching wall suspended by carbon nanotubes." *Applied Thermal Engineering*, Vol. 113, (2017), 1107–1117. <https://doi.org/10.1016/j.applthermaleng.2016.11.104>
  25. Mohyud-Din, S., Khan, U., Ahmed, N., and Hassan, S. "Magnetohydrodynamic Flow and Heat Transfer of Nanofluids in Stretchable Convergent/Divergent Channels." *Applied Sciences*, Vol. 5, No. 4, (2015), 1639–1664. <https://doi.org/10.3390/app5041639>
  26. Zang, Q., Liu, J., Lu, L., and Lin, G. "A NURBS-based isogeometric boundary element method for analysis of liquid sloshing in axisymmetric tanks with various porous baffles." *European Journal of Mechanics - B/Fluids*, Vol. 81, (2020), 129–150. <https://doi.org/10.1016/j.euromechflu.2020.01.010>
  27. Hashemi, M. S. "A novel simple algorithm for solving the magneto-hemodynamic flow in a semi-porous channel." *European Journal of Mechanics - B/Fluids*, Vol. 65, (2017), 359–367. <https://doi.org/10.1016/j.euromechflu.2017.05.008>
  28. Srinivasacharya, D., and Jagadeeshwar, P. "Flow Over an Exponentially Stretching Porous Sheet with Cross-diffusion Effects and Convective Thermal Conditions." *International Journal of Engineering, Transaction A: Basics*, Vol. 31, No. 1, (2018), 120–127. <https://doi.org/10.5829/ije.2018.31.01a.17>
  29. Sureshkumar, D., and Ethiraj, N. "Experimental and Finite Element Analysis of Single Stage Single Point Incremental Forming." *International Journal of Engineering, Transaction A: Basics*, Vol. 34, No. 10, (2021), 2259–2265. <https://doi.org/10.5829/ije.2021.34.10a.07>
  30. Bhaskara Rao, J., and Beatrice Seventline, J. "Estimation of Roughness Parameters of A Surface Using Different Image Enhancement Techniques." *International Journal of Engineering, Transaction B: Applications*, Vol. 30, No. 5, (2017), 652–658. <https://doi.org/10.5829/idosi.ije.2017.30.05b.04>
  31. Fereidoon, A., and Mohammadian, M. "Young's Modulus of Single and Double Walled Carbon Nanocones Using Finite Element Method." *International Journal of Engineering, Transaction C: Aspects*, Vol. 27, No. 9, (2014), 1467–1474. <https://doi.org/10.5829/idosi.ije.2014.27.09c.17>
  32. Sheel, T. K., and Obi, S. "Acceleration of bluff body calculation using MDGRAPE-2." *International Journal of Engineering, Transactions A - Basics*, Vol. 23, No. 2, (2010), 169–176. Retrieved from <https://www.sid.ir/en/Journal/ViewPaper.aspx?ID=213089>

---

### Persian Abstract

#### چکیده

این مقاله انتقال حرارت و سرعت زاویه‌ای نانوسیال اتیلن گلیکول میکروقطبی را بر روی باله‌های مثلثی، مستطیلی و پخ روی ورق کششی تحلیل می‌کند. نوآوری این مقاله بررسی پارامترهای جریان نانوسیال عبوری از باله‌های مختلف روی سطح کششی است. روش اجزای محدود برای حل معادلات حاکم انتخاب شده است. دمای نانوسیال در فضای باله‌ها گرم و برابر با دمای سطح است. مقدار دما ۳۰ درجه سانتی‌گراد است. حداکثر مقادیر دمای نانوسیال در آخرین باله سطوح وجود دارد. با عبور جریان نانوسیال از اولین باله‌های سطح، دمای جریان از ۲۵ درجه سانتی‌گراد به ۳۱ درجه سانتی‌گراد می‌رسد و در انتهای سطح، دما از ارزش بالایی برخوردار است. حداکثر سرعت زاویه‌ای اتیلن گلیکول در  $x=0.9$  برای حالت پخ و مستطیل و حداقل دما در  $x=0.8$  برای ۳ باله مختلف رخ می‌دهد. سرعت زاویه‌ای برای نانوسیال در حالت‌های مثلثی و پخ ۷۵ درصد بزرگتر از بافل‌های دیگر است.

---



## Influence of Mixing Conditions of Modified Bitumen on Moisture Sensitivity of Asphalt Compounds

H. Bahmani<sup>a</sup>, H. Khani Sanij<sup>a</sup>, R. Roshani<sup>a</sup>, M. M. Majidi Shad<sup>a</sup>, S. H. Hosseini<sup>\*b</sup>, M. Edalati<sup>c</sup>, M. Olazar<sup>d</sup>, S. A. Almasi<sup>e</sup>

<sup>a</sup> Department of Civil Engineering, Yazd University, Yazd, Iran

<sup>b</sup> Department of Chemical Engineering, Ilam University, Ilam, Iran

<sup>c</sup> Department of Civil Engineering, Ilam University, Ilam, Iran

<sup>d</sup> Department of Chemical Engineering, University of the Basque Country UPV/EHU, Bilbao, Spain

<sup>e</sup> Department of Transportation Planning, Imam Khomeini International University, Qazvin, Iran

### PAPER INFO

#### Paper history:

Received 09 December 2021

Received in revised form 21 January 2022

Accepted 27 January 2022

#### Keywords:

Bitumen

Epoxy Resin

Mixing Time

Moisture Sensitivity

Surface Free Energy

### ABSTRACT

Modification of bitumen allows an improving the properties of bitumen, which can be a useful technique to enhance asphalt's characteristics. Therefore, this research intended to study the effect of mixing time of different percentages of epoxy resin, between 0 to 8%, doped into bitumens on the moisture sensitivity of asphalt compounds containing two types of aggregates, i.e. limestone and siliceous. For this aim, the Sessile Drop Method (SDM) was employed, and moisture resistant parameters associated to surface free energy concept such as surface free energy components, work of cohesion, work of adhesion, work of debonding, adhesion bitumen to aggregate, and wetting bitumen around aggregate surface were assessed. The results revealed that the effect of the mixing time of bitumen and epoxy resin on moisture resistance properties of asphalt compounds significantly depends on the percentage of epoxy resin used in bitumen mixture. For bitumens with 4 and 6% epoxy resin, adhesion and wetting parameters had a similar performance for both mixing times of 10 and 60 minutes. However, asphalt compounds containing 2 and 8% epoxy resin modified bitumens prepared for 10 min mixing time had a better adhesion and wetting performance than those prepared for the longer mixing time, 60 minutes. The effect of mixing time of bitumen modified with epoxy resin on the bitumen and asphalt compound' performance depend on the percent of additive in the bitumen.

doi: 10.5829/ije.2022.35.05b.02

## 1. INTRODUCTION

The Moisture sensitivity of asphalt compounds is one of the most common damages that occurs in asphalt pavements [1–8]. The reduction in the pavement integrity due to moisture damage plays an important role in other types of distresses, such as rutting, fatigue cracking, and raveling [9].

There are three mechanisms in which moisture is capable of degrading the asphalt compound: (1) loss of cohesion within the bitumen, (2) adhesive failure between aggregate and bitumen, and (3) degradation of the aggregates. The cohesive failure occurs due to the rupture of bonds between molecules in the bitumen, and

the work of cohesion describes the resistance of bitumen against cohesive failure. On the other hand, adhesive failure happens when the bonds between bitumen and aggregate are ruptured, and work of adhesion explains the resistance of asphalt compounds against this type of failure. Moreover, the work of debonding is the measure of the work of adhesion between bitumen and aggregate in the presence of water [10].

The moisture damage is usually studied using experimental laboratory testing methods. A number of laboratory tests have been developed over the years to determine the moisture susceptibility of bituminous compounds. They include the modified Lottman test, Tunnickliff and Root method, Hamburg wheel tracking,

\*Corresponding Author Institutional Email: [s.h.hosseini@ilam.ac.ir](mailto:s.h.hosseini@ilam.ac.ir)  
(S. H. Hosseini).

asphalt pavement analyzer, saturation ageing tensile stiffness (SATS), Marshall immersion test, resilient modulus test, and immersion-compression test [11–14]. Nevertheless, these approaches are not able to examine fundamental features of materials to predict adhesion and wetting ability of each bitumen-aggregate composition [15]. An important material property concerning the moisture sensitivity of asphalt compounds is the surface free energy of the asphalt binder and the aggregate. The surface free energy of these materials can be used to determine work of cohesion, work of adhesion, and work of debonding [15]. In the surface free energy method, surface free energy properties of the materials are used to assess both the adhesion and wetting characteristics of bitumen and aggregate composition, and thereby the moisture sensitivity of asphalt compounds [15]. It was already shown that the surface free energy method is suitable for the selection of materials resistant to moisture [16–19]. There are different methods of measuring surface energy of asphalt compounds. In some researches, the surface free energy of bitumen and components of aggregates have been measured using the Wilhelmy plate method and the universal sorption device (USD), respectively [20–22]. On the same subject, the sessile drop method (SDM) has been used to measure the surface free energy of bitumen [23]. Using the SDM by a number of researchers, the effect of additives on the adhesion mechanism of bitumen and aggregates was investigated [24–26]. These studies showed that the SDM is a suitable technique for assessing the effect of moisture on the bitumen-aggregate system.

The bitumen modification with additives is one of the common methods to reduce moisture damage of asphalt compounds [27, 28]. Also, the epoxy resin is a type of polymer, which has many applications in engineering industries. The effect of this additive on improving the performance of bitumen and asphalt compounds has been previously studied [29]. Bitumen modification process is usually accomplished at a high temperature and a specified mixing time. The available studies in the open literature proved that changing the conditions such as mixing time, mixing temperature, and mixing speed during the preparation of the modified bitumen, affected on the performance of the bitumen [30–32]. Pérez-Lepe [33] showed the influence of the conditions during the bitumens modification process with polymer additives on their rheological properties. In another study, the influence of the processing of bitumen modified with tire crumb rubber and polymeric additives was studied [31]. The results showed that a mixing time above 45 minutes exponentially increased the viscosity of the bitumen. Although the influence of the conditions for the preparation of the modified bitumens on their performance has been proven, their effect on the performance of asphalt

compounds in terms of moisture sensitivity, has been rarely studied.

This study focuses on the effect of amount of epoxy resin percentage and its mixing time during the bitumen modification process on the moisture sensitivity of asphalt compounds including two kinds of aggregates. Accordingly, two times, i.e. 10 and 60 minutes as a short and a long mixing times, respectively, are chosen to prepare bitumen modified with epoxy resin. In addition, the SDM is used to evaluate the moisture sensitivity of each asphalt compound by the measuring of moisture sensitivity parameters associated to the surface free energy of bitumen and aggregate.

## 2. SURFACE FREE ENERGY CONCEPT

The surface free energy is defined as the amount of energy required to create a unit surface area of a material under vacuum [34]. The surface free energy of a material ( $\gamma^{total}$ ) consists of two components: a non-polar or Lifshitz-van der Waals component ( $\gamma^{LW}$ ) and a polar component or acid-base component ( $\gamma^{AB}$ ). Consequently, the surface free energy is given by Equation (1) as follows:

$$\gamma^{total} = \gamma^{LW} + \gamma^{AB} \quad (1)$$

The acid-base component ( $\gamma^{AB}$ ) can be calculated according to Equation (2):

$$\gamma^{AB} = 2\sqrt{\gamma^+\gamma^-} \quad (2)$$

where ( $\gamma^+$ ) is the Lewis acid parameter of the surface free energy and ( $\gamma^-$ ) is the Lewis base parameter of the surface free energy [35].

**2. 1. Work of Cohesion** The work of cohesion for a material is the required work for splitting a column of the material with a unit cross sectional area into two separate columns. From the definition of surface free energy, it is easy to derive the work of cohesion,  $W_{BB}$ , of the bitumen (material 'B') as follows:

$$W_{BB} = \gamma_B^{total} \quad (3)$$

the higher value of this parameter indicates the more resistant of the bitumen against cohesive failure [15].

## 2. 2. Work of Adhesion and Work of Debonding

The adhesive bond strength under dry conditions refers to the work done by adhesion phase between bitumen and aggregate. The adhesive bond strength in the presence of water is termed the work of debonding. The work of adhesion and the work of debonding can be calculated using Equations (4) and (5), respectively, i.e., from the surface free energy components of the bitumen, aggregate and water. A higher value of the

work of adhesion and work of debonding indicates the more resistance to moisture damage [34].

$$W_{AB} = 2\sqrt{\gamma_A^{LW}\gamma_B^{LW}} + 2\sqrt{\gamma_A^+\gamma_B^-} + 2\sqrt{\gamma_A^-\gamma_B^+} \quad (4)$$

$$W_{AWB}^{wet} = 2\gamma_W^{LW} + 2\sqrt{\gamma_A^{LW}\gamma_B^{LW}} - 2\sqrt{\gamma_A^{LW}\gamma_W^{LW}} - 2\sqrt{\gamma_B^{LW}\gamma_W^{LW}} + 4\sqrt{\gamma_W^+\gamma_W^-} - 2\sqrt{\gamma_W^+(\gamma_A^- + \gamma_B^-)} - 2\sqrt{\gamma_W^-(\gamma_A^+ + \gamma_B^+)} + 2\sqrt{\gamma_A^+\gamma_B^-} + 2\sqrt{\gamma_A^-\gamma_B^+} \quad (5)$$

where  $\gamma^{LW}$ ,  $\gamma^+$  and  $\gamma^-$  are the surface energy components. In addition, A, B, and W denote aggregate, bitumen, and water, respectively.

### 2. 3. Energy Parameter Related to Moisture Sensitivity of Asphalt Compound

The two main factors of asphalt compound stripping are the reduction of bitumen adhesion to aggregates (EP1) and the reduction of bitumen wetting on the aggregate surface (EP2), which they are given by Equations (6) and (7).

$$EP1 = \frac{W_{AB}}{W_{AWB}^{wet}} \quad (6)$$

$$EP2 = \frac{W_{AB} - W_{BB}}{W_{AWB}^{wet}} \quad (7)$$

The greater the energy EP1 parameter, the higher the asphalt compound resistance against moisture [15]. Even though EP1 is an important parameter in determining the stripping of asphalt compound, it does not determine the degree of wettability of aggregates surface by a bitumen, which is represented by EP2 parameter. A higher the EP2 parameter indicates more wettability the bitumen on the aggregate surface, so that the stripping of bitumen-aggregate is less probable [15].

## 3. MATERIALS AND METHOD

In this study, nine types of bitumens were used, namely, eight modified ones at two mixing times and base bitumen, along with two types of aggregate, i.e., siliceous matter and limestone. Different amounts of epoxy resin (2, 4, 6 and 8%) were used to prepare the modified bitumen that is within the range used by Çubuk et al. [36]. As reported in the open literature, epoxy resin, as a bitumen modifier, has also been applied at high percentages, up to 50% [37]. In this study, a lower amount of epoxy resin (2–8%) was utilized to modify bitumen, from the economic point of view [38]. The prolonged mixing time can age bitumen and reduce the performance of bitumen and asphalt compounds containing it, during the modification process. Nevertheless, when bitumen is mixed with additives for a short mixing time, bitumen and additives fail to mix

properly, leading to a weak in bitumen and asphalt pavement structure. Therefore, it is imperative to determine the influence of mixing time and its optimal value for bitumen modification with additives. A minimum mixing time of 10 minutes was chosen to ensure the additive adequately mixes with bitumen, and a maximum 60 minutes was selected to avoid aging bitumen at a constant temperature and speed of mixing condition.

In overall, 18 types of asphalt compounds were evaluated. By measuring the surface free energy of each type of the bitumen and aggregate, the energy parameters associated to the moisture sensitivity of each asphalt compounds were calculated, thereby the moisture resistance of each bitumen and aggregate composition was evaluated. Figure 1 shows the methodology used in this study to obtain the effect of mixing time on adhesion and wetting performances.

### 3. 1. Materials

The commonly used bitumen in Iran which has been provided by Isfahan refinery with 60–70 penetration grade, was used. The main characteristics of the used bitumen are set out in Table 1. Two types of aggregates, i.e. limestone and siliceous, which have a considerable range of characteristics in aspect of mineralogy and degree of moisture resistant variety were also used, here. The chemical compositions of the aggregates that were obtained by performing XRF test are listed in Table 2. The epoxy resin applied in all experiments as the modifying agent was a type of Bisphenol-A Diglycidyl Ether, whose characteristics and chemical open formula are listed in Table 3 and Figure 2, respectively.

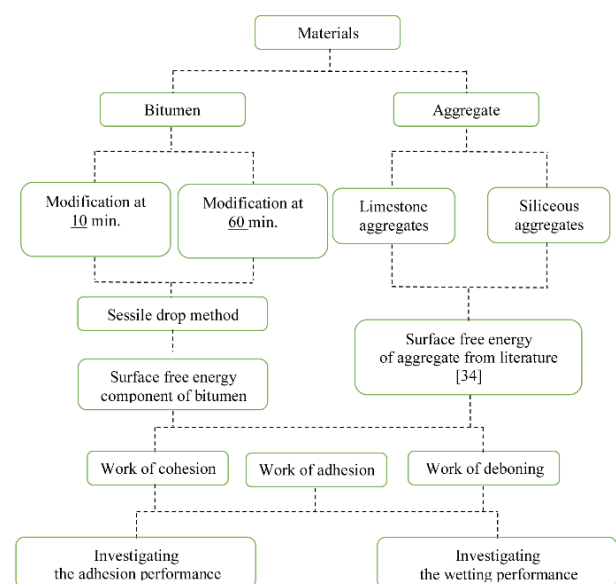


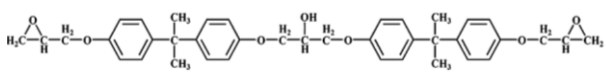
Figure 1. Research plan

**TABLE 1.** Properties of the bitumen used

Characteristic	Standard	Value
Specific gravity at 25 °C, (g/cm <sup>3</sup> )	ASTM D70	1.02
Penetration (100 g, 5 s, 25 °C), 0.1 mm	ASTM D5	65
Softening point (°C)	ASTM D36	50
Flash point (°C)	ASTM D92	324
Kinematic viscosity at 135 °C, (c.st)	ASTM D2170	344
Ductility (25 °C, 5 cm/min), cm	ASTM D113	155

**TABLE 2.** Chemical compositions of aggregates used

Component	Limestone (%)	Siliceous (%)
K <sub>2</sub> O	0.1	0.5
Fe <sub>2</sub> O <sub>3</sub>	0.3	0.4
MgO	1.6	1.0
Al <sub>2</sub> O <sub>3</sub>	1.2	9.0
SiO <sub>2</sub>	1.3	55.0
CaO	52.1	10.0
L.O.I.	43.4	24.1

**Figure 2.** Chemical formula of BPA type epoxy resin**TABLE 3.** Chemical compositions of epoxy resin used

Characteristic	Value
Equivalent weight of epoxy (g/eq)	184-190
Viscosity (cps at 25°C)	11500-13500
Hy-Cl (wt%)	0.05 max
Specific gravity (g/cm <sup>3</sup> at 20°C)	1.17
Color (g)	0.5 max

**3. 2. Bitumen Modification Process** Bitumen modified were prepared by adding epoxy resin percentages being as follows 0, 2, 4, 6, and 8%(w/w) under a specific process. Firstly, pure bitumen preheated at 130 °C was mixed with the specified amount of the mentioned epoxy resin percentages (0, 2, 4, 6, and 8% (w/w) for two mixing times of 10 and 60 minutes at a speed of 600 rpm and temperature of 130 °C. After completing the mixing process, the bitumen samples were kept at 110°C and then 25°C for one hour and one day, respectively. According to this methodology, 8 types of modified bitumens were prepared, at which 4 types refer to mixing time of 10 minutes and 4 remaining ones refer to long mixing time of 60 minutes.

### 3. 3. Sessile Drop Method (SDM) and Measuring Surface Free Energy of Bitumen

SDM is a common method for measuring the surface free energy of solids and liquids [15]. In this study, it was used for measuring surface free energy components of bitumens. According to this method, the surface free energy is calculated using the contact angles of three probe liquids on the bitumen substrate. The probe liquids used in this study were distilled water, ethylene glycol, and formamide. These liquids always have the same magnitude of surface free energy component values, which can also be used to calculate the surface free energy components for other materials, such as bitumen, as reported by Little and Bhasin [15]. The surface free energy components of the mentioned probe liquids for the bitumen are presented in Table 4. In the process of SDM, the prepared bitumens were heated to 135 °C in a 50 ml container. The bitumen heated was poured onto the glass slide surface with dimensions of 75 \* 25 mm. The glass samples covered with bitumen were stored in a desiccator and cooled to room temperature. For each of the bitumens studied, at least 3 samples (the number of probe liquids) were prepared. The bitumen glass slides were placed between a light source and a camera. A micro syringe filled with the probe liquid was placed above the bitumen surface and a small drop of the probe liquid from the syringe was dispensed on a bitumen surface and an image of the drop was captured using a camera (Figure 3). For each bitumen sample, the contact angle at least three drops of each probe liquid were measured and their average was taken as the contact angle of that probe liquid with the bitumen.

The contact angle values are substituted into the following equation to obtain the surface free energy components of bitumen:

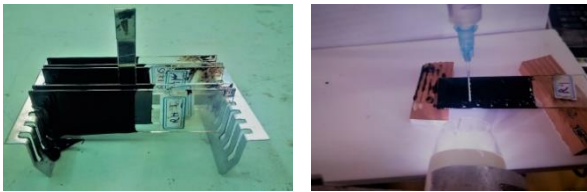
$$\gamma_{Li}(1 + \cos\theta) = 2\sqrt{\gamma_B^{LW}\gamma_{Li}^{LW}} + 2\sqrt{\gamma_B^+\gamma_{Li}^+} + 2\sqrt{\gamma_B^-\gamma_{Li}^-} \quad (8)$$

where  $\gamma_{Li}^{LW}$ ,  $\gamma_{Li}^+$ , and  $\gamma_{Li}^-$  are the surface free energy components of the probe liquid and  $\gamma_B^{LW}$ ,  $\gamma_B^+$ , and  $\gamma_B^-$  are the surface energy components of the bitumen. Furthermore,  $\gamma_{Li}$  is the total surface energy of the probe liquid and  $\theta$  represents the contact angle between the bitumen and the probe liquid. By substituting the surface free energy values of each probe liquid in Equation (8), three equations with three unknowns ( $\gamma_B^{LW}$ ,  $\gamma_B^+$ , and  $\gamma_B^-$ ) are obtained. By solving the set of these equations, the surface free energy components of the bitumen are determined.

**3. 4. Surface Free Energy of Aggregates** Table 5 presents the surface free energy components for both aggregates of limestone and siliceous. It can be seen that siliceous has the higher basic polar component than that of limestone. likewise, acidic polar component and total SFE of limestone are higher than those of siliceous.

**TABLE 4.** Surface free energy components of probe liquids

Probe liquid	Non-polar component ( $\mu\text{J}/\text{m}^2$ )	Acidic polar component ( $\mu\text{J}/\text{m}^2$ )	Basic polar component ( $\mu\text{J}/\text{m}^2$ )	Total surface free energy ( $\mu\text{J}/\text{m}^2$ )
Distilled water	21.8	25.5	25.5	72.8
Ethylene glycol	29.0	1.9	47.0	48.0
Formamide	39.0	2.3	39.6	58.0

**Figure 3.** The SDM procedure**TABLE 5.** Surface free energy values of aggregates used [15]

Aggregate type	Non-polar component ( $\mu\text{J}/\text{m}^2$ )	Acidic polar component ( $\mu\text{J}/\text{m}^2$ )	Basic polar component ( $\mu\text{J}/\text{m}^2$ )	Total surface free energy ( $\mu\text{J}/\text{m}^2$ )
Limestone	44.1	2.4	259.0	93.6
Siliceous	48.8	0	412	48.8

## 4. RESULT AND DISCUSSION

**4.1. Contact Angle Measurement** The measured contact angles for different probe liquids, i.e., distilled water, ethylene glycol and formamide, on the bitumen surface are shown in Figure 4(a, b and c). Figure 4 presents the standard deviations by error bars for the bitumen specimens with three probe liquids. For each probe liquid and asphalt binder tested in five replicates, there is a small deviation less than  $5^\circ$  in contact angle [15].

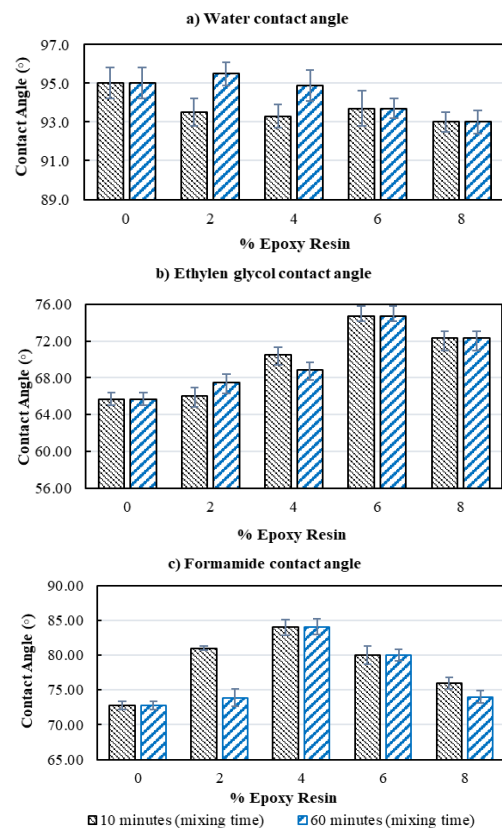
In addition, the findings show the maximum standard deviation of  $1.3^\circ$  that confirms the repeatability of results. According to the figure, for the probe liquids of distilled water and ethylene glycol, the contact angles of bitumens modified with 2 and 4% epoxy resin are different in mixing time of 10 and 60 minutes; however, the contact angles of bitumens containing 0, 6, and 8% epoxy resin are equal for both mixing times of 10 and 60 minutes. The contact angle of the formamide probe liquid for mixing time of 10 minutes is higher than that of 60 minutes for bitumens modified by 2 and 8% epoxy resin; however, these values are equal for the bitumens containing 4 and 6% epoxy resin for both mixing times. According to the results, the change of the process

mixing time and the percentage of epoxy resin in bitumen leads to a change of the contact angle of the probe liquids with the bitumen surface due to a change in the chemical nature of bitumen.

## 4.2. Surface Free Energy Component of Bitumens

The surface free energy components of each bitumen were obtained using the contact angle measured with the probe liquids by SDM. Figure 5 shows the surface free energy components of bitumens modified with 2, 4, 6 and 8% epoxy resin and mixed for different mixing times (10 and 60 minutes). The zero-minute mixing time shown in Figure 5 refers to the value of the surface free energy components for the base bitumen. As can be seen, the surface free energy components change with the epoxy resin percentage and mixing time. The values of the surface free energy components are 25, 2.4, and  $22.6 \mu\text{J}/\text{m}^2$ , respectively, for the total, polar, and non-polar surface free energy components in the case of base bitumen. These results mainly show the base bitumen, unmodified, is a kind of the non-polarity material.

The bitumen with 4% epoxy resin shows the highest polarities of 14 and  $11.8 \mu\text{J}/\text{m}^2$  for the mixing times of 10 and 60 minutes, respectively, among the other cases. Whereas the bitumen modified with 8% epoxy resin exhibits the maximum value of total surface free energy

**Figure 4.** Measurement of contact angle of probe liquids with bitumen

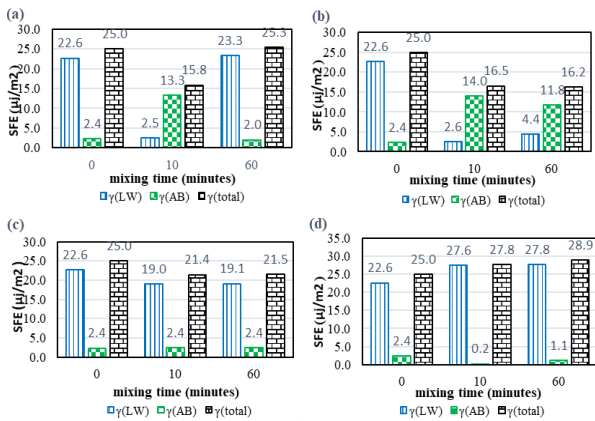


**Figure 5.** Surface free energy components for modified bitumens at different mixing times: a) 2% epoxy resin, b) 4% epoxy resin, c) 6% epoxy resin, d) 8% epoxy resin

and the non-polar surface free energy, it shows the minimum value of polar surface free energy. On the other hand, the influence of mixing time is quite different for bitumens with various epoxy resin percentages. In the surface free energy component of the bitumen containing 2% epoxy resin and mixed for 10 minutes, the total surface free energy and the non-polar surface free energy decrease; while, the polarity of the modified bitumen increases in comparison with the base bitumen. When the mixing time is 60 minutes, the surface free energy components of the modified bitumen are very close to those of base bitumen surface free energy component. These results show that at 2% epoxy resin, 10 minutes mixing time has a greater effect on the polarity of the modified bitumen than 60 minutes mixing time. There is an increase in the polar component of the surface free energy for the bitumen modified with 4% epoxy resin comparison with the base bitumen. It should be noted that modified bitumens for 10 minutes mixing time lead to more polarity than those mixed for 60 minutes. In the case of bitumens containing 6% epoxy resin, the total surface free energy and the non-polar surface free energy decrease compared to the base bitumen, while, the polar surface free energy does not change. In fact, the value of polarity of this type of modified bitumen is similar to the base bitumen independently of the mixing time. Regarding the bitumen containing 8% epoxy resin, the amount of total surface free energy and the non-polar surface free energy increased compared to the base bitumen, but the polar surface free energy decreased. Therefore, the results show that the effect of mixing time on the bitumen surface free energy components for the bitumens containing lower percentages of epoxy resin (2 and 4%) is more noticeable than the bitumens containing higher percentages, i.e. 6 and 8%.

**4. 3. Work of Cohesion of Bitumens**

As mentioned before, the cohesion energy or work of

cohesion is calculated from the surface free energy components of the bitumen using Equation (3). It should be noted that when the value of this parameter is high, the bitumen is more resistant against crack propagation and crack growth [15]. Figure 6 shows the cohesion energy for different modified bitumens. As observed, adding epoxy resin to bitumen at both mixing times alters the work of cohesion of bitumen. The bitumens modified with 4 and 6% epoxy resin for both mixing times, and with 2% epoxy resin for the mixing time of 10 minutes, decrease the work of cohesion compared to the base bitumen. When bitumen is mixed with 8% epoxy resin for 10 and 60 minutes, and also with 2% epoxy resin for 60 minutes, its cohesive performance has improved compared to the unmodified bitumen. Furthermore, the maximum and minimum values of the work of cohesion are determined by mixing of bitumen with 8% epoxy resin for 60 minutes and with 2% epoxy resin for 10 minutes, respectively. It is also found that the values of work of cohesion for the 4 and 6% epoxy resin modified bitumens are almost the same for both mixing times. Moreover, the work of cohesion improved by 4.1% for the 8% epoxy resin modified bitumen prepared at a longer mixing time. It is also observed that the work of cohesion increased by 60% for the 2% epoxy resin modified bitumen prepared at a longer mixing time. In overall, the results show that the work of cohesion is affected by the mixing time of bitumen with epoxy resin based on the amount of additive used.

**4. 4. Work of Adhesion and Debonding**

Figure 7 shows the variation of the values of work of adhesion and work of debonding for two mixing times of 10 and 60 minutes. Increasing the values of both parameters in positive direction shows the enhancing the performance of the bitumen-aggregate system against moisture. According to Figure 7a (limestone asphalt compounds) and Figure 7b (siliceous asphalt compounds), although the effect of mixing time on these parameters is negligible for bitumens containing 4 and 6% epoxy resin, the corresponding effect for bitumens containing 2 and 8% epoxy resin is considerable. These results show that

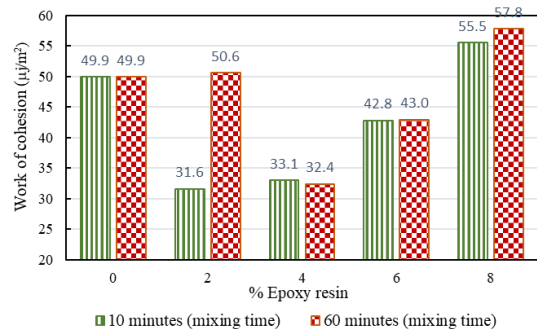


**Figure 6.** Work of cohesion for bitumens modified for 10 and 60 minutes mixing times

the effect of mixing time on the mentioned parameters depends on the percentage of additive, epoxy resin, in bitumen. As observed, both asphalt compounds (limestone and siliceous) have a similar impact on the work of adhesion and work of debonding based on the amount of epoxy resin in modified bitumen. The work of adhesion and work of debonding and thereby the performance of asphalt compound decrease with longer mixing time for the bitumen modified with 2% epoxy resin, whereas the performance of asphalt compound improves with time for the bitumen modified with 8% epoxy resin. According to Equations (6) and (7), as discussed in section 4.5, these results were used to calculate the magnitude of energy parameters related to moisture resistance of asphalt compound.

**4. 5. Energy Parameters Related To Moisture Resistance of Asphalt Compound**

EP1 and EP2 are the parameters that predict the moisture resistance of the asphalt compounds. EP1 and EP2 denote the bitumen adhesion to the aggregate and the extent of bitumen wetting on the aggregate surface, respectively. It should be noted, when EP1 and EP2 increase, the moisture resistance of bitumen-aggregate also increases. In the following, the behavior of these two parameters for the asphalt compounds containing different aggregates are studied for two mixing times.

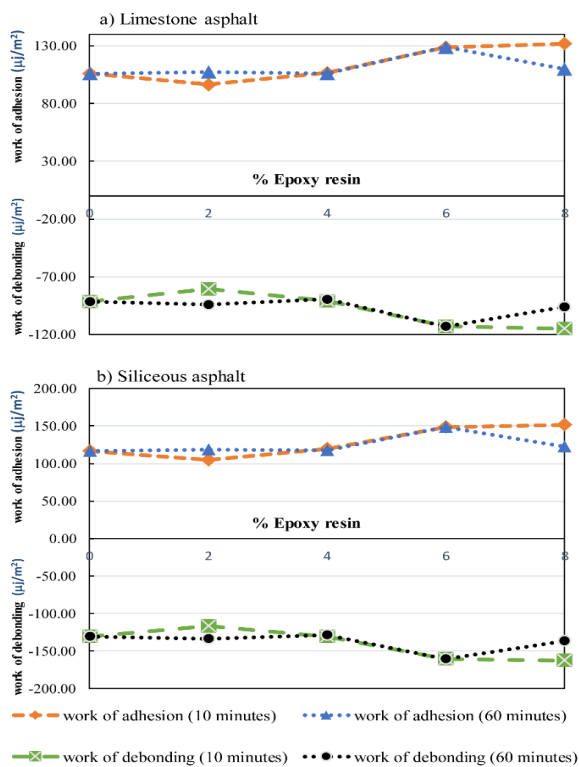


**Figure 7.** Work of adhesion and work of debonding for limestone and siliceous asphalt compounds for 10 and 60 minute mixing times

**4. 5. 1. Influence of Mixing Time on EP1**

Figure 8 shows the variation of EP1 for asphalt compounds containing limestone/siliceous aggregates and modified bitumens for mixing times of 10 and 60 minutes. The minimum and maximum values of EP1 parameter for limestone asphalt are 1.14 and 1.20, respectively, while, the corresponding values for asphalt compounds containing siliceous aggregate are 0.89 and 0.93. These results of EP1 parameter show that asphalt compounds comprising limestone aggregate leads to a better adhesion performance than that of the siliceous aggregate. It is also evident that the effect of mixing time on the EP1 parameter is insignificant. Nevertheless, for the mixing time of 10 minutes, the value of EP1 increases by a maximum 5.26% in comparison with the mixing time of 60 minutes for the asphalt compound containing limestone aggregate and bitumen modified with 2% epoxy resin. As observed, in the case of siliceous compounds, the maximum difference between the values of EP1 occurs for the modified bitumen with 8% epoxy resin under both mixing times of 10 and 60 minutes. Also, the EP1 parameter for the prepared bitumen with a mixing time of 10 minutes is 3.3% higher than that of 60 minutes. Consequently, the mixing time of the bitumen with different percentages of epoxy resin cannot be an effective parameter for improving the adhesive performance of the asphalt compounds including limestone/siliceous aggregates and modified bitumen. Also, an increase of the mixing time not only is

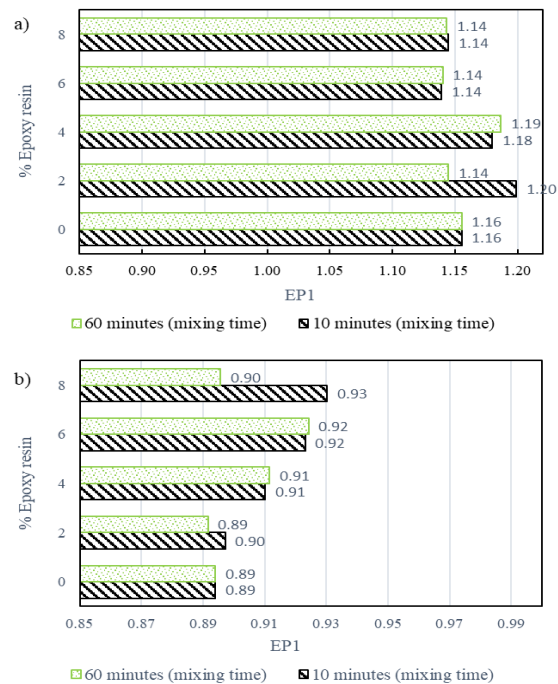


**Figure 8.** EP1 variations for asphalt mixtures containing modified bitumen using mixing times of 10 and 60 minutes: a) limestone aggregate, b) siliceous aggregate

ineffectual in improving the asphalt compound performance, but also leads to energy loss in the process. Accordingly, a mixing time of 10 minutes is sufficient to reach a suitable adhesive performance.

**4. 5. 2. Influence of Mixing Time on EP2**

Figure 9 shows the variation of EP2 when siliceous or limestone aggregates are mixed with each modified bitumen for mixing times of 10 and 60 minutes. As shown in this figure, the value of EP2 for limestone aggregate is greater than that of the siliceous aggregate for the asphalt compounds with almost all percentages of epoxy resin. This reveals that the wetting performance of limestone aggregates is higher than that of siliceous aggregates. For both aggregates in the compounds, the mixing time of 10 minutes for preparing the modified bitumens with 2 and 8% epoxy resin leads to higher values of EP2 than those preparing the modified bitumens for 60 minutes' mixing time. This finding proves the importance of the mixing time impact on the process of providing the modified bitumens, thereby on the performance of asphalt compounds. Therefore, an appropriate mixing time of modified bitumen beside the proper value of additive percentage adjust the wetting performance of the asphalt compound.

When 4 and 6% epoxy resin are used to modify the bitumen, the samples prepared using the both mixing times leads to the identical EP2 values for both

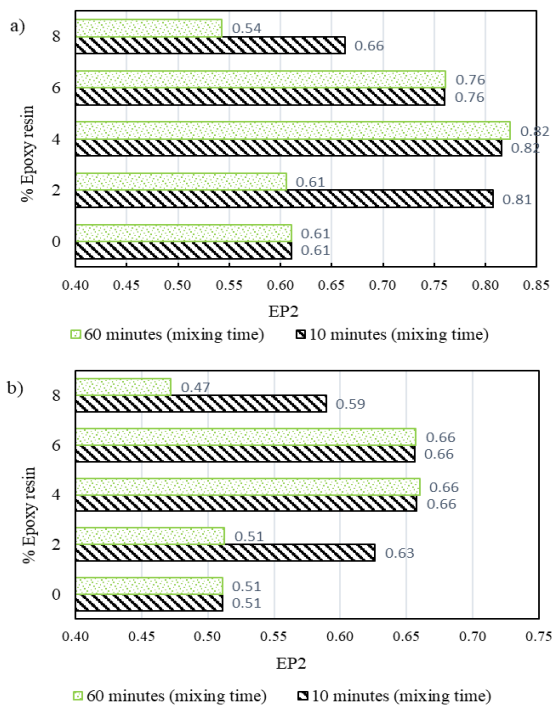


**Figure 9.** EP2 variations for asphalt mixtures containing modified bitumen using mixing times of 10 and 60 minutes: a) limestone aggregate, b) siliceous aggregate times

aggregates. However, there are significant differences between the values of EP2 for both mixing times and aggregates in the cases of the bitumens modified by 2 and 8% epoxy resin. The values of EP2 increase about 32.8 and 23.5% for the mixing time of 10 minutes in comparison with those of mixing time of 60 minutes for the modified bitumens with 2% epoxy resin mixed with limestone and siliceous aggregates, respectively. Moreover, 8% epoxy resin with limestone and siliceous aggregates at the mixing time of 10 minutes led to increasing in the values of EP2 of 22.2 and 25.5%, respectively, compared with those of 60 minutes mixing time. Generally, an increase in the mixing time of modified bitumen causes a decrease in the wetting performance of asphalt' compounds, so that the mixing time of 10 minutes is a better time than 60 minutes.

**5. CONCLUSIONS**

The effects of mixing time and additive percentage in the modified bitumen with combination of two important aggregates on the moisture sensitivity of asphalt compounds were investigated using surface free energy measurement. The main findings of the study can be summarized as follows:

- The values of total, polar, and non- polar surface free energy for the base bitumen are 25, 2.4 and 22.6  $\mu\text{J}/\text{m}^2$ , respectively; which reveals the bitumen is a kind of non-polarity material.
- The 8% epoxy resin modified bitumen produces the maximum values of total surface free energy and non-polar surface free energy. However, the minimum value of polar surface free energy is also relevant to this specimen. Also, the maximum polarity is obtained by the bitumen modified with 4% epoxy resin with the values of 14 and 11.8  $\mu\text{J}/\text{m}^2$  for the mixing times of 10 and 60 minutes, respectively.
- The effect of mixing time on bitumen surface free energy components is more noticeable in case of bitumens with the lower percentages of epoxy resin additive (2 and 4%) compared to the bitumens with higher ones (6 and 8%).
- In each modified bitumen, the value of the work of cohesion corresponding to the mixing time of 60-minutes is higher than that corresponding to 10-minutes one. In fact, an increase in the mixing time leads to enhancing the cohesion bitumen energy.
- The mixing time affects the work of adhesion and work of debonding based on the percentage of additive in bitumen. There is no important difference between the values of these parameters in the two mentioned mixing times for bitumens containing 4 and 6% epoxy resin. Nevertheless, the values of the work of adhesion and work of debonding for bitumens with the addition of 2 and 8% epoxy resin

for 10- and 60-minutes mixing time are quite different.

- The minimum and maximum values of EP1 parameter for limestone asphalt are 1.14 and 1.20, respectively. Those values for asphalt compounds containing siliceous aggregate are 0.89 and 0.93. These results show that asphalt compounds containing limestone aggregates lead to a better adhesion performance than those containing siliceous aggregates.
- The value of EP2 for limestone aggregates is greater than that of siliceous aggregates for asphalt compounds containing epoxy resin in almost all percentages. This means that limestone aggregates have a higher wetting performance than siliceous aggregates.
- In the modified bitumens with amount of epoxy resin 4 and 6%, the values of EP1 and EP2 parameters are very close to each other for both 10- and 60-minutes mixing times. This means that the mixing time of bitumen with various percentages of epoxy resin is not influential in improving the adhesion and wetting performance of asphalt compounds.
- The asphalt compounds containing bitumens with 2 and 8% epoxy resin prepared for 10 minutes' mixing time show a better performance in terms of adhesion (EP1) and wetting (EP2) compared to those prepared for mixing time 60 minutes.
- Finally, the mixing time of 10 minutes is recommended as a suitable value for bitumens with 0 to 8% epoxy resin in order to reduce the moisture sensitivity of asphalt compounds.

## 6. REFERENCES

1. Gao, J., Liu, P., Wu, Y., Xu, Y., and Lu, H. "Moisture damage of asphalt mixture and its evaluation under the long-term soaked duration." *International Journal of Pavement Research and Technology*, Vol. 14, No. 5, (2021), 607–614. <https://doi.org/10.1007/s42947-020-0176-z>
2. Jahanian, H. R., Shafabakhsh, G., and Divandari, H. "Performance evaluation of Hot Mix Asphalt (HMA) containing bitumen modified with Gilsonite." *Construction and Building Materials*, Vol. 131, (2017), 156–164. <https://doi.org/10.1016/j.conbuildmat.2016.11.069>
3. Hamzah, M. O., Kakar, M. R., Quadri, S. A., and Valentin, J. "Quantification of moisture sensitivity of warm mix asphalt using image analysis technique." *Journal of Cleaner Production*, Vol. 68, (2014), 200–208. <https://doi.org/10.1016/j.jclepro.2013.12.072>
4. Wang, W., Wang, L., Yan, G., and Zhou, B. "Evaluation on moisture sensitivity of asphalt mixture induced by dynamic pore water pressure." *International Journal of Pavement Research and Technology*, Vol. 13, No. 5, (2020), 489–496. <https://doi.org/10.1007/s42947-020-0141-x>
5. Afkhamy Meybodi, P., Khani Sanij, H., Hosseini, S. H., and Olazar, M. "Effect of Crushed Glass on Skid Resistance, Moisture Sensitivity and Resilient Modulus of Hot Mix Asphalt." *Arabian Journal for Science and Engineering*, Vol. 44, No. 5, (2019), 4575–4585. <https://doi.org/10.1007/s13369-018-3475-9>
6. Jitsangiam, P., Nusit, K., and Nikraz, H. "An Evaluation of Moisture Damage Resistance of Asphalt Concrete based on Dynamic Creep Characteristics." *KSCE Journal of Civil Engineering*, Vol. 23, No. 4, (2019), 1610–1616. <https://doi.org/10.1007/s12205-019-1369-3>
7. Mosa, A. M., Jawad, I. T., and Salem, L. A. "Modification of the properties of warm mix asphalt using recycled plastic bottles." *International Journal of Engineering, Transaction C: Aspects*, Vol. 31, No. 9, (2018), 1514–1520. <https://doi.org/10.5829/ije.2018.31.09c.06>
8. Ghasemi, M., and Marandi, S. M. "Laboratory Studies of the Effect of Recycled Glass Powder Additive on the Properties of Polymer Modified Asphalt Binders." *International Journal of Engineering - Transactions A: Basics*, Vol. 26, No. 10, (2013), 1183–1190. Retrieved from <https://www.sid.ir/en/Journal/ViewPaper.aspx?ID=355404>
9. Cho, D.-W., and Kim, K. "The mechanisms of moisture damage in asphalt pavement by applying chemistry aspects." *KSCE Journal of Civil Engineering*, Vol. 14, No. 3, (2010), 333–341. <https://doi.org/10.1007/s12205-010-0333-z>
10. Copeland, A. R., Youtcheff, J., and Shenoy, A. "Moisture Sensitivity of Modified Asphalt Binders." *Transportation Research Record: Journal of the Transportation Research Board*, Vol. 1998, No. 1, (2007), 18–28. <https://doi.org/10.3141/1998-03>
11. Birgisson, B., Roque, R., Tia, M., and Masad, E. A. Development and evaluation of test methods to evaluate water damage and effectiveness of antistripping agents, University of Florida, Gainesville, (2005). Retrieved from <https://trid.trb.org/view/758967>
12. Solaimanian, M., Harvey, J., Tahmoressi, M., and Tandon, V. "Test methods to predict moisture sensitivity of hot-mix asphalt pavements." In Transportation research board national seminar, San Diego, California (2003), 77–110. Retrieved from [https://www.researchgate.net/profile/Tim-Aschenbrener/publication/286140774\\_Introduction\\_and\\_Seminar\\_Objectives/links/5e83f239299bf130796dc230/Introduction-and-Seminar-Objectives.pdf#page=82](https://www.researchgate.net/profile/Tim-Aschenbrener/publication/286140774_Introduction_and_Seminar_Objectives/links/5e83f239299bf130796dc230/Introduction-and-Seminar-Objectives.pdf#page=82)
13. Bahmani, H., Sanij, H. K., and Peiravian, F. "Estimating Moisture Resistance of asphalt mixture containing epoxy resin using Surface Free Energy Method and Modified Lottman test." *International Journal of Pavement Engineering*, (2021), 1–13. <https://doi.org/10.1080/10298436.2021.1904236>
14. Mehrara, A., and Khodaii, A. "Moisture Damage Evaluation Using Energy Based Responses." *Journal of Civil Engineering and Management*, Vol. 23, No. 1, (2016), 47–58. <https://doi.org/10.3846/13923730.2014.975742>
15. Little, D. N., and Bhasin, A. Using surface energy measurements to select materials for asphalt pavement, Washington DC: Transportation Research Board, Final Report for NCHRP 9-37, (2007). Retrieved from <http://worldcat.org/isbn/9780309431743>
16. Zhang, F., Muhammad, Y., Liu, Y., Han, M., Yin, Y., Hou, D., and Li, J. "Measurement of water resistance of asphalt based on surface free energy analysis using stripping work between asphalt-aggregate system." *Construction and Building Materials*, Vol. 176, (2018), 422–431. <https://doi.org/10.1016/j.conbuildmat.2018.05.055>
17. Kim, S.-H., Jeong, J.-H., and Kim, N. "Use of surface free energy properties to predict moisture damage potential of Asphalt concrete mixture in cyclic loading condition." *KSCE Journal of Civil Engineering*, Vol. 7, No. 4, (2003), 381–387. <https://doi.org/10.1007/BF02895836>
18. Hamed, G. H., Asadi, M., Moghadas Nejad, F., and Esmaceli, M. R. "Applying asphalt binder modifier in reducing moisture-induced damage of asphalt mixtures." *European Journal of*

- Environmental and Civil Engineering*, Vol. 25, No. 11, (2021), 2039–2056. <https://doi.org/10.1080/19648189.2019.1615554>
19. Azarhoosh, A., Moghaddas Nejad, F., and Khodaii, A. "Evaluation of the effect of nano-TiO<sub>2</sub> on the adhesion between aggregate and asphalt binder in hot mix asphalt." *European Journal of Environmental and Civil Engineering*, Vol. 22, No. 8, (2018), 946–961. <https://doi.org/10.1080/19648189.2016.1229227>
  20. Howson, J., Masad, E., Bhasin, A., Little, D., and Lytton, R. "Comprehensive analysis of surface free energy of asphalts and aggregates and the effects of changes in pH." *Construction and Building Materials*, Vol. 25, No. 5, (2011), 2554–2564. <https://doi.org/10.1016/j.conbuildmat.2010.11.098>
  21. Nejad, F. M., Asadi, M., and Hamedi, G. H. "Determination of moisture damage mechanism in asphalt mixtures using thermodynamic and mix design parameters." *International Journal of Pavement Research and Technology*, Vol. 13, No. 2, (2020), 176–186. <https://doi.org/10.1007/s42947-019-0099-8>
  22. Kingery, W. D., and Humenik, M. "Surface Tension at Elevated Temperatures. I. Furnace and Method for Use of the Sessile Drop Method; Surface Tension of Silicon, Iron and Nickel." *The Journal of Physical Chemistry*, Vol. 57, No. 3, (1953), 359–363. <https://doi.org/10.1021/j150504a026>
  23. Xiao, F., and Amirkhanian, S. N. "Laboratory investigation of moisture damage in rubberised asphalt mixtures containing reclaimed asphalt pavement." *International Journal of Pavement Engineering*, Vol. 10, No. 5, (2009), 319–328. <https://doi.org/10.1080/10298430802169432>
  24. Zhou, L., Huang, W., Zhang, Y., Lv, Q., and Sun, L. "Mechanical evaluation and mechanism analysis of the stripping resistance and healing performance of modified asphalt-basalt aggregate combinations." *Construction and Building Materials*, Vol. 273, (2021), 121922. <https://doi.org/10.1016/j.conbuildmat.2020.121922>
  25. Lambert, J., Shalaby, A., and Enieb, M. "Wettability, surface tension and surface free energy behavior of short-term aging and liquid antistrips modified HMA binders." *IJPC-International Journal of Pavements, At: São Paulo, Brazil*, Vol. 199, (2013).
  26. Koc, M., and Bulut, R. "Evaluation of a warm mix asphalt additive using direct contact angle measurements." In *International Journal of Pavements Conference*, (2013), 161–167.
  27. Iskender, E., Aksoy, A., and Ozen, H. "Indirect performance comparison for styrene-butadiene-styrene polymer and fatty amine anti-strip modified asphalt mixtures." *Construction and Building Materials*, Vol. 30, (2012), 117–124. <https://doi.org/10.1016/j.conbuildmat.2011.11.027>
  28. Bala, N., Napiyah, M., and Kamaruddin, I. "Influence of nanosilica on moisture resistance of polymer modified bitumens." *Petroleum Science and Technology*, Vol. 36, No. 3, (2018), 244–250. <https://doi.org/10.1080/10916466.2017.1419480>
  29. Cong, P., Chen, S., and Yu, J. "Investigation of the properties of epoxy resin-modified asphalt mixtures for application to orthotropic bridge decks." *Journal of Applied Polymer Science*, Vol. 121, No. 4, (2011), 2310–2316. <https://doi.org/10.1002/app.33948>
  30. Mastrofini, D., and Scarsella, M. "The application of rheology to the evaluation of bitumen ageing." *Fuel*, Vol. 79, No. 9, (2000), 1005–1015. [https://doi.org/10.1016/S0016-2361\(99\)00244-6](https://doi.org/10.1016/S0016-2361(99)00244-6)
  31. González, V., Martínez-Boza, F. J., Gallegos, C., Pérez-Lepe, A., and Páez, A. "A study into the processing of bitumen modified with tire crumb rubber and polymeric additives." *Fuel Processing Technology*, Vol. 95, (2012), 137–143. <https://doi.org/10.1016/j.fuproc.2011.11.018>
  32. Khani, H., Bahmani, H., and Roshani, R. "Evaluating the Effect of Modified-Bitumens Mixing Temperature and Their Surface Free Energy Variations on Moisture Resistance Performance of Bitumen-Aggregates System." *Journal of Transportation Infrastructure Engineering*, Vol. 6, No. 1, (2020), 29–44. <https://doi.org/10.22075/JTIE.2019.18740.1417>
  33. Perez-Lepe, A. "Influence of the processing conditions on the rheological behaviour of polymer-modified bitumen." *Fuel*, Vol. 82, No. 11, (2003), 1339–1348. [https://doi.org/10.1016/S0016-2361\(03\)00065-6](https://doi.org/10.1016/S0016-2361(03)00065-6)
  34. Van Oss, C. J., Chaudhury, M. K., and Good, R. J. "Interfacial Lifshitz-van der Waals and polar interactions in macroscopic systems." *Chemical Reviews*, Vol. 88, No. 6, (1988), 927–941. <https://doi.org/10.1021/cr00088a006>
  35. Bhasin, A. "Development of methods to quantify bitumen-aggregate adhesion and loss of adhesion due to water", Doctoral dissertation, Texas A&M University, (2003). Retrieved from <https://hdl.handle.net/1969.1/5934>
  36. Çubuk, M., Gürü, M., and Çubuk, M. K. "Improvement of bitumen performance with epoxy resin." *Fuel*, Vol. 88, No. 7, (2009), 1324–1328. <https://doi.org/10.1016/j.fuel.2008.12.024>
  37. Yu, J., Cong, P., and Wu, S. "Laboratory investigation of the properties of asphalt modified with epoxy resin." *Journal of Applied Polymer Science*, Vol. 113, No. 6, (2009), 3557–3563. <https://doi.org/10.1002/app.30324>
  38. Zarei, M., Rahmani, Z., Zahedi, M., and Nasrollahi, M. "Technical, Economic, and Environmental Investigation of the Effects of Rubber Powder Additive on Asphalt Mixtures." *Journal of Transportation Engineering, Part B: Pavements*, Vol. 146, No. 1, (2020), 04019039. <https://doi.org/10.1061/JPEODX.0000142>

---

### Persian Abstract

#### چکیده

اصلاح قیر، امکان بهبود خواص آن را فراهم می‌کند و می‌تواند به عنوان یک روش مناسب در جهت بهبود خواص ترکیب‌های آسفالتی مورد استفاده قرار گیرد. بنابراین این مطالعه به بررسی اثر زمان اختلاط قیرهای اصلاح شده با درصد‌های متفاوت رزین اپوکسی از صفر تا ۸ درصد وزنی قیر، بر حساسیت رطوبتی ترکیب‌های آسفالتی حاوی دو نوع سنگدانه آهکی و سیلیسی پرداخته است. به این منظور، روش قطره چسبیده مورد استفاده قرار گرفت و پارامترهای حساسیت رطوبتی مربوط به انرژی آزاد سطحی شامل اجزای انرژی آزاد سطحی، انرژی پیوستگی، انرژی چسبندگی، انرژی شکست پیوند، میزان ترشوندگی قیر بر سطح سنگدانه، و میزان چسبندگی قیر به سنگدانه محاسبه و مورد ارزیابی قرار گرفتند. نتایج نشان دادند میزان اثر زمان اختلاط قیرهای اصلاح شده با رزین اپوکسی بر حساسیت رطوبتی ترکیب‌های آسفالتی به طور قابل توجهی وابسته به درصد رزین اپوکسی موجود در قیر است. برای قیرهای با ۴ تا ۶ درصد اپوکسی رزین، عملکرد چسبندگی و ترشوندگی قیر به سنگدانه برای زمان‌های اختلاط ۱۰ دقیقه و ۶۰ دقیقه مشابه بود. با این حال، در ترکیب‌های آسفالتی حاوی ۲ و ۸ درصد رزین اپوکسی، قیرهای اصلاح شده با زمان اختلاط ۱۰ دقیقه عملکرد بهتری نسبت به قیرهای با زمان اختلاط ۶۰ دقیقه از خود نشان دادند. اثر زمان اختلاط قیرهای اصلاح شده با رزین اپوکسی بر عملکرد قیر و ترکیب آسفالتی وابسته به درصد افزودنی به کارگرفته شده در قیر است.



## Decision Support System for Analyzing Key Performance Indicators in Construction Projects Management

R. Ansari<sup>\*a</sup>, S. A. Banihashemi<sup>b</sup>, R. Taherkhani<sup>a</sup>, S. Moradi<sup>a</sup>

<sup>a</sup> Department of Civil Engineering, Imam Khomeini International University, Qazvin, Iran

<sup>b</sup> Department of Industrial Engineering, Payame Noor University, Tehran, Iran

### PAPER INFO

#### Paper history:

Received 24 December 2021

Received in revised form 01 February 2022

Accepted 03 February 2022

#### Keywords:

Construction

Claim Management

Performance Management

Decision Support System

### ABSTRACT

Many factors play a role in the life cycle of construction industry projects, focusing on human resources and relationships as the main axis of business development. Thus, the conflict of interests between the stakeholders in the construction industry projects is a clear and challenging problem. The increased number of stakeholders in the project complicates human relationships and, consequently, increases the possible conflicts. The conflicts may result in claims if not resolved. The success of construction projects and their cost and time management can be affected by the poor management of claims. Therefore, this research aims to take a significant step to improve the efficiency of projects by identifying and ranking the causes of claims and analyzing their effects on key efficiency indicators. Firstly, causes of claim are collected according to experts' opinions and literature and classified based on key efficiency indicators using the integrated analytic hierarchy process-technique for order preference by similarity to ideal solution (AHP-TOPSIS) technique. According to findings, delays with a proximity coefficient of 0.728 are the most significant factors in making claims with a great effect on the key efficiency indicators of the construction project. The changes in most construction projects are ranked in second place, followed by acceleration command, extra work, changing workshop conditions, and contractual ambiguities. The present study results may reduce the challenges in managing the construction industry claims and ensure the successful completion of projects.

doi: 10.5829/ije.2022.35.05b.03

### NOMENCLATURE

AHP	Analytic Hierarchy Process	PIS	Positive Ideal Solution
TOPSIS	Technique for Order of Preference by Similarity to Ideal Solution	NIS	Negative Ideal Solution
EPC	Engineering, procurement, and construction	KPIs	Key Performance Indicators

### 1. INTRODUCTION

The term 'claim' can be confusing and have several meanings. The following are two definitions of claims in the Cambridge English Dictionary: 1) To say that something is true or real, though you cannot prove it and people might not believe it, and 2) To ask for something valuable because you think it is yours or has a right to it.

As defined by the Project Management Institute, a party may submit a claim when it believes that the

counterparty should not be met the contractual obligation or expectations and is deserved to financial and time compensation [1]. In the Oxford Advanced Learner's Dictionary, claim means demanding something as right. In Webster Dictionary, the claim is defined as proving and demanding what is right or seems right. According to the Canadian Law Dictionary, a claim can be 'an assertion to the right to remedy, relief, or property or a 'failure to fulfill obligations under the contract' [2]. Other terms used for a claim are conflict and disputes. In

\*Corresponding Author Institutional Email:  
[raminansari@eng.ikiu.ac.ir](mailto:raminansari@eng.ikiu.ac.ir) (R. Ansari)

the construction industry, claims are usually used to describe any request by the contractor for payments other than the contractual payments [3].

Conflict can be a factor in making a claim, and the dispute can be seen as the result. Disputes in the construction industry arise when claims can not be resolved, while claims arise because of mismanagement of conflicts [4]. Claims can be examined from two points of view, the party that submits the claim and the party that rejects or accepts the claim. What distinguishes claims from 'change' is the agreed element from both parties about what was promised. If the agreement is reached, the claim becomes a 'change'; otherwise, it becomes a 'dispute.' Conflicts in human relationships are unavoidable, so construction projects involving many factors can also occur. The more parties involved in a project, the more relationships, so there are more potential sources for conflict [5]. The use of the word 'claim' creates a kind of emotional confrontation usually accompanied by a charge and retaliation. The consequences of these claims are, in many cases, the disruption of relationships, arbitration, or litigation with all its delays and costs [6]. Claims are a major source of problems for the construction industry, and construction claims by any of the parties involved in the project are considered one of the most destructive and unpleasant events in a project [7]. In fact, claims are made when one party is harmed, and the other party has to make up for it [8]. More simply, a claim may be regarded as a claim for compensation for damages incurred by any party to the contract [2].

Due to the nature of the contracts, their complexity, the number of involved parties, risk, and pressure of time constraints in preparing contract documents, claims are unavoidable [4]. The claims are of concern to all parties involved in the construction project contract. Claims may result in increased costs and scheduling delays or jeopardize the working relationship between the parties involved in the contract. Claims and their causes are the main drivers of rising costs [9].

A survey conducted in western Canada showed that a large proportion of claims had been accompanied by delay and, in many cases delayed by more than 100% of the original contract period, as to the project cost, more than half of the claims resulted in an additional cost of at least 30% of their original contract value [2]. Other research work done in the United States and Thailand showed similar results: The average cost increase due to the claim is approximately 7% of the original contract price [10, 11].

In general, any construction contract is challenging because it seeks to provide a specific solution in violation of any terms or conditions. Therefore, it is essential for the parties involved in the contract to be well aware of its provisions [12].

Claims unknowingly consume project resources and are considered as one of the important reasons for project cost increases [13]. In fact, they divert resources away from project goals and thereby increase costs [14]. This may lead to project failure [15]. Completing projects without a claim is a key factor in the success of construction projects [16]. In fact, early identification of potential differences will help complete the project successfully [17].

In the construction industry, project managers must be able to make reliable predictions about the future status of the project. Such forecasts may help contractors control projects during the construction phase and give them early warning of potential problems. However, predicting performance is a complex and dynamic process involving many distinct indicators [18]. At the same time, changes in one performance index due to their very complex structures and interactions may affect other indicators [19]. Numerous other factors have an impact on these indicators and, ultimately, the overall performance of construction projects; one of them is the claims and their causes.

According to previous research, claims are unavoidable at various stages of the project. All efforts have been made to reduce claims, provide preventive solutions, and finally establish these claims, which is necessary to improve the performance of projects.

In fact, construction claims management is critical to success in executing construction projects. Research has also shown that poor claims management can affect the success of construction projects and their budgeting and scheduling. Despite the challenges of construction claims, different controls can be adopted to manage these claims to ensure that projects with minimal claim impact are implemented. In addition, claim control guarantees the successful completion of construction projects and minimizes delays and disputes [20].

The concept of project success is difficult to find because projects are complex and dynamic. The definition of this concept can vary depending on the type of industry, project team, or individual perspective [21]. An architect may evaluate success in aesthetic terms, and an engineer may be technically qualified, an accountant in terms of budgeted expenses, a human resources manager in terms of employee satisfaction, and an executive in terms of market shares [22]. In previous years, the simple definition of project success was based solely on project life cycle implementation stages. But it is now that project success needs to be defined from the beginning to the end of the project life cycle.

Their success can be evaluated and controlled through project efficiency measurement. Different techniques and approaches have been used in recent years to predict and evaluate the efficiency of construction, some of which are on the basis of key efficiency indicators. As can be

concluded from the review of previous research, the study of the causes of claims in construction projects from the key efficiency indicators' perspective has received less attention from researchers. Hence, integrating key efficiency indicators and determining their importance in construction projects is the first achievement of this paper, which has not been fully and comprehensively examined in other related studies. Examining the effect of claims on key efficiency indicators and, consequently, the construction project's success is the second achievement. According to different researches on the causes of claims and their resolution, a study that examines the effect of each reason on project efficiency was not observed in the literature.

Accordingly, in this study, the key efficiency indicators are ranked based on the causes of claims, following identifying the key efficiency indicators of construction projects and identifying the reasons for making claims using integrated AHP-TOPSIS and multi-criteria decision-making MCDM techniques. The association between the causes of claims and the key efficiency indicators helps project managers have a better view relative to the effect of their activities on the objectives and development of the project over time.

## 2. LITERATURE REVIEW

Projects completed in the construction industry receive different claims from stakeholders based on projects' specific conditions. These claims by project stakeholders significantly affect project efficiency and success [23].

In recent years, different definitions of the claim have been raised, but they all share the concept that a dispute arises between parties after a claim based on a rejected change [24-26]. Given the negative impact of possible claims on the ultimate goals and project success, more studies have been conducted on construction claims management in the past two decades [27-29]. One study conducted in 1993 showed that the causes of claims often include poor forecasting and review of workplace conditions, bidding with incomplete maps, early introduction of design reviews, and construction disturbance [30]. Half of the contractual claims are related to design errors [3]. Another study in Canada showed that the common causes of all claims are project acceleration, limited access, climate, and increased scope [4].

Likewise, studies have been conducted in different countries to examine the causes of claims, the types of claims, and the claims management process. One of these studies has been conducted in the UAE. The causes of claims concerning their priority include changes, extra-work, delays, different site conditions, acceleration, and contract ambiguity. In this research, the claims settlement methods were also examined and classified according to

the priority used in the projects (negotiation, mediation, arbitration, and litigation) [31].

Most research has focused on two factors, delay, and change, which are the main drivers of claims in construction projects. According to a study in the state of Colorado, the delay is the main reason behind claims in the projects under consideration, and even more important than change and additional orders. It also proves that projects with fixed completion dates are more susceptible to claims than projects with more flexible planning [9]. Further research has also been done to prove that changes in employers' requirements are the most important reason for making a claim [32].

Since claim management is a process that requires analyzing a large amount of diverse information, old documentation methods developed by industry experts can be considered as one of the most important challenges for successful claims management. The feasibility of existing claim management systems is questionable due to problems with input and document information. For this reason, a study has been conducted to develop a BIM-based claim management system [13].

In a study aimed by Bakhary et al. [33] at categorizing the claim management process-related problems from the contractors' and consultants' viewpoints, classified conventional claim management procedures into six main stages, including identification, notification, examination, documentation, presentation, and negotiation. The findings of this study emphasize the need for a proper documentation and recording system with qualified staff to identify the claims during the project. Researchers also state that a standard and transparent procedure needs to be established by which contractors can make the right claim by following it.

Construction claims are now an unavoidable concern and have a major impact on project efficiency. The timely completion of construction projects is an important criterion for measuring project success. However, most construction projects are delayed due to problems with claims and their management, which will have a negative impact on project efficiency. Claims also have a significant impact on the cost of construction projects and cause negative cost performance [34]. A study has also been conducted to enhance understanding of the relationship between conflict management, team coordination, and project efficiency [35].

In another study [36] project claim management has been investigated to minimize project cost and time functions using a meta-heuristic algorithm with the EPC project as a case study. The experimental results demonstrate the minimum time and delay of the project with better stability and effectiveness of the system.

Since 1980, more emphasis has been placed on non-financial and multidimensional performance indicators to understand better and manage construction projects' performance [37, 38].

Asgari et al. [39] have examined the key success factors in the construction industry from the owners, contractors, and consultants' point of view. They classified the identified indicators into five main categories, including financial, interactive processes, human resources, contract agreements, and project specifications. Their results showed that the human resources group-related indicators from the owners' and contractors' point of view and financial and project specifications-related indicators from the consultants' point of view are the main features for project success [39]. In 2009, the effect of rework on project efficiency was evaluated both in terms of employer and contractor [40]. In 2016, another researcher evaluated and modeled the competence of construction projects and their relationships to project efficiency [41]. In the next study, the system dynamics approach was used to model the relationship between tender strategy and construction project efficiency [42]. In the same year, a model was presented for predicting the performance of construction projects to manage the performance of construction projects with a system dynamic approach [18]. In recent years, many studies have been complete in the field of performance management, key performance indicators, and different performance management systems in different countries [43-46].

**2. 1. CAUSES of CLAIM** According to the literature review of claims in the construction projects, there are several reasons for making claims, the most important of which were considered to determine their impact on the performance of construction projects in this study, changes, delays, acceleration, extra work due to change commands, different site conditions, and contract ambiguity.

**2. 1. 1. Changes** The complexity and uniqueness of construction projects and the involvement of different individuals and stakeholders in these projects are characteristic of these projects. In fact, these features result in changes. Changes in construction projects are common and appear to be the main source of conflict but are sometimes required to complete the project. From the perspective of the employer or the main contractor, the changes are undesirable because some of them have indirect effects on the cost and schedule of the project [47]. Changes should not include removing something intended to be done by others. Claims for changes made while executing a project are inevitable because all possible states cannot be predicted. The main source of dispute is what changes are and are not. Any change from the specified sequence or timing stated in a program submitted by the contractor and instructed by the engineer would therefore qualify as a change. The employer is not permitted to make changes without giving instructions, and these instructions must be in

written form. We should know that extra work does not mean change because extra work is not in the contract, but change means changing what was in the contract and done before. Changes can occur at any stage, including design, specifications, and implementation. A change announcement can be written or structured; a structured announcement means making the change and reacting immediately [48].

**2. 1. 2. Delays** Claims due to delays in the construction industry are among the most common types of claims. This claim relates to a period of time when construction is prolonged or activities are not performed as expected and are not in agreement with the parties. The delay must be justified to provide a basis for the cost or additional payment. However, types of justifiable delays occur once in a contract and naturally relate to events beyond the control of the contract [49]. To complete the project within the designated time, the contractor and the employer must make every effort. Failure in this area will create a claim and eventually a dispute.

But in most cases, 'extension of time' is considered a need for the project, and in fact, the extension of time is 'money,' and the same claim for compensation by each factor causes a great deal of conflict and dispute [48]. Employer delays are one of the most important issues for contractor claims, and contractors can raise claims by documenting claims that, in most cases, result in employer financial and non-financial compensation. Employer delays include delays in delivery of the site, suspensions, delays in delivering documents, delays in payments, and so on.

**2. 1. 3. Acceleration** Construction contracts clearly consider important milestone times, completion date together with probably liquidated damages for delay or additions for completing on time. Thus time is a key factor in project decisions. Speeding up arises when the work of the contractor is accelerated to finish a specific task earlier than the designated time. Acceleration in construction projects is classified into two types: directed acceleration and constructive acceleration [50]. To compensate for lost time, most employers order contractors to speed up work. To achieve this goal, more resources may be employed, which is inconsistent with productivity and the planned linear performance and can be costly [48]. In fact, another reason for the claim is an acceleration order by the employer, and because it is unforeseen, it will impose additional costs on the contractor and is, therefore, one of the foundations of the claim. Accelerated costs include additional labor costs, overtime costs, additional equipment costs, stacking of trade costs, increased overhead costs, loss of labor efficiency costs, additional supervision costs, increased material delivery costs, and so on [48].

**2. 1. 4. Extra Work Due to Change Commands**

Any changes to the project will cause extra work. But there is a difference between overtime and extra work. Because extra work is freelance and off-contract, overtime is for the full realization of the contract terms. One of the inevitable cases of project implementation is the change in the technical specifications and the order of change in the execution of works for various reasons. One of the inevitable cases of project implementation is the change in technical specifications and execution of works for various reasons. These changes cause extra work on the project, including change orders according to the employer’s opinion, changes due to inevitable and executive reasons, deficiencies in technical specifications and schedules, confusion in technical specifications, lack of transparency in decisions, and previous executive measures [48].

**2. 1. 5. Different Site Conditions** Claims due to different site conditions after the contract are one of the common claims, and these changes may occur during soil testing and drilling of boreholes, excavation, leveling, or construction of buildings and installations. Changing workplace conditions may increase the cost of implementation, an unpredictable delay, the need to employ sophisticated technical practices, and ultimately disrupt the normal operation of the project. If, in the condition of a tender or before the contract, the contractor is required to visit the site and then submit an offer, then it will be extremely difficult for the contractor to submit a claim on the condition of the site. If the contractor is not fully aware of the environmental conditions of the workshop or somehow hidden from the contractor’s view, in this case, secrecy may cause the contractor to make a claim, even in court [47].

**2. 1. 6.Contract Ambiguity** Mistakes in the preparation of documents as well as bid-offer are a fairly common topic. Mistakes can take many forms. Common mistakes include computational or written errors, deletion of some rows, mistaken assumptions, different or inaccurate understanding of concepts, and dual interpretation. Other types of errors are related to the contractor’s viewpoint in setting and bidding. These errors include estimation with an error about the project completion time or workforce or materials and equipment. Mistakes due to ignoring facts or legal matters or the essential requirements of the contract do not normally have no way of getting rid of the legal consequences [48].

**2. 2. Analytical Hierarchy Process Method (AHP)**

Analytical Hierarchy Process is one of the most widely used Multiple Criteria Decision Making methods,

developed by Saaty [51]. The principles of the AHP process are:

- The reverse condition
- The principle of homogeneity
- The principle of dependency
- The principle of expectations
- This method can do two things: find the relative importance of the indexes and rank the options.

**2. 2. 1. Steps of the Analytical Hierarchy Process Method**

**Step 1:** First, a logical pairwise comparison matrix is created using a scale ranging from 1-9. The scale (1-9) is shown in Table 1. The number of pairwise comparisons is calculated using Equation (1).

$$number\ of\ Pairwise = \binom{n}{2} \tag{1}$$

where n is the number of factors.

**Step 2:** Normalizing the Matrix Values Pairwise Comparisons. To do this, we divide the values of each matrix component into the sum of the column components containing the same component.

**Step 3:** Calculating the relative importance of each index. The arithmetic mean of each row is the relative importance of each index.

**Step 4:** Determining the incompatibility rate. If the rate is greater than 0.1, the comparisons should be revised; otherwise, there is compatibility, and work can continue.

**2. 3. TOPSIS<sup>1</sup> Method**

The TOPSIS method is another multi-criteria decision-making method used by Hwang et al. [40]. In this research, this method was used in combination with the AHP method. The basic concept of this method is that the chosen option should be the shortest distance from the best possible and the longest distance from the worst possible [52, 53].

**2. 3. 1. Steps of TOPSIS Method**

1) Determining the decision matrix. Given a set of alternatives,  $A = \{A_k | k = 1, \dots, m\}$  [7], and a set of criteria,  $C = \{C_j | j = 1, \dots, n\}$ , where  $X = \{x_{kj} | k = 1, \dots, m; j = 1, \dots, n\}$  denotes the set of performance ratings and  $w = \{w_j | j = 1, \dots, n\}$  is a set of

**TABLE 1.** Scale (1-9) [51]

Definition	Standard values	Inverse values
The same importance	1	1/1
Weak dominance	3	1/3
Strong dominance	5	1/5
Very strong dominance	7	1/7
Absolute dominance	9	1/9
Inter values	2,4,6,8	1/2,1/4,1/6,1/8

<sup>1</sup> Technique for Order Preference by Similarity to ideal Solution

weights as follows:

$$W = [w_1 \quad w_2 \quad \dots \quad w_n] \tag{2}$$

(2) Calculating the normalized decision matrix. The normalized value  $r_{ij}$  is calculated as follows:

$$R = \begin{bmatrix} r_{11} & \dots & r_{1n} \\ \vdots & \dots & \vdots \\ r_{m1} & \dots & r_{mn} \end{bmatrix} \tag{3}$$

$$r_{ij} = \frac{x_{ij}}{\sqrt{\sum_{i=1}^m x_{ij}^2}} \tag{4}$$

(3) Calculating the weighted normalized decision matrix. The weighted normalized value  $v_{ij}$  is calculated as follows:

$$v_{ij} = w_j * r_{ij} \quad , \quad \begin{matrix} i = 1, 2, \dots, m \\ j = 1, 2, \dots, n \end{matrix} \tag{5}$$

where  $w_j$  is the weight of the  $i^{\text{th}}$  attribute or criterion, and  $\sum_{j=1}^n w_j = 1$ .

(4) Determining the positive ideal solution (PIS) and negative ideal solution (NIS):

$$A^+ = \{v_1^+, \dots, v_j^+, \dots, v_n^+\} = \{(\max_j v_{ij} | i \in I), (\min_j v_{ij} | i \in J)\} \tag{6}$$

$$A^- = \{v_1^-, \dots, v_j^-, \dots, v_n^-\} = \{(\min_j v_{ij} | i \in I), (\max_j v_{ij} | i \in J)\} \tag{7}$$

where  $I$  is associated with benefit criteria, and  $J$  is associated with cost criteria.

(5) Calculating the separation measures using the  $n$ -dimensional Euclidean distance. The separation of each alternative from the ideal solution is given by:

$$S_i^+ = \sqrt{\sum_{j=1}^n (V_{ij} - V_j^+)^2} \tag{8}$$

$$S_i^- = \sqrt{\sum_{j=1}^n (V_{ij} - V_j^-)^2} \tag{9}$$

(6) Calculating the relative closeness to the ideal solution. The relative closeness of the alternative  $A_i$  with respect to  $A^+$  is defined as follows:

$$C_i = \frac{S_i^-}{S_i^- + S_i^+} \tag{10}$$

Finally, the preferred orders can be obtained according to the similarities to PIS ( $C_i$ ) in descending order to choose the best alternatives

### 3. RESEARCH METHODOLOGY

According to the literature review, 42 key performance indicators were obtained, the number of these indices

reached 22 by the Delphi method with a statistical population consisting of 10 experts. All steps performed in this study are shown in Figure 1.

A total of 24 indicators were assessed by distributing the questionnaire based on the Likert scale between experts. Cronbach's alpha was used to measure the internal consistency of the questionnaire and, in fact, its reliability. Cronbach's alpha is obtained at 0.83, which is good according to Table 2. At this stage, 130 questionnaires were distributed and ranked according to Table 3 to select the most important indicators.

**TABLE 2.** Cronbach's alpha values [54]

Reliability	Cronbach's alpha coefficients
Excellent	$\alpha \geq 0.9$
Good	$0.8 \leq \alpha \leq 0.9$
Acceptable	$0.7 \leq \alpha \leq 0.8$
Questioned	$0.6 \leq \alpha \leq 0.7$
Poor	$0.5 \leq \alpha \leq 0.6$
unacceptable	$\alpha \leq 0.5$

**TABLE 3.** Selection of the most important key performance indicators

KPIs	Mean Index	Rank
Cost	4.289	1
Schedule	4.273	2
Safety	4.260	3
Quality	4.242	4
Environment	4.210	5
Client satisfaction	4.202	6
Team satisfaction	4.192	7
Profitability	4.172	8
Productivity	4.140	9
Sustainability	4.120	10
Stakeholder satisfaction	4.111	11
Integration	4.091	12
User expectation and satisfaction	4.091	13
Communication	4.061	14
Functionality	4.050	15
Risk	4.040	16
Billing	4.020	17
Procurement	4.020	18
Technical performance	4.010	18
Supply chain	4.000	19
Scope	3.990	20
Innovation	3.959	21

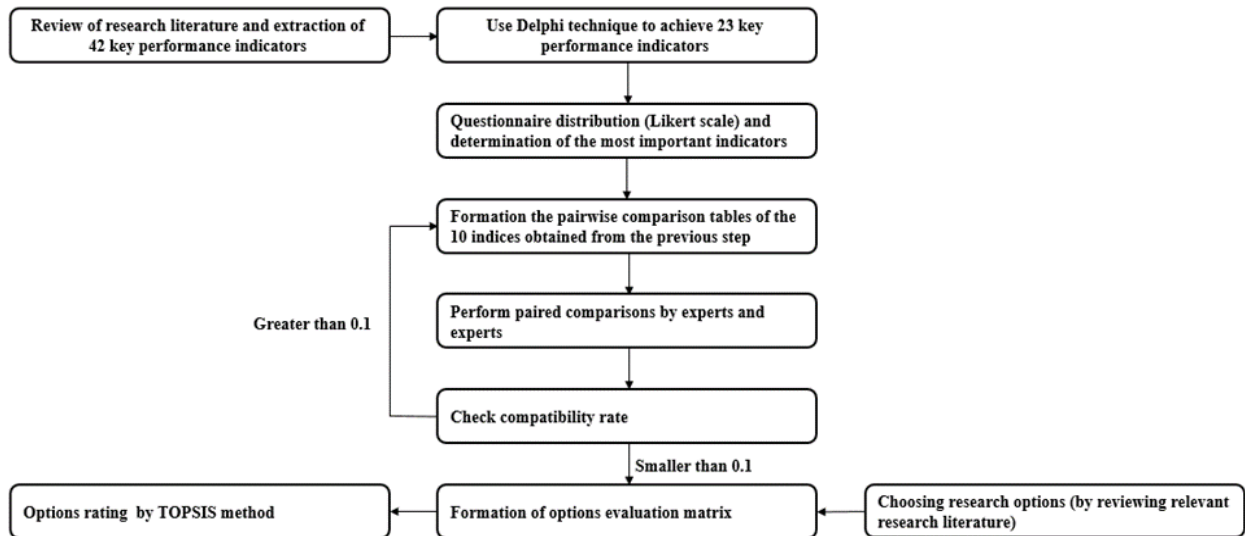


Figure 1. Diagram of Research Methodology

Ranking Key Performance Indicators Based on The Causes of Claims

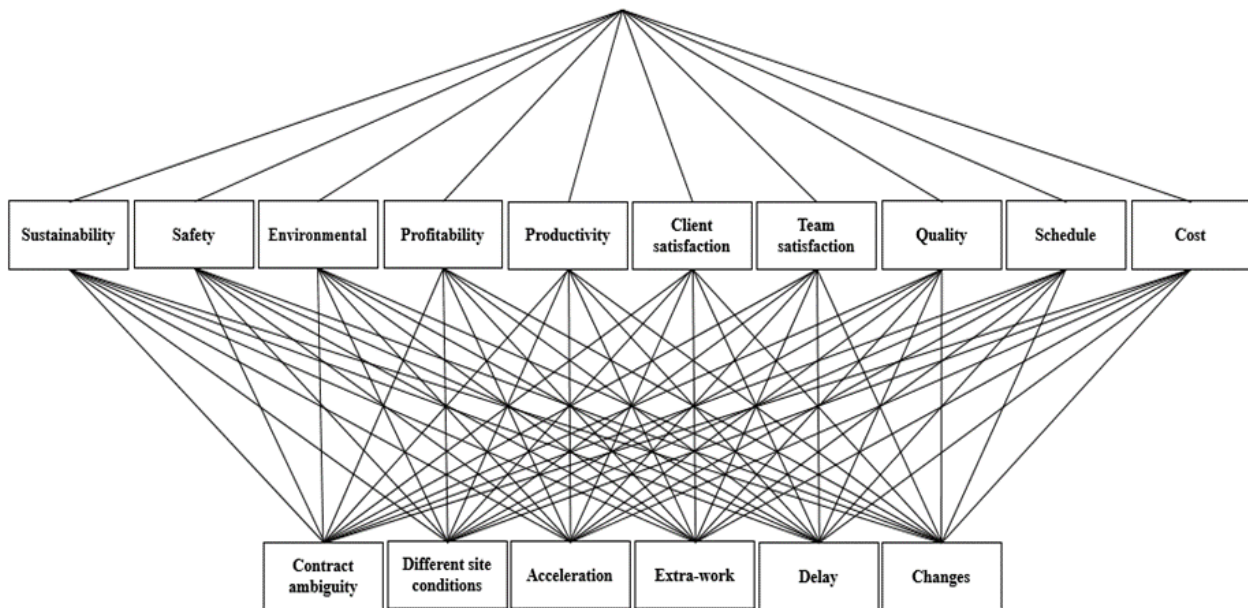


Figure 2. Research hierarchy model

#### 4. RESULTS

In this study, due to a large number of options and factors resulting in increased pairwise comparisons, a hybrid approach was used to ensure accuracy. The relative importance of the indicators was determined by the AHP method and the ranking of options by the TOPSIS method. In fact, using the hybrid method reduces the number of computations and even comparisons by at least half, which is an acceptable and

reasonable solution besides accurately calculating and computing results. Quantitative and qualitative criteria can also be involved in the evaluation at the same time. The ranking hierarchy for the research is shown in Figure 3.

We examined the performance indicators of scheduling, safety, cost, customer satisfaction, quality, team satisfaction, profitability, productivity, sustainability, and the environment, among the questionnaire’s first 10 performance indicators.

Thus, 10 factors obtained from the analysis of the questionnaire results were ranked by the AHP method, and each weight was determined as required by the TOPSIS method. Since the software incompatibility rate is 0.03, then the compatibility is found in paired comparisons, and the results can be trusted. The ratings and weights of the AHP are summarized in Table 4.

The options were then ranked by the TOPSIS method, and the results from the analysis of the answers are listed in Table 5.

**TABLE 4.** Relative importance of key performance indicators

KPIs	Wi	Rank
Safety	0.212	1
Environmental	0.107	2
Cost	0.101	3
Profitability	0.094	4
Schedule	0.093	5
Productivity	0.092	6
Sustainability	0.082	7
Quality	0.082	7
Client satisfaction	0.076	8
Team satisfaction	0.063	9

**TABLE 5.** Ranking the causes of claim

Causes of claim	Pi	Rank
Delays	0.728	1
Changes	0.640	2
Acceleration	0.632	3
Extra work	0.519	4
Different site conditions	0.493	5
Contract ambiguity	0.114	6

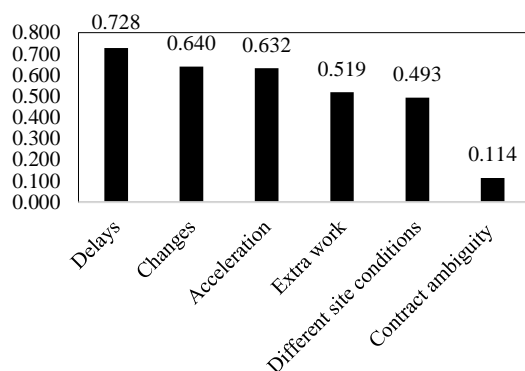


**Figure 3.** Comparative graph of the proximity coefficients of options

## 5. DISCUSSION AND CONCLUSIONS

According to the relevant literature review results, it can be said that claims occur in most construction projects. But most of these claims are not treated correctly. A lot of research has been done in this field in different countries. Every year a lot of time and money is spent around the world settling construction claims. Therefore, it is crucial to use a correct management process to reduce the claims to resolve the problems. The claim management process involves a number of steps useful to improve project efficiency if performed correctly and accurately by experts. Claims have a major impact on the performance of construction projects and their success or failure. Construction projects and their related contracts are a large and complex collection of documents. Often these documents are not properly understood by various factors involved in the project or each with a different interpretation of the contract clauses, leading to a conflict. If these claims are not resolved correctly, they will cause disputes in construction projects. For this reason, having a good documentation system has become an essential requirement in resolving claims. In fact, this documentation system will assist the claim management process to prevent disputes. For correctly claim management, time, cost, and an expert workforce trained in the proper use of the documentation and reporting system are required. If all are followed, an effective step will be taken to improve project efficiency in all areas.

According to the results, the reasons for making claims in construction projects in Iran are delays, changes, acceleration, extra-work, different site conditions, and contract ambiguity. The key performance indicators used in this ranking, in order of priority, include safety, environment, cost, profitability, scheduling, productivity, sustainability, quality, customer satisfaction, and team satisfaction.

Delays with a proximity factor of 0.728 are the most important cause of claims that significantly impact key performance indicators of the project. Changes also occur in most construction projects, with a coefficient of 0.640 seconds. Then, acceleration, extra-work, different site conditions, and contract ambiguity with coefficients of 0.632, 0.519, 0.493, and .114 are placed in the next priorities, respectively. As such, the importance of having a documentation and reporting system in projects is clear. It needs serious scrutiny. Training team members and project staff about the requirements of contract clauses and clearly defining the purpose of contract clauses are essential steps in construction projects. This can partially help to partially alleviate and resolve claims to improve performance and minimize disagreements.

## 6. REFERENCES

- Hadikusumo, B.H. and Tobgay, S., "Construction claim types and causes for a large-scale hydropower project in bhutan", *Journal of Construction in Developing Countries*, Vol. 20, No. 1, (2015), 49, doi.
- Semple, C., Hartman, F.T. and Jergeas, G., "Construction claims and disputes: Causes and cost/time overruns", *Journal of Construction Engineering Management*, Vol. 120, No. 4, (1994), 785-795, [https://doi.org/10.1061/\(ASCE\)07339364\(1994\)120:4\(785\)](https://doi.org/10.1061/(ASCE)07339364(1994)120:4(785))
- Jergeas, G.F. and Hartman, F.T., "Contractors' construction-claims avoidance", *Journal of Construction Engineering Management*, Vol. 120, No. 3, (1994), 553-560, doi. [https://doi.org/10.1061/\(ASCE\)07339364\(1994\)120:3\(553\)](https://doi.org/10.1061/(ASCE)07339364(1994)120:3(553))
- Perrigot, R., López-Fernández, B. and Basset, G., "Conflict management capabilities in franchising", *Journal of Retailing Consumer Services*, Vol. 63, (2021), 102694, <https://doi.org/10.1016/j.jretconser.2021.102694>
- Kumaraswamy, M.M., "Conflicts, claims and disputes in construction", *Engineering Construction Architectural Management*, Vol. 4, No. 2, (1997), 95-111, <https://doi.org/10.1108/eb021042>
- Vidogah, W. and Ndekugri, I., "Improving management of claims: Contractors' perspective", *Journal of Management in Engineering*, Vol. 13, No. 5, (1997), 37-44, <https://doi.org/10.1080/014461998372385>
- Ho, S.P. and Liu, L.Y., "Analytical model for analyzing construction claims and opportunistic bidding", *Journal of Construction Engineering Management*, Vol. 130, No. 1, (2004), 94-104, [https://doi.org/10.1061/\(ASCE\)0733-9364\(2004\)130:1\(94\)](https://doi.org/10.1061/(ASCE)0733-9364(2004)130:1(94))
- Kululanga, G., Kuotcha, W., McCaffer, R. and Edum-Fotwe, F., "Construction contractors' claim process framework", *Journal of Construction Engineering Management*, Vol. 127, No. 4, (2001), 309-314, [https://doi.org/10.1061/\(ASCE\)07339364\(2001\)127:4\(309\)](https://doi.org/10.1061/(ASCE)07339364(2001)127:4(309))
- Hashem M. Mehany, M.S. and Grigg, N., "Causes of road and bridge construction claims: Analysis of colorado department of transportation projects", *Journal of Legal Affairs Dispute Resolution in Engineering Construction*, Vol. 7, No. 2, (2015), 04514006, [https://doi.org/10.1061/\(ASCE\)LA.1943-4170.0000162](https://doi.org/10.1061/(ASCE)LA.1943-4170.0000162)
- Callahan, J.T., "Managing transit construction contract claims, Transportation Research Board, (1998).
- Khanchitvorakul, S., "Development of construction claim supporting system", Master of Engineering King Mongkut University of Technology Thonburi, (2000).
- Suryawanshi, C., *Analysis of claims based on provisions in 4th edition of fidic contracts*. 2010, Retrieved from the NBMCW website: <https://www.nbmcw.com/project-mgmt> ....
- Shahhosseini, V. and Hajarolasvadi, H., "A conceptual framework for developing a bim-enabled claim management system", *International Journal of Construction Management*, Vol. 21, No. 2, (2021), 208-222, doi. <https://doi.org/10.1080/15623599.2018.1512182>
- Riad, N., Arditi, D. and Mohammadi, "A conceptual model for claim management in construction: An ai approach", *Computers Structures*, Vol. 40, No. 1, (1991), 67-74, [https://doi.org/10.1016/0045-7949\(91\)90458-X](https://doi.org/10.1016/0045-7949(91)90458-X)
- Shahhossein, V., Afshar, M.R. and Amiri, O., "The root causes of construction project failure", *Scientia Iranica*, Vol. 25, No. 1, (2018), 93-108, <https://doi.org/10.24200/sci.2017.4178>
- Enshassi, A., Choudhry, R.M. and El-Ghandour, S., "Contractors' perception towards causes of claims in construction projects", *International Journal of Construction Management*, Vol. 9, No. 1, (2009), 79-92, <https://doi.org/10.1080/15623599.2009.10773123>
- Richbell, D., "Mediation of construction disputes, John Wiley & Sons, (2009).
- Leon, H., Osman, H., Georgy, M. and Elsaid, M., "System dynamics approach for forecasting performance of construction projects", *Journal of Management in Engineering*, Vol. 34, No. 1, (2018), 04017049, [https://doi.org/10.1061/\(ASCE\)ME.1943-5479.0000575](https://doi.org/10.1061/(ASCE)ME.1943-5479.0000575)
- Korde, T., Li, M. and Russell, A.D., "State-of-the-art review of construction performance models and factors", in Construction Research Congress 2005: Broadening Perspectives. (2005), 1-14.
- Fung, H.P. and Siow, H., "Relationship between team satisfaction and project performance as perceived by project managers in malaysia—a mixed methods study", *Open Journal of Social Science Research OJSSR*, Vol. 1, No. 9, (2013), 238-249, <https://doi.org/10.12966/OJSSR.12.02.2013>
- Parfitt, M.K. and Sanvido, V., "Checklist of critical success factors for building projects", *Journal of Management in Engineering*, Vol. 9, No. 3, (1993), 243-249, [https://doi.org/10.1061/\(ASCE\)9742-597X\(1993\)9:3\(243\)](https://doi.org/10.1061/(ASCE)9742-597X(1993)9:3(243))
- Freeman, M. and Beale, P., "Measuring project success, Project Management Institute. (1992).
- Alvanchi, A., Shiri, N. and Alikhani, H., "In-depth investigation of project planning and control software package application in the construction industry of iran", *International Journal of Engineering*, Vol. 33, No. 10, (2020), 1817-1825, <https://doi.org/10.5829/ije.2020.33.10.a01>
- Pmi, A., "Guide to the project management body of knowledge", in Project Management Institute. Vol. 130, (2008).
- Reid, A. and Ellis, R.C., "Common sense applied to the definition of a dispute", *Structural Survey*, (2007), <https://doi.org/10.1108/02630800710772827>
- Ndekugri, I. and Russell, V., "Disputing the existence of a dispute as a strategy for avoiding construction adjudication", *Engineering, Construction Architectural Management*, Vol., No., (2006), doi. <https://doi.org/10.1108/09699980610680180>
- Le-Hoai, L., Dang, C.N., Lee, S.B. and Lee, Y.D., "Benchmarking claim causes against contractors in emerging markets: Empirical case study", *International Journal of Construction Management*, Vol. 19, No. 4, (2019), 307-316, <https://doi.org/10.1080/15623599.2018.1435156>
- Sibanyama, G., Muya, M. and Kaliba, C., "An overview of construction claims: A case study of the zambian construction industry", *International Journal of Construction Management*, Vol. 12, No. 1, (2012), 65-81, <https://doi.org/10.1080/15623599.2012.10773185>
- Stamatiou, D.R.I., Kirytopoulos, K.A., Ponis, S.T., Gayialis, S. and Tatiopoulos, I., "A process reference model for claims management in construction supply chains: The contractors' perspective", *International Journal of Construction Management*, Vol. 19, No. 5, (2019), 382-400, <https://doi.org/10.1080/15623599.2018.1452100>
- Revay, S., "Can construction claims be avoided? Building owners and engineers frequently occurring claims identified", *Building Research and Information*, Vol. 21, No. 1, (1993), 56-58, doi.
- Zanelidin, E.K., "Construction claims in united arab emirates: Types, causes, and frequency", *International Journal of Project Management*, Vol. 24, No. 5, (2006), 453-459, <https://doi.org/10.1016/j.ijproman.2006.02.006>
- Hayati, K., Latief, Y. and Sarasati, A.D., "Causes and problem identification in construction claim management", in IOP

- Conference Series: Materials Science and Engineering, IOP Publishing. Vol. 469, No. 1, (2019), 012082.
33. Bakhary, N.A., Adnan, H. and Ibrahim, A., "A study of construction claim management problems in malaysia", *Procedia Economics Finance*, Vol. 23, (2015), 63-70, [https://doi.org/10.1016/S2212-5671\(15\)00327-5](https://doi.org/10.1016/S2212-5671(15)00327-5)
  34. Yusuwan, N.M. and Adnan, H., "Issues associated with extension of time (eot) claim in malaysian construction industry", *Procedia Technology*, Vol. 9, (2013), 740-749, <https://doi.org/10.1016/j.protcy.2013.12.082>
  35. Tabassi, A.A., Abdullah, A. and Bryde, D.J., "Conflict management, team coordination, and performance within multicultural temporary projects: Evidence from the construction industry", *Project Management Journal*, Vol. 50, No. 1, (2019), 101-114, <https://doi.org/10.1177/8756972818818257>
  36. Mukilan, K., Rameshbabu, C. and Velumani, P., "A modified particle swarm optimization for risk assessment and claim management in engineering procurement construction projects", *Materials Today: Proceedings*, Vol. 42, (2021), 786-794, <https://doi.org/10.1016/j.matpr.2020.11.315>
  37. Neely, A., Mills, J., Platts, K., Richards, H., Gregory, M., Bourne, M. and Kennerley, M., "Performance measurement system design: Developing and testing a process-based approach", *International Journal of Operations Production Management*, (2000), <https://doi.org/10.1108/01443570010343708>
  38. Leong, T.K., Zakuan, N., Mat Saman, M.Z., Ariff, M., Md, S. and Tan, C.S., "Using project performance to measure effectiveness of quality management system maintenance and practices in construction industry", *The Scientific World Journal*, Vol. 2014, (2014), <https://doi.org/10.1155/2014/591361>
  39. Asgari, M., Kheyroddin, A. and Naderpour, H., "Evaluation of project critical success factors for key construction players and objectives", *International Journal of Engineering, Transactions B: Applications*, Vol. 31, No. 2, (2018), 228-240, <http://doi.org/10.5829/ije.2018.31.02b.06>
  40. Hwang, B.-G., Thomas, S.R., Haas, C.T. and Caldas, C.H., "Measuring the impact of rework on construction cost performance", *Journal of Construction Engineering and Management*, Vol. 135, No. 3, (2009), 187-198.
  41. Omar, M.N. and Fayek, A.R., "Modeling and evaluating construction project competencies and their relationship to project performance", *Automation in Construction*, Vol. 69, (2016), 115-130, <https://doi.org/10.1016/j.autcon.2016.05.021>
  42. Wibowo, M.A., Astana, I.N.Y. and Rusdi, H., "Dynamic modelling of the relation between bidding strategy and construction project performance", *Procedia Engineering*, Vol. 171, (2017), 341-347, <http://doi.org/10.1016/j.proeng.2017.01.342>
  43. Bourne, M., Franco-Santos, M., Micheli, P. and Pavlov, A., "Performance measurement and management: A system of systems perspective", *International Journal of Production Research*, Vol. 56, No. 8, (2018), 2788-2799, <https://doi.org/10.1080/00207543.2017.1404159>
  44. Lop, N., Ismail, K., Isa, H.M. and Khalil, N., "An effective approach of performance measurement systems (pms) for adoption in construction projects", *Journal of Engineering Science and Technology*, Vol. 13, No. 12, (2018), 3951-3963.
  45. Marzouk, M.M. and Gaid, E.F., "Assessing egyptian construction projects performance using principal component analysis", *International Journal of Productivity and Performance Management*, Vol. 67, No. 9, (2018), 1727-1744.
  46. Sulieman, H. and Alfaraidy, F., "Influences of project management capabilities on the organizational performance of the saudi construction industry", *Engineering, Technology & Applied Science Research*, Vol. 9, No. 3, (2019), 4144-4147.
  47. Sun, M. and Meng, X., "Taxonomy for change causes and effects in construction projects", *International Journal of Project Management*, Vol. 27, No. 6, (2009), 560-572. <https://doi.org/10.1016/j.ijproman.2008.10.005>
  48. Patil, Y., Bhatt, D. and Kambekar, A., "Anatomy of construction claims", AR, Anatomy of Construction Claims (February 22, 2019), (2019).
  49. Callahan, M.T., "Construction delay claims, Aspen publishers, (2010).
  50. Sanders, D. and Eagles, W., "Delay, disruption and acceleration claims", Borden Ladner Gervais LLP, Vol. 3, (2001).
  51. Saaty, T.L., "The analytic hierarchy process for decision in a complex world", Pittsburgh: RWS Publications, (1980).
  52. Zavadskas, E.K., Vilutiene, T., Turskis, Z. and Tamosaitiene, J., "Contractor selection for construction works by applying saw-g and topsis grey techniques", *Journal of Business Economics Management*, Vol. 11, No. 1, (2010), 34-55.
  53. Banihashemi, S.A., Khalilzadeh, M., Antucheviciene, J. and Šaparauskas, J., "Trading off time-cost-quality in construction project scheduling problems with fuzzy swara-topsis approach", *Buildings*, Vol. 11, No. 9, (2021), 387, <https://doi.org/10.3390/buildings11090387>
  54. Siswaningsih, W., Firman, H. and Khoirunnisa, A., "Development of two-tier diagnostic test pictorial-based for identifying high school students misconceptions on the mole concept", in Journal of Physics: Conference Series, IOP Publishing. Vol. 812, No. 1, (2017), 012117.

---

### Persian Abstract

---

#### چکیده

در چرخه حیات پروژه‌های صنعت ساخت، عوامل بسیاری نقش دارند که منابع و روابط انسانی محور اصلی پیشرفت فعالیت هاست. بنابراین تضاد منافع بین ذینفعان در پروژه های این صنعت مساله ای بدیهی و چالش برانگیز است. افزایش تعداد ذینفعان در پروژه، موجب پیچیدگی روابط انسانی و در نتیجه سیر صعودی احتمال تعارضات می شود. این تعارضات در صورت عدم حل و فصل می تواند منجر به ایجاد ادعا خواهند شد. مدیریت ضعیف دعاوی بر موفقیت پروژه‌های عمرانی و مدیریت هزینه و زمان آنها تأثیرگذار است. از این رو هدف از انجام این تحقیق آن است تا با شناسایی و رتبه‌بندی علل ایجاد دعاوی و تحلیل اثرات آنها بر شاخص‌های کلیدی عملکرد، گامی جهت بهبود عملکرد پروژه‌ها برداشته شود. در ابتدا دلایل ایجاد ادعا طبق نظر خبرگان و ادبیات پژوهش جمع‌آوری گردیده و براساس شاخص‌های کلیدی عملکرد و با روش ترکیبی AHP-TOPSIS رتبه‌بندی شده است. یافته ها نشان داد که تأخیرات با ضریب نزدیکی ۰.۷۲۸ مهمترین عامل ایجاد ادعاها هستند که تأثیر زیادی بر شاخص‌های کلیدی عملکرد پروژه دارند. تغییرات هم که در اغلب پروژه‌های عمرانی ایجاد می‌شوند، در رتبه دوم قرار دارند. سپس دستور تسریع، کار اضافی، تغییر شرایط کارگاهی، و ابهامات قراردادی در اولویت‌های بعدی قرار دارند. نتایج این تحقیق می‌تواند چالش‌های موجود در مدیریت دعاوی صنعت ساخت‌وساز را کاهش داده و اتمام موفقیت‌آمیز پروژه‌ها را تضمین کند.

---



## Stable Operation Limits in Dual Active Bridge for SuperCapacitor Applications

A. Bandani, F. Barati\*

Division of Energy, Materials and Energy Research Center, Karaj, Iran

### PAPER INFO

#### Paper history:

Received 04 December 2021

Received in revised form 26 January 2022

Accepted 01 February 2022

#### Keywords:

Dual-Active Bridge

SuperCapacitor Energy Storage

Phase-Shift Angle

Stable Operation Limits

### ABSTRACT

This paper presents an idea for limiting the phase-shift angle in Dual Active Bridge (DAB) which ensures the converter's stability. The stability is the main criterion in a converter's operation without which the converter will stop working. In an ideal DAB which comprises of ideal components, the phase-shift angle limit is  $90^\circ$ . We developed a detailed model in Matlab/Simulink for DAB based on which the limits for the stable operation of converter are derived. In the developed model, attempts are made to employ as accurate as possible models for the components. In this way, the limits are expected to be very close to the practice. The DAB is a bi-directional converter; meaning that the power flow occurs in both forward and reverse directions. We derived the limits separately for forward and reverse modes. It is shown that the limits are the same for both directions confirming the fact that the DAB is symmetrical. We employed the DAB as the SuperCapacitor (SC) energy storage's interface in this paper.

doi: 10.5829/ije.2022.35.05b.04

## 1. INTRODUCTION

Renewable energy sources such as Photovoltaic (PV), Wind, and etc. have fluctuations in their generated power, since they depend on the climate and environmental conditions. On the other hand, there are loads which need constant powers. So, there is always a mismatching between the generation and the demand in renewable energy systems. To resolve this problem, electrical energy storage elements are employed. These elements such as batteries, Supercapacitors (SC), and etc. need interfacing converters which perform their charging and discharging properly. The interfacing converters employed for energy storage elements must be bi-directional to perform both charging and discharging operations [1-5].

The Dual-Active Bridge (DAB) is a bi-directional isolated dc/dc converter as shown in Figure 1. The main reasons for galvanic isolation between sources in multiple-source systems are personal security, noise reduction and voltage matching. The isolation is performed by a high frequency transformer. The DAB is employed in various applications such as renewable energies, power systems, hybrid storage elements,

military equipment, and etc. [6, 7]. In Figure 2, a generic schematic is shown for the isolated bi-directional dc/dc converters.

The DAB is proposed in 1990 for the first time [8, 9]. After many years, the advances in power electronics devices and magnetic materials have resulted in a more efficient converter [10, 11]. The power rating in a bi-directional converter is proportional to the number of switches. Therefore, the power rating in a DAB is more than other types of bi-directional converters such as the push pull, half bridge, and etc. [12].

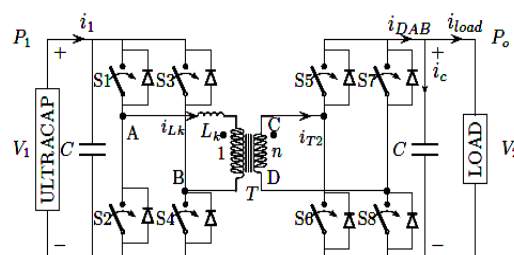
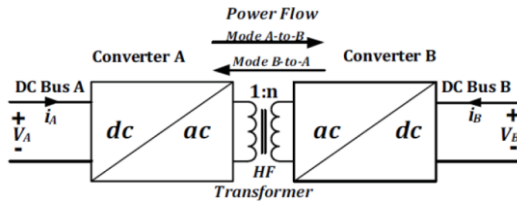


Figure 1. A dual-active bridge utilized for supercapacitor applications

\*Corresponding Author Institutional Email: [f.barati@merc.ac.ir](mailto:f.barati@merc.ac.ir) (F. Barati)



**Figure 2.** A generic schematic for a dc/dc isolated bi-directional converter

The SCs are among the most advanced energy storage elements. They have features such as high power density, suitable and safe for the environment, low shelf discharge, wide operating temperature range, fast charging and discharging capabilities, high capacities and very high life cycles. Because of the limited energy stored in SCs, their associated converters can operate only at some limited periods of time. This type of converters' operation is called the intermittent operation [13]. They are also combined with batteries and fuel cell which form hybrid energy storage [14].

Base on literature [15-17], the modelling, design, and control of DAB in different conditions and applications are presented. Stability and power transfer analysis of DAB are presented [18-20]. Ghani et al. [21] employed an online particle swarm technique to optimize the DAB phase-shift angle; for a bi-directional dc-dc converter, a current-limit control scheme is presented. The presented scheme aimed to prevent the converter from becoming unstable. The similar work presented by Ahmadi et al. [22] for the DAB; we need to make sure that the converter is prevented from becoming unstable condition. In an ideal DAB, the phase-shift angle limit above which the converter becomes unstable is 90°. Based on this, all of the previous works considered 90° as the stability limit of DAB.

In this paper, by employing a detailed model, we will show that it is not valid to consider 90° as the stability limit of DAB. In fact, we will show that, depending on the converter's parameters, a phase-shift angle less than 90° must be considered as the DAB's stability limit.

## 2. OPERATION PRINCIPLES OF DUAL- ACTIVE BRIDGE

In this section, the operation principles of DAB are presented. The DAB's operation is based on the Phase-Shift Modulation (PSM). This means that the switching signals for one of the bridges are phase-shifted with respect to those of the other bridge.

### A. Different Types of Phase-Shift Modulation

There are four types of phase-shift modulation including the Single Phase-Shift (SPS), Extended Phase-Shift

(EPS), Dual Phase- Shift (DPS), and Triple Phase-Shift (TPS) as discussed by Kayaalp et al. [23]. We employed a SPS as shown in Figure 3 in this paper. As seen, the bridge 2's AC voltage is phase-shifted with respect to the bridge 1's AC voltage. The phase-shift angle  $\varphi$  can be positive or negative. A positive phase-shift angle results in a power flow from bridge 1 to bridge 2 which is called the forward mode of operation. The reverse mode of operation occurs when the phase-shift angle is negative resulting in a power flow from bridge 2 to bridge 1. The DAB with the SPS has the advantages of simplicity and great stability. It also provides the maximum power delivery capability. It has, however, the disadvantages such as lower efficiency and dynamic response compared to the other types of phase-shift modulation [23].

In the SPS modulation, by considering ideal components, the equation for power delivered to the output can be obtained as follows [23, 24].

$$P_o = \frac{nv_1v_2}{2\pi^2f_sL_s} \varphi(\pi - \varphi) \tag{1}$$

which  $V_1$  is the input voltage,  $V_2$  is the output voltage,  $n$  is the transformer turns ratio,  $\Phi$  is the phase-shift angle in radians,  $f_s$  is the switching frequency and  $L_s$  is the total inductance when everything is moved to the secondary of transformer. It can also be shown that the following equation can be derived for the output voltage.

$$V_2 = \frac{nv_1}{2\pi^2f_sL_s} R_L \varphi(\pi - \varphi) \tag{2}$$

where,  $R_L$  is the load. Based on this equation, for fixed  $V_1$  and  $R_L$ , the output voltage is dependent on the phase-shift angle  $\varphi$ . So, by changing in  $\varphi$ , the output voltage varies accordingly.

### B. Parameters for Designed DAB

We designed a DAB for the SC's applications with the parameters shown in Table 1 for which the idea of phase-shift angle limiting is presented. We, however, want to confirm that the idea is generic and can be employed for a DAB with any parameters. According to Equation (1),

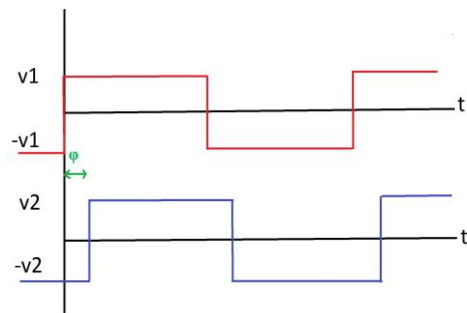


**Figure 3.** AC side voltages of bridge 1 and bridge 2 with SPS modulation

**TABLE 1.** Parameters of designed DAB for SC applications

Symbol	Description	Value
$L_s(\mu H)$	Total inductance	120
$n = \frac{n_2}{n_1}$	Transformer turns ratio	8
$f_s(kHz)$	Switching frequency	20
$V_{CE}(V)$	On-state IGBT's collector to emitter voltage	3
$V_{FD}(V)$	Forward biased anti-parallel diode voltage	1.6
$t_{db}(\mu s)$	Dead-beat	2
$R_1(\Omega)$	Transformer primary winding resistance	0.06
$R_2(\Omega)$	Transformer secondary winding resistance	0.13
$C_{sc}(F)$	Capacitance of SC	18
$V_1(V)$	Input voltage nominal value	48
$V_2(V)$	Output voltage nominal value	400
$i_{load}(A)$	Output current nominal value	10

the amounts of power delivered to the output in DAB depends on  $V_1$ ,  $V_2$ ,  $n$ ,  $f_s$ ,  $\Phi$ , and  $L_s$ . For a DAB with given parameters, the values of  $n$ ,  $f_s$ , and  $L_s$  are fixed. In order to regulate the output voltage at a desired value, despite the SC's voltage varies, the phase-shift angle must be adjusted appropriately by the closed-loop control system. In the case of a voltage drop at the output, the phase-shift angle will be increased in the positive direction to restore the output voltage. This leads to the SC discharging. Also, in the case of a voltage swell at the output, the phase-shift angle will be increased in the negative direction to restore the output voltage which leads to the SC charging. However, in both cases of DAB's forward and reverse modes, the phase-shift angle must be appropriately limited in order to keep the converter stable.

### C. Limits for Phase-Shift Angle in Ideal DAB

As seen in Equation (2),  $V_2$  versus  $\varphi$  is a quadratic parabolic function whose maximum is obtained if the derivative of  $V_2$  with respect to  $\varphi$  is set to zero. That is:

$$\frac{dV_2}{d\varphi} = 0 \rightarrow \varphi = \frac{\pi}{2} \quad (3)$$

This means that, in the ideal DAB, at the phase-shift angle equals to  $+90^\circ$ , the maximum output voltage is obtained. So,  $+90^\circ$  is considered as the phase-shift angle limit above which the DAB becomes unstable.

## 3. STABLE OPERATION LIMITS FOR NON-IDEAL DAB

In order to obtain the phase-shift angle limits for the stable operation of the DAB, we developed a detailed model in Matlab/Simulink. To have a model close to the reality, we, at the first step, include the power switches'

voltage drops, transformer and inductor windings resistances. We call this model a lossy one without the deadbeat. The model is then equipped with the deadbeat as well.

Attempts are made to employ as accurate as possible models for each component. In this way, the obtained limits will be very close to the practice. The model is run in the open-loop mode in which the converter's performance can be evaluated at steady-states for different values of the phase-shift angle.

### D. Lossy Model without Deadbeat

The open-loop simulations of DAB are done in five positive phase-shift angles, i.e.  $5^\circ$ ,  $20^\circ$ ,  $50^\circ$ ,  $70^\circ$ , and  $75^\circ$  which are for the forward mode of operation. Also, five negative phase-shift angles i.e.  $-5^\circ$ ,  $-20^\circ$ ,  $-50^\circ$ ,  $-70^\circ$ , and  $-75^\circ$  are considered for the reverse mode of operation. The results are shown in Figures 4 to 7.

In both cases of forward and reverse modes, we start to increase the phase-shift angle until the exchanged power starts to decrease. The phase-shift angle at which the exchanged power starts to decrease is considered as the limit. We derive the limits separately for the forward and reverse modes.

According to Figures 4 and 5, in the forward mode, by increasing the phase-shift angle up to  $70^\circ$ , the output

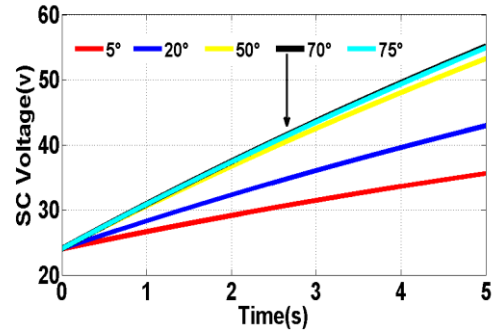


**Figure 4.** Output voltage in forward mode for different phase-shift angles

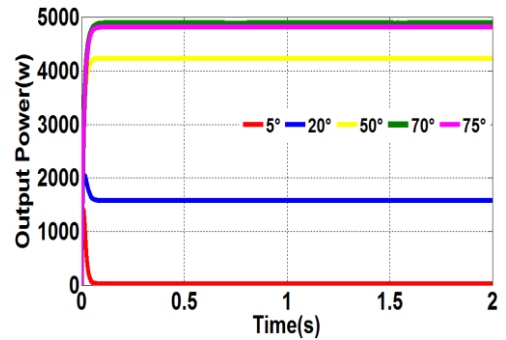


**Figure 5.** Output power in forward mode for different phase-shift angles

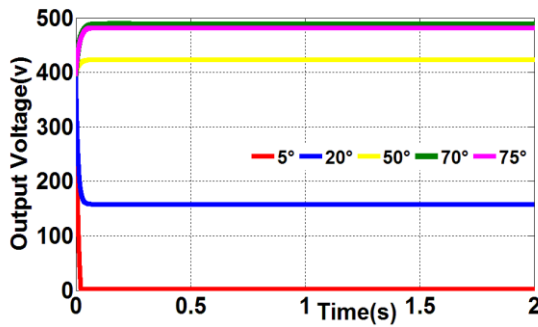


Figure 6. Voltage of SC in reverse mode for different phase-shift angles

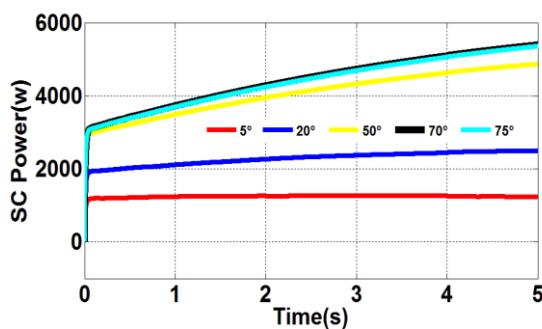


Figure 7. Power absorbed by SC in reverse mode for different phase-shift angles

voltage as well as the power delivered to the output increase. However, for higher phase-shift angles, the output voltage and the power delivered decrease. Therefore, for the stability of converter in this mode, any increase in the phase-shift angle above  $70^\circ$  must be avoided. Note that, tests in the forward mode are performed with nominal input voltage and output current as listed in Table 1.

For the reverse mode, according to Figures 6 and 7, by increasing the phase-shift angle up to  $-70^\circ$ , the SC's voltage as well as the absorbed power by the SC increase. However, for higher phase-shift angles, the SC's voltage and absorbed power decrease. So, the same as the forward mode, in the reverse mode, any increase in the phase-shift angle above  $-70^\circ$  must be avoided in order to keep the converter stable. Tests in the reverse mode are performed with the nominal output voltage and nominal output current injected to the converter's output. Note that, the results in Figures 6 and 7 are dynamic ones, since the SC's charging is in progress. It is also worth mentioning that the limits obtained for the forward and reverse modes are the same implying the fact that the converter is symmetrical.

For different load currents, the output voltage is shown against the phase-shift angle in Figure 8. It is clear that for a specific phase-shift angle, by increasing in the load current, the output voltage decreases which is

expected. Also, for any load current, the output voltage increases as the phase-shift angle is increased until the phase-shift angle reaches the limit, i.e.  $70^\circ$ . Increasing the phase-shift angle above  $70^\circ$  results in decreasing the output voltage and therefore, the power delivered to the output is decreased. This means that  $70^\circ$  is the phase-shift angle limit for the DAB with the listed parameters regardless of the load current.

#### E. Lossy Model with Deadbeat

A  $2\mu\text{s}$  deadbeat is considered for the DAB with the listed parameters in Table 1. It guarantees that no short-circuit occurs in any of the converter's legs. However, it has adverse effects on the converter's performance which are inevitable [25]. In this section, we investigate the deadbeat effects on the power delivery capability as well as the limits of the phase-shift angle.

For a specific load current, the output voltage is shown against the phase-shift angle both for with and without the deadbeat in Figure 9. As clear, in both cases, by increasing in the phase-shift angle, the output voltage increases until the phase-shift angle reaches the limit. The limit equals to  $70^\circ$  for the case of without deadbeat as shown before. It is, however, higher for the case of with deadbeat as clear.

For a specific phase-shift angle, by including the deadbeat, the output voltage is decreased especially at low phase-shift angles as shown. The case gets better as the phase-shift angle increases. This means that, including the deadbeat, which is necessary for the proper operation of converter in practice, has an adverse effect on the power delivery capability of the DAB. We, therefore, want to conclude that including the deadbeat reduces the effective phase-shift angle. As a result of this, the power delivery capability is reduced and the phase-shift angle limit is increased.

In Figure 10, by including the deadbeat, the output voltage is shown against the phase-shift angle for different load currents. As clear, for a specific phase-shift angle, by reducing the load current, the output voltage increases as expected. Also, for a specific load current, by increasing the phase-shift angle, the output voltage increases until the phase-shift angle reaches the limit. As clear, the limit is different for different load currents. In fact, for 1A load current, the limit equals to  $85^\circ$ , for 5A load current, the limit equals to  $80^\circ$ , for 10A load current, the limit equals to  $75^\circ$ , and for 15A load current, the limit equals to  $70^\circ$ . So, by considering 10A as the nominal load current, the limit for the phase-shift angle for the DAB with the listed parameters equals to  $75^\circ$ . Comparing Figures 8 and 10 for 10A load current shows that the phase-shift angle limit is higher for the case of with deadbeat confirming the fact that the deadbeat reduces the effective phase-shift angle. We also want to conclude that the phase-shift angle limit for the reverse mode equals to  $-75^\circ$ , since the converter is symmetrical.

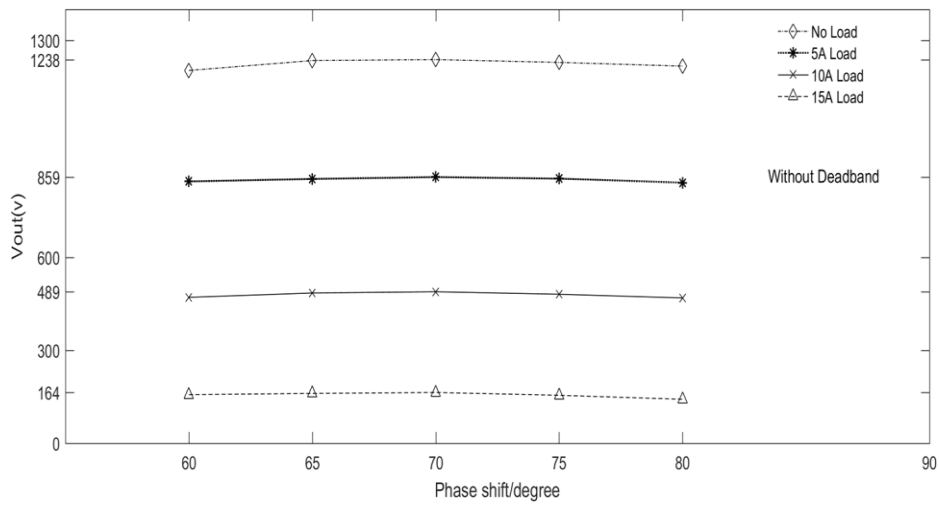


Figure 8. Output voltage versus phase-shift angle for different load currents without including deadband

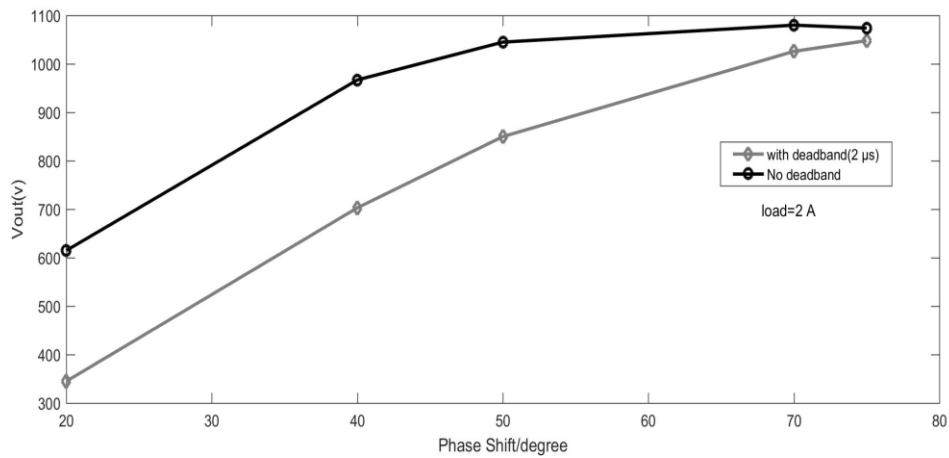


Figure 9. Output voltage versus phase-shift angle for with and without deadband

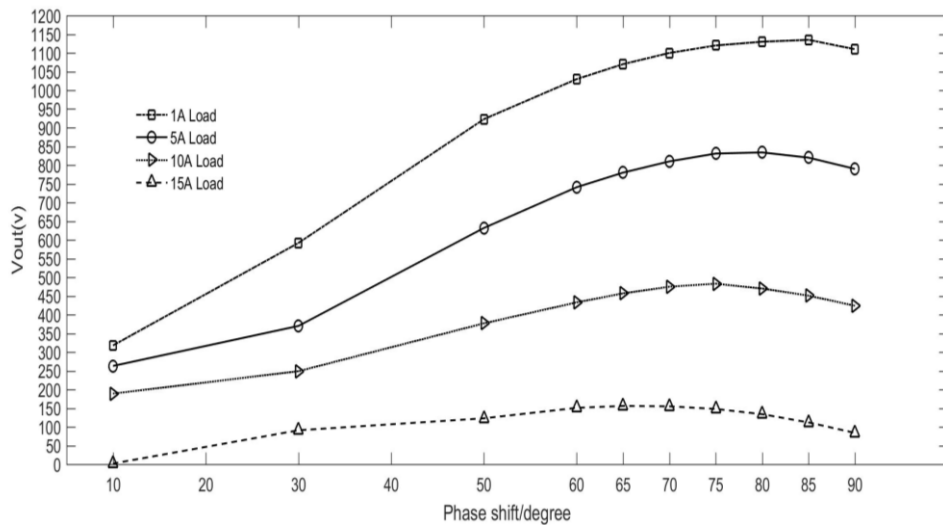


Figure 10. Output voltage versus phase-shift angle with deadbeat for different load currents

#### 4. DISCUSSION

In this section, we present a discussion about the idea of phase-shift angle limiting as well as the results obtained. As said, we limit the phase-shift angle in order to make sure that the converter is stable.

The stability is the main criterion in a power electronics converter's operation. This is because of the fact that, without stability, the converter will stop working soon. So, we limited the phase-shift angle in the DAB according to the stability criterion. There are, of course, other criteria too such as the efficiency, current stress, and etc. However, in the DAB, because of its structure, the efficiency is inherently high. So, it is believed that the most limiting criterion in the DAB's operation is the stability. In the other words, by ensuring the stability, other important criteria such as the efficiency are well met.

For fixed input voltage and output current, the output voltage is shown against the phase-shift angle for different conditions as shown in the previous section. Starting from low phase-shift angles, the output voltage increases as the phase-shift angle is increased up to a certain value. Increasing in the phase-shift angle above the certain value leads to the output voltage decreasing.

This value is considered as the stability limit for the phase-shift angle. This is due to the fact that, the closed-loop control systems' efforts to restore the output voltage, which is through increasing the phase-shift angle in the case of output voltage drop, will result in the output voltage decreasing if the phase-shift angle is moved above the limit. Since the output voltage is not restored, the closed-loop control system increases the phase-shift angle more and more resulting in the output voltage decreasing more and more until the output voltage reaches to zero. The derived limits for the forward and reverse modes, which are the same since the DAB is symmetrical, are employed in the closed-loop control system which guarantees that no increasing above the limits occurs either at dynamic or steady-states [26].

According to Equation (1), imposing limitations on the phase-shift angle means that the maximum power which can be delivered by the converter is accordingly limited. The same happens for the voltage gain as clear from Equation (2). Also, it slows down the dynamic performance of the converter. We call these as the adverse effects of phase-shift angle limiting.

Although the limit for an ideal DAB is  $90^\circ$  regardless of the converter's parameters, the derived limits are for the DAB with the listed parameters. This means that the limits can be different for a DAB with different parameters. So, the same procedure, as shown, must be followed to obtain the limits for any DAB with given parameters. We, however, want to confirm that the derived limits are the converter's characteristics. This

means that they are valid regardless of the converter's application or the converter's input source or output load.

#### 5. CONCLUSIONS

Based on a detailed model developed in Matlab/Simulink, we derived the limits for the phase-shift angle in DAB both for the forward and reverse modes. The operation of converter above these limits must be prevented in order to keep the converter stable. In contrast to the ideal model for which the allowable range of phase-shift angle is  $-90^\circ < \varphi < 90^\circ$ , the non-ideal model's allowable range is  $-75^\circ < \varphi < 75^\circ$  for the converter with the listed parameters. In the non-ideal model, we considered the power switches' voltage drops, transformer and inductor windings resistances, and, of course, the deadbeat. It is also confirmed that the deadbeat reduces the effective phase-shift angle in DAB's operation.

#### 6. REFERENCES

1. Mirhosseini Moghadam, M., Tavakoli, A. and Alizadeh, B., "Stability analysis of ac/dc microgrids in island mode", *International Journal of Engineering, Transactions A: Basics*, Vol. 34, No. 71750-1765, doi: 10.5829/ije.2021.34.07a.20.
2. Sagar, G. and Debela, T., "Implementation of optimal load balancing strategy for hybrid energy management system in dc/ac microgrid with pv and battery storage", *International Journal of Engineering, Transactions A: Basics*, Vol. 32, No. 10, (2019), 1437-1445, doi: 10.5829/ije.2019.32.10a.13.
3. Peng, F.Z., Li, H., Su, G.-J. and Lawler, J.S., "A new zvs bidirectional dc-dc converter for fuel cell and battery application", *IEEE Transactions on Power Electronics*, Vol. 19, No. 1, (2004), 54-65.
4. Su, G.-J. and Peng, F.Z., "A low cost, triple-voltage bus dc-dc converter for automotive applications", in Twentieth Annual IEEE Applied Power Electronics Conference and Exposition, 2005. APEC 2005., IEEE. Vol. 2, (2005), 1015-1021.
5. Chiu, H.-J. and Lin, L.-W., "A bidirectional dc-dc converter for fuel cell electric vehicle driving system", *IEEE Transactions on Power Electronics*, Vol. 21, No. 4, (2006), 950-958.
6. Mi, C., Bai, H., Wang, C. and Gargies, S., "Operation, design and control of dual h-bridge-based isolated bidirectional dc-dc converter", *IET Power Electronics*, Vol. 1, No. 4, (2008), 507-517.
7. Zhang, Z., Ouyang, Z., Thomsen, O.C. and Andersen, M.A., "Analysis and design of a bidirectional isolated dc-dc converter for fuel cells and supercapacitors hybrid system", *IEEE Transactions on power electronics*, Vol. 27, No. 2, (2011), 848-859, doi.
8. De Doncker, R.W., Divan, D.M. and Kheraluwala, M.H., "A three-phase soft-switched high-power-density dc/dc converter for high-power applications", *IEEE Transactions on Industry Applications*, Vol. 27, No. 1, (1991), 63-73.
9. Kheraluwala, M., Gascoigne, R.W., Divan, D.M. and Baumann, E.D., "Performance characterization of a high-power dual active

- bridge dc-to-dc converter", *IEEE Transactions on Industry Applications*, Vol. 28, No. 6, (1992), 1294-1301.
10. Biela, J., Schweizer, M., Waffler, S. and Kolar, J.W., "Sic versus si—evaluation of potentials for performance improvement of inverter and dc-dc converter systems by sic power semiconductors", *IEEE Transactions on Industrial Electronics*, Vol. 58, No. 7, (2010), 2872-2882.
  11. Lee, M.-C., Lin, C.-Y., Wang, S.-H. and Chin, T.-S., "Soft-magnetic fe-based nano-crystalline thick ribbons", *IEEE Transactions on Magnetics*, Vol. 44, No. 11, (2008), 3836-3838.
  12. Zhao, B., Song, Q., Liu, W. and Sun, Y., "Overview of dual-active-bridge isolated bidirectional dc-dc converter for high-frequency-link power-conversion system", *IEEE Transactions on Power Electronics*, Vol. 29, No. 8, (2013), 4091-4106.
  13. Gurusinge, N., Kularatna, N., Round, W.H. and Steyn-Ross, D.A., "Energy-limited transient-mode fast supercapacitor charger topology", *IEEE Transactions on Power Electronics*, Vol. 32, No. 2, (2016), 911-914.
  14. Ibanez, F.M., Echeverria, J.M., Vadillo, J. and Fontan, L., "A step-up bidirectional series resonant dc/dc converter using a continuous current mode", *IEEE Transactions on Power Electronics*, Vol. 30, No. 3, (2014), 1393-1402.
  15. Costinett, D., Maksimovic, D. and Zane, R., "Design and control for high efficiency in high step-down dual active bridge converters operating at high switching frequency", *IEEE Transactions on Power Electronics*, Vol. 28, No. 8, (2012), 3931-3940.
  16. Zhao, B., Yu, Q. and Sun, W., "Extended-phase-shift control of isolated bidirectional dc-dc converter for power distribution in microgrid", *IEEE Transactions on Power Electronics*, Vol. 27, No. 11, (2011), 4667-4680.
  17. Krismer, F. and Kolar, J.W., "Accurate small-signal model for the digital control of an automotive bidirectional dual active bridge", *IEEE Transactions on Power Electronics*, Vol. 24, No. 12, (2009), 2756-2768.
  18. Barlik, R., Nowak, M. and Grzejszczak, P., "Power transfer analysis in a single phase dual active bridge", *Bulletin of the Polish Academy of Sciences. Technical Sciences*, Vol. 61, No. 4, (2013), doi: 10.2478/bpasts-2013-0088.
  19. Shi, L., Lei, W., Li, Z., Cui, Y., Huang, J. and Wang, Y., "Stability analysis of digitally controlled dual active bridge converters", *Journal of Modern Power Systems Clean Energy*, Vol. 6, No. 2, (2018), 375-383.
  20. Jafari, M., Malekjamshidi, Z. and Zhu, J.G., "Analysis of operation modes and limitations of dual active bridge phase shift converter", in 2015 IEEE 11th International Conference on Power Electronics and Drive Systems, IEEE. (2015), 393-398.
  21. Ab-Ghani, S., Daniyal, H., Ramlan, N.H. and Tiong, M.C., "Online pso-tuned phase shift angle controller for dual active bridge dc-dc converter", *SN Applied Sciences*, Vol. 2, No. 1, (2020), 1-8, doi: 10.1007/s42452-019-1782-8.
  22. Ahmadi, B., Barati, F. and Karimi, C., "A variable current-limit control scheme for a bi-directional converter used in ultracapacitor applications", *Electric Power Components Systems*, Vol. 46, No. 3, (2018), 278-289.
  23. Kayaalp, I., Demirdelen, T., Koroglu, T., Cuma, M.U., Bayindir, K.C. and Tumay, M., "Comparison of different phase-shift control methods at isolated bidirectional dc-dc converter", *International Journal of Applied Mathematics Electronics Computers*, Vol. 4, No. 3, (2016), 68-73.
  24. Liu, B., Davari, P. and Blaabjerg, F., "An enhanced generalized average modeling of dual active bridge converters", in 2020 IEEE Applied Power Electronics Conference and Exposition (APEC), IEEE. (2020), 85-90.
  25. Wang, D., Peng, F., Ye, J., Yang, Y. and Emadi, A., "Dead-time effect analysis of a three-phase dual-active bridge dc/dc converter", *IET Power Electronics*, Vol. 11, No. 6, (2018), 984-994.

## 7. APPENDIX

The closed-loop control system for the designed DAB for SC applications is shown in Figure (A-1). It is based on the output voltage control for which a Proportional-Integral-Derivative (PID) control is employed. The output voltage reference value is set to 400V which is the output nominal voltage. The modulator from which switching signals are generated is a Single Phase-Shift (SPS) one as explained before. It generates eight switching signals for the switches in bridges 1 and 2. The switching signal of a switch in bridge 2 is phase-shifted with respect to the switching signal of its counterpart in bridge 1.

The idea presented in this paper for limiting the phase-shift angle is implemented in the closed-loop control system as shown. In fact, we limit the controller output appropriately such that the phase-shift angle does not exceed the obtained limits. Note that, the limits are implemented both for the forward and reverse modes of operation. In this way, we make sure that the DAB's operation is stable.

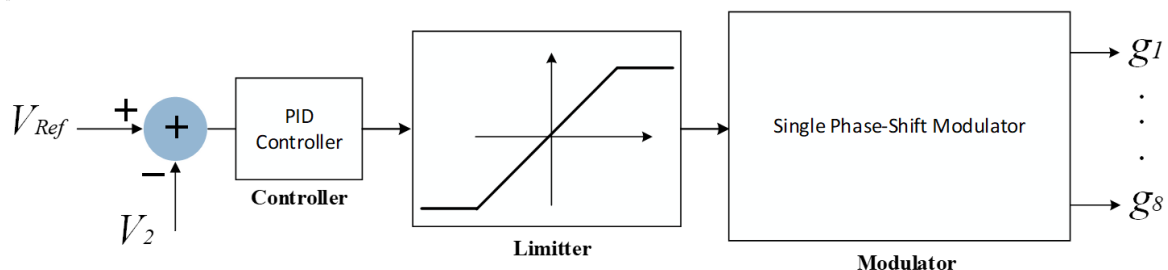


Figure (A-1). Closed-loop control system of DAB with implemented phase-shift angle limits

## Persian Abstract

## چکیده

در این مقاله به ارائه ایده ای برای محدود کردن زاویه شیفیت فاز در مبدل پل فعال دوگانه با هدف پایداری مبدل پرداخته میشود. پایداری، اصلی ترین معیار در کار یک مبدل است چرا که بدون آن مبدل به سرعت از کار می افتد. در مبدل پل فعال دوگانه ایده آل، محدوده مجاز زاویه شیفیت فاز  $90^\circ \pm$  است. در این مقاله با بکارگیری یک مدل دقیق از مبدل که در نرم افزار Matlab/Simulink ایجاد کردیم به استخراج محدوده مجاز شیفیت فاز می پردازیم. در مدل پیاده سازی شده تلاش شده است تا از دقیق ترین مدل المانها بهره جسته شود و بدین ترتیب بتوان محدوده استخراج شده را به واقعیت نزدیک دانست. مبدل پل فعال دوگانه یک مبدل دوجته است. بدین معنی که شارش توان در آن هم در جهت مستقیم و هم در جهت معکوس امکان پذیر است. ما محدوده مجاز شیفیت فاز را جداگانه برای کارکردهای مستقیم و معکوس استخراج کردیم هر چند نشان داده شد که محدوده مجاز برای کارکردهای مستقیم و معکوس یکسان است. این موضوع به دلیل وجود تقارن در مبدل است. در این مقاله، مبدل پل فعال دوگانه برای کاربردهای ابرخازن مورد استفاده قرار گرفته است.



## Experimental Study on Performance Assessment of Hydraulic Power Take-off System in Centipede Wave Energy Converter Considering Caspian Sea Wave Characteristics

M. Aghanezhad, R. Shafaghat\*, R. Alamian, S. M. A. Seyedi, M. J. Raji Asadabadi

Sea-Based Energy Research Group, Babol Noshirvani University of Technology, Babol, Iran

### PAPER INFO

#### Paper history:

Received 13 January 2022

Received in revised form 29 January 2022

Accepted 01 February 2021

#### Keywords:

Centipede Wave Energy Converter

Hydraulic Power Take-off System

Experimental Study

Wave Tank

Simcenter Amesim

### ABSTRACT

Considering the characteristics of the Caspian Sea waves, using a centipede wave energy converter might lead to satisfactory performance. The present paper introduced a pilot wave energy converter (WEC) called IRWEC2. Moreover, the performance of the hydraulic power take-off (PTO) system developed for the WEC was assessed experimentally in the wave tank of Babol Noshirvani University of Technology (BNUT). The Simcenter Amesim software was used so as to design the hydraulic PTO system and to initially evaluate the system performance. For two separate buoys were used, different series and parallel configurations were employed for the separate hydraulic cylinders connected to each buoy to achieve the optimum performance of the PTO system. The characteristics of input wave, resistant load, and flow control valve opening were defined as the most important parameters affecting the converter performance. Accordingly, the maximum value of generator output was obtained based on the certain values of these parameters. To validate the processes defined, the simulation results obtained through the Simcenter Amesim software were compared to the experimental ones and a good agreement was found. According to the results, the maximum power of the PTO system was 46 watts (for laboratory scale), which is related to the parallel configuration. In this case, the efficiency of the PTO system was 23%. Moreover, the output of the generator increased by about 12% compared to the case where only one buoy was used.

doi: 10.5829/ije.2022.35.05b.05

### NOMENCLATURE

$\bar{x}$	Average of measured data
$x_i$	Measured data
<b>Greek Symbols</b>	
$v$	Piston velocity ( $m/s$ )
$\Delta P$	Pressure difference (bar)
$\Delta x$	Piston displacement (cm)
$\Delta y$	Buoy displacement (cm)
$\omega$	Angular frequency ( $rad/s$ )
$\omega_{out}$	Rotational velocity (for G & HM) (RPM)
$\omega_{W.M}$	Wave maker angular frequency ( $rad/s$ )
$\sigma_m$	Standard uncertainty
$\eta_{PTO}$	PTO Efficiency (%)
$\eta_t$	Hydromotor Efficiency (%)
<b>Subscripts</b>	
G	Generator
HM	HydroMotor
i	Data item
W.M	Wave Maker
$a$	Amplitude (cm)
$A$	Piston area ( $mm^2$ )
$F$	Applied force to the cylinder ( $N$ )
GDP	Generator dissipation (%)
$I$	electric current (A)
$N$	Experiment perform number
$P_G$	Output generator power ( $W$ )
$P_{HM}$	Output hydromotor power ( $W$ )
$P_{in}$	Applied power to the cylinder ( $W$ )
$P$	Hydraulic cylinder pressure (bar)
$Q$	Hydromotor flowrate ( $l/min$ )
RPM	Wave maker rotational velocity (RPM)
$s$	Standard deviation
$t$	Time (s)
$T$	Period (s)
$V$	Voltage (V)
$V_g$	Displacement ( $cm^3$ )

\*Corresponding Author Institutional Email: [rshafaghat@nit.ac.ir](mailto:rshafaghat@nit.ac.ir) (R. Shafaghat)

Please cite this article as: M. Aghanezhad, R. Shafaghat, R. Alamian, S. M. A. Seyedi, M. J. Raji Asadabadi, Experimental Study on Performance Assessment of Hydraulic Power Take-off System in Centipede Wave Energy Converter Considering Caspian Sea Wave Characteristics, *International Journal of Engineering, Transactions B: Applications*, Vol. 35, No. 05, (2022) 883-899

## 1. INTRODUCTION

Nowadays, using renewable energy is among the programs and policies of developed and developing countries. With their significant energy density, the waves of seas and oceans are known as one of the sustainable subsets of renewable energy sources [1]. A variety of methods to harness the energy of seas' and oceans' waves have been submitted in the form of hundreds of ideas and research works. It is worth mentioning that many ideas and designs have been utilized as the final product as wave energy converters (WECs). Considering every single of the energy absorption mechanisms, WECs can have different power take-off (PTO) systems. Mechanical, pneumatic, hydraulic PTOs and also direct power transmission system are different types as following researchers studied. Tri et al. [2] used such a mechanical PTO system driven by a continuously variable transmission system (CVT) for point absorber type WEC. Yazdi et al. [3] studied pneumatic one in OWC WEC. Henderson [4] tested hydraulic PTO in Pelamis. Waters et al. [5] examined a linear generator configured with a buoy and sea cable. Centipede wave energy converters are designed to use an array of buoys to attain wave energy. Each of these absorbent units is attached to an arm as the first element of the PTO chain to transmit the heave motion, which is created in the primary interaction (PI) with the wave, to the other components of the PTO system (see Figure 1). At the end of the PTO chain, the reciprocating motions of the buoy are converted into rotational motion and accordingly electrical energy in a generator. The PTO system in a centipede converter could be mechanical, hydraulic, or direct (linear generators). The mechanical PTO system tends to be used in laboratory studies. In the semi-industrial and industrial models, hydraulic PTO systems are commonly utilized. The operational nature of the hydraulic PTO systems is appropriately in accordance with the attributes of sea waves. Using the hydraulic PTO systems in wave energy converters is very prevalent, amongst which Wavestar, Pelamis, AW-Energy, SEAREV, and ETC can be mentioned [6]. In this study, a hydraulic PTO system was utilized for the centipede WEC.

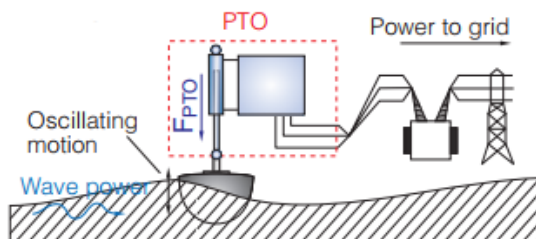


**Figure 1.** Primary interaction between absorber and wave to produce useful power electricity (wave to wire scheme) [7]

A great deal of research has been conducted on WECs, a part of which has been relevant to the absorber's shape, type, and connection method, and the other part deals with the optimization and control of the PTO system.

Sarлак et al. [8] numerically assessed the hydrodynamic parameters, efficiency, and dynamic response for different geometric shapes. Their results demonstrated that the horizontal cylinder shape is the most optimal geometry for the Offshore Wave Buoy WEC system between all samples. Alamian et al. [9] conducted a similar study utilizing NEMOH software for a point absorber converter. In this study, the optimization of the geometric shape considering its construction costs was investigated.

Babarit et al. [10] studied the two-way cylinder in a PTO system and used a gas accumulator to prevent fluctuations. Hansen et al. [11] also examined two different combinations in cylinders to control the power absorption by single and multiple point absorbers. One of the two systems studied was a symmetrical cylinder system with two oil chambers, and the other system contained two cylinders and four nonsymmetrical oil chambers that were tested in three different sea conditions. Cargo et al. [12] evaluated a type of point absorber WEC through numerical simulation in both ideal conditions and conditions with the loss. They achieved the optimal state by changing the features of some components of the hydraulic circuit. Moreover, their results indicated that there is no difference between optimization in the ideal circuit and the circuit with loss. This can assist in the numerical research to optimize the circuit of hydraulic transmission systems. Bayani et al. [13] used a wide variety of wave characteristics to examine the IRWEC1 in BNUT's wave tank. Considering the 1:8 scale, 145 kilowatts power is expected. Hassan et al. [14] used different configuration of turbines during a virtual experiment. In an experimental study, Coiro et al. [15] examined two different configurations of point absorbers in the two positions of the buoyant arm, one in the parallel position to the water surface and the other being angled to the water surface. Alamian et al. [16] utilized various mechanical PTO systems for the centipede wave converter system such as axles and flywheels, gear systems, and also wheels and chains, to name but a few. Another sample of a mechanical combination was conducted by Tri et al. [2]. They tested a system, including a CVT (continuously variable transmission) gearbox, a flywheel, and a WEC-CVT-EHA electrohydraulic actuator. Using an electrohydraulic system to maintain the generator at the rated speed, they dramatically increased the converter efficiency. In both configurations, the hydraulic cylinder is perpendicular to the arm. They also re-conducted this research numerically with two methods of potential theory and

URANS to parametrically analyze the system. Liu et al. [17] carried out an experimental and numerical examination of the hydraulic PTO system of the Pelamis wave energy converter in Aqua software and delineated the effect of different hydraulic parameters. They investigated the effect of several parameters, including the rod-to-piston diameter ratio, various wave conditions at sea, hydromotor displacement volume, and accumulator volume, on the efficiency. Kim et al. [18] tested a WEC, consisting of two hemispherical buoys with the same geometric attributes to maximize the power, that can be extracted in different positions in terms of the distance between the buoys and the pressure difference in the hydraulic motor. Other parameters investigated on the aforementioned wave converter system were the collision wave angle with the wave converter under different wave frequencies. Tian et al. [19] first modeled the small-scale impact (WEC) system by Simulink in MATLAB and then validated it. They used a combined electrohydraulic system to transmit power. Another parameter they studied was the pre-charged accumulator gas pressure. Aghanezhad et al. [20] defined dry tests to study the hydraulic PTO system of a centipede wave converter and examined various parameters to optimize the output power.

To utilize any PTO system in a WEC, it is of utmost importance to pay attention to crucial factors such as sea wave attributes, environmental conditions, and the compatibility of power transmission chain elements. This topic, coupled with the lack of sufficient maturity during using the industrial samples of wave energy converters [6], reveals the need to study and search on tuning and optimizing the PTO system more than ever. In some cases, replacing equipment, adjusting processes, or changing the configuration of PTO systems can improve the performance. In a centipede WEC, these changes can include changes in the size and shape of the absorber buoy, the length of the buoy arm, the size and volume of the hydraulic motor and accumulator, the settings of some parameters (e.g., accumulator pre-charge pressure, flow control valve opening), and resistive load determined for generator and hydraulic motor.

In order to optimize the hydraulic PTO system, it should be inspected in various conditions, and its dependence on effective parameters should also be considered. In this research, the centipede WEC having a hydraulic PTO system was assessed experimentally and numerically. To this end, the operation of the PTO system in the different conditions of the wave, resistive load, and the characteristics of hydraulic elements of the hydraulic circuit will be regarded. In light of the nature of centipede converters, two buoys were utilized together with two separate PTO systems. Thus, to evaluate the performance of the converter, different configurations of the two converters together with the two PTO systems were used. It is noteworthy that two hydraulic cylinders in different

series and parallel positions were inspected to acquire an effectual output in different configurations. By choosing the best configuration using the Simcenter Amesim program, the output power of the PTO system was calculated while the appropriate number of buoys and cylinders were configured. Experimental data were used to validate the simulation results. It should be noted that the output power of the converter significantly depended on the features of the input wave. Accordingly, all changes in the system were made considering constant input waves so that the results were comparable.

## 2. MATERIALS AND METHODS

**2. 1. Problem Statement** In this research, the hydraulic PTO system in the IRWEC2 centipede WEC was assessed experimentally and numerically. To conduct experimental tests, considering the waves of the Caspian Sea, the wave tank of Babol Noshirvani University of Technology (BNUT) was utilized [21]. However, the laboratory study phase of this converter equipped with a mechanical PTO system was completed for two different arrays, including 6 and 10 buoys (see Figure 2). In order to complete laboratory tests and to approach the industrial model, the hydraulic PTO system was used due to the favorable features and performance of the hydraulic PTO system and its appropriate adaptation to the attributes of sea waves (see Figure 3). At this step, to ensure the performance of the hydraulic PTO system, the performance of the system in dry tests outside the tank was examined [20].

As mentioned before, a converter with two hemispherical buoys was used. The diameter of the both buoys was 110 cm, which was connected to the rotary joint using a 2.5m arm. The hydraulic cylinder connection point to the arm was considered at a point between the buoy and the rotary joint. To install the converter in the wave tank, it was essential to adjust the movement of the hydraulic cylinder. The hydraulic cylinder's movement stroke depends on the depth of water and the characteristics of the incoming waves. Figure 4 shows one of the converters installed in the tank. To accomplish the converter's appropriate performance points, two objective functions of the WEC efficiency and the output power were assessed. Various strategies were used in the experimental study to enhance the performance of the converter.

**2. 2. Caspian Sea** As mentioned earlier, to assess the performance of the centipede WEC, the characteristics of the Caspian Sea waves were considered. The Caspian Sea has significant potential to generate electricity from waves. Figure 5 demonstrates a combined diagram of wave distribution and energy according to two parameters of significant wave height and wave period in

the Caspian Sea in the beach of Babolsar city. The colored scale embodies the total annual energy per wavefront length unit, and the bold numbers indicate the probability of occurrence of any particular wave conditions according to the number of hours per year. As shown in Figure 5, the waves with a significant height of 0.5 to 1 m and a period of 4 to 6 seconds have the highest annual energy. However, another significant category of waves is the waves with a height of 0 to 0.5 meters and a period of 2 to 4 seconds, which are most likely to occur in the Caspian Sea (see Table 1).



**Figure 2.** Centipede WEC constructed and tested in BNUT, at Sea-based Energy Research group test rig by mechanical PTO system in 6 and 10 buoy arrays [20]

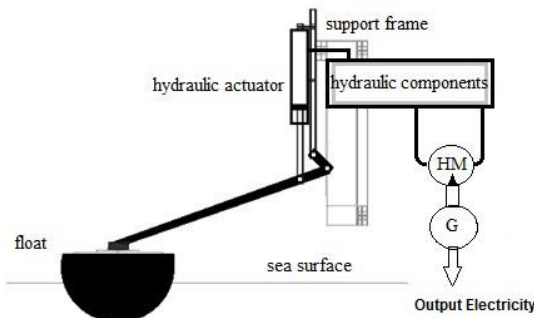


**Figure 3.** Centipede WEC scheme with hemisphere buoy and hydraulic PTO system [20]



**Figure 4.** installation mode of centipede WEC in the wave tank

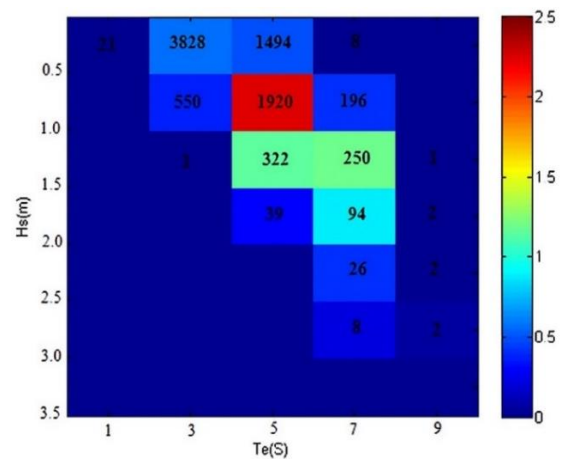


**Figure 5.** Combined scatter and energy diagrams of the annual energy corresponding to sea states in different ranges of Hs and Te for Caspian Sea (near Babolsar) [16]

**TABLE 1.** Caspian Sea wave classification for tests

Waves	Period (s)	Height (m)
<b>Class I</b>	4-6	0.5-1
<b>Class II</b>	2-4	0-0.5

To model the waves in the wave tank, it is very important to consider the WEC scaling. In this study, for the developed semi-industrial sample was used directly in the sea, the scale of the converter was 1:1, and the dimensions of the buoys in the experimental tests were equal to those of the buoys installed in the sea. Therefore, the wave characteristics will not be different compared to the sea wave features. Furthermore, the second group of waves presented in Table 1 was used for experimental tests (class II). To this end, to implement the final tests in most of the experiments, a wave with a height of 40 cm and a period of 3 seconds was utilized in the wave tank.

Nevertheless, the stronger and weaker waves were also used whenever they were required.

## 2. 3. Experimental Study

**2. 3.1. Experimental Equipment** According to the energy transmission chain initiated from the sea waves, the centipede WEC was composed of various subsets and components (see Table 2). The mechanical components of the converter were a buoy and an intermediary arm to transmit the motion. In this converter, after the collision of the input wave, the wave energy was absorbed by the buoy and was then transferred by the arms to the hydraulic cylinder. The increased pressure of working fluid in the hydraulic cylinders was transferred to a hydromotor, which allowed the reciprocating motion of waves to convert into rotational motion. A single-acting hydraulic cylinder was applied in the system, generating the power only when the buoy moved upward followed by the arm. At the end of the process, mechanical energy was converted into electrical one by transferring the rotational motion to the generator. A schematic of the electrical circuit is shown in Figure 6.

Based on the energy conversion chain, the proper selection of elements for hydraulic PTO system and

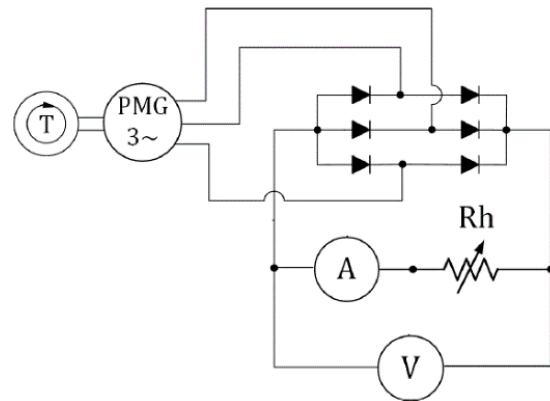


**Figure 6.** Electric circuit including Diode Bridge (bridge rectifier), rheostat and voltage and current measurement elements [20]

correct adjustment of them are of great importance. Figure 7 shows a schematic of the hydraulic power transmission system. As can be seen, check valves are considered on both sides of the hydraulic cylinder to prevent backflow generation. Moreover, an accumulator was used to reduce the fluctuations.

The technical specifications of measurement equipment with their accuracy range are presented in Table 3. Regarding the importance of knowing the wave characteristics and measuring the buoy fluctuations, analytical equations were used to determine the incident wave characteristics, and image analysis was employed to measure the buoyancy fluctuations. Tracker software was also used for image analysis. It should be mentioned that there was a red mark on the buoy for such a purpose, which was traceable to the software after capturing images and in the post-processing step. The incoming wave collision with the buoy and the piston movement made it possible to transfer the wave energy. An ultrasonic level-meter sensor was applied to measure the velocity and displacement of the piston. The force arising

**TABLE 2.** The technical information of setup components

Item	Properties	
Buoy	Diameter	110 cm
	Draft	45.7 cm
	Weight	63 kg
Arm	Length	2.5 m
	Weight	16.3 kg
Hydraulic Cylinder	Piston Diameter	18 mm
	Cylinder Diameter	40 mm
	Stroke	245 mm
Oil Tank	Capacity	50 lit
Check valve	¾ and ¼ inch	
Accumulator	Nominal Capacity	2.5 lit
Relief valve	Pressure relief valve set at 15 bar	
Throttle valve	Needle valve	
Hydromotor	Type	Gerotor-fixed displacement
	Displacement	12.5 cc
Generator	Synchronous permanent magnet (AFPMG) (100W, 100RPM)	
Hydraulic oil	HLP 51524 part 2	
Rheostat	50 Ω, 50 V, 5 A	
Resistors	10 Ω, 10 W	

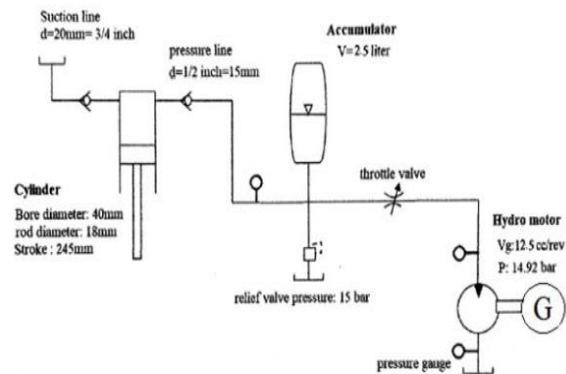


**Figure 7.** Schematic of hydraulic circuit and components [20]

**TABLE 3.** The technical information of measurement equipment

Item	Specification	Accuracy
Pressure Gauge	Dial type (10, 25, and 40 (bar))	±0.5%
Multimeter (voltage)	HIOKI 3256	±0.6%
Multimeter (current)	HIOKI 3200	±1.5%
Force Gauge	Radex digital weighing (50 kg)	±0.05%
Tachometer	Lutron tachometer DT-2268	±0.05%
Level meter	HC-SR04	±0.3 cm

from the wave in the hydraulic cylinder led to increasing the oil pressure in the hydraulic circuit. Several pressure gauges were employed to measure the oil pressure at different points of the hydraulic circuit. The output load was simulated using a rheostat and several resistors. Both voltage and current were measured by two multi-meters. Finally, the rotational speed of the generator and hydro-motor shafts was measured using a digital tachometer as shown in Figure 8.

An incident wave was produced in the form of regular waves by a paddle wave-maker system in a tank of dimensions 11 x 3 x 3 m (see Figure 9).

**2.3.2. Uncertainty Analysis** Because of numerous parameters measured and diversity of experiments, uncertainties were calculated for all measured data. The equations of average value, standard deviation, and mean dispersion were used to compute the percentage error of each quantity.

$$\bar{x} = \frac{\sum_{i=1}^N x_i}{N}$$

$$s = \sqrt{\frac{\sum_{i=1}^N (x_i - \bar{x})^2}{N-1}} \tag{1}$$

$$\sigma_m = \frac{s}{\sqrt{N}}$$



**Figure 8.** hydraulic and electric output data measurement equipment



**Figure 9.** overall view of wave tank [16]

where  $X_i$  is the measured data,  $\bar{X}$  is the average of the measured data,  $N$  is the number of the performed experiments, and  $s$  and  $\sigma_m$  are the standard deviation and standard uncertainty parameters, respectively. As the experiments were repeated three times in each case, the uncertainty calculated for the voltage, flow, pressure, and rotational speed parameters are presented in Table 4.



**Figure 10.** Flow control valve and related settings for opening positions [20]

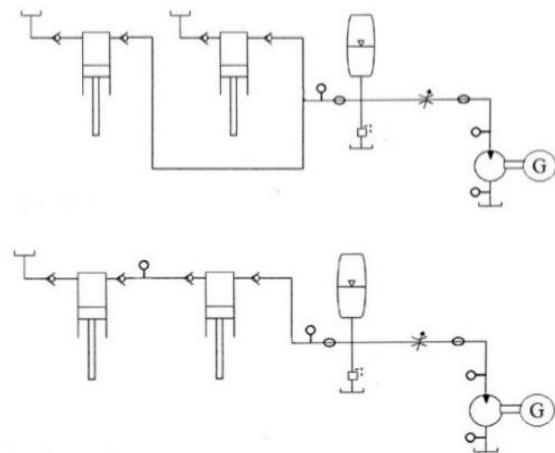


**Figure 11.** installation modes of parallel (a) and series (b) configurations

**2. 3. 3. Test Method**

As mentioned above, a centipede WEC with two buoys was used where the tests were conducted for single-buoy and double-buoy cases. First, the tests were carried out for a single-buoy system. In this case, the effect of two parameters on the opening angle of the flow control valve and the output load was evaluated considering an incident wave with a height of 40 cm and a period of 3s. In these conditions, the goal was to achieve the maximum output power of the converter. As shown in Figure 10, the control valve opening angle was calibrated with the number of turns to open it. To this end, the odd number of turns was considered to adjust the opening angle of the flow control valve. The resistance variation was used in order to change the output load. In this regard, to determine the maximum throughput of the PTO system, the resistance changes starting from 20 ohms were increased by 10 ohms at each step. Thus, by determining proper operating points for the flow control valve and resistive load, it can be tested for other waves of heights 20, 25, and 30 cm.

Considering a buoy followed by a PTO system (a hydraulic cylinder), the wave height was determined by the most appropriate output and the optimum opening angle of the flow control valve. In the next step, the hydraulic cylinders of two separate PTO systems were tested in the series and parallel arrangements for double-buoy configuration.

The experimental steps are shown in Figure 12.

**2. 3. 4. Output Data Processing**

To evaluate the performance of the IRWEC2 WEC, the converter output power was measured compared to the input power. The output power of the converter was determined by the measurement equipment; however, it was necessary to recognize the input wave characteristics to examine the input power to the WEC. Several desired waves were generated in the wave tank using a paddle wave-maker in

which two inputs, including stroke length and wave-maker frequency, were applied to adjust it. The wave period was directly dependent on the wave-maker frequency on the basis of Equation (2); also, the wave height was adjusted by changing the stroke length.

$$RPM = \omega_{W.M} \times \frac{60}{2\pi} = \frac{2\pi}{T} \times \frac{60}{2\pi} = \frac{60}{T} \tag{2}$$

Table 5 shows the wave period for every single desired frequency of the wave-maker. Since the wave period for all experiments was assumed to be a fixed value of 3s, the waves with various heights could be generated by varying the wave-maker stroke (see Table 6). Each specific wave height was named according to its obtained value.

As the Wave Mode I experiment had the maximum wave height, it was considered to evaluate the conformance between the buoy fluctuations and the incoming wave conditions. To define the incoming wave based on the specified wave-maker frequency, the target wave height would be determined by varying the length of the wave-maker stroke. Therefore, Equation (3) could be applied to the incoming wave in this test; image

**TABLE 4.** uncertainty for all parameters in specific test condition (Wave Mode I, R=20 ohms, single configuration)

<i>N</i> = 3	<i>V</i>	<i>I</i>	<i>P<sub>cylinder</sub></i>	$\Delta P$	$\omega_{out}$
Certainty in 95% level	±2.82%	±0.03%	±0.76%	±0.60%	±7.25%

**TABLE 5.** wave period converted to RPM as an input

<i>T</i> (s)	1.5	2	2.15	2.4	2.6	3	3.5	4
RPM	40	30	28	25	23	20	17	15

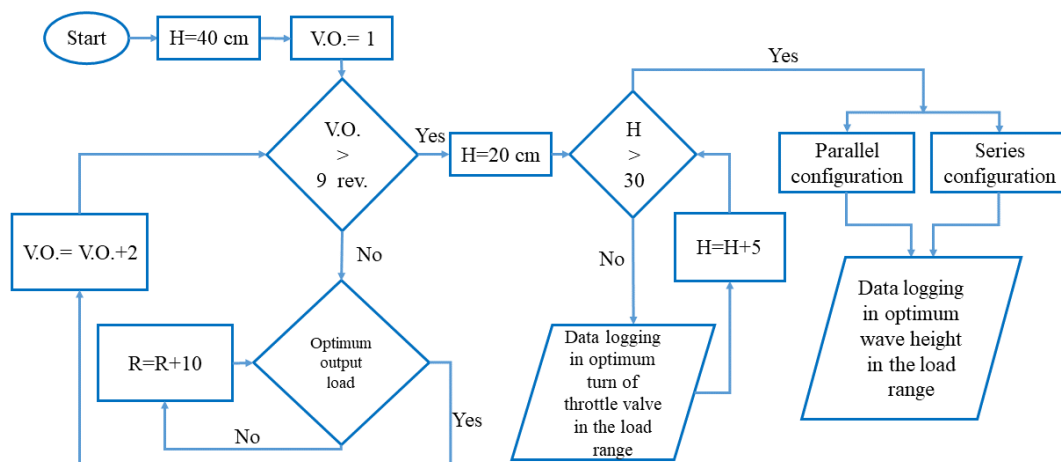


**Figure 12.** test flowchart

analysis was also used to evaluate the buoy fluctuations. Figure 13 depicts the comparison of the incoming wave profile and the buoy fluctuations.

$$y = \text{asin}(\omega t) = 20 \sin(2.093t) \tag{3}$$

As discussed above, the buoy displacements directly affect the hydraulic cylinder performance. If the power transmitted from the buoy to the hydraulic cylinder is considered equivalent to the PTO input power, Equation (4) can be applied to calculate the input power.

$$P_{in} = F * v \tag{4}$$

where  $F$  is the piston force (N) obtained using the cylinder pressure (Equation 5),  $v$  is the piston average velocity (m/s), and  $P_{in}$  is the system input power (W).

$$F = \frac{P \times A}{10} \tag{5}$$

$P$  is the cylinder pressure (bar) measured through the experiment, and  $A$  is the piston cross-sectional area ( $mm^2$ ).

To obtain the piston average velocity, its displacement was first calculated using the level-meter sensor (see Figure 14), then the average velocity was calculated by given piston displacement in the hydraulic circuit charging stage and the piston displacement duration.

TABLE 2. nominated wave modes for tests

T (s)	H (cm)	Wave Mode (W.M.)
3	40	I
3	30	II
3	25	III
3	20	IV

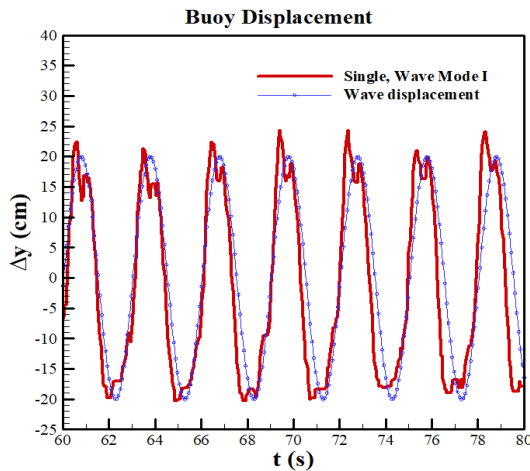


Figure 13. Buoy displacement due to wave motion W.M. I

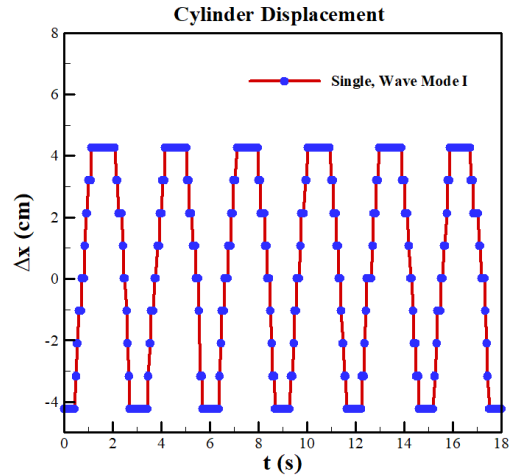


Figure 14. Piston displacement in W.M. I condition

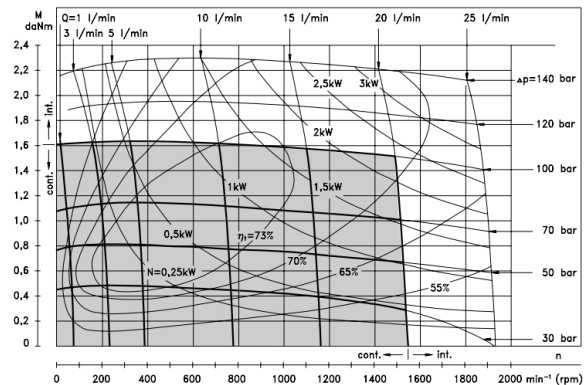


Figure 15. Hydromotor performance diagram [22]

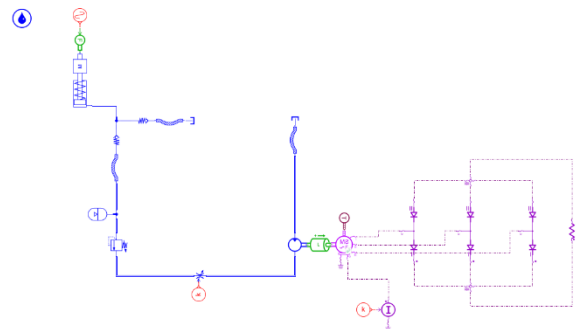


Figure 16. Amesim simulation diagram for hydraulic and electric circuits

After charging the hydraulic circuit by the buoy motion and the piston displacement in the hydraulic cylinder, a high-pressure fluid was transferred through the hydraulic circuit to the hydromotor. According to the information from the hydromotor manufacturer, the hydromotor power was obtained from Equation (6) [23]:

$$P_{HM}(w) = Q * \Delta p * \frac{\eta_t}{600} * 1000 \quad (6)$$

where  $Q$  denotes the volume flow rate passed through hydromotor ( $l/min$ ), and  $\Delta p$  is the pressure difference between the hydromotor inlet and outlet (bar). The parameter  $\eta_t$  represents the efficiency of the hydromotor in different operating conditions that were calculated at all the operating points based on Figure 15 [22]. The flow rate passing through hydromotor was obtained from Equation (7):

$$Q(l/min) = \frac{\omega_{out}(RPM) * V_g(cm^3)}{1000} \quad (7)$$

where  $\omega$  is the rotational speed of hydromotor measured in all different conditions through the experiments and  $V_g$  is a constant parameter indicating the displacement of hydromotor and is equal to  $12.9 \text{ cm}^3$ .

The hydromotor drove a generator to produce electric power. The output power of the generator, as the output power of the wave energy converter, was calculated by Equation (8):

$$P_G = I * V \quad (8)$$

where  $I$  is the electric current (A) and  $V$  is the voltage between the consumer ends (V).

The power transmission setting included some subsets such as plumbing, hydraulic cylinder, accumulator, throttle valve, relief valve, hydromotor, and generator, which every one of them could contribute to the power loss. Equation (9) was applied to obtain the overall efficiency of the PTO system:

$$\eta_{PTO} = \frac{P_G}{P_{in}} * 100 \quad (9)$$

where  $P_G$  is the output power of the generator and  $P_{in}$  is the input power to the hydraulic cylinder.

In addition to the overall efficiency of the PTO system, there is a parameter called generator power dissipation, which is the amount of power that is not converted to the useful power by the generator and coupling. The GDP parameter was employed to analyze this problem [20]:

$$GDP = \left(1 - \frac{P_G}{P_{HM}}\right) * 100 \quad (10)$$

**2. 4. Numerical Study** Simcenter Amesim software was utilized to initially design the hydraulic circuit and evaluate the performance of the hydraulic PTO system at the optimal operating points. In this regard, to evaluate the performance, different configurations were examined, including one hydraulic cylinder and two hydraulic cylinders, in series and parallel mode configurations. This software is a multi-purpose toolbox so as to model and analyze a system with various mechanical, electrical, and control components. Figure

16 shows, for example, the hydraulic and electric circuits of the PTO system simulated in Simcenter Amesim software.

In order to simulate the wave-induced force, a force transducer and an input signal were used to apply the wave sinusoidal motion. The incoming signal was set based on the force exerted on the buoy and its movement period. By defining this force, it was exerted to the cylinder through the force transducer. In this circuit, a single-acting cylinder was used according to the experimental prototype, and a cylinder-attached mass was considered in simulations due to the buoy and arm weights. All features of the hydraulic cylinder, including its internal dimensions, motion stroke, cylinder movement speed, and hydraulic fluid properties, were determined established upon the experimental prototype. The hydraulic circuit was considered similar to the experimental one. Furthermore, the hydromotor power was transmitted using a coupling to a generator. Concerning the defined electric circuit, it is possible to measure voltage and current as electrical outputs of the circuit.

#### 2. 4. 1. Numerical Method Validation

The results obtained from the Wave Mode I experiment were used to examine the validity of the simulation results. In the first step, to validate the numerical method, the single-buoy experimental tests were applied only. According to the circuit designed for this case, the outputs of the software, including the hydromotor pressure, voltage, and current and the generator power, are presented in Figure 17. It is worthy to mention that the outputs were extracted when the results were stabilized. The numerical and experimental results are in good agreement, so the numerical data errors were computed as 5.4, 5.7, and 6.5% for the differential pressure, voltage, and current of hydromotor, respectively. The electric power parameter was obtained by multiplying the voltage and current parameters.

According to the validation of the results obtained from the single-buoy case, validations are presented for several series and parallel configurations (see Figure 18). As can be seen, the experimental and simulation results are in good agreement; the mean difference between the experimental and simulation data is 5.4 and 6.4% in series and parallel modes, respectively.

### 3. RESULTS

In this section, the results of the experimental tests are presented. To this end, the WEC performance with a buoy is compared to the WEC with two buoys. It is worthy to note that about the WEC with two buoys, the results are presented for two parallel and series configurations. After selecting the more preferred

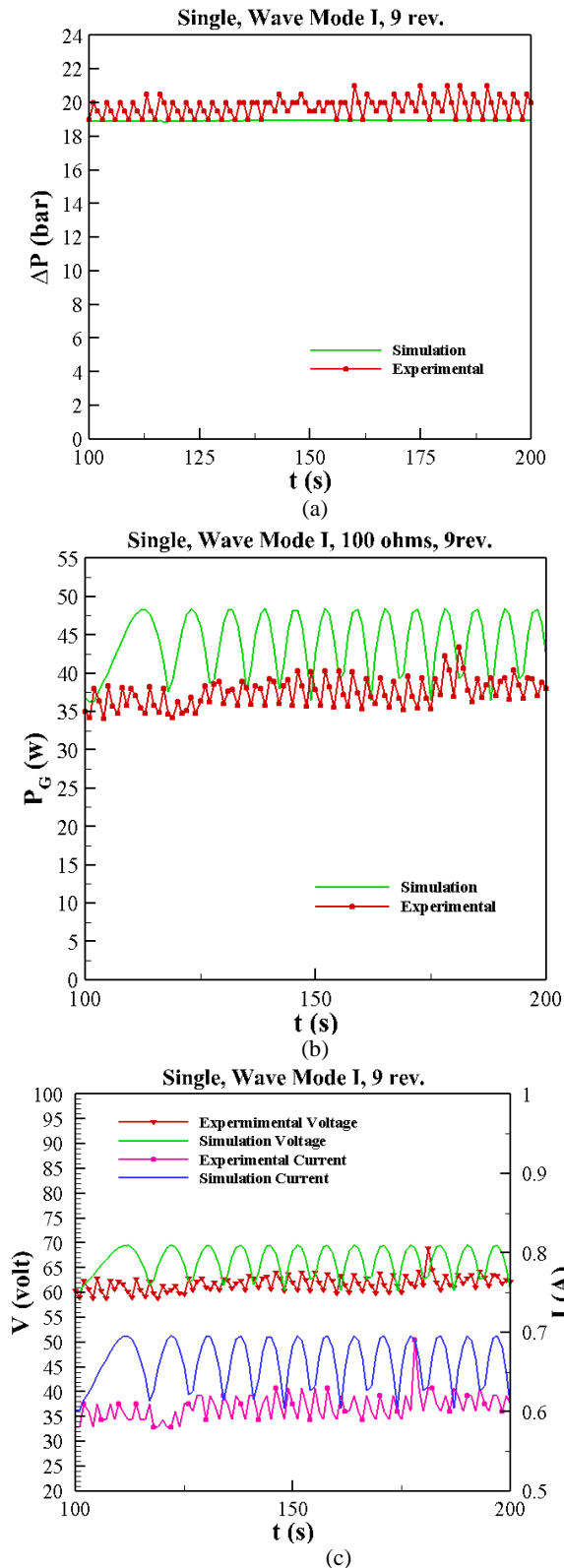


**Figure 17.** Numerical validation for single-cylinder mode in a 100-ohm resistance and 9 turns mode, a: experimental and numerical pressure results comparison, b: experimental and numerical power results comparison, c: experimental and numerical V and I results comparison

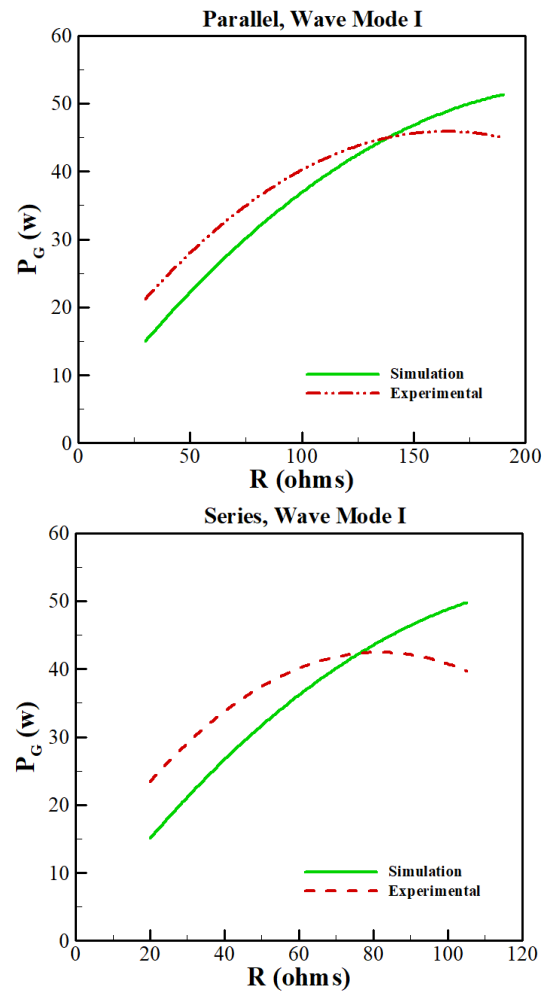


**Figure 18.** Parallel and series configuration validation

configuration in terms of performance, the results concerning Simcenter Amesim software are first validated with the experimental results, and the effect of an increased number of buoys is then examined for the selected configuration.

**3. 1. Experimental Results**

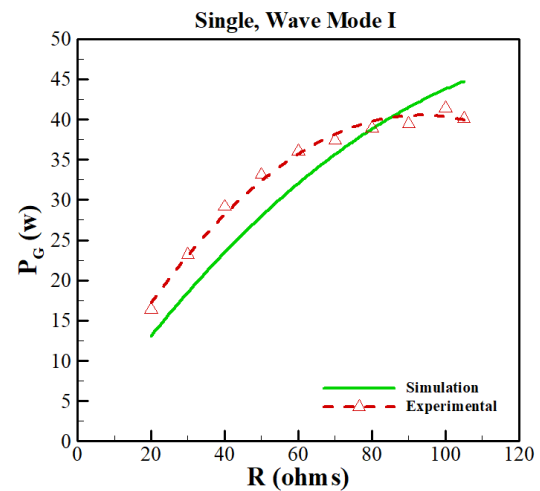
To provide the experimental results, the results of the Wave Mode I experiment are first presented. In this experiment, the wave height and period were considered to be 40 cm and 3 seconds, respectively. Figure 19a shows the output power versus the resistive load of the rheostat for different opening modes of the flow control valve. According to Figure 19a, by increasing the rheostat resistance, the output power increases first to reach a maximum value, and the output power is fixed initially by a further increase in the resistance, and is then decreased gradually. The ideal output power is achieved as 41.37 W for a 100-ohm resistor and 9 turns of the flow control valve. It should be noted that the power increase in the resistance range from 20 to 100 ohms is equal to

153%, followed by a decreasing trend. Moreover, for a 100-ohm resistor, the output power for 9 turns of flow control valve increases by about 7.8% relative to 1 turn. Figure 19b shows that the experimental results are in good consistency with the simulation ones in such a way that the minimum difference is about 0.7% for an 80-ohm resistor and the maximum difference is about 18.8% for a 40-ohm resistor.

The hydromotor power is calculated using the flow rate passed through it. Figure 20 indicates the hydromotor output power in terms of the resistive load for different turns of the flow control valve. Similar to the generator power, the hydromotor maximum power is also achieved for a 100-ohm resistor, which is equivalent to 41.87 W. A negligible difference between the output power of hydromotor and generator indicates very low power losses.

Figure 21a shows the efficiency of the PTO system. The maximum efficiency of the PTO is calculated as 26% for a 100-ohm resistor and 9 turns of the flow control valve. This value is as approximately the same as a 105-ohm resistor. The efficiency curve unlike the power curves has an ascending trend. It seems that by increasing the resistive load, efficiency increases, but it is not considerable due to the loss of the generator output power and the interruption of the output power. Figure 21b shows the loss curves between the hydromotor and the generators for various opening modes. Based on the presented plots, it is observed that the curves' trend is the same for the rest of the cases except for one turn of the flow control valve.

The reason of this difference is attributed to the significant losses of the system to open the flow control valve in one turn. It should be mentioned that in the maximum values of the output power and efficiency, the power loss is negligible, almost equal to zero. This power loss is an indication of the power that the generator



(b) Experimental and numerical power results comparison in resistance range

Figure 19. Captured power in test unit and the simulation

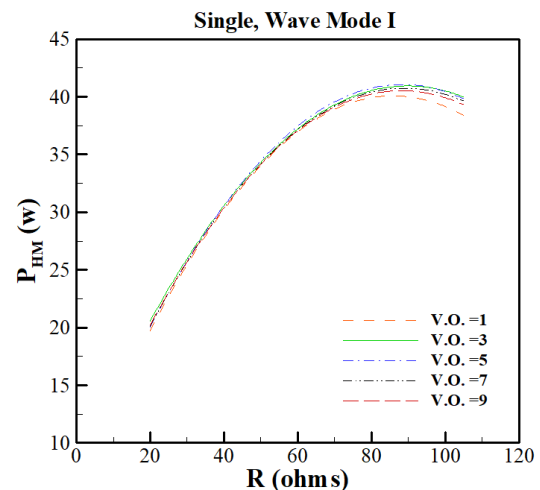
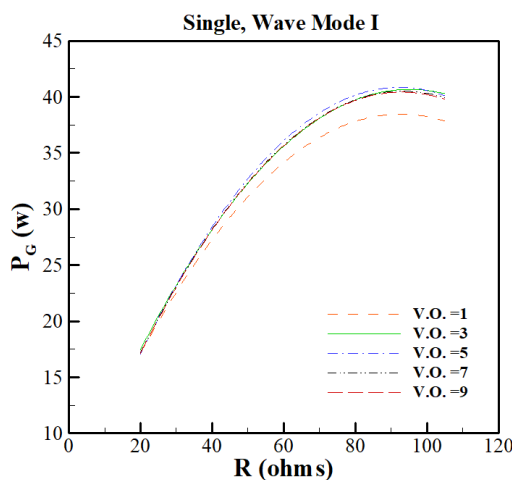


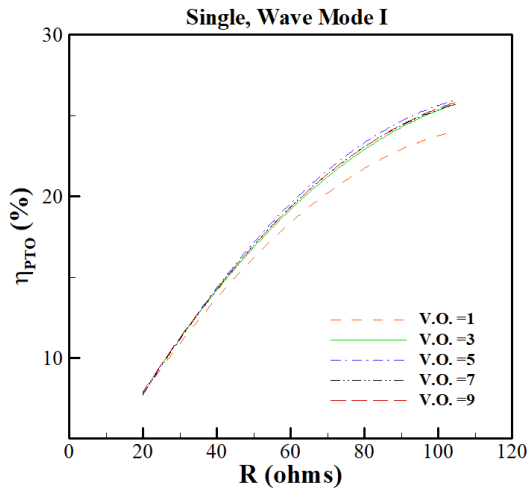
Figure 20. Hydromotor output power in different flow control valve modes



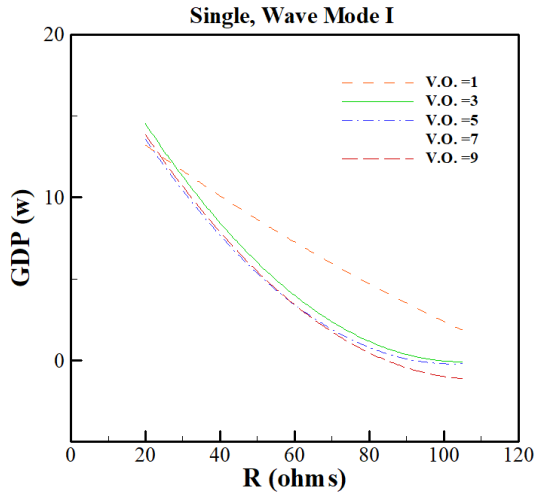
(a) Experimental power in different throttle valve turns

cannot transform to the useful power. Figure 22 illustrates the difference between one opening turn of the flow control valve with the other modes. As can be seen, there is no tangible variation in the generator power of around 40 W in all opening turns except one case. For a better analysis of the result, a closer look at the control valve should be considered. Figure 23 depicts the flow control valve diagram.

The data presented in Figure 23 can confirm why the opening mode of the flow control valve does not affect in some cases. The maximum value of the flow rate passed through hydromotor is 1.9 l/min in this experiment. According to this Figure, for flow rates of less than 20 l/min, the variation of the pressure drop is not distinguishable in different opening modes of the flow



(a) PTO system efficiency in different valve opening modes



(b) Dissipation among generator and hydromotor in different valve opening modes

Figure 1. efficiency and dissipation of the PTO system

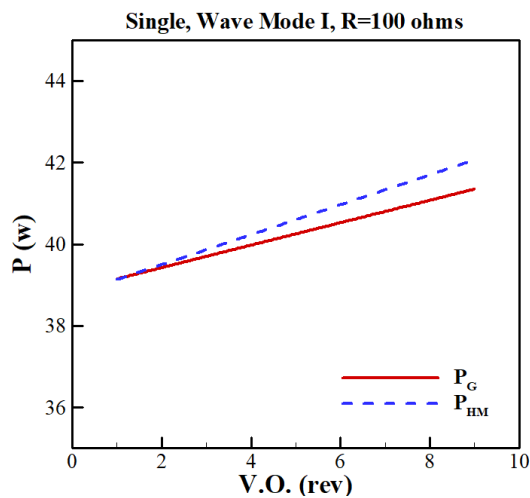


Figure 22. Output power changes with respect to valve opening turns in a 100-ohm resistance

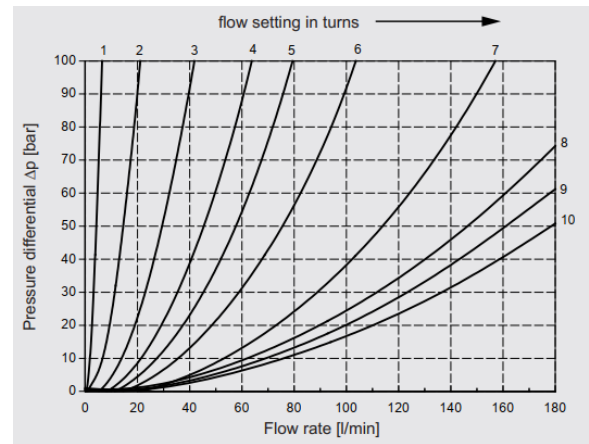


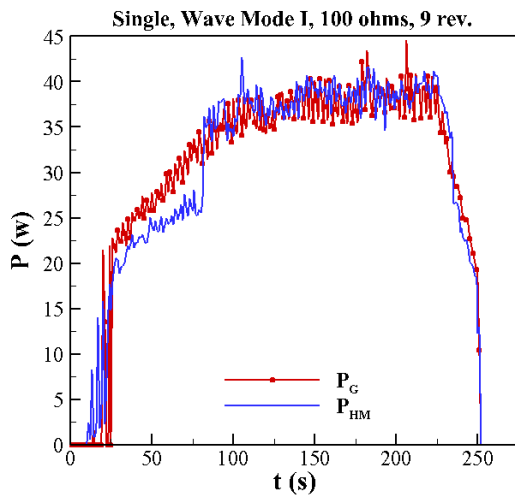
Figure 23. throttle valve performance diagram [24]

control valve, and it is the same for all values of opening turns. However, for the conditions prevailing in the experiment, two initial turns of the valve have a larger pressure drop, but for other numbers of turns, the pressure drop is not significant. Hence, it can be inferred that the total amount of losses is relatively great for the single-turn mode. It should be noted that the pressure drop is 1.5 bar in the oil path from the hydraulic cylinder to the hydromotor for 9 turns of the flow control valve opening. Therefore, the pressure drop is insignificant in the hydraulic circuit path, and a great percentage of pressure loss is attributed to the hydromotor.

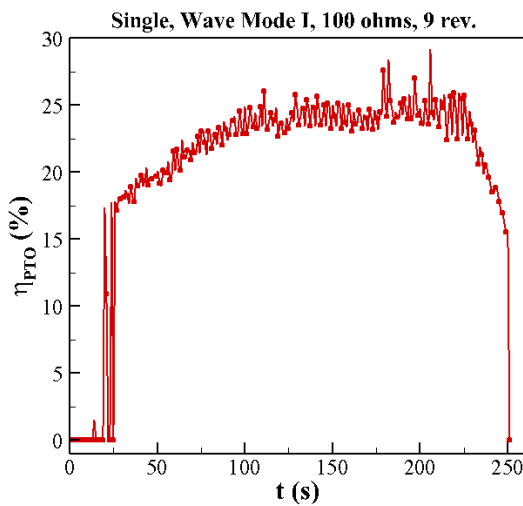
In the experiments conducted, the data collection started by turning on the wave-maker and continued until its shutdown. Figure 24 indicates the outputs related to power, efficiency, and pressure difference for 9 turns of the flow control valve and 100-ohm resistive load. As can be seen, all mentioned graphs are stabilized in the approximate duration of 100 seconds. In 100-226 seconds, the outputs are almost constant, and the fluctuations are very negligible. The power changes in the range of 36 to 42 W, and pressure fluctuation is also around 1 bar.

Figure 25 shows the output power of the WEC for different wave heights (20, 25, and 31 cm). The experiment was carried out for 9 turns of the flow control valve. Obviously, with increasing the wave height, the output power will experience a significant increase. For example, the maximum power generated by a 20 cm wave is 3.9 W, and the output is interrupted by increasing the resistance to more than 30 ohms, while this occurs for 25 cm wave in resistance values higher than 90 ohms.

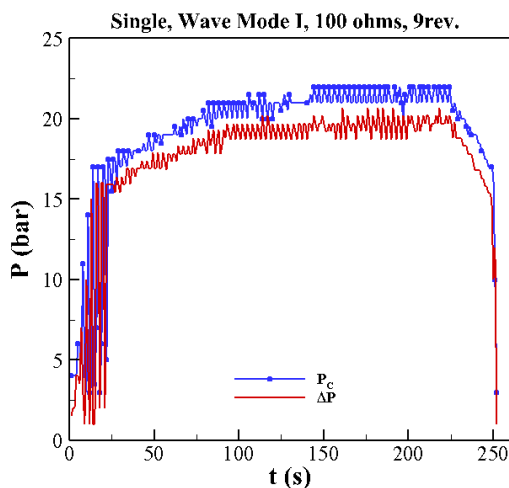
The efficiency curve for the studied heights is presented in Figure 26. The increasing trend of efficiency with wave height is not similar to the power variations. The efficiency at 25 cm wave height is higher than the other wave heights; this is indicated by both the hydromotor and generator performance curves.



(a) Hydromotor and generator output power



(b) PTO system efficiency



(c) Hydromotor pressure difference and cylinder pressure  
**Figure 2.** Diagrams related to the continuous working of the system in 9th turn valve opening and a 100-ohm resistance

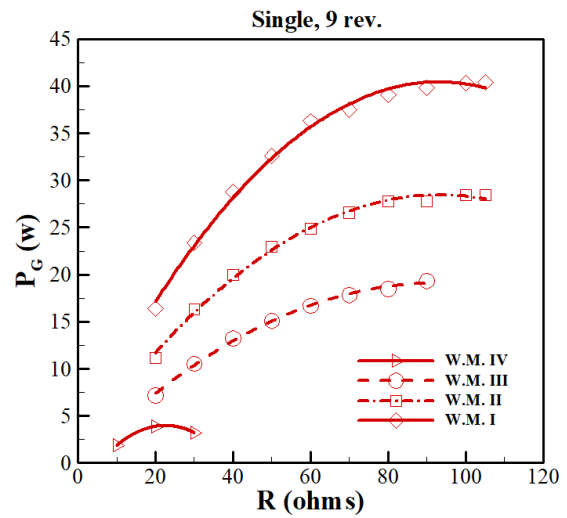


**Figure 3.** Generator output power for various wave heights in resistance load range by 9 turn applied to the throttle valve

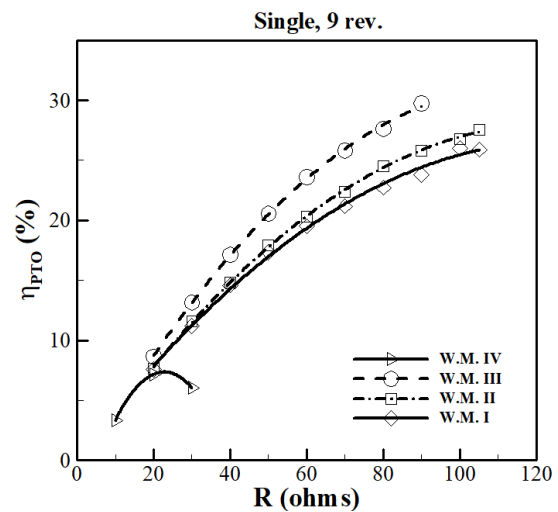


**Figure 4.** PTO efficiency for various wave heights in resistance load range by 9 turn applied to the throttle valve

Concerning the hydromotor and generator performance curves (Figures 15 and 27), the range of the generator rotational speed is more limited than that of the hydromotor. The rotational speed of the generator and the hydromotor shafts is presented for 4 wave height in the variation range of rheostat resistance as shown in Figure 28. As can be seen, the rotational speed of the generator for a wave with 25 cm height is located at the rated speed limit of the generator, which operates at maximum output power condition.

For the greater height waves, this rotational speed exceeds the nominal speed of the generator, which can explain the difference in the presented efficiency

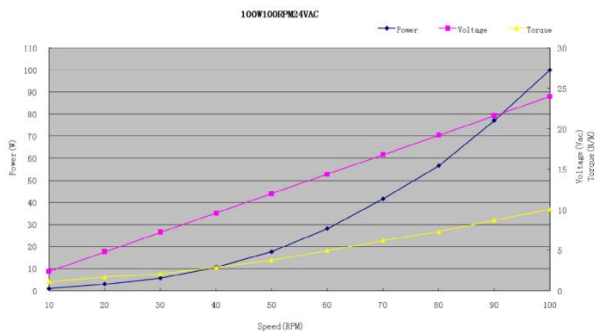


Figure 5. Generator performance diagram [25]

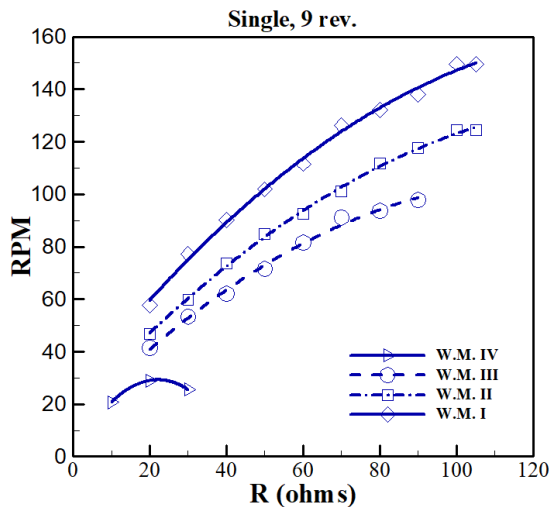


Figure 6. Common shaft rotational velocity for various wave heights in resistance load range by 9 turn applied to the throttle valve

diagrams. The efficiency with a 25 cm wave height and maximum power is equal to 29.7%. Regarding higher power generation with the greater height waves, the generator can be selected according to its rotational speed. Hence, the rated rotational speed of the generator should be placed in the range of rotational speeds determined by the maximum energy and maximum probable waves to achieve the maximum efficiency.

**3. 2. Configurations Evaluations**

The results have been presented for experiments considering a single buoy with a hydraulic cylinder thus far. It should be noted that, as one of the critical results, the maximum output power is recorded for a 100-ohm resistor in the single-buoy single-cylinder case, and achieving the maximum efficiency is subjected to overlap between the rotational speed range of the hydromotor and the generator nominal speed. Since more than a buoy is deployed at the same time in the centipede wave energy converters, the performance of the PTO system is also evaluated by allowing for two buoys to get a better understanding of

different configurations of the hydraulic PTO system. Consequently, there are three cases, involving a buoy and a hydraulic cylinder, two buoys connected in series and two buoys connected in parallel that are separately investigated.

The procedure for conducting the tests for series and parallel configurations is similar to the single-buoy test procedure. Figure 29 depicts the power generated in three different configurations of the hydraulic circuit against the resistance variation. Given that the highest power is different between the three configurations of the hydraulic circuit, the diagrams are presented for the single-cylinder and parallel configuration in 9-turn opening mode and for the series configuration in 7-turn opening mode. To this end, the maximum output power is computed as 41.4 W for the single-cylinder state with a 100-ohm resistor, while this value is 41.8 W and 46.43 W in the series and parallel state with an 80-ohm and a 170-ohm, respectively. Therefore, in the series and single-cylinder cases, especially in high resistances, the values are very close together and an increase of about 2.25% is observed, but in the parallel case, the two cylinders' synergy is considerable, so a 12.23% increase is achieved relative to the single-cylinder case.

Figure 30 illustrates a comparison of the efficiency in 3 cases. As can be seen, the efficiency in the single-cylinder case is more than that of the parallel and series configurations. Hence, concerning the power and efficiency results, it can be stated that the parallel configuration can be applied to generate the higher power and the single-cylinder counterpart to achieve higher efficiency. The very important achievement obtained from these comparisons is to employ two individual systems in the parallel mode.

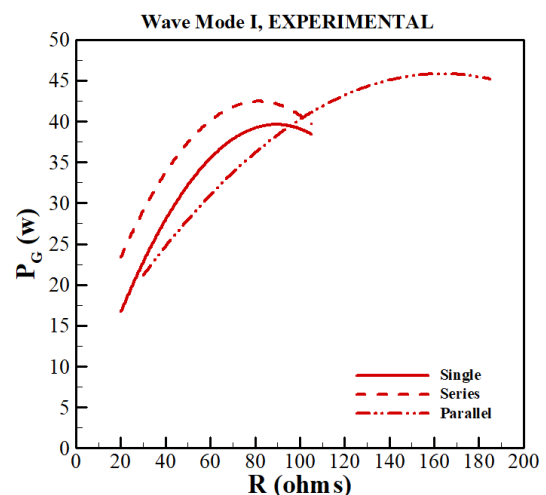
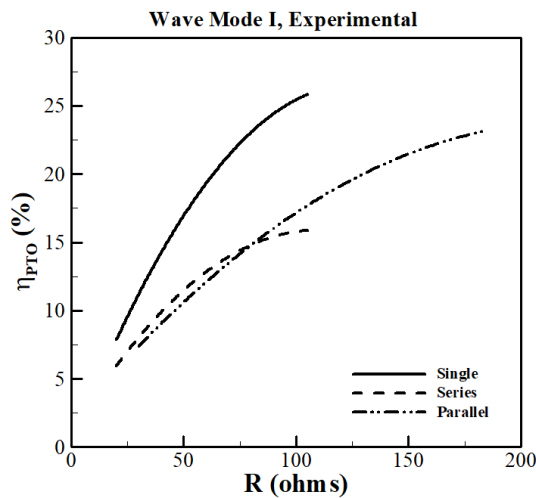


Figure 7. Output PTO system power for single-cylinder and the double type in series and parallel configurations in the range of resistance load (9 turns applied to single and parallel, and 7 turns for series configurations)



**Figure 8.** PTO efficiency for single-cylinder and the double type in series and parallel configurations in the range of resistance load (9 turns applied to single and parallel, and 7 turns for series configurations)

According to the obtained results, both maximum efficiency and generated power can be obtained if two systems are considered completely separate. The point is that for the case where large number of buoys are applied, this strategy results in an increased cost and is not economical. Therefore, the parallel configuration is used in the following to evaluate the increased number of the buoys. In this context, simulations were carried out using Simcenter Amesim software for two, three, and ten buoys. In the curve of efficiency against resistance, the highest efficiency was achieved at the highest resistance at all three configurations. However, the result is that the higher power does not mean higher efficiency. Experimental and simulation results are presented in parallel mode for the 170-ohm resistor in Figure 31. The difference between experimental and simulation results is about 9%.

Due to the appropriate conformance of the numerical and experimental data, the simulation is applied to change the circuit arrangement and to find the optimal number of the hydraulic cylinders in the series and parallel circuits. On the other hand, for the series and parallel cylinders, the results show that, the maximum power is increased by 2.25 and 12.23%, respectively, so the parallel configuration is applied to the numerical simulation considering a wave height of 40 cm and a wave period of 3s. Figure 32 depicts the simulation results for parallel configuration with 2, 3, and 10 cylinders. As can be seen, the resistive load variation is continued to maximize the power generated by the converter. It is worth mentioning that the maximum power for 2, 3, and 10 cylinders are obtained in resistance values of 180, 320, and 1200 ohms, respectively. The interesting point is that by increasing the number of

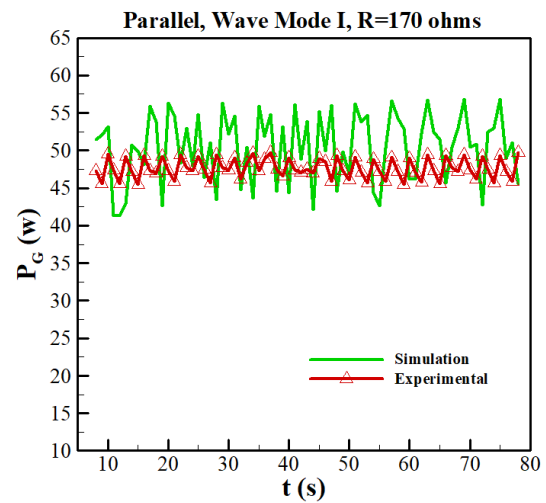


**Figure 9.** Experimental and numerical contrast for power production in parallel type configuration by applying a 170-ohm resistance

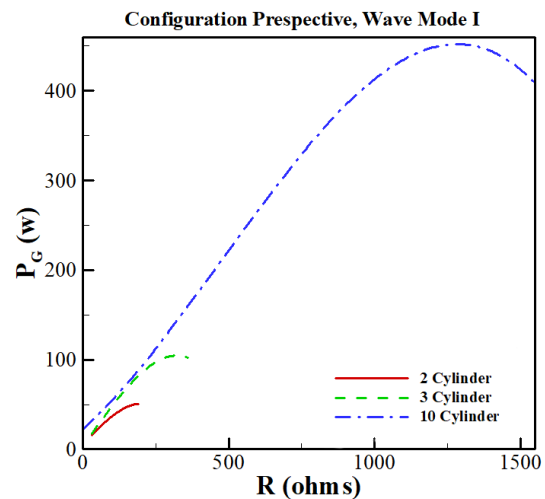


**Figure 10.** Multi-cylinder influence under the condition of W.M. I

cylinders from 2 to 3, the efficiency of the PTO system decreases from 17.22 to 16.13% while increasing the number of cylinders to 10 leads to a 25.9% increase in the efficiency.

#### 4. CONCLUSION

In this study, the centipede WEC was investigated experimentally and numerically. Experimental tests were performed in the wave tank, and numerical simulations were carried out using Simcenter Amesim software. As the results suited the experiments in terms of compatibility, Simcenter Amesim can be used in more future simulations for hydraulic PTOs. The main

objective of this research was to evaluate the output power and the performance of the PTO system for various configurations of the centipede wave converter. To this end, the maximum output power and efficiency of the PTO system were calculated by defining the resistive load. The effect of the flow rate passing through the flow control valve on the system performance was investigated to achieve maximum power and desired operating conditions of the PTO system. According to the type of Centipede WEC, using separate PTO systems for each arm is not efficient economically. So choosing a proper configuration is of high importance. In the experimental study, three connection configurations were considered for installing hydraulic cylinders together in the hydraulic PTO, including single-buoy (a closed hydraulic loop running by a single buoy, driving the PTO), double-buoy with the series arrangement, and double-buoy with the parallel arrangement (a closed hydraulic loop running by two buoys, driving the same PTO.). First, numerical results were validated by comparing them with experimental results, and then, the best configuration selected. At last numerical simulations were performed for 3- and 10-buoy modes of the selected configuration. Some of the important concluded remarks are stated below:

- The experimental results showed that by increasing the resistive load, the output power increases to a maximum value and then slowly decreases.
  - In the experimental tests, the maximum output power of 41.37, 41.8, and 46.43W was obtained considering three different configurations of single-buoy, double-buoy connected in series, and double-buoy connected in parallel, respectively.
  - The pressure losses in the hydraulic circuit from cylinder to hydromotor are about 1.5 bar, achieving its maximum value in the hydromotor, but the results showed that the hydromotor output power with optimal resistances is almost completely converted to the output power in the generator.
  - In low flow rates, the output power of the generator is not changed significantly by varying the opening mode of the flow control valve, so the increase in the power output from the lowest to the highest opening mode is 7.8%; this parameter can be very effective at high flow rates.
  - The PTO system efficiency is 26, 16, and 23% in three different configurations of single-buoy, double-buoy connected in series, and double-buoy connected in parallel, respectively. The efficiency for the single-buoy mode is maximum, but the output power is greater in the parallel configuration than the others. The maximum power and efficiency do not occur at the same time. The parallel configuration is suited to achieve the highest output power, and the single-buoy for maximum efficiency.
- Concerning the selection of the parallel configuration as the desired case, the results obtained from the numerical study showed that the output power significantly increases by increasing the number of buoys followed by the number of hydraulic cylinders in the parallel configuration. Hence, in the configuration of 10 parallel cylinders, with a significant increase in output power, efficiency has also an acceptable increase.

## 5. ACKNOWLEDGEMENTS

The results presented in this article are the outcome of a research project approved by the Supreme Council for Science, Research and Technology (SCSRT). We would like to express our gratitude for the spiritual and funding support of the Mazandaran Provincial Government, the Deputy Governor for Economic Affairs and Resource Development.

## 6. REFERENCES

1. Tafazzoli, S., Shafaghat, R. and Alamian, R., "Numerical investigation on the multi-body hydrodynamic interactions under Caspian Sea environmental conditions", *Ocean Engineering*, Vol. 232, (2021), 109048, DOI: 10.1016/j.oceaneng.2021.109048.
2. Tri, N. M., Binh, P. C. and Ahn, K. K., "Power take-off system based on continuously variable transmission configuration for wave energy converter", *International Journal of Precision Engineering and Manufacturing-Green Technology*, Vol. 5, (2018), 89-101, DOI: 10.1007/s40684-018-0010-0.
3. Yazdi, H., Shafaghat, R. and Alamian, R., "Experimental Assessment of a Fixed On-Shore Oscillating Water Column Device: Case Study on Oman Sea", *International Journal of Engineering, Transactions C: Aspects*, Vol. 33, (2020), 494-504, DOI: 10.5829/ije.2020.33.03c.14.
4. Henderson, R., "Design, simulation, and testing of a novel hydraulic power take-off system for the Pelamis wave energy converter", *Renewable Energy*, Vol. 31, (2006), 271-283, DOI: 10.1016/j.renene.2005.08.021.
5. Waters, R., Stålberg, M., Danielsson, O., Svensson, O., Gustafsson, S., Strömstedt, E., Eriksson, M., Sundberg, J. and Leijon, M., "Experimental results from sea trials of an offshore wave energy system", *Applied Physics Letters*, Vol. 90, (2007), 034105, DOI: 10.1063/1.2432168.
6. Hansen, R. H., *Design and control of the powertake-off system for a wave energy converter with multiple absorbers*. Videnbasen for Aalborg UniversitetVBN, Aalborg Universitet, The Faculty of Engineering and Science. 2013: Department of Energy Technology, Aalborg University. 266.
7. López, I., Andreu, J., Ceballos, S., De Alegría, I. M. and Kortabarria, I., "Review of wave energy technologies and the necessary power-equipment", *Renewable and Sustainable Energy Reviews*, Vol. 27, (2013), 413-434, DOI: 10.1016/j.rser.2013.07.009.
8. Sarlak, H., Seif, M. S. and Abbaspour, M., "Experimental investigation of offshore wave buoy performance", *Journal of Marine Engineering*, Vol. 6, (2010).

9. Alamian, R., Shafaghat, R. and Safaei, M. R., "Multi-objective optimization of a pitch point absorber wave energy converter", *Water*, Vol. 11, (2019), 969, DOI: 10.3390/w11050969.
10. Babarit, A., Guglielmi, M. and Clément, A. H., "Declutching control of a wave energy converter", *Ocean Engineering*, Vol. 36, (2009), 1015-1024, DOI: 10.1016/j.oceaneng.2009.05.006.
11. Hansen, R. H., Andersen, T. O. and Pedersen, H. C., *Analysis of discrete pressure level systems for wave energy converters*, in *Proceedings of 2011 International Conference on Fluid Power and Mechatronics*. 2011, IEEE. 552-558.
12. Cargo, C. J., Plummer, A. R., Hillis, A. J. and Schlotter, M., "Determination of optimal parameters for a hydraulic power take-off unit of a wave energy converter in regular waves", *Proceedings of the Institution of Mechanical Engineers, Part A: Journal of Power and Energy*, Vol. 226, (2012), 98-111, DOI: 10.1177/0957650911407818.
13. Bayani, R., Farhadi, M., Shafaghat, R. and Alamian, R., "Experimental Evaluation of IRWEC1, a Novel Offshore Wave Energy Converter", *International Journal of Engineering, Transactions C: Aspects*, Vol. 29, (2016), 1292-1299. doi: 10.5829/idosi.ije.2016.29.09c.15
14. Hassan, F. A., Mahmoud, M. and Almohammed, O. A., "Analysis of the Generated Output Energy by Different Types of Wind Turbines", *Journal of Human, Earth, and Future*, Vol. 1, (2020), 181-187.
15. Coiro, D. P., Troise, G., Calise, G. and Bizzarrini, N., "Wave energy conversion through a point pivoted absorber: Numerical and experimental tests on a scaled model", *Renewable Energy*, Vol. 87, (2016), 317-325, DOI: 10.1016/j.renene.2015.10.003.
16. Alamian, R., Shafaghat, R. and Ghasemi, M., "Experimental evaluation of attenuator WEC in a laboratory wave tank", *Journal of Marine Engineering*, Vol. 14, (2019), 1-9, DOI: 20.1001.1.17357608.1397.14.28.8.7.
17. Liu, C., Yang, Q. and Bao, G., "Influence of hydraulic power take-off unit parameters on power capture ability of a two-raft-type wave energy converter", *Ocean Engineering*, Vol. 150, (2018), 69-80, DOI: 10.1016/j.oceaneng.2017.12.063.
18. Kim, S.-J., Koo, W. and Shin, M.-J. *Numerical study on multi-buoy-type wave energy converter platform with hydraulic PTO system*. in *Oceans 2017-Aberdeen*. 2017. IEEE. DOI: 10.1109/OCEANSE.2017.8084920.
19. Tian, H., Zhou, Z. and Sui, Y., "Modeling and Validation of an Electrohydraulic Power Take-Off System for a Portable Wave Energy Converter with Compressed Energy Storage", *Energies*, Vol. 12, (2019), 3378, DOI: 10.3390/en12173378.
20. Aghanezhad, M., Shafaghat, R. and Alamian, R., "Experimental Performance Evaluation of a Hydraulic PTO System for Centipede Wave Energy Converter", *International Journal of Coastal and Offshore Engineering*, Vol. 3, (2020), 35-46, DOI: 10.29252/ijcoe.3.4.35.
21. Alamian, R., Shafaghat, R., Shadloo, M. S., Bayani, R. and Amouei, A. H., "An empirical evaluation of the sea depth effects for various wave characteristics on the performance of a point absorber wave energy converter", *Ocean Engineering*, Vol. 137, (2017), 13-21, DOI: 10.1016/j.oceaneng.2017.03.036.
22. HYDRAULIC MOTORS MM. <https://www.dynahydraulics.com/wp-content/uploads/2017/03/1-MM-1.pdf>
23. Hydraulic Motors, Variable Displacement, in HY30-8223/UK, P. Hannifin, Editor. 2014: sweden.
24. Needle Valves with and without Reverse Flow Check Direct-Acting, HYDAC, Editor. p. 1-4.
25. TGET-260-I-100W-100R (AFPMG Three Phase inner rotor). Available from: [http://www.china-topgrand.com/product\\_new/?tid=74&type=85](http://www.china-topgrand.com/product_new/?tid=74&type=85).

---

### Persian Abstract

#### چکیده

با توجه به شرایط امواج دریای مازندران، به کارگیری مبدل‌های انرژی امواج هزارپایی در این دریا، می‌تواند از عملکرد قابل قبولی برخوردار باشد. در این مقاله ضمن معرفی یک مبدل نیمه‌صنعتی تحت عنوان IRWEC2 جهت نصب در دریا، عملکرد سامانه‌ی انتقال توان هیدرولیکی توسعه‌یافته برای این مبدل، به صورت تجربی مورد ارزیابی قرار می‌گیرد. آزمون‌های تجربی در استخر موج دانشگاه صنعتی نوشیروانی بابل انجام شده‌اند. برای طراحی سامانه‌ی انتقال توان هیدرولیکی و ارزیابی اولیه‌ی عملکرد سامانه‌ی PTO، از نرم‌افزار امسیم استفاده شده است. با توجه به استفاده از دو بویه‌ی مجزا، برای استخراج عملکرد بهینه‌ی سامانه‌ی انتقال توان از پیکربندی‌های مختلف سری و موازی برای به کارگیری سیلندرهای هیدرولیک مجزا برای هر بویه استفاده شده است. مشخصات موج ورودی، بار مقاوم و نیز میزان گشودگی شیر کنترل جریان، به عنوان مهم‌ترین پارامترهای تأثیرگذار بر روی عملکرد مبدل تعریف شده‌اند که مقدار ماکزیمم خروجی ژنراتور در مقادیر معینی از پارامترهای نام‌برده به دست می‌آیند. در ابتدا برای اعتبارسنجی فرایندهای تعریف‌شده، نتایج به دست آمده از شبیه‌سازی با نرم‌افزار امسیم به نتایج تجربی مقایسه شده است که نتایج شبیه‌سازی‌ها هم‌خوانی بسیار خوبی با نتایج تجربی داشته‌اند. با توجه به نتایج به دست آمده، بیشینه توان سامانه‌ی انتقال توان معادل ۴۶ وات به پیکربندی موازی مربوط می‌شود؛ بازدهی سیستم انتقال توان در این حالت ۲۳٪ بوده، خروجی ژنراتور نسبت به حالتی که تنها از یک بویه استفاده شده است، حدود ۱۲٪ افزایش یافته است.

---



## Evaluation of a Mobile Highway Management System at Roadwork Zones

J. Skovajsa<sup>a</sup>, O. Přibyl<sup>b</sup>, P. Přibyl<sup>b</sup>, M. Ščerba<sup>b</sup>, A. Janota<sup>\*c</sup>

<sup>a</sup> Ministry of Transport of Czech Republic, Prague, Czech Republic

<sup>b</sup> Czech Technical University, Faculty of Transportation Sciences, Prague, Czech Republic

<sup>c</sup> University of Žilina, Faculty of Electrical Engineering and Information Technology, Žilina, Slovakia

### PAPER INFO

#### Paper history:

Received 31 August 2021

Received in revised form 02 February 2022

Accepted 03 February 2022

#### Keywords:

Road Traffic

Congestion

Mobile

Intelligent Transportation System

### ABSTRACT

Road construction and maintenance activities cause traffic congestions and delays and present challenges for ensuring the safety of both motorists and road workers. While urban areas are well-equipped with traffic devices, in the case of highways our chances to collect traffic data and control traffic flows may be limited. Then the use of a temporary Highway Traffic Management System seems to be a suitable solution. Although the impacts of its deployment are addressed by many theoretical studies and demonstrated on traffic simulation models, there are not many references dealing with field tests. We provide results of the practical evaluation of the temporary Highway Management System installed and tested on the main highway in the Czech Republic during the road works period. Before-after analysis of collected traffic data was performed to prove the importance and positive impact of the proposed solution. We demonstrate an over 20% increase in the capacity of the roadwork zone and an almost 30 seconds decrease in average delay for one vehicle Highway administrators can use the results to justify investments into the temporary deployment of mobile traffic management systems.

doi: 10.5829/ije.2022.35.05b.06

## 1. INTRODUCTION

The highway D1 is a backbone of the road network in the Czech Republic, running west-east and connecting the capital Prague with other major cities, Brno and Ostrava. In addition to being the longest, it is also the oldest highway in the country, with the highest traffic volumes. It was not until November 1980 that the final section, allowing highway travel from the capital to Brno, was completed. An average daily traffic volume is over 37,500 vehicles per day. The highest value reaches almost 90,000 vehicles per day and occurs near the capital city of Prague. The age of the highway and the high volume of traffic naturally lead to traffic problems. Driving comfort is limited due to the old road surfaces, which require regular maintenance. For these reasons, the Ministry of Transport of the Czech Republic together with the Roads and Motorways Directorate of the Czech Republic (RSD), have decided to invest in the complete renovation of highway D1. Responsible authorities had

to choose a suitable alternative from various solutions, taking into account different and conflicting criteria. The decision-making process concerned four basic alternatives – modernization, reconstruction, new construction, and zero alternatives:

A) *Modernization* concerns a solution where both directions of the highway are extended by 75 cm, i.e., change from the category D26.5 to D28 according to local classification regulations. This solution allows driving in four lanes in one work zone and assumes the laying of a new concrete surface.

B) *Reconstruction* consists of fragmenting the current concrete cover and laying a new asphalt carpet. In this case, category D26.5 remains unchanged.

C) *New construction* means a complete reconstruction of the 6-lane highway.

D) *Zero's* solution is to preserve and maintain the status quo.

All these alternatives were evaluated using the Statistic Failure Modes and Effect Analysis (SAFMEA)

\*Corresponding Author Institutional Email: [ales.janota@uniza.sk](mailto:ales.janota@uniza.sk)  
(A. Janota)

methodology [1]. Finally, the *Modernization* option was chosen [2]. The planned duration of the whole process was 7 years, while several work zones with a length of 5 to 7 km each were established at the same time. Each work zone used two lanes in each direction with limited width and the maximum speed limit of 80 km/h. Maintenance work was expected to be completed in 2021.

The principal question was how to manage highway traffic under those extraordinary situations. A Highway Traffic Management System (HTMS) is one of the important functional systems of Intelligent Transportation Systems (ITS) [3]. Its purpose is to collect data from roadside equipment, to provide more efficient services to highway users, and to prevent or react to hazardous situation occurrences. The latest HTMS usually relies on multiple technologies creating different installed sub-systems: variable message signs, portable information displays, emergency call boxes, incident detection systems, meteorological data systems, automatic traffic counters and classifiers, CCTV, speed enforcement systems, etc. [3]. While urban areas are well-equipped with traffic devices [4], our chances to collect traffic data and control traffic flows on highways may be limited. In case of exceptional circumstances, such as roadworks and maintenance works, permanent installations are not available and the only solution to the traffic situation is based on the deployment of a mobile version of the HTMS. Jacobson [5] discussed the main benefits of such solutions as identified in many international projects: travel time decrease 20 to 48%; travel speed increase 16 to 62%; highway capacity increase 17 to 25%; and others. This paper aims to provide results of the practical evaluation of the mobile HTMS temporarily installed and practically tested on the longest highway in the Czech Republic (D1) during the roadworks period. The evaluation is based on collecting data before and after deployment of the mobile HTMS to demonstrate how the capacity of the roadwork zone increases.

**1. 1. State-of-art** Speeding as a key factor causing rear-end and roadside accidents and collisions between vehicles and traffic facilities and construction personnel is analyzed by Cheng and Cheng [6]. A qualitative study of safety aspects introduced by Yang et al. [7], analyzing worker perceptions of common hazards and their mitigating measures in work zones. Methodological approaches to work zone safety were reviewed and assessed by Ackaah et al. [8]. It is well-known that any roadwork causes traffic problems, including traffic congestions, delays, and even increased safety hazards. While the theoretical effects and implications of HTMS are well known and broadly discussed. There are not so many literature providing practical results from real applications. At the same time, the implementations

differ concerning the boundary conditions as well as the actual implementation. We believe that the research presented here is significant in the way it provides results from a real-world study and not a simulation experiment. It follows the evaluation principles described by Sinha and, Fwa [9]. The following paragraphs analyze and compare the findings to the existing literature review.

Requirements and limitations of HTMS are discussed by Harbord and Jones [10]. Speed harmonization project on the M25 Motorway in the UK, focusing on congestion management, led clearly to the reduction of the number of accidents by over 10%. The HTMS also caused a decrease in travel times in one direction while travel times in the other direction were increased. This is caused not only by imposed speed limits but also by more strict enforcement [11]. Also, further investigations on this highway could not demonstrate a statistically significant decrease in travel times [12]. Another experiment in Utrecht and Rotterdam (the Netherlands) led to an increase in the capacity of about 1 to 2 % [13]. It is worth mentioning that sometimes in the case of developing countries highway capacity analyses should be adjusted for prevailing traffic composition and driver behavior [14]. Interesting results of speed management on road arterials were provided by Talebpour et al. [15]. The authors addressed many different aspects and various scenarios that might have influence. However, the impact is demonstrated on a microscopic traffic simulation model in PTV Vissim. While authors explain the calibration procedure, their own experience in demonstrating the effects of speed harmonization is strongly dependent on drivers' compliance [16] and the results cannot be compared to real-world studies (as presented in this paper). Similar results were also discussed in literature [17-19].

An important study by Strömberg and Lind [20] presents the results of a field-test experiment on the E4 highway south of Stockholm. The authors reported on real implementation and evaluation during 18 months. Similar to our field test, they implemented their solution in two phases: first the queue warning was implemented and two years later the speed harmonization. The evaluation method was also similar: before-after analysis. One important result was a significant decrease in drivers' speed compliance after introducing the system. This significantly decreases the effectiveness of the system. The authors were dealing with a road segment where they had a maximum speed of 100 kph. Overall, the authors reached an increase in the maximum throughput of about 10%.

Astarita et al. [21] analyzed various technologies (Internet of Things, connected vehicles, new sensors, clouds, blockchains, etc.) applied to mobile systems and their impact on traffic management and safety. Many recent publications discuss the benefits of connected and automated vehicles in highway management. Most of the

studies however provide only theoretical foundations [22] or show the impact within a simulated environment [23-28]. The effects of connected, cooperative, and/or autonomous vehicles are discussed in literature [29-32]. The main control objective is the work zone throughput. Yulong and Leilei [33] proposed the control flow of Intelligent Lane Merge Control System with Intelligent Transportation System (ITS) techniques. The ITS is also considered by Jacob et al. [34], utilized reinforcement learning-based optimal control. Yanli et al. [35] presented research of adaptive speed control of freeway work zone to decrease the speed difference between the upstream and downstream vehicles. General recommendations for intelligent vehicle highway systems are available even reported by Nanda [36]. Traffic management systems being a part of smart cities may also implement other functionalities, such as prioritizing emergency vehicles [37] which was not our case. Ambros et al. [38] focus on the effectiveness of section speed control in highway work zones in the Czech Republic. We believe that the results presented within this paper set the basis for a better comparison of the real impact of connected vehicles.

**1. 2. Evaluation Framework** The main aim of the pilot project was to implement, test, and evaluate a comprehensive modular mobile telematics system for traffic management in road closures, or temporarily

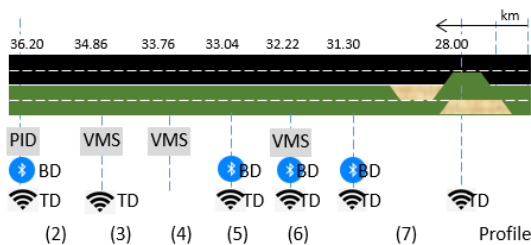


**Figure 1.** The configuration of the temporary highway traffic management system (simplified)

**TABLE 1.** Legend to Figure 1

Profile No.	Position [km]	Sensors		Actuators
		Traffic detector TD	Bluetooth detector BD	PID/VMS
1	36.22	Yes	Yes	PID
2	34.86	Yes	No	VMS
3	33.76	No	No	VMS
4	33.04	Yes	Yes	-
5	32.20	Yes	Yes	VMS
6	31.30	Yes	Yes	-
7	28.00	Yes	No	-

exposed locations within the road network. The system was expected to harmonize traffic flow, inform about the situation, and/or respond to the actual traffic. The pilot field test was realized on the highway D5 in the Czech Republic (a work zone between 28.5 and 30.8 km on the D5 highway was selected). However, the results were used as an indicator for future purchase and implementation of more such systems for the planned modernization of the main highway D1.

**2. EVALUATION RESULTS**

**2. 1. Principle of Operation** Two major technological systems were tested within the evaluation process—the warning system and the speed harmonization system. Both of them belong to the field of mobile highway management, but they use different means to address a driver. It is rather well-known that sudden changes in the driving speed (i.e., quick deceleration) and interactions of vehicles with significant speed differences are risky [39-40]; that can cause shock waves [41-42].

The *Warning System*: reacts to the situation when the traffic flow increases, the drivers are affected by the adjacent traffic and must decrease their speeds. If the speed decreases to 30 km/h, the traffic sign “Warning – Congestion ahead” is activated about 6 km ahead of the work zone. This warns the drivers, but further does not limit their behaviors.

The *Speed Harmonization system* is similar to the previous system but it also addresses the problem of sudden breaking, large differences in speeds, and shock waves. It affects the traffic flow using changes in the speed limits, which are dynamically decreased based on the actual traffic flow conditions.

**2. 2. Evaluation Methodology** The methodology for the pilot testing was in advance accepted by the Roads and Motorway Directorate of the Czech Republic (RSD). Preliminary analysis of the data from highway D5 showed the necessity of collecting data and warning the drivers at least 5 kilometers ahead of the work zone. Technologies were installed ahead of the selected work zone as depicted in Figure 1. The overall length of the road equipped with the technology (both data collection and warning and speed harmonization) was 8.2 km. Portable Information Displays (PID) and Variable Message Signs (VMS) were used as actuators. The road network segment was also covered by the GPRS – 3G (i.e., wireless technology) as a preferred mode of data exchange. To allow better understanding and confirmation of the results, there were cameras placed on the entire length of the monitored area, and the visual information was transmitted to the National Traffic Information Centre (NDIC) located in the eastern part of the country (Ostrava city). This also brought a possibility

of manual intervention by road operators (not used during our measurements). There are different ways how to evaluate a certain measure in the transportation field. Morris et al. [43] mention modeling, simulation; or before-after analysis which does not place any assumptions on the underlying model nor requires detailed calibration. For that reason, three evaluation phases (see Table 2) were used to collect statistically significant data.

The transmission layer in each profile contains 2G-2,5G (GPRS-HSDPA) and WiFi communication. The power supply layer varies according to the required consumption: Profile 1 – 2x 180 Ah batteries connected in parallel; Profile 2 - fuel cell, 360 Ah backup battery, connection to the SOS system, 360 Ah backup battery; Profile 3 - fuel cell, 2x 360 Ah backup battery, connection to the SOS system; Profile 4 - fuel cell, 180 Ah backup battery, 420 Ah battery; Profile 5 - fuel cell, 180 Ah backup battery, 420 Ah battery; Profile 6 - fuel cell, 180 Ah backup battery; and Profile 7 – solar panel, 40 Ah backup battery.

The 1<sup>st</sup> phase (Sept 5 – Oct 3, 2016) was essential as it described the situation without any warning or speed harmonization. Only reference data were collected to make later comparison with all other modes possible. The 2<sup>nd</sup> phase (Oct 3 – Oct 22, 2016) clearly denoted a phase,

in which the warning system was activated, but there was no speed harmonization function. Finally, the 3<sup>rd</sup> phase (Oct 22 – Nov 11, 2016) covered the situation with the speed harmonization system activated. The overall traffic volumes for each phase were similar, i.e., 17541 Veh/day, 16954 Veh/day, and 18138 Veh/day for each phase, respectively.

Table 3 shows values of daily traffic volumes (given in vehicles/day) as observed during the 10-weeks. Their graphical representation is available in Figure 2.

To be sure that we can assume the daily volumes to be from the same distribution, we tested the hypothesis that the second and third phases have the same daily average flow as the first phase. Using an independent two-sample t-test, we got a p-value of 0.355 and 0.404 respectively. That means that we cannot reject either of the hypotheses on a confidence level of 95% (<https://www.scribbr.com/statistics/t-test/>) and can assume the same traffic volumes for all phases.

The control unit of the local control system works in principle according to the schematic diagram shown in Figure 3. The whole system works basically automatically. In case of certain extraordinary and emergency situations, it will be possible to control each actor via the local control system or from the superior level (NDIC). The principal functions of the local control system include in particular:

**TABLE 2.** Evaluation phases and scenarios

Evaluation Phase	Data Collection	Warning System	Speed Harmonization
1 <sup>st</sup> Before: Basic Scenario	ON	OFF	OFF
2 <sup>nd</sup> After: Active Warning Only	ON	ON	OFF
3 <sup>rd</sup> After: Active Speed Harmonization	ON	OFF	ON

**TABLE 3.** Daily traffic volumes [Veh/day]

Mo	Tue	Wed	Thu	Fri	Sat	Sun
-	-	-	-	-	17066	15925
17331	17975	18779	20870	19412	16893	12257
17003	18441	16951	19601	20758	14876	13390
16542	18704	16892	18718	19647	20136	15265
15833	16197	17757	17691	19130	15437	13438
16525	17757	17425	19458	20057	13059	14541
16618	18254	18517	18882	17599	16958	14892
16654	18690	18417	19821	20287	19462	15922
17597	14997	17372	18479	20386	15748	12403
21878	20759	20792	17518	17433	-	-

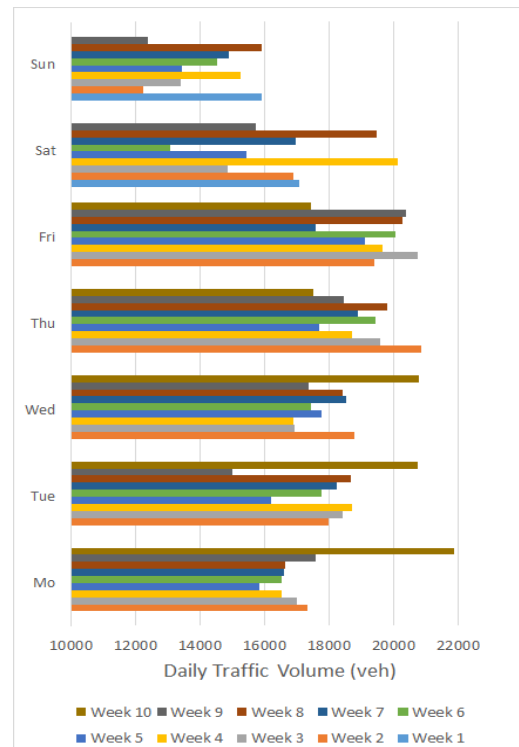


**Figure 2.** Comparison of aggregated daily volumes for particular days of the week

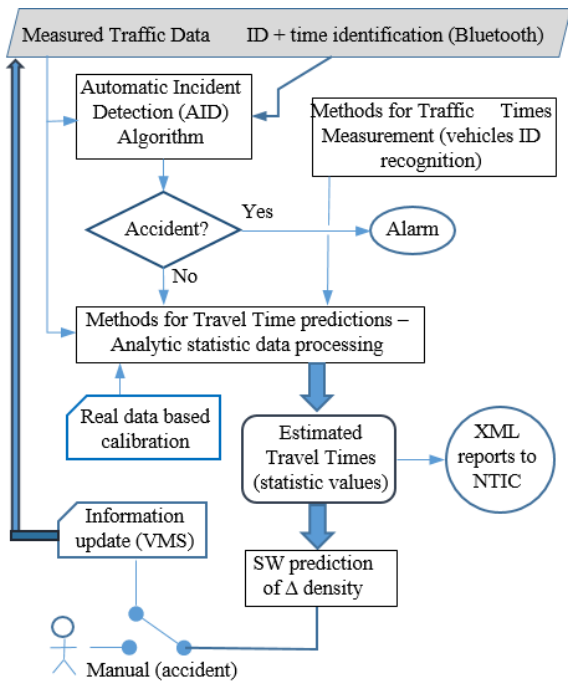


**Figure 3.** Schematic diagram of processes processed by the local control system

1. Communication between peripheral elements on the infrastructure (traffic detectors, driving time detectors, and at the same time all types of VMS);
2. Supervision of connected technology and sending status information to NDIC;
3. Data collection from detectors and their processing for the needs of control algorithms incl. sending selected information to NDIC;
4. Transmission of commands for displaying symbols on the VMS.

**3. RESULTS**

We provide selected results demonstrating its impact on traffic. In the pilot project, we focused on several aspects (variables) addressing the performance and impact of the mobile highway management system, particularly impact on road capacity; impact on the duration of traffic congestion, and impact on delay.

**3.1. Impact on Road Capacity** Table 4 provides the maximum and average flow per minute and average occupancy data.

**3.2. Impact on the Duration of Traffic Congestions** The traffic congestion was defined as the time when the average speed of the traffic flow is lower than 30 km/h

(based on speed reduction index as stated by Afrin and Yodo [44]) anywhere between the 1st and the 5th measurement points. In every evaluation phase, data were measured over 120 hours. The results are presented in Table 5.

**3.3. Impact on Delay** Another important parameter indicating the quality of the traffic management is delay (in seconds). The parameter was evaluated using floating car data from the project RODOS<sup>1</sup> where a large fleet of vehicles collected data and evaluated them. The data were collected and aggregated for segments 34 km – 32 km (i.e., profiles No. 3, 4, and 5).

Let us explain the parameter average delay. A delay of 0 seconds means, that a vehicle went through the segment with an average speed of 120 km/h so that the vehicle passed through the measured segment of 2 km in about 60 seconds. A delay of 30 seconds means that the vehicle passed through the segment in about 90 seconds, i.e., with an average speed of 80 km/h. The measurements from the RODOS vehicle fleet were collected for particular project phases as depicted in Table 6. The table indicates a significant improvement of 25.09 seconds already in the 2nd phase with an active warning system only. In the case of the 3rd phase with a speed harmonization system, the delay further improves by additional 4.58 seconds. The values and decrease of the average values can be seen in Figure 4.

**TABLE 4.** Resulting maximum and average flow per minute

Evaluation Phase	1 <sup>st</sup> Before Basic Scenario	3 <sup>rd</sup> After Active Speed Harmonization	Δ [%]
Max flow (Veh/min)	26.6	32.4	+21.8
Max flow (Veh/h)	1596	0.1	+21.8
Avg. flow (Veh/min)	21.4	21.7	+1.4
Avg. occupancy (%)	9.0	11.2	+24.4

**TABLE 5.** Impact on the duration of traffic congestions

Evaluation Phase: Ratio of congestions to the total time	1 <sup>st</sup>	2 <sup>nd</sup>	3 <sup>rd</sup>
Mo	11.5	8.0	5.5
Tue	17.0	6.0	11.0
We	23.5	32.5	8.5
Thu	35.0	31.0	33.0
Sat	11.0	4.5	0.0
Sun	22.0	9.0	6.0
Total	23.4	18.3	12.7

<sup>1</sup>[http://www.centrum-rodos.eu/about\\_the\\_rodos\\_center.aspx](http://www.centrum-rodos.eu/about_the_rodos_center.aspx)

**TABLE 6.** Impact on average delay for segments 34-32 km

1 <sup>st</sup> Evaluat. Phase		2 <sup>nd</sup> Evaluat. Phase		3 <sup>rd</sup> Evaluat. Phase	
Date	Avg daily delay [s]	Date	Avg daily delay [s]	Date	Avg daily delay [s]
10.IX	6.90	08.X	8.09	22.X	8.45
11.IX	106.99	09.X	3.09	23.X	4.14
12.IX	14.24	10.X	28.19	31.X	7.78
13.IX	7.79	11.X	7.61	01.XI	23.69
14.IX	9.53	12.X	68.21	02.XI	8.05
15.IX	102.27	13.X	50.41	03.XI	39.09
16.IX	125.20	14.X	48.21	04.XI	29.40
17.IX	68.48	15.X	10.28	05.XI	8.49
18.IX	107.55	16.X	10.07	06.XI	9.47
19.IX	10.84	17.X	6.40	07.XI	15.72
20.IX	18.45	18.X	6.56	08.XI	10.37
21.IX	41.98	19.X	45.72	09.XI	10.14
22.IX	50.24	20.X	16.39	10.XI	119.60
23.IX	117.48	21.X	127.51	11.XI	78.21
Average delay per phase [s]					
56.28		31.20		26.61	
Average daily improvements in delay between phases [s]					
25.09			4.58		

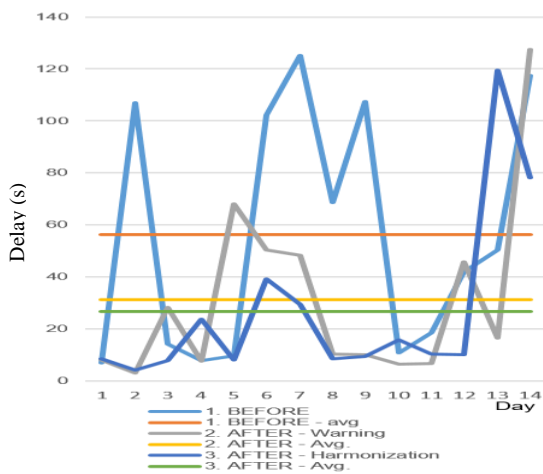


**Figure 4.** Delays and their average values as observed over 3 evaluation phases

We can observe a larger improvement between the 3<sup>rd</sup> phase (with active speed harmonization) and the 2<sup>nd</sup> phase (with warning system only). This is a significant contribution with a high positive impact on the overall traffic flow.

The achieved results demonstrate the importance of such a system deployment. The mobile highway

management system increased the road capacity by over 21%. Overall, there was a more than 5% decrease in the time of congestions for the 2nd phase. For the 3rd phase, this decrease reached over 10%. Similarly, the average daily delay decreased by almost 30 seconds.

#### 4. CONCLUSIONS

The major objective of this paper was to evaluate a pilot operation of the mobile highway management system consisting of warning and speed harmonization subsystems. A before-after analysis was conducted in 2016. With all other variables kept constant (mainly the traffic flow), the system measured various parameters. We described results dealing with the road capacity and the time in congestions, defined as the time when the speed was lower than 30 km/h.

Concerning the relatively short measurement period, we do not report on the impact of our system on road safety, even though quite important improvements could be expected there. During the 1<sup>st</sup> phase, there were 7 incidents reported, and during the following two phases only 2 incidents. This result could be expected, due to the speed harmonization. The results are however not statistically significant and require a long-term evaluation. Overall, the presented results have a huge impact, especially for a highway with such high traffic demand as D1. As the modernization of the highway takes years, such an increase has a major impact not only on the lost time but also on produced CO<sub>2</sub> emissions and fuel consumption. Without a doubt, an investment into a mobile highway management system for work zones has also a high societal impact.

In addition, the growth of cooperative vehicles will also influence the behavior of traffic flow in work zones. The cooperative vehicles can be used as further sensors measuring parameters of the traffic flow and simultaneously, they can be used as actuators. The control system can for example warn such vehicles in case of dangerous situations or provide recommendations for speed adaptation. This behavior will also be further investigated.

Based on the results and clear demonstration of savings the Roads and Motorways Directorate of the Czech Republic decided to order six sets of mobile highway management systems. They will be applied to future work zones on highways. This statement can be proved by tender-based information published in the tender area under the ID number VZ0084077 of the General Directorate of the Roads and Motorways Directorate of the Czech Republic (ŘSD ČR) and available online<sup>1</sup>.

<sup>1</sup> <https://tenderarena.cz/dodavatel/seznam-profilu-zadavatelu/detail/Z0003026/zakazka/310542>

We believe that our findings are important not only for researchers but also for highway managers as they support investments in new research as well as the implementation of mobile highway management systems in work zones.

## 5. ACKNOWLEDGEMENTS

This work was partially supported by the VEGA Grant Agency under the project VEGA-1/0241/2022.

## 6. REFERENCES

- Čížek, P. "Risk analysis using extended SAFMEA methodology on example of incubated companies", *Scientific papers of the University of Pardubice. Series D, Faculty of Economics and Administration*, (2017), <https://dk.upce.cz/handle/10195/67944>
- Příbyl, P., Příbyl, O. "Effective decision support system based on statistical tool", *CCIS*, Vol. 640, (2016), 378-387. DOI: 10.1007/978-3-319-49646-7
- Sreelatha, R., Roopalakshmi, R. "Highway Traffic Management System: Recent Trends and Future Challenges", in Proceedings of the International Conference on Intelligent Computing Systems (ICICS 2017 – Dec 15th - 16th 2017) organized by Sona College of Technology, Salem, Tamilnadu, India, Available at SSRN: 9 (2017). DOI: 10.2139/ssrn.3122193
- Amini, B., Shahi, J. "The Influence of Urban Network Features on the Quality of Traffic Service (RESEARCH NOTE)", *International Journal of Engineering*, Vol. 11, No. 3, (1998), 167-174.
- Jacobson, L. N. "Highway traffic operations and freeway management: State-of-the-practice", Final Report FHWA-OP-03-076, (2003)
- Cheng, Gz., Cheng, R. "Optimizing speed limits upstream of freeway reconstruction and expansion work zones based on driver characteristics", *Journal of Transportation Engineering Part A-Systems*, Vol. 146, No. 7, (2020), DOI: 10.1061/JTEPBS.0000389
- Yang, H., Ozbay, K., Ozturk, O., Xie, K. "Work zone analysis and modeling: A state-of-the-art review", *Traffic Injury Prevention*, Vol. 16, No. 4, (2015), 387-396, DOI: 10.1080/15389588.2014.948615
- Ackaah, W., Huber, G., Bogenberger, K., Bertini, R. "Assessing the Harmonization Potential of Variable Speed Limit Systems", *Transportation Research Record: Journal of the Transportation Research Board*, 2554, (2016), 129-138. DOI: 10.3141/2554-14
- Sinha, K. C., Fwa, T. F. "On the Concept of Total Highway Management", *Transportation Research Record*, Vol. 1229, (1989), 79-88.
- Harbord, B., Jones, J. "Camera Enforcement of Traffic Regulations", Colloquium on Camera Enforcement of Traffic Regulations London, England, IEEE XPlore Conference Proceedings Online, & Institution of Electrical Engineers. Computing & Control Division, (1996).
- Harbord, B. "M25 controlled motorway: Results of the first two years", in 9<sup>th</sup> International Conference on Road Transport Information and Control (Conf. Publ. No. 454), 149-154, (1998). DOI: 10.1049/cp:19980173
- Van Toorenburg, J.A.C. "Homogeniseren: effect van aangepaste adviessnelheden op de verkeersafwikkeling", Ministerie van Verkeer en Waterstaat, Rijkswaterstaat, Dienst Verkeerskunde, Rotterdam, (1983), 26.
- Suleiman, G. M., Bezgin, N. Ö., Ergun, M., Mustafa, G., Kardeş, M. "Effects of speed management and roadway parameters on traffic flow along arterials", in Proceedings of the Institution of Civil Engineers – Transport, Vol. 170, No. 6, (2017), 346-362. DOI: 10.1680/jtran.16.00035
- Vaziri, M. "Traffic Flow Characteristics of Isolated Off-ramps in Iranian Expressways", *International Journal of Engineering*, Vol. 11, No. 3, (1998), 135-146.
- Talebpour, A., Mahmassani, H. S., Hamdar, S. H. "Speed Harmonization: Evaluation of Effectiveness under Congested Conditions", *Transportation Research Record - Journal of the Transportation Research Board*, Vol. 2391, No. 1, (2013), 69-79. DOI: 10.3141/2391-07
- Grumert, E. F., Tapani, A., Ma, X. "Characteristics of variable speed limit systems", *European Transport Research Review*, Vol. 10, No. 21, (2018), 1-12. DOI: 10.1186/s12544-018-0294-8
- Vadde, R., Sun, D., Sai, O. J., Faruqi, M. A., Leelani, P. T. "A simulation study of using active traffic management strategies on congested freeways", *Journal of Modern Transportation*, 20, (2012), 178-184. DOI: 10.1007/BF03325796
- Debnath, A.K., Blackman, R., and Haworth, N. "Common hazards and their mitigating measures in work zones: A qualitative study of worker perceptions", *Safety Science*, Vol. 72, (2015), 293-301.
- Oskarbski, J., Kamiński, T., Kyamakya, K., Chedjou, J. Ch., Żarski, K., Pędzierska, M. "Assessment of the Speed Management Impact on Road Traffic Safety on the Sections of Motorways and Expressways Using Simulation Methods", *Sensors* 2020, Vol. 20, No. 5057, (2020). DOI: 10.3390/s20185057
- Strömgren, P., Lind, G. "Harmonization with Variable Speed Limits on Motorways", *Transportation Research Procedia*, Vol. 15, (2016), 664-675. DOI: 10.1016/j.trpro.2016.06.056
- Astarita, V., Festa, D. C. and Giofrè, V. P. "Mobile Systems applied to Traffic Management and Safety: a state of the art", *Procedia Computer Science*, Vol. 134, (2018), 407-414.
- Xiaodong, P., Xiang, W., Zhen, Y., Haozhe, C. "Highway Traffic Safety Management System Based on the Theory of Dissipative Structures and Catastrophe Theory", in 2009 Int. Conf. on Information Management, Innovation Management and Industrial Engineering, (2009), 42-45. DOI: 10.1109/ICIII.2009.320
- Dowling, R., Nevers, B., Jia, A., Skabardonis, A., Krause, C., Vasudevan, M. "Performance Benefits of Connected Vehicles for Implementing Speed Harmonization", *Transportation Research Procedia*, 15, (2016), 459-470. DOI: 10.1016/j.trpro.2016.06.039
- Malikopoulos, A. A., Hong, S., Park, B. B., Lee, J., Ryu, S. "Optimal Control for Speed Harmonization of Automated Vehicles", *IEEE Transactions on Intelligent Transportation Systems*, Vol. 20, No. 7, (2019), 2405-2417. DOI: 10.1109/TITS.2018.2865561
- Grumert, E., Tapani, A. "Impacts of a Cooperative Variable Speed Limit System", *Procedia- Social and Behavioral Sciences*. Vol. 43, (2012), 595-606. DOI: 10.1016/j.sbspro.2012.04.133
- Grumert, E., Ma, X., Tapani, A. "Analysis of a cooperative variable speed limit system using microscopic traffic simulation, Transportation" *Research Part C-emerging Technologies*, Vol. 52, (2015), 173-186. DOI: 10.1016/j.trc.2014.11.004
- Akinboro, S. A., Adeyiga, J. A., Omotosho, A., Akinwumi, A. O. "Mobile Road Traffic Management System Using Weighted

- Sensor”, *Int. Journal of Interactive Mobile Technologies*, Vol. 11, No. 5, (2017), 147-160.
28. Ingle, R. M., Williams, B. D., Sobhi, N., “An advanced traffic management system simulator for intelligent vehicle-highway systems research”, in Proceedings of Winter Simulation Conference, (1994), 1455-1460. DOI: 10.1109/WSC.1994.717550
  29. Wu, W. J., Sun, R. C., Ni, A. N., Liang, Z. K. and Jia, H. F. “Simulation and evaluation of speed and lane-changing advisory of CAVS at work zones in heterogeneous traffic flow”, *International Journal of Modern Physics B*, Vol. 34, No. 21, (2020), DOI: 10.1142/S021797922050201X
  30. Ramezani, H., Benekohal, R. “Optimized Speed Harmonization with Connected Vehicles for Work Zones”, in 18th IEEE Int. Conf. on Intelligent Transportation Systems, Las Palmas, Gran Canaria, Spain, (2015), 1081-1086. DOI: 10.1109/ITSC.2015.179
  31. Thandavarayan, G., Sepulcre, M., Gozalez J. “Cooperative Perception for Connected and Automated Vehicles: Evaluation and Impact of Congestion Control”, *IEEE Access*, Vol. 8, (2020), 197665-197683. DOI: 10.1109/ACCESS.2020.3035119
  32. Chehardoli, H., Homaienezhad, M. “Third-order Decentralized Safe Consensus Protocol for Inter-connected Heterogeneous Vehicular Platoons”, *International Journal of Engineering, Transactions C: Aspects*, Vol. 31, No. 6, (2018), 967-972. DOI: 10.5829/IJE.2018.31.06C.14
  33. Yulong, P., Leilei, D. “Study on Intelligent Lane Merge Control System for Freeway Work Zones”, in IEEE Intelligent Transportation Systems Conference, Seattle, WA, USA, (2007), 586-591. DOI: 10.1109/ITSC.2007.4357778
  34. Jacob, C., Abdulhai, B. Hadayeghi, A. and Malone, B. J. “Highway Work Zone Dynamic Traffic Control Using Machine Learning”, In IEEE Intelligent Transportation Systems Conference, Toronto, Ont., 267-272, DOI: 10.1109/ITSC.2006.1706753, (2006)
  35. Yanli, M., Gaofeng, G., Yuan, J., Xuesheng, Z. “Speed Control System Analysis of Freeway Work Zone Based on ITS”, in 5<sup>th</sup> Int. Conf. on Intelligent Systems Design and Engineering Applications (ISDEA), Hunan, China, (2014), 918-921. DOI: 10.1109/ISDEA.2014.267
  36. Nanda, R. S. “Intelligent Vehicle Highway Systems (Ivhs) Issues and Recommendations”, *International Journal of Engineering*, Vol. 8, No. 3, (1995), 121-132.
  37. Sumi, L., Ranga, V. “Intelligent Traffic Management System for Prioritizing Emergency Vehicles in a Smart City (TECHNICAL NOTE)”, *International Journal of Engineering, Transactions B: Applications*, Vol. 31, No. 2, (2018), 278-283.
  38. Ambros, J., Turek, R. Elgner, J., Krivankova, Z., Valentova, V. “Effectiveness evaluation of section speed control in Czech Motorway work zones”, *Safety*, Vol. 6, No. 3, (2020), DOI: 10.3390/safety6030038
  39. Hegyi, A., De Schutter, B., Hellendoorn, J. “Optimal Coordination of Variable Speed Limits to Suppress Shock Waves”, *IEEE Transactions on Intelligent Transportation Systems*, Vol. 6, No. 1, (2005), 102-112. DOI: 10.1109/TITS.2004.842408
  40. Zovak, G., Kos, G., Huzjan, B. “The Driver Behaviour and Impact of Speed on Road Safety on the Motorways in Croatia”, *Promet - Traffic & Transportation*, Vol. 29, No. 2, (2017), 155-164. DOI: 10.7307/ptt.v29i2.2071
  41. Ou, H., Tang, T. Q. “Impacts of moving bottlenecks on traffic flow”, *Physica A - Statistical Mechanics and Its Applications*, Vol. 500, (2018), 131-138. DOI: 10.1016/j.physa.2018.02.044
  42. Şahin, İ., Kuşakci, S. Ş., Aydin, G. “Shockwaves in Highway Traffic: Macroscopic and Microscopic Analysis with Wavelet Transform”, *Teknik Dergi*, Vol. 27, No. 2, (2016), 7429-7452.
  43. Morris, T. P., White, I. R., Crowther, M. J. “Using simulation studies to evaluate statistical methods”, *Statistics in Medicine*, Vol. 38, No. 11, (2019), 2074-2102. DOI: 10.1002/sim.8086
  44. Afrin, T., Yodo, N. “A Survey of Road Traffic Congestion Measures towards a Sustainable and Resilient Transportation System”, *Sustainability*, Vol. 12, No. 11, (2020), 4660. DOI: 10.3390/su12114660

---

### Persian Abstract

#### چکیده

فعالیت‌های ساخت و ساز و نگهداری راه‌ها باعث ازدحام و تأخیر در ترافیک می‌شود و برای تضمین ایمنی رانندگان و کارگران جاده‌ای چالش‌هایی ایجاد می‌کند. در حالی که مناطق شهری به خوبی مجهز به وسایل ترافیکی هستند، در مورد بزرگراه‌ها، شانس ما برای جمع‌آوری داده‌های ترافیکی و کنترل جریان ترافیک ممکن است محدود باشد. سپس استفاده از سیستم موقت مدیریت ترافیک بزرگراه راه حل مناسبی به نظر می‌رسد. اگرچه تأثیرات استقرار آن توسط بسیاری از مطالعات نظری مورد توجه قرار گرفته و بر روی مدل‌های شبیه‌سازی ترافیک نشان داده شده است، اما مراجع زیادی در مورد آزمایش‌های میدانی وجود ندارد. ما نتایج ارزیابی عملی سیستم مدیریت موقت بزرگراه نصب شده و آزمایش شده در بزرگراه اصلی جمهوری چک را در طول دوره کار جاده ارائه می‌دهیم. تجزیه و تحلیل قبل و بعد از داده‌های ترافیک جمع‌آوری شده برای اثبات اهمیت و تأثیر مثبت راه حل پیشنهادی انجام شد. ما بیش از ۲۰ درصد افزایش در ظرفیت منطقه کار جاده‌ای و تقریباً ۳۰٪ کاهش میانگین تأخیر برای یک وسیله نقلیه را نشان می‌دهیم. مدیران بزرگراه می‌توانند از نتایج برای توجیه سرمایه‌گذاری در استقرار موقت سیستم‌های مدیریت ترافیک بسیار استفاده کنند.

---



## Partial Replacement of Conventional Material with Stabilized Soil in Flexible Pavement Design

S. D. Turkane\*, S. K. Chouksey

Department of Civil Engineering, National Institute of Technology, Raipur, India

### PAPER INFO

#### Paper history:

Received 21 October 2021

Received in revised form 28 January 2022

Accepted 03 February 2022

#### Keywords:

Low Plastic Soil

Fly Ash

Geopolymer

Flexible Pavement

IIT PAVE

### ABSTRACT

Due to rapid urbanization and industrialization, the construction of roads increases rapidly for easy and fast transportation. Adequate land is not available everywhere to construct good roads; hence, roads are forcefully built on locally available soil such as loose soil or expansive soil. In this paper, an experimental investigation was carried out on low plastic soil (LPS) to enhance engineering properties by using chemical soil stabilization (fly ash-based geopolymer). The design of flexible pavement thickness was carried out for conventional and stabilized soil material using IITPAVE software as per IRC 37 guidelines. The results show the feasibility of fly ash-based geopolymer significant enhancement of strength were observed in terms of unconfined compressive strength (UCS) for various curing days (0 to 128 days), California bearing ratio (CBR), and Resilient modulus ( $M_R$ ). The microstructural analysis via Scanning Electronic Microscope (SEM) and X-Ray Diffraction Analysis (XRD) was also revealing the formation of geopolymeric gel which leads to the dense matrix to soil mass. The flexible pavement thickness significantly reduces with the application of stabilized low plastic soil.

doi: 10.5829/ije.2022.35.05b.07

## 1. INTRODUCTION

The road is the lifeline of any developing country; the economic growth is majorly dependent on the development of the road network. India has the second-largest road network in the world, spanning a total of 5.89 million kilometers. This road network transports 64.5% of all goods in the country and 90% of India's total passenger traffic uses the road network to commute as per Indian Road Industry Report [1]. Road transportation has gradually increased over the years with an improvement in connectivity between cities, towns, and villages in the country. With this increasing road transport, a huge amount of natural resources get consumed which is not healthy from an environmental perspective. Also, the stability of the road is a major issue caused due to the underlying subgrade or sub-base layer material. Therefore, to reduce the use of natural resources and construct sustainable roads by means of maximizing the use of locally available material or industrial

byproducts. Generally, the majority of roads are constructed on locally available soil which may not have adequate properties to bear the upcoming loads.

The local soil has low shearing strength, high swelling-shrinkage behaviour, large deformation [2]. Therefore, it is necessary to treat the existing land through ground improvement techniques to fulfill the increasingly demanding situations. Many techniques are widely in practice to treat the existing soil as subgrade and sub-base material, out of that chemical treatment is most common, cost-effective, and widely used. Traditionally, cement and/or lime are the most common stabilizers (binders), which form the cementitious material and hold the soil particles closely by internal chemical reactions in the presence of water. However, the production of this stabilizer causes more emissions of a greenhouse gas like carbon dioxide ( $\text{CO}_2$ ) which is hazardous to the environment. Therefore, researchers or engineers always search for new, sustainable, cost-effective stabilizer alternatives to ordinary portland cement and lime [3].

\*Corresponding Author Email: [sagarturkane24@gmail.com](mailto:sagarturkane24@gmail.com)  
(S. D. Turkane)

In this context, the use of local soil and an industrial byproduct such as cement kiln dust, calcium carbide residue, granulated blast furnace slag, fly ash, and geopolymeric binder in soil stabilization has been studied by several researchers [4–7] in recent years. Davidovits [8] proposed the geopolymer as an inorganic aluminosilicate material formed from the polycondensation of silica and alumina. The silica and alumina-rich precursors are majorly found in the coal ashes (fly ash), which are available in a tremendous amount. In India, coal ash production is nearly 226.13 million metric tons and utilization is about 187.87 million metric tons, i.e. 83.05% [9]. Therefore, a fly ash-based geopolymer could also be a better option for soil stabilization already proposed by Zhang et al. [10] and has become a green area for research in soil stabilization. Although, numbers of literature are available on fly ash-based geopolymer in building material applications [11–13]. All this literature explains the significant applicability of fly ash-based geopolymer as building materials, especially as concrete or mortar that shows the high mechanical strength, more durable, and sustainable material. However, selected studies are available on fly ash-based geopolymer in expansive soil stabilization [7, 12, 14–19]. The stabilization of clay soil by means of geopolymerization would improve the mechanical strength (UCS, CBR, etc.). For the alkaline activation of fly ash, sodium hydroxide and sodium silicate are the best combinations [20–22]. The modular ratio (sodium silicate /sodium hydroxide) is greater than 1.5 strength of stabilized soil decreases [16]. Therefore, looking at the rare application of fly ash-based geopolymer in soil stabilization, this paper deals with the feasibility of the fly ash-based geopolymer for locally available soil stabilization, that can be suitable as a road pavement material.

The contribution of various authors shows the importance of fly ash-based geopolymer for soil stabilization and its potential to provide eco-friendly solutions for various geotechnical projects. However, the application of these stabilized materials for actual road pavement design is very selected [23]. Thus, this paper aimed to design the flexible pavement with low plastic soil and fly ash-based geopolymer as a stabilizer. It also aimed to provide the application of fly ash in pavement construction, in an eco-friendly manner and to develop a sustainable methodology. The paper consists of the material used for the study followed by the sample preparation and testing methodology adopted. The mechanical performance in terms of UCS, CBR, and resilient modulus along with microstructural analysis was carried out to understand the micro-level changes that occurred in soil samples. Furthermore, the application of stabilized soil is demonstrated in the flexible road pavement with a comparison of conventional soil.

## 2. MATERIALS

Experimental investigations are performed on low plastic soil (LL < 50), collected from Raipur city, Chhattisgarh, India. The engineering properties of LPS and fly ash, such as specific gravity (G), liquid limit (LL), plastic limit (PL), plasticity index (PI) and maximum dry density (MDD), optimum moisture content (OMC) are determined according to IS:2720 (Part 3)-1980, IS:2720 (Part 5)-1985, and the values are tabulated in Table 1. Fly ash (FA) used for the experiments were obtained from the National Thermal Power Corporation and Steel Authority of India Limited (NSPCL), Bhilai, Chhattisgarh, India. The chemical composition of low plastic soil and fly ash is determined by Energy-dispersive X-ray spectroscopy (EDX) analysis and presented in Table 2. The results show that the major components in fly ash are  $\text{SiO}_2$ ,  $\text{Al}_2\text{O}_3$ , and  $\text{Fe}_2\text{O}_3$ , suitable precursors for forming a good geopolymer [24, 25]. Also, fly ash is non-plastic, non-swelling material which acts as a filler in the soil mass also helps to the reduction of plastic characteristics of the soil. According to ASTM C 618 – 05, 2005 [26], it is categorized as F-type fly ash. Figure 1 presents the particle size distribution curve for LPS and FA, respectively. The percentage variation of various sizes of particles is presented in Table 1.

For the geopolymerization of fly ash, a proportionate mixture of sodium hydroxide (NaOH) and sodium silicate ( $\text{Na}_2\text{SiO}_3$ ) solutions were used. The liquid sodium silicate consists of  $\text{Na}_2\text{O}$ = 14.35% and  $\text{SiO}_2$ = 33.10%, while sodium hydroxide solution of 6 molar (M). The researchers suggested a suitable concentration for NaOH between 4.5 to 18 molar [27–29]. Hence, from an economic and safety point of view, low concentrated

**TABLE 1.** Engineering Properties

Sr. No.	Properties	Low Plastic Soil	Fly Ash
1	G	2.59	2.44
2	LL (%)	42.3	34.56
3	PL (%)	20.16	NA
4	PI (%)	22.14	-
5	Sand (%)	30.21	-
6	Silt & Clay (%)	69.8	100
7	Classification	CL	F Class [26]
8	MDD ( $\text{kN/m}^3$ )	18.42	11.56
9	OMC (%)	15.8	18.18
10	UCS (kPa)	238	-
11	CBR (%)	4.8	-

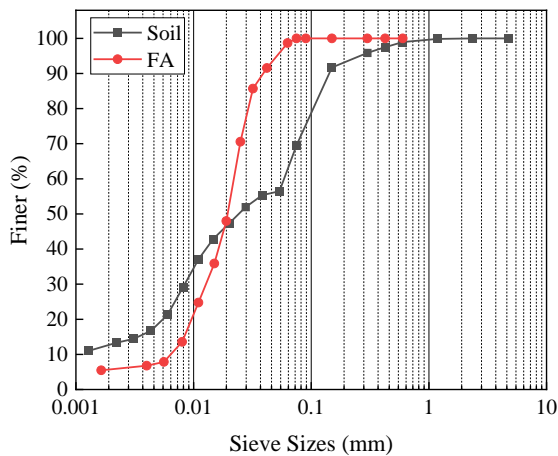


Figure 1. Particle Size Distribution

NaOH, i.e., 6 molar, were adopted for the experimental investigation.

The chemical composition of LPS and fly ash is summarized in Table 2.

### 3. SAMPLE PREPARATION AND TESTING

Many researchers studied on stabilization of soil [6, 30–34]. They found the optimized percentage of various binders, such as fly ash content, lime content, rice husk ash, etc., lies between 15 to 25%. Therefore, LPS blended with various proportions of fly ash (10, 15, 20, 25, and 30%) with an alkaline activator to form a geopolymer. The NaOH of 6M solution was prepared just one day before casting of samples for the test by mixing 240 g (NaOH molecular weight 40 g/mole\* 6M) of NaOH flakes to make a 1-liter solution in water. The  $\text{Na}_2\text{SiO}_3/\text{NaOH}$  ratio was selected as 1.5 to see the effect of activator on LPS-FA composite as per the recommendation [16].

A predetermined (calculated based on MDD) proportion of LPS and FA was mixed homogeneously, and then an activator (calculated based on OMC) was

TABLE 1. Chemical Composition

Constituents (%)	LPS	FA
Silica ( $\text{SiO}_2$ )	66.99	62.39
Alumina ( $\text{Al}_2\text{O}_3$ )	12.89	24.47
Iron Oxide ( $\text{Fe}_2\text{O}_3$ )	12.09	5.74
Calcium Oxide (CaO)	2.22	1.79
Magnesium Oxide (MgO)	1.32	0.62
Potassium (K)	3.4	2.75
Titanium (Ti)	0.93	2.25

TABLE 2. Sample Details

Samples	LPS (%)	FA (%)	No. of Samples	Curing Periods
FA•	100	0	3	0 days
FA10	90	10	18	
FA15	85	15	18	
FA20	80	20	18	0, 7, 14, 28, 56 and 128 days
FA25	75	25	18	
FA30	70	30	18	

added. The sample was filled into UCS mould and compacted for making a cylindrical sample of 50 mm diameter and 100 mm height. For the result consistency average of 3 samples, were prepared. The total number of samples with respect to curing days cast was 93 as mentioned in TABLE 2. After compaction, the samples were extracted and placed in an airtight plastic bag for curing according to the standard method suggested [35]. Under ambient temperature or room temperature (25–28 °C), all samples were cured for 0, 7, 14, 28, 56, and 128 days and, after curing, tested as per IS 4332 Part V (1970). The specimen prepared at their respective MDD and OMC for the CBR test and tested for unsoaked and soaked conditions. The resilient modulus of all samples was estimated according to AASHTO: T 307-99 [36]. Scanning Electronic Microscope (SEM), and X-ray Diffraction (XRD) were also carried out to understand the microstructural characteristics of stabilized LPS after 28 days curing period, and also to check the formation of geopolymer.

### 4. RESULT AND DISCUSSION

**4. 1. Unconfined Compression Test** The LPS stabilized with fly ash-based geopolymer for various fly ash content and curing periods of 0, 7, 14, 28, 56, and 128 days to understand the effect of fly ash content and time effect on strength enhancement. The UCS results were reported using the average UCS value of three samples to assure the test result consistency. It can be observed that from Figure 2 with the increase in fly ash content up to 25% UCS value increases further replacement it decreases. This UCS increment is may due to a higher amount of alumina and silica leached from the available fly ash content, which may lead to geopolymer gel/matrix formation. That indicates up to 25% of fly ash as it gets consumed to form geopolymer gel. However, further reduction may occur due to some particles remaining unreacted with further fly ash replacement, and that act as filler material.

Curing of sample promotes the polymeric reaction at the ambient temperature samples become hardened

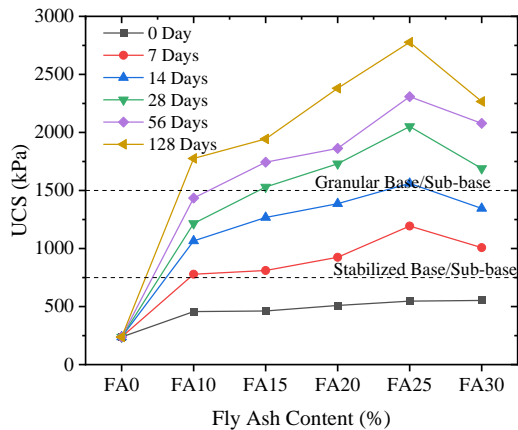


Figure 2. UCS Result

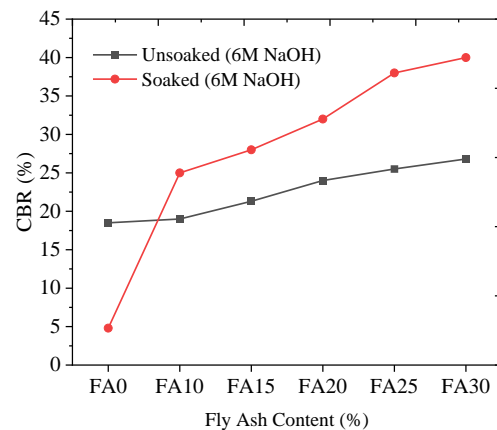


Figure 3. CBR Strength Result

slowly. As shown in Figure 2, with an increasing curing period, strength increases, indicating that at ambient temperature the polymeric reaction takes place, which binds the soil particles closely. The continuous increment in the UCS value was observed with curing days. However, UCS value for 7 and 14 days curing periods of FA10 % to FA30 % containing soil specimen satisfy the minimum required strength (750 kPa) for stabilized sub-base layer at the end of 28 days curing period. Further, increasing in curing periods 28 to 128 days the stabilized LPS satisfies the minimum strength requirement for the granular base/sub-base. A similar trend of results was observed by the various researchers [14–17, 37]. These strength enhancements show the continuous formation of polymeric reaction and binding of soil particles due to more silicate and aluminate availability for geopolymer formation [17, 38].

#### 4. 2. California Bearing Ratio (CBR) and Resilient Modulus ( $M_R$ )

CBR test performed on soil specimen for unsoaked and 28 days (4 days soaking + 24 days curing) cured samples. Figure 3 shows the variation of CBR value to fly ash content. It has been observed that the CBR value for LPS is 18.5 % for unsoaked conditions and 4.8% for soaked conditions. The CBR value for unsoaked conditions increases due to mixes offering more resistance due to better packing of different sized fractions. Further, for curing samples rapid improvement in the CBR value has been observed this can be attributed to the less attraction of water during the curing process as a result of the dense microstructure of soil particles due to gel formation [17, 19, 39, 40].

Resilient Modulus ( $M_R$ ) is a fundamental material property used to characterize unbound pavement materials [36]. The variation of resilient modulus ( $M_R$ ) to the fly ash content is shown in Figure 4. The result showed a similar type of trend as observed in CBR tests. The  $M_R$  value of fly ash-based geopolymer treated soil is

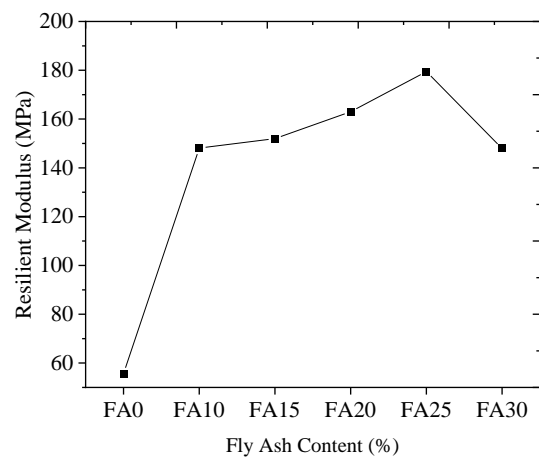


Figure 4. Resilient Modulus for untreated and treated LPS

in the range of 148 to 179 MPa which is much higher than the untreated LPS (55.62 MPa).

#### 4. 3. Microstructural Analysis

The microstructural and morphologic study on the fly ash-based geopolymer specimens was elaborated via XRD and SEM an advanced tool for monitoring the microstructural changes.

##### 4. 3. 1. X-Ray Diffraction Analysis (XRD)

The X-ray diffraction technique is the most widely used method to identify soil minerals and study their crystal structure. Figure 5 shows the XRD pattern for the various fly ash content for stabilized LPS after 28 days of curing. The LPS shows the presence of clay minerals such as montmorillonite (M), illite (I) along with quartz (Q), and a small amount of muscovite (Ms) & feldspar (F). Thus, LPS with fly ash-based geopolymer altered the diffraction pattern significantly; new reflection patterns were also seen, namely sillimanite (S), phillipsite (P),

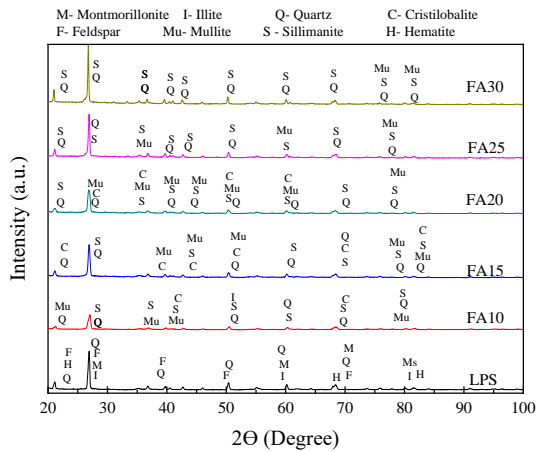


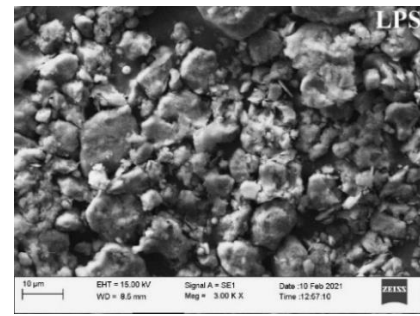
Figure 5. XRD

mullite (Mu), and cristobalite (C) approximately at  $2\theta = 21.22^\circ, 27.07^\circ, 35.49^\circ, 39.87^\circ, 42.75^\circ, 50.50^\circ, 60.30^\circ, 68.53^\circ, 75.97^\circ, 81.70^\circ, \text{ and } 82^\circ$ . These minerals roughly belong to crystalline phases detected in the formed gel by the active dissolution of sodium aluminosilicate compounds with pozzolanic particles [21, 22].

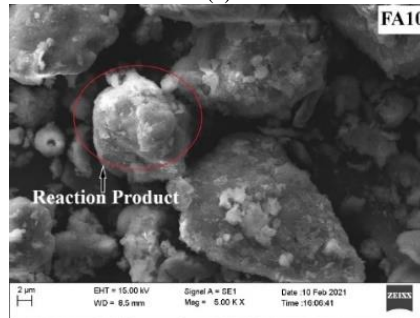
Furthermore, it was also observed that low-intensity peaks of LPS show participation in the process of geopolymerization [41]. Also, some of the peaks were absent compared to the virgin LPS, indicating the disturbance of the layered structure of clay mineralogy [22]. It could be said that the binding effect of geopolymer gel renders the improvement in the mechanical strength of the soil. Moreover, due to the formation of new crystalline minerals which disturbed the original layered structure that controls the swelling behaviour of soil. As stabilized LPS becomes less prone to swelling and shrinkage behaviour. Hence, it can be concluded that the binding effect of geopolymeric gel due to the presence of aluminosilicate and zeolite group (Sillimanite & Phillipsite) would improve the mechanical strength of LPS.

4. 3. 2. Scanning Electronic Microscope (SEM)

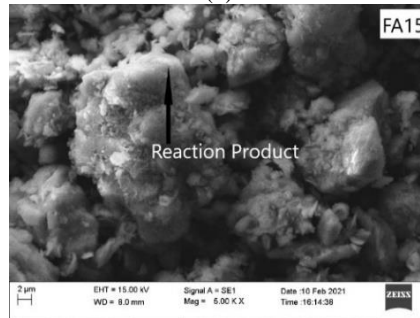
The microstructural changes of LPS are understood by SEM images analysis after 28 days of curing. Figure 6 (b to f) shows SEM images for fly ash content of 10, 15, 20, 25 and 30%. The images reveal that the fly ash was consumed for the formation of geopolymeric gel or reaction product. This product form mainly due to the dissolution of silica and alumina ions leading to leaching of sodium aluminate hydrate gel (NASH) and further with polymerization reaction in the presence of calcium at ambient temperature, it produces the calcium aluminosilicate hydrate (CASH). However, a few quantities of unreacted or partially reacted fly ash particles were also observed especially in the FA30 sample.



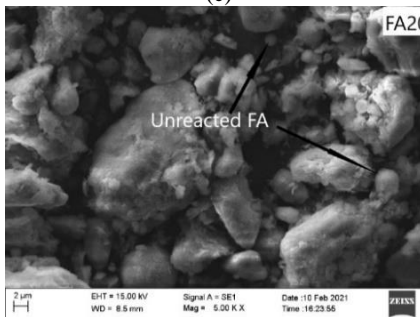
(a)



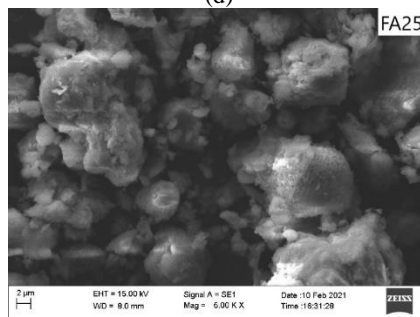
(b)



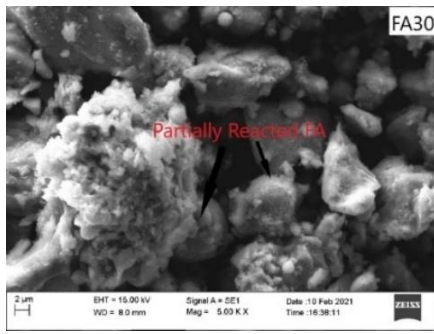
(c)



(d)



(e)



(f)

**Figure 6.** SEM for (a) LPS (b) FA10 (c) FA15 (d) FA20 (e) FA25 and (f) FA30

## 5. DESIGN OF FLEXIBLE PAVEMENT THICKNESS USING STABILIZED SOIL

The application of stabilized soil is demonstrated in terms of the design of flexible pavement thickness for high-volume roads as per IRC:37-2018 [42]. The pavement thickness using low plastic soil is tabulated in Table 4. The CBR value of the LPS subgrade is 4.8%; therefore, the stabilized soil having a CBR more or equal to 10% should be laid. As per IRC:37-2012, from Figure 7, the effective CBR is found to be 8%. The resilient modulus of LPS from the experiment is 55 MPa.

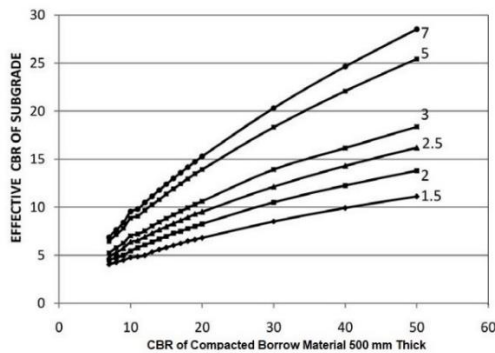


**Figure 7.** Effective CBR for Subgrade as per IRC: 37-2012 [43]

The elasticity modulus for the binder course and surface course is considered to be 3000 MPa, whereas the elastic modulus of Wet Mix Macadam (WMM) and Granular Sub-Base (GSB) is estimated together using Equation (1). The horizontal tensile strain ( $\epsilon_t$ ) and vertical compressive strain ( $\epsilon_v$ ) of the conventional material are analyzed from IITPAVE (pavement analysis software), and the results are tabulated in Table 4.

$$MR_{gain} = 0.2 * (h)^{0.45} * MR_{Support} \quad (1)$$

As from the above experimental analysis, fly ash-based geopolymer could find a good soil stabilizer of fly ash 25% and 6M NaOH (FA25+6M). the proposed pavement thickness with stabilized LPS is calculated and tabulated as per IRC 37 in Table 5. The stabilized LPS CBR value was found to be 38% so, from Figure 7, the effective CBR is 22%, and the resilient modulus for the modified subgrade is 179 MPa should be limited to 100 MPa.

The elastic modulus of the WMM course is considered as 350 MPa and for the binder course and surface course together is 3000 MPa. As per IRC SP 89-2018, the cement-treated sub-base (CTSB) should have a minimum elastic modulus of 2000 MPa, and using Eq. (2) the resilient modulus ( $M_R$ ) of stabilized LPS is calculated. The UCS value for stabilized soil (FA25+6M) after 28 days of curing is 2.050 MPa, and the resilient modulus is found to be 2050 MPa. Hence, the conventional subbase material can be replaced with CTSB of LPS+FA25+6M. The calculated resilient modulus of stabilized soil is too high, thus 600 MPa is considered for the analysis as per IRC 37. The cross-section of the proposed high-volume road pavement is as shown in Figure 8. The estimated horizontal tensile ( $\epsilon_t$ ) and vertical compressive ( $\epsilon_v$ ) strain calculated through IITPAVE software were found to be less than the conventional material pavement material.

$$M_R = 1000 * UCS_{28\text{ Days}} \quad (2)$$

Table 6 compares pavement thickness using conventional pavement material and fly ash-based geopolymer LPS used as a sub-base material. A

**TABLE 4.** Pavement Thickness Using Conventional Material

Design Traffic (MSA)	Pavement Thickness (mm)				Total Thickness (mm)	$M_R$ (MPa)	$\epsilon_v$ ( $10^{-4}$ )	$\epsilon_t$ ( $10^{-4}$ )
	GSB	WMM	BC	SC				
5	150	250	50	30	480	163	6.17	3.22
10	200	250	60	30	540	172	4.98	2.93
20	200	250	90	40	580	172	3.94	2.27
30	200	250	95	40	585	172	3.83	2.2
40	200	250	105	40	595	172	3.62	2.06
50	200	250	115	40	605	172	3.42	1.93

Surface Course $M_R = 3000$ MPa
Binder Course $M_R = 3000$ MPa
WMM $M_R = 350$ MPa
CTSB $M_R = 600$ MPa
Modified Soil CBR = 38% $M_R = 100$ MPa
Subgrade of CBR = 4.8 %

**Figure 8.** Proposed Cross Section of High-Volume Road Pavement

significant reduction of pavement thickness was observed that indicates the reduction in the use of natural resources such as aggregates, moorum, etc. Also, for soil stabilization, the traditional stabilizer such as cement and lime can be replaced with sustainable soil stabilizers (fly ash geopolymer). Furthermore, the industrial by-product can be effectively utilized in an eco-friendly manner for construction activity. Based on the above observations, applying fly ash-based geopolymer to stabilizing LPS in subgrade and subbase layers becomes economical; partially replacing inert material and saving natural recourse leads to a more sustainable solution.

**TABLE 3.** Pavement Thickness Using Stabilized LPS

Design Traffic (MSA)	Pavement Thickness (mm)				Total Thickness (mm)	$\epsilon_v (10^{-4})$	$\epsilon_t (10^{-4})$
	CTSB	WMM	BC	S C			
5	200	150	0	40	390	4.30	1.03
10	200	150	0	40	390	4.30	1.03
20	200	150	50	30	430	3.55	0.82
30	200	150	50	40	440	3.37	0.77
40	200	150	55	40	445	3.28	0.75
50	200	150	65	40	455	3.12	0.71

**TABLE 4.** Comparison of Pavement Thickness

Design Traffic (MSA)	Pavement Thickness (mm)		Total Thickness Reduction (mm)	% Reduction Thickness
	Conventional Material	Stabilized LPS		
5	480	390	90	18.75
10	540	390	150	27.78
20	580	430	150	25.86
30	585	440	145	24.79
40	595	445	150	25.21
50	605	455	150	24.79

## 6. CONCLUSIONS

Following conclusions were drawn based on the laboratory experimental results, and application of fly ash-based geopolymer stabilized LPS for the design of pavement thickness for high volume roads.

- Low plastic soil treated with fly ash-based geopolymer significantly increases strength characteristics (UCS and CBR). The fly ash content of 25% with 6M NaOH concentration shows the highest strength.
- The strength improvement with fly ash-based geopolymer stabilized LPS after 7 days of curing is

greater than the minimum strength requirement for sub-base course of road pavement as per IRC: 37-2012.

- The microstructure of stabilized LPS shows the formation of geopolymer gel; as a result, particles are closely packed with each other and form a dense matrix.
- The granular sub-base material can be replaced with cement-treated sub-base material.
- A significant reduction of pavement thickness was observed with the application of fly ash-based geopolymer.

Fly ash-based geopolymer can be the found effective chemical stabilizer for stabilizing low plastic soil, but the

challenge lies in its effective application. Also, the exact dosage of fly ash and activator needs to be checked before a particular field application. This research could also contribute to waste mitigation as well as the development of sustainable soil stabilizers in the road construction industry.

## 7. REFERENCES

- IBEF, R. India Brand Equity Foundation 2019.
- Mitchell J.K., and Soga K. Fundamentals of Soil Behavior. John Wiley & Sons, Inc. (2005).
- Turkane S.D., and Chouksey S.K. "Application of Response Surface Method for Optimization of Stabilizer Dosages in Soil Stabilization". *Innovative Infrastructure Solutions*, (2022), 1-12. <https://doi.org/10.1007/s41062-021-00704-9>
- Ghosh P., Kumar H., and Biswas K. "Fly Ash and Kaolinite-Based Geopolymers: Processing and Assessment of Some Geotechnical Properties". *International Journal of Geotechnical Engineering*, Vol. 10, No. 4, (2016), 377-386. <https://doi.org/10.1080/19386362.2016.1151621>
- Leong H.Y., Ong D.E.L., Sanjayan J.G., and Nazari A. "Strength Development of Soil-Fly Ash Geopolymer: Assessment of Soil, Fly Ash, Alkali Activators, and Water". *Journal of Materials in Civil Engineering*, Vol. 30, No. 8, (2018), [https://doi.org/10.1061/\(ASCE\)MT.1943-5533.0002363](https://doi.org/10.1061/(ASCE)MT.1943-5533.0002363)
- Kanthe V., Deo S., and Murmu M. "Combine Use of Fly Ash and Rice Husk Ash in Concrete to Improve Its Properties". *International Journal of Engineering, Transactions A: Basics*, Vol. 31, No. 7, (2018), 1012-1019. <https://doi.org/10.5829/ije.2018.31.07a.02>
- Phummiphon I., Horpibulsuk S., Sukmak P., Chinkulkijniwat A., Arulrajah A., and Shen S.L. "Stabilisation of Marginal Lateritic Soil Using High Calcium Fly Ash-Based Geopolymer". *Road Materials and Pavement Design*, Vol. 17, No. 4, (2016), 877-891. <https://doi.org/10.1080/14680629.2015.1132632>
- Davidovits J. "Geopolymers". *Journal of Thermal Analysis*, Vol. 37, No. 8, (1991), 1633-1656. <https://doi.org/10.1007/bf01912193>
- Central Electricity Authority "Report on Fly Ash Generation at Coal/Lignite Based Thermal Power Stations and Its Utilization in the Country for the Year 2019-20" (2020), 1-32
- Zhang M., Guo H., El-Korchy T., Zhang G., and Tao M. "Experimental Feasibility Study of Geopolymer as the Next-Generation Soil Stabilizer". *Construction and Building Materials*, Vol. 47, (2013), 1468-1478. <https://doi.org/10.1016/j.conbuildmat.2013.06.017>
- Amran M., Debbarma S., and Ozbakkaloglu T. "Fly Ash-Based Eco-Friendly Geopolymer Concrete : A Critical Review of the Long-Term Durability Properties". *Construction and Building Materials*, Vol. 270, (2021), 121857. <https://doi.org/10.1016/j.conbuildmat.2020.121857>
- Toniolo N., and Boccaccini A.R. "Fly Ash-Based Geopolymers Containing Added Silicate Waste. A Review". *Ceramics International*, Vol. 43, No. 17, (2017), 14545-14551. <https://doi.org/10.1016/j.ceramint.2017.07.221>
- Rashad A.M. "A Brief on High-Volume Class F Fly Ash as Cement Replacement - A Guide for Civil Engineer". *International Journal of Sustainable Built Environment*, Vol. 4, No. 2, (2015), 278-306. <https://doi.org/10.1016/j.ijsbe.2015.10.002>
- Abdullah H.H., Shahin M.A., Walske M.L., and Karrech A. "Systematic Approach to Assessing the Applicability of Fly-Ash-Based Geopolymer for Clay Stabilization". *Canadian Geotechnical Journal*, Vol. 57, No. 9, (2020), 1356-1368. <https://doi.org/10.1139/cgj-2019-0215>
- Corrêa-Silva M., Araújo N., Cristelo N., Miranda T., Gomes A.T., and Coelho J. "Improvement of a Clayey Soil with Alkali Activated Low-Calcium Fly Ash for Transport Infrastructures Applications". *Road Materials and Pavement Design*, Vol. 20, No. 8, (2019), 1912-1926. <https://doi.org/10.1080/14680629.2018.1473286>
- Murmu A.L., Jain A., and Patel A. "Mechanical Properties of Alkali Activated Fly Ash Geopolymer Stabilized Expansive Clay". *KSCE Journal of Civil Engineering*, Vol. 23, No. 9, (2019), 3875-3888. <https://doi.org/10.1007/s12205-019-2251-z>
- Murmu A.L., Dhole N., and Patel A. "Stabilisation of Black Cotton Soil for Subgrade Application Using Fly Ash Geopolymer". *Road Materials and Pavement Design*, (2018), 1-19. <https://doi.org/10.1080/14680629.2018.1530131>
- Parhi P.S., Garanayak L., Mahamaya M., and Das S.K. "Stabilization of an Expansive Soil Using Alkali Activated Fly Ash Based Geopolymer". In: Hoyos LR, McCartney J (eds) *Advances in Characterization and Analysis of Expansive Soils and Rocks, GeoMEast 2017, Sustainable Civil Infrastructures*. Springer International Publishing, Cham, [https://doi.org/10.1007/978-3-319-61931-6\\_4](https://doi.org/10.1007/978-3-319-61931-6_4)
- Varma N., Kumar T., and Nagaraju V. "Compressive Strength of High Plastic Clay Stabilized with Fly Ash-Based Geopolymer and Its Synthesis Parameters". In: *Transportation, Water and Environmental Geotechnics Proceedings of Indian Geotechnical Conference 2020*. 25-37, [https://doi.org/10.1007/978-981-16-2260-1\\_3](https://doi.org/10.1007/978-981-16-2260-1_3)
- Hardjito D., Wallah S.E., Sumajouw D.M.J., and Rangan B.V. "On the Development of Fly Ash-Based Geopolymer Concrete". *ACI Materials Journal*, Vol. 101, No. 6, (2004), 467-472. <https://doi.org/10.14359/13485>
- Syed M., GuhaRay A., and Kar A. "Stabilization of Expansive Clayey Soil with Alkali Activated Binders". *Geotechnical and Geological Engineering*, Vol. 38, No. 6, (2020), 6657-6677. <https://doi.org/10.1007/s10706-020-01461-9>
- Miao S., Shen Z., Wang X., Luo F., Huang X., and Wei C. "Stabilization of Highly Expansive Black Cotton Soils by Means of Geopolymerization". *Journal of Materials in Civil Engineering*, Vol. 29, No. 10, (2017), 1-9. [https://doi.org/10.1061/\(ASCE\)MT.1943-5533.0002023](https://doi.org/10.1061/(ASCE)MT.1943-5533.0002023)
- Amulya S., and Ravi Shankar A.U. "Replacement of Conventional Base Course with Stabilized Lateritic Soil Using Ground Granulated Blast Furnace Slag and Alkali Solution in the Flexible Pavement Construction". *Indian Geotechnical Journal*, Vol. 50, No. 2, (2020), 276-288. <https://doi.org/10.1007/s40098-020-00426-2>
- Khale D., and Chaudhary R. "Mechanism of Geopolymerization and Factors Influencing Its Development: A Review". *Journal of Materials Science*, Vol. 42, No. 3, (2007), 729-746. <https://doi.org/10.1007/s10853-006-0401-4>
- Zhuang X.Y., Chen L., Komarneni S., Zhou C.H., Tong D.S., Yang H.M., Yu W.H., and Wang H. "Fly Ash-Based Geopolymer: Clean Production, Properties and Applications". *Journal of Cleaner Production*, Vol. 125, (2016), 253-267. <https://doi.org/10.1016/j.jclepro.2016.03.019>
- ASTM C 618 - 05 "Standard Specification for Coal Fly Ash and Raw or Calcined Natural Pozzolan for Use in Concrete"
- Mustafa Al Bakri A.M., Kamarudin H., Bnhussain M., Rafiza A.R., and Zarina Y. "Effect of Na<sub>2</sub>SiO<sub>3</sub>/NaOH Ratios and NaOH Molarities on Compressive Strength of Fly-Ash-Based

- Geopolymer". *ACI Materials Journal*, Vol. 109, No. 5, (2012), 503-508. <https://doi.org/10.14359/51684080>
28. Nematollahi B., and Sanjayan J. "Effect of Different Superplasticizers and Activator Combinations on Workability and Strength of Fly Ash Based Geopolymer". *Materials and Design*, Vol. 57, (2014), 667-672. <https://doi.org/10.1016/j.matdes.2014.01.064>
  29. Yaghoubi M., Arulrajah A., Disfani M.M., Horpibulsuk S., Bo M.W., and Darmawan S. "Effects of Industrial By-Product Based Geopolymers on the Strength Development of a Soft Soil". *Soils and Foundations*, Vol. 58, No. 3, (2018), 716-728. <https://doi.org/10.1016/j.sandf.2018.03.005>
  30. Çokça E. "Use of Class C Fly Ashes for the Stabilization of an Expansive Soil". *Journal of Geotechnical and Geoenvironmental Engineering*, Vol. 127, No. 7, (2001), 568-573. [https://doi.org/10.1061/\(ASCE\)1090-0241\(2001\)127:7\(568\)](https://doi.org/10.1061/(ASCE)1090-0241(2001)127:7(568))
  31. Kate J.M. "Strength and Volume Change Behavior of Expansive Soils Treated with Fly Ash". In: *Innovations in Grouting and Soil Improvement*. American Society of Civil Engineers, Austin, Texas, 1-15, [https://doi.org/10.1061/40783\(162\)19](https://doi.org/10.1061/40783(162)19)
  32. Mahajan S.M., and Parbat D.K. "Effects of Fly Ash on Engineering Properties of BC Soil". *International Journal of Research in Engineering, Science and Technologies*, Vol. 1, No. 5, (2015),
  33. Trivedi J.S., Nair S., and Iyyunni C. "Optimum Utilization of Fly Ash for Stabilization of Sub-Grade Soil Using Genetic Algorithm". *Procedia Engineering*, Vol. 51, (2013), 250-258. <https://doi.org/10.1016/j.proeng.2013.01.034>
  34. Turkane S.D., and Chouksey S.K. "Partial Replacement of Moorum with Fly Ash in Embankment". *Lecture Notes in Civil Engineering*, Vol. 77, (2021), 381-391. [https://doi.org/10.1007/978-981-15-5195-6\\_30](https://doi.org/10.1007/978-981-15-5195-6_30)
  35. Kaniraj S.R., and Gayathri V. "Factors Influencing the Strength of Cement Fly Ash Base Courses". *Journal of Transportation Engineering*, Vol. 129, No. 5, (2003), 538-548. [https://doi.org/10.1061/\(ASCE\)0733-947X\(2003\)129:5\(538\)](https://doi.org/10.1061/(ASCE)0733-947X(2003)129:5(538))
  36. AASHTO T 307-99 "Standard Method of Test for Determining the Resilient Modulus of Soils and Aggregate Materials of Soils and Aggregate Materials" (2012).
  37. Syed M., GuhaRay A., Agarwal S., and Kar A. "Stabilization of Expansive Clays by Combined Effects of Geopolymerization and Fiber Reinforcement". *Journal of The Institution of Engineers (India): Series A*, Vol. 101, No. 1, (2020), 163-178. <https://doi.org/10.1007/s40030-019-00418-3>
  38. Zuhua Z., Xiao Y., Huajun Z., and Yue C. "Role of Water in the Synthesis of Calcined Kaolin-Based Geopolymer". *Applied Clay Science*, Vol. 43, No. 2, (2009), 218-223. <https://doi.org/10.1016/j.clay.2008.09.003>
  39. Teerawattanasuk C., and Voottipruex P. "Comparison between Cement and Fly Ash Geopolymer for Stabilized Marginal Lateritic Soil as Road Material". *International Journal of Pavement Engineering*, Vol. 20, No. 11, (2019), 1264-1274. <https://doi.org/10.1080/10298436.2017.1402593>
  40. Phetchuay C., Horpibulsuk S., Arulrajah A., Suksiripattanapong C., and Udomchai A. "Strength Development in Soft Marine Clay Stabilized by Fly Ash and Calcium Carbide Residue Based Geopolymer". *Applied Clay Science*, Vol. 127-128, (2016), 134-142. <https://doi.org/10.1016/j.clay.2016.04.005>
  41. Murmu A.L., and Patel A. "Studies on the Properties of Fly Ash-Rice Husk Ash-Based Geopolymer for Use in Black Cotton Soils". *International Journal of Geosynthetics and Ground Engineering*, Vol. 6, No. 3, (2020), 1-14. <https://doi.org/10.1007/s40891-020-00224-z>
  42. Indian Road Congress. "Guidelines for the design of flexible pavements (Fourth Revision). IRC 37-2018. New Delhi, India." (2018).
  43. Congress, Indian Roads. "IRC: 37-2012, Guidelines for the Design of Flexible Pavements." In *Indian Roads Congress, New Delhi, India*. (2012).

---

### Persian Abstract

#### چکیده

به دلیل شهرنشینی و صنعتی شدن سریع، ساخت جاده‌ها برای حمل و نقل آسان و سریع به سرعت افزایش می‌یابد. خاک مناسب در همه جا برای ساخت جاده‌های خوب در دسترس نیست. از این رو، جاده‌ها به اجبار بر روی خاک در دسترس محلی مانند خاک سست یا خاک گسترده ساخته می‌شوند. در این مقاله، یک بررسی تجربی بر روی خاک کم پلاستیک (LPS) برای افزایش خواص مهندسی با استفاده از تثبیت شیمیایی خاک (ژئوپلیمر مبتنی بر خاکستر بادی) انجام شد. طراحی ضخامت روسازی انعطاف پذیر برای مصالح خاک معمولی و تثبیت شده با استفاده از نرم افزار IITPAVE طبق دستورالعمل IRC 37 انجام شد. نتایج نشان می‌دهد که امکان‌پذیری ژئوپلیمر مبتنی بر خاکستر بادی، افزایش قابل توجهی استحکام از نظر مقاومت فشاری محدود (UCS) برای روزهای مختلف پخت (۰ تا ۱۲۸ روز)، نسبت باربری کالیفرنیا (CBR) و مدول ارتجاعی (MR) مشاهده شد. تجزیه و تحلیل ریزساختاری از طریق میکروسکوپ الکترونیکی روبشی (SEM) و تجزیه و تحلیل پراش پرتو ایکس (XRD) همچنین تشکیل ژل ژئوپلیمری را که منجر به ماتریکس متراکم به توده خاک می‌شود، آشکار کرد. ضخامت روسازی منعطف به طور قابل توجهی با استفاده از خاک کم پلاستیک تثبیت شده کاهش می‌یابد.

---



## Elevated Temperature Performance of Concrete Reinforced with Steel, Glass, and Polypropylene Fibers and Fire-proofed with Coating

H. R. Moosaei, A. R. Zareei\*, N. Salemi

Department of Civil Engineering, Isfahan (Khorasgan) Branch, Islamic Azad University, Isfahan, Iran

### PAPER INFO

#### Paper history:

Received 27 September 2021

Received in revised form 02 February 2022

Accepted 03 February 2022

#### Keywords:

Elevated Temperatures

Fire Behavior

Fireproof Coating

Glass Fibers

Mechanical Properties

Polypropylene Fibers

Steel Fibers

### ABSTRACT

Concrete has good strength and durability; however, it suffers from spalling and significant reduction of strength when exposed to fire. This study was aimed to enhance the fire resistance of concrete by applying two different techniques: 1) reinforcing with fiber, and 2) applying a fire-proof coating. For this purpose, mixes were made with steel fiber (SF), glass fiber (GF), and polypropylene fiber (PPF) applied at 0.5-2% of cement weight; in addition to a mix prepared with a 15 mm layer of fireproof coating material and a control mix. All mixes were subjected to elevated temperatures of 200-800 °C, and physical and mechanical properties were evaluated. According to the test results, both techniques were effective in enhancing the fire resistance of concrete mixes. The maximum residual compressive and flexural strengths were obtained for mix containing 0.5% GF, which were 117% and 145% higher than that of the control mix at 800 °C, respectively. Also, concrete with fireproof coating showed up to 76% and 113% higher compressive and flexural strengths compared to that of the control mix, respectively. It was found that addition of fibers in the manufacturing process of the concrete is a more desirable and economically-efficient approach to enhance the fire resistance. However, for an existing concrete structure, applying fireproof coating is the only option and can enhance the fire resistance comparably.

doi: 10.5829/ije.2022.35.05b.08

## 1. INTRODUCTION

Concrete is one of the most used construction materials worldwide due its good mechanical and durability properties, availability of raw materials, and relatively low maintenance cost [1]. However, concrete shows a significant strength loss when exposed to fire due to moisture loss, excessive cracking, and impairment of the cement matrix [2]. The study of concrete under fire dates back to the early 1900's and it was mainly focused on the behavior of cement paste and mortars [3]. Ma et al. [4] presented a comprehensive review on the effects of high temperatures on the mechanical properties of concrete. Exposure of concrete to elevated temperatures results in spalling [5], i.e., removal of some portions of the surface layer of the concrete, and external cracking, which is caused by the evaporation of the free water and decomposition of the paste [6]. The previously

mentioned phenomena can expose the steel reinforcements inside the concrete to heat, which can have devastating effects on the load-bearing capacity and stability of the concrete structure. Furthermore, the alkalinity tends to reduce as a result of carbonation, which is intensified by fire, and thus the corrosion risk of steel rebars escalates [7, 8]. At temperatures beyond 400 °C, the paste begins to shrink and the aggregates expand, which cause a significant strain gradient in the matrix [9]. It increases the cracking in the matrix and reduces the bond between paste and aggregates, resulting in further degradation of strength. At extreme temperatures, e.g., 800-1000 °C, the decomposition of the hydration products and loss of chemically-bound water lead to significant impairment of the microstructure and result in 60-80% reduction of strength [10].

Due to the risks associated with exposure of concrete to fire and its widespread application in civil engineering

\*Corresponding Author Institutional Email: [a.r.zareei@khuisf.ac.ir](mailto:a.r.zareei@khuisf.ac.ir)  
(A. R. Zareei)

structures such as buildings, bridges, tunnels, etc, it is of paramount importance to enhance the fire resistance of concrete through effective and cost-efficient techniques [11]. In order to enhance the performance of concrete under fire, various methods have been proposed and examined. One of the most effective practices is the utilization of fibers such as steel, glass, basalt, and polypropylene fiber (PPF) in concrete [12–16]. The use of fibers can improve the fire resistance of concrete by mitigating the formation and propagation of thermal induced cracks [17, 18]. Furthermore, fibers enhance the load-bearing capacity of concrete by providing additional strength by sewing effect and bridging over the cracks [19, 20]. Afroughsabet and Ozbakkaloglu [21] studied the performance of concrete incorporating a combination of PPF and steel fiber (SF) and reported that the highest enhancement in strength was achieved for PPF and SF contents of 0.15% and 0.85%, respectively. Serrano et al. [22] studied the compressive and tensile behavior of concrete subjected to an open flame with temperature of 400°C. It was shown that PPF-reinforced concrete was more resistant to fire than the SF-reinforced counterpart, and addition of 2% PPF increased the residual compressive strength of concrete by 68% over that of the control mix. Sun and Xu [23] showed that using 0.9% PPF in concrete leads to the optimal compressive strength, fatigue, and dynamic performance. However, the melting of PPF can create channels for the evaporated water to escape [24], and Lee et al. [25] reported that using high contents of PPF resulted in the formation of micro-cracks in concrete subjected to 400°C. Similar findings were reported by Yermak et al. [26] that PPF-reinforced concrete mixes were more porous than the SF-reinforced counterparts. Jameran et al. [27] studied the fire behavior of concrete with SF and PPF. The total fiber content was kept constant at 1.5% and different proportions of SF and PPF were incorporated into the concrete. The highest residual strength after fire exposure was achieved at 100% SF and 0% PPF contents. Moghadam and Izadifard [28] compared the performance of SF and glass fiber (GF) in improving the fire resistance of concrete. It was observed that mix reinforced with 0.25% GF showed the highest tensile strength, which was 213% higher than that of the control mix.

The addition of fiber for enhancing the fire resistance of concrete can only be done during the manufacturing process, and thus this method cannot be used for retrofitting purposes. In order to enhance the fire behavior of existing concrete structures, a layer of fireproof coating material can be applied. In this context, several studies proposed and examined different types of coatings for improving the behavior of the concrete at elevated temperature [29–31]. Temuujin et al. [32] investigated the utilization of a metakaolin-based geopolymer coating for fireproofing concrete. The coating exhibited a thermal expansion of 3% at 800°C

and concrete specimens maintained their strength for one hour at 1000°C. Hou et al. [33] used a type of cementitious thermal insulation material as fire-retardant coating to improve the fire resistance of concrete beams reinforced with 2% SF and 0.2% PPF. Results showed that the insulated beam exhibited about 38% higher fire endurance compared to that of the uninsulated one. Furthermore, several studies have investigated the effect of thermal insulation on the fire behavior of concrete structures strengthened with fiber-reinforced polymer (FRP) composites [34–37]

In the light of the previous studies, this paper aimed to present a direct comparison between the performance of concrete reinforced with different types of fibers and concrete with fireproof coating, which has not been done before. The objectives of the present research are: (1) Determining the type and content of the fiber, which leads to the maximum enhancement of fire resistance of the concrete; (2) Answering the question how effectively a fireproof coating can enhance the fire resistance of an existing concrete structure; and (3) Comparing the fire behavior of fiber-reinforced and fireproof coated concretes. The fresh and hardened properties of concrete mixes were evaluated. Furthermore, the residual compressive and flexural strengths as well as the mass loss of mixes were measured after exposure to elevated temperatures ranging from 200 to 800 °C.

## 2. EXPERIMENTAL PROGRAM

### 2. 1. Materials

**2. 1. 1. Portland Cement** In this study, Type II Portland cement from Ardestan cement plant was used with a density of 3.15 g/cm<sup>3</sup>. The chemical and physical characteristics of the cement and the values recommended by the Iranian Standard No. 389 in Tables 1 and 2, respectively.

**2. 1. 2. Fine Aggregate** Natural sand with particle size of 0-5 mm from Isfahan Soffeh mine was used as fine aggregate in this study (Table 3). The fineness modulus of the sand was equal to 3.1 based on determined based on ASTM C-125 standard [38]. The gradation curve of the sand and the recommended upper and lower bounds of ASTM C33 [39] are shown in Figure 1.

**2. 1. 3. Coarse Aggregate** Natural gravel with maximum size of 19 mm was used as coarse aggregate in the present research. Sieve analysis was done for the gravel based on ASTM C33, and the gradation curve is shown in Figure 2 and the physical characteristics are given in Table 4.

**TABLE 1.** Chemical characteristics of the cement used in this study

Chemical composition	Type II cement	
	Iranian Standard ISIRI 389 result (%)	Test result (%)
SiO <sub>2</sub>	> 20	22±0.4
Al <sub>2</sub> O <sub>3</sub>	< 6	5±0.3
Fe <sub>2</sub> O <sub>3</sub>	< 6	3.82±0.2
CaO	62-66	64±0.5
MgO	< 5	1.9±0.2
SO <sub>3</sub>	< 3	1.5±0.2
K <sub>2</sub> O	0.5-1	0.49±0.15
Na <sub>2</sub> O	0.2-0.4	0.25±0.15
C <sub>3</sub> A	5-8	6.51±1
Free CaO	-	1.2±0.2
L.O.I.	< 3	1±0.2

**TABLE 2.** Physical characteristics of the cement used in this study

	Specific surface area (g/cm <sup>2</sup> )	Setting time (min)		Compressive strength (kg/cm <sup>2</sup> )		
		Initial	Final	3 days	7 days	28 days
Allowable value (ISIRI 389)	> 2800	> 45	< 360	> 100	> 175	> 315
Measured value	3000±50	90±5	150±10	≥ 170	≥ 275	≥ 370

**TABLE 3.** Physical characteristics of fine aggregate (sand)

Property	Value
Apparent specific weight (kg/m <sup>3</sup> )	2570
Water absorption (%)	4.6
Apparent density (g/cm <sup>3</sup> )	2.54
Fineness module (F.M)	3.1
Percent passing #200 sieve (%)	3.4

**2. 1. 4. Fibers**

The fibers used in this study consisted of SF, GF, and PPF. SF was two-way hooks with length of 30-50 mm. Since SF can remain functional even at high temperature of 1200 °C, the incorporation of these fibers can enhance the resistance of concrete in fire condition as well as the mechanical properties [18, 40]. The GF used in the present work was of type “High Silica” with length of 12 mm. GF consists of very thin and flexible fibers, which are produced with diameters ranging from 5 to 25 μm. These fibers are more

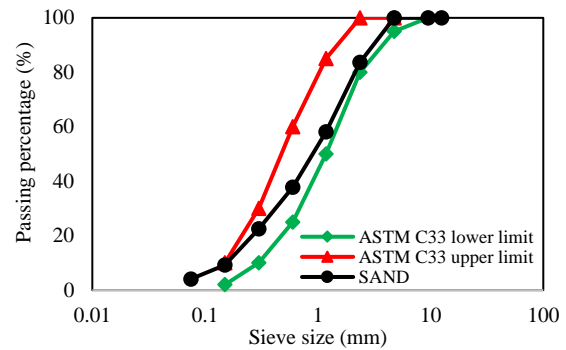


**Figure 1.** Gradation curve of fine aggregate (sand)

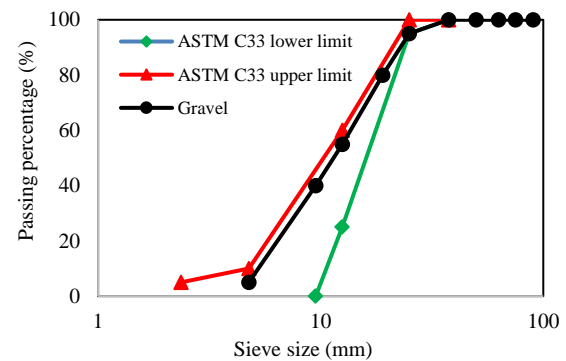


**Figure 2.** Gradation curve of gravel

**TABLE 4.** Physical characteristics of coarse aggregate (gravel)

Property	Value
Apparent specific weight (kg/m <sup>3</sup> )	2693
Water absorption (%)	1.2
Apparent density (g/cm <sup>3</sup> )	2.68
Saturated moisture with a dry surface (%)	0.5

economically efficient than the other types of fibers and also possess high tensile strength. The PPF used in this study was provided from Afzir company, Iran, Tehran, and was chopped to increase their grip with paste. The properties of fibers used in the present study are summarized in Table 5 (see Figure 3).

**TABLE 5.** Characteristics of fibers used in this paper

Fiber type	Length (mm)	Color	Elasticity module (GPa)	Diameter (mm)	Specific weight (g/cm <sup>3</sup> )	Melting temperature (°C)
SF	30-50	Copper	200	0.8	7.85	-
GF	12	White	70	0.011-0.015	2.6	550
PPF	12-13	White	5	0.02	0.91	160



Figure 3. Fibers used in this study: (a) GF, (b) PPF, (c) SF

**2. 1. 5. Fireproof Coating** In this study, mineral coatings were used, which can be applied to the concrete by spraying or manual application. This coating is a powder (Figure 4), which is a combination of mineral adhesives, lightweight fine materials, fibers, and additives. It can turn into fireproof mortar when mixed with water. Fire retardant coating or fire resistance coating has some special additives in it, which provide a very high durability against fire and reduces the potential of cracking and spalling. It was purchased from Iran Construction Clinic located in Tehran. The properties and technical information of the coating used are given in Table 6. The mix design for the fireproof coating and the mix design for the subbase used for better adhesion between concrete and coating are shown in Table 7.



Figure 4. Fireproof coating used in this study

TABLE 6. Physical characteristics of the fireproof coating

Test result	Test standard	Technical characteristic
Specific weight (kg/m <sup>3</sup> )	ASTM E-605	About 700
Compressive strength (kg/m <sup>2</sup> )	ASTM E-761	More than 35
Electrical conductivity (W/m.C)	-----	Less than 0.2
Surface burning spread characteristic	ASTM E-84 BS 476	Class A Class O
Fire resistance	ASTM E-119 ISO 834	More than 4 hours based on thickness

TABLE 7. Mix design of fireproof coating and subbase

Coating type	Liquid to powder ratio	Powder (kg/m <sup>3</sup> )	Water (kg/m <sup>3</sup> )	Liquid (kg/m <sup>3</sup> )
Sublayer coating	0.5	500	---	250
Fireproof coating	0.6	500	300	---

## 2. 2. Mix Design

Concrete mixes were prepared with different fiber types including SF, GF, and PPF and different fiber contents including 0.5%, 1%, 1.5%, and 2% of the cement weight. For comparison purposes, a control mix was prepared as well without any fibers. Furthermore, in order to compare the two methods of enhancing the fire resistance of concrete, the control mix was coated with a 15 mm fireproof layer and its behavior at elevated temperatures of 200, 400, 600, and 800 °C was compared to that of the other concrete mixes. The mix proportioning of concrete mixes is presented in Table 8. It should be noted that all mixes were prepared with a constant water-to-cement (w/c) ratio of 0.52. In Table 8, the control mix is denoted as Normal Concrete (NC) and fiber-reinforced mixes are referred to with a two-part code name: the first part denotes the fiber type and the second part denotes the fiber content in percentage. Also, the mix with fireproof material is referred to as FPC-NC.

The mixing process consisted of dry mixing of the coarse and fine aggregates for 2 minutes in the mechanical mixer. Then, 50% of the water was poured into the mixer with the cement and mixing was continued for 90 s. After that, fibers (if any) were gradually added to the mixture with the remaining water. The substances were mixed together until a homogenous mix was obtained and the fibers were properly dispersed. As for the concrete mix with fire proof coating, the coating layer was prepared in advance to the mixing day. In order to prepare the coating layer, the powder was mixed with water to achieve a mortar with average consistency.

The fresh mix was poured into the molds in three layers and each layer was compacted by using a standard rod. The specimens were left in the laboratory environment for 24 h and then were demolded and submerged in a water tank at  $23 \pm 2$  °C for further curing. For mix with fireproof coating, first, the concrete specimens were cured at temperature of  $23 \pm 2$  °C and humidity of  $50\% \pm 5\%$  for 24 h. Then, the surface of the specimens was carefully dried and cleaned; then, placed at the center of a 130 mm×130 mm×130 mm mold. Next, the coating was poured into the mold around the specimen. After 48 h, the molds were opened and the specimens were placed in the moist room. Note that the curing was not done inside of a water tank for mix with fireproof coating.

**TABLE 8.** Concrete mix designs (kg/m<sup>3</sup>)

Name	Cement	Water	Sand	Gravel	Fiber
NC <sup>1</sup>	420	220	800	880	---
SFC-0.5 <sup>2</sup>	420	220	800	880	2.1
SFC-1	420	220	800	880	4.2
SFC-1.5	420	220	800	880	6.3
SFC-2	420	220	800	880	8.4
PPFC-0.5 <sup>3</sup>	420	220	800	880	2.1
PPFC-1	420	220	800	880	4.2
PPFC-1.5	420	220	800	880	6.3
PPFC-2	420	220 </td <td>800</td> <td>880</td> <td>8.4</td>	800	880	8.4
GFC-0.5 <sup>4</sup>	420	220	800	880	2.1
GFC-1	420	220	800	880	4.2
GFC-1.5	420	220	800	880	6.3
GFC-2	420	220	800	880	8.4
FPC-NC <sup>5</sup>	420	220	800	880	---

<sup>1</sup> NC: Normal concrete

<sup>2</sup> SFC-0.5: Fiber-reinforced concrete with 0.5% SF

<sup>3</sup> PPFC-0.5: Fiber-reinforced concrete with 0.5% PPF

<sup>4</sup> GFC-0.5: Fiber-reinforced concrete with 0.5% GF

<sup>5</sup> FPC-NC: Normal concrete with fireproof coating

### 3. TESTING METHODS

The workability of the fresh concrete was evaluated by using slump test following the guidelines of C143/C143M-12 [41]. The compressive and flexural strengths of cubic and beam specimens with dimensions of 100 mm×100 mm×100 mm and 100 mm×100 mm×500 mm were determined based on the provisions of ASTM C39/C39M-16 [42] and ASTM C78/C78M-16 [43], respectively. Note that the tests were conducted on three specimens for each mix in order to ensure repeatability of the test results.

The specimens were heated at temperatures of 200, 400, 600, and 800 °C to evaluate the effects of fiber type and dosage as well as the fireproof coating on the elevated temperature behavior of concrete mixes. This was done in an electric oven at a heating rate of 6 °C/min until the target temperature was reached. The specimens were kept in the oven for 2 h to obtain steady-state thermal condition. Finally, after 24 h of cooling, the mass loss, residual compressive strength, and residual flexural strength of specimens were determined.

## 4. RESULTS AND DISCUSSIONS

**4.1. Slump** The results of slump test for different concrete mixes are shown in Figure 5.

Based on the test results, it is obvious that the workability of the fresh concrete was reduced when fibers were added. Furthermore, by increasing the fiber content, a higher reduction of slump was noticed. This could be attributed to the fact that when fibers are added to the mix, a network of fiber-matrix forms, which increases the internal friction. Therefore, a higher water content is required to obtain the same slump value. However, since the water-to-cement ratio has been kept constant in this study, the slump value decreases constantly with increasing fiber content. The reduction percentage in concrete mixes containing less than 1% fiber was below 10%. This is in agreement with the results of Jhatial et al. [44] who reported 8.7% reduction in slump of concrete containing 1% SF as compared to that of the control concrete. However, at the maximum dosage of fiber, i.e., 2%, about 17%, 20%, and 19% reduction in slump was observed for mixes reinforced with SF, PPF, and GF compared to that of the control mix, respectively. Mastali et al. [45] also observed 16% reduction in slump flow of concrete with 2% GF content. Also, it is observed that the SF-reinforced mixes showed a higher workability compared to PPF- and GF-reinforced mixes. A reason behind this could be the smooth surface of SF, which facilitates a better dispersion compared to other fiber types. PPF-reinforced mixes showed the highest reduction in workability, which could be related to the hydrophobic nature of PPF [46], which repels the water, and thereby air bubbles tend to attach to the fibers. This is supported by earlier findings [47, 48].

### 4.2. Effect of Elevated Temperatures on Mass Loss of Mixes

Figure 6 shows the mass loss of mixes after exposure to the elevated temperatures. According to the test results, the weight of the samples decreased with an increase in temperature. The mass losses of the control mix at temperature of 200, 400, 600, and 800 °C were

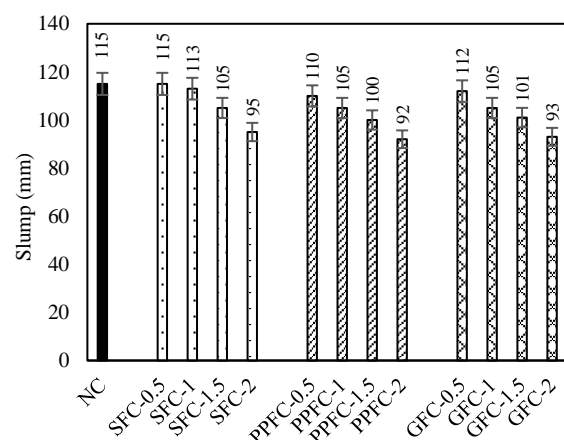


**Figure 5.** Slump of concrete mixes

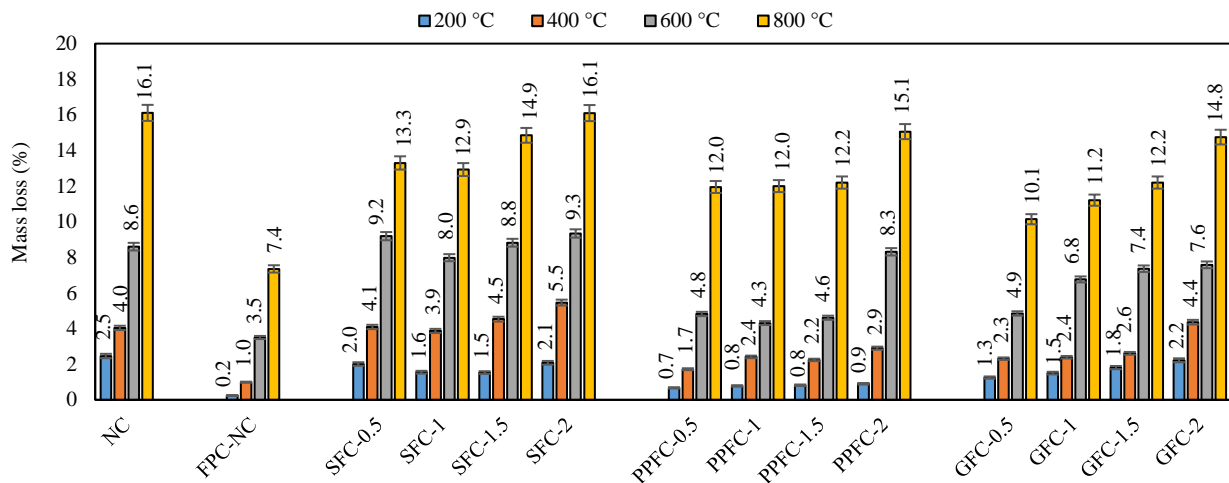


Figure 6. Mass loss of mixes at different temperatures

about 2.5%, 4%, 8.6%, and 16.1%, respectively, compared to the value of mass at room temperature. The mass loss due to exposure to temperatures in the range of 200-400 °C is mostly related to the evaporation of free water, which increased the porosity of the matrix [49]. At higher temperatures, the destruction of the hydration products of cement, i.e., calcium silicate hydrate (C-S-H) gel and calcium hydroxide ( $\text{Ca}(\text{OH})_2$ ), and the evaporation of free water are responsible for the decrease in the mass of concrete mixes [50]. At an extreme temperature of 800 °C, the impairment of the microstructure becomes more significant and the chemically-bound water evaporates, which further breaks the chemical bonds and causes severe decomposition of the hydration products [51].

In general, the mass loss of fiber-reinforced mixes was lower than that of the control mix. This could be related to the bridging effect of fibers, which mitigated the formation and propagation of micro-cracks due to heat exposure [15]. As a result, the stability of the specimens was enhanced at elevated temperature as less channels were available for the evaporated water to escape [52], and thereby less moisture loss occurred. The lower mass loss of fiber-reinforced mixes was more obvious at lower fiber contents. Mix with 0.5% GF demonstrated the lowest mass loss, and the weights of the specimens containing 0.5% GF were decreased by 1.25%, 2.31%, 4.85%, and 10.14% at temperature of 200, 400, 600, and 800 °C as compared to that of the plain concrete, respectively. However, the mass loss showed an increasing trend with fiber content. For example, adding 2% GF to the concrete resulted in 2.22%, 4.36%, 7.58%, and 14.75% reduction in mass at temperature of 200, 400, 600, 800 °C compared to that of the control mix, respectively. Similarly, mix containing 0.5%, 1%,

1.5%, and 2% PPF showed about 12%, 12%, 12.2%, and 15.1% mass losses at 800 °C. This could be due to the melting of fibers at elevated temperatures, which increased the porosity of concrete mixes. The higher mass loss in SF-reinforced mixes confirms this as the specific gravity of SF is much higher than that of the PPF and GF.

Moreover, test results showed that the lowest mass loss belonged to mix insulated with fireproof coating. The mass losses of mix FPC-NC were about 0.2%, 1%, 3.5%, and 7.4%, respectively, at temperatures of 200, 400, 600, and 800 °C compared to the mass at the ambient temperature. The fireproof coating prevented the heat to reach the inner parts of the specimens, and as a result, less fire-induced micro-cracks formed in the specimen and the escape of the evaporated water became more difficult.

#### 4. 3. Effect of Elevated Temperatures on the Compressive Strength of Mixes

Table 9 shows the compressive strength of mixes at different temperatures. Based on the test results, unlike the general trend of the compressive strength with increasing temperature, there was a slight increase in compressive strength at 200 °C. For example, the compressive strength of the control mix was increased about 12% when the temperature was increased from 23 °C to 200 °C. This could be due to the fact that heat treatment can promote hydration reaction of Portland cement and lead to further dissolution of  $\text{CaO}$  and  $\text{SiO}_2$  [26]. As it can be observed in the table, an increase in compressive strength at 200 °C was more pronounced for fiber-reinforced mixes. The maximum increase for the concrete reinforced with SF, PPF, and GF was 17%, 23%, and 25% compared to the corresponding value at 23 °C, respectively.

**TABLE 9.** Compressive strength of mixes before and after exposure to elevated temperatures

Mix/ Temperature	23 °C	200 °C	400 °C	600 °C	800 °C
NC	45.0	50.5	40.3	25.3	11.45
FPC-NC	43.6	48.5	42.5	31.1	20.1
SFC-0.5	47.1	53.9	43.1	26.7	11.9
SFC-1	48.0	55.3	45.0	27.7	12.8
SFC-1.5	51.0	59.5	48.6	33.1	14.8
SFC-2	41.8	47.0	38.0	22.7	10.4
PPFC-0.5	52.4	64.6	50.5	37.6	22.3
PPFC-1	45.4	52.9	42.3	30.4	14.9
PPFC-1.5	44.9	51.6	41.7	28.7	14.3
PPFC-2	38.2	42.9	35.4	23.4	10.7
GFC-0.5	53.1	66.2	51.8	39.1	24.8
GFC-1	50.8	60.9	48.0	35.8	17.3
GFC-1.5	47.0	55.4	43.9	30.3	15.0
GFC-2	39.4	44.9	36.5	24.6	12.0

However, compressive strength was reduced at temperatures in the range of 400-800 °C. Exposure to temperatures of 400, 600 and 800 °C reduced the compressive strength of the control mix by 10%, 44%, and 75% compared to the corresponding value at the room temperature, respectively. The highest drop in the 28-day compressive strength of the control mix happened as the temperature increased from 400 °C to 800 °C. Such high temperatures weakens the van der Waal's forces between C-S-H layers and reduces the surface energy, thereby resulting in the formation of weaker silanol groups with Si-OH:OH-Si bonds [53]. Furthermore, the evaporation of the free water and the chemically-bound water resulted in the formation of micro-cracks, which contributed to the loss of strength.

Generally, adding fibers to the concrete enhanced the compressive strength. In SF-reinforced mixes, the highest compressive strength at room temperature was obtained by adding 1.5% SF, which led to 13% higher compressive strength than that of the control mix as shown in Figure 7. In PPF- and GF-reinforced mixes, the maximum compressive strength at room temperature was achieved by adding 0.5% fiber, which led to 17% and 18% higher compressive strength than that of the control mix, respectively. The strength gain can be justified by the sewing effect of fibers, which bridged over the micro-cracks and increased the load-bearing capacity of concrete mixes [54]. However, it was observed that a

high content of fiber has an adverse effect. For example, concrete mixes reinforced with 2% fiber, regardless of the fiber type, showed a lower compressive strength compared to that of the control mix. When the amount of fibers increases, it reduces the workability of the mixture due to the friction between fibers and paste. This has a negative effect both on the compaction of the fresh mix and dispersion of the fibers. The non-uniform dispersion of fibers can cause fiber balling, which in turn increases the porosity of the concrete and lowers the strength [55]. In addition, fibers used in this study are hydrophobic, and therefore air bubbles can attach to their surface and become entrapped inside the concrete, which further increases the porosity [20].

The test results at elevated temperature indicated that the addition of fibers benefited the fire resistance of concrete mixes. In SF-reinforced mixes, the highest residual compressive strength was obtained by using 1.5% SF, which increased the compressive strength by 18%, 21%, 31%, and 29% at 200, 400, 600, and 800 °C compared to the corresponding residual compressive strength of the control mix, respectively. On the other hand, the residual compressive strength of the PPF- and GF- reinforced mixes was reduced with fiber content, i.e., the minimum fiber content (0.5%) led to the maximum fire resistance. Among all fiber-reinforced mixes, the mix reinforced with 0.5% GF showed the highest residual compressive strength. Based on the test results, the compressive strength of mix GFC-0.5 after exposure to temperatures of 200, 400, 600, and 800 °C was 31%, 29%, 54%, and 116% higher than that of the control mix, respectively. It can be observed that adding 0.5% GF can have a significant contribution to the fire resistance of concrete due to the bridging effect of fibers, which limited the formation and propagation of micro-cracks. However, using a higher content of GF resulted in a constant reduction in the residual compressive strength. For example, the residual compressive strength of mix containing 2% GF was about half of that of the mix containing 0.5% GF at 800 °C. Similarly, increasing the fiber content in PPF-reinforced mixes reduced the residual compressive strength. For example, the compressive strength of mix with 2% PPF was about half of that of the mix with 0.5% PPF at 800 °C. This can be attributed to the low melting point of PPF, which resulted in an increase in void content when fibers melted at elevated temperatures [56].

Moreover, the results showed that insulating the concrete with fireproof coating can be effective in maintaining the compressive strength after heat exposure. According to Table 9, mix FPC-NC showed a strength reduction of 3%, 29%, and 54% after being subjected to the elevated temperatures of 400, 600, and 800 °C, respectively. Also, consistent with the other concrete mixes, there was an increase of about 11% at 200 °C compared to the corresponding value at the room

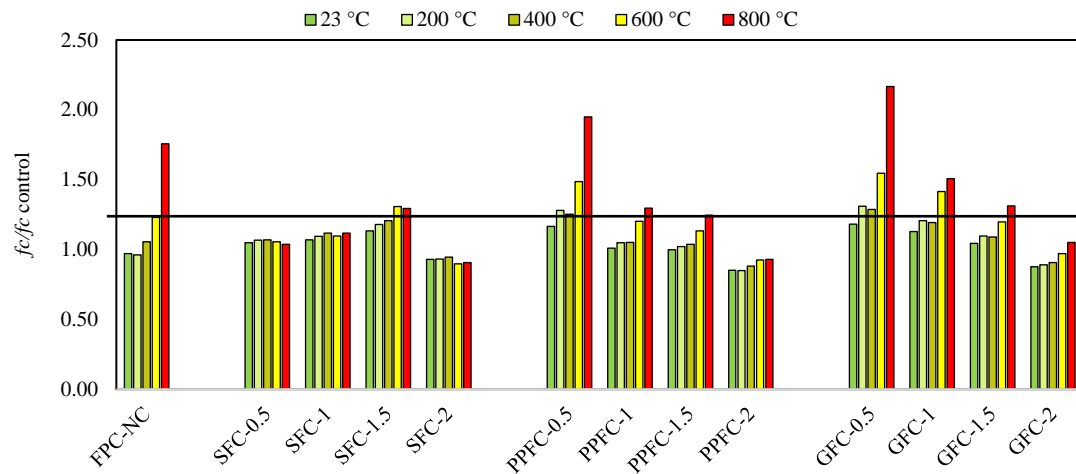


Figure 7. Ratio of compressive strength of mixes to compressive strength of the control mix

temperature. Comparing the results with fiber-reinforced mixes indicated that the fire resistance of mix FPC-NC was comparable to that of the mix GF-0.5. Thus, it can be concluded that using a 15 mm layer of the fireproof coating used in this study is as effective as reinforcing the concrete with 0.5% GF in enhancing the fire resistance of the concrete. In the insulated concrete, the fireproof layer reduces heat transfer to the inside of the concrete, and thereby mitigates the moisture loss and degradation of the microstructure. On the other hand, in fiber-reinforced mixes with fiber content up to 1.5%, the additional strength provided by the fiber-matrix bond and the bridging effect of fibers outweighed the negative influence of fiber agglomeration and increased void content.

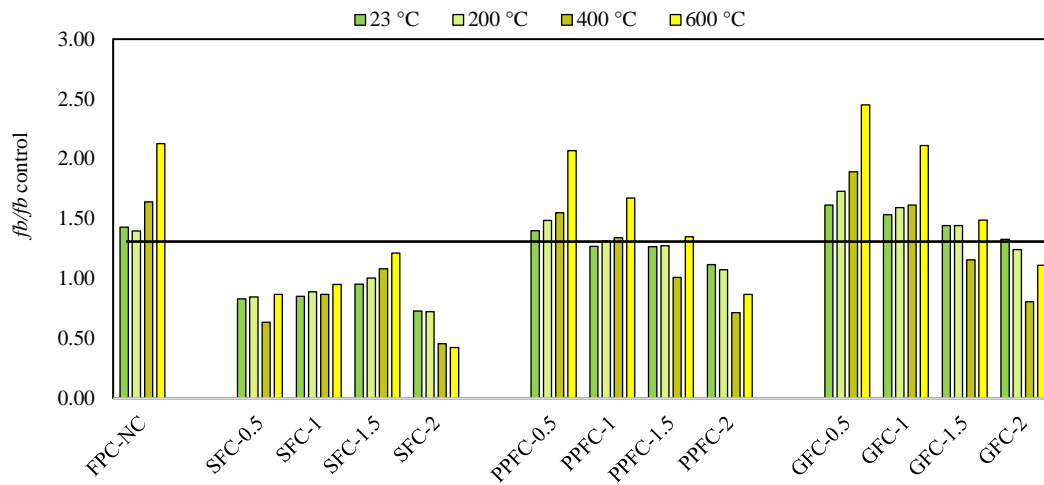
#### 4. 4. Effect of Elevated Temperature on the Flexural Strength of Concrete Mixes

Table 10 shows the flexural strength of mixes at different temperatures. Generally, the reduction in the flexural strength was more pronounced than the compressive strength. This could be related to the higher dependency of the flexural behavior of the concrete on cracking as compared to the compressive strength [46, 57]. Exposure of concrete to elevated temperatures creates numerous cracks as a result of loss of moisture and degradation of the microstructure through decomposition of the hydration products. When subjected to bending, cracks tend to open and propagate, which negatively affects the flexural strength. However, the compressive load applied to the specimens can help in closing the micro-cracks and the compressive strength is more affected by the strength of the matrix itself and also the interlocking between aggregate and paste [58].

TABLE 10. Flexural strength of mixes before and after exposure to elevated temperatures

Mix\ Temperature	23 °C	200 °C	400 °C	600 °C	800 °C
NC	4.91	5.68	4.03	2.41	0.00
FPC-NC	7.02	7.95	6.62	5.12	2.55
SFC-0.5	6.13	7.22	3.84	3.14	0.00
SFC-1	6.27	7.57	5.24	3.43	0.93
SFC-1.5	7.03	8.57	6.54	4.38	1.43
SFC-2	5.37	6.16	2.75	1.53	0.43
PPFC-0.5	6.87	8.45	6.25	4.98	2.30
PPFC-1	6.24	7.47	5.41	4.03	1.11
PPFC-1.5	6.22	7.25	4.07	3.25	0.57
PPFC-2	5.49	6.11	2.89	2.09	0.24
GFC-0.5	7.92	9.83	7.63	5.90	3.29
GFC-1	7.54	9.05	6.51	5.08	2.11
GFC-1.5	7.08	8.20	4.66	3.58	1.09
GFC-2	6.52	7.07	3.25	2.68	0.79

All fiber-reinforced mixes exhibited a higher flexural strength than that of the plain concrete. The optimum fiber content for different types of fibers based on the flexural strength test results was the same as that obtained



**Figure 8.** Ratio of flexural strength of mixes to flexural strength of the control mix

from the compressive strength results. Maximum flexural strength in SF-, PPF-, and GF-reinforced mixes was achieved by using 1.5%, 0.5%, and 0.5% fiber, respectively. The flexural strengths of mix SF-1.5, PPF-0.5, and GF-0.5 were about 43%, 40%, and 61%, respectively, higher than that of the control mix at the ambient temperature. As it can be observed, GF-0.5 with 28-day flexural strength of 7.92 MPa showed the highest flexural strength among all mixes.

At elevated temperature, consistent with the results of the compressive strength test, the flexural strength of mixes exhibited an increase at 200 °C, and then was reduced monotonically as the temperature was increased. For example, the control mix showed 16% higher flexural strength after exposure to 200 °C, which could be ascribed to the positive effect of heat exposure on the hydration of Portland cement and formation of C-S-H gel. Similarly, fiber-reinforced mixes showed enhancements in the flexural strength at this temperature. In agreement with the compressive strength, the maximum level in the residual flexural strength of fiber-reinforced mixes at 200 °C with respect to the ambient temperature was obtained in mix GF-0.5, which was about 24%. The lowest level in the flexural strength at this temperature was observed in mix FPC-NC, which was 13%. Since the fireproof coating limited the heat transfer to the inside of the concrete specimen, the increase in strength was limited as well. By increasing the temperature, the flexural strength of the concrete mixes started to decrease. For example, the residual flexural strength of the control mix after exposure to temperatures of 400 and 600 °C was 18% and 51% lower than the corresponding value at the ambient temperature. At 800 °C, spalling occurred in the specimen and it exploded in the oven, and thus no data is available

regarding the flexural strength of the plain concrete at this temperature. It could be related to the higher surface-to-volume ratio of the beam samples as compared to that of the cube samples, which increased the area of the surface exposed to heat. The degradation of the flexural strength at elevated temperature could be due to evaporation of free water, decomposition of the dehydrated products, and mismatch between the strain of the paste and that of the aggregates due to high temperature gradient. Upon exposure to fire, the paste tends to shrink as it loses water and the binding gel becomes damaged, whereas aggregates tend to expand [59, 60]. The difference between the change in the volume of the paste and aggregates reduces the paste-aggregate bond, and thereby reduces the load-bearing capacity of the concrete.

In line with the results of compressive strength, fiber-reinforced mixes showed a superior performance at elevated temperature compared to the plain concrete. In SF-reinforced mixes, the residual flexural strength increased up to a fiber content of 1.5%. Similar to the control mix, mix containing 0.5% SF failed at 800 °C and did not show any strength; however, at 200-600 °C, it showed 27%-30% higher residual flexural strength than that of the control mix as shown in Figure 8. Mix reinforced with 1% SF performed slightly better than mix with 0.5% SF; whereas, mix with 1.5% SF showed the highest residual flexural strength in SF-reinforced mixes. The residual flexural strengths of mix SFC-1.5 at 200, 400, and 600 °C were 51%, 62%, and 82% higher than that of the control mix, respectively. However, using 2% SF resulted in the lowest flexural strength in SF-reinforced mixes, which was even lower than that of the control mix. For example, the residual flexural strengths of mix SFC-2 at 400 and 600 °C were 54% and 58% lower

than that of the control mix, respectively. Heat treatment had a negative effect on the fiber-matrix bond as the fibers start to soften and the paste starts to contract. Therefore, additional strength provided by the fiber-matrix bond reduces with temperature, lowering the contribution of fibers to the flexural strength [61]. Furthermore, as the amount of fibers exceed a critical value, the fiber balling effect increases the porosity of the concrete, which is further intensified when fibers melt at extreme temperatures and leave behind pores and gaps.

Moreover, the PPF-reinforced mixes performed superior to SF-reinforced mixes at elevated temperature. The flexural strengths of the optimal mix, i.e., mix PPF-0.5, were reduced by 9%, 27%, and 66%, respectively, at 400, 600, and 800 °C. It may be attributed to the flexibility of PPF, which enables it to bend in different directions and fill in the pores and gaps more effectively than SF. Also, mix PPF-0.5 outperformed the control mix by showing 49%, 55%, and 107% higher flexural strength at the same temperatures. The crack arrestment by fibers mitigated the propagation of the thermal-induced micro-cracks and the bridging action of fibers over the cracks contributed to the strength gain [16]. As the fiber content was increased, the fire resistance of PPF-reinforced mixes began to decline. For the sake of illustration, the residual flexural strengths of mix PPF-0.5, PPF-1, PPF-1.5, and PPF-2 at 800 °C were 66%, 82%, 91%, and 96% lower than the corresponding value at 23 °C, respectively. As mentioned earlier, as the content of fiber increases in the mix, the workability drops, and thus the quality of compaction of the mix and fiber dispersion reduce as well. As a result, the porosity of the concrete increases, which has a negative effect on its strength. The exposure to elevated temperatures can further increase the gaps and pores in the concrete as a result of degradation of C-S-H gel and melting of fibers.

In agreement with the compressive strength results, the highest residual flexural strength was obtained in GF-reinforced mixes. Addition of 0.5% GF led to minimum losses of strength after heat treatment at 400, 600, and 800 °C, which were 4%, 25%, and 58%, respectively. Furthermore, the residual flexural strengths were enhanced by 73%, 89%, and 145% at 200, 400, 600 °C compared to that of the control mix, respectively. Although the flexural strength was reduced with increasing fiber content in GF-reinforced mixes, the residual flexural strength of all GF-reinforced mixes was still higher than that of the control mix at all temperatures. For the sake of illustration, the strength losses at 800 °C in mix containing 0.5%, 1%, 1.5%, and 2% GF were 58%, 72%, 85%, and 88%,

respectively. Similar reports can be found in the previous studies. Ravikumar and Thandavamoorthy [62] showed that the compressive strength losses at 300 °C in concrete reinforced with 0.5% and 1% GF were 25% and 10%, while the strength loss of the control mix was 32%.

Moreover, the fireproof coating has shown to be effective in increasing the residual flexural strength when exposed to fire. The strength reductions at 400, 600, and 800 °C were 6%, 27%, and 64%, respectively; however, the residual flexural strengths were still 40%, 64%, and 113% higher than that of the control mix at the same temperatures. Fire insulation improved the resistance and stability of the concrete against fire by limiting the amount of heat reaching to the core of the concrete [37].

#### 4. 5. Analysis of Variance (ANOVA)

In this section, ANOVA method was employed to quantify the influence of temperature, fibers, and their interaction on compressive strength and flexural strength of concrete mixtures. ANOVA is a widely used method to calculate the contribution of variables involved in a problem [63, 64]. Since two variables were involved in this study, two-way ANOVA was performed to rank the input parameters including temperature, fiber percentage, and their interaction based on their significance to the problem.

Figure 9(a)-(f) shows the ANOVA results of compressive strength and flexural strength. Figure 9(a)-(c) illustrates the ANOVA results regarding compressive strength. As seen, the contribution of temperature was significantly higher than that of the fiber percentage. For example, the contribution of temperature for concrete reinforced with SF was 90% while the contribution of fiber percentage was 4.2%. Furthermore, it was observed that the contribution of fiber percentage was higher in case of PPF and GF and it increased to 12% and 18%,

respectively. This owed to the higher melting point of these fibers, which increased their influence on strength of mixtures at elevated temperatures. This agreed with the compression test results, where concrete containing SF showed the highest reduction in strength at elevated temperature. For example, the compressive strength of mix with the optimum SF content was reduced from 50 MPa at 23 °C to 14 MPa at 800 °C, while that of the mix with the optimum GF content was reduced from 53 MPa to 24 MPa. Similar results were observed for flexural strength. With reference to Figure 9(d)-(f), the contribution of fiber percentages for concrete containing SF, PPF, and GF were 9.8%, 14.7%, and 23.3%, respectively.

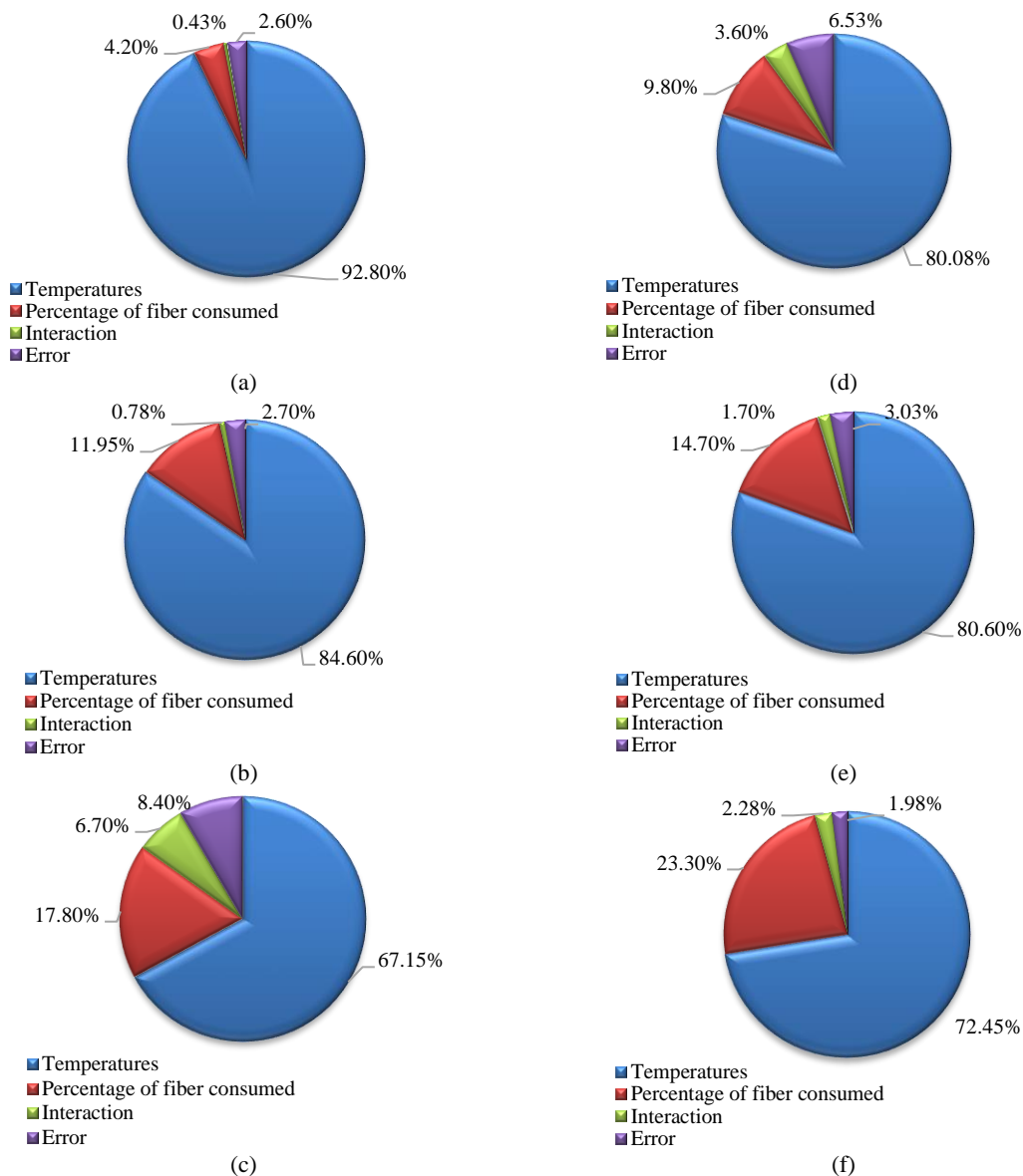


**Figure 9.** ANOVA results for the compressive strength of (a) SF-reinforced mixes, (b) PPF-reinforced mixes, (c) GF-reinforced mixes; and ANOVA results for the flexural strength of (d) SF-reinforced mixes, (e) PPF-reinforced mixes, (f) GF-reinforced mixes

### 5. CONCLUSIONS

This study investigated the fire resistance of concrete reinforced with three different types of fibers including SF, PPF, and GF incorporated at four different fiber contents including 0.5%, 1%, 1.5%, and 2%. The elevated temperature performance of the mixes was compared to that of the concrete insulated with a 15 mm layer of fireproof coating. The workability, mass loss, residual compressive and flexural strengths of mixes were evaluated. Based on the test results, the following conclusions are drawn:

- The inclusions of fibers results in reduced workability. The reduction is below 10% generally for fiber content less than 2%; however, by adding 2% fiber, the slump value reduced by up to 20%. PPF-reinforced mixes showed the lowest workability among fiber-reinforced mixes and SF-reinforced mixes are the most workable.
- Concrete mixes exhibit an increase of 8%-25% in the mechanical strength at 200 °C compared to the corresponding value at the ambient temperature. The use of fibers enhances the fire resistance. The optimum fiber content for SF-, PPF-, and GF-

reinforced mixes were 1.5%, 0.5%, and 0.5%, respectively.

- The reduction of the flexural strength was more obvious compared to the compressive strength. It can be related to the higher sensitivity of flexural strength to the presence of thermal-induced cracks than compressive strength.
- The maximum residual compressive and flexural strengths were obtained for mix containing 0.5% GF, which were up to 117% and 145% higher than that of the control mix, respectively.
- The insulation of the concrete with fireproof coating is a very effective technique to enhance the fire resistance of an existing concrete structure. As the temperature increases, the effectiveness of the fireproof coating becomes more pronounced. At 800 °C, the insulated concrete exhibits up to 76% and 113% higher compressive and flexural strengths compared to that of the control mix, respectively.

It can be concluded that in order to achieve the highest fire resistance of concrete, 0.5% GF should be added during the construction process. Whereas, fireproof coating technique can be applied after the construction process, which can enhance the fire resistance to a level comparable to that of the mix reinforced with 0.5% GF.

## 6. REFERENCES

- Zareei, S. A., Ameri, F., Bahrami, N., Shoaeei, P., Moosaei, H. R., and Salemi, N. "Performance of sustainable high strength concrete with basic oxygen steel-making (BOS) slag and nano-silica." *Journal of Building Engineering*, Vol. 25, (2019), 100791. <https://doi.org/10.1016/j.jobe.2019.100791>
- Zareei, S. A., Ameri, F., Shoaeei, P., and Bahrami, N. "Recycled ceramic waste high strength concrete containing wollastonite particles and micro-silica: A comprehensive experimental study." *Construction and Building Materials*, Vol. 201, (2019), 11–32. <https://doi.org/10.1016/j.conbuildmat.2018.12.161>
- Husem, M. "The effects of high temperature on compressive and flexural strengths of ordinary and high-performance concrete." *Fire Safety Journal*, Vol. 41, No. 2, (2006), 155–163. <https://doi.org/10.1016/j.firesaf.2005.12.002>
- Ma, Q., Guo, R., Zhao, Z., Lin, Z., and He, K. "Mechanical properties of concrete at high temperature—A review." *Construction and Building Materials*, Vol. 93, (2015), 371–383. <https://doi.org/10.1016/j.conbuildmat.2015.05.131>
- Phan, L., and Carino, N. "Effects of the Test Conditions and Mixture Proportions on Behavior of High-Strength Concrete Exposed to High Temperatures." *ACI Materials Journal*, Vol. 99, No. 1, (2002), 54–66. Retrieved from [https://tsapps.nist.gov/publication/get\\_pdf.cfm?pub\\_id=860335](https://tsapps.nist.gov/publication/get_pdf.cfm?pub_id=860335)
- Ameri, F., Shoaeei, P., Zareei, S. A., and Behforouz, B. "Geopolymers vs. alkali-activated materials (AAMs): A comparative study on durability, microstructure, and resistance to elevated temperatures of lightweight mortars." *Construction and Building Materials*, Vol. 222, (2019), 49–63. <https://doi.org/10.1016/j.conbuildmat.2019.06.079>
- Madhkhani, M., and Saedian, P. "Mechanical Properties of Ultra-high Performance Concrete Reinforced by Glass Fibers under Accelerated Aging." *International Journal of Engineering, Transaction B: Applications*, Vol. 34, No. 5, (2021), 1074–1084. <https://doi.org/10.5829/ije.2021.34.05b.01>
- Kashyzadeh, K. R., Ghorbani, S., and Forouzanmehr, M. "Effects of Drying Temperature and Aggregate Shape on the Concrete Compressive Strength: Experiments and Data Mining Techniques." *International Journal of Engineering, Transaction C: Aspects*, Vol. 33, No. 9, (2020), 1780–1791. <https://doi.org/10.5829/ije.2020.33.09c.12>
- Horszczaruk, E., Sikora, P., Cendrowski, K., and Mijowska, E. "The effect of elevated temperature on the properties of cement mortars containing nanosilica and heavyweight aggregates." *Construction and Building Materials*, Vol. 137, (2017), 420–431. <https://doi.org/10.1016/j.conbuildmat.2017.02.003>
- Sivathanu Pillai, C., Santhakumar, A. R., Poonguzhali, A., Pujar, M. G., Ashok Kumar, J., Preetha, R., and Kamachi Mudali, U. "Evaluation of microstructural and microchemical aspects of high density concrete exposed to sustained elevated temperature." *Construction and Building Materials*, Vol. 126, (2016), 453–465. <https://doi.org/10.1016/j.conbuildmat.2016.09.053>
- Kulkarni, P., and Muthadhi, A. "Improving thermal and mechanical property of lightweight concrete using n-butyl stearate/expanded clay aggregate with alccofine1203." *International Journal of Engineering, Transactions A: Basics*, Vol. 33, No. 10, (2020), 1842–1851. <https://doi.org/10.5829/IJE.2020.33.10A.03>
- Varghese, A., Anand, N., and Arulraj, P. G. "Influence of fiber on shear behavior of concrete exposed to elevated temperature." *International Journal of Engineering, Transactions A: Basics*, Vol. 33, No. 10, (2020), 1897–1903. <https://doi.org/10.5829/IJE.2020.33.10A.08>
- Thomas, C., Rico, J., Tamayo, P., Ballester, F., Setién, J., and Polanco, J. A. "Effect of elevated temperature on the mechanical properties and microstructure of heavy-weight magnetite concrete with steel fibers." *Cement and Concrete Composites*, Vol. 103, (2019), 80–88. <https://doi.org/10.1016/j.cemconcomp.2019.04.029>
- Hamad, R. J. A., Megat Johari, M. A., and Haddad, R. H. "Mechanical properties and bond characteristics of different fiber reinforced polymer rebars at elevated temperatures." *Construction and Building Materials*, Vol. 142, (2017), 521–535. <https://doi.org/10.1016/j.conbuildmat.2017.03.113>
- Li, Y., Tan, K. H., and Yang, E.-H. "Synergistic effects of hybrid polypropylene and steel fibers on explosive spalling prevention of ultra-high performance concrete at elevated temperature." *Cement and Concrete Composites*, Vol. 96, (2019), 174–181. <https://doi.org/10.1016/j.cemconcomp.2018.11.009>
- Li, Y., Yang, E.-H., and Tan, K. H. "Flexural behavior of ultra-high performance hybrid fiber reinforced concrete at the ambient and elevated temperature." *Construction and Building Materials*, Vol. 250, (2020), 118487. <https://doi.org/10.1016/j.conbuildmat.2020.118487>
- Al Qadi, A. N. S., and Al-Zaidyeen, S. M. "Effect of fibre content and specimen shape on residual strength of polypropylene fibre self-compacting concrete exposed to elevated temperatures." *Journal of King Saud University - Engineering Sciences*, Vol. 26, No. 1, (2014), 33–39. <https://doi.org/10.1016/j.jksues.2012.12.002>
- Novák, J., and Kohoutková, A. "Fibre reinforced concrete exposed to elevated temperature." *IOP Conference Series: Materials Science and Engineering*, Vol. 246, (2017), 012045. <https://doi.org/10.1088/1757-899X/246/1/012045>
- Xie, J., Zhang, Z., Lu, Z., and Sun, M. "Coupling effects of silica fume and steel-fiber on the compressive behaviour of recycled aggregate concrete after exposure to elevated temperature." *Construction and Building Materials*, Vol. 184, (2018), 752–764. <https://doi.org/10.1016/j.conbuildmat.2018.07.035>

20. Pakravan, H. R., and Ozbakkaloglu, T. "Synthetic fibers for cementitious composites: A critical and in-depth review of recent advances." *Construction and Building Materials*, Vol. 207, (2019), 491–518. <https://doi.org/10.1016/j.conbuildmat.2019.02.078>
21. Afroughsabet, V., and Ozbakkaloglu, T. "Mechanical and durability properties of high-strength concrete containing steel and polypropylene fibers." *Construction and Building Materials*, Vol. 94, (2015), 73–82. <https://doi.org/10.1016/j.conbuildmat.2015.06.051>
22. Serrano, R., Cobo, A., Prieto, M. I., and González, M. de las N. "Analysis of fire resistance of concrete with polypropylene or steel fibers." *Construction and Building Materials*, Vol. 122, (2016), 302–309. <https://doi.org/10.1016/j.conbuildmat.2016.06.055>
23. Sun, Z., and Xu, Q. "Microscopic, physical and mechanical analysis of polypropylene fiber reinforced concrete." *Materials Science and Engineering: A*, Vol. 527, No. 1–2, (2009), 198–204. <https://doi.org/10.1016/j.msea.2009.07.056>
24. Lura, P., and Terrasi, G. Pietro. "Reduction of fire spalling in high-performance concrete by means of superabsorbent polymers and polypropylene fibers." *Cement and Concrete Composites*, Vol. 49, (2014), 36–42. <https://doi.org/10.1016/j.cemconcomp.2014.02.001>
25. Lee, J., Terada, K., Yamazaki, M., and Harada, K. "Impact of melting and burnout of polypropylene fibre on air permeability and mechanical properties of high-strength concrete." *Fire Safety Journal*, Vol. 91, (2017), 553–560. <https://doi.org/10.1016/j.firesaf.2017.04.026>
26. Yermak, N., Pliya, P., Beaucour, A.-L., Simon, A., and Noumowé, A. "Influence of steel and/or polypropylene fibres on the behaviour of concrete at high temperature: Spalling, transfer and mechanical properties." *Construction and Building Materials*, Vol. 132, (2017), 240–250. <https://doi.org/10.1016/j.conbuildmat.2016.11.120>
27. Jameran, A., Ibrahim, I. S., Yazan, S. H. S., and Rahim, S. N. A. A. "Mechanical Properties of Steel-polypropylene Fibre Reinforced Concrete Under Elevated Temperature." *Procedia Engineering*, Vol. 125, (2015), 818–824. <https://doi.org/10.1016/j.proeng.2015.11.146>
28. Abdi Moghadam, M., and Izadifard, R. A. "Effects of steel and glass fibers on mechanical and durability properties of concrete exposed to high temperatures." *Fire Safety Journal*, Vol. 113, (2020), 102978. <https://doi.org/10.1016/j.firesaf.2020.102978>
29. Cai, Z., Liu, F., Yu, J., Yu, K., and Tian, L. "Development of ultra-high ductility engineered cementitious composites as a novel and resilient fireproof coating." *Construction and Building Materials*, Vol. 288, (2021), 123090. <https://doi.org/10.1016/j.conbuildmat.2021.123090>
30. Ma, X., Pan, J., Cai, J., Zhang, Z., and Han, J. "A review on cement-based materials used in steel structures as fireproof coating." *Construction and Building Materials*, Vol. 315, (2022), 125623. <https://doi.org/10.1016/j.conbuildmat.2021.125623>
31. Wei, W., and Zhong-nian, F. "Effects of crystallized fire proof material on the fire resistance of concrete." *Fire Science and Technology*, Vol. 40, No. 8, (2021), 1137–1141.
32. Temuujin, J., Rickard, W., Lee, M., and van Riessen, A. "Preparation and thermal properties of fire resistant metakaolin-based geopolymer-type coatings." *Journal of Non-Crystalline Solids*, Vol. 357, No. 5, (2011), 1399–1404. <https://doi.org/10.1016/j.jnoncrysol.2010.09.063>
33. Hou, X., Ren, P., Rong, Q., Zheng, W., and Zhan, Y. "Effect of fire insulation on fire resistance of hybrid-fiber reinforced reactive powder concrete beams." *Composite Structures*, Vol. 209, (2019), 219–232. <https://doi.org/10.1016/j.compstruct.2018.10.073>
34. Palmieri, A., Matthys, S., and Taerwe, L. "Experimental investigation on fire endurance of insulated concrete beams strengthened with near surface mounted FRP bar reinforcement." *Composites Part B: Engineering*, Vol. 43, No. 3, (2012), 885–895. <https://doi.org/10.1016/j.compositesb.2011.11.061>
35. Firmo, J. P., Correia, J. R., and França, P. "Fire behaviour of reinforced concrete beams strengthened with CFRP laminates: Protection systems with insulation of the anchorage zones." *Composites Part B: Engineering*, Vol. 43, No. 3, (2012), 1545–1556. <https://doi.org/10.1016/j.compositesb.2011.09.002>
36. Firmo, J. P., and Correia, J. R. "Fire behaviour of thermally insulated RC beams strengthened with EBR-CFRP strips: Experimental study." *Composite Structures*, Vol. 122, (2015), 144–154. <https://doi.org/10.1016/j.compstruct.2014.11.063>
37. Cree, D., Chowdhury, E. U., Green, M. F., Bisby, L. A., and Bénichou, N. "Performance in fire of FRP-strengthened and insulated reinforced concrete columns." *Fire Safety Journal*, Vol. 54, (2012), 86–95. <https://doi.org/10.1016/j.firesaf.2012.08.006>
38. ASTM C125, "Standard terminology relating to concrete and concrete aggregates", Annual Book ASTM Standards, 2003.
39. ASTM C33/C33M-16, "Standard Specification for Concrete Aggregates", ASTM International, West Conshohocken, PA, 2016.
40. Mirzazadeh, M. M., Noël, M., and Green, M. F. "Effects of low temperature on the static behaviour of reinforced concrete beams with temperature differentials." *Construction and Building Materials*, Vol. 112, (2016), 191–201. <https://doi.org/10.1016/j.conbuildmat.2016.02.216>
41. ASTM C143/C143M-15a, "Standard Test Method for Slump of Hydraulic-Cement Concrete", ASTM International West Conshohocken, PA, 2015.
42. ASTM C39/C39M-16, "Standard Test Method for Compressive Strength of Cylindrical Concrete Specimens" ASTM International West Conshohocken, PA, 2016.
43. ASTM C78/C78M-16, "Standard Test Method for Flexural Strength of Concrete (Using Simple Beam with Third-Point Loading)", ASTM International West Conshohocken, PA, 2016.
44. Jhatial, A. A., Sohu, S., Bhatti, N. K., Lakhari, M. T., and Oad, R. "Effect of steel fibres on the compressive and flexural strength of concrete." *International Journal of Advanced and Applied Sciences*, Vol. 5, No. 10, (2018), 16–21. Retrieved from <https://scholar.google.com/citations?user=SoKy-gUAAA&hl=en&oi=sra>
45. Mastali, M., Dalvand, A., Sattarifard, A. R., and Abdollahnejad, Z. "Effect of different lengths and dosages of recycled glass fibres on the fresh and hardened properties of SCC." *Magazine of Concrete Research*, Vol. 70, No. 22, (2018), 1175–1188. <https://doi.org/10.1680/jmacr.17.00180>
46. Rajaei, S., Shoaee, P., Shariati, M., Ameri, F., Musaei, H. R., Behforouz, B., and de Brito, J. "RETRACTED: Rubberized alkali-activated slag mortar reinforced with polypropylene fibres for application in lightweight thermal insulating materials." *Construction and Building Materials*, Vol. 270, (2021), 121430. <https://doi.org/10.1016/j.conbuildmat.2020.121430>
47. Afroughsabet, V., Biolzi, L., and Ozbakkaloglu, T. "High-performance fiber-reinforced concrete: a review." *Journal of Materials Science*, Vol. 51, No. 14, (2016), 6517–6551. <https://doi.org/10.1007/s10853-016-9917-4>
48. Thirumurugan, S., and Anandan, S. "Compressive strength index of crimped polypropylene fibres in high strength cementitious matrix." *World Applied Sciences Journal*, Vol. 24, (2013), 698–702. <https://doi.org/10.5829/idosi.wasj.2013.24.06.714>
49. Sedaghatdoost, A., Behfarnia, K., Bayati, M., and Vaezi, M.

- sadegh. "Influence of recycled concrete aggregates on alkali-activated slag mortar exposed to elevated temperatures." *Journal of Building Engineering*, Vol. 26, (2019), 100871. <https://doi.org/10.1016/j.jobe.2019.100871>
50. Xiao, J., and Falkner, H. "On residual strength of high-performance concrete with and without polypropylene fibres at elevated temperatures." *Fire Safety Journal*, Vol. 41, No. 2, (2006), 115–121. <https://doi.org/10.1016/j.firesaf.2005.11.004>
51. Novak, J., and Kohoutkova, A. "Mechanical properties of concrete composites subject to elevated temperature." *Fire Safety Journal*, Vol. 95, (2018), 66–76. <https://doi.org/10.1016/j.firesaf.2017.10.010>
52. Memon, S. A., Shah, S. F. A., Khushnood, R. A., and Baloch, W. L. "Durability of sustainable concrete subjected to elevated temperature – A review." *Construction and Building Materials*, Vol. 199, (2019), 435–455. <https://doi.org/10.1016/j.conbuildmat.2018.12.040>
53. Naus, D. J. The Effect of Elevated Temperature on Concrete Materials and Structures - a Literature Review, Report Number: ORNL/TM--2005/553. Oak Ridge, TN (United States). <https://doi.org/10.2172/974590>
54. Aslani, F., and Samali, B. "High Strength Polypropylene Fibre Reinforcement Concrete at High Temperature." *Fire Technology*, Vol. 50, No. 5, (2014), 1229–1247. <https://doi.org/10.1007/s10694-013-0332-y>
55. Zareei, S. A., Ameri, F., Bahrami, N., Shoaee, P., Musaei, H. R., and Nurian, F. "Green high strength concrete containing recycled waste ceramic aggregates and waste carpet fibers: Mechanical, durability, and microstructural properties." *Journal of Building Engineering*, Vol. 26, (2019), 100914. <https://doi.org/10.1016/j.jobe.2019.100914>
56. Lourenco, L. A. P., Barros, J. A. O., and Alves, J. G. A. "Fiber Reinforced Concrete of Enhanced Fire Resistance for Tunnel Segments." *Special Publication*, Vol. 276, (2011), 1–34. Retrieved from <https://www.concrete.org/restrictedcountry.aspx>
57. Toghroli, A., Mehrabi, P., Shariati, M., Trung, N. T., Jahandari, S., and Rasekh, H. "Evaluating the use of recycled concrete aggregate and pozzolanic additives in fiber-reinforced pervious concrete with industrial and recycled fibers." *Construction and Building Materials*, Vol. 252, (2020), 118997. <https://doi.org/10.1016/j.conbuildmat.2020.118997>
58. Behnood, A., and Ghandehari, M. "Comparison of compressive and splitting tensile strength of high-strength concrete with and without polypropylene fibers heated to high temperatures." *Fire Safety Journal*, Vol. 44, No. 8, (2009), 1015–1022. <https://doi.org/10.1016/j.firesaf.2009.07.001>
59. Guerrieri, M., Sanjayan, J., and Collins, F. "Residual strength properties of sodium silicate alkali activated slag paste exposed to elevated temperatures." *Materials and Structures*, Vol. 43, No. 6, (2010), 765–773. <https://doi.org/10.1617/s11527-009-9546-3>
60. Manjunath, R., Narasimhan, M. C., and Umesha, K. M. "Studies on high performance alkali activated slag concrete mixes subjected to aggressive environments and sustained elevated temperatures." *Construction and Building Materials*, Vol. 229, (2019), 116887. <https://doi.org/10.1016/j.conbuildmat.2019.116887>
61. Chen, G. M., He, Y. H., Yang, H., Chen, J. F., and Guo, Y. C. "Compressive behavior of steel fiber reinforced recycled aggregate concrete after exposure to elevated temperatures." *Construction and Building Materials*, Vol. 71, (2014), 1–15. <https://doi.org/10.1016/j.conbuildmat.2014.08.012>
62. Ravikumar, C. S., and Thandavamoorthy, T. S. "Glass fibre concrete: Investigation on Strength and Fire Resistant properties." *IOSR Journal of Mechanical and Civil Engineering*, Vol. 9, No. 3, (2013), 2320–2334. Retrieved from [https://www.academia.edu/download/32785136/Glass\\_Fibre\\_Concrete-Investigation\\_on\\_Strength\\_and\\_Fire\\_Resistant\\_Properties.pdf](https://www.academia.edu/download/32785136/Glass_Fibre_Concrete-Investigation_on_Strength_and_Fire_Resistant_Properties.pdf)
63. Shoaee, P., Tahmasebi Orimi, H., and Zahrai, S. M. "Seismic reliability-based design of inelastic base-isolated structures with lead-rubber bearing systems." *Soil Dynamics and Earthquake Engineering*, Vol. 115, (2018), 589–605. <https://doi.org/10.1016/j.soildyn.2018.09.033>
64. Khaneghahi, M. H., Najafabadi, E. P., Shoaee, P., and Oskouei, A. V. "Effect of intumescent paint coating on mechanical properties of FRP bars at elevated temperature." *Polymer Testing*, Vol. 71, (2018), 72–86. <https://doi.org/10.1016/j.polymertesting.2018.08.020>

---

### Persian Abstract

#### چکیده

بتن استحکام و دوام خوبی دارد. با این حال، هنگام قرار گرفتن در معرض آتش از پوسته پوسته شدن و کاهش قابل توجه استحکام رنج می برد. هدف از این مطالعه افزایش مقاومت بتن در برابر آتش با استفاده از دو تکنیک مختلف: (۱) تقویت با الیاف، و (۲) اعمال پوشش ضد حریق. برای این منظور، مخلوط‌هایی با الیاف فولادی (SF)، الیاف شیشه (GF) و الیاف پلی پروپیلن (PPF) با ۰/۵ تا ۲ درصد وزن سیمان، علاوه بر مخلوطی که با لایه ۱۵ میلی‌متری پوشش نسوز تهیه شده بود، ساخته شد. مواد و یک مخلوط کنترل همه مخلوط‌ها در معرض دماهای بالای ۲۰۰–۸۰۰ درجه سانتیگراد قرار گرفتند و خواص فیزیکی و مکانیکی مورد ارزیابی قرار گرفتند. با توجه به نتایج آزمایش، هر دو تکنیک در افزایش مقاومت در برابر آتش مخلوط‌های بتن مؤثر بودند. حداکثر مقاومت فشاری و خمشی باقیمانده برای مخلوط حاوی GF ۰/۵ درصد به دست آمد که به ترتیب ۱۱۷ و ۱۴۵ درصد بیشتر از مخلوط کنترل در ۸۰۰ درجه سانتیگراد بود. همچنین بتن با پوشش نسوز به ترتیب تا ۷۶ درصد و ۱۱۳ درصد مقاومت فشاری و خمشی بالاتری نسبت به مخلوط شاهد نشان داد. مشخص شد که افزودن الیاف در فرآیند تولید بتن، رویکردی مطلوب‌تر و از نظر اقتصادی کارآمدتر برای افزایش مقاومت در برابر آتش است. با این حال، برای یک سازه بتنی موجود، اعمال پوشش نسوز تنها گزینه است و می‌تواند مقاومت در برابر آتش را به طور قابل مقایسه‌ای افزایش دهد.

---



## Influencing Parameters of Exterior Reinforced Concrete Beam-Column Joint Shear Strength: A Depth Review of Recent Advances

S. Ravikumar\*, S. Kothandaraman

Department of Civil Engineering, Pondicherry Engineering College, Puducherry, India

### PAPER INFO

#### Paper history:

Received 28 September 2021

Received in revised form 03 February 2022

Accepted 11 February 2022

#### Keywords:

Anchorage Length

Beam Column Joints

Compressive Strength of Concrete

Confinement of Joint

Shear Strength

Transverse Reinforcement

### ABSTRACT

Beam-Column Joints (BCJ) manage the structural behaviour and failure mechanisms under severe events, blast, earthquakes, and impacts. Thus, they are the critical constituents in a building. Disparate deficiencies, say beam weak on flexure, shear, and column weak in shear, are present in this joint assembly to account for limits in design rule. To analyze the Reinforced Concretes (RC) Beam-Column (BC) connections behaviour, systematic research was performed amid the past '20' years. The influence parameters in favor of the Shear Strength (SS) of external RC-BCJ are investigated here. (a) The Concretes Compressive Strength (CCS), (b) confinement joint by the beam, (c) anchorage length, (d) beam and column reinforcement, and (e) the columns axial load are the '5' main parameters intended for the joint SS, which is found through the outcome. The most considerable correlation to the joint SS was found with the CCS amongst the influence aspects. This study reveals the vital features of the RC-BCJ shear strength.

doi: 10.5829/ije.2022.35.05b.09

### NOMENCLATURE

M	Moment (kN.m)	Col, c	Column
T	Tensile force	s	Sagging
C	Compressive force	jh	Horizontal joint force

## 1. INTRODUCTION

Recently, numerous experimentation researches on the composite connection have focused on steel-RC column connection and RC column connection [1]. For carrying service loads and providing stress protection against bending, torsion, vibration, shear, impact, and fatigue under particular conditions, RC beams were created, which are Fibers-Reinforced Polymer (FRP) [2]. Lots of researchers analyzed the RC's performance in structural concrete. On an extensive scale, the RC beams' use was investigated. A 13%–18% decrease was seen on the SS of longitudinally RC beams [3]. If cracks occur in the BCJ region after the earthquake load, the BC adjoining to the joint won't work effectively. Significantly, the requirement of crack resistance capacity is high for the

structures in the corrosive surroundings [4]. The data were gathered from past earthquakes. It exhibited that the flawed model of the connections between the columns and beams and the bad design details for the structural members caused the precast and RC systems to collapse [5]. Vast dynamic loads, which might be more prominent, contrasted to the design loads of utmost structures rooted via the blast within or close to construction, could bring about catastrophic damage to structural frame systems structures [6]. High temperature has a huge role in the changes of material properties and strength diminution in reinforcement and concrete of RC column [7]. The construction engineers and steel fixers have to discover rebar spatial clashes and shun rebar clashes just once a spatial clash occurs. These clashes are tedious and impact the quality and construction expenditure [8]. Brittle

\*Corresponding Author Institutional Email: [srkce@pec.edu](mailto:srkce@pec.edu)  
(S. Ravikumar)

failure occurs on the joints devoid of shear reinforcement under cyclic loading. However, with augmented concrete strength, their ductility increases [9]. Disparate parametric conditions, say beams longitudinal Reinforcements Ratios (RR), concrete strength, joint Aspects Ratio (AR), column RR, and also the joint stirrups impact at the joint were taken, and in that, '18' specimens were cast and tested [10]. The influence parameters of exterior RC-BCJ shear strength are exhibited in Figure 1. These studies' outcomes reveal the exterior RC-BCJ Shear Strength's behavior and contrast the behavior with the joints that lack shear reinforcement. The research also facilitates the methods to ascertain RC-BCJ's strength and identify the influencing parameters for an RC-BC shears strength.

**2. LITERATURE SURVEY**

The influence parameters of exterior BCJ-SS are surveyed here. The behavior RC-BCJ is surveyed in section 2.1. The strut and truss mechanism is elucidated in section 2.2. Section 2.3 illustrates the parameter influence of joint SS.

**2. 1. Behavior RC Beam-Column Joint** The seismic behavior of RC external vast BC connections is investigated. This study concentrates mainly on the load transfer paths and disparate performances of the joints with traditional and wide beams.

**2. 1. 1. Behavior of Beam-Column Joint under Lateral (Seismic) Loading** An essential factor that affects the utilization of vast beam systems in practice is the difference in Seismic Performance (SP) between a comprehensive BC system and a conventional BC system. This section surveys the SP of BCJ along with its drawbacks.

Kamakshi and Vinu [11] examined the structural activities of hybrid RC exterior BCJ. A hybridized

reinforcement system encompassed the on-sites fabricated, Hand Layup Carbons-FRP (CFRP-HL) stirrups, together with the customary steel reinforcements. Concerning ductility (2.19 times), load-carrying capacity (2.09 times), Energy Dissipation (ED) capacity (5.32 times), along with initial stiffness (2.29 times) high contrasted with the steel-RC specimen SJ, the hybridized reinforcement impact in joint HJ1 was comprehended. In addition, the greater complexity of on-site modifications was brought about by the constructability and the fabrication of FRP rebars.

Snehal and Dahake [12] elucidated the RC-BCJ analysis subjected to lateral seismic loading. The BCJ was a vital part of RC frames concerning lateral seismic loading. Amid severe earthquake shaking, the avoidance of anchorage in tandem with Shear Failures (SF) was not adequately addressed by design in addition to detailing provisions on BCJ in IS13920:1993. Failure might occur because utilizing the concrete does not encompass enough resistance. These were found via analyzing the damages that were incurred in an instant opposing RC framed structures that were subjugated to precedent earthquakes.

Marimuthu and Kothandaraman [13] illustrated the reverse cyclic behaviors of RC external BCJ with coupler anchors. In reversed cyclic loading conditions, '2' groups of joint specimens were cast as well as tested. The '1st' crack load of the coupler fitted specimen was enhanced. However, on account of the effectual anchorage of longitudinal beam bars via coupler arrangements, the '1st' crack load was delayed. Some drawbacks in RC BCJ with coupler anchors were the bad behavior of epoxy resins at temperatures over the glass transitions temperature in addition to the comparatively higher price of epoxy together with polymer materials.

Khan et al. [14] generated ultra-high performances fiber RC (UHPFRC) to SP of shear-deficient BCJ. Aimed at strengthening the concrete BCJ specimens, '2' disparate methods were employed. It comprised of: a) sand-blasting the usual concrete substrates surface of

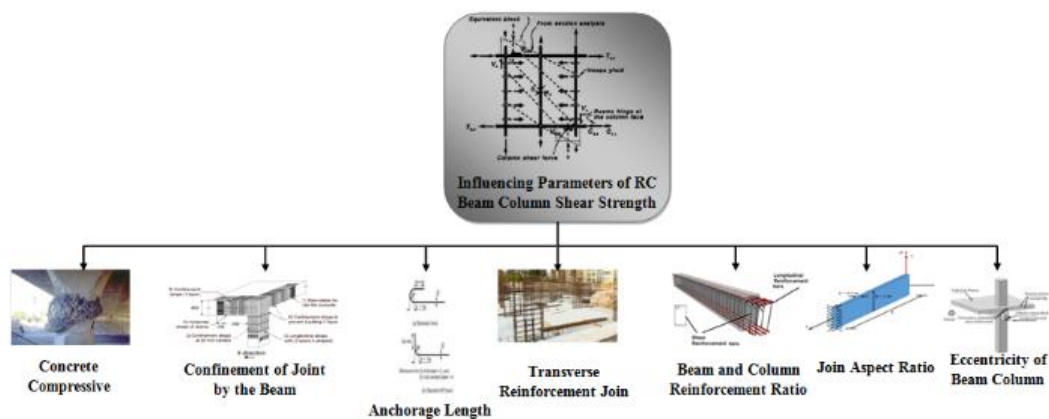


Figure 1. Influence parameters of exterior RC-BCJ shear strength

BCJ together with in-situ casting of a thirty mm thick UHPFRC and b) bonding thirty mm thick pre-fabricated UHPFRC plates for deficient BCJ utilizing epoxy resins together with special fillers. In contrast with the 2nd method, the 1st technique of strengthening was highly effective regarding shear capacity, stiffness, deformation capacity, and ED capacity. On the other hand, strength degradation and sudden diminution in the ductility were brought about by the issues of the detachment of pre-fabricated UHPFRC plates fixed to the joint utilizing epoxy.

Mosallam et al. [15] studied the RC-BCJ's structural behavior retrofitted with disparate sorts of FRP composites laminates together with hybridized connectors. Non-linear numerical simulations were evaluated aimed at the RC-BCJ behavior. A numerical appraisal of the behavior of an '8' full-scale interior RC-BC specimens was done. Simulated gravity in tandem with lower-frequency full-cyclic reversal, a load was carried out on the interior RC-BCJ specimens. A good correlation was attained between numerical and experimentation outcomes, in contrast to wood or unpainted lower-carbon steel.

Pimanmas and Chaimahawan [16] rendered the strengthening intended for an interior RC-BCJ centered upon the joint expansion conception. Cast-in-situ concrete expanded the BCJ two-dimensionally around the joint's corners. Interior BC specimens with the extended joint zone were taken to experiment. A good performance in upgrading the joint SS, ED, and ductility was found. The joint SF could be averted by augmenting the joint size. The joint expansion lessened the joint shear stress. It effectively changed failure mode as of brittle joint SF to flexural failure in beams. The corrosion was increased on account of the materials used.

Pampanin [17] illustrated the slab's impact on the seismic responses of sub-standard meticulous external RC-BCJ. Centered upon equations derived as of modern detailed BCJ subassembly test, the impact of the cast-in-situ slab and transverse beams was gauged. A minimal of about 2.2 times the beam depth was the effectual flange width while gauging the negative beam instant aimed at the seismic appraisal of non-ductile external b-c joints. Equal participation was not rendered by the reinforcement on the whole width of the slab in opposing the exterior instant with high strain levels close to the beam interface.

Santarsiero and Masi [18] examined an Italian seismic code mechanism for slab contribution to the BCJ's strength. The motivation was obtained on the apparent discordance between the findings of precedent experiments and analytical research and the rules rendered in present seismic codes considering the RC-BC connections' design for complying with capacity model principles. This effect represented the slab steel quantity

function. The slab reinforcements orthogonal to the beam were also highlighted. The collapse mechanism would shift column flexure to joint shear with augmented shear stress. It was not favourable. All these researches have a common ideology on improving the performance on behaviour of beam-column joint through either materials, anchorage system through the experimental test, model or simulation. So there is the necessity to understand the joint behavior to improve the performance effectively.

**2. 1. 2. Forces in the Joint** The joint reaction force is the force produced in a joint in response to forces on the joint are shown in Table 1. Ms, Mh are sagging and hogging moment of lateral beams, T, C are Tension in bars and Compression in bars, and lc - length of column. The force developed during earthquake in the moment-resisting frame BC joint is complex, with shear force dominating, from the joint portion's static equilibrium. At the moment frame, the horizontal joint shear force is shown in Joint A (knee/corner), Joint B (exterior), and Joint C (interior). The disparate forces on the joints and drawbacks were elucidated here.

Najafgholipour et al. [19] generated the Finite Elements Analysis (FEA) of RC-BC connections with governing joint SF mode. The ductile model philosophy and the anticipated overall structure performance were compromised via the brittle activities on the joint area. The crushing of the concrete diagonal strut on the joint area led to the connection specimen's failure. Bond slip of reinforcing steel and the intrinsic interaction within reinforcement and concrete on RC members have not been considered by the utmost finite element examination of RC structures.

Najafgholipoura and Arabi [20] generated a semi-analytical constitutive design for implementing the joint core shear deformation and unwanted joint SF mode on the non-linear examination of RC moment-opposing frames. The influential properties of the joint core were regarded in the equation. It included CCS, joint panel ARs, BC dimensions, and beam flexural RR. The design execution was also done on non-linear frame examination software SAP2000. The simple method presented a simulation analysis of '3' connections with disparate governing failure modes. The competence of

**TABLE 1.** Column Shear & horizontal Shear force in joint

Joint Type	Shear in Column	Horizontal Joint Shear Strength
Interior Joint (IJ)	$V_{col} = \frac{M_s + M_h}{l_c}$	$V_{jh} = C + T - V_{col}$
Exterior Joint (EJ)	$V_{col} = \frac{M_h}{l_c}$	$V_{jh} = T - V_{col}$
Corner Joint (CJ)	$V_{col} = T$	$V_{jh} = T$

capturing disparate failure modes on the joint area was found. Nevertheless, the SF of the joint panels was given concentration by some numerical studies.

Pan et al. [21] illustrated the BCJ modelling for non-linear examination of RC frames. A devoid of holistic frame examination was found to simulate the joint behavior and vital worldwide failure modes, like column axial, beam shear, column shear, and soft story failure. The ratio of the envisaged to the observed peak load encompassed a 1.05 mean and a 16.3% coefficient of variation for the '9' interior joint subassemblies modelled. Nevertheless, the compressive stresses in reinforcing bars were not anticipated together with the tensile stresses.

**2. 2. Strut and Truss Mechanism** The truss assembly of beams or other constituents generates a rigid structure. In engineering, it is a structure that "comprises of '2'-force members only, wherein the structural members are assembled so that, it behaves as a single object". Together with the truss mechanism in BCJ, the strut is elucidated here.

Zhang and Li [22] exhibited a customized strut-and-tie model (S.T.M.) for corroded RC external joints. Under '2' levels of representative columns axial force ratio, '8' same RC external joints with disparate corrosion levels of reinforcements were tested. Lateral loading resisting, ED, ductility, and the stiffness of corroded specimens were elucidated and contrasted with un-corroded control specimens. Together with the development length of beam longitudinal reinforcements, joint shears stress were examined and contrasted with available model code. The examination of the joint interior force flow of the corroded joint was done. The reinforcement's corrosion had a strong adverse impact on the joints' strength and lateral drifts capability with other mechanical properties. Highly specialized equipment was utilized by STM, which was fragile and luxurious.

Choi et al. [23] estimated the equal diagonal strut mechanisms and SS of the URM wall in-fill RC frames. Utilizing principal compressive strains on the concretes block wall, the diagonal strut means of the concrete block wall were elucidated. The sum of SS of RC columns and CB wall did not align well with lateral strength recorded on specimens. The SS of CB wall on IFRB and IFFB specimens in cyclic loadings was somewhat lower than those under monotonic loadings.

Mansouri et al. [24] generated a Gene Expression Programming (GEP) aimed at the predictive formulation of the SS of RC exterior BCJ devoid of Transverses Reinforcement (TR). The contribution of every variable of the BCJ comprised on the GEP could be appropriately reflected via the model. The disparate parameters influencing the joint's SS, such as material features, model variables, and joint geometrical and detailing configurations, were evaluated. Compared to prevailing

models, the rendered GEP more precisely predicted the SS of RC-BCJ. However, the system encompassed slow convergence together with low solution accuracy.

Choi et al. [25] elucidated the diagonal Strut means of URM Wall in-fill RC Frame. Static cyclic loading tests to comprehend the lateral force resistances mechanisms in the in-plane direction. In specimen 1S-2B, the compressive struts were generated individually in both walls in a way similar to the strut generated on specimen 1S-1B. However, specimen 1S-1B did not exhibit good accord with the lateral length.

Paul et al. [26] posited the diagonal Strut Mechanism of URM Wall Infill RC frames intended for Single and Double-Bays. A simple technique was discussed for estimating the lateral response of the URM in-fill RC frame. All through the loading cycle, the wall response for '1' bay and '2' bay specimens was accurately estimated by the equal diagonal strut method. Treating in-fill walls as a non-structural element should be trounced well at the design phase as it was not right.

Xue and Lam [27] examined the plane equivalent micro-truss element intended for RC structures. It was cost-effective to properly replace the continuum design with micro-truss elements, particularly for automatically forming the STM. The relative error of deflection designed with '2' elements with augmenting element number quickly decreased. The solution agreed with the theoretical value having the element size around 1/10 to 1/15 height of the beam. However, presenting the concrete modeled with the utilized-defined element was hard.

Lee et al. [28] suggested the diagonal strut actions on masonry in-fill RC frames. Customized Compressions Field Theory together with Disturbed Stress Fields design was employed. However, the diagonal strut actions in the cracked masonry in-fill along with consequent failure mode relied on model variables, say the masonry thickness, cohesion on the mortar joint-bricks interface, together with the bad mortar filling presence. In addition, the columns and beams were lightly reinforced members and did not satisfy the needs of intermediary and special instance frame members.

Wu et al. [29] elucidated the mechanical performances of steels truss RC transfer beam. It analyzed the development of crackdown the beam, strains of reinforcements, and steel truss, together with force transference mechanisms of the deep beam. In contrast to the normal RC transfer beam, the bearing capability and the rigidity of the STRC transfers beam were ameliorated considerably. In the STRC transfer beam, the STM force transference mechanism was generated. The diagonal shear cracks chiefly appeared down the diagonal strut on account of the STM force transferences mechanism of the deep flexural members.

Van den Hoogen [30] explicated the beam truss mechanism aimed at shear on concrete. Beam or truss

mechanism in concrete for shear was discussed. Higher load failure was brought about by the artificial cracks (i.e.) by crushing the concrete instead of SF. Additionally, the truss mechanism occurred in this circumstance. The regular beam bending or shear cracks, when occurred, would result in the failing of the beam without the truss mechanism's occurrence. However, the crack is not straight in reality. It would be curved via the influence of shear stresses. Additionally, the actual depth is hard to predict.

Abdul-Razzaq et al. [31] illustrated the concrete and steel strengths endeavour on deep beams with reinforced struts. The experimentation tests were executed on '9' specimens. These specimens were split into '3' groups. The outcomes showed that in the specimens, merely the STM was reinforced. The augmentation in the ultimate capability and diminish on mid-span deflection were around 26-40% and 19-28% correspondingly, for the RC frames. The model's capacity seemed lower because of a lessening midspan deflection.

Wang and Hsu [32] estimated the activities of RC moment-opposing frames with badly reinforcing details. The main aim was to predict the RC moment-resisting frames' behaviour, particularly for the joints with badly reinforcing details utilizing truss mechanism examination. However, the reinforcement strain forecast on the column seemed better than that on the beam compared to the detailed comparison between experimentation and analytical outcomes. The reason could be in the joint modelling aimed at the beam prediction with lesser accuracy.

### 3. PARAMETER INFLUENCE OF JOINT SHEAR STRENGTH

The research community still debates the influence of disparate parameters on the joint SS. Therefore, the critical aspects of the joint SS of BCJ and the significance of these factors are elucidated. Various researchers developed empirical research on the joint shear strength model prediction and discussed their limitations, the empirical-based joint shear strength models derived with various parameter. On comparisons of those models, significant difference identified between among various models to predict joint shear strength. The difference in prediction models with experimental results caused due to non-uniformity on selection of actual influence of parameters of joint shear strength.

**3. 1. Concrete Compressive Strength** The capacity of failure under the action of compressive forces is termed the compressive strength of a material. Compressive strength is vital for ascertaining the material's performance amid service conditions, particularly concrete.

Murad [33] research carried out a model for predicting joint shear strength using the GEP technique. For the model, the following parameters were considered compressive strength of concrete, amount of transverse reinforcement, geometric property of joint panel (width and depth), concrete strength, the ratio of reinforcement, and axial column load. The results confirm that concrete compressive strength after the crack and the contribution of concrete in resisting shear force was significantly reduced.

Pauletta et al. [34] proposed semi-empirical models to find the shear strength capacity of the joint with the parameters of axial load on column with formation concrete strut. Concrete strut strength mainly depends on concrete compressive strength. The shear strength depends on the concrete strut transverse and longitudinal reinforcements. The reinforcement with proper transverse reinforcements gives the confinement effect to achieve higher ductility.

**3. 2. Confinement of Joint by the Beams** This section surveys the different confinements of joints. The joint is controlled via the longitudinal reinforcing steel and the confinement provided by the TR. Wu et al. [35] conducted their work on curing process optimization based on curing degree considered the shear strength of joints.

Karthik et al. [36] formed a Compatibility-STM (C-STM) for tested C-beam specimens. It was subjugated to differing degrees of ASR or DEF deterioration together with differing degrees of related corrosion of the rebars. The simulation accounted for age-modified cover in tandem with core concrete material properties. Additionally, the resultant passive prestress took endeavor on the longitudinal together with T.R. With an augmentation on the passive prestress effect, an augmentation in strength and the stiffness of the specimens was observed. The progression of non-linear events brought about the large BCJ failure. Differing levels of ASR or DEF deterioration affected it, which was tracked successfully via the C-STM. However, the system encompassed inadequate anchorage lengths.

Khan et al. [37] rendered a simplified BCJ modeling method aimed at the inelastic examination of RC moment-opposing frames. A zero-length link constituent with an instant-rotation lumped plasticity hinge was presented in the joint model. To simulate the non-linear shear activities of the joint panel, it was rendered at the intersection of BC elements. '2' portal frames were tested on quasi-static cyclic loads. To envisage the cyclic force-displacement hysteretic response, the modeling technique was implemented. Nevertheless, critical damage wasn't attained via the shear strains of the joint panel.

Gao and Lin [38] posited that XG Boost intended for exceptional classification outcomes of the BCJ's failure

modes. The SHAP was employed to explain the features' endeavors in the envisage models. An accurate envisage of the interior BCJs' failure mode was done. The change of failure mode from brittle to ductility failure was suggested for the BCJ. SHAP was used to consider feature interactions and render an impact examination of every feature. Nevertheless, for adjusting the failure mode of a BCJ, the model could not render the changing magnitude of the influencing parameters.

Massone and Orrego [39] formed an analytical model for SS assessment of RC-BCJ. For envisaging the non-linear activities of RC-BCJ, the execution of the model was done while considering axial together with shear stresses. It was centered on a plain formulation which regarded an average strain together with the stress field of an RC panel signifying the joint. The equilibrium was satisfied in the longitudinal direction. There was a difference in the total specimens with SF.

### 3. 3. Anchorage system for RC Beam-Column Joint

Development length, termed anchorage length, is rendered for transferring steel to concrete. Anchorage system in RC BC with different materials is were discussed in this section.

A suitable anchoring length must be given for the longitudinal beam bar at the connection. In previous earthquakes, numerous reinforced concrete structures have been badly damaged or collapsed due to insufficient joint detailing (no transverse reinforcing in the joints) and longitudinal beam bar anchoring. Additionally, the longitudinal beam bar is exposed to alternate compression and tension loads during reverse cyclic loading, resulting in bond weakening and diagonal tension cracking in both directions. As a result, the whole structure rapidly loses strength and rigidity. Rather than these, increased joint performance should be achieved via new design strategies or enhanced details.

Park and Paulay [40] examined thirteen full-scale reinforced concrete beam-column connections subjected to reversed cyclic stress. The method by which the beam steel was secured inside the joint, the presence of "U" bars, and the quantity of transverse reinforcement were crucial factors. As a consequence of diagonal stress cracking and anchoring failure, the joint progressively degenerated. Additionally, the fast degeneration of joints is accelerated by crack opening and closure during seismic excitation. As a result, effective anchoring and confinement of beam-column joints are critical for increasing their seismic performance. After extensive research, Park and Paulay [40] proposed a few approaches and processes, that fulfill the joint core's anchoring, shear, and confinement requirements. All used bend-up bars, bent-up bars incorporated into stub beams, and mechanical anchoring to the bar's end.

Leon [41] determined the anchoring length by examining the behavior of four half-scaled internal joints

with varied anchoring lengths. Significant factors were column depth, anchoring length (between 16 and 28 times the diameter of the bar), and changing joint shear stress (between 11.5 and 18.5 of compressive strength of concrete). The results indicate that 24db (dia of bars) of anchorage is required to achieve the beam's maximum strength, whereas 28db of anchorage enables adequate energy dissipation and the formation of plastic hinges (strong column and weak beam concept). However, the usage of smooth bars and conventional practice techniques contribute significantly to joint problems (inadequate detailing of reinforcement, instead of providing anchoring, hook-end was utilized).

Pampanin et al. [42] investigated the behaviour of three different types of beam-column joints when subjected to reverse cyclic load to demonstrate joint inefficiency. Each specimen was cut in half and revealed smooth bars, insufficient reinforcing features (i.e., no transverse reinforcement in the joint), and hook-ended bars (deficiencies in the anchorage). The use of smooth reinforcing bars with end-hook anchorage in the absence of transverse reinforcement results in brittle damage mechanisms, and the use of older details results in concrete "wedge" spalling, brittle local failure, and loss of bearing capacity in the exterior joint.

Adopting outmoded structural characteristics results in a shear hinge mechanism in the joint region, which results in rapid strength degradation and increases local deformation, ultimately failing the entire frame system. Additionally, the anchoring of main beam bars, the transverse strengthening of joints, and the placement of lapped splices substantially affected the joint's effectiveness.

Kuang [43] investigated the behaviour of RC exterior beam-column joints using a variety of different types of anchoring in the beam reinforcement and laps in the column bar's lower zone. The results reveal that external beam-column joints' hysteretic behaviour and shear resistance are mostly governed by the beam's reinforcing details and anchoring length. Even in places with low to moderate seismic activity, it is critical to pay attention to the design of the RC beam-column junction. Apart from anchoring the beam's primary longitudinal bar, joint confinement is a critical feature that significantly affects cooperative behaviour.

Murty et al. [44] investigated twelve RC beam-column joint subassemblies with varying details of beam bar anchoring and transverse reinforcement at the joint core. The study's results indicated that the specimen combination of full anchoring and ACI standard hook with hairclip provides excellent energy dissipation and hysteretic loop and may be used in structures located in low seismic zones.

**3. 4. Transverse Reinforcement in Joint** TR should be rendered within the joint region to resist shear

forces and confined concrete. Disparate TR joints are elucidated.

Adib et al. [45] examined non-linear designing of cyclic response of RC-BC joints reinforced via plain bars. Linear elastic elements represented the BC components. Rigid elements defined the dimensions of the joint panel. At the beam's end, the non-linear rotational spring took into deliberation the slip's effect. The BC connections that had bar slippage failure mode were considered. However, a lower moment capacity with a lower axial load was there.

Said et al. [46] elucidated the outcome of replacing the TR with cementitious composite in RC-BCJ subjugated to cyclic loading. For testing, '2' specimens of whole-scale RC-BCJ were cast and prepared. At a 5% drift ratio, the joint was damaged. At the drift ratio of 7%, the ECC specimen was damaged. Lastly, the failure happened in the joint zone due to the localization of '2' prominent cracks.

Marimuthu and Kothandaraman [47] explored the TR methods in RC-BCJ. Throughout the years, numerous techniques of reinforcing techniques were developed. Enhanced performance, lessened congestion, effortless fabrication; in addition, the simple placing of concrete on the joint was found. Superior performance was attained by headed studs aimed at the joint's conventional shear reinforcement. Headed stud joint's behavior was very close to convention behavior. When there were issues with the reinforcement congestion in the joints, the diagonal collar stirrups were not helpful.

Sengupta and Li [48] formed a customized Bouc–Wen design aimed at the hysteresis behavior of RC-BCJ with restricted TR. For solving the differential equations accompanied by executing a systematic appraisal of the parameters associated with the model, Livermore Solvers for Ordinary Differential Equations together with the Genetic Algorithm was employed. Centered on the broad parametric study, the impact of the joint physical parameters, say the column axial load ratio, plain or deformed bars aimed at longitudinal reinforcement, the joint AR, the BC longitudinal RR, concrete compressive cylinder strength, on the parameters were meticulously studied. However, the sensitive ranking of every parameter could easily be deduced after every parameter to a definite gamut of gauging error happened because of every variation.

Kotsovou and Mouzakis [49] generated a seismic design of RC exterior BCJ. The diagonal strut mechanism predominantly resisted the HDC exterior BCJ, centered on the supposition that the load transferred to the joint as the BC elements. The method's validity was experimentally verified via a comparative study of the performance of '7' full-size BCJ sub-assemblages. In accord with the present European Codes, '3' were designed along with four in compliance with the technique. Those modeled to comply with the

specifications completely fulfilled the code performance needs compared to the specimens modeled in compliance with the present code provisions. However, it was hard to place on compacting concrete.

### 3. 5. Beam and Column Reinforcement Ratio

For preventing concrete crushing, the maximum RR for beams is rendered. The minimal RR for columns is needed for providing resistance in opposition to bending that might occur regardless of analytical outcomes. The researched-on RR of disparate materials utilized in BC-SS is discussed here.

Wang et al. [50] studied the RR's effect on the competence of the RC column to oppose lateral impact loading. It discussed the consequence of lateral impact loading rates, longitudinal RR, and stir-up ratios on the failure mode, lateral load-bearing capacity, et cetera. The ultimate load-bearing capacity of columns would be the augmentation in longitudinal RR. The longitudinal RR and loading velocity did not significantly influence it. However, the column would be susceptible to SF if the stirrup space was larger or else to flexural failure.

El-Gendy and El-Salakawy [51] elucidated the flexural reinforcement sort's consequence together with the ratio on the punching activities of RC slab-column edge connections subjugated to reversed-cyclic lateral loads. Doubling GFRP-RR of 0.7 to 1.4% brought about 43 and 63% amelioration in the initial stiffness and the connections' ED capacity. However, the stiffness degradation was not significantly affected. As the strain gauge malfunctioned after the 1.00% drift ratio, the ratio couldn't be gauged to connect ES-0.7.

Ibrahim et al. [52] illustrated the steel-to-FRP RR as a tool managing the SFRC BCJs' lateral response. The outcomes displayed that instead of FRP RR, utilizing the steel RR could improve the administration of the SFRC BCJs' serviceability state. However, preventing breakage in non-structural elements was a highly complicated task worth 3 to 5 times the expense. Consequently, the non-structural elements' breakage in FRP-RC models might be higher.

Tobbi et al. [53] explicated the Concentrically Loaded Fibers-Reinforced Polymer RC Columns' activity with several reinforcement kinds together with ratios. The outcomes displayed that the FRP bars had been utilized as longitudinal reinforcement aimed at concrete columns intended for the concentric compression; in addition, the FRP transverse reinforcement's amalgamation and steel longitudinal bars provided suitable strength and flexible behavior. However, the stress computation did not consider the deprivation of concrete cover involvement following the breakage. Therefore, the concrete columns regarded the cross-sectional region from the elastic phase's start until failure was not precise.

Yavas and Goker [54] illustrated the RR's impact on shear behaviors of I-shaped UHPC beams and devoid of fiber shear reinforcement. The outcomes displayed that the SS in higher RRs via the SF-UHPC's mechanical features along with fibers' crack-bridging capacity was advanced if the steel fibers' insertion to the UHPC mixture with lower RRs adjusted the failure mode as of the shear to flexure. The present methodologies for the envisaging of SS were not employed to execute the SF-UHPC members.

Carmo et al. [55] analyzed the lightweight cumulative concrete BCJ with various strengths along with RR. The outcomes displayed that to get the benefits of tensioned rebar's capacity, a considerable quantity of concrete in compression along with concrete with higher strength was desired by the BCJs with higher RR. The proper casting of the concrete was highly complicated, with the small cross-sections possessing a higher number of rebar.

Hassan et al. [56] illustrated the column size and RR's consequence on SS of glass fiber-reinforced polymers (GFRP) RC 2-Way Slabs. The outcomes displayed the crucial factors influencing the punching shear capacities like the reinforcement and slab size, accompanied by the ratio of the slab critical section's perimeter to the effectual slab depth. The FRP grids might not provide a similar punching shear.

**3. 6. Column Axial Load Ratio** Axial load is a structural load of a beam slab and a brick wall that functions on a longitudinal axis on a column. The different methodologies aimed at increasing the axial load ratio were explicated in this section.

Karimi et al. [57] recommended an FRP-encased steel-concrete composite column for several slenderness ratios. However, the devise methodologies for Concrete-Filled Steel Tubes (CFSTs) or Concrete-Encased Steel (CES) columns were not applicable due to the FRP tube's existence. Therefore, an analytical methodology was produced to discover the composite column's activity for several slenderness ratios. The predicted values highly agreed upon the experiential outcomes from the appraisal of 6 columns between 500 mm-3000 mm in height. The parametric study was executed to scrutinize the effect of the diameter of column, FRP tube thickness, FRP tube's axial compressive modulus, steel-to-concrete region ratio on the capacity associations along with slenderness limit. Nevertheless, the composite column's constancy was reduced with an augmentation in diameter.

Mogili et al. [58] examined the impacts of BC geometry together with eccentricity on the seismic performance of RC BC knee joints. In consequence of the shortage of experiential outcomes, the performance of knee joints' impact and the beam axis's eccentricity with the column centerline was not recognized. To review the impact of the beam axis's eccentricity and the proportion

of BC flexural capacity, the 4 full-scale knee joint sub-assemblages were evaluated underneath the upturned cyclic loading. The outcomes displayed the knee joints' weaker performance. The eccentricity's declining consequence was noticed in the opening activities. To ameliorate the opening capacity, the stronger columns were employed effectively. However, the methodology possessed a torsional breakage.

Halahla et al. [59] examined Shapes Memory Alloys (SMA) on the springiness of external RC BCJs utilizing the damage plasticity method. The consequence of utilizing the SMA on the flexibility capability of exterior RC-BCJ at various column axial load levels was concentrated in this work. The experiential outcomes obtained from the literature for authentication reasons were correlated with the outcomes attained by the finite element examination; both were contrasted with theoretical solutions. The outcomes displayed that the use of SMA enhanced the springiness of RC joints without dropping load capacity. Furthermore, the finite element technique successfully executed the capture of huge strain accompanied by the super-elastic activity of SMA bars.

Zhao et al. [60] examined a macro BCJ element technique to deliberate the consequence of joint inelastic deformations aimed at an internal joint with stirrups. The force transfer methodologies and inelastic response methodologies were regarded for the evolvement of macro BCJ, utilizing axial springs demonstrating the bar-slip technique of longitudinal reinforcement, concrete, and reinforcement on the interface-shear together with joint core. Eight reinforcement materials and concrete components in the joint core were operated simultaneously to impact joint shear deformation. The outcomes displayed that the joint method could create the joint SS, hysteretic response, and BC sub assemblages' joint shear deformation. To estimate the relationship for interface-shear springs, merely small data are utilized. However, the lower ductility was possessed by the methodology.

Influencing parameters are analyzed for RC-BC joint SS Concerning RR; the BC ratio's result utilizing disparate materials and methods is estimated. Finally, the different methodologies utilized to augment the external RC-BCJ shear strength are analyzed with Figures 2 and 3.

The BC ratio's evaluation concerning RR is exhibited in Figure 2. Kaszubska et al. [61] investigated on the influence of longitudinal GFRP reinforcement ratio on shear capacity of concrete beams; GFRP has 1.85% of R.R. CFRP [62] and hybrid fiber [63] have 1.25% and 1.90%. Then, lightweight aggregate concrete (LWAC) [64] has 1.52% of RR. Then, CFRP [65] and Eurocode 8 (E8) [66] have 1.35% and 1.8%. Next, CFRP [67] has 0.68% RR, which is less RR than E8. Finally, FRP [68] has 2.01% of RR. Figure 3 shows the RR of various

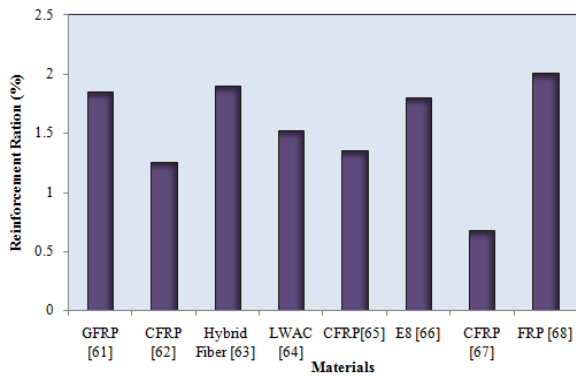


Figure 2. Evaluation of the BC ratio in terms of RR

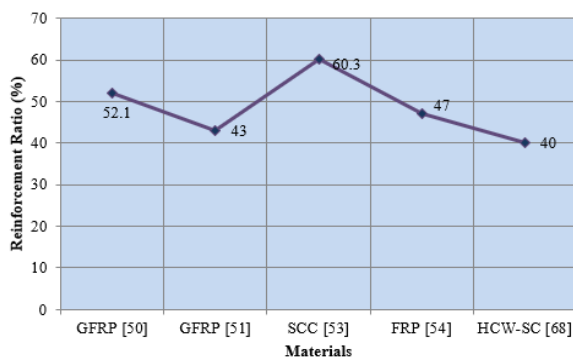


Figure 3. Evaluation of the BC ratio in terms of RR

materials used in SS GFRP [50] has 52.1% of DR. GFRP [51] and SCC [53] has 43% and 60.3% of DR. Then, FRP [54] has 47% higher DR than all other materials. Then, HCW-SC [68] has 40% of DR.

### 3. CONCLUSION

This study intends to comprehend the consequence of disparate parameters on the SS of exterior RC-BCJ. The experimentation tests' huge database is employed to assess the major role of parameter on the joint SS of exterior BCJ. The imperative levels of main parameters on the joint SS are exhibited in the data analysis. The CCS, the joint AR of the joints, anchorage of beam longitudinal reinforcement, and the number of stirrups in the joint are the most vital factors affecting the shear capacity of external RC-BCJ. The influence of higher strain rate loading on the specimens' flexural capacity modeled utilizing gravity and seismic considerations is investigated. The subassembly's ductility is enhanced with the amelioration of the reinforcement at the BCJ. The ductile subassembly exhibits high stiffness and ultimate strength under higher strain rate loading. A limited range of applicability is only there for most strengthening schemes developed so far. However,

additional research is needed to develop sufficient guidelines over a longer-term service for RC with transverse or lateral confinement.

### 4. REFERENCES

1. Tumengkol, H. A., Irmawaty, R., Parung, H., and Amiruddin, A. "Precast Concrete Column Beam Connection Using Dowels Due to Cyclic Load." *International Journal of Engineering, Transaction A: Basics*, Vol. 35, No. 1, (2022), 102–111. <https://doi.org/10.5829/ije.2022.35.01A.09>
2. Hajsadeghi, M., Jalali, M., Chin, C., Zirakian, T., and Bahrebar, M. "Flexural Performance of Fibre Reinforced Concrete with an Optimised Spirally Deformed Steel Fibre." *International Journal of Engineering*, Vol. 34, No. 6, (2021), 1390–1397. <https://doi.org/10.5829/ije.2021.34.06c.01>
3. Zhang, H., Wu, J., Jin, F., and Zhang, C. "Effect of corroded stirrups on shear behavior of reinforced recycled aggregate concrete beams strengthened with carbon fiber-reinforced polymer." *Composites Part B: Engineering*, Vol. 161, (2019), 357–368. <https://doi.org/10.1016/j.compositesb.2018.12.074>
4. Zhang Ju, Yan Changwang, and Jia Jinqing. "Crack resistance capacity of SRUHSC column to RC beam joint under frequent earthquake load." In 2010 International Conference on Mechanic Automation and Control Engineering (2010), 1106–1109. <https://doi.org/10.1109/MACE.2010.5536864>
5. Ghayeb, H. H., Razak, H. A., and Ramli Sulong, N. H. "Performance of dowel beam-to-column connections for precast concrete systems under seismic loads: A review." *Construction and Building Materials*, Vol. 237, (2020), 117582. <https://doi.org/10.1016/j.conbuildmat.2019.117582>
6. Alshaikh, I. M. H., Bakar, B. H. A., Alwesabi, E. A. H., and Akil, H. M. "Experimental investigation of the progressive collapse of reinforced concrete structures: An overview." *Structures*, Vol. 25, (2020), 881–900. <https://doi.org/10.1016/j.istruc.2020.03.018>
7. Liu, J., Xu, C., Ao, N., Feng, L., and Wu, Z. "Study Artificial Potential Field on the Clash Free Layout of Rebar in Reinforced Concrete Beam – Column Joints." In 2018 15th International Conference on Control, Automation, Robotics and Vision (ICARCV) (2018), 83–87. <https://doi.org/10.1109/ICARCV.2018.8581082>
8. Trapani, F. Di, Malavisi, M., Marano, G. C., Greco, R., and Ferrotto, M. F. "Optimal design algorithm for seismic retrofitting of RC columns with steel jacketing technique." *Procedia Manufacturing*, Vol. 44, (2020), 639–646. <https://doi.org/10.1016/j.promfg.2020.02.245>
9. Kibria, B. M. G., Ahmed, F., Ahsan, R., and Ansary, M. A. "Experimental investigation on behavior of reinforced concrete interior beam column joints retrofitted with fiber reinforced polymers." *Asian Journal of Civil Engineering*, Vol. 21, No. 1, (2020), 157–171. <https://doi.org/10.1007/s42107-019-00204-3>
10. Saravanan, J., and Kumaran, G. "Joint shear strength of FRP reinforced concrete beam-column joints." *Open Engineering*, Vol. 1, No. 1, (2011), 89–102. <https://doi.org/10.2478/s13531-011-0009-6>
11. Kamakshi, S., and Vinu, S. K. "Structural Behavior of Hybrid Reinforced Concrete Exterior Beam Column Joint." *Applied Mechanics and Materials*, Vol. 877, (2018), 254–263. <https://doi.org/10.4028/www.scientific.net/AMM.877.254>
12. Snehal, A., and Dahake, H. B. "Analysis of Beam Column Joint Subjected to Seismic Lateral Loading." *International Research Journal of Engineering and Technology*, Vol. 3, No. 5, (2016), 346–352. Retrieved from

- <https://www.academia.edu/download/54559388/IRJET-V3I575.pdf>
13. Marimuthu, K., and Kothandaraman, S. "Reverse Cyclic Behaviour of RC Exterior Beam-column Joints with Coupler Anchors: An Experimental Study." *SSRG International Journal of Civil Engineering*, (2019), 1–6. Retrieved from <https://www.internationaljournalsrg.org/uploads/specialissuepdf/ICFTESH/2019/CE/IJCE-ICFTESH-P101.pdf>
  14. Khan, M. I., Al-Osta, M. A., Ahmad, S., and Rahman, M. K. "Seismic behavior of beam-column joints strengthened with ultra-high performance fiber reinforced concrete." *Composite Structures*, Vol. 200, (2018), 103–119. <https://doi.org/10.1016/j.compstruct.2018.05.080>
  15. Mosallam, A., Allam, K., and Salama, M. "Analytical and numerical modeling of RC beam-column joints retrofitted with FRP laminates and hybrid composite connectors." *Composite Structures*, Vol. 214, (2019), 486–503. <https://doi.org/10.1016/j.compstruct.2019.02.032>
  16. Pimanmas, A., and Chaimahawan, P. "Cyclic Shear Resistance of Expanded Beam-Column Joint." *Procedia Engineering*, Vol. 14, (2011), 1292–1299. <https://doi.org/10.1016/j.proeng.2011.07.162>
  17. Pampanin, S. "Influence of slab on the seismic response of sub-standard detailed exterior reinforced concrete beam column joints." Doctoral dissertation, University of Canterbury, (2010). Retrieved from <http://hdl.handle.net/10092/3727>
  18. Santarsiero, G., and Masi, A. "Analysis of slab action on the seismic behavior of external RC beam-column joints." *Journal of Building Engineering*, Vol. 32, (2020), 101608. <https://doi.org/10.1016/j.jobe.2020.101608>
  19. Najafgholipour, M. A., Dehghan, S. M., Dooshabi, A., and Niroomandi, A. "Finite Element Analysis of Reinforced Concrete Beam-Column Connections with Governing Joint Shear Failure Mode." *Latin American Journal of Solids and Structures*, Vol. 14, No. 7, (2017), 1200–1225. <https://doi.org/10.1590/1679-78253682>
  20. Najafgholipour, M. A., and Arabi, A. R. "A nonlinear model to apply beam-column joint shear failure in analysis of RC moment resisting frames." *Structures*, Vol. 22, (2019), 13–27. <https://doi.org/10.1016/j.istruc.2019.07.011>
  21. Pan, Z., Guner, S., and Vecchio, F. J. "Modeling of interior beam-column joints for nonlinear analysis of reinforced concrete frames." *Engineering Structures*, Vol. 142, (2017), 182–191. <https://doi.org/10.1016/j.engstruct.2017.03.066>
  22. Zhang, X., and Li, B. "Seismic performance of exterior reinforced concrete beam-column joint with corroded reinforcement." *Engineering Structures*, Vol. 228, (2021), 111556. <https://doi.org/10.1016/j.engstruct.2020.111556>
  23. Choi, H., Jin, K., Matsukawa, K., and Nakano, Y. "Evaluation of equivalent diagonal strut mechanism and shear strength of URM wall in-filled R/C frame." In Second European Conference on Earthquake Engineering and Seismology, Istanbul, 2014), 1–10.
  24. Mansouri, I., Güneçyisi, E. M., and Mosalam, K. M. "Improved shear strength model for exterior reinforced concrete beam-column joints using gene expression programming." *Engineering Structures*, Vol. 228, (2021), 111563. <https://doi.org/10.1016/j.engstruct.2020.111563>
  25. Choi, H., Sanada, Y., and Nakano, Y. "Diagonal Strut Mechanism of URM Wall Infilled RC Frame for Multi Bays." *Procedia Engineering*, Vol. 210, (2017), 409–416. <https://doi.org/10.1016/j.proeng.2017.11.095>
  26. Paul, D., Choi, H., Matsukawa, K., and Nakano, Y. "Development of Diagonal Strut Mechanism of URM Wall Infilled RC Frame for Single and Double-Bays." *Bulletin of ERS*, No. 48, (2015), 125–141.
  27. Xue, Z., and Lam, E. S. "A Plane Equivalent Micro-truss Element for Reinforced Concrete Structures" (2019), 1–8. <https://doi.org/10.11159/icsect19.131>
  28. Lee, S.-J., Eom, T.-S., and Yu, E. "Investigation of Diagonal Strut Actions in Masonry-Infilled Reinforced Concrete Frames." *International Journal of Concrete Structures and Materials*, Vol. 15, No. 6, (2021), 1–14. <https://doi.org/10.1186/s40069-020-00440-x>
  29. Wu, Y., Yang, C., Li, G. X., and Zhang, C. M. "Study on Mechanical Performances of Steel Truss Reinforced Concrete Transfer Beam." *Advanced Materials Research*, Vol. 368–373, (2011), 299–302. <https://doi.org/10.4028/www.scientific.net/AMR.368-373.299>
  30. Van den Hoogen, M. G. M. "Beam or truss mechanism for shear in concrete: Problems converting a beam into a truss", Master thesis, TU Delft Repositories, (2013). Retrieved from <https://repository.tudelft.nl/islandora/object/uuid%3Aaca08b0e1-fdaf-4457-a19e-cabfb4425f11>
  31. Saleem, K., Razzaq, A.-, Jebur, S. F., and Mohammed, A. H. "Concrete and Steel Strengths Effect on Deep Beams with Reinforced Struts." *International Journal of Applied Engineering Research*, Vol. 13, No. 1, (2018), 66–73. Retrieved from [http://www.ripublication.com/ijaer18/ijaerv13n1\\_10.pdf](http://www.ripublication.com/ijaer18/ijaerv13n1_10.pdf)
  32. Wang, Y.-C., and Hsu, K. "Truss Analysis for Evaluating the Behavior of Reinforced Concrete Moment-Resisting Frames with Poorly Reinforcing Details." In The 14 th World Conference on Earthquake Engineering, China, (2008), 1–8. Retrieved from <https://citeseerx.ist.psu.edu/viewdoc/download?doi=10.1.1.488.4712&rep=rep1&type=pdf>
  33. Murad, Y. "Joint shear strength models for exterior RC beam-column connections exposed to biaxial and uniaxial cyclic loading." *Journal of Building Engineering*, Vol. 30, (2020), 101225. <https://doi.org/10.1016/j.jobe.2020.101225>
  34. Pauletta, M., Di Marco, C., Frappa, G., Somma, G., Pitacco, I., Miani, M., Das, S., and Russo, G. "Semi-empirical model for shear strength of RC interior beam-column joints subjected to cyclic loads." *Engineering Structures*, Vol. 224, (2020), 111223. <https://doi.org/10.1016/j.engstruct.2020.111223>
  35. Wu, G., Jiang, M., Das, D., and Pecht, M. "ACA Curing Process Optimization Based on Curing Degree Considering Shear Strength of Joints." *IEEE Access*, Vol. 7, (2019), 182906–182915. <https://doi.org/10.1109/ACCESS.2019.2959324>
  36. Karthik, M. M., Mander, J. B., and Hurlbauss, S. "Simulating behaviour of large reinforced concrete beam-column joints subject to ASR/DEF deterioration and influence of corrosion." *Engineering Structures*, Vol. 222, (2020), 111064. <https://doi.org/10.1016/j.engstruct.2020.111064>
  37. Khan, M. S., Basit, A., and Ahmad, N. "A simplified model for inelastic seismic analysis of RC frame have shear hinge in beam-column joints." *Structures*, Vol. 29, (2021), 771–784. <https://doi.org/10.1016/j.istruc.2020.11.072>
  38. Gao, X., and Lin, C. "Prediction model of the failure mode of beam-column joints using machine learning methods." *Engineering Failure Analysis*, Vol. 120, (2021), 105072. <https://doi.org/10.1016/j.engfailanal.2020.105072>
  39. Massone, L. M., and Orrego, G. N. "Analytical model for shear strength estimation of reinforced concrete beam-column joints." *Engineering Structures*, Vol. 173, (2018), 681–692. <https://doi.org/10.1016/j.engstruct.2018.07.005>
  40. Park, R., and Paulay, T. "Behaviour of reinforced concrete external beam-column joints under cyclic loading." In Proceedings of the 5th World Conference on Earthquake Engineering, Rome, Vol. 1, (1973), 772–781.
  41. Leon, R. T. "Anchorage requirements in interior RC Beam-Column joints." In Proceedings of Ninth World Conference on Earthquake Engineering, Vol. 4, (1988), 591–596.

42. Pampanin, S., Calvi, G. M., and Moratti, M. "Seismic Behavior of R.C. Beam-Column Joints Designed for Gravity Only", University of Canterbury, (2002). Retrieved from <https://ir.canterbury.ac.nz/handle/10092/173>
43. Kuang, J. S., and Wong, H. F. "Effects of beam bar anchorage on beam-column joint behaviour." *Proceedings of the Institution of Civil Engineers - Structures and Buildings*, Vol. 159, No. 2, (2006), 115–124. <https://doi.org/10.1680/stbu.2006.159.2.115>
44. Murty, C. V. R., Rai, D. C., Bajpai, K. K., and Jain, S. K. "Effectiveness of reinforcement details in exterior reinforced concrete beam-column joints for earthquake resistance." *Structural Journal*, Vol. 100, No. 2, (2003), 149–156. Retrieved from <https://www.concrete.org/restrictedcountry.aspx>
45. Adibi, M., Marefat, M. S., and Allahvirzizadeh, R. "Nonlinear modeling of cyclic response of RC beam-column joints reinforced by plain bars." *Bulletin of Earthquake Engineering*, Vol. 16, No. 11, (2018), 5529–5556. <https://doi.org/10.1007/s10518-018-0399-4>
46. Said, S. H., and Abdul Razak, H. "Structural behavior of RC engineered cementitious composite (ECC) exterior beam-column joints under reversed cyclic loading." *Construction and Building Materials*, Vol. 107, (2016), 226–234. <https://doi.org/10.1016/j.conbuildmat.2016.01.001>
47. Marimuthu, K., and Kothandaraman, S. "Review on the Methods of Reinforcement Technique in Reinforced Concrete Beam-Column." *International Journal of Civil Engineering and Technology*, Vol. 10, No. 01, (2019), 970–987. Retrieved from <http://iaeme.com/Home/issue/IJCIET?Volume=10&Issue=1http://iaeme.com>
48. Sengupta, P., and Li, B. "Modified Bouc-Wen model for hysteresis behavior of RC beam-column joints with limited transverse reinforcement." *Engineering Structures*, Vol. 46, (2013), 392–406. <https://doi.org/10.1016/j.engstruct.2012.08.003>
49. Kotsovu, G., and Mouzakis, H. "Seismic design of RC external beam-column joints." *Bulletin of Earthquake Engineering*, Vol. 10, No. 2, (2012), 645–677. <https://doi.org/10.1007/s10518-011-9303-1>
50. Wang, X., Zhang, Y., Su, Y., and Feng, Y. "Experimental Investigation on the Effect of Reinforcement Ratio to Capacity of RC Column to Resist Lateral Impact Loading." *Systems Engineering Procedia*, Vol. 1, (2011), 35–41. <https://doi.org/10.1016/j.sepro.2011.08.007>
51. El-Gendy, M., and El-Salakawy, E. "Effect of flexural reinforcement type and ratio on the punching behavior of RC slab-column edge connections subjected to reversed-cyclic lateral loads." *Engineering Structures*, Vol. 200, (2019), 109703. <https://doi.org/10.1016/j.engstruct.2019.109703>
52. Ibrahim, H. A., Fahmy, M. F. M., and Wu, Z. "Numerical study of steel-to-FRP reinforcement ratio as a design-tool controlling the lateral response of SFRC beam-column joints." *Engineering Structures*, Vol. 172, (2018), 253–274. <https://doi.org/10.1016/j.engstruct.2018.05.102>
53. Tobbi, H., Farghaly, A. S., and Benmokrane, B. "Behavior of Concentrically Loaded Fiber-Reinforced Polymer Reinforced Concrete Columns with Varying Reinforcement Types and Ratios." *ACI Structural Journal*, Vol. 111, No. 2, (2014), 375–386. <https://doi.org/10.14359/51686528>
54. Yavas, A., and Goker, C. O. "Impact of Reinforcement Ratio on Shear Behavior of I-Shaped UHPC Beams with and without Fiber Shear Reinforcement." *Materials*, Vol. 13, No. 7, (2020), 1525. <https://doi.org/10.3390/ma13071525>
55. Carmo, R. N. F. do, Costa, H., Gomes, G., and Valença, J. "Experimental evaluation of lightweight aggregate concrete beam-column joints with different strengths and reinforcement ratios." *Structural Concrete*, Vol. 18, No. 6, (2017), 950–961. <https://doi.org/10.1002/suco.201600166>
56. Hassan, M., Fam, A., Benmokrane, B., and Ferrier, E. "Effect of Column Size and Reinforcement Ratio on Shear Strength of Glass Fiber-Reinforced Polymer Reinforced Concrete Two-Way Slabs." *ACI Structural Journal*, Vol. 114, No. 4, (2017), 937–950. <https://doi.org/10.14359/51689869>
57. Karimi, K., Tait, M. J., and El-Dakhkhni, W. W. "Analytical modeling and axial load design of a novel FRP-encased steel-concrete composite column for various slenderness ratios." *Engineering Structures*, Vol. 46, (2013), 526–534. <https://doi.org/10.1016/j.engstruct.2012.08.016>
58. Mogili, S., Kuang, J. S., and Huang, R. Y. C. "Effects of beam-column geometry and eccentricity on seismic behaviour of RC beam-column knee joints." *Bulletin of Earthquake Engineering*, Vol. 17, No. 5, (2019), 2671–2686. <https://doi.org/10.1007/s10518-019-00562-y>
59. Halahla, A. M., Abu Tahnat, Y. B., Almasri, A. H., and Voyiadjis, G. Z. "The effect of shape memory alloys on the ductility of exterior reinforced concrete beam-column joints using the damage plasticity model." *Engineering Structures*, Vol. 200, (2019), 109676. <https://doi.org/10.1016/j.engstruct.2019.109676>
60. Zhao, W., Yang, H., Chen, J., and Sun, P. "A proposed model for nonlinear analysis of RC beam-column joints under seismic loading." *Engineering Structures*, Vol. 180, (2019), 829–843. <https://doi.org/10.1016/j.engstruct.2018.09.068>
61. Kaszubska, M., Kotynia, R., and Barros, J. A. O. "Influence of Longitudinal GFRP Reinforcement Ratio on Shear Capacity of Concrete Beams without Stirrups." *Procedia Engineering*, Vol. 193, (2017), 361–368. <https://doi.org/10.1016/j.proeng.2017.06.225>
62. Ashour, A. F., and Kara, I. F. "Size effect on shear strength of FRP reinforced concrete beams." *Composites Part B: Engineering*, Vol. 60, (2014), 612–620. <https://doi.org/10.1016/j.compositesb.2013.12.002>
63. You, Z., Chen, X., and Dong, S. "Ductility and strength of hybrid fiber reinforced self-consolidating concrete beam with low reinforcement ratios." *Systems Engineering Procedia*, Vol. 1, (2011), 28–34. <https://doi.org/10.1016/j.sepro.2011.08.006>
64. Dias-da-Costa, D., Carmo, R. N. F., Graça-e-Costa, R., Valença, J., and Alfaiate, J. "Longitudinal reinforcement ratio in lightweight aggregate concrete beams." *Engineering Structures*, Vol. 81, (2014), 219–229. <https://doi.org/10.1016/j.engstruct.2014.09.016>
65. Osman, B. H., Wu, E., Ji, B., and Abdulhameed, S. S. "Effect of reinforcement ratios on shear behavior of concrete beams strengthened with CFRP sheets." *HBRC Journal*, Vol. 14, No. 1, (2018), 29–36. <https://doi.org/10.1016/j.hbrj.2016.04.002>
66. Kassoul, A., and Bougara, A. "Maximum ratio of longitudinal tensile reinforcement in high strength doubly reinforced concrete beams designed according to Eurocode 8." *Engineering Structures*, Vol. 32, No. 10, (2010), 3206–3213. <https://doi.org/10.1016/j.engstruct.2010.06.009>
67. Peng, S., Xu, C., and Liu, X. "Truss-arch model for shear strength of seismic-damaged SRC frame columns strengthened with CFRP sheets." *Frontiers of Structural and Civil Engineering*, Vol. 13, No. 6, (2019), 1324–1337. <https://doi.org/10.1007/s11709-019-0557-z>
68. Ferreira, D., Oller, E., Marí, A., and Bairán, J. "Numerical Analysis of Shear Critical RC Beams Strengthened in Shear with FRP Sheets." *Journal of Composites for Construction*, Vol. 17, No. 6, (2013), 04013016. [https://doi.org/10.1061/\(ASCE\)CC.1943-5614.0000434](https://doi.org/10.1061/(ASCE)CC.1943-5614.0000434)

## Persian Abstract

## چکیده

اتصالات تیر-ستون (BCJ) رفتار سازه و مکانیسم‌های شکست را تحت حوادث شدید، انفجار، زلزله و ضربه مدیریت می‌کند. بنابراین، آنها اجزای حیاتی در یک ساختمان هستند. کمبودهای متفاوت، مثلاً تیر ضعیف در خمش، برش، و ستون ضعیف در برش، در این مجموعه مشترک وجود دارد تا محدودیت‌ها در قاعده طراحی در نظر گرفته شود. برای تجزیه و تحلیل رفتار اتصالات تیر-ستون (BC) بتن مسلح (RC)، تحقیقات سیستماتیک در میان ۲۰ سال گذشته انجام شد. پارامترهای تأثیر به نفع مقاومت برشی (SS) RC-BCJ خارجی در اینجا بررسی می‌شوند. (الف) مقاومت فشاری بتن (CCS)، (ب) اتصال محصور شده توسط تیر، (ج) طول لنگر، (د) آرمانور تیر و ستون، و (ه) بار محوری ستون‌ها پارامترهای اصلی 'ه' هستند. برای SS مفصل، که از طریق نتیجه یافت می‌شود. قابل توجه‌ترین همبستگی با SS مشترک با CCS در میان جنبه‌های تأثیر یافت شد. این مطالعه ویژگی‌های حیاتی مقاومت برشی RC-BCJ را نشان می‌دهد.



## Numerical Investigation of Geometric Parameters Effects on Heat Transfer Enhancement in a Manifold Microchannel Heat Sink

M. R. Babaei, G. A. Sheikhzadeh\*, A. A. Abbasian Arani

Department of Mechanical Engineering, University of Kashan, Kashan, Iran

### PAPER INFO

#### Paper history:

Received 15 January 2022

Received in revised form 05 February 2022

Accepted 10 February 2022

#### Keywords:

Manifold Microchannel Heat Sink  
Thermophysical Properties  
Heat Transfer Enhancement  
Performance Evaluation Criterion

### ABSTRACT

Microchannel heat sink has been employed and as a part of electronic equipment extensively investigated. In this investigation, heat transfer and fluid flow features of laminar flow of water in a manifold microchannel heat sink (MMHS) was numerically simulated. Selected heat flux was  $100 \text{ W/m}^2$  and water was as working fluid. The effect of length of inlet/outlet ratio ( $\lambda=L_{\text{inlet}}/L_{\text{outlet}}$ ), the height of microchannel ( $H_{\text{ch}}$ ), and width of the microchannel ( $W_{\text{ch}}$ ) at Reynolds number (Re) range from 20 to 100 as independent parameters on the fluid flow and heat transfer features were examined. Obtained results demonstrate that in MMHS, the impinging jet on the bottom channel surface, inhibits the growth of hydrodynamic and thermal boundary layers, resulting in an enhanced heat transfer rate. Also, by increasing Re and keeping the geometric parameters constant, the heat transfer rate increases. Based on the present investigation, for low Re, it is better to choose a  $\lambda=L_{\text{inlet}}/L_{\text{outlet}} > 1$  and for high Re, choose a  $\lambda < 1$ . For low Re, maximum of performance evaluation criterion ( $\text{PEC}_{\text{max}}$ ) is obtained at  $H_{\text{ch}}=300\mu\text{m}$ , and for high Re,  $\text{PEC}_{\text{max}}$  is obtained at  $H_{\text{ch}}=240\mu\text{m}$ . for  $\text{Re}=20$  to  $100$ , the maximum of  $\text{PEC}_{\text{max}}$  is  $1.765$  and obtained at  $\text{Re}=100$  and  $H_{\text{ch}}=240\mu\text{m}$ .

doi: 10.5829/ije.2022.35.05b.10

### NOMENCLATURE

$W_{\text{ch}}$	width of the microchannel ( $\mu\text{m}$ )	$q''$	heat flux ( $\text{W/m}^2$ )
$W_{\text{f}}$	width of the fin ( $\mu\text{m}$ )	Re	Reynolds number
$H_{\text{ch}}$	height of microchannel ( $\mu\text{m}$ )	T	temperature (K)
$H_{\text{m}}$	height of manifold ( $\mu\text{m}$ )	$T_{\text{in}}$	Inlet temperature (K)
$H_{\text{s}}$	height of substrate ( $\mu\text{m}$ )	$T_{\text{out}}$	Outlet temperature (K)
$L_{\text{in}}$	length of inlet path ( $\mu\text{m}$ )	$T_{\text{m}}$	mean Bulk temperature (K)
$L_{\text{m}}$	length of manifold ( $\mu\text{m}$ )	$\bar{T}_{\text{s}}$	average temperature of microchannel wall (K)
$L_{\text{out}}$	length of outlet path ( $\mu\text{m}$ )	u	velocity (m/s)
$\lambda$	length of inlet/outlet ratio ( $L_{\text{inlet}}/L_{\text{outlet}}$ )	$u_{\text{in}}$	Inlet velocity (m/s)
MMHS	manifold microchannel heat sink	L	Length of microchannel ( $\mu\text{m}$ )
MMHE	manifold microchannel heat exchanger	$\text{Nu}_{\text{ave}}$	average Nusselt number
TMHS	Traditional microchannel heat sink	$\text{Nu}_{\text{ave,r}}$	reference average Nusselt number
PEC	performance evaluation criterion	f	friction coefficient
FFMHS	Force-fed microchannel heat sink	$f_{\text{r}}$	reference friction coefficient
JIHS	Jet impingement heat	$k_{\text{f}}$	thermal conductivity of fluid ( $\text{W/mK}$ )
p	Pressure (Pa)	$\mu_{\text{f}}$	dynamic viscosity ( $\text{Ns/m}^2$ )
$\Delta p$	pressure drop (Pa)	$c_{\text{p}}$	specific heat capacity ( $\text{J/kg K}$ )
$\dot{m}$	mass flow rate (kg/s)	$A_{\text{ch}}$	Microchannel cross section ( $\text{m}^2$ )

\*Corresponding Author Institutional Email: [sheikhz@kashanu.ac.ir](mailto:sheikhz@kashanu.ac.ir) (G. A. Sheikhzadeh)

## 1. INTRODUCTION

In the electronic equipment industry, using microchannel heat sink as one of the effective methods for achieving high electronic components thermal performance. Therefore, modeling different types of microchannel heat sink is one of the important topics of interest of researchers [1-3]. Also, Attempts had been made by many authors to develop improved models suitable for various processes [4-6].

Traditional microchannel heat sink (TMHS) and manifold microchannel heat sink (MMHS) are two categories of the microchannel heat sink. TMHS has two fundamental problems: major variation of temperature within the heat source and high-pressure drop. In the MMHS, compared with TMHS, as shown in Figure 1, the coolant flow path to a small part is reduced, and also cold fluid impinges on the microchannel bottom surface. Therefore, the pressure drop is reduced, and the growth of thermal and hydrodynamic boundary layers is limited and leads to better heat transfer. Many researches have been done on the application of MMHS in the electronics industry and for the purpose to cool the electronic chips. At present, researchers are now trying to find MMHS that can not only improve heat transfer but also be economically viable and have a low pressure drop. Therefore, they are studying on MMHS geometry and etc. Some of these studies are discussed as follows:

Kermani [7] by experimental method, showed major enhancement in heat transfer coefficient in the MMHS for cooling the solar cells than TMHS. His result showed that for MMHS, 37% of total pressure drop were obtained in the microchannel with a hydraulic diameter of  $36 \mu\text{m}$  and 13% of total pressure drop were obtained in the microchannel with a hydraulic diameter of  $67 \mu\text{m}$ . The remaining total pressure drop occurs in the manifold. Escher et al. [8] introduced a 3D flow modeling of MMHS. They studied the hydrodynamics performance and thermal performance for one-unit cell of MMHS. Also, they determined thermal performance and total

hydrodynamical structure of the system. Their observations showed that the width of the channel and  $L_{\text{inlet}}/L_{\text{outlet}}$ , change the thermal performance. Cetegen [9] for achieving the minimum pumping power and maximum heat transfer coefficients, by numerical simulation studied tree type of microchannel heat sink: Force-fed microchannel heat sink (FFMHS), TMHS, and Jet impingement heat sink (JIHS). Her results showed that at the same pumping power, for FFMHS, heat transfer coefficients are 306% higher than JIHS and are 72% higher than TMHS. Kasten et al. [10] for microchannel unit cell, numerically modeled a 3D conjugate heat transfer. In the next step, they simulated a 3D complete heat sink model. They concluded that if the flow rate increases, the thermal resistance of MMHS decreases and, pressure drop increases. Boteler et al. [11] by a numerical analysis and one phase mode, studied flow field and heat transfer for a manifold microchannel heat exchanger. They concluded that two parameters, such as a microchannel fin and width of microchannel, have a significant effect on thermal performance. Husain and Kim [12] numerically modeled a 3D model of MMHS. The key parameters of their research were thermal resistance and water pumping power. Their results showed that the nozzle height to the microchannel height ( $H_{\text{nz}}/H_{\text{ch}}$ ) and the ratio of the microchannel width to the microchannel height ( $W_{\text{ch}}/H_{\text{ch}}$ ) are more effective parameters on pumping power of water and thermal resistance. Sarangi et al. [13], by 3D numerical simulation, studied the influence of geometrical variables such as manifold height, manifold inlet/outlet ratio, microchannel width, and microchannel depth on the performance of MMHS. Their study consisted of two sections: porous-medium pattern and unit-cell pattern. Their observations showed that the optimum value of the manifold inlet/outlet ratio is equal to 3. In the study of Arie et al. [14] the air was used as a cooling fluid in MMHS. To obtain the best design variables, they used an optimization function. Their investigation showed that, by using MMHS, improvement in heat sink thermal performance is observed. Arie et al. [15] for achieving

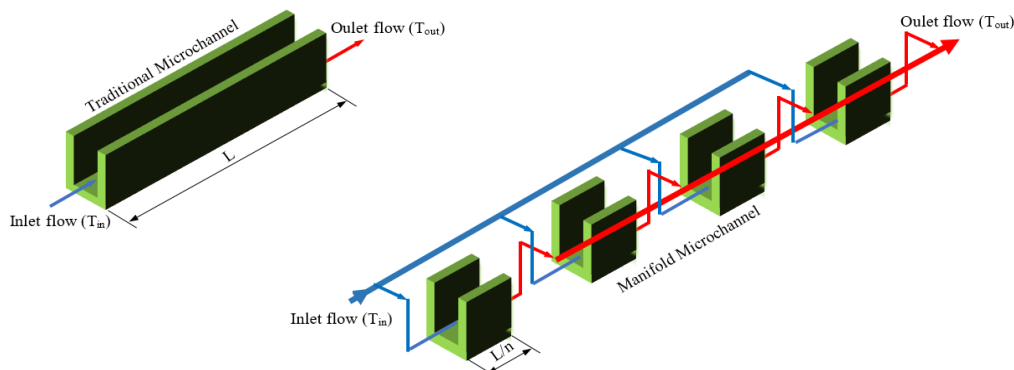


**Figure 1.** Comparison of Traditional microchannel with Manifold microchannel

the optimal thermal performance of manifold microchannel heat exchanger (MMHE) and for determining the best design parameters, used a numerical method. Their observations showed that friction coefficient and Nusselt number compared to chevron categories of the plate heat exchanger are effective parameters in optimizing the manifold microchannel. Yue et al. [16] studied thermal performances of a MMHS in the presence of nanofluids as working fluids. Their observations showed that Nusselt number and water pumping power increases by increasing the volume fraction of nanoparticles and Re and decreases by increasing the diameter of the particles. Andhare et al. [17] designed a particular type of MMHE to study numerically and experimentally the impact of this type of microchannel heat sink on thermal performance. Their observations showed that for  $\dot{m} < 20 \text{ g/s}$ , the total heat transfer coefficient  $h_{\text{total}} = 20000 \text{ W/m}^2\text{K}$  was obtained. Li et al. [18] numerically studied flow field and heat transfer for both MMHS and TMHC for non-Newtonian fluid such as dilatant fluid and pseudo-plastic fluid. Their result showed that drag resistance decreased for pseudo-plastic fluid flow up to 2 orders and increased for dilatant fluid flow up to 3 orders. Arie et al. [19] enhanced the performance of an air-water MMHE, used multi-objective optimization and compared the results with optimized conventional heat exchangers, such as louvered fin, plain plate-fin, pin fin, wavy fin and wavy fin surfaces. Their results showed that the sophisticated design of the manifolds and fins could significantly improve the performance of MMHE. Compared to a wavy-fin heat exchanger, MMHE can up to 60% increase heat transfer density.

Drummond et al. [20] experimentally studied a hierarchical MMHC. They studied the effect aspect ratio and channel width on the thermal and hydraulic performance. They showed that the case with a larger hydraulic diameter compared to the case with a smaller hydraulic diameter lead to lower thermal resistance and higher heat transfer coefficient. Ju et al. [21] presented numerical modeling to analyze thermal and hydrodynamic performances of the micro-pin-fin heat sink. Their result showed that heat sinks with square and circular micro-pin-fins with the same cross-sectional area have the same thermal performance. Zhang et al. [22] by numerical simulation, studied both steady and pulsating flow in MMHS. Their result showed that pulsating flow inlet, in comparison to the steady flow, improves thermal performance. Also, in comparison to other pulsating types, sinusoidal-wave pulsating flow plays a more effective role in enhancing heat transfer. Jung et al. [23] studied experimentally and numerically a 3D MMHS was made of silicon. Their experimental result showed that at a flow rate of 0.1 l/min and a maximum temperature of 90 C°, 250 W/cm<sup>2</sup> is removed by the

MMHS with a pressure drop of less than 3 kPa. Tiwari et al. [24] designed and studied experimentally single-phase flow in a MMHE. Their result showed that for the tube-side with  $\dot{m} = 806 \text{ g/s}$  and for the shell-side with  $\dot{m} = 82 \text{ g/s}$ , shell-side heat transfer coefficient of 45,000 W/m<sup>2</sup>K and overall heat transfer coefficient of 22,000 W/m<sup>2</sup>K can be obtained. Luo et al. [25], studied heat transfer in a MMHS for two-phase flow boiling process. Their observations showed that for the manifold divider, the manifold ratio ranges from 1 to 2 is suitable to reduce the pressure drop of the MMHS. Yang et al. [26] numerically studied performance enhancement of hybrid microchannel heat sink. Their result showed that compared to the usual MMHS, the best heat sink could decrease thermal resistance by 19.15% and reduce pressure drop by 1.91% at Re = 295. Drummond et al. [27] experimentally studied two-phase flow morphology in high aspect ratio manifold microchannels. Their results showed that for manifold microchannels, the two-phase flow regime plays an important role in heat transfer improvement and must be with accuracy considered in heat sink design. Luo et al. [28] by 3D numerical methods, studied two-phase flow boiling in MMHS for different manifolds configurations (C-type, H-type, Z- and, U-type). Their results showed that compared with C-type and Z-type, H-type and the U-type manifolds due to their lower pressure drop and better heat transfer performance are recommended. Yang et al. [29] performed an experimental comparison between a hybrid microchannel heat sink (HMHS) and a typical manifold microchannel heat sink (CMMHS). Their results showed that the HMHS reduce thermal resistance and pressure drop. Luo et al. [30] studied numerically pressure loss and thermal performance of subcooled flow boiling in an MMC with various sizes of fin widths and channel widths and various inlet volume flow rates. Their observations showed that the thermal resistance of heat sink reduced when the volume flow rate increases, but pressure drop increased.

In the current study, the effects of variation of geometric dimension of MMHS such as length of inlet/outlet ratio, the height of microchannel and, width of microchannel at Re=20 to 100 on the flow field and heat transfer to find the optimal geometric dimension are numerically investigated. According to the obtained results, the best geometry is selected in terms of thermal improvement. In addition, for more precise results, the water thermophysical properties of the working fluid and silicon as a solid part (manifold and microchannels) are considered temperature-dependent, which had not been considered in previous similar articles. The PEC is also considered as a criterion for selecting the optimal microchannel rather than Nusselt number, and pressure drop.

At first of the current investigation, the model under consideration and boundary condition are presented. Then, system of governing equations and boundary conditions, numerical procedure, grid independency study and validation are done. Finally results and discussion are presented for investigation of heat transfer and fluid flow features of laminar flow of water in a manifold microchannel heat sink. Figure 2 shows the research methodology.

**2. MODEL DESCRIPTION**

**2. 1. Geometrical Model and Boundary Conditions**

The effect of variable geometric parameters such as  $\lambda$ ,  $H_{ch}$  and  $W_{ch}$  for  $Re=20$  to  $100$  on the flow field and heat transfer was investigated. Manifolds, microchannels and substrate are made of silicon. MMHS schematic in the current study is shown in Figure 3. The manifolds are distributed above the microchannels. The coolant fluid, after passing through the inlet channels of the manifolds, rotates  $90^\circ$  and enters the microchannels, removes the heat from the substrate along the microchannel length

and, finally  $90^\circ$  turn and exits upward and enters the output channels in the manifold. Figure 4 shows the computational domain and geometric dimension for a unit cell of MMHS. Due to symmetry boundary conditions and to reduce the computational cost, a unit cell of MMHS is chosen. At the inlet of manifold, mass flow inlet and, at the outlet of manifold, pressure outlet have been selected as boundary conditions. Also, constant heat flux of  $100 \text{ W/cm}^2$  on the bottom wall and no-slip velocity boundary condition on the walls of the microchannel has been considered. Figure 5 indicates the boundary conditions for the unit cell of MMHS.

**3. THERMOPHYSICAL PROPERTIES**

In the present simulation, silicon has been used as a solid part (manifold and microchannels) and, water is used as a working fluid. Temperature-dependent thermophysical properties between  $300\text{K}$  to  $400\text{K}$ , including thermal conductivity and dynamic viscosity of water and thermal conductivity of silicon were considered as the function of temperature [31-32]. Variations of the other

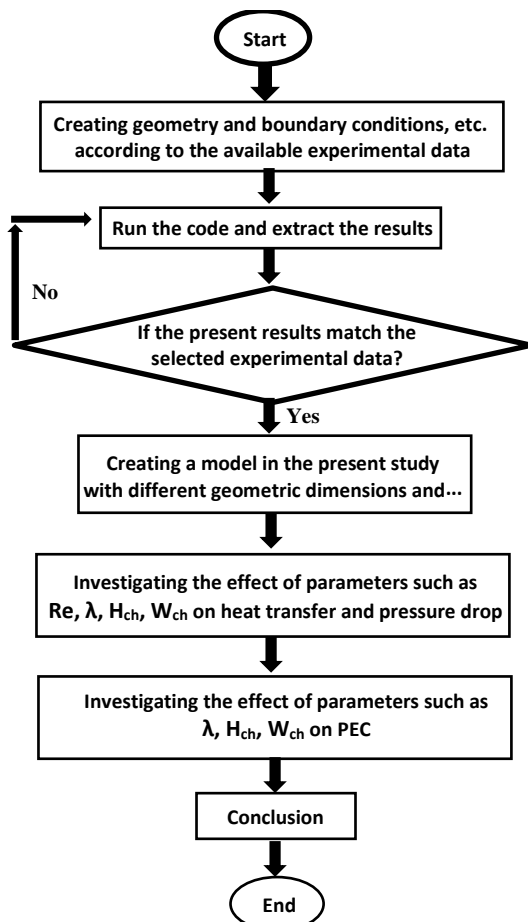


Figure 2. Research methodology

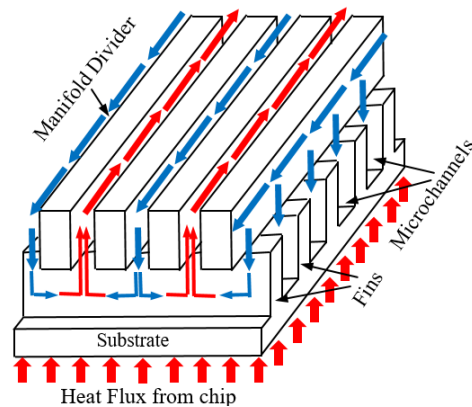


Figure 3. Schematic of MMHS

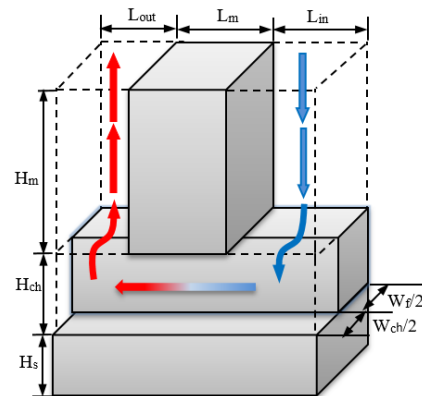
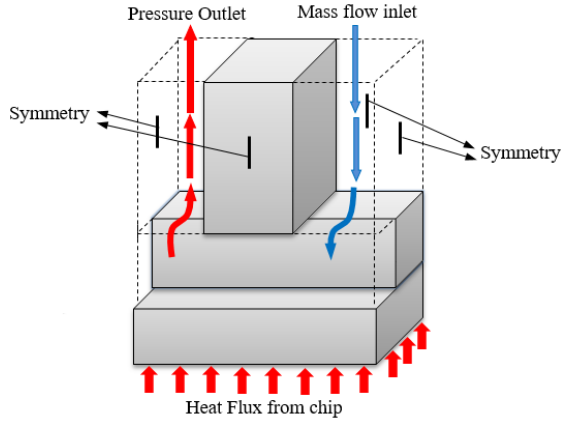


Figure 4. Computational domain and geometric dimension for the unit cell of MMHS



**Figure 5.** Applied boundary conditions for the unit cell of MMHS

thermophysical properties of water and silicon between the temperature ranges of 300K to 400K have no significant effect on the results.

#### 4. GOVERNING EQUATIONS

Single-phase fluid flow and laminar flow governing equations at steady states condition in Cartesian coordinate is:

Continuity equation:

$$\frac{\partial}{\partial x_j}(u_j) = 0 \quad (1)$$

Momentum equation:

$$\frac{\partial}{\partial x_j}(\rho u_j u_i) = -\frac{\partial p}{\partial x_i} + \frac{\partial}{\partial x_j}(\mu_f \frac{\partial u_i}{\partial x_j}) \text{ (fluid)} \quad (2)$$

Energy equation:

$$\frac{\partial}{\partial x_j}(\rho u_j c_p T_f) = \frac{\partial}{\partial x_j}(k_f \frac{\partial T_f}{\partial x_j}) \text{ (solid)} \quad (3)$$

$T$ ,  $p$ , and  $u_j$  represent the temperature, pressure, and velocity, while the subscripts f and s refer to the fluid and solid, respectively. For the flow to justify the assumption of laminar flow, the low Re (Re=20 to 100) is considered. The liquid to the solid interface was coupled by continuity of both heat flux and temperature:

$$T_{s_{interface}} = T_{f_{interface}} \quad (4)$$

$$-k_s \left( \frac{\partial T_s}{\partial n} \right)_{interface} = -k_f \left( \frac{\partial T_f}{\partial n} \right)_{interface} \quad (5)$$

##### 4. 1. Important Parameters in the Three-dimensional Flow

The friction coefficient, which is one of the parameters for evaluation of the microchannel operation, is defined as follows:

$$f = 2\Delta p \frac{D_h}{L} \frac{1}{\rho u_{in}^2} \quad (6)$$

where,  $L$ ,  $D_h$ ,  $u_{in}$ , and  $\rho$  are the length, hydraulic diameter, inlet velocity, and density, respectively.

The average Nusselt number defined as follows:

$$Nu_{ave} = \frac{q'' D_h}{k_f (\bar{T}_s - T_m)} \quad (7)$$

where,  $T_m$  and  $\bar{T}_s$  are the mean Bulk temperature and microchannel wall temperature, respectively.

Performance Evaluation Criterion parameter (PEC), is defined as follows [33]:

$$PEC = (Nu_{ave} / Nu_{ave,r}) / (f / f_r)^{1/3} \quad (8)$$

Re based on flow in the straight part of the microchannel according of Figure 6 defined as follows:

$$Re = \frac{\dot{m}_{ch} D_h}{\mu A_{ch}} \quad (9)$$

where

$$A_{ch} = w_{ch} / 2 \times H_{ch} \quad (10)$$

$$D_h = \frac{2H_{ch}w_{ch}}{H_{ch}+w_{ch}} \quad (11)$$

#### 5. GRID INDEPENDENCY

Several meshes with different cell numbers have been used to ensure that the results are independent of the grid. The mesh and results are plotted for the microchannel middle plate. According to Figure 7, for one case, a mesh with the 1420800 cells is sufficient for conducting simulation. By increasing the cell numbers more than 1420800, the obtained results do not have significant variations (heat transfer coefficient difference between 1420800 and 1965600 cells is 0.50%).

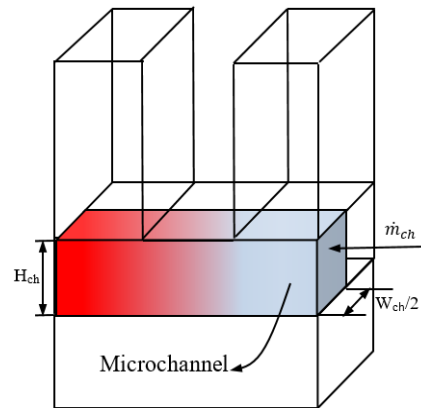


**Figure 6.** Microchannel section and microchannel geometrical characteristics

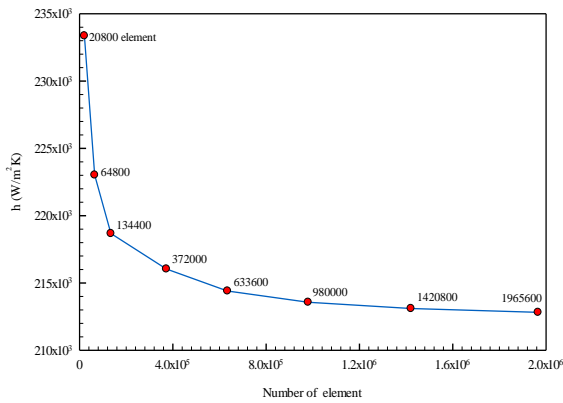


Figure 7. Mesh independence study.  $H_{ch} = 360\mu\text{m}$ ,  $W_{ch}=60\mu\text{m}$

6. MODEL VALIDATION

For assurance of the accuracy of numerical simulations, the numerical results are compared with available experimental data. In Kermani’s study, heat transfer enhancement of MMHS with hydraulic diameter  $D_h=36\mu\text{m}$  examined. Figure 8 show validation with kermani result for  $D_h=36\mu\text{m}$ . according to Figure 7, it can be seen that the current results have good match with Kermani’s experimental data [7].

7. RESULTS AND DISCUSSIONS

In this section, the results of the numerical simulation of fluid flow and heat transfer inside the MMHS are presented. Nu and  $\Delta p$  are two important parameters that are presented. Also, to study from an engineering and economic viewpoint, the PEC has been presented for different cases. Also, the results are presented as temperature contours and velocity contours.

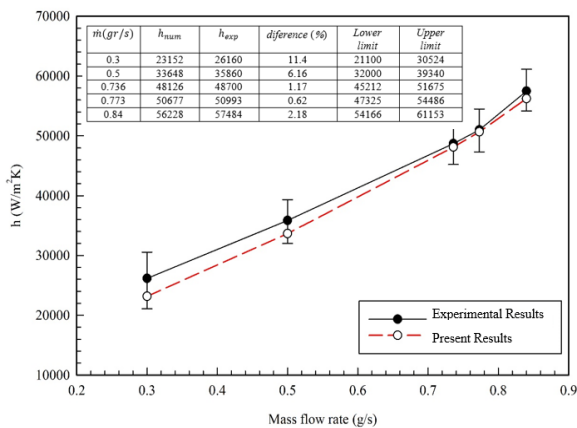


Figure 8. Heat transfer coefficient variations versus mass flow rate: comparison of present numerical results with experimental result [7] for  $D_h=36\mu\text{m}$

7. 1. Effect of Re on Heat Transfer and Pressure Drop

The cooling fluid, after passing through the inlet nozzle, impacts the microchannel floor. In the MMHC flow, due to the direct impact of the flow perpendicular to the microchannel floor and the short flow path length, most of the flow is developing along the microchannel, thus limiting the growth of the hydrodynamic and thermal boundary layer. Therefore, a small diffusion length from the solid wall to the convective flow and better heat transfer rate is achieved. At the subsequent region, the rate of heat transfer decreases due to the growth of the hydrodynamic and thermal boundary layer. The results are plotted for the microchannel middle plate. Figure 9 shows temperature contours and velocity contours at various Re for  $H_{ch}=600\mu\text{m}$ ,  $W_{ch}=60\mu\text{m}$ ,  $W_f=60\mu\text{m}$ ,  $L_{in}=120\mu\text{m}$ , and  $L_{out}=200\mu\text{m}$ . According to Figure 9(a), as the Re increases, the temperature of the microchannel floor and, consequently, the surface temperature in contact with the heat source decreases; this is due to the increase in flow rate and fluid velocity on the microchannel floor. The maximum temperature of the microchannel floor is 311.3K at Re=20 and is 306.3K at Re=100. Also, the thermal and hydrodynamic boundary layer thickness is reduced, and therefore, the heat transfer rate is increased. At the inlet zone of the flow from the nozzle to the microchannel, due to the reduction of cross-section, the velocity in this zone increases (according to Figure 9(b)) and formed a rotational zone near this zone. The Muximum velocity is related to the microchannel input at Re=20 is 1.07m/s and at Re=100 is 5.27m/s. Also, by increasing the Re, the flow injection velocity on the microchannel floor increases, and the formed rotational zone becomes larger.

7. 2. Effect of  $\lambda = L_{inlet}/L_{outlet}$  on Heat Transfer and Pressure Drop

Figure 10 shows temperature contours and velocity contours at various  $\lambda$  for  $H_{ch}=600\mu\text{m}$ ,  $W_{ch}=60\mu\text{m}$ ,  $W_f=60\mu\text{m}$  and  $L_{out}=200\mu\text{m}$  at Re=100. Studies were performed for  $\lambda = 0.6$  to 1.3, but contours from  $\lambda=1$  to  $\lambda=1.3$  are similar, and their changes are not significant and not shown. Figure 10(a) shows that by increasing in  $\lambda$ , the temperature of the microchannel floor increases. Due to the increase in cross-sectional area and decrease in inlet velocity from the nozzle to the microchannel, the flow injection velocity on the microchannel floor decreases. The maximum temperature of the microchannel floor is 306.3K at  $\lambda=0.6$  and is 307.8K at  $\lambda=1$ . Figure 10(b) show with an increase in  $\lambda$ , inlet velocity from the nozzle to the microchannel decreases, and as a result, flow injection velocity on the microchannel floor decreases. The input velocity at  $\lambda=0.6$  is 5.27m/s and at  $\lambda=1$  is 3.45m/s. Also as  $\lambda$  increases, the maximum velocity zone is also seen in the output manifold, and in  $\lambda=1$ , the maximum velocity is seen in the output manifold zone.

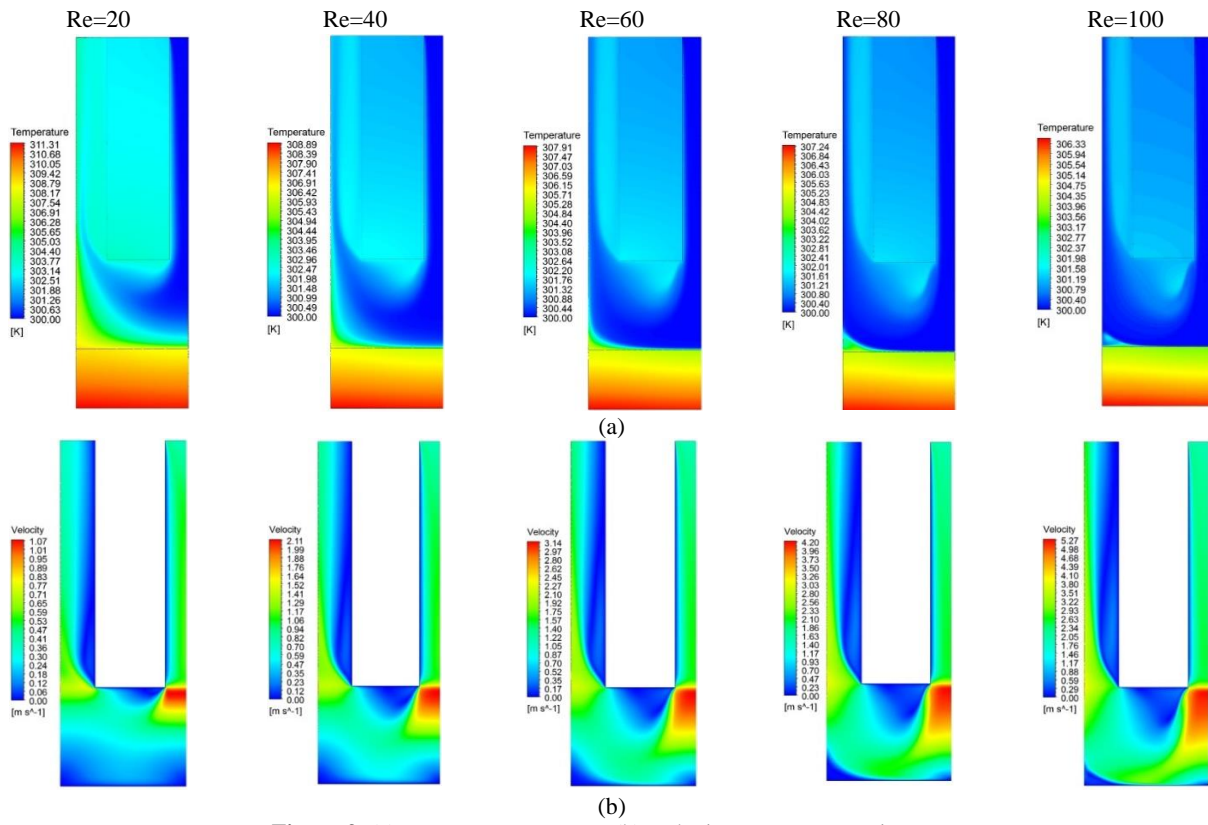


Figure 9. (a)Temperature contours (b) Velocity contours at various Re

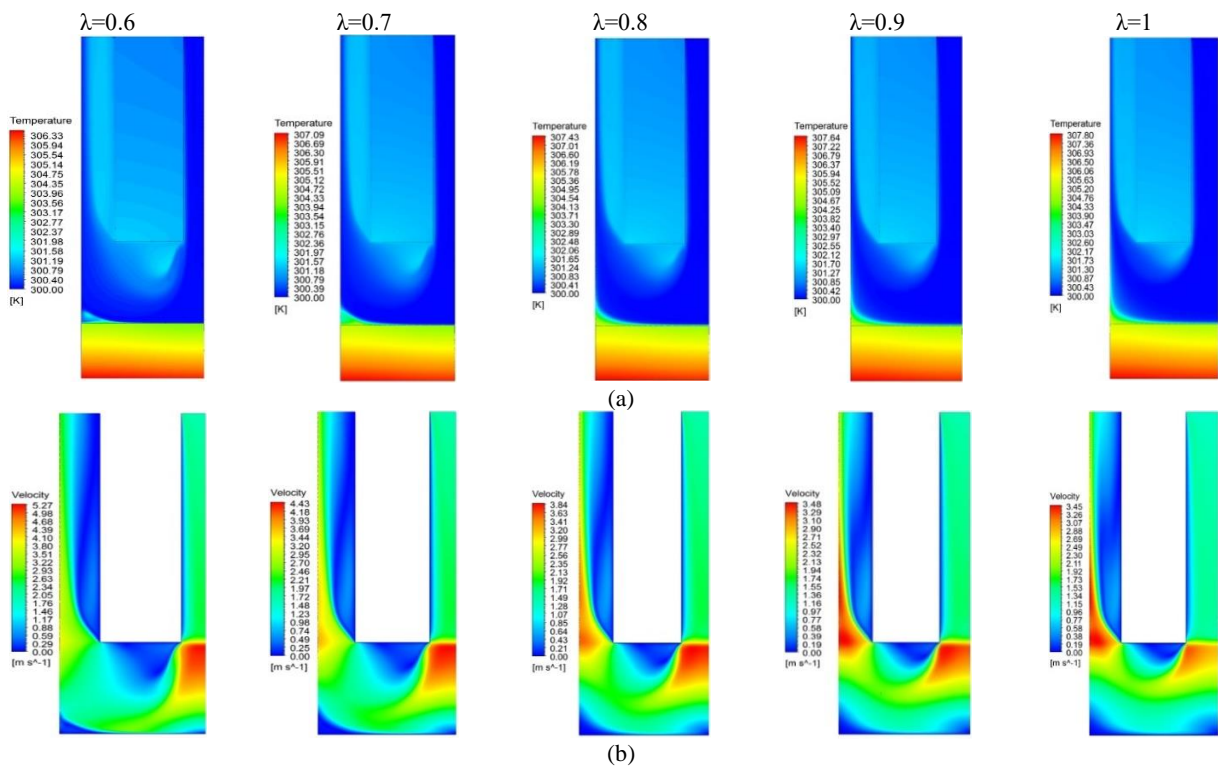
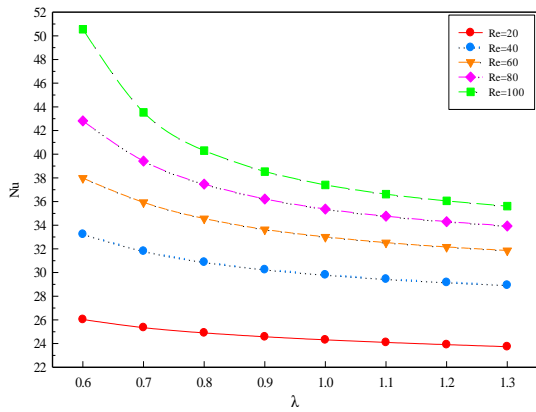


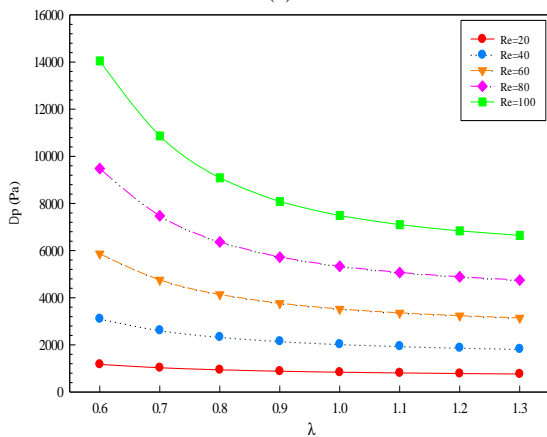
Figure 10. (a)Temperature contours (b) Velocity contours at various λ

Figures 11(a) and 11(b) respectively show variations of the Nu and  $\Delta p$  versus  $\lambda$  for different Re on the microchannel floor. By increasing Re, Nu and  $\Delta p$  are increased. At higher Re and smaller  $\lambda$ , the slope of variations of Nu and  $\Delta p$  is greater and for lower Re the slope of the changes is imperceptible. By increasing in  $\lambda$ , the amount of Nu and  $\Delta p$ , as well as their variations are reduced.

**7. 3. Effect of  $\lambda$  on PEC** Figure 12 shows PEC for various  $\lambda$  and Re. by increasing  $\lambda$ , PEC is increased for Re=20, 40 and 60 and for  $\lambda > 1$ , PEC variations are insignificant. For Re=80, the PEC values are close to 1. For Re=100, by increasing in  $\lambda$ , PEC is decreased. The highest PEC is occurred at Re=100 and  $\lambda = 0.6$ . It seems that due to the smaller inlet section of the microchannel at  $\lambda = 0.6$  than other  $\lambda$  values, with increasing Reynolds number, the increase in heat transfer is greater than the pressure drop increase. For lower Re, it is better to choose a  $\lambda > 1$  and for higher Re, choose a  $\lambda < 1$ .



(a)



(b)

**Figure 11.** Variations of the (a) Nu (b)  $\Delta p$  versus  $\lambda$  for various Re

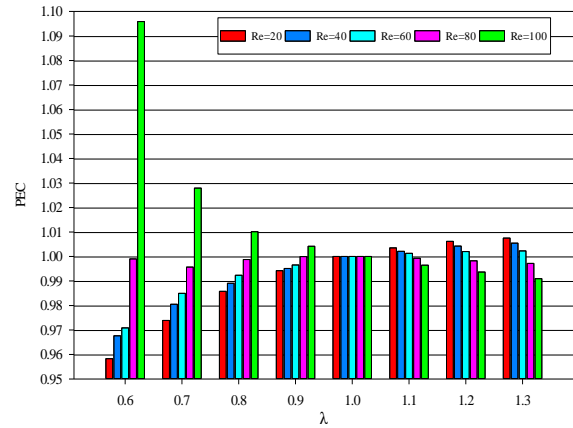


**Figure 12.** Variations of the PEC versus  $\lambda$  for different Re

**7. 4. Effect of  $H_{ch}$  and  $W_{ch}$  on Heat Transfer and Pressure Drop**

In this section, variations of the Nu and  $\Delta p$  at various  $H_{ch}$  and  $W_{ch}$  for Re=20 and 100 were studied. Before presenting the results and analyzing them, it is notable that: according to that the results are presented for a constant Re, according to the definition of Re in Equation (9) and ratio of mass flow rate in Equation (12), with variation of  $H_{ch}$  and  $W_{ch}$ , mass flow rate changes so that the Re remains constant.

$$\dot{m}_{ch_2} / \dot{m}_{ch_1} = \frac{A_{ch_2} D_{h1}}{A_{ch_1} D_{h2}} \tag{12}$$

Figures 13 and 14 show variations of Nu and  $\Delta p$  versus  $H_{ch}$  for different values of  $W_{ch}$  for Re=20 and Re=100, respectively. The following can be seen from Figures 13 and 14:

By increasing the  $H_{ch}$ , the Nu increases at first and decreases slightly at the end. The effect of  $W_{ch}$  is more evident in larger values of  $H_{ch}$ . As the  $H_{ch}$  increases, the effect of  $W_{ch}$  on the Nu becomes more evident.

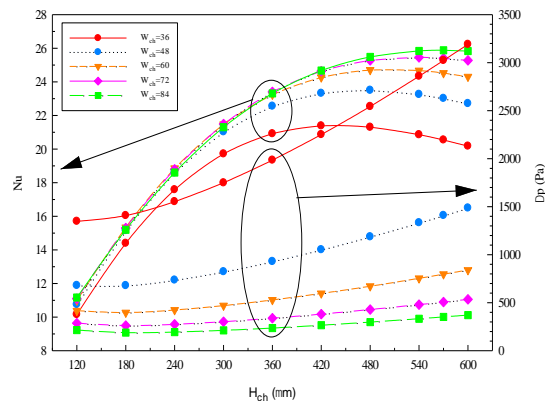


**Figure 13.** Variations of the Nu and  $\Delta p$  versus  $H_{ch}$  for different  $W_{ch}$  for Re=20

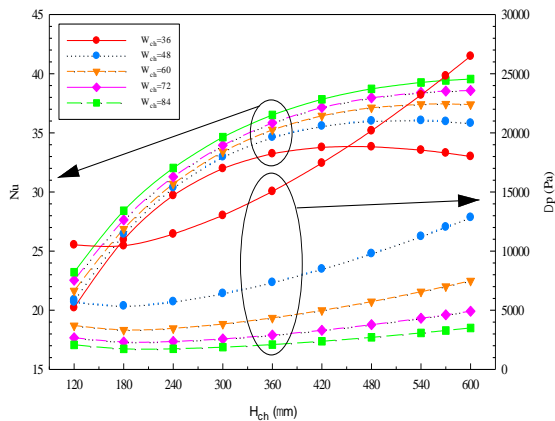


**Figure 14.** Variations of the Nu and  $\Delta p$  versus  $H_{ch}$  for different  $W_{ch}$  for  $Re=100$

Also, as the  $W_{ch}$  increases, the  $Nu_{max}$  is obtained at a greater  $H_{ch}$ . Table 1 shows  $Nu_{max}$  and corresponding  $H_{ch}$ , for which  $Nu_{max}$  is obtained for various  $W_{ch}$  at  $Re=20$  and  $Re=100$ . As can be seen, by increasing  $Re$ , the  $Nu_{max}$  is received at a higher  $H_{ch}$ . According to Figure 13, for  $W_{ch}=48\mu m$  to  $W_{ch}=84\mu m$ , as the  $H_{ch}$  increases,  $\Delta p$  first decreases slightly and then increases, so that at higher  $H_{ch}$  and lower  $W_{ch}$ , a more severe pressure drop is observed.

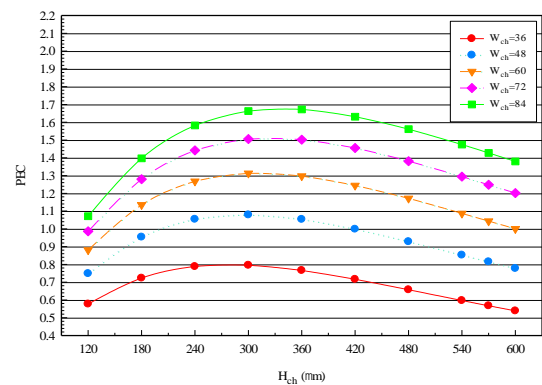
**TABLE 1.**  $Nu_{max}$  for various  $W_{ch}$  at  $Re=20$  and  $Re=100$

$W_{ch}(\mu m)$	Re	$Nu_{max}$	$H_{ch}(\mu m)$
36	20	21.38	420
	100	33.83	480
48	20	23.51	480
	100	36.06	540
60	20	24.71	480
	100	37.45	570
72	20	25.46	540
	100	38.59	600
84	20	25.89	570
	100	39.55	600

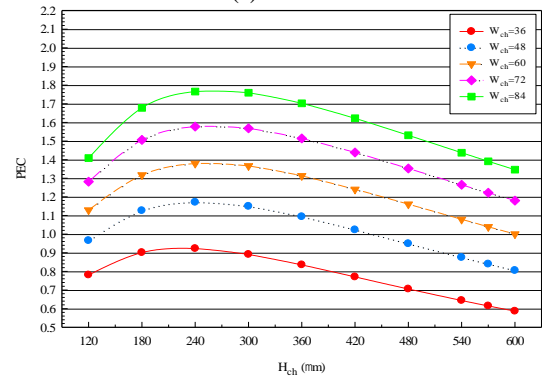
But for  $W_{ch}=36\mu m$ , an increasing trend is observed from the beginning to the end. The same trend is observed for Figure 14, with the difference that, firstly, for all values of the  $W_{ch}$ , the  $\Delta p$  first decreases slightly and then increases, and secondly, the  $\Delta p$  values are higher than  $Re=20$ .

**7. 5. Effect of Channel Height and Channel width on PEC**

Figure 15 shows variations of PEC with respect to  $H_{ch}$  for various  $W_{ch}$  at  $Re=20$  and  $Re=100$ . Table 2 shows  $PEC_{max}$  and corresponding  $H_{ch}$  for various  $W_{ch}$  and  $Re$ . According to Figure 15, for all  $Re$ , by increasing  $H_{ch}$ , PEC increases at first and then decreases. By



(a)  $Re=20$



(b)  $Re=100$

**Figure 15.** PEC for different values of  $H_{ch}$  and  $W_{ch}$  for (a)  $Re=20$  and (b)  $Re=100$

**TABLE 2.** Maximum PEC and corresponding  $H_{ch}$  for various  $W_{ch}$  and  $Re$

$W_{ch}(\mu m)$	PEC				
	Re=20	Re=40	Re=60	Re=80	Re=100
36	0.795 at $H_{ch}=300$	0.867 at $H_{ch}=240$	0.896 at $H_{ch}=240$	0.915 at $H_{ch}=240$	0.922 at $H_{ch}=240$
48	1.078 at $H_{ch}=300$	1.118 at $H_{ch}=300$	1.136 at $H_{ch}=240$	1.160 at $H_{ch}=240$	1.171 at $H_{ch}=240$
60	1.313 at $H_{ch}=300$	1.328 at $H_{ch}=300$	1.342 at $H_{ch}=300$	1.358 at $H_{ch}=240$	1.379 at $H_{ch}=240$
72	1.505 at $H_{ch}=300$	1.504 at $H_{ch}=300$	1.520 at $H_{ch}=300$	1.541 at $H_{ch}=300$	1.578 at $H_{ch}=240$
84	1.672 at $H_{ch}=360$	1.650 at $H_{ch}=300$	1.671 at $H_{ch}=300$	1.705 at $H_{ch}=300$	1.765 at $H_{ch}=240$

comparing the PEC for  $Re=20$  and  $100$ , it is observed PEC is increased with  $W_{ch}$ ; this increase is more for middle  $H_{ch}$  (PEC<sub>max</sub> is occurred between  $H_{ch}=240\mu m$  and  $H_{ch}=300\mu m$ ).

Similar trend for above parameter were reported by previous researchers [8-10]. But study on the PEC was rarely considered in the previous investigations. Based on the obtained results, one can say current investigation is more applicable than previous reported investigation.

## 8. CONCLUSION

The effect of  $\lambda$ ,  $H_{ch}$ , and  $W_{ch}$  at  $Re=20$  to  $100$  on the heat transfer and flow field characteristics including  $Nu$ ,  $\Delta p$ , and PEC for laminar flow regime of water in the MMHS have been simulated numerically. The results showed that:

- As the  $Re$  increases, the thermal and hydrodynamic boundary layer thickness is reduced, and therefore, the heat transfer rate is increased.
- For  $H_{ch}=600\mu m$ ,  $W_{ch}=60\mu m$ ,  $W_f=60\mu m$  and  $\lambda=0.6$ , by increasing the  $Re$  from  $20$  to  $100$ , the maximum temperature of the microchannel floor is reduced from  $311.3K$  to  $306.3K$ .
- For  $H_{ch}=600\mu m$ ,  $W_{ch}=60\mu m$ ,  $W_f=60\mu m$  and  $Re=100$ , by decreasing  $\lambda$  from  $1$  to  $0.6$ , the maximum temperature of the microchannel floor is reduced from  $307.8K$  to  $306.3K$ .
- By increasing in  $\lambda$ , the amount of  $Nu$  and  $\Delta p$  is reduced.
- For low  $Re$ , it is better to choose a  $\lambda>1$  and for high  $Re$ , choose a  $\lambda<1$ . The highest PEC is for  $Re=100$  and  $\lambda=0.6$  (PEC = 1.095).
- By increasing  $Re$ , the  $Nu_{max}$  is occurred at higher  $H_{ch}$  (for example at  $W_{ch}=84\mu m$ ,  $Nu_{max}=25.89$  for  $H_{ch}=570\mu m$  &  $Re=20$ , and  $Nu_{max}=39.55$  for  $H_{ch}=600\mu m$  &  $Re=100$ ).
- At the highest  $H_{ch}$  and the least  $W_{ch}$ , the highest  $\Delta p$  is observed ( $\Delta p = 2700Pa$  at  $H_{ch}=600\mu m$  &  $W_{ch}=36\mu m$ ).
- By increasing  $W_{ch}$ , PEC increases. PEC<sub>max</sub> is occurred at middle  $H_{ch}$ ; between  $H_{ch}=240\mu m$  and  $H_{ch}=300\mu m$ .

To complete this work and in the future simulations, the authors intend to consider the micro-scale phenomena such as charge accumulation or slip effect near the walls. Also, investigation about the effect of using hybrid nanofluids as a cooling fluid to improve the cooling in this system is of interest to the authors.

## 9. REFERENCES

1. Bailina, F., Pei, Z., Ganghan, H., YanJun, W., "Research on Properties of Fluid Pressure Drop for Electric Vehicle IGPT Pin

- Fin Heat Sink", *International Journal of Engineering, Transactions A: Basics*, Vol. 28, No. 4, (2015), 627-633. DOI: 10.5829/idosi.ije.2015.28.04a.18.
2. Sarabandi, A. H., Jabari Moghadam, A., "Slip Velocity in Flow and Heat Transfer of Non-newtonian Fluids in Microchannels", *International Journal of Engineering, Transactions A: Basics*, Vol. 30, No. 7, (2017), 1054-1065. DOI: 10.5829/ije.2017.30.07a.15.
3. Safikhani, H., Shaabani, H., "Numerical Simulation of Frost Formation in Interrupted Micro Channel Heat Sinks Considering Microfluidic Effects in Slip Regime", *International Journal of Engineering, Transactions C: Aspects*, Vol. 33, No. 12, (2020), 2556-2562. DOI: 10.5829/ije.2020.33.12c.17
4. Tan, H., Wu L., Wang, M., Yang Z., Du, P., Heat transfer improvement in microchannel heat sink by topology design and optimization for high heat flux chip cooling, *International Journal of Heat and Mass Transfer*, Vol. 129, (2019). <https://doi.org/10.1016/j.ijheatmasstransfer.2018.09.092>
5. Adeyemi, T.S., Rufus, D.O., "Analytical Development of an Improved Inflow Performance Relationship (IPR) Model for Solution Gas Drive Reservoirs," *Journal of Human, Earth and Future*, Vol. 2, No. 2, (2021). Doi: 10.28991/HEF-2021-02-02-04.
6. Kapeller, H., Dvorak, D., Šimić, D., "Improvement and Investigation of the Requirements for Electric Vehicles by the use of HVAC Modeling," *HighTech and Innovation Journal*, Vol. 2, No. 1, (2021). Doi: 10.28991/HIJ-2021-02-01-07
7. Kermani, E., "Manifold micro-channel cooling of photovoltaic cells for high efficiency solar energy conversion", M.S. Thesis, University of Maryland, (2008).
8. Escher, W., Michel, B., Poulikakos, D., "A novel high performance ultra-thin heat sink for electronics, *International Journal of Heat and Fluid Flow*, Vol. 31, (2010), 586-598. <https://doi.org/10.1016/j.ijheatfluidflow.2010.03.001>.
9. Cetegen, E., "Force Fed Microchannel High Heat Flux Cooling Utilizing Microgrooved Surface", Dissertation submitted to the Faculty of the Graduate School of the University of Maryland, College Park, in partial fulfillment of the requirements for the degree of Doctor of Philosophy, (2010).
10. Kasten, P., Zimmermann, S., Tiwari, M.K., Michel, B., Poulikakos, D., "Hot water-cooled heat sinks for efficient data center cooling: towards electronic cooling with high exergetic utility", *Frontiers in Heat and Mass Transfer*, Vol. 1, (2010). <http://dx.doi.org/10.5098/hmt.v1.2.3006>.
11. Boteler, L., Jankowski, N., McCluskey, P., Morgan, B., "Numerical investigation and sensitivity analysis of manifold microchannel coolers", *International Journal of Heat and Mass Transfer*, Vol. 55, (2012) 7698-7708. <https://doi.org/10.1016/j.ijheatmasstransfer.2012.07.073>.
12. Husain, A., Kim, K.Y., "Design Optimization of Manifold Microchannel Heat Sink Through Evolutionary Algorithm Coupled with Surrogate Model", *IEEE Transactions on Components, Packaging and Manufacturing Technology*, Vol. 3, (2013), 617-624. <https://doi.org/10.1109/95.588554>.
13. Sarangi, S., Bodla, K.K., Garimella, S.V., Murthy, J.Y., "Manifold microchannel heat sink design using optimization under uncertainty", *International Journal of Heat and Mass Transfer*, Vol. 69, (2014), 92-105. <https://doi.org/10.1016/j.ijheatmasstransfer.2013.09.067>.
14. Arie, M.A., Shoostari, A.H., Dessiatoun, S.V., Ohadi, M.M., "Thermal optimization of an air-cooling heat exchanger utilizing manifold-microchannels", Fourteenth Intersociety Conference on Thermal and Thermomechanical Phenomena in Electronic Systems (ITherm), (2014), 807-815. <https://doi.org/10.1109/ITHERM.2014.6892364>

15. Arie, M.A., Shooshtari, A.H., Dessiatoun, S.V., Al-Hajri, E., Ohadi, M.M., "Numerical Modeling and Thermal Optimization of a Single-phase Flow Manifold-Microchannel Plate Heat Exchanger", *International Journal of Heat and Mass Transfer*, Vol. 81 (2015), 478-489. <https://doi.org/10.1016/j.ijheatmasstransfer.2014.10.022>.
16. Yue, Y., Mohammadian, S.K., Zhang, Y., "Analysis of performances of a manifold microchannel heat sink with nanofluids", *International Journal of Thermal Sciences*. Vol. 89, (2015), 305-313. <https://doi.org/10.1016/j.ijthermalsci.2014.11.016>.
17. Andhare, R.S., Shooshtari, A.H., Dessiatoun, S.V., Ohadi, M.M., "Heat Transfer and Pressure Drop Characteristics of a Flat Plate Manifold Microchannel Heat Exchanger in Counter Flow Configuration", *Applied Thermal Engineering*. Vol. 96, (2016), 178-189. <https://doi.org/10.1016/j.applthermaleng.2015.10.133>.
18. Li, S.N., Zhang, H.N., Li, X.B., Li, Q., Li, F.C., Sang, S. Q., Joo, W., "Numerical study on the heat transfer performance of non-Newtonian fluid flow in a manifold microchannel heat sink", *Applied Thermal Engineering*, Vol. 115, (2017), 1213-1225. <https://doi.org/10.1016/j.applthermaleng.2016.10.047>.
19. Arie, M.A., Shooshtari, A.H., Rao, V.V., Dessiatoun, S.V., Ohadi, M.M., "Air-Side Heat Transfer Enhancement Utilizing Design Optimization and an Additiv Manufacturing Technique", *ASME, Journal of Heat Transfer*, Vol. 139, (2017). <https://doi.org/10.1115/1.4035068>.
20. Drummond, K.P., Back, D., Sinanis, M.D., Janes, D.B., Peroulis, D., Weibel, J.A., Garimella, S.V., "A Hierarchical Manifold Microchannel Heat Sink Array for High-Heat-Flux Two-Phase Cooling of Electronics", *International Journal of Heat and Mass Transfer*, Vol. 117, (2018), 319-330. <https://doi.org/10.1016/j.ijheatmasstransfer.2017.10.015>.
21. Ju, X., Xu, C., Zhou, Y., Liao, Z., Yang, Y., "Numerical investigation of a novel manifold micro-pin-fin heat sink combining chessboard nozzle-jet concept for ultra-high heat flux removal", *International Journal of Heat and Mass Transfer*, Vol. 126, (2018), 1206-1218. <https://doi.org/10.1016/j.ijheatmasstransfer.2018.06.059>.
22. Zhang, H., Li, S., Cheng, J., Zheng, Z., Li, X., Li, F., "Numerical study on the pulsating effect on heat transfer performance of pseudoplastic fluid flow in a manifold microchannel heat sink", *Applied Thermal Engineering*. Vol. 129, (2018), 1092-1105. <https://doi.org/10.1016/j.applthermaleng.2017.10.124>.
23. Jung, K.W., Kharangate, C.R., Lee, H., Palko, J., Zhou, F., Asheghi M., Dede, E.M., Goodson, K.E., "Embedded cooling with 3D manifold for vehicle power electronics application: Single-phase thermal-fluid performance", *International Journal of Heat and Mass Transfer*, Vol. 130 (2019), 1108-1119. <https://doi.org/10.1016/j.ijheatmasstransfer.2018.10.108>.
24. Tiwari, R., Andhare, R.S., Shooshtari, A., Ohadi, M.M., "Development of an Additive Manufacturing-Enabled Compact Manifold Microchannel Heat Exchanger", *Applied Thermal Engineering*. Vol. 147, (2019), 781-788. <https://doi.org/10.1016/j.applthermaleng.2018.10.122>.
25. Luo, Y., Li, J., Zhou, K., Zhang, J., Lia, W., "A numerical study of subcooled flow boiling in a manifold microchannel heat sink with varying inlet-to-outlet width ratio", *International Journal of Heat and Mass Transfer*, Vol. 139, (2019), 554-563. <https://doi.org/10.1016/j.ijheatmasstransfer.2019.05.030>.
26. Yang, M., Cao, B.Y., "Numerical study on flow and heat transfer of a hybrid microchannel cooling scheme using manifold arrangement and secondary channels", *Applied Thermal Engineering*. Vol. 159, (2019). <https://doi.org/10.1016/j.applthermaleng.2019.113896>.
27. Drummond, K.P., Weibel, J.A., Garimella, S.V., "Two-phase flow morphology and local wall temperatures in high-aspect-ratio manifold microchannels", *International Journal of Heat and Mass Transfer*, Vol. 153, (2020). <https://doi.org/10.1016/j.ijheatmasstransfer.2020.119551>.
28. Luo, Y., Zhang, J., Li, W., "A comparative numerical study on two-phase boiling fluid flow and heat transfer in the microchannel heat sink with different manifold arrangements", *International Journal of Heat and Mass Transfer*, Vol. 156, (2020). <https://doi.org/10.1016/j.ijheatmasstransfer.2020.119864>.
29. Yang, M., Li, M.T., Hua, Y.C., Wang, W., Cao, B.Y., "Experimental study on single-phase hybrid microchannel cooling using HFE-7100 for liquid-cooled chips", *International Journal of Heat and Mass Transfer*, Vol. 160, (2020). <https://doi.org/10.1016/j.ijheatmasstransfer.2020.120230>.
30. Luo, Y., Li, W., Zhang, J., Minkowycz, W.J., "Analysis of thermal performance and pressure loss of subcooled flow boiling in manifold microchannel heat sink", *International Journal of Heat and Mass Transfer*, Vol. 162, (2020). <https://doi.org/10.1016/j.ijheatmasstransfer.2020.120362>.
31. Bergman, T.L., Avine, A.S., Incropera, F.P., Dewitt, D.P., *Fundamentals of Heat and Mass Transfer*, Seventh ed., John Wiley & Sons, Hoboken, 2011.
32. Glassbrenner, C.J., Slack, G.A., "Thermal Conductivity of Silicon and Germanium from 3K to the Melting Point", *Physical Review*. Vol. 134, (1964), 1058-1069. <https://doi.org/10.1103/PhysRev.134.A1058>.
33. Ghorbani, M., Salimpour, M.R., Vafai, K., "Microchannel thermal performance optimization utilizing porous layer configurations", *International Journal of Heat and Mass Transfer*, Vol. 133, (2019), 62-72. <https://doi.org/10.1016/j.ijheatmasstransfer.2018.12.063>.

---

### Persian Abstract

#### چکیده

در این تحقیق، انتقال حرارت و رفتار جریان سیال در حالت آرام و برای سیال آب در یک چاه حرارتی میکروکانال منیقولدی بطور عددی شبیه‌سازی شده است. برای اطمینان از صحت روش عددی، نتایج با اطلاعات تجربی موجود مقایسه شده است. در شبیه‌سازی جریان سیال و انتقال حرارت، خواص ترموفیزیکی سیال آب و سیلیکون متغیر (وابسته به دما) در نظر گرفته شده است. تاثیر نسبت طول ورودی به خروجی جریان، ارتفاع میکروکانال و پهنای میکروکانال به عنوان پارامترهای مستقل در اعداد رینولدز ۲۰ تا ۱۰۰ بر جریان سیال و انتقال حرارت بررسی شده است. نتایج نشان داد که در چاه حرارتی میکروکانال منیقولدی، جت برخوردی بر سطح پایین کانال، رشد لایه مرزی هیدرودینامیکی و حرارتی را محدود می‌کند و در نتیجه نرخ انتقال حرارت افزایش می‌یابد. همچنین با افزایش عدد رینولدز و ثابت نگه داشتن ابعاد هندسی، نرخ انتقال حرارت افزایش می‌یابد. بر اساس نتایج حاضر، برای اعداد رینولدز کوچک، بهتر است  $\lambda > 1$  و برای اعداد رینولدز بزرگ  $\lambda < 1$  انتخاب شود. در محدوده مطالعه، برای اعداد رینولدز کوچک، ماکزیمم معیار ارزیابی عملکرد ( $PEC_{max}$ ) در  $H_{ch}=300\mu m$  بدست می‌آید و برای اعداد رینولدز بزرگ در  $H_{ch}=240\mu m$  بدست می‌آید. برای اعداد رینولدز ۲۰ تا ۱۰۰، ماکزیمم معیار ارزیابی عملکرد برابر با ۱.۷۶۵ و در  $Re=100$  و  $H_{ch}=240\mu m$  بدست می‌آید.

---



## Use of Random Vortex Method in Simulating Non-Newtonian Fluid Flow in a T-junction for Various Reynolds Numbers and Power-law Indexes

Y. Noori<sup>a</sup>, A. R. Teymourtash<sup>\*a</sup>, B. Zafarmand<sup>b</sup>

<sup>a</sup> Department of Mechanical Engineering, Faculty of Engineering, Ferdowsi University of Mashhad, Mashhad, Iran

<sup>b</sup> Department of Mechanical Engineering and Power Plant, Khorasan Water and Power Industry Higher Educational and Research Complex, Mashhad, Iran

### PAPER INFO

#### Paper history:

Received 08 January 2022

Received in revised form 09 February 2022

Accepted 09 February 2022

#### Keywords:

Random Vortex Method

Non-Newtonian

power-law Fluid

T-junction

Navier-Stokes Equations

Schwarz-christoffel Conformal Mapping

### ABSTRACT

Past studies show that until now the Random Vortex Method (RVM) has only been used to solve the flow of Newtonian fluids. In this paper, by presenting a new approach, the RVM is developed for the first time with the aim of simulating the flow of non-Newtonian fluids. For this purpose, a numerical simulation of two-dimensional flow of non-Newtonian power-law fluid in a T-junction is presented. The simulation is conducted for  $Re = 50-200$  at the inlet of the channel and different power-law indexes ( $n = 0.2-1.4$ ). The RVM solves the Navier–Stokes equations as a function of time and determines the velocity at any point of the channel directly and without determining a mesh on the geometry. Potential velocity, an initial condition for the flow analysis by the RVM, is obtained using the Schwarz–Christoffel conformal mapping. The effect of two parameters of power-law index and Reynolds number on the recirculation zone has been investigated. Acceptable agreement among the results of the present study and the existing numerical and experimental results shows the capability of the proposed method, according to which the RVM can be considered a powerful promising method in simulating the non-Newtonian fluids in laminar and turbulent flow regimes.

doi: 10.5829/ije.2022.35.05b.11

### NOMENCLATURE

$U$	inlet velocity of the channel (m/s)	$b$	heterogeneous source term in the vorticity equation
$H$	inlet height of the channel (m)	$Gr(x,t)$	Green function
$n$	power-Law index	$\Delta t$	time step (s)
$m$	power-Law consistency index	$Re$	Reynolds number at the inlet section of the channel
$Q_1$	inlet flow rate of the channel (m <sup>3</sup> /s)	$Re_r$	local Reynolds number
$Q_2$	outlet flow rate from the longitudinal branch (m <sup>3</sup> /s)	$u_x$	velocity profile in x direction (m/s)
$Q_3$	outlet flow rate from the lateral branch (m <sup>3</sup> /s)	$u_{ave}$	average velocity (m/s)
$z$	complex number on z-plane	$L_r$	recirculation length (m)
$t$	complex number on t-plane	<b>Greek Symbols</b>	
$\bar{t}$	conjugate of $t$	$\nabla$	Del operator
$dt/dz$	Schwarz-Christoffel transfer function	$\mu$	dynamic viscosity (pa.s)
$N$	total number of vortexes	$\omega^*$	dimensionless vorticity in normal direction to the x-y plane
$F(t_j)$	Schwarz-Christoffel transfer function	$\rho$	fluid density (kg/m <sup>3</sup> )
$\bar{w}(z_j)$	induced velocity equation on the vortex $j$	$\sigma$	standard deviation of Gaussian distribution
$t^*$	dimensionless time	$\dot{\gamma}$	shear rate (s <sup>-1</sup> )
$V^*$	dimensionless velocity vector	$\dot{\gamma}^*$	dimensionless shear rate
$x^*$	x-dimensionless coordinates	$\mu_a$	apparent viscosity (pa.s)
$y^*$	y-dimensionless coordinates	$\omega$	vorticity in normal direction to the x-y plane (s <sup>-1</sup> )
$u^*$	dimensionless velocity in x direction	<b>Superscript</b>	
$v^*$	dimensionless velocity in y direction	$*$	dimensional variable

\*Corresponding Author Institutional Email: teymourtash@um.ac.ir (A. R. Teymourtash)

## 1. INTRODUCTION

One of the most promising and accurate methods for studying the viscous flow in the laminar and turbulent regimes, is the Random Vortex Method (RVM). So far, all studies performed with this method are limited to Newtonian fluids. However, the behavior of most real fluids used in the food, petroleum and petrochemical industries, such as solutions and molten polymers, industrial oils, as well as materials that have viscous and elastic properties (viscoelastic) is considered non-Newtonian, and because of its wide application in industry, it is a topic that is always discussed and various methods are used to study and simulate such process.

Numerous methods for studying and modeling non-Newtonian fluid flow have been discovered and identified. Each has proven its strengths and weaknesses through repeated research. But, what is certain is that the discovery and appearance of an accurate method to simulate fluid flow has always been of interest. For this reason, this paper develops the RVM in order to simulate the flow of non-Newtonian fluids by introducing a new approach for the first time. For this purpose, the non-Newtonian power-law fluid in a T-junction is simulated using RVM.

The T-junctions are often used as phase separators for raw materials (liquid-gas) in industrial applications such as refrigeration system, advanced thermodynamic cycle, nuclear reactors, petroleum exploitation pipelines and so on [1]. More applications of T-junction have been mentioned in the research of Yang et al. [1]. The junctions (T or Y) are commonly located in such a way that the inlet two-phase flow to the branch is unequal separated between the side and main branches, and puts the gas-rich flow in the side branch and the liquid-rich flow in the main branch.

In the RVM, a limited number of vortexes are generated and are followed in the form of a numerical algorithm using the Lagrangian perspective. To solve the unsteady flow, each time step is divided into two half steps. In the first half step, the effects of the viscosity are neglected and this time step is passed by the convection mechanism. In the second half step, the viscosity effects are influenced by the random movement of the vortex bubbles generated by the diffusion mechanism.

RVM is employed to solve the two-dimensional equations of motion and the time function of incompressible fluids in laminar and turbulent flows. The method is based on solving the time-dependent vorticity equation, which is obtained from the effect of the Curl operator on the Navier-Stokes equations and its integration with the continuity equation.

The condition of no-slip on the wall at any point in time is the boundary condition for solving the fluid flow equations. In the RVM, to reduce the wall velocity

tangential component to zero, a number of definite constant rotational vortexes are produced and their movements are generated due to both mechanisms of convection, diffusion and Lagrangian perspective accordingly. The motion of each vortex stems from the potential velocity of the fluid in addition to the total instantaneous velocities induced by the other vortexes and their images at the center of the intended vortex. Similarly, the instantaneous velocity at any point in the field is obtained using the instantaneous velocities induced by the vortexes, their images, and the velocity of the potential velocity passing through that point.

The RVM was first introduced by Alexandre Chorin who proposed a model for turbulent flow around a cylinder in 1973 [2]. He modified this method in 1978 to import the boundary conditions to the calculations for the boundary layer analysis, and named it the Random Vortex Method [3]. Thereafter, RVM became known as a numerical method for solving the flow field.

Gagnon and Giovannini [4] were other people who did their research using the RVM. In this study numerical simulation and physical analysis of high Reynolds number recirculating flows behind sudden expansions have been investigated.

Many researchers have recently done their investigation using RVM, some of which are mentioned here. Noori and Zafarmand [5] simulated the laminar and turbulent flow inside some divergent channels and investigated the effects of the divergence angle and Reynolds number on the reverse flow inside the channel using RVM. In this study, the flow inside divergent channels with different angles and Reynolds numbers was investigated; while, instantaneous and average velocities being calculated. A demonstration of the production of vortexes and their distribution was presented. The movement of the produced vortexes instantly and at different times was well depicted. In addition to the above results in this study, the effect of divergence angle and Reynolds number on flow separation within divergent channels was investigated and the results are presented in a useful graph.

Zafarmand et al. [6] studied the turbulent flow in a channel using the vortex blob method. They obtained and discussed the physical concepts of turbulence and entropy generation. At first, time-averaged velocities and then their fluctuations were calculated. It was observed that turbulence structures occupy different positions and move with convection velocity. To verify the second law of thermodynamics, averaged vorticity and its fluctuations as well as averaged entropy and its fluctuations were calculated. In this research, for the first time, the turbulence structures were visualized and presented by employing the vector of velocity fluctuations, vorticity and entropy generation fluctuations.

Zafarmand and Ghadirzad [7] studied high Reynolds viscous flow simulation past a cylinder as well as an elliptical airfoil by random vortex blob. In both cases, the obtained mean time velocities were compared with available numerical and experimental results. Having known the velocity field, by employing momentum balance, the drag and lift coefficients caused by flow past the elliptical airfoil with different diameter ratios were calculated.

Tadayoni-Navaei and Zafarmand [8] used the RVM for geometries with the unsolvable Schwarz-Christoffel formula. In this paper, the Schwarz-Christoffel mapping function for a square cavity is numerically obtained. Then, the instantaneous and the average velocity fields were calculated inside the cavity using the RVM. The advantage of this modeling is that for calculation of velocity at any point of the geometry. There is no need to use meshing in the entire flow field and the velocity in a special point can be obtained directly; also, no need to the other points.

Jin et al. [9] suggested a circle theorem technique to handle 2-D flows around arbitrary cylinders in discrete vortex method. In this work, a novel boundary method is proposed based on the circle theorem technique. Under this algorithm, the identical vortices were introduced outside the body to counteract the lost strengths of vortices through the use of the circle theorem and surface curvature. A series of numerical simulations of flow over various cross-sectional bodies at high Reynolds numbers were performed to validate the accuracies in predicting the hydrodynamic loads, including flow past elliptic, foil, square, and triangular cylinders.

Mimeau et al. [10] compared the semi-Lagrangian Vortex Method (VM) and Lattice Boltzmann Method (LBM) for incompressible flows. In this study, a proven version of each method was used and compared on different three dimensional benchmarks in terms of numerical accuracy, convergence, numerical diffusion and dissipation. It was shown that both methods converge to the same solution but in a different way. The VM performs better than the LBM for the lowest resolution whereas LBM appears to be more accurate for the growing resolutions.

Qian and Yao [11] studied the McKean–Vlasov type stochastic differential equations (SDEs) arising from the random vortex method, which arise from the random vortex dynamics and other physics models. By introducing a new approach, they resolved the existence and uniqueness of both the weak and strong solutions for the McKean–Vlasov stochastic differential equations whose coefficients are defined in terms of singular integral kernels such as the Biot–Savart kernel.

Extensive studies have been performed on T-junctions as well as non-Newtonian fluids. Hayes et al. [12] studied the flow specification of a Newtonian fluid in a two-dimensional, planar, right angled Tee branch by

solving the Navier-Stokes equations. In this work the effects of the branch length and the grid size on the interior flow field were examined to assess the accuracy of the solutions. They concluded that the length of the side branch has very little influence on the interior flow field, particularly at higher Reynolds number.

Khandelwal et al. [13] studied the treatment of power-law fluid in a T-channel in the laminar regime. The two-dimensional numerical calculations have been done using Ansys Fluent. In this paper the parameters such as wake length, critical Reynolds number and the variation of viscosity were calculated by using constant density and non-Newtonian power-law viscosity model. The results showed that for a particular power-law index ( $n$ ), length of recirculation zone increases in the side branch with increasing  $Re$ . Also, it increases with decreasing  $n$  for the fixed  $Re$ . The critical Reynolds number decreases with decreasing  $n$ .

Brandi et al. [14] carried out research using the Direct Numerical Simulation (DNS) and Linear Stability Theory (LST) analysis on an Oldroyd-B fluid flowing between two parallel plates. In this paper, the laminar-turbulent transition was studied and the convection of Tollmien–Schlichting waves was investigated for the incompressible, two-dimensional flow between two parallel plates. The viscoelastic fluid adopted was modeled by the Oldroyd-B constitutive equation. DNS and LST were used to verify the stability of the viscoelastic fluid flow to unsteady disturbances.

Zhou et al. [15] examined the dynamics and interfacial evolution for bubble breakup in shear-thinning, non-Newtonian fluids in a microfluidic T-junction. The result showed that the length of the bubble tip is linearly stretched with time, and the elongation rate increases with the concentration of CMC solution. Also, the rheological property of the CMC solution could significantly affect the bubble breakup process in the microfluidic T-junction.

Kwak and Nam [16] presented a simple factor for the vortex formation in power-law fluids flowing inside a channel. Their research explored the feasibility of applying the flow reversal condition on the Couette–Poiseuille (C–P) power-law fluid to predict the vortex generation.

Luo et al. [17] presented the results of mixing the non-Newtonian inelastic fluids in a turbulent patch of T-junction. Results were obtained based on a Direct Numerical Simulation (DNS) of a turbulent flow in a converging T-junction for both Newtonian (water) and non-Newtonian inelastic fluid (dilute Xanthan Gum solution). Based on experimental data, the Bird-Carreau law was used to capture the inelastic shear thinning property of the solution and passive scalar was introduced in the transverse branch to investigate the mixing in such configuration.

Yang et al. [18] carried out an experimental investigation to compare the phase separation performance between the single and double branching T-junctions. The experimental data were compared with the predicted values produced by theoretical models based on water-air mixture, and they found out that there is no suitable model for the refrigerants. It was concluded that the inlet mass flux has little influence on phase separation while the phase separation efficiency drops sharply with the increase of inlet quality.

Rostami and Morini [19] experimentally studied the production of the Newtonian droplets with non-Newtonian and Newtonian bearer flows inside the micro T-junctions. In this paper the generation of Newtonian microdroplets in both Newtonian and non-Newtonian carrier fluids through a commercial micro T-junction under an opposed-flow configuration was analyzed experimentally.

Moghimi et al. [20] examined the effect of non-uniform magnetic field on non-Newtonian fluid separation in a diffuser. The purpose of this study is to investigate the boundary layer separation point in a magnetohydrodynamics diffuser. As an innovation, the  $Re$  value on the separation point is determined for the non-Newtonian fluid flow under the influence of the non-uniform magnetic field due to an electrical solenoid, in an empirical case. The impact of the magnetic field intensity on the separation point analyzed from the physical point of view. It was observed the wall shear stress increases by increasing magnetic field intensity that leads to delaying the boundary layer separation.

Maurya et al. [21] examined the combined effects of the power-law rheology and isothermal rotating cylinder on the characteristics of the power-law fluid flow inside the T-junctions. The range of parameters considered in this work is as: Reynolds number,  $1 < Re \leq 50$ , power-law index,  $0.2 \leq n \leq 1$ , Prandtl number,  $10 \leq Pr \leq 100$  and non-dimensional circumferential velocity of the cylinder,  $-5 \leq \alpha \leq 5$ . Results suggest that the rotating cylinder can be used as a technique to create and/or reduce the formation of momentum and thermal boundary layers in the flow domain.

Motahar [22] estimated non-Newtonian behavior of nanofluid phase change material containing mesoporous silica particles using a neural network approach. In this paper, the rheological properties of nanofluid phase change material containing mesoporous silica nanoparticles are predicted by the artificial neural networks (ANNs) method based on the experimental database reported in literature. The results showed that the developed ANN has a very low mean squared error for the training and test dataset. Also, the predicted dynamic viscosity and shear stress also have the maximum relative error of 6.26 and 0.418%, respectively.

Vatani and Domiri-Ganji [23] experimentally studied the patterns of the two-phase flow (gas-liquid) inside a rectangular channel with  $90^\circ$  bend. The aim of this study was to analyze the behavior of two-phase flow in an inclined rectangular channel with  $90^\circ$  bend for various vertical lengths. The fluids used in this study were air and water. In this study, the effects of vertical length on flow regimes and pattern transition borders are examined. According to the flow visualization, no vortex was observed in the vertical section. The results showed that the flow regime in the vertical section is churn flow regime. Finally, it can be seen that the flow pattern structures are not greatly affected by changing the vertical length.

In the continuation, this research uses the RVM to simulate the non-Newtonian fluid flow following a new approach for the first time. The target of this research is to develop the RVM in the non-Newtonian fluids simulation. For this purpose, the non-Newtonian power-law fluid in a T-junction is simulated using RVM for  $Re=50-200$  at the inlet of the channel and different power-law indexes ( $n=0.2-1.4$ ).

## 2. CONFIGURATION OF THE CASE GEOMETRY AND FINDING THE POTENTIAL VELOCITY

Figure 1 shows a channel with the specifications. The inlet velocity of the channel is  $U$ , and the inlet height of the channel is  $H$ .  $Q_1$ ,  $Q_2$  and  $Q_3$  are the input flow rate, the output flow rate from the longitudinal branch and the output flow rate from the lateral branch, respectively.

Since potential flow analysis for complicated geometries is a very difficult process, the mentioned geometries can be simplified using the conformal mapping. In this approach, a complicated geometry in the  $z$ -plane is transformed to a simpler geometry in the  $t$ -plane. The Schwartz-Christoffel conformal transfer is used to compute the potential velocity in internal flows. The transformation converts the channel and its inner region, which is located on the  $z$ -plane axis, into the upper half of the transfer  $t$ -plane axis.

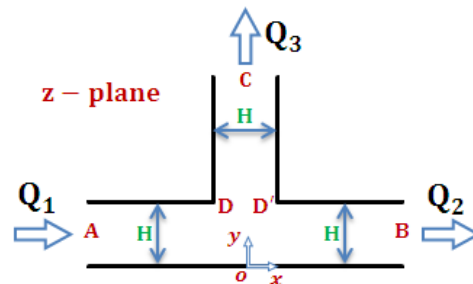


Figure 1. Configuration of channel with a T-junction

The conversion of the channel shown in Figure 1 by the Schwartz-Christofel conformal mapping to its corresponding  $t$  transfer plane is illustrated in Figure 2.

As mentioned before, to find the potential flow as an initial condition, the Schwartz-Christofel transfer function is used, which is obtained for a T-junction as shown in Equation (1) [25]:

$$\frac{dt}{dz} = \pi \frac{1-t^2}{\sqrt{5-t^2}} \tag{1}$$

According to Figure 2, the input flow to the channel is equivalent to one source and the output flows from the channel are equivalent to two sinks in the complex transfer  $t$ -plane.

### 3-THE GOVERNING EQUATIONS

The governing equation in RVM is the two-dimensional vorticity transport equation where its dimensionless form for the incompressible non-Newtonian fluid flow is derived as follows:

$$\frac{\partial \omega^*}{\partial t^*} + (V^* \cdot \nabla) \omega^* = \frac{1}{Re} \nabla^2 \omega^* + b(x, y, t) \tag{2}$$

$$b = \frac{\partial \mu}{\partial x^*} \left( \frac{\partial^2 v^*}{\partial x^{*2}} + \frac{\partial^2 v^*}{\partial y^{*2}} \right) - \frac{\partial \mu}{\partial y^*} \left( \frac{\partial^2 u^*}{\partial x^{*2}} + \frac{\partial^2 u^*}{\partial y^{*2}} \right) + \left( \frac{\partial^2 \mu}{\partial x^{*2}} - \frac{\partial^2 \mu}{\partial y^{*2}} \right) \left( \frac{\partial u^*}{\partial y^*} + \frac{\partial v^*}{\partial x^*} \right) - 2 \frac{\partial^2 \mu}{\partial y^* \partial x^*} \left( \frac{\partial u^*}{\partial x^*} - \frac{\partial v^*}{\partial y^*} \right) + \frac{\partial \mu}{\partial x^*} \frac{\partial \omega^*}{\partial x^*} + \frac{\partial \mu}{\partial y^*} \frac{\partial \omega^*}{\partial y^*} \tag{3}$$

In the above relations,  $u^*$  and  $v^*$  are the fluid velocity in  $x$  and  $y$  directions respectively,  $\mu$  is the dynamic viscosity and  $\omega^*$  is the vorticity in normal direction to the  $x$ - $y$  plane.  $b$  is the heterogeneous term of the source term in the vorticity equation, which becomes to zero ( $b=0$ ) for the Newtonian fluid. Furthermore,  $Re$  is the liquid phase Reynolds number at the inlet section of the channel which is derived for the non-Newtonian fluid flow as follows [26]:

$$Re = \frac{\rho H^n U^{2-n}}{m} \tag{4}$$

where  $\rho$  is the density of fluid,  $H$  is the inlet height of the channel,  $U$  is the inlet velocity of the channel,  $n$  is the Power-law index and  $m$  is the consistency index.

The RVM scheme is based on the vorticity transport equation solution in two steps of convection and diffusion which for non-Newtonian flow, these two steps will be as follows, respectively [4]:

$$\frac{\partial \omega^*}{\partial t^*} + V^* \cdot \nabla \omega^* = 0 \tag{5}$$

$$\frac{\partial \omega^*}{\partial t^*} = \frac{1}{Re} \nabla^2 \omega^* + b \tag{6}$$

The general solution of the vorticity transport equation is obtained by the summation of the above equations. In the RVM, the no-slip condition or zero relative velocity on the wall at any moment is considered as a boundary condition of the fluid flow equations. In order to zero the sliding velocity on the walls, a number of similar vortexes with the same circulation are generated, and are separated from the wall by the diffusion mechanism and enter the flow field. In the next step, these vortexes continue their motion by both diffusion and convection mechanisms. In addition, to eliminate the normal induced velocity by the vortexes, the vortexes image is used.

To solve the diffusion equation, the Green function is used. According to Andrei Polyanin solution [27], the Green function of Equation (6) is:

$$Gr(x, t) = \left( \frac{Re}{4\pi t} \right)^{1/2} \exp\left( -\frac{Re}{4t} x^2 \right) \tag{7}$$

According to the above relation, the derived Green functions in Newtonian and non-Newtonian fluids are similar. This means that in the non-Newtonian fluid, as in a Newtonian fluid, the diffusion mechanism can be solved using the random perpendicular motion. The motion due to the diffusion of the vortexes is as two perpendicular displacements which are the random variables with Gaussian distribution and a mean value of zero and a standard deviation of  $\sigma = \sqrt{\frac{2\Delta t}{Re}}$  ( $\Delta t$  is the time step).

As a matter of fact, term  $b$  has its effects on the standard deviation  $\sigma$ . The effect of adding  $b$  to the diffusion equation for a non-Newtonian fluid (despite the same Green functions) could be simulated by an alternative approach. According to this approach, for a non-Newtonian power-law fluid, after calculating the shear rate and apparent viscosity in each time step for any location of the vortex, the local Reynolds and its standard deviation ( $\sigma = \sqrt{\frac{2\Delta t}{Re_r}}$ ); where  $Re_r$  is the local Reynolds in

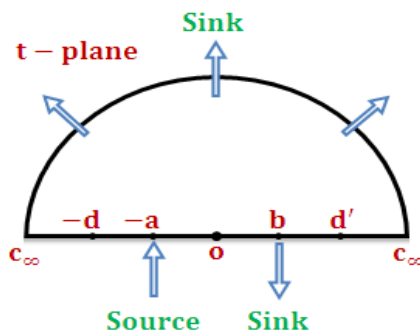


Figure 2. Transmission  $t$ -plane for the T-junction

any point of fluid, are determined for a random motion. In other words, in this approach, it is assumed that for a non-Newtonian fluid in each time step, each point of the fluid that indicates the position of a vortex has different viscosity. To determine the apparent viscosity, after finding the instantaneous velocities of  $u^*$  and  $v^*$  at any point of the geometry using the RVM, according to power-law model, the shear rate could be computed by the following relations [26]:

$$\begin{aligned} \dot{\gamma} &= \sqrt{2\left(\frac{\partial u}{\partial x}\right)^2 + 2\left(\frac{\partial v}{\partial y}\right)^2 + \left(\frac{\partial u}{\partial y} + \frac{\partial v}{\partial x}\right)^2} \\ &= \frac{U}{H} \sqrt{2\left(\frac{\partial u^*}{\partial x^*}\right)^2 + 2\left(\frac{\partial v^*}{\partial y^*}\right)^2 + \left(\frac{\partial u^*}{\partial y^*} + \frac{\partial v^*}{\partial x^*}\right)^2} = \frac{U}{H} \dot{\gamma}^* \end{aligned} \tag{8}$$

where  $\dot{\gamma}$  is the shear rate. In the power-law model,  $\mu_a$  is the apparent viscosity which is derived as follows [26]:

$$\mu_a = m \dot{\gamma}^{n-1} = m \left(\frac{U}{H} \dot{\gamma}^*\right)^{n-1} \tag{9}$$

where  $\dot{\gamma}^*$  is the dimensionless shear rate,  $n$  is the power-law index and  $m$  is the consistency index. Now, a relation can be derived between the local Reynolds and the liquid flow Reynolds number at the inlet of the channel as follows:

$$Re_r = \frac{\rho U H}{\mu_a} = \frac{\rho U H}{m \left(\frac{U}{H} \dot{\gamma}^*\right)^{n-1}} = \frac{\rho U^{2-n} H^n}{m} \frac{1}{\dot{\gamma}^{*n-1}} = \frac{Re}{\dot{\gamma}^{*n-1}} \tag{10}$$

In this equation,  $Re_r$  is the local Reynolds number and  $Re$  is the Reynolds number at the inlet of channel, which in this study is  $Re=50-200$ . After calculating the fluid shear rate in each time step for each point inside each vortex locations, the local Reynolds and the standard deviation

$\sigma = \sqrt{\frac{2\Delta t}{Re_r}}$  for a random motion is determined. In other

words, in fluid flow simulation using RVM, the difference between the non-Newtonian and Newtonian fluids is the random motion of the vortices. In Newtonian fluid, all vortices in every time step move with the same constant standard deviation. Whereas, for a non-Newtonian fluid, each vortex in each time step performs its random motion with a determined standard deviation and at the same time different.

According to RVM, if  $N$  is the total number of vortices, the induced velocity equation is shown below [5]:

$$\begin{aligned} \bar{w}(z_j) &= \\ &\left[ \sum_{\substack{i=1 \\ i \neq j}}^N w(t_j, t_i) - \sum_{i=1}^N w(t_j, \bar{t}_i) + w_p(t_j) \right] F(t_j) \end{aligned} \tag{11}$$

In this equation, the first term is the set of velocities induced by all vortices on the vortex  $j$ . The second term is the set of velocities induced by the images of all vortices on the vortex  $j$ , and the third term is the velocity of the passing potential at point  $t_j$  corresponding to point  $z_j$ . Also,  $t$  is the complex coordinate in the transfer plane,  $\bar{t}$  is the conjugate of  $t$ , and  $F(t_j)$  is also a Schwarz-Christoffel transfer function.

#### 4. VALIDATION OF RESULTS

To validate the results of this research and indicate the ability of the presented method, first the non-Newtonian flow between two infinite parallel flat plates is solved by RVM and was compared with analytical results. Also, the results of the present study were compared with the results of Hayes et al. [12] and Khandelwal et al. [13].

Consider a unidirectional non-Newtonian flow between two infinite parallel flat plates in the  $x$  direction, which located at  $y=\pm H/2$ . The velocity field  $u_x$ , normalized by the mean velocity is given by Rakotomalala et al. [28]:

$$\frac{u_x(y)}{u_{ave}} = \frac{2n+1}{n+1} \left[ 1 - \left( \frac{2|y|}{H} \right)^{\frac{n+1}{n}} \right] \tag{12}$$

where  $n$  represents the Power-law index. The comparison between the analytical solution and the present results for a non-Newtonian flow between two infinite parallel flat plates with different power-law indexes is illustrated in Figure 3. According to this figure, there is a very good conformation between the presented method results and the analytical solution. Figure 4 shows the horizontal velocity profiles between two plates for various power-law indexes resulting from the recent study. For the identical flow rate, when  $n>1$  (shear thickening fluid) the profile of velocity becomes sharper. Whereas, when  $n<1$  (shear thinning fluid) the profile of velocity changes to plug flow profile.

To validate the present method in solving non-Newtonian flow, the output results have been compared with numerical and experimental results by Hayes et al. [12] and Khandelwal et al. [13]. This comparison is performed for the recirculation length  $L_r$  inside the side branch of the T-junction which is studied as the dimensionless ratio of  $L_r/H$  ( $H$  is the inlet height of the channel) for various power-law indexes ( $n=0.2, 0.4, 0.6$  and  $1$ ) at different Reynolds numbers. The results of this comparison can be observed in Figure 5. As this figure shows, a very good conformation exists between the results which show a promising performance of the current method for non-Newtonian fluid flow simulations.

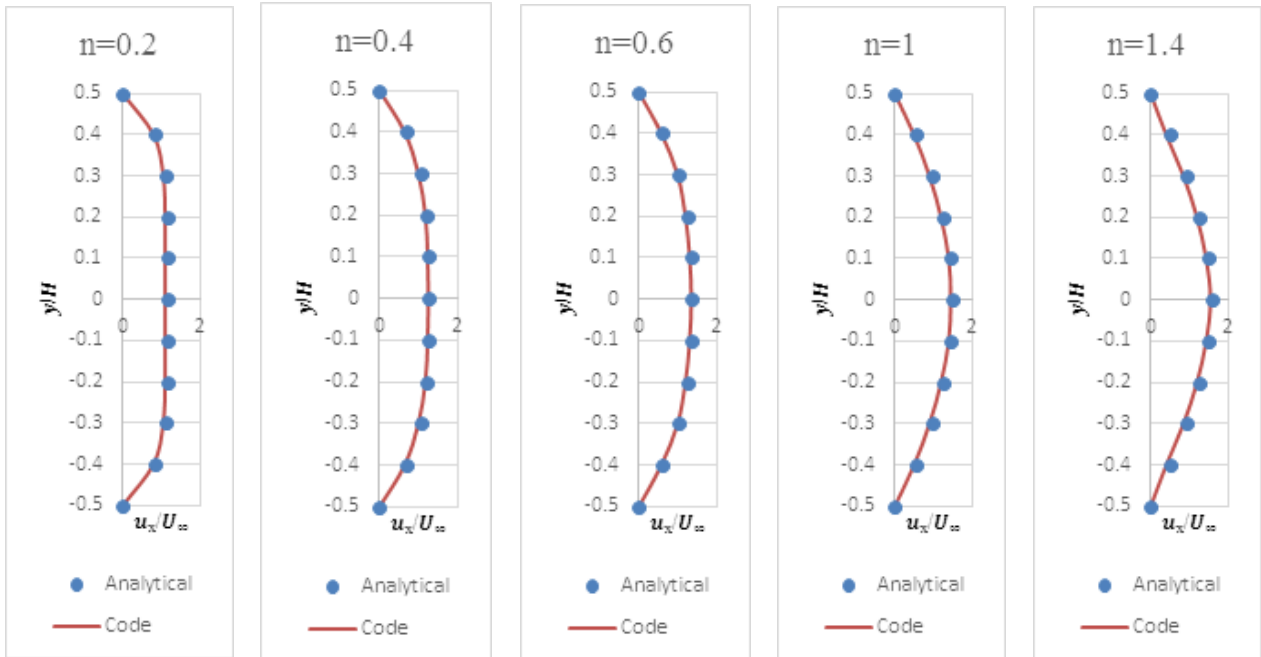


**Figure 3.** Comparison of the analytical solution and the present results of RVM for a non-Newtonian flow between two infinite parallel flat plates with different power-law indexes

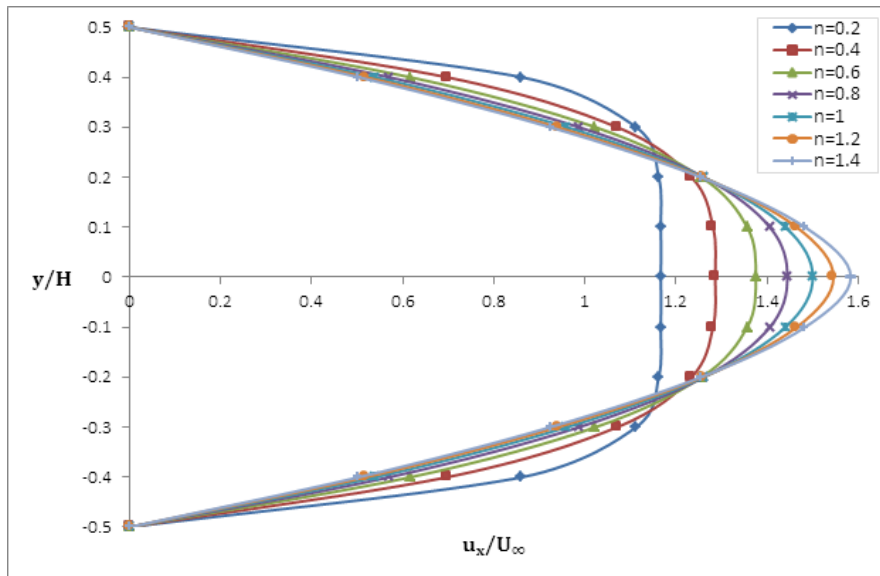


**Figure 4.** Horizontal velocity profiles of non-Newtonian fluid flow between two infinite parallel flat plates with different power-law indexes (Obtained from present study)

For  $n=0.2, 0.4, 0.6$  and  $1$ , the minimum percentage of deviation of the values obtained in present study in comparison with the outcomes of Khandelwal et al. [13] were about 0.41%, 0.26%, 0.56% and 0%, respectively; while the maximum deviations were about 5.17%, 2.45%, 1.61% and 2.93%, respectively.

Furthermore, for  $n=1$ , the minimum percentage deviation of the values in comparison with the results of Hayes et al. [12] is about 0.29%; while the maximum deviation is about 3.87%. As the figure shows, there is an acceptable conformation between the present study results and the both sets of results.

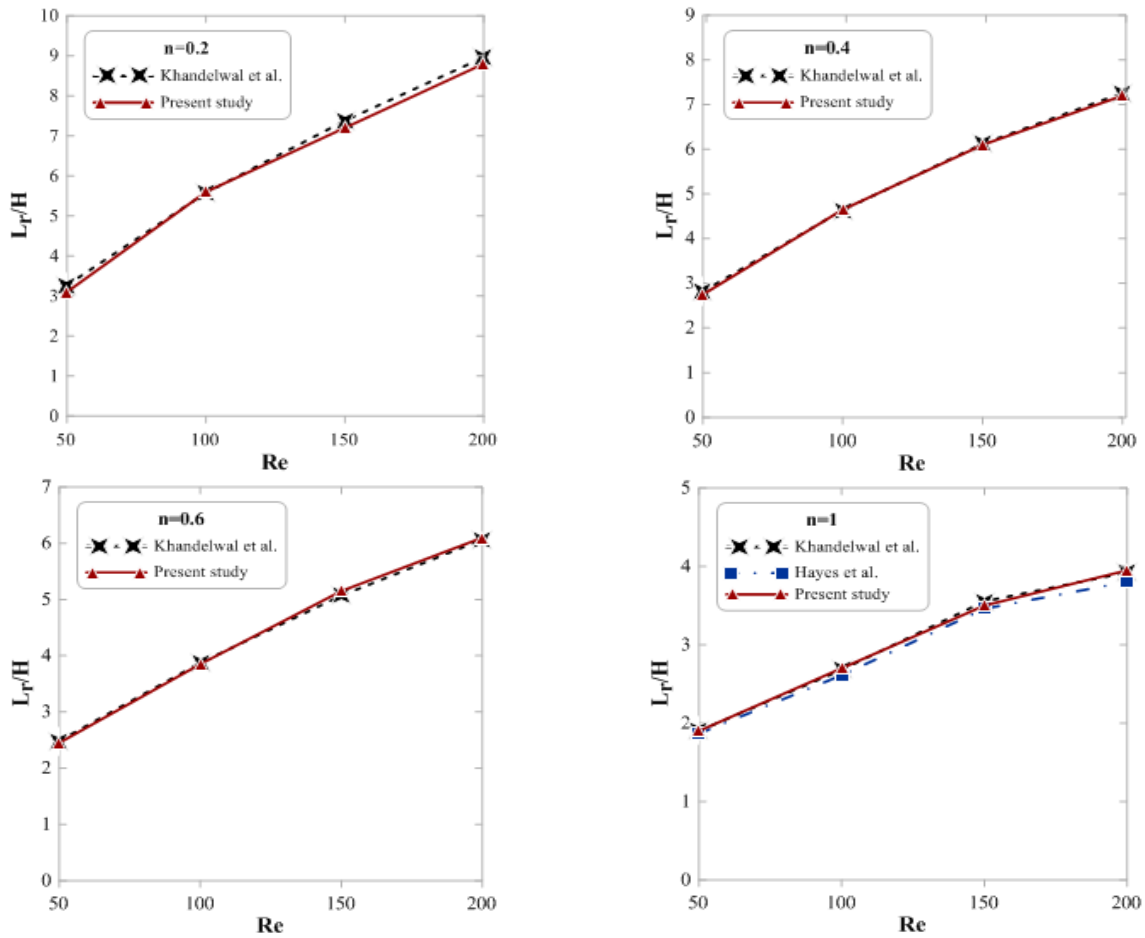


**Figure 5.** Comparison of recirculation length ( $L_r/H$ ) with that of Khandelwal et al. [13] for  $n=0.2, 0.4, 0.6$  and with that of Khandelwal et al. [13] and Hayes et al. [12] for  $n=1$  at different values of  $Re$

### 5. RESULTS AND DISCUSSION

The computation begins with the initial condition of the potential flow. Starting with a potential flow, the flow develops by generating vorticity along solid walls to annihilate the slip velocity. The vortices motion stems from both convection and diffusion mechanisms. Vortices that move away from the computational domain are neglected in the computational process.

Once the vortices fill all the computing domain, their number is almost constant; which means:  $\frac{dN}{dt} \approx 0$  ( $N$  is

the total number of vortices within the computing domain). Afterwards, velocity can be evaluated anywhere in the flow. Such a velocity field is instantaneous, and to obtain the average velocity, the computation must be repeated in several time steps and then averaged.

In order to investigate the effect of the parameters of power-law index and Reynolds number on the recirculation zone, after solving the non-Newtonian fluid

flow using RVM, the streamlines inside the T-junction can be drawn. Figure 6 illustrates the streamlines inside a T-junction for  $Re=50, 100, 150$  and  $200$ , respectively. To demonstrate the effect of the power-law index over the flow, seven cases ( $n=0.2, 0.4, 0.6, 0.8, 1, 1.2$  and  $1.4$ ) are investigated, which is shown here as an example of one case ( $n=0.2$ ). This figure shows that for a specific power-law index, increasing the Reynolds number increases the length of the recirculation zone.

Figure 7 shows the streamlines inside a T-junction for  $n=0.2, 0.4, 0.6, 0.8, 1$  and  $1.2$ , respectively for four fixed Reynolds numbers  $Re=50, 100, 150$  and  $200$  (here for  $Re=100$ ). The results show that, by increasing the value of the power-law index, the length of the recirculation zone decreases. This is due to that by increasing the power-law index, the local Reynolds number decreases in the whole flow field. In other words, with increasing the power-law index, the shear thickening treatment of the fluid rises and as a consequence, the fluid viscosity grows higher which leads to a decrease into the length of the recirculation zone.

After finding the length of the recirculation zone in the lateral branch for different values of the Reynolds number and the power-law indexes, these values can be displayed on a graph to compare results. Figure 8 illustrates the length of the recirculation zone within the T-junction in terms of the Reynolds number for the various power-law indexes. For a particular power-law index, this length increases nonlinearly with increasing Reynolds number. Also, for a fixed Reynolds number, the recirculation length increases with decreasing power-law index. Therefore, it can be concluded that the recirculation length is a function of the power-law index and the Reynolds number. Another important conclusion that can be drawn from this figure is that the lower the power-law index, the greater the effect of the Reynolds number on the length of the recirculation zone. In contrast, increasing the Reynolds number for the power-law indexes with high values does not have a significant effect on the length of the recirculation zone.

It is important to determine the critical Reynolds number in which the start of the recirculation zone appears in the lateral branch, is very important. In present study critical Reynolds numbers are obtained for several of the power-law indexes. For this purpose, for a specific power-law index, the Reynolds number is gradually increased from the lower values with a tolerance of  $\pm 1$ ,

and for each value of the Reynolds number, the change of the velocity sign in the y-direction inside the lateral branch is checked. The change in the velocity sign indicates the presence of a recirculation zone there. For instance, Figure 9 illustrates the streamlines in a T-junction for the critical Reynolds number for the cases of  $n=0.2$  and  $1.2$ , respectively. As can be seen from this figure, for  $n=0.2$ , up to  $Re=8$ , no sign change in velocity and therefore no wake is observed in the flow, but as the Reynolds number increases to  $Re=9$ , a recirculation zone in the lateral branch appears. In the same way, for  $n=1.2$ , no recirculation zone exists until  $Re=19$  but this zone appears at  $Re=20$ .

Figure 10 illustrates the critical Reynolds number in terms of power-law index obtained from present study in comparison with the results of Khandelwal et al. [13]. As the figure shows, there is very good conformation between both sets of results. By incrementing the power-law index, the critical Reynolds number is enhanced, meaning that the start of the recirculation zone appearing in the lateral branch occurs at a higher Reynolds number. In the other words, with increasing the power-law index, the shear thickening treatment of the fluid rises and as a consequence, the fluid viscosity grows higher which leads to recirculation zones occurring at a higher Reynolds number.

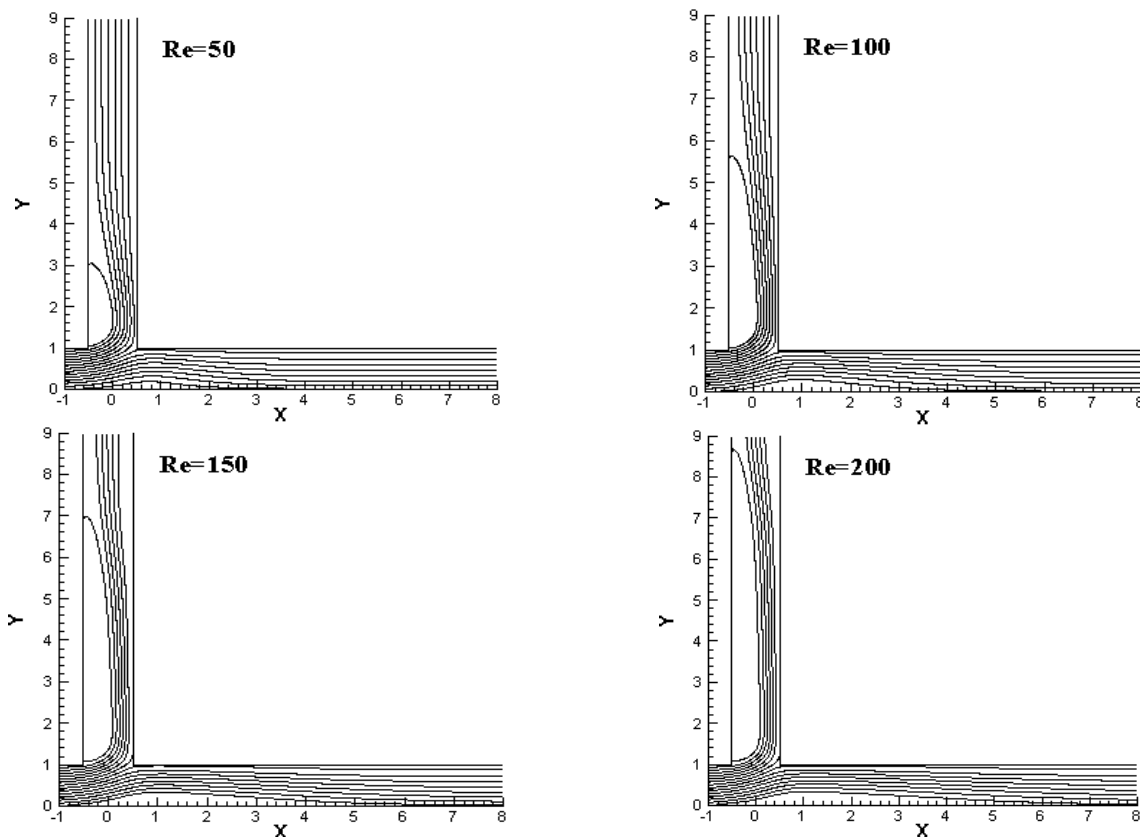


Figure 6. Streamlines inside a T-junction at different values of Re for  $n=0.2$  (Obtained from present study)

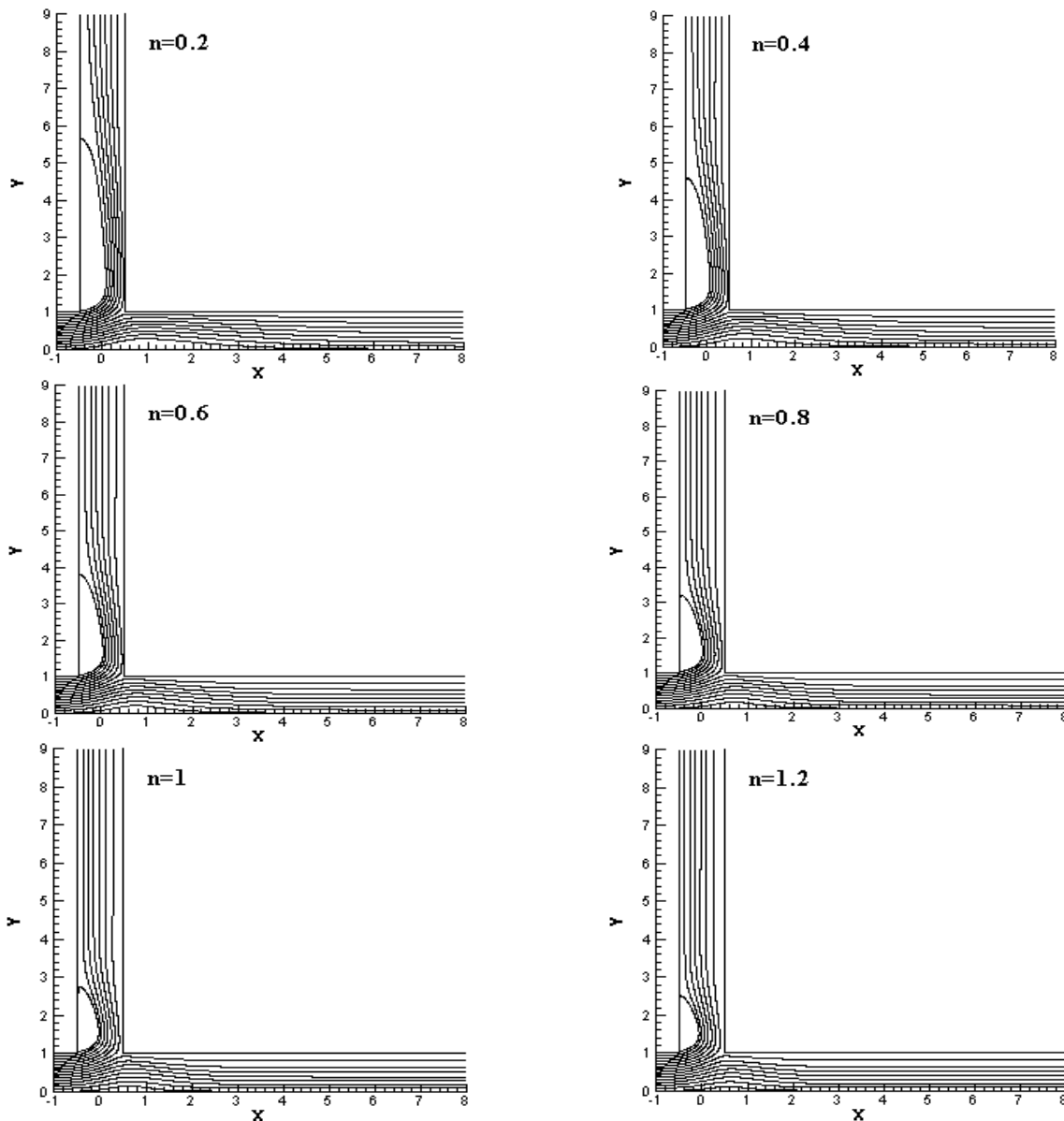


Figure 7. Streamlines inside a T-junction at different values of  $n$  for  $Re=100$  (Obtained from present study)

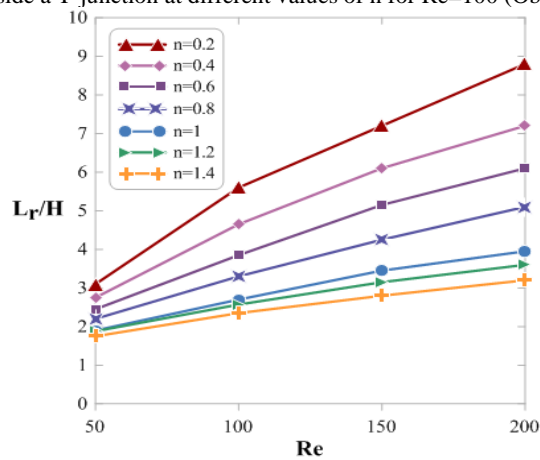
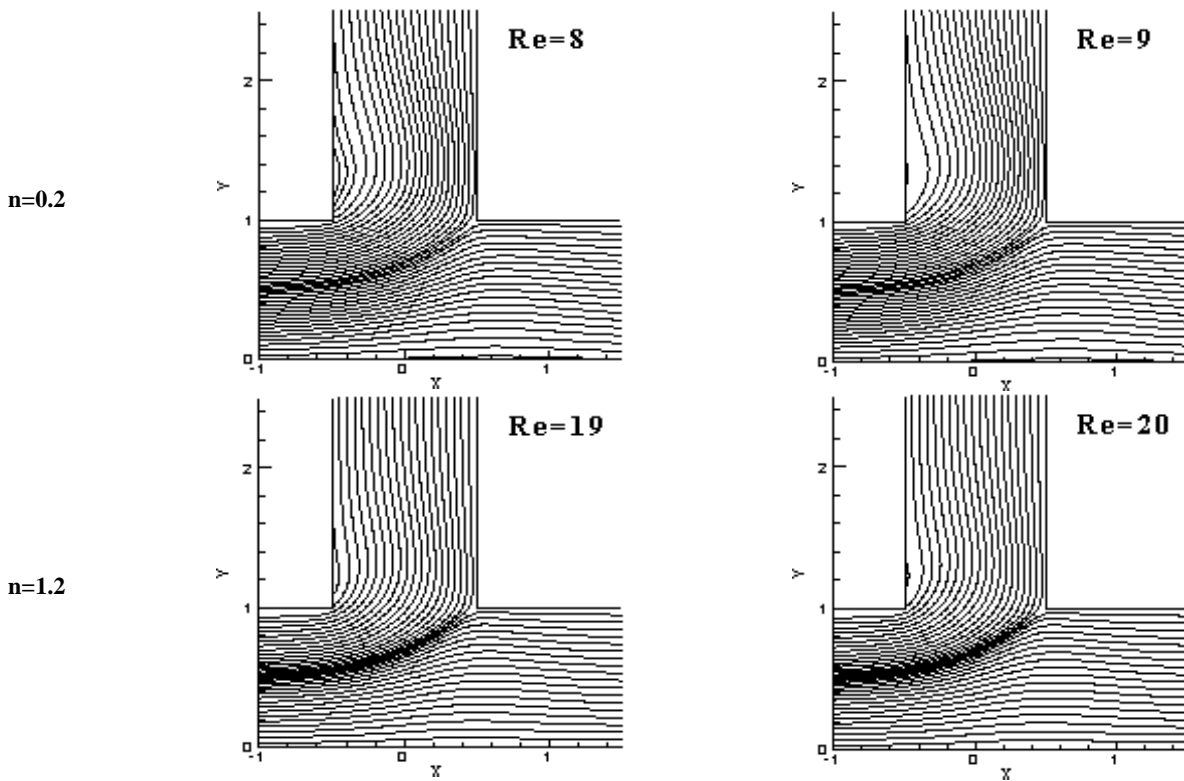
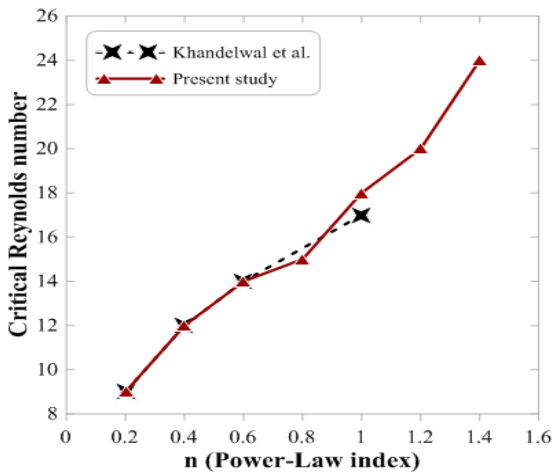


Figure 8. Variation of recirculation length ( $L_r/H$ ) with  $Re$  at different values of power-law indexes (Obtained from present study)



**Figure 9.** Streamlines for critical Reynolds number in which the start of the recirculation zone appears in the side branch for  $n=0.2$  and  $1.2$  (Obtained from present study)



**Figure 10.** Comparison of critical Reynolds number for the onset of flow separation at different values of power-law indexes with that of Khandelwal et al. [13]

### 6. CONCLUSION

As mentioned earlier, the main purpose of this study is to develop the Random Vortex Method in simulating and solving the flow of non-Newtonian fluids, which in this research is offered for the first time with the introduction of a new approach. By observing the obtained results and

comparing them with the numerical and experimental results of other researchers, there is a very good and acceptable agreement, which proves that the proposed method is very capable in simulating the flow of non-Newtonian fluids. Therefore, from now on, the RVM can be considered as one of the reliable and accurate methods in non-Newtonian fluid analysis and many existing non-Newtonian fluid problems can be investigated by this method.

Important advantages of the RVM include its ability to study the fluid flow in a wide range of Reynolds numbers, including laminar and turbulent regimes, solving time-based equations, and no need to simplify governing equations. Therefore, this method can be used for two-phase flows that need to determine the instantaneous velocities. Also, simulation of turbulent flow in this method is possible easily and with very high accuracy and can be considered as future work. In addition to internal flows, this method can also be used to simulate external flows.

In conclusion, it can be said that in this study, the capability of the RVM in simulating and solving the flow of non-Newtonian fluids has been proven. Therefore, it is suggested that other studies be performed to investigate the flow of non-Newtonian fluids with this method, especially the simulation of turbulent flows, which this method is able to solve with high accuracy.

## 7. REFERENCES

- Yang, B., Su, W., Deng, Sh., Zhao, L., Lu, P., "State-of-art of impacting T-junction: Phase separation, constituent separation and applications", *International Journal of Heat and Mass Transfer*, Vol. 148, (2020), 119067. DOI: <https://doi.org/10.1016/j.ijheatmasstransfer.2019.119067>
- Chorin, A. J., "Numerical study of slightly viscous flow", *Journal of Fluid Mechanics*, Vol. 57, (1973), 785-796. DOI: <https://doi.org/10.1017/S0022112073002016>
- Chorin, A. J., "Vortex sheet approximation of boundary layers", *Journal of Computational Physics*, Vol. 27, (1978), 428-442. DOI: [https://doi.org/10.1016/0021-9991\(78\)90019-0](https://doi.org/10.1016/0021-9991(78)90019-0)
- Gagnon, Y., Giovannini, A., "Numerical simulation and physical analysis of high Reynolds number recirculating flows behind sudden expansions", *Journal of Physics Fluids*, Vol. 5, (1993), 2377-2389. DOI: <https://doi.org/10.1063/1.858752>
- Noori, Y., Zafarmand, B., "Simulating of laminar and turbulent flows inside diverging channels with Random Vortex Method (RVM) and investigating the effects of the angle of divergence and the Reynolds number on the recirculating flow inside the channels", *Journal of Applied and Computational Sciences in Mechanics*, Vol. 26, (2015), 17-34. DOI: 10.22067/fum-mech.v26i1.23642
- Zafarmand, B., Souhar, M., Hossein Nezhad, A., "Analysis of the characteristics, physical concepts and entropy generation in a turbulent channel flow using Vortex Blob Method", *International Journal of Engineering, Transactions B: Applications*, Vol. 29, No. 7, (2016), 985-994. DOI: 10.5829/idosi.ije.2016.29.07a.14
- Zafarmand, B., Ghadirzad, N., "High Reynolds viscous flow simulation past the elliptical Airfoil by Random Vortex Blob", *International Journal of Engineering, Transactions B: Applications*, Vol. 30, No. 12, (2017), 1903-1910. DOI: 10.5829/ije.2017.30.12c.12
- Tadayoni Navaei, I., Zafarmand, B., "Random Vortex Method for Geometries with Unsolvable Schwarz-Christoffel Formula", *International Journal of Engineering, Transactions B: Applications*, Vol. 31, No. 1, (2018), 38-44. DOI: 10.5829/ije.2018.31.01a.06
- Jin, G., Zou, L., Jiang, Y., Zong, Z., Sun, Z., "A circle theorem technique to handle 2-D flows around arbitrary cylinders in discrete vortex method", *Journal of Wind Engineering & Industrial Aerodynamics*, Vol. 209, (2021), 104496. DOI: <https://doi.org/10.1016/j.jweia.2020.104496>
- Mimeau, Ch., Marie, S., Mortazavi, I., "A comparison of semi-Lagrangian vortex method and lattice Boltzmann method for incompressible flows", *Computers and Fluids*, Vol. 224, (2021), 104946. DOI: <https://doi.org/10.1016/j.compfluid.2021.104946>
- Qian, Z., Yao, Y., "McKean-Vlasov type stochastic differential equations arising from the random vortex method", *Partial Differential Equations and Applications*, Vol. 3, No. 1, (2021). DOI: <https://doi.org/10.1007/s42985-021-00146-z>
- Hayes, R. E., Nandakumar, K., Nasr-El-Din, H., "Steady laminar flow in a 90 degree planar branch", *Computers and Fluids*, Vol. 17, (1989), 537-553. DOI: [https://doi.org/10.1016/0045-7930\(89\)90027-3](https://doi.org/10.1016/0045-7930(89)90027-3)
- Khandelwal, V., Dhiman, A., Baranyi, L., "Steady laminar flow in a 90 degree planar branch", *Computers and Fluids*, Vol. 17, No. 4, (2014). DOI: <http://dx.doi.org/10.1016/j.compfluid.2014.11.030>
- Brandi, A.C., Mendonca, M.T., Souza, L.F., "DNS and LST stability analysis of Oldroyd-B fluid in a flow between two parallel plates", *Journal of Non-Newtonian Fluid Mechanics*, Vol. 267, (2019). DOI: <https://doi.org/10.1016/j.jnnfm.2019.03.003>
- Zhou, H., Zhu, Ch., Fu, T., Ma, Y., Li, H. Z., "Dynamics and interfacial evolution for bubble breakup in shear-thinning non-Newtonian fluid in microfluidic T-junction", *Chemical Engineering Science*, Vol. 208, (2019), 115-158. DOI: <https://doi.org/10.1016/j.ces.2019.115158>
- Kwak, H., Nam, J., "Simple criterion for vortex formation in the channel flow of power-law fluids", *Journal of Non-Newtonian Fluid Mechanics*, Vol. 284, (2020). DOI: <https://doi.org/10.1016/j.jnnfm.2020.104372>
- Luo, H., Delache, A., Simoens, S., "Mixing of non-Newtonian inelastic fluid in a turbulent patch of T-junction", *Journal of Non-Newtonian Fluid Mechanics*, (2020). DOI: <https://doi.org/10.1016/j.jnnfm.2020.104307>
- Yang, B., Deng, Sh., Sub, W., Zhao, L., Wang, D., "Experimental investigation on phase separation comparison between single and double T-junctions", *Experimental Thermal and Fluid Science*, Vol. 118, (2020). DOI: <https://doi.org/10.1016/j.expthermflusci.2020.110171>
- Rostami, B., Morini, G. L., "Generation of Newtonian droplets in Newtonian and non-Newtonian carrier flows in micro T-junctions under opposed-flow configuration", *Journal of Non-Newtonian Fluid Mechanics*, Vol. 281, (2020). DOI: <https://doi.org/10.1016/j.jnnfm.2020.104297>
- Moghim, S. M., Abbasi, M., Khaki Jamei, M., Domirri Ganji, D., "Effect of Non-uniform Magnetic Field on Non-newtonian Fluid Separation in a Diffuser", *International Journal of Engineering, Transactions A: Basics*, Vol. 33, No. 7, (2020), 1354-1363. DOI: 10.5829/ije.2020.33.07a.23
- Maurya, A., Tiwari, N., Chhabra, R.P., "Controlling the flow and heat transfer characteristics of power-law fluids in T-junctions using a rotating cylinder", *International Journal of Thermal Sciences*, Vol. 163, (2021). DOI: <https://doi.org/10.1016/j.ijthermalsci.2021.106854>
- Motahar, S., "A Neural Network Approach to Estimate Non-Newtonian Behavior of Nanofluid Phase Change Material Containing Mesoporous Silica Particles", *International Journal of Engineering, Transactions B: Applications*, Vol. 34, No. 8, (2021), 1974-1981. DOI: 10.5829/ije.2021.34.08b.18
- Vatani, M., Domirri Ganji, D., "Experimental Examination of Gas-liquid Two-phase Flow Patterns in an Inclined Rectangular Channel with 90° Bend for Various Vertical Lengths", *International Journal of Engineering, Transactions A: Basics*, Vol. 35, No. 4, (2022), 685-691. DOI: 10.5829/ije.2022.35.04a.07
- Streeter, V. L., Wylie, E. B., K. Bedford, W., "Fluid Mechanics", 9th Edition, W.C. Brown Pub. Co, ISBN-13: 978-0070625372, (1997).
- Nehari, Z., "Conformal Mapping", New York, McGraw-Hill, ISBN 978-0-486-61137-2, (1952).
- Chhabra, R. P., Richardson, J. F., "Non-Newtonian Flow and Applied Rheology", Second Edition, ISBN 978-0-7506-8532-0, (2008). DOI: <https://doi.org/10.1016/B978-0-7506-8532-0.X0001-7>
- Polyanin, A. D., "Handbook of Linear Partial Differential Equations for Engineers and Scientists", Chapman and Hall/CRC, Edition, ISBN 978-1-58488-299-9, (2002).
- Rakotomalala, N., Salin, D., Watzky, P., "Simulations of viscous flows of complex fluids with a Bhatnagar, Gross, and Krook lattice gas", *Physics of Fluids*, Vol. 8, (1996). DOI: <https://doi.org/10.1063/1.869093>

---

**Persian Abstract**

---

**چکیده**

مطالعات گذشته نشان می دهد که تاکنون از روش ورتکس های تصادفی (RVM) فقط برای حل جریان سیالات نیوتنی استفاده می شده است. در این مقاله با ارائه یک رویکرد جدید، روش ورتکس های تصادفی برای اولین بار با هدف شبیه سازی جریان سیالات غیر نیوتنی توسعه داده شده است. برای این منظور، جریان دوبعدی سیال غیرنیوتنی پاورلا در یک اتصال T به صورت عددی شبیه سازی شده است. این شبیه سازی برای عدد رینولدز ورودی کانال در محدوده  $Re = 50-200$  و شاخص های مختلف پاورلا در طیف  $n = 0.2-1.4$  انجام شده است. روش ورتکس های تصادفی معادلات ناویر-استوکس را به صورت تابعی از زمان حل می کند و بدون نیاز به شبکه بندی بر روی هندسه و همچنین بدون نیاز به تعیین سرعت در تمام میدان سیال، سرعت در هر نقطه از کانال را تعیین می نماید. سرعت پتانسیل به عنوان شرط اولیه در تحلیل جریان به روش ورتکس های تصادفی است که در این مقاله با استفاده از تبدیل همدیس شوارتز-کریستوفل به دست آمده است. اثر دو پارامتر شاخص پاورلا و عدد رینولدز بر ناحیه گردش مجدد بررسی شده است. توافق قابل قبول بین نتایج مطالعه حاضر و نتایج عددی و تجربی موجود، قابلیت روش ارائه شده را نشان می دهد که با توجه به آن می توان روش ورتکس های تصادفی را یک روش امیدوارکننده قدرتمند در شبیه سازی جریان سیالات غیرنیوتنی در رژیم های جریان آرام و درهم در نظر گرفته گرفت.

---



## An Application of Artificial Neural Network to Predict the Compressive Strength of Concrete using Fly Ash and Stone Powder Waste Products in Central Vietnam

V. L. Thang, L. Cung\*, D. S. Nguyen

University of Science and Technology, The University of Danang, Vietnam

### PAPER INFO

#### Paper history:

Received 03 January 2022

Received in revised form 04 February 2022

Accepted 11 February 2022

#### Keywords:

Concrete

Compressive Strength

Fly Ash and Stone Powder

Artificial Neural Network

Ultrasonic Pulse Velocity

Amplitude Attenuation Ratio

### ABSTRACT

In Central Vietnam, the traditional materials for making concrete are usually of natural origin. The overexploitation of these materials causes many adverse effects on the natural environment. Local industrial plants and quarries generate millions of tons of waste products such as fly ash and stone powder. However, when used for the partial replacement of cement and sand, these waste products can affect the compressive strength of concrete. Therefore, it is necessary to build models to predict compressive strength for this type of concrete. The paper aimed to apply artificial neural network models to predict the compressive strength of concrete using fly ash and stone powder waste products. The input of the ANN model includes six parameters: ultrasonic pulse velocity, wave amplitude attenuation ratio, and 4 parameters of concrete materials. Experimental data were obtained from 72 cubic specimens of different mixtures using available materials in Central Vietnam. These models allow predicting the 28-day compressive strength of concrete within the range of 9-62MPa (90-620daN/cm<sup>2</sup>). Furthermore, these models can predict compressive strength with any mixture. It is significant when re-evaluating whether the actual compressive strength value is as reliable as the one provided by the manufacturer.

doi: 10.5829/ije.2022.35.05b.12

### NOMENCLATURE

ANN	Artificial neural network	C	Binder
$f_c$	Concrete compressive strength	D	Water
A	Fine aggregate	UPV	Ultrasonic pulse velocity
B	Coarse aggregate	$A_2/A_1$	Amplitude attenuation ratio

## 1. INTRODUCTION

In Central Vietnam, as shown in Figure 1, the traditional materials for making concrete are sand, gravel, Portland cement, and water. The sources of these materials are often natural, such as sand mined from rivers, stone powder from quarries, cement formed by fine grinding clinker, natural gypsum, shells, and clay. The over-exploitation of these materials causes adverse effects on nature. Especially sand mining in rivers causes landslides and floods in this area. Therefore, it is necessary to find alternative sources of materials for those traditional ones. Some studies in Vietnam use waste products to partially replace traditional materials such as autoclaved aerated

concrete after the autoclaving process to replace 25% of natural sand [1], rice husk ash, and fly ash, partially replacing cement [2, 3]. This research axis of using waste products has received significant attention in many countries. The mechanical properties of the concrete using these materials have been considered in literature [4, 5] and the compressive strength was also studied by Kanthe et al. [6] and Sadowski et al. [7]. Therefore, it helps to benefit waste products and limit the use of traditional materials, helping to reduce adverse effects on the natural environment [8, 9].

One problem arises: waste products can affect compressive strength, an essential parameter of concrete quality. Therefore, it is necessary to study the

\*Corresponding Author Institutional Email: [lcung@dut.udn.vn](mailto:lcung@dut.udn.vn)  
(L. Cung)



**Figure 1.** Origin of fly ash and stone powder in Central Vietnam

compressive strength of concrete using these new alternative materials. Scientists have examined the application of ultrasonic pulse velocity (UPV) to evaluate concrete compressive strength for decades due to its distinct advantages over conventional compression measurements. The widely used relationship between concrete compressive strength and UPV is expressed in the exponential formulation. However, examining the performance coefficients of these models shows that the single nonlinear regression with exponential formulation provides bad fitting curves since some concrete ingredients affect much on compressive strength but at a low rate on UPV [10, 11]. The multivariable model with many input parameters, including UPV and other parameters such as concrete ingredient materials, age, and temperature is recommended to enhance the situation. Regression models and artificial neural network models are commonly used to predict the compressive strength of concrete [12, 13]. The accuracy of the regression model depends on the selection of input parameters and the amount of input data of the model [14, 15]. For the artificial neural network model, the choice of the artificial neural network structure determines the prediction results [16, 17]. The sensitivity analysis to predict the compressive strength of concrete based on the artificial neural network has been mentioned by Heidari and Hashempour [18].

Each year, about one million tons of fly ash are generated at Vung-Ang thermal power plants. At Phuoc-Tuong quarry, there is a large amount of waste stone powder (as shown in Figure 1). The paper proposes to reuse fly ash and stone powder to replace cement and sand partially. At construction sites in the area, the required compressive strength for concrete is from 20-50MPa (200-500daN/cm<sup>2</sup>). Some studies have predicted the compressive strength of concrete in this range. However, no studies have been available for predicting compressive strength in such a wide range as above using fly ash and stone powder to replace cement and sand. This paper aimed to build an artificial neural network model to predict the compressive strength of concrete using two waste products, fly ash and stone powder. The input of the ANN model will be the concrete mixtures, UPV, and wave amplitude attenuation ratio. The number of specimens for the experiment is determined by the design of the experiment method. Many different structures of artificial neural networks are elaborated to choose the most optimal one. The model allows predicting compressive strength in the range of 8.65-62.13MPa (86.5-621.3daN/cm<sup>2</sup>). The research results help concrete manufacturers evaluate the concrete mixtures and determine the optimal mix to ensure the design compressive strength requirements. In addition, the model allows the supervision consultant to re-evaluate the compressive strength provided by the concrete manufacturer.

## 2. MATERIALS AND METHODS

**2. 1. Materials** Compressive strength value is influenced by many factors such as mixtures, concrete mixing method, curing conditions, specimen shape, concrete age. Therefore, the Ishikawa diagram was used to analyze the effect of the affecting factors as shown in Figure 2. Because the concrete using fly ash and stone powder waste is the object of study, the concrete mixture will be a factor to be included in the research model. Other factors are assumed to be in standard conditions according to Vietnamese standards.

The traditional local material for making concrete are sand, gravel, cement, and water. Based on actual data at concrete factories in the area, the study uses fly ash and stone powder waste products to replace 20% cement and sand.

**2. 2. Design of Experiments** Based on the analysis of the Ishikawa diagram as shown in Figure 2, the concrete mixture is the input parameter of the artificial neural network model to predict the compressive strength. By consulting the Vietnamese Ministry of Construction, for concrete of compressive strength from 20 to 50MPa (200-500daN/cm<sup>2</sup>), the essential material

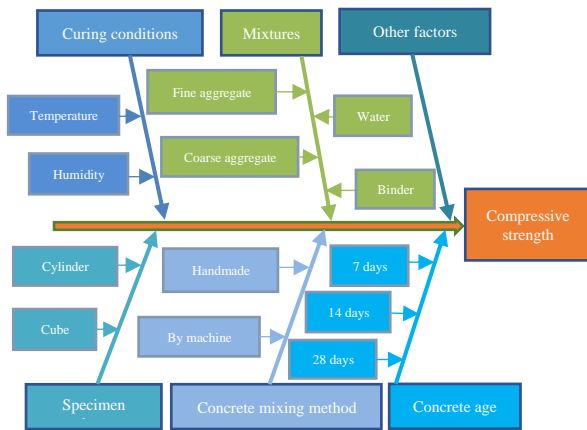


**Figure 2.** Ishikawa diagram: Main factors affecting the compressive strength

components for making concrete are shown in Table 1. The result indicates that the binder has the most considerable variation with 58.9% compared to the full content of this material. The remaining parameters such as fine aggregates, water, and coarse aggregates (a mixture of aggregate particles with sizes from 10-20mm) are changed by 32.2, 17.4, and 8.3%, respectively.

The study uses the design of experiments method to determine the number of specimens to be taken. The number of levels of each parameter such as fine aggregate, coarse aggregate, binder, and water is 3, 2, 4 and 3, respectively, as given in Table 2. The number of experimental specimens was determined according to the full factorial experiment design method as follows:

$$\text{Experimental mixture number} = 2^1 \times 3^2 \times 4^1 = 72 \quad (1)$$

All component materials of 72 concrete mixtures are shown in Table A1 in the appendix.

**2. 3. Artificial Neural Network** Using fly ash and stone powder with different mixtures can change the compressive strength of concrete. Therefore, it is necessary to predict the compressive strength of concrete using these waste products. The paper proposes to use an

**TABLE 1.** Content range of specimen concrete components

Concrete components	Unit	Content range	Total
Fine aggregate	Sand (80%)	kg	512-755.2
	Stone powder (20%)	kg	128-188.8
Coarse aggregate (gravel)	kg	1100-1200	1100-1200
Binder	Cement (80%)	kg	172.8-420
	Fly ash (20%)	kg	43.2-105
Water	liter	190-230	190-230

**TABLE 2.** Content level of each specimen component

Label	Concrete components	Level of variation				Number of levels
		1	2	3	4	
A	Fine aggregate (kg)	640	792	944	*	3
B	Coarse aggregate (kg)	1100	1200	*	*	2
C	Binder (kg)	216	319	422	525	4
D	Water (liter)	190	210	230	*	3

artificial neural network to predict the compressive strength of concrete using waste products in central Vietnam. The model inputs are four concrete materials such as fine aggregate, coarse aggregate, binder, and water and two ultrasonic wave characteristics such as ultrasonic pulse velocity and wave amplitude attenuation ratio measured at 28 days. Three prediction models with different inputs are elaborated to compare their performances in order to find the best model.

**Model 1:** There are five input parameters including fine aggregate (A) [kg], coarse aggregate (B) [kg], binder (C) [kg], water (D) [liter] and ultrasonic pulse velocity (UPV) [m/s]. The output is the compressive strength at 28 days ( $f_c$ ) [daN/cm<sup>2</sup>].

**Model 2:** There are five input parameters including fine aggregate (A) [kg], coarse aggregate (B) [kg], binder (C) [kg], water (D) [liter] and amplitude attenuation ratio ( $A_2/A_1$ ). The output is the compressive strength at 28 days ( $f_c$ ) [daN/cm<sup>2</sup>].

**Model 3:** There are six input parameters including fine aggregate (A) [kg], coarse aggregate (B) [kg], binder (C) [kg], water (D) [liter], UPV [m/s] and amplitude attenuation ratio ( $A_2/A_1$ ). The output is the compressive strength at 28 days ( $f_c$ ) [daN/cm<sup>2</sup>].

The neural network is a backward propagation consisting of 3 layers including one input layer, one hidden layer, and one output layer. A total of 72 experimental datasets is randomly split into training, validation, and testing datasets by MATLAB software. The training data has 50 samples accounting for 70% of the total dataset. The validation and testing data have 11 samples respectively.

Three coefficients such as standard deviation (S), coefficient of determination ( $R^2$ ), and mean squared error are used to evaluate the prediction model accuracy, as given in Equation (2). Where  $y_i$  is the  $i^{\text{th}}$  observed response value;  $\bar{y}$  is the mean response;  $\hat{y}_i$  is the  $i^{\text{th}}$  fitted response and  $n$  is the number of observations.

$$S = \sqrt{MSE} = \sqrt{\frac{1}{n} \sum_{i=1}^n (\hat{y}_i - y_i)^2}$$

$$R^2 = 1 - \frac{\sum_{i=1}^n (\hat{y}_i - y_i)^2}{\sum_{i=1}^n (\bar{y} - y_i)^2} \quad (2)$$

$$MSE = \frac{1}{n} \sum_{i=1}^n (\hat{y}_i - y_i)^2$$

**3. EXPERIMENTS AND RESULTS**

**3. 1. Specimen Preparation**

According to Vietnam Standard TCVN 5574:2018, the concrete specimen is a cube with an edge of 15cm as given in Figure 3. The specimen is fabricated and cured at the University of Science and Technology Laboratory, The University of Da Nang in Vietnam. Specimen curing in the laboratory at a temperature of  $25\pm 2^{\circ}\text{C}$  and relative humidity of  $80\pm 7\%$  as shown in Figure 4.



**Figure 3.** Mold for making concrete samples



**Figure 4.** Curing concrete samples

**3. 2. Experiment Results**

At the age of 28 days, ultrasonic pulse velocity (UPV), wave amplitude attenuation ratio ( $A_2/A_1$ ), and compressive strength of the specimen are measured. There are three ways to determine the ultrasonic pulse velocity based on the propagation of ultrasonic waves as shown in Figure 5. The paper uses direct transmission through the sample using the Tico Proceq ultrasound device.

Waves emitted from the Tico Proceq ultrasound device with a frequency of 54kHz and connected to a digital signal acquisition as shown in Figure 6. Figure 7 shows the device connection diagram to receive wave signals. The amplitudes of the emitted wave ( $A_1$ ) and received wave ( $A_2$ ) are illustrated in Figures 8 and 9. The amplitude attenuation ratio when propagating through the

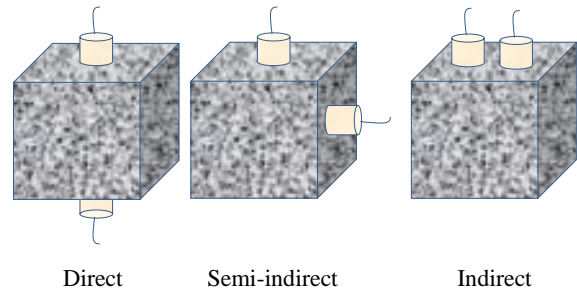


**Figure 5.** Positions of ultrasonic transducers



**Figure 6.** Tico Proceq ultrasound and SYSAM-SP5 signal acquisition



**Figure 7.** Device connection diagram to receive wave signal

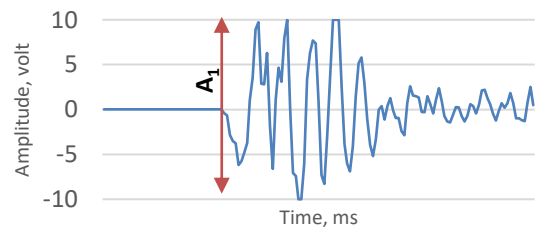


**Figure 8.** Wave signal from the emitting source

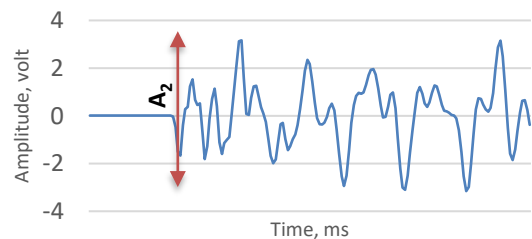


**Figure 9.** Wave signal from the receiving source

concrete specimen is determined. The concrete compressor used for measuring the compressive strength is a hydraulic compressor SYE-2000A with a maximum compressive force of 200 tons. Then, the characteristic compressive strength is calculated by Equation (3).

$$f_c = \frac{P}{A} \tag{3}$$

where P is the destructive compressive force, and A is the cross-sectional area of the specimen. The ultrasonic pulse velocity (UPV), wave amplitude attenuation ratio ( $A_2/A_1$ ), and compressive strength of 72 mixtures are shown in Table A1 in the appendix.

### 3. 3. Results of the Artificial Neural Network

The artificial neural network structure proposed in the paper to predict the compressive strength consists of three layers including the input, hidden, and output layer, as given in Figure 10. In order to determine the appropriate number of neurons in the hidden layer, the trial-and-error method is proposed to use for many cases with different hidden neuron numbers. Table 3 illustrates the results of three prediction models with different numbers of neurons in the hidden layer. The results show that the ANN model with ten hidden neurons gives the highest accuracy of compressive strength prediction. Therefore, the three most suitable models to predict compressive strength are selected including model 1 (5x10x1), model 2 (5x10x1), and model 3 (6x10x1).

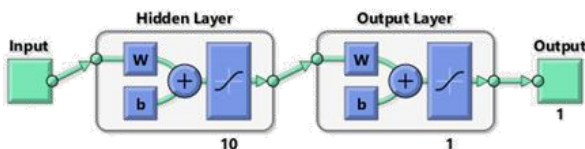


Figure 10. ANN network structure

TABLE 3. Coefficients of determination of ANN networks

Networks ANN	The structure of layers	The coefficient (R <sup>2</sup> )
Model 1	5x8x1	88.36%
	5x10x1	93.66%
	5x15x1	91.7%
	5x20x1	90.6%
Model 2	5x8x1	86.89%
	5x10x1	93.38%
	5x15x1	92.7%
Model 3	5x20x1	90.7%
	6x8x1	89.31%
	6x10x1	94.55%
	6x15x1	93.07%
	6x20x1	92.87%

The training procedure of the three ANN models is shown in Figure 11. In this figure, the vertical axis is the mean squared error (MSE), and the horizontal axis is the number of training iterations. The meaning of Figure 11 is to evaluate the training process of the artificial neural network model. The best validation performance indicates the iteration at which the validation performance reached a minimum. The training work continues for six more iterations and then stops. If the test curve increased significantly before the validation curve has increased, it is possible that some overfitting may

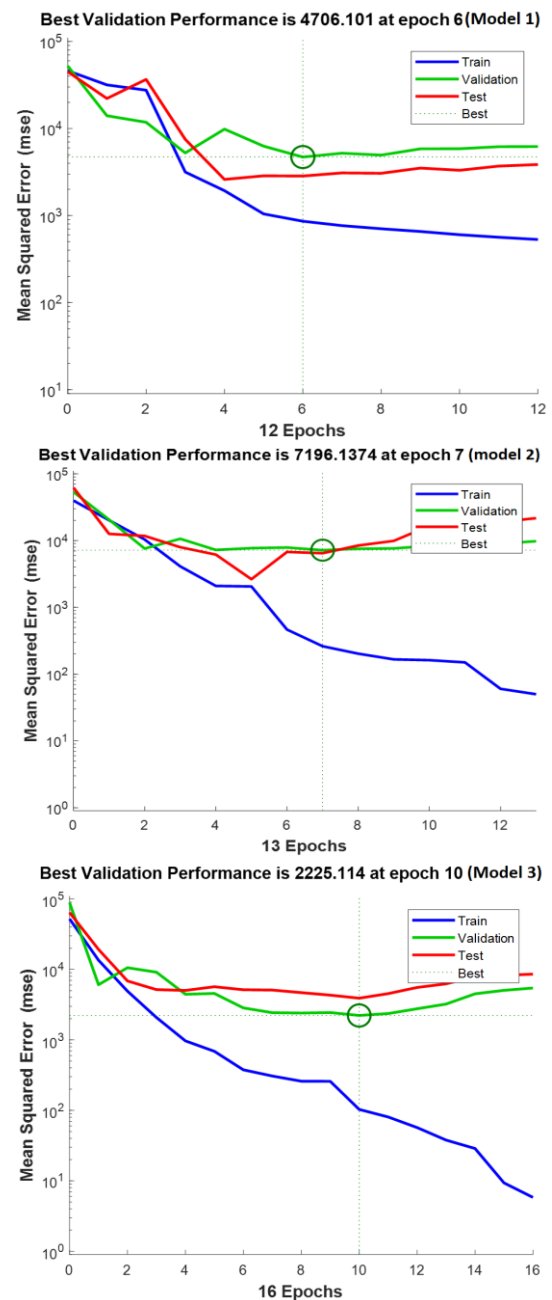
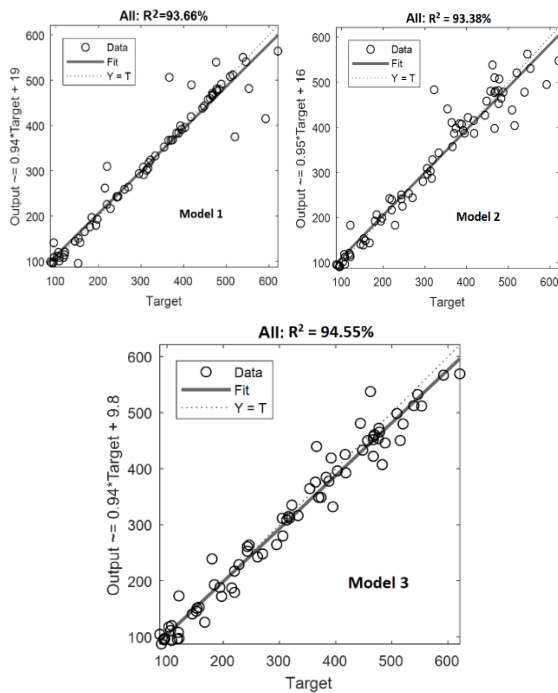


Figure 11. Training procedure of three ANN models

have occurred. The results show that the validation and test curves are similar in all three prediction models. In which model 3 has the minor mean squared error (MSE). Therefore, model 3 has the best training among the three predictive models.

Figure 12 shows the relationship between the outputs of the network and the targets. The three graphs represent training, validation, and testing data. The dashed line in each graph represents the perfect result as the output equals the target. The solid line represents the best-fit linear regression line between the output and the target. The predicted compressive strength (output) compared with the experimental results (target) of all three models has a good agreement. At the same time, the line approximating the predicted compressive strength for both cases above coincides with the straight-line  $Y=T$  of the graphs. However, the evaluation parameters of model 3 are the best of the three models, as given in Table 4.



**Figure 12.** Prediction results of compressive strength of three ANN models

**TABLE 4.** Performance parameters of models 1, 2, and 3

Performance coefficients	Deviation (S), daN/cm <sup>2</sup>	Determination coefficient (R <sup>2</sup> ), %
ANN model		
Model 1	38.05	93.66
Model 2	38.89	93.38
Model 3	35.26	94.55

#### 4. DISCUSSIONS

The results of the training process and the prediction of compressive strength, as given in Figures 11 and 12, show that the artificial neural network models have high accuracy. Model 3 is the most accurate predictor and the most suitable model to predict the compressive strength of concrete using fly ash and stone powder. However, model 1 and 2 can be very suitable for predicting the compressive strength for manufacturers corresponding to selected concrete ingredients using fly ash and stone powder.

In addition to predicting the compressive strength for 72 existing grades, the ANN can predict the compressive strength for any mix when the model's input parameters are known. For example, it is necessary to check whether the supplier's actual compressive strength value of concrete ensures the designed one or not. Then, with the known concrete mix provided by the concrete manufacturer, while the UPV values and the amplitude attenuation ratio were measured experimentally, with an established ANN network (model 3), it is facilitated to predict the compressive strength of concrete. For illustration, Table 5 shows the expected compressive strength value based on the given mixtures, known UPV, and amplitude attenuation ratio values.

**TABLE 5.** Predicting compressive strength of concrete according to model 3 by ANN

Concrete components		UPV (m/s)	A <sub>2</sub> /A <sub>1</sub>	Predicted results (daN/cm <sup>2</sup> )
Fine aggregate (kg)	Sand	515		
	Stone powder	129		
Coarse aggregate (kg)		1200	4395	0.277
Binder (kg)	Cement	224		
	Fly ash	56		
Water (liter)		195		

#### 5. CONCLUSIONS

The paper proposes three artificial neural network models that allow predicting the compressive strength of concrete using ingredient materials in Central Vietnam. The highlight is the reuse of fly ash and stone powder waste products. The inputs of ANN models are concrete mixtures, ultrasonic pulse velocity (UPV), and amplitude attenuation ratio. These models allow predicting the compressive strength of concrete at 28 days within the range of 8.65-62.13MPa (86.5- 621.3daN/cm<sup>2</sup>).

The outstanding advantage of the built neural network model is that it can predict the compressive strength for

any concrete mixture. It is significant when it is necessary to evaluate the compressive strength provided by the concrete supplier. Then, with the concrete manufacturer's known concrete mix, while ultrasonic pulse velocity and amplitude attenuation ratio were experimentally measured, using the built ANN model, it is easy to predict the compressive strength of concrete.

## 6. ACKNOWLEDGEMENTS

This work was supported by the University of Science and Technology, The University of Danang, under code number of project: T2021-02-20.

## 7. REFERENCES

1. Nguyen Ngoc, L., "Recycling of aac waste in the manufacture of autoclaved aerated concrete in vietnam", *GEOMATE Journal*, Vol. 20, No. 78, (2021), 128-134, doi: 10.21660/2021.78.j2048.
2. Van Nguyen, C., Lambert, P. and Hung Tran, Q., "Effect of vietnamese fly ash on selected physical properties, durability and probability of corrosion of steel in concrete", *Materials*, Vol. 12, No. 4, (2019), doi: 10.3390/ma12040593.
3. Tran, H.-B., Le, V.-B. and Phan, V.T., "Mechanical properties of high strength concrete containing nano SiO<sub>2</sub> made from rice husk ash in southern vietnam", *Crystals*, Vol. 11, No. 8, (2021), doi: 10.3390/cryst11080932.
4. Teixeira, E.R., Camões, A., Branco, F.G., Aguiar, J.B. and Figueiro, R., "Recycling of biomass and coal fly ash as cement replacement material and its effect on hydration and carbonation of concrete", *Waste Management*, Vol. 94, (2019), 39-48, doi: 10.1016/j.wasman.2019.05.044.
5. Hafez, H., Kurda, R., Cheung, W.M. and Nagaratnam, B., "Comparative life cycle assessment between imported and recovered fly ash for blended cement concrete in the uk", *Journal of Cleaner Production*, Vol. 244, (2020), 118722, doi: 10.1016/j.jclepro.2019.118722.
6. Kanthe, V., Deo, S. and Murmu, M., "Combine use of fly ash and rice husk ash in concrete to improve its properties (research note)", *International Journal of Engineering, Transactions A: Basics*, Vol. 31, No. 7, (2018), 1012-1019, doi: 10.5829/ije.2018.31.07a.02.
7. Sadowski, Ł., Piechówka-Mielnik, M., Widziszowski, T., Gardynik, A. and Mackiewicz, S., "Hybrid ultrasonic-neural prediction of the compressive strength of environmentally friendly concrete screeds with high volume of waste quartz mineral dust", *Journal of Cleaner Production*, Vol. 212, No., (2019), 727-740, doi: 10.1016/j.jclepro.2018.12.059.
8. Shariq, M., Prasad, J. and Masood, A., "Studies in ultrasonic pulse velocity of concrete containing ggbfs", *Construction and Building Materials*, Vol. 40, (2013), 944-950, doi: 10.1016/j.conbuildmat.2012.11.070.
9. Jin, R., Yan, L., Soboyejo, A.B.O., Huang, L. and Kasal, B., "Multivariate regression models in estimating the behavior of frp tube encased recycled aggregate concrete", *Construction and Building Materials*, Vol. 191, (2018), 216-227, doi: 10.1016/j.conbuildmat.2018.10.012.
10. Trtnik, G., Kavčič, F. and Turk, G., "Prediction of concrete strength using ultrasonic pulse velocity and artificial neural networks", *Ultrasonics*, Vol. 49, No. 1, (2009), 53-60, doi: 10.1016/j.ultras.2008.05.001.
11. Bogas, J.A., Gomes, M.G. and Gomes, A., "Compressive strength evaluation of structural lightweight concrete by non-destructive ultrasonic pulse velocity method", *Ultrasonics*, Vol. 53, No. 5, (2013), 962-972, doi: 10.1016/j.ultras.2012.12.012.
12. Ashrafian, A., Taheri Amiri, M.J., Rezaie-Balf, M., Ozbakkaloglu, T. and Lotfi-Omran, O., "Prediction of compressive strength and ultrasonic pulse velocity of fiber reinforced concrete incorporating nano silica using heuristic regression methods", *Construction and Building Materials*, Vol. 190, (2018), 479-494, doi: 10.1016/j.conbuildmat.2018.09.047.
13. Shahmansouri, A.A., Yazdani, M., Ghanbari, S., Akbarzadeh Bengar, H., Jafari, A. and Farrokhi Ghatte, H., "Artificial neural network model to predict the compressive strength of eco-friendly geopolymer concrete incorporating silica fume and natural zeolite", *Journal of Cleaner Production*, Vol. 279, (2021), 123697, doi: 10.1016/j.jclepro.2020.123697.
14. Vuong, L.T., Le, C. and Nguyen, D.S., "Prediction of compressive strength of concrete using recycled materials from fly ash based on ultrasonic pulse velocity and design of experiment", in *Computational Intelligence Methods for Green Technology and Sustainable Development*, Cham, Springer International Publishing., (2021), 600-612.
15. Zhang, Y., Aslani, F. and Lehane, B., "Compressive strength of rubberized concrete: Regression and ga-bpnn approaches using ultrasonic pulse velocity", *Construction and Building Materials*, Vol. 307, (2021), 124951, doi: 10.1016/j.conbuildmat.2021.124951.
16. Tenza-Abril, A.J., Villacampa, Y., Solak, A.M. and Baeza-Brotons, F., "Prediction and sensitivity analysis of compressive strength in segregated lightweight concrete based on artificial neural network using ultrasonic pulse velocity", *Construction and Building Materials*, Vol. 189, (2018), 1173-1183, doi: 10.1016/j.conbuildmat.2018.09.096.
17. Ranjbar, A., Barahmand, N. and Ghanbari, A., "Hybrid artificial intelligence model development for roller-compacted concrete compressive strength estimation", *International Journal of Engineering, Transactions A: Basics*, Vol. 33, No. 10, (2020), 1852-1863, doi: 10.5829/ije.2020.33.10a.04.
18. Heidari, A. and Hashempour, M., "Investigation of mechanical properties of self compacting polymeric concrete with backpropagation network", *International Journal of Engineering, Transactions C: Aspects*, Vol. 31, No. 6, (2018), 903-909, doi: 10.5829/ije.2018.31.06c.06.

## APPENDIX

**TABLE A1.** Designation of mixture, ultrasonic pulse velocity (UPV), amplitude attenuation ratio ( $A_1/A_1$ ), and compressive strength ( $f_c$ )

Mixture	Designation of mixture	Fine aggregate (A), kg/m <sup>3</sup>			Gravel (B) kg/m <sup>3</sup>	Binder (C) (kg/m <sup>3</sup> )			Water (D) liter	UPV (m/s)	Amplitude attenuation ratio	Compressive strength
		Sand (80%)	Stone (20%)	Total (100%)		Cement (80%)	Fly ash (20%)	Total (100%)			$A_2/A_1$	$f_c$ (daN/cm <sup>2</sup> )
1	A1B1C1D1	512	128	640	1100	172.8	43.2	216	190	4250	0.074	144.7
2	A1B1C1D2	512	128	640	1100	172.8	43.2	216	210	4055	0.112	108.1
3	A1B1C1D3	512	128	640	1100	172.8	43.2	216	230	3935	0.093	90.4
4	A1B1C2D1	512	128	640	1100	255.2	63.8	319	190	4495	0.472	315.8
5	A1B1C2D2	512	128	640	1100	255.2	63.8	319	210	4360	0.347	215.4
6	A1B1C2D3	512	128	640	1100	255.2	63.8	319	230	4355	0.128	193.9
7	A1B1C3D1	512	128	640	1100	337.6	84.4	422	190	4695	0.390	447.5
8	A1B1C3D2	512	128	640	1100	337.6	84.4	422	210	4560	0.309	403.3
9	A1B1C3D3	512	128	640	1100	337.6	84.4	422	230	4515	0.453	317.7
10	A1B1C4D1	512	128	640	1100	420	105	525	190	4715	0.618	545.7
11	A1B1C4D2	512	128	640	1100	420	105	525	210	4675	0.194	553.3
12	A1B1C4D3	512	128	640	1100	420	105	525	230	4520	0.308	467.0
13	A1B2C1D1	512	128	640	1200	172.8	43.2	216	190	4440	0.051	152.3
14	A1B2C1D2	512	128	640	1200	172.8	43.2	216	210	4215	0.016	103.3
15	A1B2C1D3	512	128	640	1200	172.8	43.2	216	230	4185	0.034	95.2
16	A1B2C2D1	512	128	640	1200	255.2	63.8	319	190	4690	0.021	121.4
17	A1B2C2D2	512	128	640	1200	255.2	63.8	319	210	4525	0.088	246.1
18	A1B2C2D3	512	128	640	1200	255.2	63.8	319	230	4465	0.054	220.4
19	A1B2C3D1	512	128	640	1200	337.6	84.4	422	190	4760	0.027	354.1
20	A1B2C3D2	512	128	640	1200	337.6	84.4	422	210	4745	0.110	417.0
21	A1B2C3D3	512	128	640	1200	337.6	84.4	422	230	4715	0.205	364.3
22	A1B2C4D1	512	128	640	1200	420	105	525	190	4900	0.097	592.2
23	A1B2C4D2	512	128	640	1200	420	105	525	210	4705	0.408	509.3
24	A1B2C4D3	512	128	640	1200	420	105	525	230	4680	0.499	469.1
25	A2B1C1D1	633.6	158.4	792	1100	172.8	43.2	216	190	4410	0.037	157.1
26	A2B1C1D2	633.6	158.4	792	1100	172.8	43.2	216	210	4120	0.040	120.0
27	A2B1C1D3	633.6	158.4	792	1100	172.8	43.2	216	230	4080	0.062	96.5
28	A2B1C2D1	633.6	158.4	792	1100	255.2	63.8	319	190	4560	0.049	306.2
29	A2B1C2D2	633.6	158.4	792	1100	255.2	63.8	319	210	4485	0.065	242.9
30	A2B1C2D3	633.6	158.4	792	1100	255.2	63.8	319	230	4330	0.025	196.8
31	A2B1C3D1	633.6	158.4	792	1100	337.6	84.4	422	190	4705	0.058	443.9
32	A2B1C3D2	633.6	158.4	792	1100	337.6	84.4	422	210	4680	0.092	373.6
33	A2B1C3D3	633.6	158.4	792	1100	337.6	84.4	422	230	4540	0.050	369.9
34	A2B1C4D1	633.6	158.4	792	1100	420	105	525	190	4775	0.249	539.3
35	A2B1C4D2	633.6	158.4	792	1100	420	105	525	210	4625	0.057	475.6

Mixture	Designation of mixture	Fine aggregate (A), kg/m <sup>3</sup>			Gravel (B) kg/m <sup>3</sup>	Binder (C) (kg/m <sup>3</sup> )			Water (D) liter	UPV (m/s)	Amplitude attenuation ratio	Compressive strength
		Sand (80%)	Stone (20%)	Total (100%)		Cement (80%)	Fly ash (20%)	Total (100%)			A <sub>2</sub> /A <sub>1</sub>	f <sub>c</sub> (daN/cm <sup>2</sup> )
36	A2B1C4D3	633.6	158.4	792	1100	420	105	525	230	4445	0.235	457.0
37	A2B2C1D1	633.6	158.4	792	1200	172.8	43.2	216	190	4245	0.076	179.6
38	A2B2C1D2	633.6	158.4	792	1200	172.8	43.2	216	210	3945	0.070	106.2
39	A2B2C1D3	633.6	158.4	792	1200	172.8	43.2	216	230	3905	0.102	107.6
40	A2B2C2D1	633.6	158.4	792	1200	255.2	63.8	319	190	4490	0.144	304.8
41	A2B2C2D2	633.6	158.4	792	1200	255.2	63.8	319	210	4310	0.036	243.2
42	A2B2C2D3	633.6	158.4	792	1200	255.2	63.8	319	230	4260	0.143	184.5
43	A2B2C3D1	633.6	158.4	792	1200	337.6	84.4	422	190	4630	0.195	487.7
44	A2B2C3D2	633.6	158.4	792	1200	337.6	84.4	422	210	4500	0.109	387.6
45	A2B2C3D3	633.6	158.4	792	1200	337.6	84.4	422	230	4510	0.083	333.4
46	A2B2C4D1	633.6	158.4	792	1200	420	105	525	190	4650	0.189	461.7
47	A2B2C4D2	633.6	158.4	792	1200	420	105	525	210	4550	0.116	322.1
48	A2B2C4D3	633.6	158.4	792	1200	420	105	525	230	4505	0.161	483.4
49	A3B1C1D1	755.2	188.8	944	1100	172.8	43.2	216	190	4105	0.084	166.8
50	A3B1C1D2	755.2	188.8	944	1100	172.8	43.2	216	210	3975	0.082	120.8
51	A3B1C1D3	755.2	188.8	944	1100	172.8	43.2	216	230	3720	0.082	93.8
52	A3B1C2D1	755.2	188.8	944	1100	255.2	63.8	319	190	4445	0.119	294.7
53	A3B1C2D2	755.2	188.8	944	1100	255.2	63.8	319	210	4285	0.097	269.7
54	A3B1C2D3	755.2	188.8	944	1100	255.2	63.8	319	230	4175	0.137	219.9
55	A3B1C3D1	755.2	188.8	944	1100	337.6	84.4	422	190	4580	0.084	467.3
56	A3B1C3D2	755.2	188.8	944	1100	337.6	84.4	422	210	4620	0.100	417.8
57	A3B1C3D3	755.2	188.8	944	1100	337.6	84.4	422	230	4495	0.113	394.5
58	A3B1C4D1	755.2	188.8	944	1100	420	105	525	190	4645	0.143	365.8
59	A3B1C4D2	755.2	188.8	944	1100	420	105	525	210	4555	0.118	514.9
60	A3B1C4D3	755.2	188.8	944	1100	420	105	525	230	4455	0.045	392.2
61	A3B2C1D1	755.2	188.8	944	1200	172.8	43.2	216	190	4135	0.028	152.9
62	A3B2C1D2	755.2	188.8	944	1200	172.8	43.2	216	210	3965	0.033	118.2
63	A3B2C1D3	755.2	188.8	944	1200	172.8	43.2	216	230	3765	0.010	86.5
64	A3B2C2D1	755.2	188.8	944	1200	255.2	63.8	319	190	4415	0.016	313.0
65	A3B2C2D2	755.2	188.8	944	1200	255.2	63.8	319	210	4370	0.012	261.4
66	A3B2C2D3	755.2	188.8	944	1200	255.2	63.8	319	230	4215	0.042	228.0
67	A3B2C3D1	755.2	188.8	944	1200	337.6	84.4	422	190	4540	0.194	478.1
68	A3B2C3D2	755.2	188.8	944	1200	337.6	84.4	422	210	4460	0.105	477.2
69	A3B2C3D3	755.2	188.8	944	1200	337.6	84.4	422	230	4400	0.032	383.4
70	A3B2C4D1	755.2	188.8	944	1200	420	105	525	190	4555	0.175	621.3
71	A3B2C4D2	755.2	188.8	944	1200	420	105	525	210	4525	0.057	466.8
72	A3B2C4D3	755.2	188.8	944	1200	420	105	525	230	4520	0.039	519.6

---

**Persian Abstract**

---

**چکیده**

در مرکز ویتنام، مواد سنتی برای ساخت بتن معمولاً منشأ طبیعی دارند. بهره برداری بیش از حد از این مواد اثرات نامطلوب زیادی بر محیط طبیعی ایجاد می کند. کارخانه ها و معادن صنعتی محلی میلیون ها تن مواد زائد مانند خاکستر بادی و پودر سنگ تولید می کنند. با این حال، هنگامی که برای جایگزینی جزئی سیمان و ماسه استفاده می شود، این مواد زائد می توانند بر مقاومت فشاری بتن تأثیر بگذارند. بنابراین ساخت مدل هایی برای پیش بینی مقاومت فشاری این نوع بتن ضروری است. هدف این مقاله استفاده از مدل های شبکه عصبی مصنوعی برای پیش بینی مقاومت فشاری بتن با استفاده از خاکستر بادی و مواد زائد پودر سنگ بود. ورودی مدل ANN شامل شش پارامتر است: سرعت پالس اولتراسونیک، نسبت تضعیف دامنه موج و ۴ پارامتر مصالح بتن. داده های تجربی از ۷۲ نمونه مکعبی از مخلوط های مختلف با استفاده از مواد موجود در ویتنام مرکزی به دست آمد. این مدل ها امکان پیش بینی مقاومت فشاری ۲۸ روزه بتن را در محدوده (90-620daN/cm<sup>2</sup>) ۹-۶۲ MPa فراهم می کنند. علاوه بر این، این مدل ها می توانند مقاومت فشاری را با هر مخلوطی پیش بینی کنند. هنگام ارزیابی مجدد اینکه آیا مقدار مقاومت فشاری واقعی به اندازه مقدار ارائه شده توسط سازنده قابل اعتماد است یا خیر، مهم است.

---



# Understanding the Effect of Interfacial Interphase on the Elastic Response of Hollow Glass Microsphere Reinforced Microcomposites

M. Karevan\*

Department of Mechanical Engineering, Isfahan University of Technology, Isfahan, 84156-83111, Iran

## PAPER INFO

### Paper history:

Received 31 December 2021

Received in revised form 05 February 2022

Accepted 09 February 2022

### Keywords:

Hollow Glass Microsphere Young's Modulus

Micromechanics

Halpin-Tsai

Micro-composite

Interphase

## ABSTRACT

The hollow glass microspheres (HGMS) has been recently used in the fabrication of low-density polymeric composites due to rather high stiffness nature of the fillers together with their lightweight that in turn results in the development of micro-composites of engineered properties with enhanced mechanical properties. Interfacial interactions at the filler/polymer interface control the load transfer and, thus, bulk properties of composites leading to unpredictable performance of composites embedded with inclusions. Nevertheless, useful analytical models are required to estimate the mechanical behavior of the HGMS based composites with the incorporation of the effect of interfacial interactions and possible agglomeration of fillers. No studies so far have reported the analytical modeling of HGMS reinforced thermosetting composites emphasizing the role of the interphase shaped at the vicinity of fillers. This study aims at the fabrication of 0-20 wt% HGMS/polyester micro-composites followed by micromechanical modeling of the fabricated parts whilst the effect of the interphase region is emphasized by models modification. The results indicated a strong correlation between the interphase characteristics and Young's modulus of the specimens revealing the dependency of the modulus on the thickness and modulus of the interphase as well as the level of agglomeration and interfacial debonding of the HGMSs. The results demonstrated that with considering no interphase, the models underestimate the modulus of the parts, which suggests the presence of stiff interphase around the HGMS governed by changes in the interfacial cross-link density of the parent polymer as hypothesized supported by the mechanical response of the parts.

doi: 10.5829/ije.2022.35.05b.13

## NOMENCLATURE

$A_i$	Constants used on Eshelby's tensor	$f$	Fillers volume fraction (%)
$d$	Filler diameter (mm)	$l$	Filler length (mm)
$E_{11}$	Composite elastic modulus (GPa)	<b>Greek Symbols</b>	
$E_C$	Composite elastic modulus (GPa)	$\zeta$	Shape factor in Halpin-Tsai relation, $l/d$
$E_f$	Filler tensile modulus (GPa)	$\eta$	Halpin-Tsai constant as a function of modulus and shape factor
$E_i$	Interphase tensile modulus (GPa)	$\nu_m$	Matrix Poisson's ratio
$E_m$	Matrix tensile modulus (GPa)	$\eta$	Halpin-Tsai constant as a function of modulus and shape factor

## 1. INTRODUCTION

The fabrication of lightweight high stiff composites has drawn increasing attention due to their extensive applications mainly due to the energy conservation aspects, the decrease in the processing costs and energy consumption during the processing. Therefore, the

development of lightweight thermosetting composites with no or minimal decrease in their mechanical properties has drawn a great body of interest due to their broad applications in structures, automotive industries or energy sectors [1, 2]. However, due to the presence of multiple variables such as the interfacial interactions at the surface of filler, the agglomeration of fillers and the

\*Corresponding Author Institutional Email: [mkarevan@iut.ac.ir](mailto:mkarevan@iut.ac.ir)  
(M. Karevan)

modified properties of the polymers at the surface of the fillers, the eventual mechanical properties of reinforced polymers cannot be easily predicted through analytical or computational tools. Interfacial interactions either repulsive or attractive can modify the physical properties of polymer chains at the interface of filler/polymer and, thus, result in either an imperfect or strong bonding at the contact of filler/polymer, respectively [3].

Most often, attractive interactions lead to the generation of a third stiff layer called “interphase” that is responsible for the quality of load transfer from the matrix to the filler. The interactions, moreover, may result in the formation of the agglomeration phase which suppresses the mechanical properties of the reinforced composites [4, 5]. One main challenge still existing is the unknown properties of the interphase for many composite systems as the thickness and mechanical properties of the interphase are remarkably material specific. In addition, the small size of the interphase requires sophisticated and advanced techniques for its accurate characterization [6]. The latter would lead to even more issues in the incorporation of the interphase as a second mechanism into modeling tools [7].

The challenges arise when, for reliable characterization, the lack of any filler/polymer shear slippage, filler debonding and additional voids, micro-cracks and imperfections at the interface is assumed [8, 9]. Such phenomena significantly result in mechanical response exhibited by nano/micro-composites that cannot be easily predicted or engineered through even extensive experimental observations [10, 11]. Therefore, for a better understanding of the effect of interfacial interactions on mechanical performance of composites, although micromechanical models have been frequently employed, there is a need for approaches through which the effect of the interactions could be assessed.

Based on previous studies, numerous thermosetting-based composite systems have been designed and developed using micro size fillers from metal oxides, carbon-based materials to natural fibers [12, 13]. It could be consequently understood that the utilization of glass based reinforcements has been widely reported in the enhancement of mechanical properties of composites [14, 15]. Although this body of research reveals the dependence of mechanical and physical behavior thermosetting composites reinforced with fillers, the use of the hollow glass microspheres (HGMSs) as lightweight high stiff reinforcements has been rarely reported in respect of the elastic response of polyester-based composites filled with HGMS as the reinforcement [16]. In one study, Chen et al. [17] reported the use of HGMSs coated with silver particle aiming at the fabrication of electrically conductive microspheres to be employed as one of the reinforcement phase in epoxy-based liquid molded composites. The composites exhibited electromagnetic interference shielding

properties whilst the HGMSs acted as materials to fill up the vacancies generated by the network of carbon fibers. Jiang et al. [18] have recently revealed their work on the use of HGMSs in reinforcing expanded polystyrene (EPS) and epoxy resin (EP) to develop compression molded foam balls of enhanced compressive strength. In another study, Altay et al. [19] incorporated HGMSs together with polystyrene (PS) microfiber membrane to examine the effect of HGMSs on the thermal insulation and sound absorption insulation behavior of glass fiber fabric-reinforced epoxy composites. Moreover, no research has been reported on the correlations amongst the elastic performance of the HGMS reinforced thermosetting micro-composites emphasizing the effect of interphase [20, 21]. To do so, this study aims at the analytical modeling of 0-20 wt% HGMS reinforced polyester micro-composites using the Halpin-Tsai and Tandon-Weng models accounting for the interphase thickness and elastic modulus for a better understanding of the role of the reinforcing mechanism, the interphase, in overall tensile behavior of the HGMSs based micro-composites.

To examine the interphase impact on the elastic modulus of the fabricated parts, tensile testing was performed and the moduli of the composites were compared with the models' predictions. Upon parametric changes in the interphase properties, best result fitting based on the experimental values was determined and possible links with the interfacial modification of the polyester matrix such as degree of cross-links at the surface of HGMS and the possible presence of agglomeration phase as an adverse clustered region at higher filler loading were discussed.

## 2. EXPERIMENTAL

**2. 1. Material** Industrial-grade HGMS was used as the micro-reinforcement with the density of 0.38 g/cm<sup>3</sup>, the modulus of 1.99 GPa and an approximate diameter of ~30-40 μm. An industrial-grade polyester thermoset resin was used as the polymer matrix. The resin components of hardener and catalyst were mixed as described by the manufacturer. Figure 1 represents the SEM image of the fractured surface of polyester composites reinforced with HGMS illustrating the surface morphology and the average size of the HGMS fillers.

**2. 2. Fabrication of HGMS/Polyester Micro-composites** Micro-composites of polyester resin reinforced with 0 to 20 wt% of as-received HGMS were fabricated using direct mixing of the fillers within the resin utilizing a high shear mixer (HSM) consisting a rotor/stator mechanism at 3000 rpm for 30 minutes. The mixture of resin/hardener/catalyst was then mixed and cast into silicon molds per the ASTM standard required

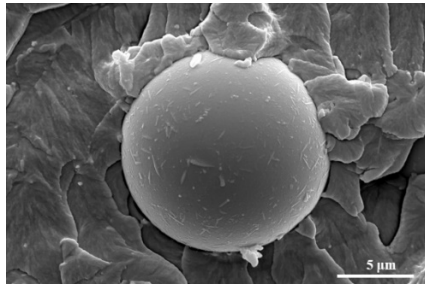


**Figure 1.** SEM image of a single HGSM particle exposed from the surface of HGMS/polyester composites

for each test near its gel time to avoid HGMS floating onto the surface of the resin due to its lightweight. To fabricate specimens, the curing process was performed at the ambient condition taking  $\sim 24$  hours for the specimens to be cured. No surface modification of HGMSs was used in the fabrication process of the current study [22]. The summary of the fabrication route and dispersion technique is given in Table 1.

## 2. 3. Characterization of HGMS/Polyester Composites

**2. 3. 1. Tensile Properties** To understand the effect of HGMSs on the tensile response of the composites including Young's modulus and tensile strength, tensile testing was performed per to the ASTM D638 test method using a universal tensile testing machine (Sanaf Co., Iran).

Three tensile test specimens were used in the case of each composite system and at least an average of two specimens were reported. The tensile values were obtained at the deformation rate (stroke speed) of 2.54 mm/min at the ambient temperature. The slope of stress-strain curve over the linear region was used to determine the modulus of the samples and the highest point on the curves were as the tensile strength of the composites.

**2. 3. 2. Impact Measurement** The Izod impact resistance of the composites was measured according to the ASTM D256 using an Impact machine (Sanaf Co.,

Iran). At least three specimens were used for the impact resistance performance of each composite system and the average and standard deviation were reported. The test was performed to better correlate the presence of stiffer interphase with the assumptions used in the incorporation of the interphase into the modeling techniques used.

**2. 3. 3. Drop Weight Testing** HGMS reinforced composites of  $120 \times 120 \times 10$  mm<sup>3</sup> were fabricated to conduct the drop-weight analysis. A digital drop testing system based on the changes on the deflection of a single cantilever beam load-cell and electric out-put current of strain gages on a Whetstone Bridge was used for assessing the toughness of the parts. The system works in such a way that upon damage onto the specimens, a fraction of the potential energy applied is absorbed by the parts and the rest of the energy is to be transferred to the loadcell. The energy received by the cantilever leads to the deflection of the beams to be a measure of the absorbed energy by the composites in a differential manner.

## 2. 3. 4. Scanning Electron Microscopy (SEM) Studies

The morphology, HGMS/polyester bonding conditions, dispersion quality and microstructure of the fractured surface of the composites were evaluated on a FE-SEM (QUANTA FEG 450-USA). The surface of the SEM composite samples cut from the fractured surface of the composites was gold sputtered before the analysis to eliminate electron charging effects created by the non-conductive nature of the polymer-based specimens.

## 3. MICROMECHANICAL APPROACH

To understand the effect of interactions on the elastic response of HGMSs reinforced composites, micromechanical models were utilized emphasizing the role of the interphase properties [23]. Assumptions including the perfect dispersion and distribution of HGMSs, linear elastic properties of the filler and matrix, isotropic properties of the constituents were made. The aspect ratio of HGMSs was assumed to be  $\sim 1$  as the fillers with spherical geometry as clearly demonstrated in Figure 1. Moreover, it was assumed that perfect interfacial bonding exists at the interface of HGMSs/polyester as one main factor, although this assumption proved to be invalid at higher fillers content due to weakened interfacial strength. Therefore, it was assumed that any debonding conditions and micro-voids resulting in shear slippage of agglomerated phase are not generally present in the bulk micro-composites as confirmed by the SEM image represented in Figure 2. It is illustrated in this study upon the addition of further HGMS loadings, interfacial debonding is likely due to

**TABLE 1.** Fabrication process specification

Parameter	Value
HSM rotational speed	3000 (rpm)
HSM diameter	20 (mm)
Mixing time	30 (minutes)
Curing time	24 (hours)
Curing temperature	ambient
Mold cavity dimension	$120 \times 120 \times 10$ mm <sup>3</sup>
	$3.2 \times 12 \times 70$ mm <sup>3</sup>

the suppressed wettability of the polymer due to excess surface area of the fillers to be wetted by the polyester resin. In the current study, three analytical models were employed to examine the effect of the interphase.

The Halpin-Tsai (H-T) model and Tandon-Weng extracted from Eshelby's tensor components first introduced in the case of ellipsoidal particles into an infinite matrix were used as the modeling technique [24].

Required modifications were considered to incorporate the interphase modulus and thickness per to a parametric study using the core-shell concept as the interphase acts like the matrix for the filler. The properties of a single entity homogenized filler being a new filler previously consisting of a filler and surrounding matrix, thus, were approximated using the micromechanical models. In addition, as the models are normally utilized in the case of short-fibers and function more accurately for inclusions of considerable aspect ratios, the rule of mixtures (ROM) was also used for the case of comparison to understand the reinforcing effect of the filler/interphase entity embedded in the polyester. The Halpin-Tsai equations used for the estimation of Young's modulus of the composites are expressed as the following equation [25]:

$$E_c = E_m \left( \frac{1+\zeta\eta f}{1-\zeta f} \right) \quad (1)$$

where

$$\eta = \frac{\left( \frac{E_f}{E_m} \right) - 1}{\left( \frac{E_f}{E_m} \right) + \zeta} \quad (2)$$

in which  $E_f$ ,  $E_m$  and  $E_c$  are Young's modulus of the fillers, matrix and the composites, respectively and  $f$  the fillers volume fraction.

$\xi = 2 \frac{l}{d}$  is to be  $\sim 2$  in the case of spherical particles.  $\xi$  is a correction factor depending upon the shape and geometry of fillers reportedly exists in the literature [26]. Tandon-Weng (T-W) explicit model initially introduced based on the Mori-Tanaka method was used to compare the modeling results with those represented by the experimental observations and the H-T model. The

Tandon-Weng model can be described as the equation below [26, 27]:

$$\frac{E_{11}}{E_m} = \frac{1}{1+f(A_1+2\nu_m A_2)/A'} \quad (3)$$

where  $E_{11}$  is the longitudinal Young's modulus in the direction of fibers/fillers,  $\nu_m$  the Poisson's ratio of the polyester in this study and  $A$  constants were obtained using the Eshelby's tensor depending on the aspect ratio, Poisson's ratio of the matrix as well as the elastic Lamé constants of the filler and matrix. The Young's modulus of the HGMSs was assumed to be 1.99 GPa based on the literature [28] and industrial-grade fillers. The modulus of 4.54 GPa for the neat polyester based on the experimental testing results, the density of 1.23 and 0.38 g/mm<sup>3</sup> based on the densitometry results and the manufacturer datasheet, respectively, and 0.23 and 0.40 as the Poisson's ratio of the HGMSs and the polyester-based on the literature values and manufacturer were used. The Lamé constants were used based on the elasticity theory in respective constituents from literature as needed unless otherwise mentioned.

The hypothesis is that the vol% of the interphase region is significantly governed by the interphase thickness, the geometry of fillers and the agglomeration phase accordingly resulting in variations in the modulus of HGMS/polyester composites. To examine the effect of the ratio of interphase vol% to that of the filler, the interphase thickness was estimated to vary from 1 to 8  $\mu\text{m}$  based on reasonable values reported in the case of micro-reinforced composites in literature [29]. The effect of interphase modulus, thus, was evaluated using the assumed values whilst the generation of a stiffer interphase compared to that of the matrix was hypothesized based on the experimental tensile moduli. In all cases, simultaneous variations in the interphase modulus as well as the changes in the interphase thickness were taken into account. It is pointed out that multiple variables exist to be considered in the

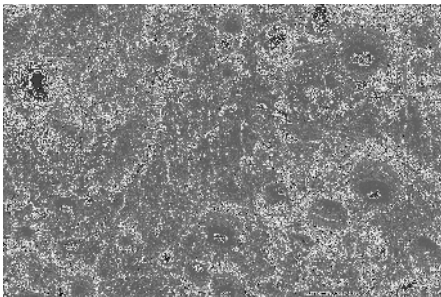


**Figure 2.** SEM image of the fractured surface of HGMS/polyester representing bonding conditions of HGMS/polyester

**TABLE 2.** Summary of the values used in the micromechanical modeling of the composites

Parameter	Value
HGMS diameter	30 ( $\mu\text{m}$ )
HGMS modulus	1.99 (GPa)
HGMS density	0.38 (g/mm <sup>3</sup> )
HGMS wt. %	0-20
HGMS aspect ratio	$\sim 1$
Interphase thickness	0-8 ( $\mu\text{m}$ )
Interphase modulus	2-15 (GPa)
Neat polyester modulus	4.54 (GPa)
Neat polyester density	1.23 (GPa)

incorporation of the interphase region into the analytical models. However, the thickness and modulus of this region are markedly affected by the interfacial strength and, thus, are taken into consideration as underlying parameters. Table 2 summarizes the parametric and experimental values employed in the micromechanical modeling of the HGMS/polyester composites.

## 4. RESULTS AND DISCUSSION

**4. 1. Tensile Properties** Figure 3 illustrates the tensile properties of polyester composites reinforced with 0-20 wt% of HGMS. As understood from the results, addition of HGMS results in a sharp decrease in the tensile strength whilst an increase in the modulus is observed. The decrease in the tensile strength as shown in Figure 3a is attributed to the highly porous nature of the fabricated parts with lower packing density and integrity of the specimens. It is hypothesized that an increase in the observed modulus as revealed in Figure 3b is correlated to the increased degree of interfacial cross- links generated at the filler surface and, thus, the enhanced stiffness of the composites. It is suggested that due to the lower Young's modulus of the HGMSs used compared to that of polyester, the second mechanism of reinforcement contributes to an increase in the modulus. However, upon the addition of HGMS up to the 12 wt% loadings, the modulus reaches a plateau suggesting the presence of opposing effects such as the formation of HGMSs agglomeration at higher loadings resulting in the decrease in the effective interfacial bonding and, thus, the interphase quality [5]. The latter is believed to decrease the shear resistance of the bulk composites as a result of weaker filler's wettability and, thus, suppressed load transfer at the interface of HGMSs and polyester matrix [30].

**4. 2. Impact Behavior of the Composites** The impact response of the specimens as a function of the HGMS wt% is demonstrated in Figure 4. As shown, the impact resistance of the composites experiences an overall increase with addition of filler content reaching an optimum value at 10 wt% of HGMSs. The observations could be ascribed to the generation of the greater volume of stiff interphase around the fillers as the HGMSs containing hollow structures cannot be essentially considered as a contributing phase to the enhanced impact performance of the composites. The hypothesis of stiffer interphase concerning the parent polymer matrix is interrelated to the polymer chains of cross-linking nature with significant growth in the degree of chains immobilization. The formation of constrained chains is thought to be occurred due to the presence of attractive interfacial forces, chains mechanical interlocking due to the fillers surface adsorption effect

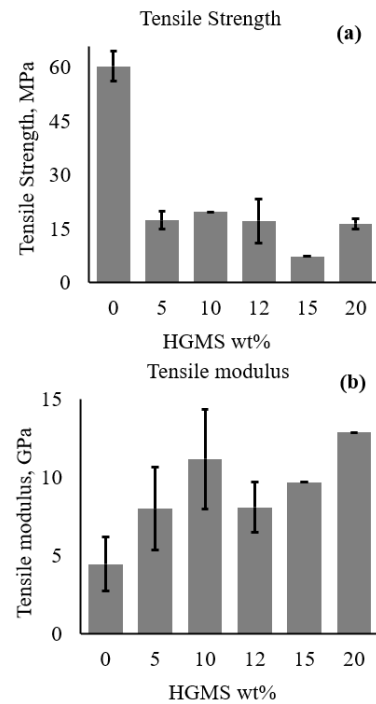


**Figure 3.** (a) Tensile strength and (b) tensile modulus of HGMS reinforced micro-composites as a function of HGMS loading

and interfacial van der Waals forces [31, 32]. The decrease in the results beyond this filler content is attributed to the increased agglomeration of the HGMS phase resulting from several competing factors. First, it is widely believed that at higher filler ratios, there is a lack of enough polymer available to wet the surface of fillers due to the extensive surface of fillers compared to that of polymer resin. Moreover, the agglomeration phase not only encourages crack propagation through the cluster phase with no polymer bonding, but also the agglomerated region leads to a decrease in effective interfacial interactions and, consequently, lowered interphase properties in terms of thickness and modulus [33].

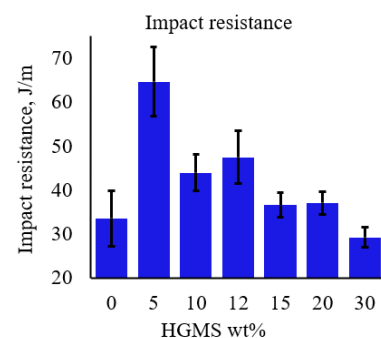


**Figure 4.** Impact resistance of HGMS filled micro-composites

**4. 3. Toughness Performance of HGMS/Polyester Composites**

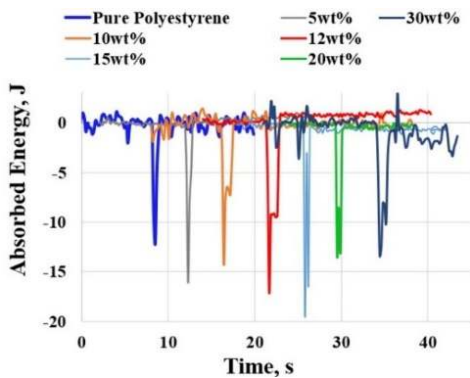
The HGMS/polyester composites energy consumption obtained from the drop weight impact as a measure of the toughness against the HGMS content is displayed in Figure 5. It is clearly understood from the figure that the addition of HGMSs into the polyester leads to an overall enhancement in the toughness exhibiting the greatest values in the case of composites at 12-15 wt% of HGMS loading. The findings support the creation of a stronger interfacial bonding and hence the formation of interphase with a stiffer nature compared to the neat polyester as earlier confirmed by the impact test results. As clearly understood, the results are in good agreement with the tensile response and impact performance of the parts where the presence of agglomeration phase at higher HGMSs loading adversely influences the toughness of the fabricated composites due to the factors discussed earlier.

**4. 4. Micromechanical Predictions**

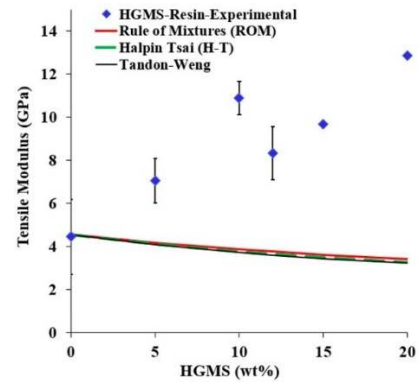
Figure 6 illustrates the micromechanical results predicted by the models compared to the experimental moduli. It is clearly shown that unmodified models underestimate the elastic modulus, which is ascribed to the lower modulus of the HGMS than that of the neat polyester. The presence of stiffer interphase is hypothesized. It is revealed by the findings as the aspect ratio of the fillers is  $\sim 1$ , the moduli are predicted the same regardless of the model used.

Several factors further contribute to the models underestimation including inadequate load transfer in the case of spherical particles, the assumption of uniform distribution of fillers in the matrix and perfect filler/polymer interfacial bonding.

Figures 7a to 7d depict the effect of incorporating the interphase of varying thickness while its modulus changes from 2 to 15 GPa. It is well defined that after the increase in the modulus beyond 12 GPa, the models start predicting more accurately concerning the experimental

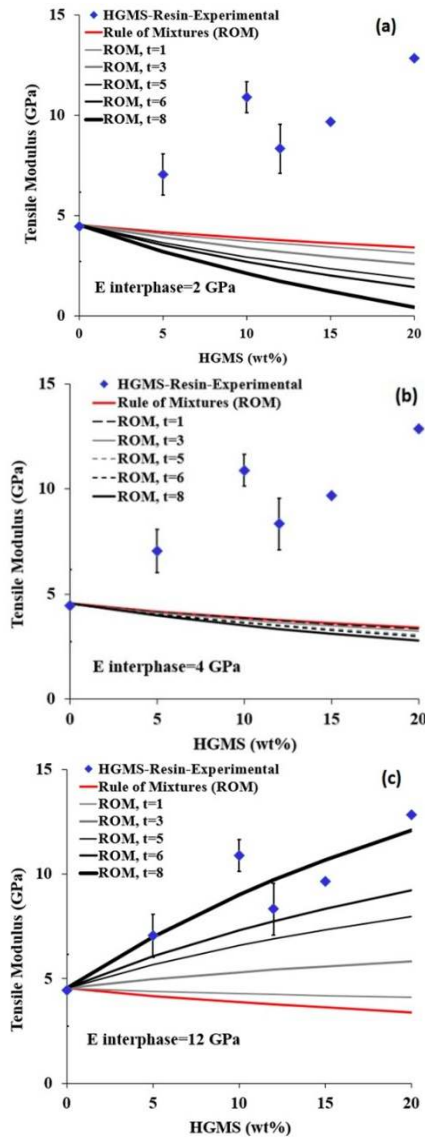


**Figure 5.** Drop weight energy absorption vs. time on based on absorbed energy difference. The downward peaks represent maximum energy absorbed upon damage by the specimens



**Figure 6.** Modeling predictions as a function of HGMS wt%

values and the increase is more intensified as the interphase thickness increases.



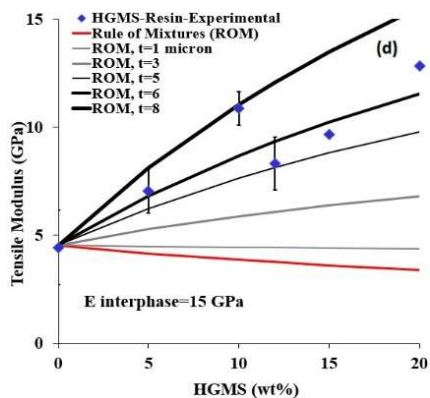


**Figure 7.** Modeling predictions as a function of HGMS wt% and interphase thickness in  $\mu\text{m}$  and modulus of: (a) 2, (b) 4, (c) 12, and (d) 15 GPa

The findings are correlated to and support the occurrence of a stiffer interfacial region as a result of an enhanced degree of cross-links at the vicinity of the HGMS surface forming stiff interphase. As mentioned earlier, a core-shell technique was employed to incorporate the interphase into the models. As expected with the addition of an interfacial phase surrounding the HGMSs, the overall elastic properties of the matrix changes resulting from the neat matrix replaced by either softer (at the interphase modulus of 2 GPa) or stiffer (at the interphase modulus of 15 GPa) material. Beside this phenomenon, as the interphase region of a given thickness occupies the neat matrix, the resulted shell material around the HGMS is expected to contribute to the overall modulus of the core-shell entity. Consequently, the modulus of the new filler (consisting of the interphase as the shell and the original HGMS as the core) is dramatically influenced by the thickness and the assumed modulus of the interphase.

As shown in Figure 7a, with the increase in the interphase thickness, the overall modulus of the composites is further decreased due to the addition of softer phase (modulus of 2 GPa) compared to the parent matrix (modulus of 4.54 GPa). The finding suggests that the interphase modulus is likely to be greater than 2 GPa based on the experimental value. As represented in Figure 7b, the presence of the interphase adversely contributes to the elastic response of composites. Nevertheless, the interphase thickness exhibits only a slight impact on the modulus as the interphase modulus and that of the neat polyester are comparable. Figures 7c and 7d clearly illustrate that the existence of a stiff interphase compared to the neat matrix not only leads to the enhancement in the modulus of the composites but also results in the sensitivity of the models to the interphase thickness. As discussed earlier, in this case, the interphase region of high modulus replaces the softer matrix, and, consequently, results in a marked improvement in the elastic response of the composites.

As shown in Figure 7d, the impact of interphase thickness on the composites modulus is more intensified when the interphase gains greater degree of elastic properties.

Figures 8a and 8b in addition demonstrate the sensitivity of the models to the interphase thickness (6 and 8  $\mu\text{m}$  represented) whilst the modulus varies. As understood from Figures 7 and 8, the composites modulus is more sensitive to both interphase thickness and modulus at lower HGMS wt%. It could be understood from the modulus curves represented in Figure 9 that there exists a trade-off between the interphase modulus and thickness suggesting that stiffer interphase of lower thickness may virtually lead to the same prediction as thick interphase of lower modulus. However, it is clearly understood from Figure 9 that the modulus predictions are more sensitive to the thickness of the interphase than the modulus resulting in a greater reinforcing efficiency [34]. The findings suggest that even though spherical particles, irrespective of their size, show an aspect ratio of 1, fillers of small diameters might contribute to the more effective interfacial load transfer than those with larger diameters. This effect could be thought of as the enhancement in the surface to volume ratio of fillers and, thus, an increase in overall volume fraction of the created interphase. The effect of the agglomeration phase on the overall elastic response of the fabricated part was also examined to give a better insight

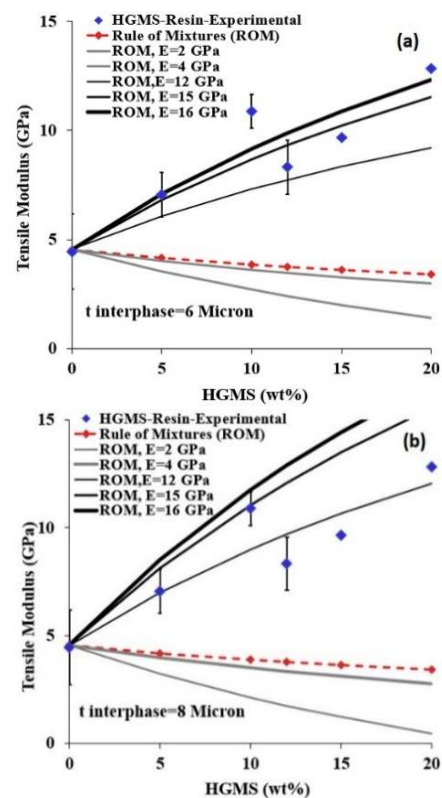


**Figure 8.** Modeling predictions as a function of HGMS wt% and modulus at the thickness of: (a) 6 and (b) 8  $\mu\text{m}$

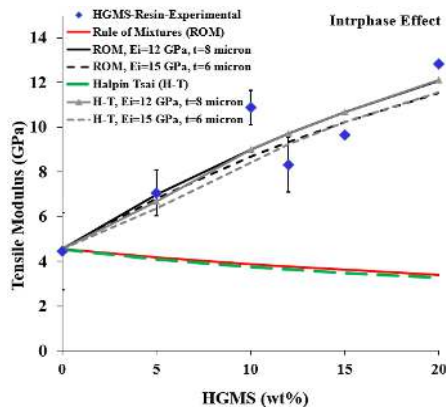


**Figure 9.** Optimized modeling predictions as a function of HGMS wt%

into the effect of interfacial interactions in particular at higher HGMSs loadings. As shown in Figure 10, the level of agglomeration phase was incorporated into the models considering the cluster size based on of a representative SEM image at high filler loading above 20 wt%. It is shown that with the incorporation of no agglomeration, the models somewhat overpredict the modulus depending on the models used (considering interphase); however, with the agglomeration involved, the modified models predict optimally closer to the experimental tensile modulus values. The agglomeration level/size was assumed using the SEM images of the fractured surface considering the equivalent particle size based on an average number of 4 HGMSs within each cluster as shown in Figure 11 (distinguished by circles) as discussed later in this work. It was found that each equivalent radius of HGMS is around 48-50  $\mu\text{m}$  (v.s. 15-20  $\mu\text{m}$  in the case of isolated HGMSs).

**4. 5. Morphological Properties** Figure 11 represents the SEM micrographs of HGMS reinforced polyester micro-composites filled with 3, 10, 20 and 30

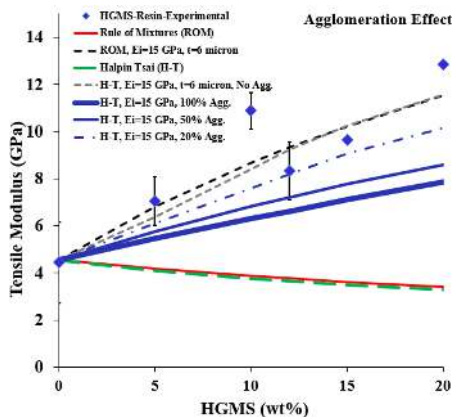


**Figure 10.** Modeling predictions as a function of HGMS wt% and agglomeration level from 0 to 100%

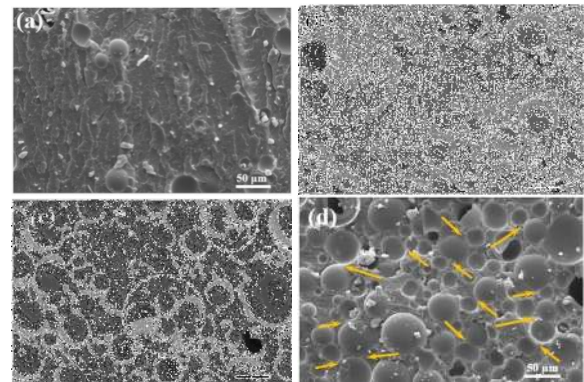


**Figure 11.** SEM fracture surfaced of HGMS/polyester composites filled with HGMS loading of (a) 3 wt% representing isolated single fillers dispersed within the matrix, (b) 10 wt% illustrating grown number density of fillers, (c) 20 wt% suggesting the presence of fillers clusters besides a dispersed phase and (d) 30 wt% as a high ratio filled composites displaying tangential interconnected spherical surface demonstrating lowered wettability of fillers due to their excess surface area compared to available polyester

wt% of the reinforcements. It is revealed that at low fillers loading, there exists uniform dispersion of HGMSs within the matrix illustrated in Figure 11a and composites where the models take into account high-level dispersion of fillers. Nevertheless, with an increase in the filler content, a higher number density of the fillers is observed, which leads to the possible presence of agglomerated phase as shown in Figures 11c and 11d. As reported frequently elsewhere, the existence of the agglomeration phase results in numerous mechanisms shown to be unfavorable to the interfacial load transfer at the filler/polymer matrix. Some factors adversely compete with the reinforcing mechanisms, which, accordingly, lead to the discrepancy between the model's prediction and the experimental elastic behavior of the composites as described in previous parts [35]. First, the agglomeration would result in the interparticle slippage against the shear forces upon loading because no bonding exists between the surface of fillers. Second, the lowered mechanical response of the fabricated part could be ascribed to the decrease in the effective surface area of the reinforcement phase due to the excess of fillers compared to the available polymer content and, thus, lower wettability of the HGMSs at the higher loadings [36, 37]. This observation could be better explained by the interconnected HGMSs surface where the fillers interspace is not enriched with polymer phase as clearly understood from Figures 11c and 11d (shown by arrows). Moreover, the higher number density of the fillers prohibits the formation of the interphase region with the assumed thickness due to the pinning effect of HGMSs sites [5, 38].

The exhibition confirms the agreement between the micro-mechanical model's prediction and the experimental elastic response resulting from the interfacial detachment at the interface of the HGMSs and polyester as understood from the SEM images.

## 5. CONCLUSION

Micro-composites of HGMS/polyester reinforced with 0-20 wt% of filler were fabricated and the effect of the presence of the interphase region and agglomeration on the overall elastic response of the composites was examined. The results indicated the existence of stiffer interphase as a result of perfect bonding at the contact of filler/polymer concerning the neat polyester leading to the increase in the modulus of the specimens upon the addition of fillers. It was further revealed that the elastic modulus of the composites is highly sensitive to the interphase modulus and thickness resulting in more accurate predictions with respect to the experimental values using the Halpin-Tsai, Tandon-Weng and the rule of mixtures when the interphase of a few microns up to 8 and modulus of 12-15 GPa are incorporated into the models. The findings confirmed the higher sensitivity of models to the interphase properties at lower filler content. It was shown through the morphological studies a perfect bonding of HGMS/polymer exists in the bulk specimens at loadings of lower filler ratio; however some levels of agglomeration leading to interconnected HGMSs and suppressed wettability of fillers were observed and accounted into the models to understand the effect of agglomerated phase on Young's modulus. The findings were linked to their severe number density of filler at higher HGMS content and, thus, models underestimation at such loadings. The study provided a methodology to give a better insight into the effect of interfacial interactions generated in thermosetting-based composites filled with HGMS reinforcements on the overall elastic response of the parts.

## 6. REFERENCES

- Kumar, N., Mireja, S., Khandelwal, V., Arun, B. and Manik, G., "Light-weight high-strength hollow glass microspheres and bamboo fiber based hybrid polypropylene composite: A strength analysis and morphological study", *Composites Part B: Engineering*, Vol. 109, (2017), 277-285. doi: 10.1016/j.compositesb.2016.10.052.
- Saindane, U.V., Soni, S. and Menghani, J.V., "Dry sliding behavior of carbon-based brake pad materials", *International Journal of Engineering, Transactions B: Applications*, Vol. 34, No. 11, (2021), 2517-2524. doi: 10.5829/ije.2021.34.11b.14.
- Jones, F., "A review of interphase formation and design in fibre-reinforced composites", *Journal of Adhesion Science and Technology*, Vol. 24, No. 1, (2010), 171-202. doi: 10.1163/016942409X12579497420609.
- Feng, J., Venna, S.R. and Hopkinson, D.P., "Interactions at the interface of polymer matrix-filler particle composites", *Polymer*, Vol. 103, (2016), 189-195. doi: 10.1016/j.polymer.2016.09.059.
- Ashraf, M.A., Peng, W., Zare, Y. and Rhee, K.Y., "Effects of size and aggregation/agglomeration of nanoparticles on the interfacial/interphase properties and tensile strength of polymer nanocomposites", *Nanoscale Research Letters*, Vol. 13, No. 1, (2018), 1-7. doi: 10.1186/s11671-018-2624-0.
- Jancar, J., "Review of the role of the interphase in the control of composite performance on micro-and nano-length scales", *Journal of Materials Science*, Vol. 43, No. 20, (2008), 6747-6757. doi: 10.1007/s10853-008-2692-0.
- Tandon, G.P., "Average stress in the matrix and effective moduli of randomly oriented composites", *Composite Science and Technology*, Vol. 27, No. 2, (1986), 111-132. doi: 10.1016/0266-3538(86)90067-9.
- Kang, D., Hwang, S.W., Jung, B.N. and Shim, J.K., "Effect of hollow glass microsphere (HGM) on the dispersion state of single-walled carbon nanotube (SWNT)", *Composites Part B: Engineering*, Vol. 117, (2017), 35-42. doi: 10.1016/j.compositesb.2017.02.038.
- Saindane, U.V., Soni, S. and Menghani, J.V., "Friction and wear performance of brake pad and optimization of manufacturing parameters using grey relational analysis", *International Journal of Engineering, Transactions C: Aspects*, Vol. 35, No. 3, (2022), 552-559. doi: 10.5829/ije.2022.35.03C.07.
- Zare, Y. and Rhee, K.Y., "Study on the effects of the interphase region on the network properties in polymer carbon nanotube nanocomposites", *Polymers*, Vol. 12, No. 1, (2020), 182. doi: 10.3390/polym12010182.
- Saindane, U.V., Soni, S. and Menghani, J.V., "Recent research status on synthesis and characterization of natural fibers reinforced polymer composites and modern friction materials—an overview", *Materials Today: Proceedings*, Vol. 26, (2020), 1616-1620. doi: 10.1016/j.matpr.2020.02.334.
- Rahmi, R., Lubis, S., Az-Zahra, N., Puspita, K. and Iqhrammullah, M., "Synergetic photocatalytic and adsorptive removals of metanil yellow using TiO<sub>2</sub>/grass-derived cellulose/chitosan (TiO<sub>2</sub>/gc/ch) film composite", *International Journal of Engineering, Transactions B: Applications*, Vol. 34, No. 8, (2021). doi: 10.5829/ije.2021.34.08b.03.
- Surendra, I., Rao, K.V. and Chandu, K., "Fabrication and investigation of mechanical properties of sisal, jute & okra natural fiber reinforced hybrid polymer composites", *International Journal of Engineering Trends and Technology*, Vol. 19, No. 2, (2015), 116-120. doi: 10.14445/22315381/IJETT-V19P220.
- Teja Prathipati, S., Rao, C. and Dakshina Murthy, N., "Mechanical behavior of hybrid fiber reinforced high strength concrete with graded fibers", *International Journal of Engineering, Transactions B: Applications*, Vol. 33, No. 8, (2020), 1465-1471. doi: 10.5829/IJE.2020.33.08B.04.
- Jesthi, D., Nayak, A., Routara, B. and Nayak, R., "Evaluation of mechanical and tribological properties of glass/carbon fiber reinforced polymer hybrid composite", *International Journal of Engineering, Transactions A: Basics*, Vol. 31, No. 7, (2018), 1088-1094. doi: 10.5829/ije.2018.31.07a.12.
- Yung, K.C., Zhu, B., Yue, T.M. and Xie, C., "Preparation and properties of hollow glass microsphere-filled epoxy-matrix composites", *Composites Science and Technology*, Vol. 69, No. 2, (2009), 260-264. doi: 10.1016/j.compscitech.2008.10.014.
- Chen, W., Qin, Y., He, X., Su, Y. and Wang, J., "Light-weight carbon fiber/silver-coated hollow glass spheres/epoxy composites as highly effective electromagnetic interference shielding material", *Journal of Reinforced Plastics and Composites*, Vol. 0, No. 007316844211065183. doi: 10.1177/07316844211065183.

18. Jiang, T., Wu, X., Gao, Y., Wang, Y., Yang, K., Liu, T., Yu, J., Sun, K., Zhao, Y. and Li, W., "Fabrication and mechanical performance of glass fiber reinforced, three-phase, epoxy syntactic foam", *Chemistry Select*, Vol. 7, No. 1, (2022), e202103556. doi: 10.1002/slct.202103556.
19. Altay, P. and Uçar, N., "Improvement of insulation properties of glass fiber fabric/epoxy composites modified by polymeric and inorganic fillers", *Polymer Composites*, Vol. 43, No. 1, (2022), 225-238. doi: 10.1002/pc.26369.
20. Imran, M., Rahaman, A. and Pal, S., "Thermo-mechanical and mechanical properties of epoxy/cnt composite modified by hollow glass microspheres", *Materials Today: Proceedings*, Vol. 22, No., (2020), 2469-2474. doi: 10.1016/j.matpr.2020.03.374.
21. Ding, J., Liu, Q., Zhang, B., Ye, F. and Gao, Y., "Preparation and characterization of hollow glass microsphere ceramics and silica aerogel/hollow glass microsphere ceramics having low density and low thermal conductivity", *Journal of Alloys and Compounds*, Vol. 831, (2020), 154737. doi: 10.1016/j.jallcom.2020.154737.
22. Mutua, F.N., Lin, P., Koech, J.K. and Wang, Y., "Surface modification of hollow glass microspheres", *Materials Sciences and Applications* Vol., (2012), 4. doi: 10.4236/msa.2012.312125.
23. Raju, B., Hiremath, S. and Mahapatra, D.R., "A review of micromechanics based models for effective elastic properties of reinforced polymer matrix composites", *Composite Structures*, Vol. 204, (2018), 607-619. doi.org/10.1016/j.compstruct.2018.07.125
24. Tandon, G.P. and Weng, G.J., "The effect of aspect ratio of inclusions on the elastic properties of unidirectionally aligned composites", *Polymer Composites*, Vol. 5, No. 4, (1984), 327-333. doi.org/10.1002/pc.750050413
25. Sheng, N., Boyce, M.C., Parks, D.M., Rutledge, G.C., Abes, J.I. and Cohen, R.E., "Multiscale micromechanical modeling of polymer/clay nanocomposites and the effective clay particle", *Polymer*, Vol. 45, No. 2, (2004), 487-506. doi: 10.1016/j.polymer.2003.10.100.
26. Montazeri, A., Javadpour, J., Khavandi, A., Tcharkhtchi, A. and Mohajeri, A., "Mechanical properties of multi-walled carbon nanotube/epoxy composites", *Materials & Design*, Vol. 31, No. 9, (2010), 4202-4208. doi: 10.1016/j.matdes.2010.04.018.
27. Tucker III, C.L. and Liang, E., "Stiffness predictions for unidirectional short-fiber composites: Review and evaluation", *Composites Science and Technology*, Vol. 59, No. 5, (1999), 655-671. doi: 10.1016/S0266-3538(98)00120-1.
28. Dzenis, Y. and Maksimov, R., "Prediction of the physical-mechanical properties of hollow-sphere reinforced plastics", *Mechanics of Composite Materials*, Vol. 27, No., (1991), 263-270. doi: 10.1007/BF00616873.
29. Downing, T., Kumar, R., Cross, W., Kjerengtroen, L. and Kellar, J., "Determining the interphase thickness and properties in polymer matrix composites using phase imaging atomic force microscopy and nanoindentation", *Journal of Adhesion Science and Technology*, Vol. 14, No. 14, (2000), 1801-1812. doi: 10.1163/156856100743248.
30. Rubel, R.I., Ali, M.H., Jafar, M.A. and Alam, M.M., "Carbon nanotubes agglomeration in reinforced composites: A review", *AIMS Materials Science* Vol. 6, No. 5, (2019), 756-780. doi: 10.3934/matrs.2019.5.756.
31. Zare, Y., Rhee, K.Y. and Hui, D., "Influences of nanoparticles aggregation/agglomeration on the interfacial/interphase and tensile properties of nanocomposites", *Composites Part B: Engineering*, Vol. 122, (2017), 41-46. doi: 10.1016/j.compositesb.2017.04.008.
32. Karevan, M. and Kalaitzidou, K., "Formation of a complex constrained region at the graphite nanoplatelets-polyamide 12 interface", *Polymer*, Vol. 54, No. 14, (2013), 3691-3698. doi: 10.1016/j.polymer.2013.05.019.
33. Tyson, B.M., Al-Rub, R.K.A., Yazdanbakhsh, A. and Grasley, Z., "A quantitative method for analyzing the dispersion and agglomeration of nano-particles in composite materials", *Composites Part B: Engineering*, Vol. 42, No. 6, (2011), 1395-1403. doi: 10.1016/j.compositesb.2011.05.020.
34. Zare, Y. and Rhee, K.Y., "Accounting the reinforcing efficiency and percolating role of interphase regions in tensile modulus of polymer/cnt nanocomposites", *European Polymer Journal*, Vol. 87, (2017), 389-397. doi: 10.1016/j.eurpolymj.2017.01.007.
35. Kundalwal, S.I., "Review on micromechanics of nano-and micro-fiber reinforced composites", *Polymer Composites*, Vol. 39, No. 12, (2018), 4243-4274. doi: 10.1002/pc.24569.
36. Mutua, F.N., Lin, P., Koech, J.K. and Wang, Y., "Surface modification of hollow glass microspheres", *Materials Sciences and Applications*, Vol. 3, No. 12 (2012), Article ID: 25408, doi: 10.4236/msa.2012.312125
37. Qiu, S., Fuentes, C.A., Zhang, D., Van Vuure, A.W. and Seveno, D., "Wettability of a single carbon fiber", *Langmuir*, Vol. 32, No. 38, (2016), 9697-9705. doi: 10.1021/acs.langmuir.6b02072.
38. Ozkutu, M., Dilek, C. and Bayram, G., "Effects of hollow glass microsphere density and surface modification on the mechanical and thermal properties of poly (methyl methacrylate) syntactic foams", *Composite Structures*, Vol. 202, (2018), 545-550. doi: 10.1016/j.compstruct.2018.02.088.

---

**Persian Abstract**

---

**چکیده**

میکروگوییچه های توخالی شیشه ای (HGMS) اخیراً در ساخت کامپوزیت های پلیمر با چگالی کم به دلیل سفتی بالای این تقویت کننده ها به همراه وزن سبک آنها که به نوبه خود منجر به توسعه میکروکامپوزیت ها با خواص مهندسی شده و خواص مکانیکی بالا مورد استفاده قرار گرفته اند. برهم کنش های سطح فیلر/پلیمر مقدار انتقال نیرو و خواص بالک کامپوزیت ها را کنترل کرده که موجب خواص غیرقابل پیش بینی کامپوزیت ها با ذرات می گردد. با این وجود، مدل های تحلیلی مفید بمنظور تخمین خواص مکانیکی کامپوزیت های پایه HGMS با در نظر گرفتن اثر برهم کنش های سطح فیلر و آگلوومراسیون احتمالی مورد نیاز است. تاکنون مطالعاتی بر اساس مدل تحلیلی HGMS کامپوزیت های ترموست تقویت شده با این ذرات گزارش نشده در حالیکه بر نقش فاز میانی تشکیل شده در اطراف فیلر تاکید کرده باشد. این مطالعه بر ساخت میکرو کامپوزیت های پلی استر/HGMS تقویت شده با ۰ تا ۲۰ درصد ذرات تمرکز داشته که به دنبال آن مدل های میکرومکانیک صورت گرفته درحالیکه نقش ناحیه فاز میانی در اصلاح مدل ها تاکید می گردد. نتایج ارتباط قوی بین مشخصات فازی میانی و مدول یانگ در کامپوزیت ها را نشان داده که وابستگی ضخامت و مدول فاز میانی و سطح آگلوومراسیون و جدایش سطح مشترک ذرات HGMS را مشخص می کند. نتایج همچنین نشان داد که در نظر نگرفتن فاز میانی منجر به پیش بینی کمتر خواص شده که بیانگر وجود فاز میانی با سفتی بیشتر در اطراف HGMS بوده که مطابق با فرضیه تحقیق توسط تغییر در چگالی پیوندهای عرضی در پلیمر زمینه تعیین شده و توسط پاسخ مکانیکی نمونه ها تائید می گردد.

---



## Extraction of Catechin as a Flavonoid Compound via Molecularly Imprinted Polymers

A. Jahanbakhsh, M. Hosseini\*, M. Jahanshahi, A. Amiri

Department of Chemical Engineering, Babol Noshirvani University of Technology, Babol, Iran

## P A P E R I N F O

## Paper history:

Received 26 May 2021

Received in revised form 14 January 2022

Accepted 31 January 2022

## Keywords:

Catechin

Molecularly Imprinted Polymers

Selectivity

Green Tea

Separation

Bioactive

## A B S T R A C T

The aim of this study is synthesis of molecularly imprinted polymers (MIPs) and evaluation for extraction of catechin. Catechin is a bioactive compound which is found abundantly in green tea. In this paper, MIPs was synthesized by precipitation polymerization technique for catechin, acrylic acid and trimethylolpropane trimethacrylate as a template, functional monomer and cross-linker in a molecular ratio of (1:12:12), respectively. Surface morphology in the MIPs by scanning electron microscopy (SEM) demonstrated spheres with nanometric scale. Fourier transform infrared spectroscopy (FTIR) of the polymers showed that catechin molecule was captured in the network copolymers. Porosity of the polymers were analyzed using Brouneur Emmet Teller (BET) technique. Based on BET analysis, specific surface area of the MIPs was  $45.5 \text{ m}^2 \cdot \text{g}^{-1}$  while it was  $42.2 \text{ m}^2 \cdot \text{g}^{-1}$  for non-imprinted polymers (NIPs). It means that the imprinting process was carried out successfully. Adsorption properties of the polymers were characterized too. The best binding capacity of the MIPs was reported equal to  $440 \text{ mg} \cdot \text{g}^{-1}$  in 750 ppm of the feed concentration whereas it was  $84 \text{ mg} \cdot \text{g}^{-1}$  for quercetin (similar structure of catechin). It confirms that the MIPs technology can be introduced as a good candidate for separation process with a satisfactory result in selectivity. The binding capacity of the MIPs was evaluated for natural extract of green tea using a high-performance liquid chromatography (HPLC) device which similar results were obtained. According to above mentioned results, separation and pre-concentration of the bioactive compounds from the extract of medicinal plants can be suggested *via* MIPs technique.

doi: 10.5829/ije.2022.35.05.14

## 1. INTRODUCTION

Catechin is a flavonoids compound which is found in a variety of fruits, vegetables and herbal plants. Although catechins are not nutritionally- nutrition for humans, they help improve human health by preventing various diseases [1]. Some Fruits like grapes, apples, strawberries, cherries, and various types of tea, especially green tea are the main sources of catechins [2]. Figure 1 shows the structure of catechin molecule contain five hydroxyl groups. Thanks to their hydroxyl groups, polyphenols such as catechin and quercetin are the most common food antioxidants.

These compounds play an important role in preventing chronic diseases like cancer by inhibiting free radicals. Due to the presence of flavonoid bioactive compounds such as catechins in green tea, Chinese people use green tea as a medicinal beverage. Recently,

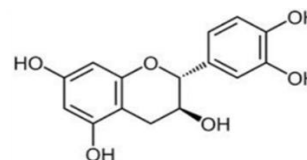


Figure 1. Chemical structure of Catechin molecule

green tea became very popular in many countries including Iran [3]. There are many different methods for separation of the bioactive or special compounds. Using eco-friendly technique is well known for human safety. Adsorption of methylene blue by silk cocoon as a natural adsorbent and extraction of the bioactive compound from gringer *via* subcritical water extraction can be mentioned as green methods [4-5]. Intra molecular interaction is a very old concept. Fisher's lock-and-key theory which are analogous to the substrate-enzyme interaction, relates to

\*Corresponding Author Institutional Email: [m.hosseini@nit.ac.ir](mailto:m.hosseini@nit.ac.ir)  
(M. Hosseini)

this concept. Today, the molecular imprinting technique is a method for designing and detecting the molecules according to a mimic system, such as antibodies and biological receptors [6-9]. The MIPs are three dimensional network polymers with specific binding sites for template molecules which are obtained by polymerization of functional monomers and cross-linker molecules in the presence of template molecules [10]. Then by elimination of the template molecule, some cavities with a similar structure will be created. Identification and selection of the template molecule is depend on covalent or non-covalent bonding (such as ionic, hydrogen and van der Waals bond) [10-12]. Figure 2 shows a general schem for creating the cavities (especially for Catechin molecule) after tempelate removal from MIPs.

MIPs are three-dimensional network copolymers with specific binding sites that are obtained during the polymerization process, in presence of the effective compounds. Fast preparation, easy, cheap, reproducibility and high selectivity are the main reasons that this technique can be suggested for separation of the bioactive compounds. Various polymerization methods (such as bulk and precipitation polymerization) have been developed for the synthesis of the MIPs. Radical polymerization, as the first method with a great adaptability in selecting functional monomers, in both bulk and precipitation polymerization, has been the most common method [13]. Five original compounds are present in the process of creating MIPs: a template molecule, a functional monomer, a cross-linker, an initiator and a solvent. High selectivity, high mechanical and chemical stability, easy synthesis and cost-effectiveness are the main advantages of the MIPs [14]. These advantages have led to numerous applications of this technique. Applications of the MIPs include sensors, solid phase extraction (SPE), enzymes, biosensors, food safety, detection of micro organisms and especially drug delivery [15-22]. In a study, imprinting of the polymers with herbicides was carried out to produce the adsorbents which could be used to isolate these hazardous compounds from contaminated water [23]. Synthesis of the MIPs was reported to isolate naphthoquinone compound from the extract of the plants [24]. Recently, this technique has also been reported to isolate antifungal

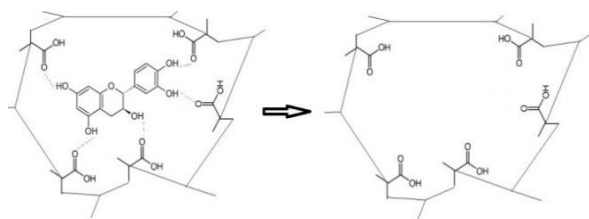


**Figure 2.** Creating of cavity in MIPs after removing of Catechin

compounds from secondary metabolites of *T. virens* [25]. In this study Catechin was used as a target molecule for MIPs synthesis in a molar ratio of (1:12:12) for template, functional monomer and cross-linker respectively via precipitation polymerization technique for the first time. According to the produced adsorbents with great bonding capacities, utilization of this type of intelligent polymers for extraction of the bioactive compounds from medicinal plants can be investigated.

## 2. EXPERIMENTAL

**2. 1. Materials and Methods** The most materials which were used in the polymerization process, the chemicals were HPLC grade. Methanol and acetic acid with high purity were supplied by Merck (Darmstadt, Germany). The list of used chemicals are summarized in Table 1.

The equipments used in this study include analytical balance manufactured by A&D company, magnetic stirrer model R-50 (Italy), water bath manufacture by Memmert model WB22 (Germany), sonicator model QTD1730 (Korea), Centrifuge manufactured by Hermle company (Germany) and oven. Jenway 6305 UV/Visible spectrometer was used to determine amount of the templates in loading process on the polymers at 278 nm wavelength. The porosity was evaluated by nitrogen gas adsorption/desorption analysis using Brouneur Emmet Teller (BET) analysis (PHS1020-China). The porosity measuring is based on the results of isothermal adsorption at 77 K. Surface morphological information of the MIPs was obtained by scan electron microscope (SEM) model VEGA\\TESCAN (Czech). Amount of Catechin measured by HPLC equipment (Agilent Technologies, Palo Alto, CA, USA) with A G1328B manual injector and C18 Column. Fourier transform infrared spectra (400-4000  $\text{cm}^{-1}$ ) were recorded for NIPs, Catechin, leached and un-leached MIPs on a

**TABLE 1.** The used Chemical materials in synthesis of MIPs

Chemical material	Function	Producer
Quercetin	Similar structure for template molecule	Sigma-Aldrich
Catechin	Template molecule	
Acrylic acid	Functional monomer	Merck
Trimethylolpropane trimethacrylate	Cross-linker	Sigma-Aldrich
Azobisisobutyronitrile	Initiator	
Acetonitrile	Porogene	
Methanol/Acetic acid	Elution	Merck
Acetone	Solvent	

Bruker spectrometer (model vector 22; Bruker, Germany).

## 2. 2. Synthesis of the MIPs And NIPs

For synthesis of MIPs, the target molecule (catechin), acrylic acid monomer (AA), and trimethylolpropane trimethacrylate crosslinker (TRIM) with molecular ratio of 1:12:12 were used [26]. Precipitation polymerization reaction was carried out in a flat-bottom flask. Initiator of the reaction was 2,2-azobisisobutyronitrile and acetonitrile was used as a porogene. At first catechin was dissolved in acetonitrile solvent and then other reactants were added at 0°C. Ultrasonic process was performed for 5 min after adding each compound. The mixture was purged for 5 min using nitrogen gas to remove oxygen molecules from the flask. The flask took place in a water bath at 60°C on the stirrer for polymerization reaction for duration of 24 h. Finally the synthesized polymer was centrifuged and kept in oven at 50°C over night. The synthesis of non-imprinted polymer (NIPs) was performed according to the same method but without the presence of any template.

## 2. 3. Removal of the Catechin From The MIPs

For separation of the catechin molecules from the synthesized polymer, the MIPs were eluted on the stirrer with methanol/acetic acid as a elutant (9:1v/v) for several times in room temperature. The process was continued until the absorbance of the extracted solution at the wavelength of 278 nm, reached to zero. The leached MIPs was washed with pure methanol and distilled water respectively and put in oven at 60°C for further use.

## 2. 4. Evaluation of the MIPs

### 2. 4. 1. Catechin Standard Absorption Curve

At first the standard curve for different concentration of catechin in acetonitrile/water solvent(1:1v/v) vs absorbance in wavelength at 278 nm was drawn to measure the binding capacity of the MIPs (see Figure 3).

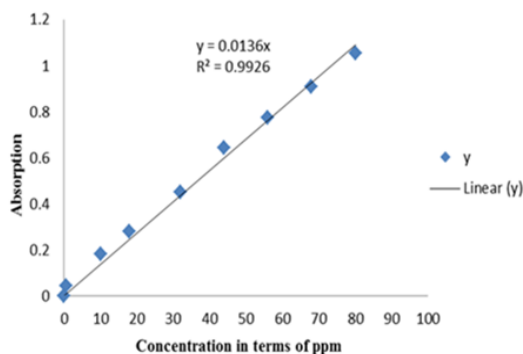


Figure 3. The standard curve for catechin in acetonitrile/distilled water (1:1 v/v)

According to the chart with the equation of  $y = 0.0136x$ , the correlation coefficient was 0.9926, which is very desirable.

### 2. 4. 2. Measuring Binding Capacity of the MIPs

In order to evaluate the data obtained from the adsorption analysis, a parameter was defined as the adsorption capacity, which determines the adsorbent performance and is an index to compare the adsorbent's performance. The binding capacity ( $Q_e$ ) of the adsorbent (MIPs) was defined as the difference of the initial ( $C_0$ ) and final ( $C_e$ ) amount (ppm) of catechin in the solution multiple loading value ( $V$ ) over the amount of the used adsorbent ( $m$ ), based on Equation (1):

$$Q_e = \frac{(C_0 - C_e)}{m} V \quad (1)$$

where  $Q_e$  (mg/g) is known as binding capacity.

### 2. 4. 3. Imprinting Factor

The imprinting factor (IF) is defined according to Equation (2):

$$IF = \frac{Q_{MIPs}}{Q_{NIPs}} \quad (2)$$

in which,  $Q_{MIPs}$  and  $Q_{NIPs}$  are binding capacity of the MIPs and NIPs, respectively.

### 2. 4. 4. Yield of the Extraction

The yield of extraction or percent of the MIPs adsorption can be calculated as Equation (3):

$$\%Extraction = \frac{C_0 - C_e}{C_0} * 100 \quad (3)$$

where  $C_0$  and  $C_e$  are initial and final concentration of the feed in loading process.

### 2. 4. 5. Selectivity of the MIPs

In general, the MIPs were evaluated for their diagnostic properties relative to the template molecule. Chromatographic and equilibrium adsorption analyses on the discontinuous system are commonly used to study the selectivity of the imprinted materials. In such experiments, a certain mass of the chemical compound which is similar to the template molecule (base on its structure) is added to the solution containing the MIPs. After loading procedure, by measuring amount of the remained molecule in solution, the quantity of the adsorbed by MIPs can be calculated [27]. Figure 4 shows the structure of Quercetin molecule (a flavonoid compound) which is similar to Catechin molecule structurally. This compound was used for selectivity test of the MIPs.

### 2. 4. 6. Selectivity Factor ( $\alpha$ )

For measuring selectivity factor ( $\alpha$ ), at first distribution coefficient ( $K_d$ ) of the template should be calculated. Distribution coefficient is introduced by Equation (4):

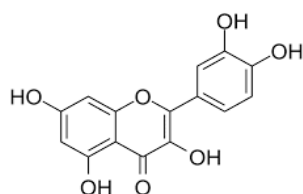


Figure 4. Chemical structure of Quercetin molecule

$$K_d = \frac{Q_e}{C_e} \quad (4)$$

where  $Q_e$  and  $C_e$  are the binding capacity (mg.g-1) and final concentration (mg/l) of the feed in loading process, respectively. Selectivity factor ( $\alpha$ ) of MIPs is an important parameter that establishes the selectivity of the polymers. Selectivity factor is defined as Equation (5):

$$\alpha = \frac{K_d(\text{catechin})}{K_d(\text{quercetin})} \quad (5)$$

where  $K_d(\text{catechin})$  and  $K_d(\text{quercetin})$  are distribution coefficients of catechin and quercetin, respectively. Utmost measure of  $\alpha$ , introduces high selectivity of the MIPs.

#### 2. 4. 7. Applicability Test for MIPs with Natural Product

##### 2. 4. 7. 1. Preparation of the Green Tea Extract

The extract of green tea was carried out in methanol solvent at 70°C for 90 min [28]. It contains several flavonoids compounds which most of them are catechin and its derivatives. Amount of catechin before and after loading procedure on MIPs can be measured by HPLC equipment at retention time of 10.567 minutes of chromatogram according to standard curve (Figure 5).

##### 2. 4. 7. 2. Loading Natural Product Extract on the MIPs

The extracted solution from green tea was

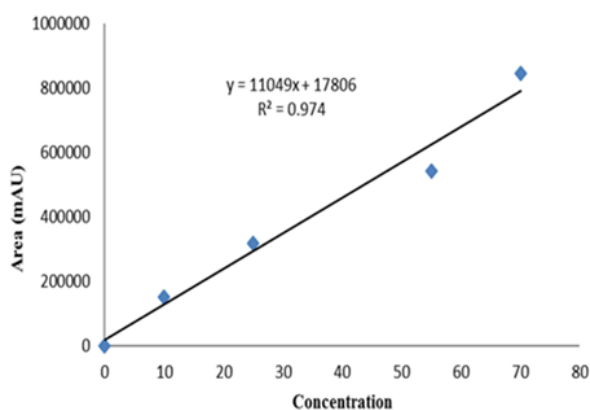


Figure 5. Standard HPLC curve for Catechin (Peak surface area vs concentration (ppm))

loaded on the MIPs. At first 20  $\mu$ l of the extract was diluted with 10 ml methanol and then 10 ml of this solution with 10 mg of the leached MIPs was put in a conical flask. Loading process took place on the magnetic stirrer for 2h. Before and after loading process, the amount of Catechin in the solution was measured by HPLC equipment. Catechin was detected at retention time 10.567 minutes after injection in C18 column. Standard HPLC curve in different concentration of pure Catechin was prepared (Figure 5) and the binding capacities were calculated.

As illustrated in Figure 5, the regression of the curve is 0.974, which shows an unexpected deviation from the straight line [28].

### 3. RESULTS AND DISCUSSION

#### 3. 1. Measurement of the Binding Capacity for MIPs

The amount of the polymer and the volume of solution in each loading was 10 mg and 20 ml, respectively, and loading was continued for two hours at the ambient temperature and in a batch system. The loading solvent at all loadings was distilled water-acetonitrile (1:1 volume ratio). Both the adsorption of the filtered solution after loading process and desorption of catechin solution in feed (before loading) was measured by UV spectrometer at a wavelength of 278 nm. The calculations and final results are summarized in Table 2. For evaluating of the MIPs, the same steps were performed using NIPs particles [29]. Measurement of the binding capacity was performed three times, and the results were relatively identical in all replicates.

TABLE 2. Evaluation of the binding capacity on MIPs and NIPs

Feed (ppm) (before loading)	Polymer	Feed (ppm) after loading	Binding capacity (mg/g)	Extraction percentage	IF
1000	MIP	897	206	10.3	2.28
	NIP	955	90	2.2	
750	MIP	492	516	34.4	2.41
	NIP	595	310	20.6	
600	MIP	493	310	25.8	2.50
	NIP	538	124	10.3	
500	MIP	401	198	19.8	2.47
	NIP	460	80	8	
400	MIP	356	88	4.4	2.44
	NIP	382	36	1.8	
250	MIP	221	58	2.9	1.98
	NIP	235	30	1.5	

The absorption curves of MIPs and NIPs showed that the utmost binding capacity was 516 ( $\text{mg.g}^{-1}$ ) for MIPs which occurred at a concentration of about 750 ppm (Figure 6). This difference in adsorption implies the presence of specific binding sites in the MIPs for catechin, that indicates the nanoporous MIPs was well synthesized.

**3. 2. Selectivity Analysis of the MIPs With Quercetin** At first, standard curve was obtained for different concentration of quercetin in acetonitrile-water solvent (1:1v/v). Measurement was carried out by UV spectrometer at 370 nm (Figure 7).

Selectivity analysis of quercetin was performed using a 750 ppm quercetin solution, because the synthesized MIPs showed the best binding capacity in this feed concentration. Quercetin had a good absorbance at the wavelength of 370nm, so the quantity of quercetin was measured in this wavelength while acetonitrile and

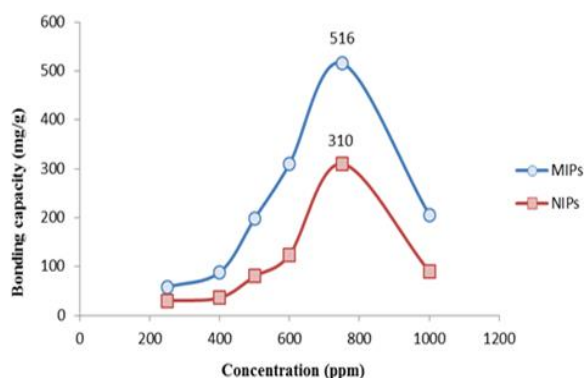


**Figure 6.** The variation of the binding capacity of the polymers Vs concentrations of Catechin

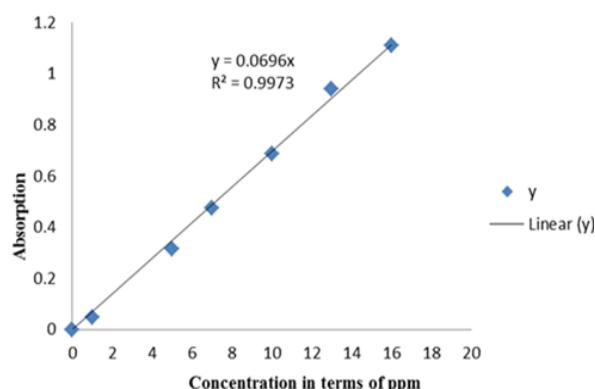


**Figure 7.** Standard curve for quercetin in distilled water/acetonitrile (1:1 v/v) (Peak surface area vs concentration (ppm))

distilled water has no absorbance. The related results were summarized in Table 3.

At a concentration of 750 ppm, the imprinted polymer with catechin had a binding capacity of 440  $\text{mg.g}^{-1}$  and 84  $\text{mg.g}^{-1}$  for catechin and quercetin, respectively. This indicates a high selectivity of the synthesized polymer imprinted the specificity of nanopores created within the AA-based molecular imprinted polymer network.

**3. 3. Evaluation of the Polymers Based on Adsorption-Desorption Analysis** Based on the adsorption-desorption analysis by nitrogen gas, the specific surface area in MIPs was 45.5, while the specific surface area in NIPs was 42.2. These values indicated that the imprinting of the polymers was desirable. The data in Table 4 presents the formation of nanopore molecular imprinted polymers. We found that MIPs had both a larger cavity volume and diameter than NIPs which indicates that MIPs had a higher specific absorption to catechin compared to NIPs. Also, based on the hole classification of the IUPAC<sup>1</sup>, the mesopores are compounds with diameters between 2 - 50 nm. Therefore, according to the obtained average diameter of the cavities, the synthesized MIPs can be classified in the mesopores group.

**3. 4. Morphology Study** Imaging by scanning electron microscopy (SEM) proved the spherical and almost uniform shape of the particles in nanometric size. According to Figure 8, the particle size of the MIPs with diameter about 142 nm was observed.

**3. 5. Infrared (IR) Spectroscopy** Infrared spectroscopy for pure catechin, NIPs, leached (after elution) and un-leached (before elution) of the MIPs was carried out by Fourier transform infrared (FTIR)

**3. 5. Infrared (IR) Spectroscopy** Infrared spectroscopy for pure catechin, NIPs, leached (after elution) and un-leached (before elution) of the MIPs was carried out by Fourier transform infrared (FTIR)

**TABLE 3.** Selectivity results with quercetin molecule for the synthesized MIPs base on Catechin template

Before loading (ppm)	Loading solution	After loading (ppm)	Binding capacity ( $\text{mg.g}^{-1}$ )	( $K_d$ )	Selectivity factor ( $\alpha$ )
750	Catechin	530	440	0.83	7.54
	Quercetin	708	84	0.11	

**TABLE 4.** BET analysis for MIPs and NIPs

Polymer	Special surface area ( $\text{m}^2.\text{g}^{-1}$ )	Volume of the cavities ( $\text{cm}^3.\text{g}^{-1}$ )	Mean diameter of the cavities (nm)
MIPs	45.521	0.049	4.338
NIPs	42.206	0.044	4.203

<sup>1</sup> International Union of Pure and Applied Chemistry

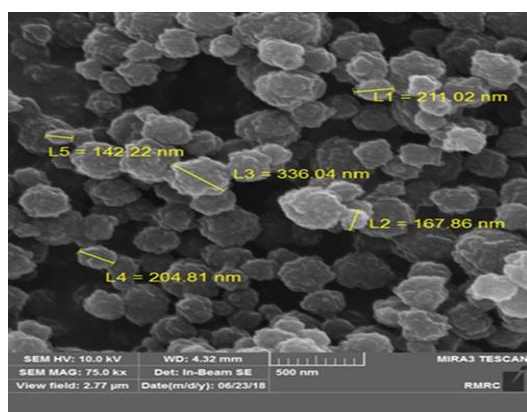


**Figure 8.** Imaging by scanning electron microscopy (SEM)

spectroscopy at the frequency of 500-4000  $\text{cm}^{-1}$  by potassium bromide (KBr) salt, and recorded infrared (IR) spectra are shown in Figure 9. Although particles exhibited similar peaks due to having the same functional groups (such as CO, -OH, and carbonyl C=O), which indicates the similarity in the solid structure of the polymers, the difference between the IR spectra of the compounds was expected. A band related to the OH group of carboxylic acids (AA) was recorded at the frequency of 3000  $\text{cm}^{-1}$ , while this band for pure catechin (related to phenol groups of catechin) was more elongated and broad in the range of 3200-3550  $\text{cm}^{-1}$ . Due to the presence of common functional groups in MIPs before elution, on top of the functional groups related to the polymer structure resulting from the catechin, some peaks like the peak at 3000  $\text{cm}^{-1}$  were wider and stronger. The peak related to C=C in the aromatic ring of catechin appeared at a frequency of about 1650  $\text{cm}^{-1}$ , and the ester C=O peak was recorded at the frequency range of 1735-1750  $\text{cm}^{-1}$ . This peak exists in catechin and un-leached MIPs spectrum while it was omitted in the leached MIPs. Also the related peak is absent in NIPs spectrum. It means that, after removal of catechin from the MIPs, most of catechin will be removed, so this peak will be disappeared in IR-Spectrum. Absorbance in 1750  $\text{cm}^{-1}$  indicates steric carbonyl group which should not be found in catechin spectrum whereas the other spectrum involve this peak. However, the carboxylic acid C=O peak was expected to appear at the 1780-1710  $\text{cm}^{-1}$  range, but due to its proximity to OH groups and intermolecular hydrogen bonds, this peak appeared at a lower frequency of about 1670  $\text{cm}^{-1}$  [30].

Frequency peaks at 2370  $\text{cm}^{-1}$  are related to the asymmetric tensile frequency of CO<sub>2</sub> molecules present in the air and combine with the sample during the formation of KBr tablets [31]. The most obvious difference between the IR spectra of the catechin molecule and other polymeric compounds originated from the C=C bond in the catechin. In the catechin

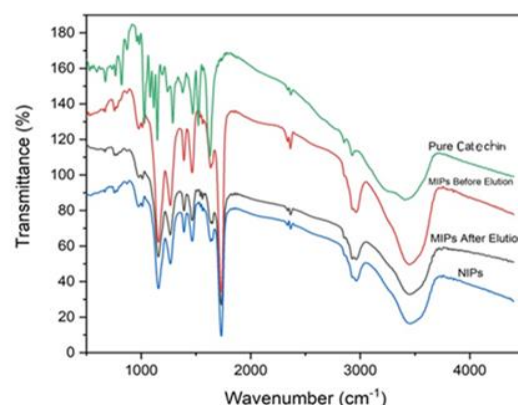


**Figure 9.** FTIR spectrum of the MIPs (after and before elution), NIPs and pure catechin molecule

spectrum, this absorption was observed at a frequency of about 1660  $\text{cm}^{-1}$  and was expected to appear in the MIPs spectrum before elution. However, it was hidden due to the presence of a peak at about 1670  $\text{cm}^{-1}$  that belonged to the carboxylic group (C=O). This group, due to the presence of hydrogen bonds, had resonance [32].

### 3. 7. Evaluation of the Synthesised MIPs for Separation of Catechin from Natural Extract of Green Tea

The amount of the absorbed catechin by MIPs was measured base on comparing of the chromatogram in before and after loading process [33-34]. Figure 10 shows the related chromatogram of green tea extract before loading on the MIPs. In this figure, catechin was appeared in retention time close 10.567 minutes. Figure 11 shows the related chromatogram of green tea extract after loading on the MIPs. In this figure, catechin was appeared at retention time of close to 10.767 minutes.

The related peak of the surface area belong to catechin was summarized in Table 5.

According to the standard curve in Figure 5, the binding capacity of the MIPs was calculated about 14.07  $\text{mg.g}^{-1}$ . It means that the adsorption of catechin by nanoporous MIPs was carried out successfully.

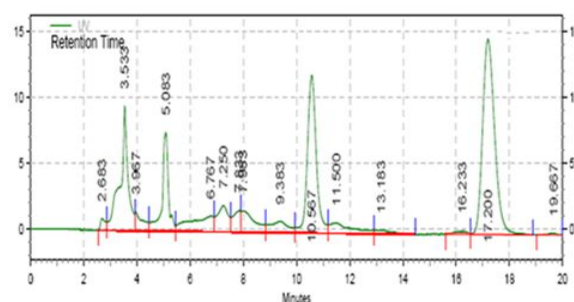


**Figure 10.** HPLC Chromatogram of green tea extract before loading

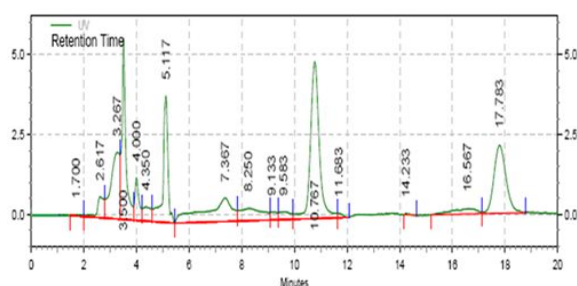


**Figure 11.** HPLC Chromatogram of green tea extract after loading

**TABLE 5.** HPLC results for natural extract of Green tea in loading process on MIPs

Green Tea Extract	Catechin (ppm)	Peak surface area (mAU)	Binding capacity ( $Q_e$ ) (mg.g <sup>-1</sup> )
Before loading	23.57	278244	-
After loading	8.81	115212	14.07

#### 4. CONCLUSION

Recently, the researches for separation of the bioactive compounds from natural extracts of medicinal plants or removal of the hazardous compounds from water has been increased. MIPs is one of the most suitable methods (adsorbent) with high selectivity in this regards. In this study, a highly stable and selective adsorbent was successfully synthesized according to precipitation polymerization reaction, in a molecular ratio of 1:12:12 for the first time. The results confirmed a good binding capacity of the synthesized MIPs with high selectivity for catechin molecule. Due to its low cost, relatively easy synthesis, high stability and selectivity, this technique has being developed in the production of enzymes, hormones, sensors, development of isolation and diagnostic methods, drug delivery, water purification, environmental chemistry, etc. Since, herbal plants contain a lot of the bioactive compounds which are very effective in treatment of the human diseases like cancer, it is necessary to find a suitable method for separation of these compounds and pre-concentration of them. Results of this research indicated that, MIPs technique can be suggested for extraction and pre-concentration of the bioactive compounds from medicinal plants.

#### 5. REFERENCES

- Jeon, H. Y., Kim, J. K., Kim, W. G., Lee, S. J. "Effects of oral epigallocatechin gallate supplementation on the minimal erythema dose and UV-induced skin damage." *Skin Pharmacology and Physiology*, Vol. 22, No. 3, (2009), 137-141. DOI: 10.1159/000201562.
- Qiu, J. "Traditional medicine: a culture in the balance." *Nature*, Vol. 448, No. 7150, (2007), 126-129. DOI: 10.1038/448126a.
- Mudgal, V., Madaan, N., Mudgal, A., Mishra, S. "Dietary polyphenols and human health." *Asian Journal of Biochemistry*, Vol. 5, No. 3, (2010), 154-162. DOI: 10.3923/ajb.2010.154.162
- Tabrizi, N.S., Yavari, M., "Adsorption of Methylene Blue Aqueous Solutions by Silk Cocoon." *International Journal of Engineering, Transactions C: Aspects*, Vol. 29, No. 9, (2016), 1191-1197. DOI: 10.5829/idosi.ije.2016.29.09c.02.
- Nourbakhsh Amiri, Z., Najafpour, G.D., Mohammadi, M., Moghadamnia, A.A., "Subcritical Water Extraction of Bioactive Compounds from Ginger (*Zingiber officinale* Roscoe)" *International Journal of Engineering, Transactions C: Aspects*, Vol. 31, No. 12, (2018), 1991-2000. DOI: 10.5829/ije.2018.31.12c.01.
- Mosbach, K., Ramström, O. "The emerging technique of molecular imprinting and its future impact on biotechnology." *Biotechnology*, Vol. 14, No. 2, (1996), 163-170. DOI: 10.1038/nbt0296-163.
- Ye, L., Mosbach, K. "Molecular imprinting: synthetic materials as substitutes for biological antibodies and receptors." *Chemistry of Materials*, Vol. 20, No. 3, (2008), 859-868. DOI: 10.1021/cm703190w.
- Piletska, E. V., Guerreiro, A. R., Whitcombe, M. J., Piletsky, S. A. "Influence of the polymerization conditions on the performance of molecularly imprinted polymers." *Macromolecules*, Vol. 42, No. 14, (2009), 4921-4928. DOI: 10.1021/ma900432z.
- Poma, A., Turner, A. P., Piletsky, S. A. "Advances in the manufacture of MIP nanoparticles." *Trends in Biotechnology*, Vol. 28, No. 12, (2010), 629-637. DOI: 10.1016/j.tibtech.2010.08.006.
- Lomenova, A., Hroboňová, K. "Polyméry s odtlačkami molekul ako chirálne stacionárne fázy v HPLC." *Chemické Listy*, Vol. 113, No. 3, (2019), 156-164.
- Machyňáková, A., Hroboňová, K. "Možnosti prípravy polymérov s odtlačkami molekul." *Chemické Listy*, Vol. 110, No. 9, (2016), 609-615.
- Halberstein, R. A. "Medicinal plants: historical and cross-cultural usage patterns." *Annals of Epidemiology*, Vol. 15, No. 9, (2005), 686-699. DOI: 10.1016/j.annepidem.2005.02.004.
- Cormack, P. A., Elorza, A. Z. "Molecularly imprinted polymers: synthesis and characterisation." *Journal of Chromatography B*, Vol. 804, No. 1, (2004), 173-182. DOI: 10.1016/j.jchromb.2004.02.013.
- BelBruno, J. J. "Molecularly imprinted polymers." *Chemical Reviews*, Vol. 119, No. 1, (2018), 94-119. DOI: 10.1021/acs.chemrev.8b00171.
- Saylan, Y., Yilmaz, F., Özgür, E., Derazshamshir, A., Yavuz, H., Denizli, A. "Molecular imprinting of macromolecules for sensor applications." *Sensors*, Vol. 17, No. 4, (2017), 898. DOI: 10.3390/s17040898.
- Sarafraz-Yazdi, A., Razavi, N. "Application of molecularly-imprinted polymers in solid-phase microextraction techniques." *TrAC Trends in Analytical Chemistry*, Vol. 73, (2015), 81-90. DOI: 10.1016/j.trac.2015.05.004.
- Mathew, D., Thomas, B., Devaky, K. S. "Biomimetic recognition and peptidase activities of transition state analogue imprinted chymotrypsin mimics." *Reactive and Functional Polymers*, Vol. 124, (2018), 121-128. DOI: 10.1016/j.reactfunctpolym.2018.01.005.
- Sener, G., Ozgur, E., Rad, A.Y., Uzun, L., Say, R., Denizli, A. "Rapid real-time detection of procalcitonin using a microcontact imprinted surface plasmon resonance biosensor." *Analyst*, Vol. 138, No. 21, (2013), 6422-6428. DOI: 10.1039/C3AN00958K.

19. Büyüktiryaki, S., Say, R., Denizli, A., Ersöz, A. "Phosphoserine imprinted nanosensor for detection of Cancer Antigen 125." *Talanta*, Vol. 167, (2017), 172-180. DOI: 10.1016/j.talanta.2017.01.093.
20. Wang, P., Sun, X., Su, X., Wang, T. "Advancements of molecularly imprinted polymers in the food safety field." *Analyst*, Vol. 141, No. 12, (2016), 3540-3553. DOI: 10.1039/C5AN01993A.
21. Jia, M., Zhang, Z., Li, J., Ma, X., Chen, L., Yang, X. "Molecular imprinting technology for microorganism analysis." *TrAC Trends in Analytical Chemistry*, Vol. 106, (2018), 190-201. DOI: 10.1016/j.trac.2018.07.011.
22. Li, L., Chen, L., Zhang, H., Yang, Y., Liu, X., Chen, Y. "Temperature and magnetism bi-responsive molecularly imprinted polymers: Preparation, adsorption mechanism and properties as drug delivery system for sustained release of 5-fluorouracil." *Materials Science and Engineering: C*, Vol. 61, (2016), 158-168. DOI: 10.1016/j.msec.2015.12.027.
23. Miao, S. S., Wu, M. S., Zuo, H. G., Jiang, C., Jin, S. F., Lu, Y. C., Yang, H. "Core-shell magnetic molecularly imprinted polymers as sorbent for sulfonyleurea herbicide residues." *Journal of Agricultural and Food Chemistry*, Vol. 63, No. 14, (2015), 3634-3645. DOI: 10.1021/jf506239b.
24. Tsermentseli, S. K., Manesiotes, P., Assimopoulou, A. N., Papageorgiou, V. P. "Molecularly imprinted polymers for the isolation of bioactive naphthoquinones from plant extracts." *Journal of Chromatography A*, Vol. 1315, (2013), 15-20. DOI: 10.1016/j.chroma.2013.09.044.
25. Shahiri Tabarestani, M., Rahnama, K., Jahanshahi, M., Nasrollanejad, S., Fatemi, M. H., "Identification of Volatile Organic Compounds from *Trichoderma virens* (6011) by GC-MS and Separation of a Bioactive Compound via Nanotechnology." *International Journal of Engineering, Transactions A: Basics*, Vol. 29, No. 10, (2016), 1347-1353. DOI: 10.5829/idosi.ije.2016.29.10a.04.
26. Abouzazadeh, A., Forouzani, M., Jahanshahi, M., Bahramifar, N. "Synthesis and evaluation of uniformly sized nalidixic acid-imprinted nanospheres based on precipitation polymerization method for analytical and biomedical applications." *Journal of Molecular Recognition*, Vol. 25, No. 7, (2012), 404-413. DOI: 10.1002/jmr.2201.
27. Galhotra, P., Navea, J. G., Larsen, S. C., Grassian, V. H. "Carbon dioxide (C16O2 and C18O2) adsorption in zeolite Y materials: effect of cation, adsorbed water and particle size." *Energy & Environmental Science*, Vol. 2, No. 4, (2009), 401-409. DOI: 10.1039/B814908A.
28. Pavia, Donald L., et al. "Introduction to spectroscopy: cengage learning." *Ainara Lopez Maestresalas*, Vol.153 (2008), 752.
29. Jiang, X., Tian, W., Zhao, C., Zhang, H., Liu, M. "A novel sol-gel-material prepared by a surface imprinting technique for the selective solid-phase extraction of bisphenol A." *Talanta*, Vol. 72, No. 1, (2007), 119-125. DOI: 10.1016/j.talanta.2006.10.006.
30. Shao, H., Zhao, L., Chen, J., Zhou, H., Huang, S., Li, K. "Preparation, characterization and application of molecularly imprinted monolithic column for hesperetin." *Journal of Pharmaceutical and Biomedical Analysis*, Vol. 111, (2015), 241-247. DOI: 10.1016/j.jpba.2015.04.006.
31. Masoumi, M., Jahanshahi, M. "Synthesis and recognition of nano pore molecularly imprinted polymers of thymol on the surface of modified silica nanoparticles." *Advances in Polymer Technology*, Vol. 35, No. 2, (2016), 221-227. DOI: 10.1002/adv.21548.
32. Amiri, A., Ramazani, A., Jahanshahi, M., Moghadamnia, A. A. "Synthesis of a nanostructured molecularly imprinted acrylic acid-based network copolymer as a solid sorbent for the quercetin extraction." *Journal of Nanostructures*, Vol. 4, No. 3, (2014), 277-283. DOI: 10.7508/jns.2014.03.004.
33. Zheng, M. M., Gong, R., Zhao, X., Feng, Y. Q. "Selective sample pretreatment by molecularly imprinted polymer monolith for the analysis of fluoroquinolones from milk samples." *Journal of Chromatography A*, Vol. 1217, No. 14, (2010), 2075-2081. DOI: 10.1016/j.chroma.2010.02.011.
34. Kwon, C.H., Choi, J.W., Lee, S.H., Park, H. L., Jung, S. H., "Chiral separation and discrimination of catechin by microbial cyclic  $\beta$ -(1 $\rightarrow$ 3), (1 $\rightarrow$ 6)-glucans isolated from *Bradyrhizobium japonicum*." *Bulletin of the Korean Chemical Society*, Vol. 28 No. 2 (2007), 347-350. DOI.org/10.5012/bkcs.2007.28.2.347

---

### Persian Abstract

---

#### چکیده

هدف از این مطالعه سنتز پلیمرهای قالب مولکولی و ارزیابی آن برای استخراج مولکول کاتچین می باشد. کاتچین یک ترکیب زیست فعال است که به وفور در چای سبز یافت می شود. در این مقاله پلیمرهای قالب گیری شده مولکولی (MIPs) به روش واکنش پلیمری شدن رسوبی در حضور کاتچین، آکرلیک اسید، تری متیلول پروپان تری متاکریلات به ترتیب به عنوان مولکول هدف، مونومر عاملی، اتصال دهنده عرضی به نسبت (۱:۱۲:۱۲)، سنتز گردید. ریخت شناسی سطحی پلیمر با استفاده از میکروسکوپ الکترونی روبشی (SEM) ذرات کروی پلیمر با ابعاد نانومتری را نشان داد. مطالعه پیوندهای شیمیایی موجود در ذرات پلیمر با استفاده از طیفسنجی تبدیل فوریه مادون قرمز (FTIR) از تسخیر شدن مولکول کاتچین در داخل پلیمر قالب گیری شده، دلالت دارند. تخلخل سطحی پلیمر، با استفاده از روش برونر، امت، تلمر (BET) مورد تجزیه و تحلیل قرار گرفت. براساس این آنالیز، سطح ویژه در پلیمرهای قالب گیری شده برابر  $45.5 \text{ m}^2 \cdot \text{g}^{-1}$  بوده در حالی که این مقدار در پلیمرهای قالب گیری نشده (NIPs) برابر  $\text{m}^2 \cdot \text{g}^{-1}$   $42.2$  بوده است. این بدان معناست که که قالب گیری در پلیمر به خوبی انجام شده است. همچنین ویژگی های جذب سطحی پلیمر نیز انجام شد. پلیمر قالب گیری شده در محلول بارگذاری با غلظت  $750 \text{ ppm}$  دارای بیشترین ظرفیت اتصال برای کاتچین به مقدار  $44.0 \text{ mg} \cdot \text{g}^{-1}$  بوده است درحالیکه ظرفیت اتصال برای مولکول کوئرستین (مولکولی با ساختار مشابه کاتچین) برابر  $8 \text{ mg} \cdot \text{g}^{-1}$  بوده است. این موضوع بیانگر آنست که فناوری قالب گیری مولکولی می تواند به عنوان یک گزینه خوب با گزینش پذیری بالای پلیمر در فرآیند جداسازی معرفی شود. همچنین اندازه گیری ظرفیت اتصال پلیمرهای قالب گیری شده بر روی عصاره طبیعی چای سبز با استفاده از دستگاه کروماتوگرافی مایع با عملکرد بالا (HPLC) انجام پذیرفت که نتایج مشابه حاصل شد. بر اساس نتایج اشاره شده، جداسازی و تغلیظ ترکیبات زیست فعال از عصاره گیاهان دارویی با استفاده از فناوری قالب گیری مولکولی، پیشنهاد می گردد.

---



## Optimum Design of Multi-layered Micro-perforated Panel Sound Absorbers in Combination with Porous Materials in an Arbitrary Frequency Range

M. Broghany<sup>a</sup>, S. Basirjafari<sup>\*b</sup>

<sup>a</sup> Graduate of Sound Engineering from IRIB University, Tehran, Iran

<sup>b</sup> Department of Sound, Faculty of Engineering, IRIB University, Tehran, Iran

### PAPER INFO

#### Paper history:

Received 27 October 2021

Received in revised form 22 January 2022

Accepted 04 February 2022

#### Keywords:

Sound Absorption Coefficient  
Micro-perforated Panel Absorber  
Optimized Composite Absorber  
Transfer Matrix Method  
Genetic Algorithm

### ABSTRACT

Optimum design of sound absorbers with optimum thickness and maximum sound absorption has always been an important issue to noise control. The purpose of this paper is an achievement of optimum design for micro-perforated panel (MPP) and its combination with a porous material and air gap to obtain maximum sound absorption with maximum overall thickness up to about 10 cm in the frequency range of (20-500 Hz), (500-2000 Hz) and (2000-10000 Hz). For this purpose, the genetic algorithm is proposed as an effective technique to solve the optimization problem. By using the precise theoretical models (i.e. simplified Allard's model and Atalla *et al.*'s model) to calculate the acoustic characteristics of each layer consisting of MPP, porous material, and airgap, we obtained more precise optimized structures. The transfer matrix method has been used to investigate the sound absorption of structures. To verify the operation of the programmed genetic algorithm, the results obtained from the optimization of the MPP absorber are compared with others that show the accuracy and efficiency of this method. After ensuring the accuracy of the proposed programmed genetic algorithm with more precise theoretical models to achieve the characteristics of each layer, new structures were obtained that have a much better sound absorption coefficient in the desired frequency range than the previous structures. The results show that the sound absorption coefficient can be reached to 0.67, 0.96, and 0.96 in the mentioned first, second, and third frequency range, respectively by optimum design parameter choosing of a composite structure.

doi: 10.5829/ije.2022.35.05b.15

### NOMENCLATURE

$f$	Frequency (Hz)	$d$	Diameter of the holes (mm)
$w$	Angular frequency (rad/s)	$D$	Depth of air gap (cm)
$L$	The thickness of the porous material (cm)	<b>Greek Symbols</b>	
$Z_s$	The specific acoustic impedance of the MPP (Rayls)	$\rho_0 c_0$	The characteristic impedance of the air (kg/m <sup>2</sup> s)
$t$	The thickness of the panel (mm)	$\sigma$	Flow resistivity of the porous material (Pa · s/m <sup>2</sup> )
$R_s$	The surface resistance of the vibrating air inside each hole	$\mathcal{E}_e$	Final correction coefficient
$p$	Perforation rate (%)	$\mu$	Kinetic coefficient of air
$Z_{in}$	Input specific acoustic impedance (Rayls)	$\alpha$	Sound absorption coefficient

### 1. INTRODUCTION

Noise pollution is an unpleasant sound that is significantly harmful to general health and it's become one of the most important environmental issues in

modern life [1-5]. Control of noise, especially, in three frequency ranges, e.g. low-frequency (20 Hz-500 Hz), mid-frequency (500 Hz-2000 Hz), and high-frequency (2000 Hz-10000 Hz) is important [6-9]. Porous materials [10] are the most applicable types of sound absorbers

\*Corresponding Author Institutional Email: [basirjafari@IRIBu.ac.ir](mailto:basirjafari@IRIBu.ac.ir)  
(S. Basirjafari)

used in noise control in high frequencies [11-14]. To increase the sound absorption in low frequencies, the thick layer of the porous absorber is needed and it takes up a lot of space. They are cheaper sound absorbers than other types of absorbers but have three major drawbacks:

- 1) They do not have adequate sound absorption in low and mid frequencies with low thickness;
- 2) They do not have adequate strength against the impact and pressure;
- 3) The separated particles from them are entered into the air and the ventilation system and thus damage human health.

In previous works, we optimized a flat multi-layer porous sound absorber by using a multi-objective genetic algorithm for application in an anechoic chamber [15]. Due to the above disadvantages for porous sound absorbers, the achieved design was only suitable for use in certain places such as anechoic rooms and music studios, not in residential and public buildings.

Hence the use of a Micro perforated panel (MPP) as a strength sound absorber in front of the porous absorber was considered by the researchers [16-19].

MPPs were introduced by Maa [20-22] for the first time. The disadvantage of this type of sound absorber is the narrow frequency range of absorption. Due to an increase in the frequency range of absorption, some suggestions have been proposed such as the use of multi-layered MPPs in succession [23-27] and the use of porous material behind the MPP [16-19].

Researchers are interested to produce sound absorbers suitable for low-frequency noise control. To increase the sound absorption in low frequencies, the insertion of the flexible plate driven by a concentrated force on the back of the MPP is used [28]. Basirjafari [29] enhanced the Helmholtz resonator sound absorption only in low-frequency by Fibonacci sequence according to the nature inspiration, for the first time.

Literature review shows that the multi-layered sound absorbers composed of porous materials and MPPs are mostly used for noise control, due to their high environmental compatibility, high strength, beautiful facing, low-cost manufacturing, simple installation, and the adjustable frequency bandwidth of sound absorption. Although, the thickness of each layer, the arrangement of layers, selection of material for each layer, determination of MPP parameters such as thickness, hole diameter, and porosity play important roles to design an optimum multi-layered sound absorber for an arbitrary frequency range of absorption.

On the other hand, a genetic algorithm is an effective tool for optimization. By using the genetic algorithm, the type of arrangement, and the characteristics of each layer in the multi-layered sound absorber can be determined in such a way that the maximum absorption coefficient of

sound is obtained in a special thickness.

The purpose of this paper is to optimize the MPPs structure and porous material by using the more precise theoretical models (i.e. simplified Allard's model [14] and Atalla *et al.*'s model [30]) than previous researches [16, 23, 26] to calculate their acoustical characteristics, and their arrangement in combination with an air gap to have a maximum average of sound absorption coefficient in desired frequency ranges with a maximum overall thickness of 10 cm.

Three frequency ranges including the first range (20 Hz - 500 Hz), the second one (500 Hz - 2000 Hz), and the third one (2000 Hz - 10000 Hz) are selected for optimization. To this aim, the use of a genetic algorithm has been proposed as an effective tool in optimization problems. By using precise theoretical models, the genetic algorithm can give a more precise optimized structure.

## 2. MATHEMATICAL MODEL

In this paper, the transfer matrix of a multi-layered structure composed of an MPP, porous material, and the air gap is used to calculate its sound absorption coefficient, as described in the previous paper [16]. The previous method has been used with the difference that the simplified Allard's model is used to calculate the characteristic impedance and the propagation constant of porous material [14] because it is more accurate than the others. Atalla *et al.* [30] model is used for calculating the acoustic impedance of MPPs as:

$$Z_s = (t + 2\varepsilon_e) \left[ (1 + j) \frac{4R_s}{pd} + \frac{jw\rho_0}{p} \right] \quad (1)$$

$$\varepsilon_e = 0.425d(1 - 1.14\sqrt{p}) \quad (2)$$

$$R_s = \sqrt{\frac{\rho_0 w \mu}{2}} \quad (3)$$

In the above equations,  $Z_s$  is the specific acoustic impedance of the MPP,  $t$  is the thickness of the panel,  $\varepsilon_e$  is the final correction coefficient,  $R_s$  is the surface resistance of the vibrating air inside each hole,  $p$  is the perforation rate,  $d$  is the diameter of the holes,  $w$  is the angular frequency, and  $\mu$  is the kinetic coefficient of air. The sound absorption coefficient can be obtained [16]:

$$\alpha = \frac{4Re\left(\frac{Z_{in}}{\rho_0 c_0}\right)}{\left[1 + Re\left(\frac{Z_{in}}{\rho_0 c_0}\right)\right]^2 + \left[\text{Im}\left(\frac{Z_{in}}{\rho_0 c_0}\right)\right]^2} \quad (4)$$

in which,  $Z_m$  an input specific acoustic impedance and  $\rho_0 c_0$  is the characteristic impedance of the air.

It can be seen that several factors affect the sound absorption coefficient of a multi-layered sound absorber composed of MPP, porous material, and air gap. For example, the absorption coefficient of the MPP depends on four factors: the diameter of the holes, the thickness of the panel, the porosity, and the depth of the air gap behind the panel. Also, the absorption coefficient of the porous absorber depends on different factors: porosity, tortuosity, Young's modulus, airflow resistivity, and the thickness of the porous material layer, which airflow resistivity and the thickness of the porous material layer is just considered in the simplified Allard's model.

With the right choice of these quantities, suitable absorption can be achieved within the desired frequency range. The number and arrangement of layers also affect the sound absorption of the structure. Therefore, for optimal structural design, the type of arrangement, and the determination of the proper characteristics of each layer is very important. Because examining the effect of each of the above factors on adsorption efficiency requires the design, fabrication, and test of several laboratory samples, the trial, and error-based method is very costly and time-consuming. Therefore, the genetic algorithm is used to optimize the sound absorption of the mentioned multi-layered structure, with commercial porous materials whose specifications are given in Table 1 of our previous paper [15]. By using the genetic algorithm, the type of arrangement, and the characteristics of each layer are determined in a way that the maximum sound absorption coefficient for the absorber with a certain thickness is obtained.

The used parameters of the genetic algorithm in this paper are as follows:

1. The maximum number of generations is 20.
2. The population size in each generation is 328.
3. The generation gap is equal to 0.5, which means that 50% of the population in each generation is replaced and the mutation rate is 5% means that in each generation, 5% of the population is jump.
4. In this case, the fitness function is the sound absorption coefficient. The transfer matrix method described in the previous section should be used to calculate it.

The design parameters are the type and thickness of the porous absorber layer, the micro-perforated panel thickness, the holes diameter, the porosity, and the air gap thickness.

### 3. RESULTS AND DISCUSSION

Because in industrial applications, optimal absorber design is required for optimum performance in the

desired frequency range, the purpose of this section is to optimize the multi-layered sound absorber composed of an MPP, porous material, and air gap for achieving the highest average of sound absorption coefficient in three frequency ranges including first range (20 Hz - 500 Hz), second range (500 Hz - 2000 Hz) and the third range (2000 Hz - 10000 Hz).

For this purpose, a genetic algorithm has been used as an effective tool for optimization problems. For the implementation of the genetic algorithm, MATLAB software has been used. In the first step, a double-layer MPP and a three-layer MPP sound absorber have been optimized by the genetic algorithm and compared with the results reported by Ruiz et al. [26] to verify the programmed genetic algorithm. At the second step, a single layer MPP and a double-layer MPP have been optimized in the mentioned three frequency range by genetic algorithm. Finally, the multi-layered sound absorber has been optimized by the genetic algorithm in the same three mentioned frequency ranges.

**3.1. Analytical Method Verification** To verify the mathematical model, the sound absorption coefficient of the single-layer micro-perforated panel and composite absorber was calculated by the transfer matrix method and compared with the experimental results illustrated in Figures 1 and 2. Sound absorption coefficients were examined in impedance tube, according to ASTM E 1050 90 and ISO 10543-2.

In Figure 1, the experimental result has been reported by Ruiz et al. [26] for the sound absorption coefficient of single layer micro-perforated panel absorber with characteristics of  $t = 1$  mm,  $d = 0.25$  mm,  $p = 3.4\%$ , and air gap with the thickness of 1.1 cm. As shown in Figure 1, the results of the proposed theory for the single-layer

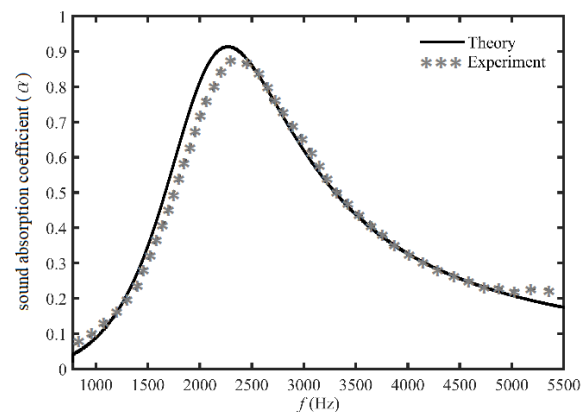


**Figure 1.** Comparison of the present theoretical result with the experimental result reported in [26] for the sound absorption coefficient of single layer micro-perforated panel absorber versus frequency; characteristics of MPP are  $t = 1$  mm,  $d = 0.25$  mm,  $p = 3.4\%$ , and thickness of air gap is 1.1 cm

MPP correspond to the experimental results with an average error of 5.8%.

In Figure 2, the experimental result has been reported by Davern [18] for the sound absorption coefficient of composite absorber consists of three layers with characteristics of the first layer: MPP absorber with  $t = 6.3$  mm,  $d = 0.75$  mm,  $p = 4.7\%$ ; second layer: porous absorber with  $\sigma = 16000$  Pa.s/m<sup>2</sup>,  $L = 2.5$  cm; third layer: air gap with  $D = 2.5$  cm thickness. As shown in Figure 2, the results of the proposed theory for the triple-layer MPP correspond to the experimental results with an average error of 15.7%.

### 3. 2. Verification of the Programmed Genetic Algorithm

As mentioned before, the absorption coefficient of the MPP sound absorber depends on four quantities: the diameter of the holes, the thickness of the panel, the porosity of the panel, and the air gap thickness between the panel and the wall.

To verify the performance of the programmed genetic algorithm for optimizing acoustic absorbers, the optimization results of MPP absorbers were compared with the optimization results reported by Ruiz et al. [26].

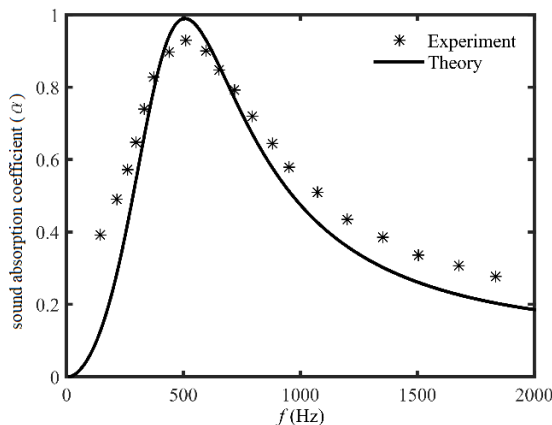


**Figure 2.** Comparison of the present theoretical result with experimental result reported in [18] for sound absorption coefficient of composite absorber versus frequency (first layer: MPP absorber with  $t = 6.3$  mm,  $d = 0.75$  mm,  $p = 4.7$  %; second layer: porous absorber with  $\sigma = 16000$  Pa.s/m<sup>2</sup>,  $L = 2.5$  cm; third layer: air gap with  $D = 2.5$  cm thickness)

They have used the Atalla model [30] to calculate the sound absorption coefficient of the MPPs. Because it is more accurate than other models. Also, they used the Simulated Annealing algorithm (SA) to optimize it. Therefore, in this paper, to compare the optimization results, the Atalla model is used to calculate the sound absorption coefficient. The relations of this model are given in Equations (1) to (3).

Also, to compare the programmed genetic algorithm results with the Simulate Annealing algorithm (SA) which Ruiz et al. [26] used to optimize the sound absorber structure, the specification of the micro-perforated panel (the diameter of holes, the thickness of the panel, the porosity, and the air gap spacing) is limited by the Ruiz method [26], which is shown in relation (5).

$$t_i = 1\text{ mm}, d_i \in [0.25, 0.75]\text{ mm}, p_i \in [3.4, 8.5]\%, \\ D_i \in [1, 5]\text{ cm} \tag{5}$$

In this regard,  $t_i$  is the thickness of the panel,  $d_i$  is the diameter of the holes,  $p_i$  is the porosity,  $D_i$  is the air gap thickness, and the subscript  $i$  represents the number of each layer. The optimization results by using the genetic algorithm and Simulate Annealing algorithm (SA) for double-layer MPP are given in Table 1 and for three-layer MPP are given in Table 2. According to Tables 1 and 2, the obtained results for the average sound absorption in comparison with Ruiz’s results clearly show the validity of the programmed genetic algorithm.

After ensuring the accuracy of the proposed programmed genetic algorithm with more precise theoretical models (i.e. simplified Allard’s model [14], and Atalla *et al.* model [30]) to achieve the characteristics of each layer, new structures will be proposed that have a much better sound absorption coefficient in the desired frequency range than the previous structures.

### 3. 3. MPP Sound Absorber Optimization

In the structural design of the N-layer micro-perforated panel, the sound absorption coefficient depends on the 4N quantities. The specifications of the panels are limited according to Equation (6).

$$t_i \in [0.5, 5]\text{ mm}, d_i \in [0.1, 1]\text{ mm}, p_i \in [1, 15]\%, \\ \sum D_i \leq 10\text{ cm} \tag{6}$$

**TABLE 1.** Comparison between the optimization results of the present genetic algorithm and the results of simulated annealing of [26] for double-layer micro-perforated panel absorber with the same thickness  $t_1 = t_2 = 1$  mm

Optimization method	1st. layer parameters			2nd. layer parameters			The average sound absorption coefficient in 800-6400 Hz
	$d_1$ (mm)	$p_1$ (%)	$D_1$ (cm)	$d_2$ (mm)	$p_2$ (%)	$D_2$ (cm)	
Simulated annealing [26]	0.25	8.4	1	0.25	3.5	1	0.65
Genetic algorithm (present work)	0.25	8.5	1	0.25	3.4	1	0.66

**TABLE 2.** Comparison between the optimization results of the present genetic algorithm and the results of simulated annealing of [26] for three-layer micro-perforated panel absorber with the same thickness  $t_1 = t_2 = t_3 = 1 \text{ mm}$ .

Optimization method	1st. layer parameters			2nd. layer parameters			3rd. layer parameters			The average sound absorption coefficient in 800 -6400 Hz
	$d_1$ (mm)	$p_1$ (%)	$D_1$ (cm)	$d_2$ (mm)	$p_2$ (%)	$D_2$ (cm)	$d_3$ (mm)	$p_3$ (%)	$D_3$ (cm)	
Simulated annealing [26]	0.25	8.5	1	0.25	4.55	1	0.25	3.4	1.3	0.74
Genetic algorithm (present work)	0.25	7.8	1	0.25	4.71	1	0.25	3.5	1.7	0.73

In practical applications of noise control, the limitation of occupied space by the sound absorber is a very important problem. The total thickness of the sound absorber is considered to be about 10 cm, most of which is air gap or porous material and is therefore very light or low cost.

In Equation (6), the maximum thickness for the total air gap is 10 cm. Tables 3 and 4 show the optimal specifications and the average sound absorption coefficient of the structure consisting of a single layer MPP (see Figure 3(a)) and double-layer MPP (see Figure 3(b)) for the desired frequency ranges, respectively.

Figures 4 and 5 show the absorption coefficient of the optimal structures in Tables 3 and 4, respectively, in terms of frequency.

According to the results of optimizing the structure of a single layer MPP, as shown in Figure 4, the genetic algorithm in each frequency range adjusts the structure characteristics so that the first resonance frequency of the structure occurs in the same range.

The optimal structure No. 1 has the highest sound absorption coefficient of 0.99 at a resonant frequency of 288 Hz. As can be seen, this structure has six resonances in the frequency range of 1 Hz to 10000 Hz, in which the

value of the absorption coefficient decreases at higher resonant frequencies.

The optimal structure No. 2 has the highest sound absorption coefficient of 0.98 at the resonant frequency of 1005 Hz. The optimal structure thickness of No. 1 is more than 3 times of No. 2 and has an average sound absorption coefficient of 21% less than the structure No. 2 in the frequency range of 500 Hz to 2000 Hz.

Therefore, increasing the thickness of the structure in the second frequency range is not necessary and if there is not considerable noise in the frequency lower than 500 Hz, structure No. 1 can not be used.

The optimal structure No. 3 has the highest sound absorption coefficient of 0.86 at a resonant frequency of 4008 Hz. As can be seen, due to the increase in the frequency range of sound absorption, the absorption coefficient of structure No. 3 in the resonance frequency has decreased by 13%. Also, the average sound absorption coefficient in this frequency range has decreased by 12.7% compared to the first frequency range and 36.4% compared to the second frequency range. Therefore, a structure consisting of a single layer of MPP is weaker in absorbing high-frequency audible sound compared to low- and mid-frequencies.

**TABLE 3.** Optimization of the sound absorption coefficient for single layer micro-perforated panel absorber.

Structure number	Frequency bandwidth (Hz)	Optimal design parameters				The average sound absorption coefficient
		$t$ (mm)	$d$ (mm)	$p$ (%)	$D$ (cm)	
1	20 – 500	1.5	0.1	1.9	10	0.62
2	500 – 2000	1.5	0.1	5.3	3	0.75
3	2000 - 10000	0.7	0.1	8.5	1	0.55

**TABLE 4.** Optimization of the sound absorption coefficient for a double-layer micro-perforated panel absorber.

Structure number	Frequency bandwidth (Hz)	Optimal design parameters								The average sound absorption coefficient
		$t_1$ (mm)	$d_1$ (mm)	$p_1$ (%)	$D_1$ (cm)	$t_2$ (mm)	$d_2$ (mm)	$p_2$ (%)	$D_2$ (cm)	
1	20 - 500	4.5	1	1.9	5	3.9	0.1	1.2	5	0.64
2	500 - 2000	2.1	0.1	14.9	3.4	4.2	0.1	7.5	2.1	0.94
3	2000 - 10000	0.5	0.1	12	1	0.8	0.1	8	1	0.78

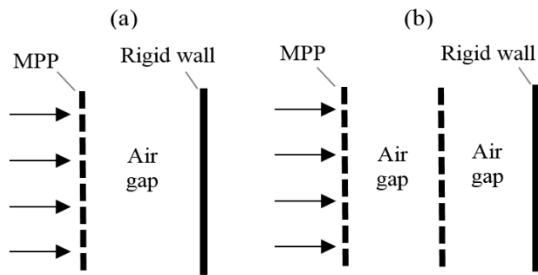


**Figure 3.** (a) single layer, (b) double-layer micro-perforated panel (MPP)

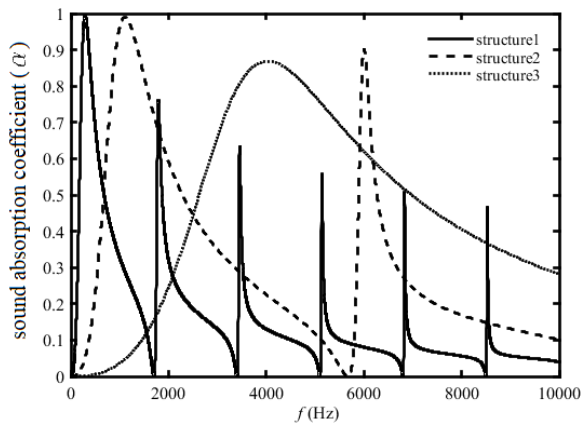


**Figure 4.** The sound absorption coefficient of optimum structures 1, 2, and 3 that are described in Table 3, for double-layer micro-perforated panel versus frequency

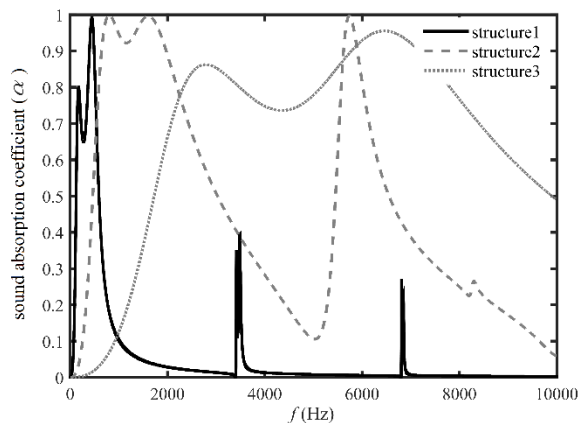


**Figure 5.** The sound absorption coefficient of optimum structures 1, 2, and 3 that are described in Table 4, for single-layer micro-perforated panel versus frequency

The average absorption coefficient of the proposed double-layer structure by Ruiz et al. [26] by assuming the fixed thickness of each layer, whose specifications are listed in Table 1, was 0.65 in the frequency range of 800 to 6400 Hz, with a total thickness of 22 mm. Whereas we considered the thickness of the MPP as a variable

quantity in the genetic algorithm and according to Table 3, by differentiating the aforementioned frequency interval, we achieved two different single-layer structures No. 2 and 3. Structure No. 2 with a thickness of 31.5 mm, provides an average absorption coefficient of 0.82 in the frequency range of 800 to 2000 Hz, and structure No. 3 with a thickness of 10.7 mm, provides an average absorption coefficient of 0.64 in the frequency range of 2000 to 6400 Hz.

Comparing Ruiz's proposed double-layer structure with our proposed single layer structures shows that according to the frequency spectrum of noise in a room, with a suitable arrangement of the structures Nos. 2 and 3 on the surfaces of the room can be achieved the average absorption coefficient of 0.73 in the frequency range of 800 to 6400 Hz, which is 12.3% better than the average absorption coefficient of the Ruiz's proposed structure.

Considering that our proposed structures are single layer, it has less manufacturing cost than Ruiz's proposed double-layer restructure, and also due to less average total thickness of 21.1 mm which is less than his structure, the average space it occupies is 4.1% lower.

The average absorption coefficient of the proposed triple-layer structure by Ruiz et al. [26] by assuming the fixed thickness of each layer, whose specifications are listed in Table 2, was 0.74 in the frequency range of 800 to 6400 Hz, with a total thickness of 36 mm.

Comparing his proposed triple-layer structure with our proposed single layer structures in Table 3, we find that with a suitable layout of these two structures Nos. 2 and 3 on the surfaces of the room, with a maximum thickness of 31.5 mm, i.e. 12.5% less than the total thickness of the Ruiz's proposed structure, can be achieved the average absorption coefficient of 0.73 in the frequency range of 800 to 6400 Hz, which with good accuracy is almost equal to the average absorption coefficient of the Ruiz's proposed structure.

Considering that our proposed structure is single-layer, it has advantages over the proposed Ruiz's triple-layer structure, including:

1. It has less manufacturing cost than the proposed Ruiz's structure.
2. Due to the lower average thickness than the proposed Ruiz's structure, the average space it occupies is 4.1% lower.
3. The diameter of MPP holes in our proposed structure is 60% reduced compared to the proposed Ruiz's structure, which is more resistant to dust passage, and as a result, over time, the space behind the perforated panel becomes less filled and polluted with dust.
4. Considering that the average thickness of the MPP in our two proposed single-layer structures is 1.1 mm. Whereas in the proposed Ruiz's triple-layer structure is used three MPP layers with an overall thickness of

3 mm. His proposed structure compared to our proposed structure, after installation on the surfaces of the room, increases the final weight of the building by 63.3% more, which is clearly, the lighter structure is more desirable and safer in earthquakes.

According to the given results for optimizing the structure of the double-layer MPP, as shown in Figure 5, using two layers of the micro-perforated panel creates the first and second resonant frequencies.

In optimized structures, the genetic algorithm in each frequency range arranges the structure specifications in such a way that the first and second resonant frequencies of the structure occur within that range. From the comparison of the optimal structure of the number 1 in Table 3 with the optimal structure of number 1 in Table 4, it can be seen that by adding single layer MPP to the single-layer structure of MPP without increasing the total thickness of 10 cm, only 3.2% has been added to the average coefficient of sound absorption in the frequency range of 20 Hz to 500 Hz. Therefore, for this frequency range, the single-layer MPP structure is more economical than the double-layer MPP. Comparison of the optimal structure No. 2 in Table 3 with the optimal structure No. 2 in Table 4 shows that by adding a perforated layer to a single-layered structure, 3 cm is added to the total thickness of structure No. 2 and the total thickness is increased to 6.13 cm, and the average sound absorption coefficient is improved by 25.3% in the frequency range of 500 Hz to 2000 Hz. Therefore, for this frequency range, the double-layer MPP structure is more appropriate than a single-layer one. According to Figure 5 for structure No. 3, it can be seen that in the optimal double-layer structure, despite the increase in the absorption frequency bandwidth, the amount of absorption at the resonance frequencies has not decreased. Besides, the use of double-layer MPP created two resonances in the frequency range of 2000 Hz to 10000 Hz, which has resulted in a 41.8% improvement in the average sound absorption coefficient of the double-layer MPP structure compared to the single-layer structure in the frequency range of 2000 Hz to 10000 Hz.

According to the results for optimal structures including single-layer and double-layer MPPs, it can be said that to improve the amount of absorption coefficient in the frequency range of 20 Hz to 500 Hz, it is necessary to increase the overall thickness of the structure.

Also, the arrangement of the three proposed structures in Table 4, with an average total thickness of 33% more than the three structures in Table 3, improves the average sound absorption coefficient in the room at all frequencies by about 23% and reaches about 80%.

### 3. 4. Optimization of a Composite Sound Absorber

To compare the results of this section with the

optimization results of the previous section, the specifications of the MPP are according to Equation (6), except for the maximum allowable depth of air gap which is considered in this section is 5 cm. The porous materials whose specifications are given in Table 1 of our previous paper [15] are used, and the maximum allowable thickness of the porous material is 5 cm. Therefore, the maximum allowable thickness for the entire air gap and porous material is 10 cm.

To accurately model the MPP and porous material, Atalla's model [30] and Allard's model [14] have been used, respectively. The optimal structural characteristics and the average sound absorption coefficient of the composite sound absorber in the three frequency range of low-, mid-, and high-frequencies are listed in Table 5. Also, the sound absorption coefficient of the optimal structures presented in Table 5 is shown in Figure 6 in terms of frequency.

According to the results of the optimization of the composite sound absorber in Table 5 and its comparison with Tables 3 and 4, it can be seen that for low-frequency range, the composite sound absorber in comparison with the single and double-layer MPP structure with the same overall thickness, has better sound absorption. Also, the use of porous material behind the MPP, due to good absorption in the high-frequency range, improves the absorption bandwidth in the composite sound absorber.

Comparison of sound absorption efficiency in optimal single-layer MPP structure which is obtained in Table 3 and composite sound absorber according to Table 5 shows that using the 5 cm of porous material behind the MPP, without a considerable increasing the thickness of the whole structures, improves the average sound absorption coefficient by 8% in the first frequency range, 28% in the second frequency range and 74.6% in the third frequency range.

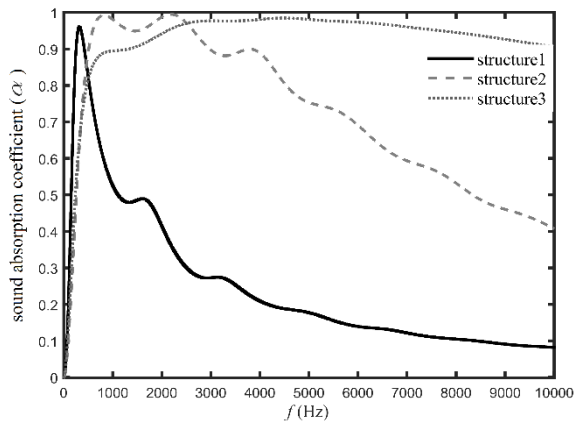
Figure 6 in comparison with Figures 4 and 5 shows that, as expected, porous material has a greater effect on improving the sound absorption coefficient at high frequencies.

Comparison of sound absorption efficiency of the optimal structure of double-layer MPP which is obtained in Table 4 and composite absorber according to Table 5, considering the high cost of making micro-perforated panels, shows that the use of 5 cm porous material behind the MPP, in addition, to reduce the manufacturing cost, improves the average sound absorption coefficient of the structure up to 4.7% in the first frequency range, up to 2% in the second frequency range and up to 23% in the third frequency range.

Therefore, it can be concluded that the use of a composite sound absorber is very suitable for sound absorption in a wider frequency range. According to the results of composite sound absorber optimization, the

**TABLE 5.** Optimization of the sound absorption coefficient for the composite absorber.

Structure number	Frequency bandwidth (Hz)	Optimal design parameters						The average sound absorption coefficient
		$t$ (mm)	$d$ (mm)	$p$ (%)	$D$ (cm)	$\sigma$ (Pa.s/m <sup>2</sup> )	$L$ (cm)	
1	20 - 500	5	0.1	9	5	6229	5	0.67
2	500 - 2000	1.5	0.9	14	3.6	10100	5	0.96
3	2000 - 10000	0.5	0.2	15	2.8	21600	5	0.96

**Figure 6.** The sound absorption coefficient of optimum structures 1, 2, and 3 that are described in Table 5, for composite absorber versus frequency

genetic algorithm in all three mentioned frequency ranges determines the maximum allowable thickness of the optimal structures with a thickness of 5 cm of porous material. Therefore, it can be said that increasing the thickness of the porous material in the composite sound absorber improves the average sound absorption coefficient in all three mentioned frequency ranges.

For future work, more accurate models such as the Johnson-Champoux-Allard (JCA) model [31] can be used to determine the acoustic characteristics of porous materials.

#### 4. CONCLUSIONS

In this paper, the optimal design of the multi-layered sound absorber composed of porous materials and the micro-perforated panel with an overall maximum thickness of up to 10 cm is presented by using the genetic algorithm for three frequency ranges. The desired frequency range includes the first range (20 Hz-500 Hz), the second range (500 Hz-2000 Hz), and the third range (2000 Hz-10000 Hz). Briefly, the results can be summarized as follows:

- The optimal design of the single-layered micro-perforated panel is only appropriate in the frequency

range of 20 Hz to 500 Hz.

- By using the precise theoretical models, we obtained single layer structures with 4.1% lower space occupation and less manufacturing cost in comparison with Ruiz's proposed double-layer structure enhance the average absorption coefficient up to 12.3% in the frequency range of 800 to 6400 Hz.
- By using the precise theoretical models, we obtained single layer structures with 41.4% lower space occupation, less manufacturing cost, 60% cleaner, and 63.3% lighter and safer in comparison with Ruiz's proposed triple-layer structure provide the same amount of the average absorption coefficient in the frequency range of 800 to 6400 Hz.
- By adding a layer to a single-layer structure MPP, the average sound absorption coefficient improves up to 25.3% in the frequency range of 500 Hz to 2000 Hz.
- The use of 5 cm porous material behind the MPP in the composite absorber, in addition, to reducing the manufacturing cost in comparison with double-layer MPP, improves the average sound absorption coefficient of the structure up to 23% in the frequency range of 2000 Hz to 10000 Hz.

#### 5. REFERENCES

1. Golmohammadi, R., Abolhasannejad, V., Soltanian, A. R., Aliabadi, M., Khotanlou, H. "Noise Prediction in Industrial Workrooms Using Regression Modeling Methods Based on the Dominant Frequency Cutoff Point", *Acoustics Australia*, Vol. 46, No. 2, (2018), 269-280. <https://doi.org/10.1007/s40857-018-0137-8>
2. Sarikavak, Y., Boxall, A. "The Impacts of Pollution for New High-Speed Railways: the Case of Noise in Turkey", *Acoustics Australia*, Vol. 47, No. 2, (2019), 141-151. <https://doi.org/10.1007/s40857-019-00154-5>
3. Kamp, I.van, Berg, F. van den. "Health effects related to wind turbine sound, including low-frequency sound and infrasound", *Acoustics Australia*, Vol. 46, No. 1, 31-57 (2018). <https://doi.org/10.1007/s40857-017-0115-6>
4. Jafari, M.J., Sadeghian, M., Khavanin, A., Khodakarim, S., Jafarpisheh, A.S. "Effects of noise on mental performance and annoyance considering task difficulty level and tone components of noise", *Journal of Environmental Health Science and Engineering*, Vol. 17, No. 1, (2019), 353-365. DOI: [10.1007/s40201-019-00353-2](https://doi.org/10.1007/s40201-019-00353-2)

5. Mehraby, K., Beheshti, H., Poursina, M. "Numerical and Analytical Investigation in Radiated Noise by a Shock-Absorber", *International Journal of Engineering, Transactions C: Aspects*, Vol. 26, No. 12, (2013), 1525-1534. DOI: 10.5829/idosi.ije.2013.26.12c.13
6. Yuan, M. "Compact and Efficient Active Vibro-acoustic Control of a Smart Plate Structure", *International Journal of Engineering, Transactions B: Applications*, Vol. 29, No. 8, (2016), 1068-1074. DOI: 10.5829/idosi.ije.2016.29.08b.06
7. Khalvati, F., Omidvar, A. "Prediction of Noise Transmission Loss and Acoustic Comfort Assessment of a Ventilated Window using Statistical Energy Analysis", *International Journal of Engineering, Transactions C: Aspects*, Vol. 32, No. 3, (2019), 451-459. DOI: 10.5829/IJE.2019.32.03C.14
8. Al-Bugharbee, H., Jubear, A. "An Experimental Investigation of Enclosure's Effect on Noise Reduction in Portable Generators", *International Journal of Engineering, Transactions B: Applications*, Vol. 33, No. 2, (2020), 350-356. DOI: 10.5829/ije.2020.33.02b.21
9. Yang, K., Zou, J., Shen, J. "Vibration and Noise Reduction Optimization Design of Mine Chute with Foam Aluminum Laminated Structure", *International Journal of Engineering, Transactions B: Applications*, Vol. 33, No. 8, (2020), 1668-1676. DOI: 10.5829/IJE.2020.33.08B.26
10. Azdast, T., Hasanzadeh, R. "Tensile and Morphological Properties of Microcellular Polymeric Nanocomposite Foams Reinforced with Multi-walled Carbon Nanotubes", *International Journal of Engineering, Transactions C: Aspects*, Vol. 31, No. 3, (2018), 504-510. DOI: 10.5829/ije.2018.31.03c.14
11. Basirjafari, S., Malekfar, R., Esmailzadeh Khadem, S. "Low loading of carbon nanotubes to enhance acoustical properties of poly (ether) urethane foams", *Journal of Applied Physics*, Vol. 112, No. 10, (2012), 104312. <https://doi.org/10.1063/1.4765726>
12. Basirjafari, S. "Effects of carbon nanotube loading on cellular structures and sound absorption of polyurethane foams", *Micro & Nano Letters*, Vol. 13, (2018). DOI: 10.1049/mnl.2018.5069
13. Basirjafari, S. "Morphological investigation of carbon nanotube reinforced polyurethane foam to analyse its acoustical and non-acoustical properties", *Micro & Nano Letters*, Vol. 16, (2021), 157-163. DOI: 10.1049/mna2.12029
14. Oliva, D., Hongisto, V. "Sound absorption of porous materials—Accuracy of prediction methods", *Applied Acoustics*, Vol. 74, No. 12, (2013), 1473-1479. DOI: 10.1016/j.apacoust.2013.06.004
15. Broghany, M., Basirjafari, S., Saffar, S. "Optimization of flat multi-layer sound absorber by using multi-objective genetic algorithm for application in anechoic chamber", *Modares Mechanical Engineering*, Vol. 16, No. 2, (2016), 215-222. DOI: 20.1001.1.10275940.1395.16.2.40.5
16. Broghany, M., Saffar, S., Basirjafari, S. "Increasing the frequency band of sound absorption for flat multi-layered absorbers consisting of porous material, perforated panel and air-gap", *Amirkabir Journal of Engineering*, Vol. 50, No. 1, (2018), 75-77. DOI: 10.22060/MEJ.2017.12042.5247
17. Liu, X., Yu, C., Xin, F. "Gradually perforated porous materials backed with Helmholtz resonant cavity for broadband low-frequency sound absorption", *Composite Structures*, Vol. 263, (2021), 113647. <https://doi.org/10.1016/j.compstruct.2021.113647>
18. Davern, W.A. "Perforated facings backed with porous materials as sound absorbers—An experimental study", *Applied Acoustics*, Vol. 10, No. 2, (1977), 85-112. DOI: 10.1016/0003-682X(77)90019-6
19. Yuan, Z.-X. "Acoustic Properties of Multilayered Structures", *Acoustics Australia*, (2020), 1-11. <https://doi.org/10.1007/s40857-020-00196-0>
20. Maa, D.-Y. "Theory and design of microperforated panel sound-absorbing constructions", *Scientia Sinica*, Vol. 18, No. 1, (1975), 55-71. DOI: 10.1360/YA1975-18-1-55
21. Maa, D.-Y. "Microperforated-panel wideband absorbers", *Noise Control Engineering Journal*, Vol. 29, No. 3, (1987), 77-84. DOI: 10.3397/1.2827694
22. Maa, D.-Y. "Potential of microperforated panel absorber", *The Journal of the Acoustical Society of America*, Vol. 104, No. 5, (1998), 2861-2866. <https://doi.org/10.1121/1.423870>
23. Lu, C.-H., Chen, W., Zhu, Y.-W., Du, S.-Z., Liu, Z.-E. "Comparison analysis and optimization of composite micro-perforated absorbers in sound absorption bandwidth", *Acoustics Australia*, Vol. 46, No. 3, (2018), 305-315. <https://doi.org/10.1007/s40857-018-0140-0>
24. Lee, W.-Y., Kim, J.-C. "A Study on Micro-Perforated Panel Absorber with Multi-Layered and Parallel-Arranged Structure to Enhance Sound Absorption Performance", *International Journal of Precision Engineering and Manufacturing*, Vol. 20, No. 6, (2019), 937-947. DOI: 10.1007/s12541-019-00072-6
25. Chen, W., Lu, C., Liu, Z., Du, S. "Simplified method of simulating double-layer micro-perforated panel structure", *Automotive Innovation*, Vol. 1, No. 4, (2018), 374-380. DOI: 10.1007/s42154-018-0040-x
26. Ruiz, H., Cobo, P., Jacobsen, F. "Optimization of multiple-layer microperforated panels by simulated annealing", *Applied Acoustics*, Vol. 72, No. 10, (2011), 772-776. <https://doi.org/10.1016/j.apacoust.2011.04.010>
27. Mosa, A.I., Putra, A., Ramlan, R., Esraa, A.-A. "Absorption Coefficient of a Double-Layer Inhomogeneous Micro-perforated Panel Backed with Multiple Cavity Depths", *Acoustics Australia*, (2020), 1-10. <https://doi.org/10.1007/s40857-020-00176-4>
28. Liu, Y., Chen, K., Zhang, Y., Ma, X., Wang, L. "Low-Frequency and Large-Scale Hybrid Sound Absorption Using Active Force Control", *Acoustics Australia*, (2020), 1-11. DOI: 10.1007/s40857-020-00207-0
29. Basirjafari, S. "Innovative solution to enhance the Helmholtz resonator sound absorber in low-frequency noise by nature inspiration", *Journal of Environmental Health Science and Engineering*, Vol. 18, (2020), 873-882. <https://doi.org/10.1007/s40201-020-00512-w>
30. Atalla, N., Sgard, F. "Modeling of perforated plates and screens using rigid frame porous models", *Journal of Sound and Vibration*, Vol. 303, No. 1-2, (2007), 195-208. <https://doi.org/10.1016/j.jsv.2007.01.012>
31. Doutres, O., Atalla, N., Dong, K. "Effect of the microstructure closed pore content on the acoustic behavior of polyurethane foams", *Journal of Applied Physics*, Vol. 110, (2011), 064901. <https://doi.org/10.1063/1.3631021>

## Persian Abstract

## چکیده

طراحی بهینه‌ی جاذب صوت با ضخامت مطلوب و حداکثر جذب صدا، همیشه مسئله مهمی در کنترل نویز بوده است. هدف از این مقاله، دستیابی به طراحی بهینه برای پانل‌های میکروسوراخ‌دار و ترکیب آن با مواد متخلخل و فاصله هوایی برای به‌دست‌آوردن حداکثر جذب صدا با حداکثر ضخامت کلی تا حدود ۱۰ سانتی‌متر در محدوده‌ی فرکانس‌های (۲۰ تا ۵۰۰ هرتز)، (۵۰۰ تا ۲۰۰۰ هرتز) و (۲۰۰۰ تا ۱۰۰۰۰ هرتز) است. برای این منظور، الگوریتم ژنتیک به عنوان یک روش مؤثر برای حل مسئله‌ی بهینه‌سازی پیشنهاد شده است. با استفاده از مدل‌های نظری دقیق همچون مدل آلارد و مدل آتالا برای محاسبه‌ی مشخصات آکوستیکی هر لایه شامل پانل میکروسوراخ‌دار، ماده متخلخل و فاصله هوایی، الگوریتم ژنتیک ساختارهای بهینه‌شده‌ی دقیقتری ارائه داده است. از روش ماتریس انتقال برای بررسی جذب صدای ساختارها استفاده شده است. برای تأیید عملکرد الگوریتم ژنتیک برنامه‌ریزی‌شده، نتایج بدست‌آمده از بهینه‌سازی جاذب میکروسوراخ‌دار با سایر تحقیقات مقایسه شده است که دقت و کارایی این روش را نشان می‌دهد. پس از اطمینان از درستی عملکرد الگوریتم ژنتیک برنامه‌نویسی‌شده با مدل‌های نظری دقیقتر برای محاسبه‌ی مشخصات آکوستیکی هر لایه، ساختارهای جدیدی بدست آمده‌اند که ضریب جذب صوتی بهتری نسبت به ساختارهای قبلی در محدوده‌ی فرکانسی موردنظر دارند. نتایج نشان می‌دهد که با انتخاب بهینه‌ی پارامترهای طراحی، ضریب جذب صوت در محدوده‌ی فرکانسی اول، دوم و سوم به ترتیب به ۰/۶۷، ۰/۹۶ و ۰/۹۶ می‌رسد.



## Single Machine Scheduling Problem with Batch Outsourcing

H. Safarzadeh, F. Kianfar\*

Department of Industrial Engineering, Sharif University of Technology, Tehran, Iran

### PAPER INFO

#### Paper history:

Received 26 June 2021

Received in revised form 13 January 2022

Accepted 28 January 2022

#### Keywords:

Single Machine Scheduling Problem

Outsourcing

Subcontracting

Batch Outsourcing

Total Completion Time

Mathematical Programming

### ABSTRACT

Outsourcing as a useful strategy in the industry can be integrated into scheduling problems. Moreover, batch outsourcing is a practical assumption owing to the logistics issues for transferring the parts between the manufacturer and the subcontractors. However, this assumption is rarely addressed in the scheduling literature. In this paper, a novel single machine scheduling problem with the option of batch outsourcing is studied. The objective is to minimize the sum of the total completion time of the jobs and the total outsourcing cost. To solve the problem, first, two mixed-integer linear programming (MILP) models, named MP1 and MP2, are developed, which respectively use a straightforward and an innovative approach to model the outsourcing batches. Next, an optimal property for the outsourcing batches is proven. This property is used to establish a valid inequality for model MP2, which is added to it to obtain a third MILP model, MP3. Extensive computational experiments showed that MP2 outperforms MP1 significantly. Moreover, including the derived valid inequality in MP3 enhances its performance considerably in comparing to MP2. Furthermore, it is observed that MP3 is capable of solving many practical-size problem instances optimally or with a low maximum optimality gap.

doi: 10.5829/ije.2022.35.05b.16

## 1. INTRODUCTION

Nowadays, companies utilize various strategies to improve their performance and sustain in the competitive market. One of those strategies is to outsource a part of the in-house tasks to relevant partners and subcontractors. This strategy can be used for various reasons in a company such as reducing production costs, compensating capacity constraints, eliminating job overloads, focusing on the main activities of a company, and improving the flexibility and robustness of the production system [1-3]. Indeed, the outsourcing strategy provides access to a widespread pool of resources out of the company that using them efficiently can significantly increase the competitiveness of the company in the market [4-6].

Outsourcing can be addressed in various fields of operations management such as supply chain management, production planning, logistics, facility layouts, health systems, and etc. Here, some of the related studies in these scopes are reviewed. Accordingly, Aksen et al. [7] studied a facility interdiction problem

with demand outsourcing. They modeled the problem as a static Stackelberg game between an attacker and a defender and developed two heuristic algorithms to solve the problem. Alizadeh et al. [8] investigated a capacitated multi-facility location-allocation problem with stochastic demands in which demands of the facilities can also be outsourced to some capacitated sub-sources. The authors proposed a stochastic non-linear mathematical model for the problem to find the optimal location of the facilities and optimal allocation of the demand points to the facilities. Mehdizadeh and Fatehi Kivi [9] addressed a single-item capacitated lot-sizing problem with various assumptions such as setup times, safety stock, backlogging, and inventory capacity. Moreover, in this problem, a part of production at each period can be outsourced to the subcontractors. The authors proposed three metaheuristic algorithms to solve the problem. Parvasi et al. [10] studied a school bus routing problem and bus stops selection in which the decisions are made in two levels, *i.e.* strategical and operational levels. At the strategical level, the location of the stops and routing of the buses are determined, while at the operational level,

\*Corresponding Author Email: [fkianfar@sharif.edu](mailto:fkianfar@sharif.edu) (F. Kianfar)

the student demands for using the transportation system are assigned to the buses. Moreover, a part of the student demands can be outsourced as well. In this study, two hybrid metaheuristic algorithms are proposed to solve the defined problem. Giri and Sarker [11] analyzed a supply chain management problem in which the logistics activities are outsourced to a third-party logistics (TPL) service provider. In this problem, there exist a manufacturer with the risk of disruption and multiple independent retailers. The design of the parameters that increases the profitability of the overall supply chain is discussed in this paper. Kim et al. [12] studied a problem related to a global supply chain embracing two divisions: one for production and another one for retailing. The production division can be offshored to a low-tax country while for the retail division, outsourcing from an outside supplier is possible. The authors analyzed the optimal choices for the supply chain structure. Heydari et al. [13] studied a supply chain consisting of a manufacturer and a retailer with stochastic demands. A part of production can be outsourced by the manufacturer, and moreover, the order quantity can be updated by the retailer as well. Mathematical models were developed for the studied problem to analyze the effect of outsourcing and the order flexibility possibilities in the problem via numerical experiments. Fathollahi-Fard et al. [14] investigated a home health care supply chain in which the patients' demand can be also outsourced to hospitals directly. A bi-level mathematical programming model representing a static Stackelberg game between nurses and patients is developed for the problem, and efficient metaheuristic algorithms are implemented to solve it.

Scheduling in the factories is a branch of the production management subject that can be integrated into the outsourcing subject as well. Scheduling generally addresses the allocation of resources to tasks over a time horizon [15]. Scheduling problems normally involve various problem constraints and one or more problem objectives to be optimized. In the presence of the outsourcing option in a scheduling problem, the subcontractors are considered as additional resources to perform the jobs over the time. Clearly, involving these extra resources in the problem can enhance the problem objectives and facilitate the problem constraints [16]. Several types of machine environments are addressed by the researchers in the scheduling literature, among which the major types are single machine, parallel machine, flow shop, and job shop [15]. The single machine environment is the simplest scheduling model in which there exists a single machine or server to process a number of jobs. This model occurs in many cases in the real world. Moreover, this model can be considered as a block of more sophisticated systems, particularly being used to analyze the bottlenecks of those systems [17].

Several research works have been conducted in the literature in recent years considering the possibility of

outsourcing in a scheduling problem. These research works can be primarily classified with regard to the machine environment type. For comprehensive reviews of this subject based on this classification, we refer the readers to Safarzadeh and Kianfar [16] and Liu [18]. However, the studies related to the context of this paper, *i.e.* the single machine environment or batch outsourcing, are reviewed in the next section in detail.

In the production systems, outsourcing the parts in batches may be a more practical assumption than outsourcing them one by one as the location of subcontractors is normally distant from the in-house plant [19]. Indeed, a considerable amount of time and/or cost is usually consumed for transporting the items between the manufacturer's and the subcontractors' shops, and outsourcing the items in batches helps reduce these logistics times and costs. Furthermore, batch outsourcing may also result in receiving order discounts from the subcontractors and prorate the preparation and setup times and costs required to start the order by them. However, a disadvantage of batch outsourcing is the issue that some parts may be ready for outsourcing while they are required to wait for other parts to be outsourced in batch. Incorporating batch outsourcing in a scheduling problem makes the problem much more complicated as most of the researchers have ignored this practical assumption. In fact, to the best of our knowledge, only four papers in the literature have addressed this assumption, *i.e.* Qi [19, 20, 21], and Ahmadizar and Amiri [22]. It should be noted that the former publication addresses a single machine environment; while, the three others consider a two-stage flow shop scheduling problem. These research works are also reviewed in the next section in detail.

In this paper, a novel single machine scheduling problem is investigated with the option of batch outsourcing. In the considered problem, outsourcing each job involves a certain time and cost for processing it and a logistics time and cost for non-processing issues like packing/unpacking, loading/unloading, and transportation. Meanwhile, all the jobs outsourced in a batch have a common logistics time and cost. The problem objective is to minimize the sum of the total completion time of the jobs and the total outsourcing cost. In order to solve the problem, first, a mixed-integer linear programming (MILP) model, named MP1, is presented using a straightforward modeling approach for the outsourcing batches. Next, a more innovative approach for modeling the outsourcing batches is proposed to develop another MILP model, named MP2. Moreover, an optimal property is proven for the outsourcing batches in the problem, using which a valid inequality for model MP2 is developed. This valid inequality is added to model MP2 to obtain a third MILP model, named MP3. Furthermore, extensive computational experiments are conducted at the end of

the paper to evaluate and compare the efficiency of the developed mathematical models.

The remainder of the paper is organized as follows: In section 2, the related literature is reviewed and discussed. In section 3, the considered problem is defined formally, and some real-world connections and applications of it are discussed. In section 4, the proposed solution approaches are presented, and in section 5, numerical experiments are conducted to evaluate the performance of the solution approaches. Finally, the conclusion of the paper is presented in section 6 and possible future studies are discussed.

## 2. LITERATURE REVIEW

Several research works in the literature have addressed a single machine scheduling problem with the option of outsourcing. Accordingly, Lee and Sung [23] studied a single machine scheduling problem in which each job is either processed in-house or subcontracted. They considered two types of problem objectives for the problem. The first one is to minimize a weighted sum of the total outsourcing cost and the maximum lateness of the jobs, while the second one is to minimize a weighted sum of the total outsourcing cost and the total tardiness of the jobs. In this study, several optimal properties are proven for the problem, based on which a branch and bound and some heuristic algorithms are proposed to solve the problem. Furthermore, the authors have also investigated another similar problem discussed by Lee and Sung [24] with a different problem objective, *i.e.* minimization of a weighted sum of the total outsourcing cost and the total completion time of the jobs. The other assumptions in this study are like the ones of the previous study, and similar solution approaches are also utilized. Qi [19] analyzed a single machine scheduling problem in which the jobs can be outsourced in batch to a single subcontractor. Various problem objectives are discussed in this paper such as makespan, total completion time, number of tardy jobs, and maximum lateness. The objective function of the problem is the sum of one of those problem objectives with the total outsourcing cost. To solve the problem, a dynamic programming approach is applied, and some characteristics of the optimal solutions are proven. Zhong and Huo [25] investigated a single machine scheduling problem in which the completion time of an outsourced job is assumed to be a step function of the job's outsourcing time. The problem is analyzed by two distinct minimization objective functions, *i.e.* the sum of the total cost and the makespan, and the sum of the total cost and the number of delayed jobs. The authors have developed pseudo-polynomial algorithms to solve the problem with the former objective function and a special case of the problem with the latter objective function. Hong and Lee [26] analyzed a single

machine scheduling problem in which the jobs can be outsourced to a limited set of subcontractors. The problem objective is to minimize the total outsourcing cost while the jobs' assigned due dates are required to be satisfied. In this paper, several optimal properties are derived for the problem solution, and a pseudo-polynomial algorithm is developed to obtain it. Ren et al. [27] studied a scheduling problem in which there exist a manufacturer with a single machine and a subcontractor with many identical parallel machines. Two problem objectives are considered for the problem, *i.e.* minimization of a weighted sum of the total cost and the total completion time of the jobs and minimization of a weighted sum of the total cost and the makespan. To solve the problem with the former objective, a polynomial-time algorithm is developed; while, for the problem with the latter objective, the problem complexity is analyzed and an approximation algorithm is proposed.

For the possibility of batch outsourcing in a scheduling problem, in addition to Qi [19], which was reviewed before, to our best knowledge, only the three papers being reviewed in the following have addressed this subject. In this regard, Qi [20] studied a flow shop scheduling problem with two serial machines in which the operations corresponding to the first machine can be assigned to a single subcontractor as well. Moreover, all the outsourced items in the scheduling horizon are returned back to the shop in a common batch with a given transportation time. The problem objective is to minimize the makespan and the total outsourcing cost at the same time. The author proposed an algorithm to extract the Pareto optimal solutions and a heuristic approach to estimate them. Furthermore, a two-machine flow shop scheduling problem with batch outsourcing is also studied by Qi [21], in which the operations corresponding to both machines are subject to outsourcing. Accordingly, three outsourcing styles are considered in this paper, *i.e.* two operations of a job are outsourced to a single subcontractor, two operations of a job are outsourced but each one to a different subcontractor, and all the operations for the first machine are outsourced to a certain subcontractor. Meanwhile, the considered problem objective is to minimize the sum of the makespan and the total outsourcing cost. Dynamic programming and other analytical approaches are utilized in this study to analyze the optimal solutions and develop optimal algorithms for the problems. Moreover, Ahmadizar and Amiri [22] considered a two-machine flow shop scheduling problem in which the jobs have different release times. Meanwhile, two certain subcontractors are considered in the problem, each of which corresponds to the operations of one of the in-house machines. As the transportation times and costs are taken into account, the jobs can be transported in batches between the manufacturer and the two subcontractors. The problem objective is to minimize the sum of the

makespan and the outsourcing costs. The authors have formulated some mathematical programming models for the problem and also developed an ant colony optimization algorithm (ACO) to solve it.

The papers reviewed above are the major research works we have observed in the literature for the subject of single machine scheduling with outsourcing as well as the subject of scheduling with batch outsourcing. Regarding the correspondence of the reviewed papers to our study, Lee and Sung [23, 24], and Zhong and Huo [25], like our study, have assumed that many subcontractors exist in the problem. However, in their considered problems, each job is outsourced solely, while in our problem, the practical assumption of batch outsourcing is addressed. Furthermore, among the reviewed research works considering batch outsourcing, only Qi [19] addressed the single machine environment. Nonetheless, he has considered a single subcontractor in the problem, and furthermore, assumed that the processing time and cost of an outsourced job are proportional to the in-house processing time of the job via fixed multipliers. However, in the problem defined in our study, the number of subcontractors are not limited like many other research works of scheduling with outsourcing *e.g.* Chen and Li, [28]; Guo and Lei, [29]; Izadi et al., [30], and the outsourcing time and cost of the jobs are arbitrary values, which are independent of the in-house processing times.

### 3. PROBLEM DESCRIPTION

In the considered problem,  $n$  jobs are available in the manufacturer's shop, which can be processed by a single in-house machine. Moreover, each job can be also outsourced to the existing subcontractors instead of being processed in the shop. It is supposed that enough number of subcontractors exist in the problem such that the jobs can be outsourced in parallel with no restriction. If job  $i$  is fulfilled in the in-house shop, then it has a processing time of  $p_i$ , and if it is outsourced, it has a processing time of  $q_i$  and a processing cost of  $c_i$ . Furthermore, it is assumed that outsourcing a job encompasses a *logistics time*,  $\alpha_1$ , and a *logistics cost*,  $\alpha_2$ , which are for the activities like packing/unpacking, loading/unloading, and transportation. Moreover, the logistics time and cost can also involve the preparation time and cost required by the subcontractor to accept and start the order. In addition, it is possible to outsource a set of jobs to a subcontractor in batch with the aim of reducing the logistics outsourcing times and costs. In this case, a common logistics time and cost are considered for the jobs included in an outsourcing batch. Moreover, it is supposed that the jobs in a batch are returned back to the shop together, *i.e.* they have identical completion times. This assumption is useful for the cases that the orders are

delivered to the customers from the in-house shop or the parts require additional production processes in the in-house shop. To have a more precise expression, suppose that jobs  $i_1, i_2, \dots, i_k$  are outsourced in a batch to a subcontractor. Then, the completion time of each job in the batch is equal to  $\alpha_1 + \sum_{j=1}^k q_{i_j}$ . Moreover, the total outsourcing cost of the jobs in the batch is equal to  $\alpha_2 + \sum_{j=1}^k c_{i_j}$ . The considered objective for the problem is to minimize the sum of the total completion time of the jobs and the total outsourcing cost. Note that the time and cost parameters are normalized before, to make aggregating the mentioned terms in the objective function rational.

A real application for the above-defined problem is the case in which a manufacturer can outsource machining of some of its raw materials to external CNC shops. This strategy is used for the times that the internal jobs are overloaded or some in-house resources are disrupted. CNC shops in some industrial areas are frequently located. For example, in the west region of Tehran, there exist many shops that do machining processes such as turning, milling, etc. They also normally have similar processing times and fees. Moreover, it is supposed that the manufacturer is distant from the location of the CNC shops, for example, it is located in the Shamsabad industrial city in the south of Tehran province which normally encompasses medium and large factories. So, transferring the parts between the manufacturer's shop and the CNC shops requires a considerable amount of logistics times and costs, which makes using the batch outsourcing strategy indispensable.

Finally, the utilized notations for the problem parameters are summarized as follows:

$n$  : number of jobs.

$p_i$  : in-house processing time of job  $i$ .

$q_i$  : outsourcing processing time of job  $i$ .

$c_i$  : outsourcing processing cost of job  $i$ .

$\alpha_1$  : logistics time for an outsourcing batch.

$\alpha_2$  : logistics cost for an outsourcing batch.

### 4. SOLUTION APPROACHES

Mathematical programming is used extensively to formulate combinatorial optimization problems, and especially, scheduling problems [31]. Although most of the scheduling problems are NP-hard, many of them, at least for a considerable segment of practical sizes, can be solved optimally or with a low optimality gap by appropriately developed MILP models. Furthermore, the efficiency of the mathematical programming approach for solving optimization problems is increasing nowadays due to the enhancement of solution techniques and development of computer technologies. This fact has made the mathematical programming solution approach

more attractive for researchers and practitioners in recent years [32,33].

In this section, three MILP models are proposed to solve the studied problem. The first MILP model is developed using a straightforward modeling approach, while a more advanced modeling approach is utilized to establish the second MILP model. Moreover, the third MILP model is an enhancement of the second MILP model based on an optimal property of the problem being proven while expressing the model. In the following, first, a simple property for the optimal solution of the problem is proven in Lemma 1, which is used in developing all the aforementioned MILP models.

**Lemma 1.** In the optimal solution of the problem, the jobs in the in-house shop are processed by the shortest processing time rule.

**Proof.** Suppose that  $J_1$  and  $J_2$  are two in-house processed jobs in the optimal solution of the problem having respectively processing times of  $p$  and  $q$ . Moreover, suppose that  $n_1$  jobs are processed after  $J_1$ , and  $n_2$  jobs are processed after  $J_2$  in the in-house shop so that  $n_1 > n_2$ , i.e.  $J_1$  is processed before  $J_2$ . If these two jobs are replaced with each other in the in-house sequence of jobs, then the amount added to the value of the objective function is equal to  $(n_1 + 1)q + (n_2 + 1)p - (n_1 + 1)p - (n_2 + 1)q$ , which is simplified as  $(n_1 - n_2)(q - p)$ . However, according to the optimality of the solution, it holds that  $q \geq p$ , which concludes the proof.

In order to use the result of Lemma 1 in the MILP models, let suppose that  $l_1, l_2, \dots, l_n$  is a sequence of job numbers in which  $p_{l_i} \geq p_{l_j}$  for  $i < j$ . This sequence gives the order of jobs with regard to the processing time, which will be used later in establishing some constraints of the proposed MILP models.

**4. 1. Model MP1** The major difference between the first and the second developed MILP models is in the way of modeling the outsourcing batches. As was mentioned before, the first MILP model, MP1, uses a straightforward approach to model the outsourcing batches. In this respect, a distinct index is considered to determine the outsourcing batches in the model. As the number of outsourcing batches in a problem solution is at most  $n$ , the considered domain for the aforementioned index is 1 to  $n$ . However, many of the  $n$  corresponding batches modeled in this way may be empty in the solution of the problem. The details of the model MP1 are presented as follows:

**Decision variables:**

$b_j$ : binary variable, equals to 1 if outsourcing batch  $j$  is non-empty; 0 otherwise.

$z_{ij}$ : binary variable, equals to 1 if job  $i$  is included in outsourcing batch  $j$ ; 0 otherwise.

$T_i$ : real variable, represents the completion time of job  $i$ .

**Model:**

$$\text{Min } \sum_{i=1}^n T_i + \alpha_2 \sum_{j=1}^n b_j + \sum_{i=1}^n (c_i \sum_{j=1}^n z_{ij}) \quad (1)$$

Subject to:

$$\sum_{j=1}^n z_{ij} \leq 1 \quad 1 \leq i \leq n \quad (2)$$

$$\frac{\sum_{i=1}^n z_{ij}}{n} \leq b_j \quad 1 \leq j \leq n \quad (3)$$

$$T_i \geq -M_1(1 - z_{ij}) + \alpha_1 + \sum_{k=1}^n q_k z_{kj} \quad 1 \leq i, j \leq n \quad (4)$$

$$T_{l_i} \geq -M_2(\sum_{j=1}^n z_{l_i j}) + p_{l_i} + \sum_{k=i+1}^n p_{l_k}(1 - \sum_{j=1}^n z_{l_k j}) \quad 1 \leq i \leq n \quad (5)$$

In the above model, Expression 1 describes the objective function of the problem. Constraint 2 guarantees that each job is included at most in one outsourcing batch. Constraint 3 indicates that if outsourcing batch  $j$  is not empty, then its corresponding decision variable,  $b_j$ , is equal to 1. Constraint 4 determines the completion times of the outsourced jobs, while constraint 5 specifies the completion times of the in-house processed jobs. Note that in these two constraints,  $M_1$  and  $M_2$  are big enough numbers that make the constraints inactive in the intended cases. In this respect, constraint 4 is trivial if job  $i$  is not included in batch  $j$ , while constraint 5 has no effect in the model if job  $i$  is outsourced. It should be noted that the minimum appropriate values for  $M_1$  and  $M_2$  are  $\alpha_1 + \sum_{k=1}^n q_k$  and  $\sum_{k=1}^n p_k$ , respectively. Moreover, note that the result given in Lemma 1 is utilized in formulating constraint 5 using notations given after Lemma 1.

**4. 2. Model MP2**

In the second proposed MILP model, MP2, a more innovative approach is utilized to model the outsourcing batches with the hope of establishing a more efficient model. It is worth noting that in model MP1, the maximum possible number of the batches were taken into account, while many of them may be empty in the obtained solution. This fact may cause increasing the dimensions of the model and wasting the computational time consumed for searching the solution space. However, in model MP2, unlike model MP1, the outsourcing batches are not directly distinguished from each other by an index. Accordingly, a binary decision variable like  $b_j$ , called the *batch indicator variable*, is utilized instead in the model to enumerate the number of outsourcing batches. This variable is equal to 1 if job  $j$  is outsourced and has the minimum job number in its outsourcing batch. In this way, for each existing outsourcing batch, one and only one of the batch indicators variables will be equal to 1. So, the number of outsourcing batches can be obtained in

the model via this variable. Moreover, another binary decision variable like  $v_{ij}$ , called the *batching variable*, is also defined, which is equal to 1 if jobs  $i$  and  $j$  are outsourced in a common batch, and 0 otherwise. The details of the model MP2 are given in the following:

**Decision variables:**

$b_i$  : binary variable, equals to 1 if job  $i$  is outsourced and has the minimum job number in its outsourcing batch; 0 otherwise.

$v_{ij}$  : binary variable ( $i < j$ ), equals to 1 if jobs  $i$  and  $j$  are outsourced in a common batch; 0 otherwise.

$f_i$  : binary variable, equals to 1 if job  $i$  is outsourced; 0 otherwise.

$T_i$  : real variable, represents the completion time of job  $i$ .

**Model:**

$$\text{Min } \sum_{i=1}^n T_i + \alpha_2 \sum_{i=1}^n b_i + \sum_{i=1}^n c_i f_i \tag{6}$$

Subject to:

$$2 v_{ij} \leq f_i + f_j \quad 1 \leq i < j \leq n \tag{7}$$

$$v_{ij} + v_{jk} - v_{ik} \leq 1 \quad 1 \leq i < j < k \leq n \tag{8}$$

$$f_i \leq b_i + \sum_{k=1}^{i-1} v_{ki} \quad 1 \leq i \leq n \tag{9}$$

$$T_i \geq -M_1(1 - f_i) + \alpha_1 + q_i + \sum_{k=1}^{i-1} q_k v_{ki} + \sum_{k=i+1}^n q_k v_{ik} \quad 1 \leq i \leq n \tag{10}$$

$$T_i \geq -M_2 f_i + \sum_{k=i+1}^n p_k (1 - f_k) \quad 1 \leq i \leq n \tag{11}$$

The objective function of the problem is presented in Expression 6. Moreover, constraint 7 ensures that if two jobs are included in the same outsourcing batch, their relevant outsourcing indicator variables are equal to 1. Constraint 8 states a *transitive* relationship between the decision variables  $v_{ij}$ , *i.e.* if jobs  $i$  and  $j$  present in the same outsourcing batch as well as jobs  $j$  and  $k$ , then jobs  $i$  and  $k$  are also in a common outsourcing batch. Constraint 9 states that if job  $i$  is outsourced, and no job exists in its outsourcing batch with a lower job number than  $i$ , then  $b_i$  is equal to 1, *i.e.* the batch is identified by job  $i$  in the model. Finally, Constraints 10 and 11 determine the completion times of the outsourced jobs and the in-house processed jobs, respectively. Meanwhile, the minimum appropriate values for  $M_1$  and  $M_2$  in this model are  $\alpha_1 + \sum_{k=1}^n q_k$  and  $\sum_{k=1}^n p_k$ , respectively.

**4. 3. Model MP3**

Although the computational results in the next section indicate that model MP2 significantly outperforms model MP1 in solving numerical problem instances, here, we modify MP2 to generate another model, named MP3, with the hope of having even a more efficient model. In this regard, first,

a notable optimal property for the outsourcing batches in the problem is proven in Lemma 2. Then, this property is used to develop a valid inequality for model MP2, which is added to the model as a new constraint to obtain the model MP3. In fact, this constraint helps to reduce the solution space of the MILP model, which may enhance its efficiency in searching for the optimal solution.

**Lemma 2.** In the optimal solution of the problem, the outsourcing batches can be represented by a sequence like  $B_1, B_2, \dots, B_k$  such that if  $i < j$ , then each job in  $B_i$  has an equal or bigger outsourcing time than each job in  $B_j$ .

**Proof.** Suppose that in the optimal solution of the problem,  $B_{i_1}$  and  $B_{i_2}$  are two arbitrary outsourcing batches containing respectively  $n_1$  and  $n_2$  jobs, such that  $n_1 \leq n_2$ . Moreover, job  $J_1$  with an outsourcing time of  $p$  and job  $J_2$  with an outsourcing time of  $q$  are included in batches  $B_{i_1}$  and  $B_{i_2}$ , respectively. Now, suppose that  $J_1$  and  $J_2$  are replaced with each other. Then, it can be easily checked that the amount of  $n_1(q - p) + n_2(p - q)$ , which is simplified as  $(n_1 - n_2)(q - p)$ , is added to the value of the objective function. However, this term must be non-negative according to the optimality of the solution. So, it is concluded that  $p \geq q$  if  $n_1 < n_2$ . Moreover, if  $n_1 = n_2$ , replacing  $J_1$  and  $J_2$  with each other has no effect on the value of the objective function, so without loss of generality, we assume  $p \geq q$  for this case. Accordingly, if we sort the outsourcing batches in the optimal solution of the problem in the form of a sequence like  $B_1, B_2, \dots, B_k$  such that for  $i < j$ , the number of jobs in  $B_i$  is smaller than or equal to the number of jobs in  $B_j$ , the proof is concluded. □

Now, we establish a valid inequality for model MP2 using the result obtained via Lemma 2. First, let suppose without loss of generality that the jobs are numbered in descending order with regard to the outsourcing processing time parameter, *i.e.*  $q_i \geq q_j$ , if  $i < j$ . According to this assumption, the batch indicator jobs in model MP2, for which the variable  $b_i$  is equal to 1, are the ones that have the maximum outsourcing time in their containing outsourcing batch since they have minimum job numbers in their batch. Regarding Lemma 2, we know that if a batch indicator variable like  $b_i$  in model MP2 is equal to 1, then any job  $k$  before job  $i$  ( $k < i$ ) and any job  $l$  after job  $i$  or job  $i$  itself ( $l \geq i$ ) cannot be included in an identical outsourcing batch. In fact, if jobs  $k$  and  $l$  are in a common outsourcing batch, and job  $i$  is also an outsourced job, then, according to Lemma 2, jobs  $k$ ,  $i$ , and  $l$  are definitely in the same outsourcing batch, which is a contradiction with the assumption  $b_i = 1$ . Regarding this result, we establish the following valid inequality for model MP2:

$$\sum_{k=1}^{i-1} \sum_{l=i}^n v_{kl} \leq (i - 1)(n - i + 1)(1 - b_i) \quad 1 \leq i \leq n \tag{12}$$

In constraint 12, if the batch indicator variable  $b_i$  is equal to zero, the constraint will be trivial as the left-hand side of it is at most  $(i - 1)(n - i + 1)$  in any case. However, if  $b_i$  is equal to one, the abovementioned result for jobs  $k, i,$  and  $l$  will be expressed by constraint 12. Hence, constraint 12 is always true for model MP2. As was discussed before, the MILP model MP3 is simply obtained by adding constraint 12 to model MP2. In the next section, the usefulness of this modification is demonstrated via numerical results.

## 5. COMPUTATIONAL EXPERIMENTS

In this section, the performance of the proposed MILP models in the previous section are examined through numerical experiments. In this respect, some appropriate numerical instances of the problem are prepared first as the test problems. Next, the problem instances are solved by the MILP models MP1, MP2, and MP3 via CPLEX software. Finally, the experimental results are presented and discussed, and the performance of the models are evaluated and compared. The models are solved by CPLEX 12.6.0 and implemented in Visual Studio 2017 via the Concert Technology of CPLEX software. The computer systems used to run the models have characteristics of CPU 2.4 GHz, 4 GB RAM, and OS of Windows 8.

### 5. 1. Test Problems

In order to conduct the computational experiments, first, it is required to provide some adequate test problems. In this respect, the problem dimensions  $n = 10, 15, 20, 25, 30, 40,$  and  $50$  are chosen to generate the test problems. Moreover, it is required to generate the values of the parameters  $p_{ij}, q_{ij}, c_{ij}, \alpha_1$  and  $\alpha_2$  for the considered problem dimensions. Accordingly, for each problem dimension, these numerical values are generated from three different sets of discrete uniform probability distributions, named  $S_1, S_2,$  and  $S_3,$  which are presented in Table 1. In this table,  $Uni[a, b]$  represents a discrete uniform probability distribution with a lower bound  $a$  and an upper bound  $b$ . Note that the considered uniform probability sets are chosen using preliminary tests such that various levels of outsourcing are obtained in the test problems. According to the considered distributions, the problem instances related to set  $S_2$  have the lowest, and the problem instances related to set  $S_3$  have the highest levels of outsourcing.

It should be noted that for each problem dimension with a set of probability distributions, 10 problem instances are generated randomly, which are named a *problem class* as a whole. Consequently, 210 problem instances organized in 21 problem classes are prepared to be used in the experiments.

### 5. 2. Experiments and Results

To conduct the numerical experiments, the developed MILP models MP1, MP2, and MP3 are solved by CPLEX software for each of the 210 problem instances generated in section 5.1. It should be noted that the values of the parameters  $M_1$  and  $M_2$  in the MILP models are set to the minimum values mentioned while expressing the models in section 4. Moreover, a time limit of one hour is considered for running each of the models for a problem instance. Note that if a problem instance is not solved optimally within the assigned time limit, an optimality gap will be reported by CPLEX, which is equal to  $\frac{\text{objective value} - \text{lower bound}}{\text{objective value}} \times 100$  in which the *objective value* is the best obtained value for the objective function, and the *lower bound* is the best obtained lower bound by the software. The optimality gap indicates the maximum relative deviation of the attained solution from the optimal solution of the problem. Accordingly, if this value is low, we can be sure that the model has attained a near-optimal or even an optimal solution.

The experimental results obtained by running the MILP models are given in Table 2. In this table, each row corresponds to the results of the problem instances of a problem class. Accordingly, the indicator *ST* represents the average solution time for the corresponding problem instances. Meanwhile, all the time indicators are reported in seconds in Table 2. Note that if a MILP model is not solved within the one-hour time limit, its solution time will be equal to 3600 seconds. Furthermore, the indicator *OF* represents the average value of the objective function obtained by the MILP model among the problem instances. Moreover, the indicator *G%* gives the average value of the optimality gap reported by CPLEX for the problem instances. Obviously, if a problem instance is solved optimally within the assigned time limit, the optimality gap will be zero. Furthermore, the number of problem instances for the corresponding problem class that are solved optimally by the MILP model is reported by the indicator *opt#*, which is out of 10. Finally, the average percentage of the outsourced jobs in the obtained problem solutions is presented by the indicator *out%*.

**TABLE 1.** The sets of probability distributions used to generate the test problems

	$p_{ij}$	$q_{ij}$	$c_{ij}$	$\alpha_1$	$\alpha_2$
$S_1$	Uni[10 100]	Uni[10 100]	Uni[10 100]	Uni[50 250]	Uni[50 250]
$S_2$	Uni[10 50]	Uni[10 100]	Uni[10 200]	Uni[50 150]	Uni[50 300]
$S_3$	Uni[10 200]	Uni[10 50]	Uni[10 100]	Uni[50 250]	Uni[50 150]

**TABLE 2.** The detailed results of the numerical experiments

Problem Class		Model MP1				Model MP2				Model MP3				
<i>n</i>	type	<i>OF</i>	<i>ST</i>	<i>G%</i>	<i>opt#</i>	<i>OF</i>	<i>ST</i>	<i>G%</i>	<i>opt#</i>	<i>OF</i>	<i>ST</i>	<i>G%</i>	<i>opt#</i>	<i>out%</i>
10	$S_1$	2346	0.53	0	10	2346	0.19	0	10	2346	0.2	0	10	27
10	$S_2$	1521	0.06	0	10	1521	0.04	0	10	1521	0.05	0	10	11
10	$S_3$	2664	1.92	0	10	2664	0.27	0	10	2664	0.23	0	10	53
15	$S_1$	3297	92	0	10	3297	4.41	0	10	3297	3.18	0	10	43
15	$S_2$	2654	1.81	0	10	2654	0.68	0	10	2654	0.61	0	10	22
15	$S_3$	3363	1295	8.2	5	3363	37	0	10	3363	2.81	0	10	65
20	$S_1$	5413	3600	24.28	0	5407	2656	3.75	4	5407	735	0.53	8	50
20	$S_2$	4408	907	2.58	8	4408	335	0	10	4408	97	0	10	29
20	$S_3$	5069	3600	32	0	5069	3283	5.35	1	5069	250	0	10	70
25	$S_1$	6815	3600	40.53	0	6809	3600	6.7	0	6805	3020	3.15	4	58
25	$S_2$	5875	3600	30.95	0	5873	3600	5.93	0	5872	2731	3.1	6	39
25	$S_3$	6331	3600	67.78	0	6314	3600	6.9	0	6314	3122	4.75	3	73
30	$S_1$	7496	3600	49.6	0	7489	3442	6.85	1	7488	3343	4.21	2	59
30	$S_2$	6828	3600	36.47	0	6827	3600	8.37	0	6824	3270	4.34	2	44
30	$S_3$	7344	3600	70.25	0	7341	3600	8.03	0	7341	3517	5.78	1	74
40	$S_1$	11772	3600	64.21	0	11720	3600	19.2	0	11697	3600	16.11	0	65
40	$S_2$	10465	3600	55.88	0	10447	3600	19.83	0	10428	3600	17.08	0	54
40	$S_3$	11137	3600	67.62	0	11107	3600	14.3	0	11093	3600	11.26	0	74
50	$S_1$	15437	3600	66.62	0	15315	3600	23.87	0	15302	3600	21.63	0	67
50	$S_2$	14487	3600	57.8	0	14436	3600	27.54	0	14413	3600	23.22	0	56
50	$S_3$	14105	3600	69.18	0	14007	3600	20.75	0	13995	3600	18.72	0	77

This quantity shows the average level of job outsourcing in each problem class. Note that the values presented in Table 2 are rounded in some cases to have a better representation of the indicators in the table.

In addition to the results reported in Table 2, the average values of the indicators *ST*, *OF*, and *G%* for each problem dimension are also given in Table 3. Therefore, each quantity in Table 3 is the average of the three related quantities in Table 2 for the corresponding problem dimension. Using the results of Table 3, the performance of the MILP models can be compared quickly. Moreover, to have an intuitive comparison of the efficiency of the MILP models, the values of the average solution time, *ST*, and the average optimality gap, *G%*, reported in Table 3 are also illustrated in Figures 1 and 2, respectively.

The experimental results indicate that model MP2 outperforms model MP1, and model MP3 outperforms model MP2 in solving the numerical problem instances. Particularly, the performance of models MP2 and MP3 in proving solution optimality or estimating the maximum optimality gap is significantly better than the

performance of model MP1. Moreover, by considering the results for the problem dimensions that the problem instances are generally solved optimally for, it is observed that the solution times of models MP2 and MP3 has been significantly lower than the solution times of model MP1. The aforementioned results are evident

**TABLE 3.** The average values of the experiment indicators for the problem dimensions

<i>n</i>	Model MP1			Model MP2			Model MP3		
	<i>OF</i>	<i>ST</i>	<i>G%</i>	<i>OF</i>	<i>ST</i>	<i>G%</i>	<i>OF</i>	<i>ST</i>	<i>G%</i>
10	2177	0.84	0	2177	0.17	0	2177	0.16	0
15	3105	462	2.73	3105	14	0	3105	2.2	0
20	4963	2702	19.62	4961	2091	3.03	4961	360	0.18
25	6340	3600	46.42	6332	3600	6.51	6330	2957	3.67
30	7223	3600	52.11	7219	3547	7.75	7218	3376	4.78
40	11125	3600	62.57	11091	3600	17.78	11073	3600	14.82
50	14676	3600	64.53	14586	3600	24.05	14570	3600	21.19

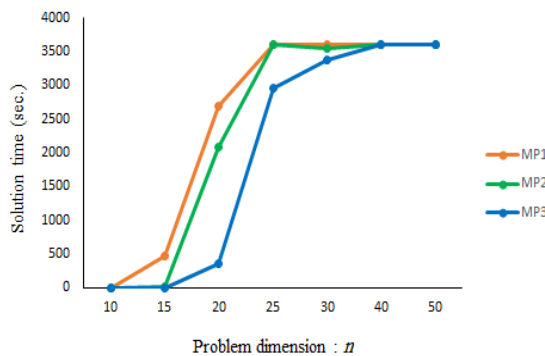


**Figure 1.** The average solution times for the problem dimensions

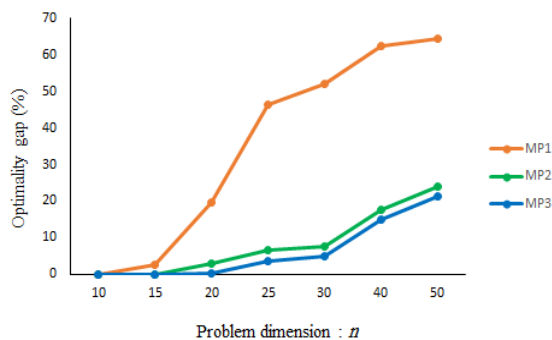


**Figure 2.** The average optimality gaps for the problem dimensions

in Table 3, Figures 1 and 2. So, we can conclude that the innovative modeling approach for the outsourcing batches utilized in MP2 and MP3 has been an effective approach. Moreover, regarding the results in Table 3, Figures 1, and 2, it is observed that the average optimality gaps obtained by MP3 have been lower than the ones of MP2, and the average solution times of MP3 have been also lower than the average solution times of MP2. So, the valid inequality obtained by the optimal property proven in Lemma 2, which is included in model MP3 has been also successful in improving the performance of the model.

Furthermore, regarding the results of Table 2, it is observed that using model MP3 as the most efficient model, almost all the problem instances with up to 20 jobs are solved optimally within the assigned time limit. Moreover, the problem instances with 25 and 30 jobs are also solved with a maximum optimality gap below 5% on average. Furthermore, this quantity is almost below 20% on average for the instances with 40 and 50 jobs. It is worth noting that the mentioned values are the maximum possible optimality gaps, and the real optimality gaps for the obtained solutions may be much lower. According to the abovementioned results, we can generally conclude

that model MP3 is an efficient model to solve practical-size problem instances of the studied problem.

Moreover, another notable result regarding the last column of Table 2 is that a considerable segment of the jobs, around 40 to 50 percent of them on average, are outsourced in the obtained solutions. This result indicates the great role that the outsourcing strategy can have in the addressed problem. However, the amount of outsourcing in the problem is evidently related to the values of the outsourcing time and cost parameters. In this regard, it is observed that when the outsourcing parameters are generated from probability distribution sets  $S_2$ , the rate of outsourcing is minimum, and when they are generated from probability distribution sets  $S_3$ , the rate of outsourcing is maximum. So, the results also indicate that the impact of the outsourcing strategy is significantly related to the combination of values of the outsourcing time and cost parameters.

## 6. CONCLUSION

In this paper, a novel single machine scheduling problem with the option of batch outsourcing was studied. The considered problem objective was to minimize the sum of the total completion time of the jobs and the total outsourcing cost. To solve the problem, three MILP models were developed. The first one, called MP1, exploited a straightforward modeling approach for the outsourcing batches, while, a more advanced approach for modeling outsourcing batches was utilized in the next MILP model, MP2. Furthermore, to enhance the efficiency of MP2 more, an optimal property for outsourcing batches was proved, which was used to develop a valid inequality for MP2. By adding this inequality to MP2 as a new constraint, another MILP model, named MP3, was also obtained.

At the end of the paper, extensive numerical experiments were conducted to evaluate and compare the efficiency of the MILP models. The results indicated that MP2 outperforms MP1, and MP3 outperforms MP2 in solving the numerical problem instances. Particularly, the results obtained by MP2 and MP3 were significantly better than the ones of MP1 with regard to the solution time and optimality reporting. Moreover, the numerical results indicated that the valid inequality included in MP3 has been effective in improving the performance of the MILP model. Furthermore, it was concluded that model MP3 can generally solve medium-size problem instances optimally or with a low optimality gap in a reasonable time. In addition, as a managerial insight, it was observed that the outsourcing strategy can have a great impact in the defined problem since a considerable segment of the jobs were outsourced in the solutions of the numerical problem instances. However, the rate of outsourcing is

dependent on the values of the outsourcing time and cost parameters.

For future studies, we propose enhancing the solution approaches given in this paper for the studied problem or utilizing other solution techniques such as heuristic and meta-heuristic algorithms. Moreover, other problem objectives, especially due-date related ones, can be also considered for the studied problem. Furthermore, the practical assumption of batch outsourcing, which is rarely addressed in the literature, can also be investigated for scheduling problems in other machine environments such as parallel machine, flow shop, and job shop.

## 7. REFERENCES

- Fakhrzad M.B., "Outsourcing through Three-dimensional Competition." *International Journal of Engineering, Transactions C: Aspects*, Vol. 27, No. 12, (2014), 1863-1871. DOI: 10.5829/idosi.ije.2014.27.12c.09
- Enayati M., Asadi-Gangraj E. and Paydar M.M., "Scheduling on flexible flow shop with cost-related objective function considering outsourcing options." *Journal of Optimization in Industrial Engineering*, Vol. 14, No. 2, (2021), 53-72. DOI: 10.22094/joie.2020.1873983.1674.
- Wang S. and Cui W., "Approximation algorithms for the min-max regret identical parallel machine scheduling problem with outsourcing and uncertain processing time." *International Journal of Production Research*, Vol. 59, No. 15, (2020), 4579-4592. DOI: 10.1080/00207543.2020.1766721.
- Gholamian K., Vakiliard H., Talebnia G. and Hejazi R., "Conceptual design of sustainable outsourcing with balanced scorecard using analytic hierarchy process: a case study for Fajr Jam gas refining company." *International Journal of Engineering, Transactions A: Basics*, Vol. 33, No. 1, (2020), 112-123. DOI:10.5829/ije.2020.33.01a.13.
- Jiang X., Zhang A., Chen Y., Chen G. and Lee K., "An improved algorithm for a two-stage production scheduling problem with an outsourcing option." *Theoretical Computer Science*, Vol. 876, (2021), 59-69. DOI: 10.1016/j.tcs.2021.05.022.
- Zhong X., Fan J. and Ou J., "Coordinated scheduling of the outsourcing, in-house production and distribution operations." *European Journal of Operational Research*, In Press, (2022). DOI: 10.1016/j.ejor.2022.01.003.
- Aksen D., Şengül Akca S. and Aras N., "A bi-level partial interdiction problem with capacitated facilities and demand outsourcing." *Computers & Operations Research*, Vol. 41, (2014), 346-358. DOI: 10.1016/j.cor.2012.08.013.
- Alizadeh M., Mahdavi I., Shiripour S. and Asadi H., "A non-linear model for a capacitated location-allocation problem with Bernoulli demand using sub-sources." *International Journal of Engineering, Transactions C: Aspects*, Vol. 26, No. 9, (2013), 1007-1016. DOI: 10.5829/idosi.ije.2013.26.09c.08.
- Mehdizadeh E. and Fatehi Kivi A., "Three meta-heuristic algorithms for the single-item capacitated lot-sizing problem." *International Journal of Engineering, Transactions, B: Applications* Vol. 27, No. 8, (2014), 1223-1232. DOI: 10.5829/idosi.ije.2014.27.08b.08.
- Parvasi S.P., Mahmoodjanloo M. and Setak M., "A bi-level school bus routing problem with bus stops selection and possibility of demand outsourcing." *Applied Soft Computing*, Vol. 61, (2017), 222-238. DOI: 10.1016/j.asoc.2017.08.018.
- Giri B.C. and Sarker B.R., "Improving performance by coordinating a supply chain with third party logistics outsourcing under production disruption." *Computers & Industrial Engineering*, Vol. 103, (2017), 168-177. DOI: 10.1016/j.cie.2016.11.022.
- Kim B., Park K.S., Jung S.Y. and Park S.H., "Offshoring and outsourcing in a global supply chain: Impact of the arm's length regulation on transfer pricing." *European Journal of Operational Research*, Vol. 266, No. 1, (2018), 88-98. DOI: 10.1016/j.ejor.2017.09.004.
- Heydari J., Govindan K., Ebrahimi Nasab H.R. and Taleizadeh A.A., "Coordination by quantity flexibility contract in a two-echelon supply chain system: Effect of outsourcing decisions." *International Journal of Production Economics*, Vol. 225, (2020), 107586. DOI: 10.1016/j.ijpe.2019.107586.
- Fathollahi-Fard A.M., Hajiaghahi Keshteli M., Tavakkoli Moghaddam R. and Smith N.R., "Bi-level programming for home health care supply chain considering outsourcing." *Journal of Industrial Information Integration*, Vol. 25, (2022), 100246. DOI: 10.1016/j.jii.2021.100246.
- Baker K.R. and Trietsch D., *Principles of Sequencing and Scheduling*. 1st edition. Hoboken, N.J: Wiley, 2009.
- Safarzadeh H. and Kianfar F., "Job shop scheduling with the option of jobs outsourcing." *International Journal of Production Research*, Vol. 57, Vol. 10, (2019), 3255-3272. DOI: 10.1080/00207543.2019.1579934.
- Pinedo M.L., *Scheduling: Theory, Algorithms, and Systems*. Springer Science & Business Media, 2012.
- Liu L., "Outsourcing and rescheduling for a two-machine flow shop with the disruption of new arriving jobs: A hybrid variable neighborhood search algorithm." *Computers & Industrial Engineering*, Vol. 130, (2019), 198-221. DOI: 10.1016/j.cie.2019.02.015.
- Qi X., "Coordinated Logistics Scheduling for In-House Production and Outsourcing." *IEEE Transactions on Automation Science and Engineering*, Vol. 5, No. 1, (2008), 188-192. DOI: 10.1109/TASE.2006.887159.
- Qi X., "Two-stage production scheduling with an option of outsourcing from a remote supplier." *Journal of Systems Science and Systems Engineering*, Vol. 18, No. 1, (2009), 1-15. DOI: 10.1007/s11518-009-5094-1.
- Qi X., "Outsourcing and production scheduling for a two-stage flow shop." *International Journal of Production Economics*, Vol. 129, No. 1, (2011), 43-50. DOI: 10.1016/j.ijpe.2010.08.011.
- Ahmadizar F. and Amiri Z., "Outsourcing and scheduling for a two-machine flow shop with release times." *Engineering Optimization*, Vol. 50, No. 3, (2018), 483-498. DOI: 10.1080/0305215X.2017.1325483.
- Lee I.S. and Sung C.S., "Minimizing due date related measures for a single machine scheduling problem with outsourcing allowed." *European Journal of Operational Research*, Vol. 186, No. 3, (2008), 931-952. DOI: 10.1016/j.ejor.2007.02.015.
- Lee I.S. and Sung C.S., "Single machine scheduling with outsourcing allowed." *International Journal of Production Economics*, Vol. 111, No. 2, (2008), 623-634. DOI: 10.1016/j.ijpe.2007.02.036.
- Zhong W. and Huo Z., "Single machine scheduling problems with subcontracting options." *Journal of Combinatorial Optimization*, Vol. 26, No. 3, (2013), 489-498. DOI: 10.1007/s10878-011-9442-y.
- Hong J.M. and Lee J.H., "Outsourcing decisions in single machine scheduling problem with multiple external facilities." *Journal of Marine Science and Technology*, Vol. 24, No. 3, (2016), 603-609. DOI: 10.6119/JMST-015-1216-1.
- Ren J., Sun G. and Zhang Y., "The Supplying Chain Scheduling with Outsourcing and Transportation." *Asia-Pacific Journal of Operational Research*, Vol. 34, No. 02, (2017), DOI: 10.1142/S0217595917500099.

28. Chen Z.L. and Li C.L., "Scheduling with subcontracting options." *IIE Transactions*, Vol. 40, No. 12, (2008), 1171-1184. DOI: 10.1080/07408170801975057.
29. Guo X. and Lei D., "Bi-objective job shop scheduling with outsourcing options." *International Journal of Production Research*, Vol. 52, No. 13, (2014), 3832-3841. DOI: 10.1080/00207543.2013.848488.
30. Izadi L., Ahmadizar F. and Arkat J., "A Hybrid Genetic Algorithm for Integrated Production and Distribution Scheduling Problem with Outsourcing Allowed." *International Journal of Engineering, Transactions B: Applications*, Vol. 33, No. 11, (2020), 2285-2298. DOI: 10.5829/ije.2020.33.11b.19.
31. Ku W.Y. and Beck J.C., "Mixed Integer Programming models for job shop scheduling: A computational analysis." *Computers & Operations Research*, Vol. 73, Supplement C, (2016), 165-173. DOI: 10.1016/j.cor.2016.04.006.
32. Ham A.M. and Cakici E., "Flexible job shop scheduling problem with parallel batch processing machines: MIP and CP approaches." *Computers & Industrial Engineering*, Vol. 102, Supplement C, (2016), 160-165. DOI: 10.1016/j.cie.2016.11.001.
33. Meng L., Zhang C., Shao X., Zhang B., Ren Y. and Lin W., "More MILP models for hybrid flow shop scheduling problem and its extended problems." *International Journal of Production Research*, (2019), 1-26. DOI: 10.1080/00207543.2019.1636324.

---

### Persian Abstract

---

#### چکیده

برون سپاری یک راهبرد متداول در صنعت است که می تواند به عنوان یک فرض در مسائل زمان بندی نیز در نظر گرفته شود. علاوه بر این، برون سپاری دسته ای کارها به دلیل وجود مسائل لجستیکی انتقال قطعات بین تولید کننده و پیمانکاران یک موضوع کاربردی است که در ادبیات مسائل زمان بندی به ندرت بررسی شده است. در این تحقیق، یک مساله جدید زمان بندی تک ماشین با امکان برون سپاری دسته ای کارها و با تابع هدف کمینه سازی مجموع زمان تکمیل کارها و هزینه های برون سپاری بررسی می شود. برای حل مساله ابتدا دو مدل برنامه ریزی خطی عدد صحیح آمیخته با نام های MP1 و MP2 ارائه می شود که به ترتیب از یک رویکرد سر راست و یک رویکرد ابتکاری جهت مدل سازی دسته های برون سپاری بهره می گیرند. سپس یک ویژگی بهینه برای دسته های برون سپاری به صورت دقیق به اثبات می رسد که با استفاده از آن یک نامساوی معتبر برای مدل MP2 توسعه داده می شود. با افزودن این نامساوی به عنوان یک محدودیت به مدل MP2، یک مدل سوم برنامه ریزی عدد صحیح آمیخته با نام MP3 نیز بدست می آید. در انتهای مقاله آزمایش های محاسباتی جهت ارزیابی عملکرد مدل های پیشنهادی انجام می شود که نتایج بدست آمده نشان دهنده برتری قابل توجه کارایی مدل MP2 نسبت به مدل MP1 و مدل MP3 نسبت به مدل MP2 است. همچنین مشاهده می شود که با استفاده از مدل MP3، تعداد زیادی از مسائل با ابعاد کاربردی به صورت بهینه و یا با درصد خطای بهینگی کم قابل حل است.

---



## Enhancement of the Shear-flexural Strength of the Rubberized Concrete Prism Beam by External Reinforcement

T. J. Mohammed<sup>\*a</sup>, K. M. Breesem<sup>b</sup>

<sup>a</sup> Department of Civil Techniques, Institute of Technology/ Baghdad, Middle Technical University, Baghdad, Iraq

<sup>b</sup> Al-Mussaib Technical Institute, Al-Furat Al-Awsat Technical University, Babylon, Iraq

### PAPER INFO

#### Paper history:

Received 24 January 2022

Received in revised form 14 February 2022

Accepted 19 February 2022

#### Keywords:

Recycle Rubber

Concrete

Prism Beam

Shear-flexural Strength

### ABSTRACT

It has become necessary to use damaged tires from various vehicles to produce rubberized concrete structures as a good solution to treat environmental pollution and reduce the total cost of construction. In general, concrete structures, for many reasons, may need to be strengthened. Recently, fiber-reinforced polymer (FRP) sheets have been used to reinforce existing concrete structural elements that were deficient. FRP is an effective solution and is moderately common for strengthening and improving the properties of the structural element. Firstly, concrete mixes were poured with replaced sand, with the percentages varying from 0, 10, 20, and 30%. Thus, some mechanical properties in terms of the workability of concrete, compressive strength, tensile strength, and density of recycled concrete were studied using rubber from tires as an alternative to fine aggregate. Secondly, concrete prisms were poured with different proportions of rubber instead of sand. Twelve rubberized concrete prisms measure 100 mm x 100 mm x 600 mm. Then, the effect of fiber reinforced polymer with different forms on concrete prisms was investigated. The results revealed a decrease in the workability, density, and compressive strength of the rubber concrete samples with an increase in the proportions of replaced sand with rubber content. It is also observed that FRP improves the strength, stiffness, and ductility of all concrete prism beams with a different ratio of recycled rubber. In addition, the test results clearly show that the strengthening by width sheets of FPR behaved more favorably than the thin sheets having the same cross-section.

doi: 10.5829/ije.2022.35.05b.17

## 1. INTRODUCTION

The consumption of rubber tires for a lot of cars has significantly increased in recent times. As a result of the increase in the amount of rubber waste generated from used tires across various means of transportation, there is an environmental problem [1]. Accumulations of tires lead to pollution as well as diseases due to the burning and the gathering of mosquitoes [2]. Therefore, a solution must be found to get rid of tires for a sustainable environment by adding recycled rubber to produce sustainable concrete [3].

There are many studies on the use of tire rubber as a substitute for aggregate in concrete mixes [4, 5]. The use of rubber recycling to produce concrete mechanical and ductile properties for improving sustainability was

investigated, but it was discovered that the dynamic properties of rubberized concrete elements had been reduced [6]. Also, the ultimate strength of specimens as beam and column was lower with an increase in the percentage of rubber used, as well as compressive strength [7]. Therefore, it is necessary to strengthen the rubberized concrete structure using fiber-reinforced polymer.

Recently, fibre reinforced polymer (FRP) sheets were used to strengthen the defective existing concrete structural elements [8]. The FPR material has extensive properties like high tensile strength and lightweight to enhance the service life of concrete elements [9]. Accordingly, the structural elements were strengthened to increase strength and durability by rehabilitating deteriorated concrete using FRP sheet [10, 11]. Many

\*Corresponding Author: [dr.thaerj.t.c@mtu.edu.iq](mailto:dr.thaerj.t.c@mtu.edu.iq) (T. J. Mohammed)

advantages have been reported by strengthening concrete using FRP compared to other traditional materials such as steel [12]. The effectiveness of the bending and shear strengthening depends on the bond between FRP and concrete, so that increase resistance by restricting external confinement [13]. The efficiency of FRP use dramatically affects the mechanical properties of rehabilitation concrete construction [14]. Various cases of strength have been depended on strip length, number and spacing or other standard methods for improving the behaviour of concrete elements [15-19].

In this paper, as in previous researches, waste tire rubber was first used as a substitute for fine aggregates to study the mechanical properties of rubber concrete. Secondly, the strengthening of rubber concrete prisms with carbon fibre was studied to improve the properties of these beams under the influence of two loading points. Thus, this research focuses on enhancing the strength of concrete containing different proportions of rubber using carbon fiber reinforced sheets.

## 2. SIGNIFICANCE OF STUDY

Concrete mixes in this paper are 1:1.5:3 (cement: sand: gravel) by weight, with a water-to-cement ratio of 0.5. Part of the sand was replaced with 10-30% rubber tire in the concrete mixes for comparison with a reference mix without rubber. Firstly, the effect of different proportions of rubber instead of sand in producing sustainable concrete must be studied. Therefore, the slump test, compressive strength at age 7, 28 days, tensile strength, and flexure strength at 28 days were examined to understand the effect of substitution on rubber concrete properties. Secondly, the use of rubber concrete in buildings subjected to increased loading needs to be strengthened properly. Therefore, twelve rubberized concrete prisms were cast. Then, some common types of external reinforcement (FRP sheets) were used to strengthen the rubber concrete prism to verify the importance of strengthening; thus, improving the shear-bending behavior.

## 3. EXPERIMENTAL WORK

In this study, rubber crumbs from car tires were used to evaluate their performance as a substitute for sand for producing concrete mixes. Rubber crumbs with dimensions less than 1 mm were obtained from mechanical shredding of car tires without any treatments. The mixes included cement, sand, gravel and water. Ordinary Portland cement (Type I) Al-Mass has been used to conform to the Iraqi standard specifications (I.Q.S 5:1984). Meanwhile, crushed coarse gravel was used from the Al-Nibae area where the sieve analysis was identical with (I.Q.S 45:1984) data as shown in

Figure 1. Also, the natural sand was from the al-Akheder area conforming to (I.Q.S45:1984) data as shown in Figure 2. Drinking water was used for concrete mixes that were designed following ACI 211.1 and for curing concrete samples. In order to prepare, the concrete mix is satisfied in the works of residential buildings. The trial and error method was also used to produce concrete grade M25.

Waste rubber tires were used as an additive to concrete at a rate of (10, 20, and 30%). As a substitute for a portion of fine aggregate (sand), use (water/cement ratio of 0.5 for all concrete mixes (1 cement: 1.5 sand: 3 gravel). Some mechanical properties in terms of the slump of concrete, compressive strength, tensile strength, and density of rubberized concrete were investigated. The main components of the reference concrete mixes (1 cement: 1.5 sand: 3 gravel) used in this research, as well as replacing the minced tires in different proportions (10, 20, and 30%), are shown in Figure 3 as a substitute for the fine aggregate, which which was encoded below:

M0: A reference concrete mix that does not contain minced used tires.

M10: A concrete mix containing 10% of the minced used tires

M20: A concrete mix containing 20% minced used tires.

M30: A concrete mix containing 30% minced used tires.

### 3. 1. FRP Strengthening

Rubberized concrete prisms have normal compressive strength fluctuate from 29-32 MPa that all prisms were cured in water at 28 days.

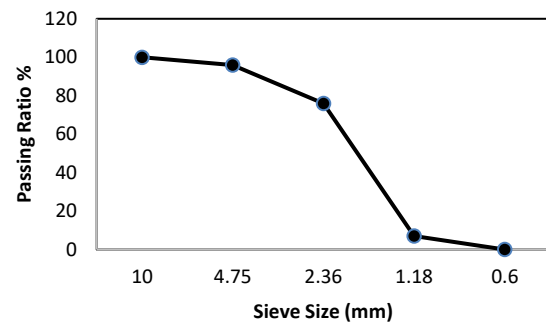


Figure 1. Sieve analysis of coarse aggregate

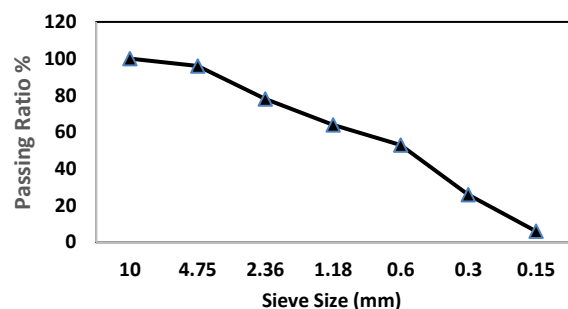


Figure 2. Sieve analysis of natural sand



Figure 3. Preparation of specimens

For strengthening prism by fiber-reinforced polymer that the type of FRP has been used Sikadur-300 Product as present in Table 1. Concrete prism is grinded to make a rough surface for perfect bonding between fiber-reinforced polymer with concrete prism [20] (see Figure 4).

**3. 2. Prism Beam Details**

The prisms were strengthened on their tension side with a glued-on fiber-reinforced polymer sheet, which was put in the middle of the prism beam. Cases of reinforcement of beams using FRP carbon fiber reinforced sheets have been identified, namely:

Prism beam without strengthening, as a control prism beam, P-R0-ST0, P-R10-ST0, P-R20-ST0, and P-R30-ST0.

The prism beam is only strengthened by FRP strip closed between the loading point and support in the shear-flexure zone with lower surface 50 mm, P-R0-ST50, P-R10-ST50, P-R20-ST50, P-R30-ST50.

The prism beam is strengthened by both FRP strip closed with a lower surface of 100 mm, P-R0-ST100, P-R10-ST100, P-R20-ST100, and P-R30-ST100.

The details of concrete prisms are described in Figure 5.

**3. 3. Setup Test**

An experimental test was set up where the rubberized concrete prism was put on supports at both ends. A two-point load test was performed on a strengthened rubberized concrete prism beam to determine its maximum failure strength, as revealed in Figure 6.



Figure 4. A rough surface for perfect bonding

**TABLE 1.** Mechanical properties of fiber-reinforced polymer

Laminate Nominal Thickness (mm)	Tensile Resistance (N/mm)	Modulus of elasticity (GPa)
0.167	585	220

\*Sikadur®-300 Product Data Sheet



Figure 5. Concrete prisms

**4. RESULTS AND DISCUSSION**

**4. 1. Slump and Workability**

The slump test was performed on all mixes containing different percentages of rubber: 0, 10, 20 and 30%, using a standard slump cone to determine the workability. It was found in Figure 7 that adding rubber to the concrete mixes reduces the slump, i.e. it notices a decrease in the workability. The addition of replaced rubber at 0, 10, 20 and 30% led to a decrease in slump at 4 cm, 3.2 cm, 2.8 cm, and 2.6 cm,



Figure 6. Testing procedures



Figure 7. Concrete prisms

respectively. The decline in the slump ratio was 20, 30 and 35% due to the rubber replacement ratio of 10, 20 and 30%, respectively, to the concrete mix without rubber due to the moisture-absorbing property of rubber as shown in Table 2. Accordingly, the slump of the concrete mix containing rubber was reduced when compared with the control concrete mix 1:1.5:3. The slump is inversely proportional to the amount of rubber added, which agrees well with another research [21].

**4. 2. Compressive Strength** The compressive strength of concrete mixes containing rubber in different proportions instead of sand has been studied. It was found from the results that increasing the amount of rubber replaced decreases the compressive strength of cubes with dimensions of 10 x 10 x 10 cm. The percentages of compressive strength at 7-day decreased by about 1.8, 3.7, and 6.2% for the proportions of rubber at 10, 20 and 30%, respectively, when compared with the reference concrete mix without rubber. While the percentages of compressive strength at 28 days were less than 1.3, 6.7 and 9.8% for proportions of rubber at 10, 20, and 30%, respectively, when compared with the reference concrete mix without rubber as indicated in Table 3. The compressive strength result showed no significant change in 10% rubber at 28 days. Meanwhile, it was observed that the lowest decrease in compressive strength was 9.8% when the rubber replacement ratio was set at 30%. Accordingly, the compressive strength decreases with an increase in the proportion of rubber replaced (see Figure 8).

**4. 3. Split Tensile Strength** It is necessary to conduct a cracking resistance test for cylinders with a diameter of 10 cm and a height of 20 cm. The results are 2.51, 2.48, 2.47, and 2.33 MPa for tensile strength for

TABLE 2. Concrete prisms

Mix code	Slump (cm)	Decrease ratio (%)
M0	4.0	0.0
M10	3.2	20%
M20	2.8	30%
M30	2.6	35%

TABLE 3. Compressive strength test results

Mix code	Compressive strength at 7 day (MPa)	Compressive strength at 28 day (MPa)
M0	23.21	31.80
M10	22.79	31.39
M20	22.35	29.67
M30	21.77	28.68

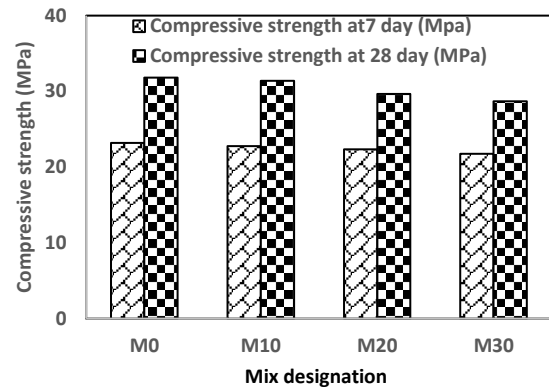


Figure 8. Compressive strength test results

rubber ratios of 0, 10, 20 and 30% at 7 days, respectively. Hence, at 28 days, tensile strength is 3.04, 2.94, 2.78, and 2.75 MPa for rubber ratios of 0, 10, 20, and 30%, respectively, as in Table 4. In other words, the higher the percentage of rubber replaced, the lower the tensile strength (see Figure 9).

**4. 4. Flexural Strength** The flexure strength of a rubberized-concrete prism with dimensions of 10 cm x 10 cm x 60 cm for 0, 10, 20 and 30% rubber substituted sand is given at 3.96, 3.80, 3.59, and 3.49 MPa at 28 days, respectively. That is, the higher the percentage of the rubber replaced, the lower the flexural resistance by 4.2, 9.53 and 12.03% with comparison without rubber

TABLE 4. Tensile strength test results

Mix code	Tensile strength at 7 day (MPa)	Decrease (%) 7 days	Tensile strength at 28 day (MPa)	Decrease (%) 28 days
M0	2.51	0%	3.04	0%
M10	2.48	-1.20%	2.94	-3.29%
M20	2.47	-1.59%	2.78	-8.55%
M30	2.33	-7.17%	2.75	-9.54%

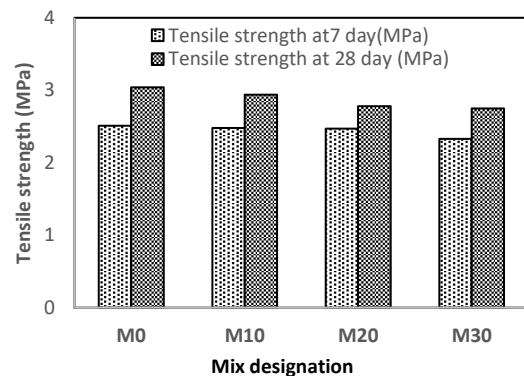


Figure 9. Tensile strength test results

is present in Table 5. The type of failure of the rubber-concrete prism is shown in Figure 10 after the testing.

#### 4. 5. External Fiber-reinforced Polymer Effect on Rubberized Concrete Prism Concrete

The types of failure of rubberized concrete prisms with fiber-reinforced polymer external are shown in Figure 10. It is observed that the FRP improves the strength and ductility of the prism beam compared to the control beam. Rubberized concrete prisms without strengthening, as control prism beams have the lowest strength. Meanwhile, the control rubber-concrete prism was observed in flexure failure, so a crack began in the middle of the concrete. Hence, strengthened rubber-concrete prisms in the shear-flexure zone with a lower surface of 50 mm of fiber-reinforced polymer, it was found that the type of failure in the flexural zone. Meanwhile, the behaviour of strengthened prism beams with both fiber-reinforced polymer strip and lower surface of 100 mm is the highest compared to other prism beams, which is consistent with the results reported by previous researchers [22, 23]. In other words, the failure rate in the shear zone was higher when the FRP external reinforcement was installed on the lower surface. The crack occurred in the protective layer for the strengthened rubber concrete prism beam. The percentage of increase in loading resulted in strengthened rubber concrete prisms as compared with control concrete prisms as well as types of failures are described in Table 6. It is also found that the strength of the rubberized concrete prism strengthened by both FRP strip with a lower surface of 100 mm is the highest and favorably the strongest.

TABLE 5. Flexure strength test results

Designation	Flexure strength at 28 day (MPa)	Increase ratio at 28 day (%)
P-R0-ST0	3.96	0%
P-R10-ST0	3.80	4.20%
P-R20-ST0	3.59	9.53%
P-R30-ST0	3.49	12.03%

TABLE 6. Flexure strength test for strengthening rubberized concrete prisms

Designation	Flexure strength at 28 day (MPa)	Increase ratio (%)	Type of failure
P-R0-ST0	3.96	0.0	Flexure
P-R10-ST50	7.73	95	Flexure
P-R10-ST100	11.42	188	Shear
P-R10-ST0	3.80	0.0	Flexure
P-R10-ST50	7.52	98	Flexure
P-R10-ST100	11.04	191	Shear

P-R20-ST0	3.59	0.0	Flexure
P-R20-ST50	7.06	97	Flexure
P-R20-ST100	10.58	195	Shear
P-R30-ST0	3.49	0.0	Flexure
P-R30-ST50	6.52	87	Shear
P-R30-ST100	10.77	209	Shear



Figure 10. Failure observation of strengthening rubberized concrete prisms

## 5. CONCLUSIONS

The tire rubber used in different proportions instead of sand effects on the properties of concrete as follows:

- The workability of concrete decreases with increasing proportions of rubber replaced.
- The compressive strength, tensile strength, and flexural strength of hardened concrete increase as the proportions of rubber substitute decrease.
- The FRP improves the strength, stiffness, and ductility of all rubberized concrete prism beams.
- The types of failure of rubberized concrete prisms were flexure failure or shear failure, which depend on the type of external strengthening.

- It was also observed that the strengthening of FRP width sheets is favourably higher than that of FRP thin sheets.

## 6. REFERENCES

- Segre, N. and Joekes, I., "Use of tire rubber particles as addition to cement paste", *Cement Concrete Research*, Vol. 30, No. 9, (2000), 1421-1425, doi: 10.1016/S0008-8846(00)00373-2.
- Antony, S.J.S., "A study on crumb rubber: Opportunities for development of sustainable concrete in the new millennium", *Indian Journal of Applied Research*, Vol. 5, No. 8, (2015), doi.
- Shahjalal, M., Islam, K., Rahman, J., Ahmed, K.S., Karim, M.R. and Billah, A.M., "Flexural response of fiber reinforced concrete beams with waste tires rubber and recycled aggregate", *Journal of Cleaner Production*, Vol. 278, (2021), 123842, doi: 10.1016/j.jclepro.2020.123842.
- Avcular, N., "Analysis of rubberized concrete as a composite material", *Cement Concrete Research*, Vol. 27, No. 8, (1997), 1135-1139, doi: 10.1016/S0008-8846(97)00115-4.
- Batayneh, M.K., Marie, I. and Asi, I., "Promoting the use of crumb rubber concrete in developing countries", *Waste Management*, Vol. 28, No. 11, (2008), 2171-2176, doi: 10.1016/j.wasman.2007.09.035.
- Zheng, L., Huo, X.S. and Yuan, Y., "Experimental investigation on dynamic properties of rubberized concrete", *Construction Building Materials*, Vol. 22, No. 5, (2008), 939-947, doi: 10.1016/j.conbuildmat.2007.03.005.
- Hassanli, R., Youssf, O. and Mills, J.E., "Experimental investigations of reinforced rubberized concrete structural members", *Journal of Building Engineering*, Vol. 10, (2017), 149-165, doi: 10.1016/j.jobe.2017.03.006.
- Mikami, C., Wu, H.-C. and Elarbi, A., "Effect of hot temperature on pull-off strength of frp bonded concrete", *Construction Building Materials*, Vol. 91, (2015), 180-186, doi: 10.1016/j.conbuildmat.2015.05.013.
- Ali, N., Samad, A.A.A., Mohamad, N. and Jayaprakash, J., "Shear behaviour of pre-cracked continuous beam repaired using externally bonded cfrp strips", *Procedia Engineering*, Vol. 53, (2013), 129-144, doi: 10.1016/j.proeng.2013.02.019.
- De Domenico, D., Fuschi, P., Pardo, S. and Pisano, A., "Strengthening of steel-reinforced concrete structural elements by externally bonded frp sheets and evaluation of their load carrying capacity", *Composite Structures*, Vol. 118, (2014), 377-384, doi: 10.1016/j.compstruct.2014.07.040.
- Shahidan, S., Zuki, S.S.M. and Jamaluddin, N., "Damage grading system for severity assessment on concrete structure", *Case Studies in Construction Materials*, Vol. 5, (2016), 79-86, doi: 10.1016/j.cscm.2016.09.001.
- Ma, S., Bunnori, N.M. and Choong, K., "Behavior of reinforced concrete box beam strengthened with cfrp u-wrap strips under torsion", in MATEC Web of Conferences, EDP Sciences. Vol. 47, (2016), 02002.
- Choi, E., Cho, B.-S., Jeon, J.-S. and Yoon, S.-J., "Bond behavior of steel deformed bars embedded in concrete confined by FRP wire jackets", *Construction Building Materials*, Vol. 68, (2014), 716-725, doi: 10.1016/j.conbuildmat.2014.06.092.
- Batikha, M. and Alkam, F., "The effect of mechanical properties of masonry on the behavior of frp-strengthened masonry-infilled RC frame under cyclic load", *Composite Structures*, Vol. 134, (2015), 513-522, doi: 10.1016/j.compstruct.2015.08.105.
- Hadhood, A., Agamy, M.H., Abdelsalam, M.M., Mohamed, H.M. and El-Sayed, T.A., "Shear strengthening of hybrid externally-bonded mechanically-fastened concrete beams using short cfrp strips: Experiments and theoretical evaluation", *Engineering Structures*, Vol. 201, (2019), 109795, doi: 10.1016/j.engstruct.2019.109795.
- Jankowiak, I., "Case study of flexure and shear strengthening of rc beams by cfrp using fea", in AIP Conference Proceedings, AIP Publishing LLC. Vol. 1922, No. 1, (2018), 130004.
- Gao, J., Koopialipoor, M., Armaghani, D.J., Ghabussi, A., Baharom, S., Morasaei, A., Shariati, A., Khorami, M. and Zhou, J., "Evaluating the bond strength of frp in concrete samples using machine learning methods", *Smart Structures Systems, An International Journal*, Vol. 26, No. 4, (2020), 403-418, doi: 10.12989/sss.2020.26.4.403.
- Rabia, B., Daouadji, T.H. and Abderezak, R., "Effect of air bubbles in concrete on the mechanical behavior of rc beams strengthened in flexion by externally bonded frp plates under uniformly distributed loading", *I*, Vol. 3, No. 1, (2021), 41, doi: 10.12989/cme.2021.3.1.041.
- Karayannis, C.G. and Goliias, E., "Strengthening of deficient rc joints with diagonally placed external C-FRP ropes", *Earthquakes Structures*, Vol. 20, No. 1, (2021), 123-132, doi: 10.12989/eas.2021.20.1.123.
- Hassen, D.R., Samad, A.A.A. and Azeez, A.A., "Strengthening of prism beam by using nsm technique with roots planted in concrete", *International Journal of Engineering Technology*, Vol. 9, No. 5, (2017), 383, doi: 10.7763/IJET.2017.V9.1003
- Velmurugan, V., Kumar, D.D. and Thanikaikarasan, S., "Experimental evaluation of mechanical properties of natural fibre reinforced polymer composites", *Materials Today: Proceedings*, Vol. 33, (2020), 3383-3388, doi: 10.1016/j.matpr.2020.05.190.
- Mazlan, S.M.S.S., Abdullah, S.R., Shahidan, S. and Noor, S.R.M., "Failure behaviour of concrete prisms strengthened by various bond widths of carbon fibre reinforced polymer (CFRP)", in MATEC Web of Conferences, EDP Sciences. Vol. 103, (2017), 02015.
- Momin, A., Khadiranaikarb, R. and Zende, A., "Flexural strength and behavioral study of high-performance concrete beams using stress-block parameters", *International Journal of Engineering, Transactions B: Applications*, Vol. 34, No. 11, (2021), 2557-2565. doi: 10.5829/ije.2021.34.11b.18.

---

**Persian Abstract**

---

**چکیده**

استفاده از لاستیک های آسیب دیده وسایل نقلیه مختلف برای تولید سازه های بتنی لاستیکی به عنوان راه حل مناسبی برای درمان آلودگی های زیست محیطی و کاهش کل هزینه های ساخت ضروری شده است. ه طور کلی سازه های بتنی به دلایل زیادی ممکن است نیاز به مقاوم سازی داشته باشند. اخیراً از ورق های پلیمری تقویت شده با الیاف (FRP) برای تقویت عناصر ساختاری بتنی موجود استفاده شده است. FRP یک راه حل موثر و نسبتاً رایج برای تقویت و بهبود خواص عنصر ساختاری است. در این مقاله ابتدا مخلوط های بتن با ماسه جایگزین ریخته شد که درصد آن از ۰، ۱۰، ۲۰ و ۳۰ درصد متغیر است. بنابراین، برخی از خواص مکانیکی از نظر کارایی بتن، مقاومت فشاری، مقاومت کششی و چگالی بتن بازیافتی با استفاده از لاستیک لاستیک به عنوان جایگزینی برای سنگدانه های ریز مورد مطالعه قرار گرفت. ثانویه، منشورهای بتنی با نسبت های مختلف لاستیک به جای ماسه ریخته شدند. دوازده منشور بتنی لاستیکی در ابعاد ۱۰۰ میلی متر در ۱۰۰ میلی متر در ۶۰۰ میلی متر هستند. سپس تأثیر پلیمرهای تقویت شده با الیاف با اشکال مختلف بر روی منشورهای بتن بررسی می شود. نتایج کاهش کارایی، چگالی و مقاومت فشاری نمونه های بتن لاستیکی را با افزایش نسبت جایگزینی ماسه با محتوای لاستیک نشان داد. همچنین مشاهده می شود که FRP استحکام، سختی و شکل پذیری تیرهای منشوری بتنی را با نسبت های مختلف لاستیک بازیافتی بهبود می بخشد. علاوه بر این، نتایج آزمایش به وضوح نشان می دهد که استحکام با ورق های پهن FPR نسبت به ورق های نازک دارای سطح مقطع یکسان رفتار مطلوب تری داشت.

---



## A Novel Curve for the Generation of the Non-circular Gear Tooth Profile

N. H. Thai<sup>\*a</sup>, N. T. Trung<sup>b</sup>

<sup>a</sup> Hanoi University of Science and Technology, Hanoi, Vietnam

<sup>b</sup> National Research Institute of Mechanical Engineering, Hanoi, Vietnam

### PAPER INFO

#### Paper history:

Received 26 January 2022

Received in revised form 20 February 2022

Accepted 21 February 2022

#### Keywords:

Non-circular Gear

Rack Cutter

Undercutting

Novel Curve

Line of Meshing

### ABSTRACT

This paper presents a novel curve generated by a point attached to an ellipse as it rolls without slipping along a datum line of rack cutter. A mathematical model of the non-circular gear profile has been developed based on the theory of gearing. The effect of an axial ratio  $\lambda$  (the ratio of the lengths of the major and minor axes of the ellipse) and the position of the point  $K_R$ , at which the novel curve starts to generate on the tooth shape and the undercut of the non-circular gear pair is also taken into consideration. A numerical program developed from the mathematical model has been proposed for the calculation and design of the non-circular gears (NCGs). Case studies are presented to show the steps of tooth shape design and to examine the geometrical profile of the NCGs in relation to design parameters of the rack cutter etc. From that, the axial ratio  $\lambda$  and position of the point  $K_R$  on the generating ellipse  $\Sigma_E$  can be selected for each specific case in order to design the appropriate profiles of the NCGs. On that basis, an experiment to determine the gear ratio of the NCGs pair based on the meshing between gears has manufactured.

doi: 10.5829/ije.2022.35.05.18

## 1. INTRODUCTION

Non-circular gears (NCGs) is designed to generate continuously variable transmission with high accuracy. Due to complexity in design and fabrication difficulties, the application of NCGs in practice still has many limitations [1]. In spite of the fact that NCGs are not commonly used as circular gear, the NCGs have been applied in various machines and equipment such as agricultural machinery [2-4]; medical equipment [5]; coal seam gas drainage machine [6]; hydraulic motors [7]; steering robotic mechanisms (with elliptical gears) [8] etc. Therefore, the NCGs have drawn a lot of interest from scientists with the following trends: (1) Generation of centrodes based on a transfer function of mechanisms [4, 5, 9]; (2) Design of the NCGs tooth profile by a number of methods such as: (a) Using shaper cutter [10, 11]; (b) Using rack cutter with an isosceles trapezoidal profile or circular arc profile [12-14]; (3) Design non-circular gearing systems for various applications [15-17]. Recently, Hao et al. [18] proposed methods to design an

NCGs pair based on an arbitrary centrode. However, those NCGs pairs could only be used for low-load application because the effect of undercutting and interference was not taken into the design process; (4) Methods for manufacturing the NCGs spur and the NCGs helical were the research object of other researchers [19-21]. Among those four trends, NCGs tooth profile design has drawn the most interest. The majority of the research focused on using circle involute [10, 12, 22]; or circular arc [13, 23] to generate the NCGs tooth profile. A setback in these works is the difference in shape and dimension of the teeth located around NCGs since these are gears with asymmetrical tooth profiles. The NCGs is different from standard cylindrical gears with the constant gear ratio [24-26]. The tooth thickness changes along with centrodes in the generation by a standard rack-cutter, and at places where the radius of the centrodes is small, the tooth are often undercutting. Thus, it is necessary to reduce the pressure angle of the cutter, but it causes undercutting or interference. In addition, when using traditional tooth profiles such as circle involute and a

\*Corresponding Author Email: [thai.nguyenhongr@hust.edu.vn](mailto:thai.nguyenhongr@hust.edu.vn)  
(N. H. Thai)

circular arc to design the tooth profile of the NCG to satisfy the condition of undercutting, the number of teeth distributed on gear must be significant. That results in often small tooth sizes reducing the gear drive load capacity.

In this study, to overcome the above problems, we proposed a novel curve in the tooth profile design of the NCGs. This primarily ensures that the teeth in different positions on the gear are more evenly distributed and the tooth size is larger to increase the load capacity of the gear drive. Compared to the other research, this paper focuses on building a mathematical model for the new curve and determining the conditions for applying it to the design of the tooth profile of the NCGs.

This paper is organized as follows: The mathematical model of the novel curve is presented in section 2. Section 3 presents the novel curve's application to the rack cutter's design. The method of applying the novel profile to the tooth design of the NCGs is presented in section 4. Conditions to avoid undercutting are presented in section 5. Meanwhile, illustrative examples verifying the applicability of the novel profile in the NCGs designs are presented in section 6. Section 7 presents the manufacturing of an NCG drive and experimental measurements to verify the applicability of the novel profile in practice. Finally, the results of the study are presented in section 8.

**2. ESTABLISHMENT OF MATHEMATICAL MODEL OF THE NOVEL CURVE**

The novel curve  $\Gamma_R$  is generated by an arbitrary point  $K_R$  attached to an ellipse  $\Sigma_E$ , with  $\Sigma_E$  rolls without sliding above or below a line  $\Delta$  as described in Figure 1a.

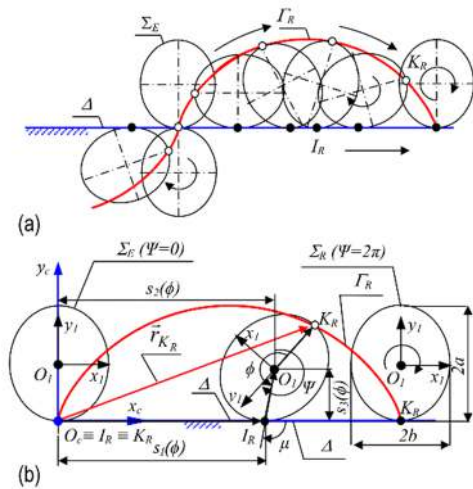


**Figure 1.** Movement of the generating ellipse with a) The novel curve and b) Principle of elliptical path traced

To establish the mathematical model of the novel curve  $\Gamma_R$ , from Figure 1b, we have:  $\mathcal{G}_c\{O_c x_c y_c\}$  is the fixed coordinate systems rigidly attached on the line  $\Delta$ ;  $\mathcal{G}_1\{O_1 x_1 y_1\}$  is a coordinate system attached to the center  $O_1$  of the generating ellipse  $\Sigma_E$ ; the point  $I_R$  is a mating point between the ellipse  $\Sigma_E$  and the line  $\Delta$  when  $\Sigma_E$  rolls without sliding on  $\Delta$ . There are two movements of the generating ellipse  $\Sigma_E$ : (1) The center  $O_1$  of  $\Sigma_E$  translates in the direction  $x_c$  by the distance  $s_2(\psi)$  and translates in the direction  $y_c$  by the distance  $s_3(\psi)$ , where  $\psi$  is the rotation angle of the coordinate system  $\mathcal{G}_1\{O_1 x_1 y_1\}$  in relation with the coordinate system  $\mathcal{G}_c\{O_c x_c y_c\}$ ; (2)  $\Sigma_E$  rotates around  $O_1$  an angle  $\psi$ . In the coordinate system  $\mathcal{G}_c\{O_c x_c y_c\}$  attached to  $\Delta$  as described in Figure 1a, beginning moment  $\Sigma_E$  contacts  $\Delta$  at the point  $O_c \equiv I_R \equiv K_R$ . After an interval of time, when the point  $I_R$  have translated a distance  $\overline{O_c I_R}$  from  $O_c$  to  $I_R$  in  $\Delta$ , the ellipse  $\Sigma_E$  will move by an arch  $\widehat{e}$  from  $I_R$  to  $K_R$  on  $\Sigma_E$  and make a rotation angle  $\psi$ . Therefore, we have: The relative position of the mating point  $I_R$  with respect to  $O_c$  is determined by:

$$s_1(\phi) = \widehat{e} = \int_0^\phi \sqrt{r_E(\phi)^2 + \left(\frac{dr_E(\phi)}{d\phi}\right)^2} d\phi \tag{1}$$

wherein:  $r_E(\phi)$  is the polar radius of  $\Sigma_E$ . From literature [23],  $r_E(\phi)$  is given by:

$$r_E(\phi) = a \sqrt{\frac{1 - \varepsilon^2}{1 - \varepsilon^2 \cos^2 \phi}} \text{ with } \varepsilon = \frac{\sqrt{a^2 - b^2}}{a} \text{ and } a, b \text{ are the major axis and minor axis of } \Sigma_E, \text{ respectively;}$$

$\phi = \angle(O_1 K_R, O_1 I_R)$  is the angle of the arch  $\widehat{e}$  on  $\Sigma_E$ .

(i) The relative position of  $O_1$  with respect to  $O_c$  when  $\Sigma_E$  rolls without sliding on  $\Delta$  is given by:

In direction of  $x_c$ :

$$s_2(\phi) = s_1(\phi) + r_{I_R}(\phi) \sin(\psi - \phi) \tag{2}$$

In direction of  $y_c$ :

$$s_3(\phi) = r_{I_R}(\phi) \cos(\psi - \phi) \tag{3}$$

(ii) The generating ellipse  $\Sigma_E$  rotates around  $O_1$  an angle  $\psi$ :

$$\phi = \psi + \mu - \frac{\pi}{2} \tag{4}$$

where:  $\mu = \arctan\left(\frac{\partial x_E(\phi) / \partial \phi}{\partial y_E(\phi) / \partial \phi}\right)$

By transformation coordinates of  $K_R$  from  $\mathcal{G}_1\{O_1 x_1 y_1\}$  system to  $\mathcal{G}_c\{O_c x_c y_c\}$ , equation of the novel curve is obtained by:

$$\mathbf{r}_{K_R} = {}^c\mathbf{r}_{I_R} + {}^c\mathbf{r}_{O_1} + {}^c\mathbf{M}_1 {}^1\mathbf{r}_{K_R} \tag{5}$$

wherein:  ${}^1\mathbf{r}_{K_R} = [0 \quad -a \quad 0]^T$ ;

$${}^c\mathbf{r}_{O_1} = [s_2(\psi) \quad s_3(\psi) \quad 0]^T; \quad {}^c\mathbf{r}_{I_R} = [s_1(\phi) \quad 0 \quad 0]^T;$$

$${}^c\mathbf{M}_1 = \begin{bmatrix} \cos \psi(\phi) & \sin \psi(\phi) & 0 \\ -\sin \psi(\phi) & \cos \psi(\phi) & 0 \\ 0 & 0 & 1 \end{bmatrix}$$

After transforming, Equation (5) is rewritten as:

$$\mathbf{r}_{K_R} = \begin{bmatrix} x_{K_R} \\ y_{K_R} \\ 0 \end{bmatrix} = \begin{bmatrix} s_2(\phi) - a \sin(\psi) \\ (-1)^g s_3(\phi) - a \cos(\psi) \\ 0 \end{bmatrix} \tag{6}$$

In Equation (6):  $g = 0$  when  $I_R$  is about  $\Delta$  and  $g = 1$  when  $I_R$  is below  $\Delta$ .

### 3. PROFILE GENERATION OF THE RACK CUTTER BY THE NOVEL CURVE

#### 3. 1. Determination of Design Parameters of the Rack Cutter by the Novel Curve

From the novel curve mathematical model set up in section 1, the formation of the rack cutter profile is shown in Figure 2.

In this figure (Figure 2, above) the datum line of the rack cutter  $\Delta$  is the dedendum profile and below  $\Delta$  is the addendum profile. The design parameters are determined as follows:

##### The pitch $p_c$

According to the method for the novel curve generation, both of the tooth thickness  $t$  and the space width  $w$  on the pitch line of the rack cutter will be equal to the perimeter of the generating ellipse  $\Sigma_E$ :

$$t = w = C_{\Sigma_{RE}} \tag{7}$$

wherein:  $C_{\Sigma_E} = \int_0^{2\pi} \sqrt{r_E(\phi)^2 + \left(\frac{dr_E(\phi)}{d\phi}\right)^2} d\phi$

Therefore, the pitch on the centrod of the rack cutter can be calculated as follows:

$$p_c = t + w = 2C_{\Sigma_{RE}} \tag{8}$$

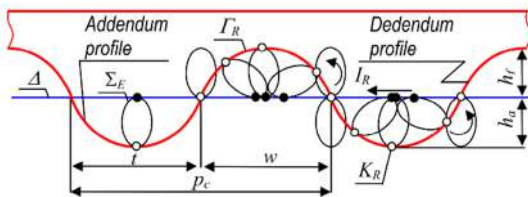


Figure 2. New rack cutter

#### The tooth height $h$

The addendum height  $h_a$  and dedendum height  $h_f$  when the point  $K_R$  is located at the major and minor axis of  $\Sigma_E$  are represented in the following equations:

$$\begin{cases} h_a = h_f = 2(pa + qb) \\ h = h_a + h_b = 4(pa + qb) \end{cases} \tag{9}$$

wherein:  $p = 1, q = 0$  when the point  $K_R$  is attached to the major axis of  $\Sigma_E$  and  $p = 0, q = 1$  when the point  $K_R$  is attached to the minor axis of  $\Sigma_E$ .

### 3. 2. Influence of the Elliptical Parameters and the Starting Point Position on the Tooth Profile of the Rack Cutter

From sections 1.1 and 1.2, it is noticeable that the profile of the rack cutter is dependent on: (1) the position of the point  $K_R$  attached to  $\Sigma_E$ ; (2) the ratio  $\lambda = a/b$  of the generating ellipse  $\Sigma_E$ . Let further consider the following two cases:

#### Case 1: Influence of the position of $K_R$ on the tooth profile of the rack cutter

We have  $\beta = \angle(O_1y_1, O_1I_0)$  is the angle defining the position of the point  $K_R$  attached to  $\Sigma_E$  (see Figure 3). Because of symmetry about the semi axes, only the position of  $K_R$  in the fourth quarter of  $\Sigma_E$  is taken into consideration. Influence of the position of  $K_R$  fixed on  $\Sigma_E$  on the tooth profile of the rack cutter is investigated with  $\beta \in [0 \div \pi/2]$ , increments  $\Delta\beta = \pi/8$ , and the pitch of centrod of the rack cutter  $p_c = 19.6$  mm. The design parameters of the rack cutter are given in Table 1 and Figure 3 shows the corresponding profile of the rack cutter.

From Figure 3 and Table 1 we have: (i) When the point  $K_R$  fixed on  $\Sigma_E$  is located on the major axis or minor axis ( $\beta = 0^\circ$  and  $\beta = 90^\circ$ ), the profile of the rack cutter will be symmetrical and the tooth heights will be as follows  $h_{|\beta=0^\circ} > h_{|\beta=90^\circ}$ ; (ii) When  $0^\circ < \beta < 90^\circ$ , the tooth height will increase in the range  $4b < h < 4a$ , and the tooth profile will be asymmetrical and deviated to the left.

#### Case 2: Influence of the ratio $\lambda = a/b$ of the generating ellipse on the tooth profile of the rack cutter

TABLE 1. Design parameter of the rack cutter by the position of  $K_R$  attached to  $\Sigma_E$

$\beta$ ( $^\circ$ )	$a$ (mm)	$b$ (mm)	$p_c$ (mm)	$h$ (mm)
0.0	1.75	1.36	19.6	7.0
22.5	1.75	1.36	19.6	6.8
45.0	1.75	1.36	19.6	6.4
90.0	1.75	1.36	19.6	5.4

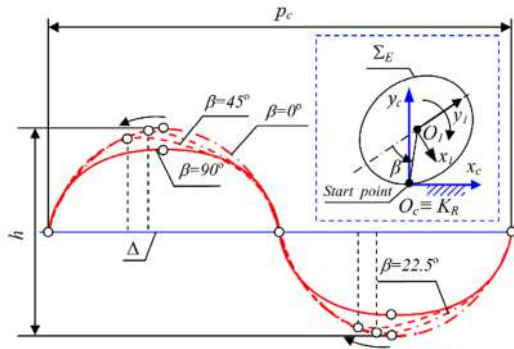


**Figure 3.** Profile of the rack cutter corresponding to different starting points  $K_R$

In this case, the ratio  $\lambda$  is obtained from Equation (7). With  $p_c$  is kept to be equal to  $19.6 \text{ mm}$ , the ratio  $\lambda$  will have the values of 1.29, 1.00, 0.78, 0.52, respectively. When the point  $K_R$  is on the semi-major axis vertex, the design parameters of the rack cutter corresponding to  $\lambda$  will be shown in Table 2. The profile of the rack cutter is presented in Figure 4.

From Figure 4 and Table 2 we have:

- (i) The tooth height  $h$  decreases with smaller values of  $\lambda$ ;
- (ii) When  $\lambda$  decreases, the tooth addendum turns into a concave form. It can be explained as while  $\lambda$  decreases, the major semi axis becomes semi-minor axis, at the position  $K_R^*$  of  $\Sigma_E$  after rolling on  $\Delta$ , distance

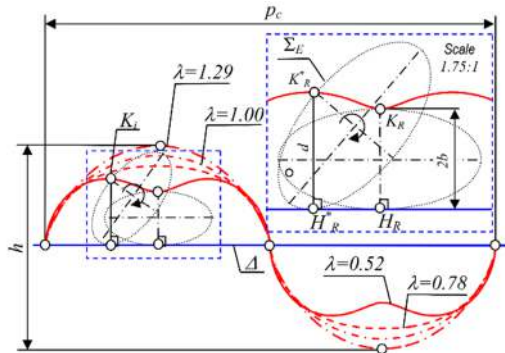


**Figure 4.** The tooth profiles corresponding to different values of  $\lambda$

**TABLE 2.** Design parameters of the rack cutter corresponding to  $\lambda$  of  $\Sigma_E$

$\lambda$	$a$ (mm)	$b$ (mm)	$p_c$ (mm)	$h$ (mm)
1.29	1.75	1.36	19.6	7.0
1.00	1.56	1.56	19.6	6.2
0.78	1.36	1.75	19.6	5.4
0.52	1.05	2.00	19.6	4.7

$d = \overline{H_R^* K_R^*} > 2b$  will cause concavity on the addendum (inside the area covered by the dashed line in Figure 4). This phenomenon will be resolved in the following section 2.3; (iii) When  $\lambda = 1$ , the ellipse  $\Sigma_E$  becomes circle, and the profile  $\Gamma_R$  of the rack cutter changes into cycloidal curve.

### 3. 3. Condition for Convexity of the Rack Cutter Profile

From Figure 4 (area bordered by the dashed line) with  $\lambda = 0.52$  (point  $K_R$  lies on the semi-minor axis vertex of  $\Sigma_E$ ), the profile will be concave. To achieve the convexity of the curve  $\Gamma_R$ , it is necessary to determine the relationship between parameters  $a$  and  $b$  of  $\Sigma_E$ . Therefore, if we consider the ellipse is fixed, the tangency  $\Delta$  only rolls on the ellipse, and  $I_R$  is the contact point between them (Figure 5); the problem will be transformed into finding distances from the point  $K_R$  on the minor semi-axis vertex to tangents  $\Delta$  of the ellipse.

The tangent  $\Delta$  to the ellipse at the point  $I_R$  can be expressed by the following equation:

$$\frac{x_{I_R}(\phi)x}{b^2} + \frac{y_{I_R}(\phi)y}{a^2} = 1 \tag{10}$$

where:  $x_{I_R}(\phi) = b \cos \phi$ ,  $y_{I_R}(\phi) = a \sin \phi$

Equation (10) can be rewritten thus:

$$\cos \phi ax + \sin \phi by - ab = 0 \tag{11}$$

Distance from the point  $K_R(b, 0)$  to the tangent  $\Delta$  of  $\Sigma_E$  at  $I_R$  is described as follows:

$$f(\phi) = d(K_R, \Delta) = \frac{|ab \cos \phi - ab|}{\sqrt{(a \cos \phi)^2 + (b \sin \phi)^2}} \tag{12}$$

By solving equation  $\frac{df(\phi)}{d\phi} = 0$ ; finding the extremes of

$f(\phi)$  at  $\sin \phi = 0$  and  $\cos \phi = \frac{-a^2}{a^2 + b^2}$ ; and substituting

into Equation (12), the maximum value of  $d$  is given by:

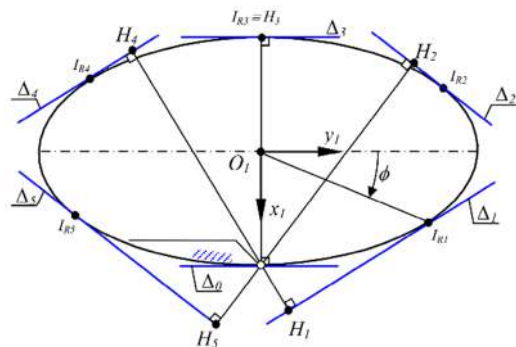


**Figure 5.** Distances from the point  $K_R$  to tangents  $\Delta$

$$d_{\max} = \frac{ab(a + a^2 + b^2)}{\sqrt{(b^4 a^2 + 3b^2 a^4 - a^4 + a^6)}} \quad (13)$$

From Figure 4, the profile becomes concave when  $d < 2b$ . Together with Equation (13), the condition of convexity of  $I_R$  can be inequality as below:

$$b \geq \frac{ab(a + a^2 + b^2)}{2\sqrt{(b^4 a^2 + 3b^2 a^4 - a^4 + a^6)}} \quad (14)$$

**4. MATHEMATICAL MODEL OF THE ELLIPSE NON-CIRCULAR GEAR SURFACES**

**4. 1. Equation of the Centrode of the NCGs Pair**

There are two usual approaches for designing the centrodes: (1) To establish the conjugated centrodes  $\Sigma_i$  ( $i = 1, 2$ ) when the gear ratio function  $i_{12}(\phi_1)$  is given in advance; (2) To determine the conjugated centrodes  $\Sigma_i$  when one centrode and the center distance of the gear pair are given. In this work, the second approach was utilized. The center distance  $A_{12}$  and one centrode, which is an eccentric circle  $\Sigma_1(O_1, R)$ , are given. From Figure 6 if  $r_1(\phi_1)$  is a polar radius of the centrode  $\Sigma_1(O_1, R)$  corresponding to an angular polar  $\phi_1$ ;  $r_2(\phi_2)$  is a polar radius of the centrode  $\Sigma_2(O_2, r_2(\phi_2))$  corresponding to an angular polar  $\phi_2(\phi_1)$ ; and the point  $I$  is the instantaneous center. According to Mundo [15], the equations of the centrodes of the NCGs is described as follows:

$$\begin{cases} r_2(\phi_2) = r_2(\phi_2(\phi_1)) = A_{12} - r_1(\phi_1) \\ \phi_2(\phi_1) = \int_0^{\phi_1} i_{21} d\phi_1 \end{cases} \quad (15)$$

where:  $i_{21}(\phi_1) = \frac{r_1(\phi_1)}{A_{12} - r_1(\phi_1)}$  is the gear ratio function of

the NCGs pair; stated in the literature [27]  $r_1(\phi_1) = \sqrt{(R^2 - e^2 \sin^2 \phi_1)} - e \cos \phi_1$  with  $R$  is a radius of a circle  $\Sigma_1(O_1, R)$  and  $e$  is an eccentricity of the rotation center  $O_1$  from the center of the circle  $\Sigma_1(O_1, R)$  as shown in Figure 6.

The relationship between the revolutions of the driving gear and the driven gear is given by the following equation [24]:

$$2\pi = n_2 \int_0^{2\pi} \left( \frac{r_1(\phi_1)}{A_{12} - r_1(\phi_1)} \right) d\phi_1 \quad (16)$$

where  $n_2$  is the number of revolutions that centrode  $\Sigma_1$  performs for one revolution of centrode  $\Sigma_2$ .

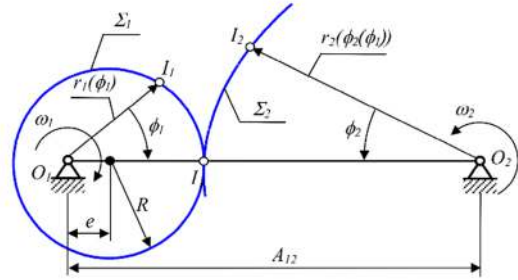


Figure 6. Illustration of mating centrodes 2 versus 1

**4. 2. A Mathematical Model of the Profile of the NCGs Pair Generated by the Novel Rack Cutter**

In general, the relative motion between the novel rack cutter and the NCGs in the fixed coordinate system  $\mathcal{G}_f\{O_f, x_f, y_f\}$  is described in Figure 7. Where  $\mathcal{G}_c\{O_c, x_c, y_c\}$  is a coordinate system connected to the datum line  $\Delta$  of the rack  $\Sigma_R$ ;  $\mathcal{G}_i\{O_i, x_i, y_i\}$  is a coordinate system connected to the gear; the point  $I$  is the instantaneous center and also is the mating point between  $\Delta$  and the centrode curve  $\Sigma_i$  of the gear ( $i = 1, 2$  when generating a profile of the driving and driven gear, respectively);  $\psi_i = \phi_i + \mu_i - \frac{\pi}{2}$  is an angular position of the coordinate system  $\mathcal{G}_i\{O_i, x_i, y_i\}$  in reference to the coordinate system  $\mathcal{G}_f\{O_f, x_f, y_f\}$  during generating

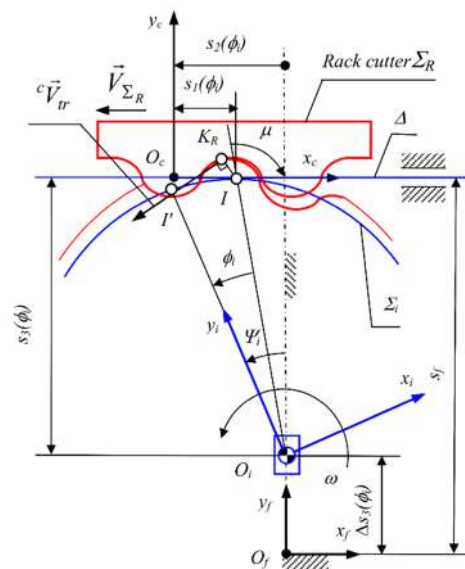


Figure 7. Relative motion between the rack cutter and the NCGs

process with  $\mu_i = \arctan\left(\frac{r_i(\phi_i)}{dr_i/d\phi_i}\right)$ ;  $s_f$  is a distance from

$x_c$  to  $x_f$ ;  $s_1(\phi_i) = \int_0^{\phi_i} \sqrt{r_i(\phi_i)^2 + \left(\frac{dr_i(\phi_i)}{d\phi_i}\right)^2} d\phi_i$  is a displacement of the rack cutter along direction  $x_f$ ,  $s_3(\phi_i) = r(\phi_i)\cos(\psi_i - \phi_i)$  is a displacement of the NCGs center  $O_i$  along direction  $y_f$  when the point  $I$  of  $\Sigma_i$  moves to the position  $I'$ .

Based on the equation of the NCGs centred in section 3.1, the profile of the NCGs will be generated by the rack cutter  $\Sigma_R$ . According to literature [1, 13, 14] and from Figure 7, the relative motion between the NCGs and the rack cutter  $\Sigma_R$  contains the following movements:

- (1) The rack cutter translates a distance  $s_2(\phi_i) = s_1(\phi_i) + r_i(\phi_i)\sin(\psi - \phi_i)$  along the direction of  $x_f$ ;
- (2) The gear sequentially moves as follows: (a) The geared center  $O_i$  translates a distance  $\Delta s_3(\phi_i) = s_{f1} - s_3(\phi_i)$  along the direction of  $y_f$ ; (b)

The gear rotates around  $O_i$  an angle  $\psi_i$ .

Therefore, if  $K_R$  is the shaping point on  $\Gamma_R$  of  $\Sigma_R$ , and by transforming the coordinates of  $K_R$  from  $\mathcal{G}_c\{O_c, x_c, y_c\}$  to  $\mathcal{G}_i\{O_i, x_i, y_i\}$  of the gear, the profile equation of the shaped gear is expressed by:

$$\mathbf{r}_{K_i} = {}^i\mathbf{M}_f \mathbf{M}_f^f \mathbf{M}_c \mathbf{r}_{K_R} \quad (17)$$

wherein:

$${}^f\mathbf{M}_c = \begin{bmatrix} 1 & 0 & s_2(\phi_i) \\ 0 & 1 & s_{f1} \\ 0 & 0 & 1 \end{bmatrix}; \quad \mathbf{M}_f = \begin{bmatrix} 1 & 0 & 0 \\ 0 & 1 & \Delta s_3(\phi_i) \\ 0 & 0 & 1 \end{bmatrix};$$

$${}^i\mathbf{M}_f = \begin{bmatrix} \cos\psi_i & \sin\psi_i & 0 \\ -\sin\psi_i & \cos\psi_i & 0 \\ 0 & 0 & 1 \end{bmatrix}; \mathbf{r}_{K_R} \text{ is determined from}$$

Equation (6). The relationship between the kinematic parameter  $\phi_i$  and the geometrical parameter  $\phi$  is expressed by the meshing equation [27]:

$$\mathbf{n}^c \mathbf{V}_{tr} = 0 \quad (18)$$

where:  $\mathbf{n}^c$  is the common normal vector of the conjugated profiles ( $\Gamma_i, \Gamma_R$ ) at the mating point  $K$ .  ${}^c\mathbf{V}_{tr}$  is the relative sliding velocity between  $K_R \in \Gamma_R$  and  $K_i \in \Gamma_i$  at  $K$ , when  $\Gamma_i$  are rolling as well as slipping with  $\Gamma_R$ . The vector  $\mathbf{n}$  is given by:

$$\mathbf{n} = \frac{\partial \mathbf{r}_{K_R}(\phi)}{\partial \phi} \times \mathbf{k} \quad (19)$$

With  $\mathbf{k} = [0 \ 0 \ 1]^T$ , and  ${}^c\mathbf{V}_{tr}$  is expressed as below:

$${}^c\mathbf{V}_{tr} = \omega_c \times {}^c\mathbf{r}_{IK} \quad (20)$$

where:  $\omega_c = \omega_c \mathbf{k}_c$  is the angular velocity of the shaped gear in relation with the coordinate system  $\mathcal{G}_c\{O_c, x_c, y_c\}$  of the rack cutter, and  ${}^c\mathbf{r}_{IK} = (s_1(\phi) - x_{K_R})\mathbf{i}_c + y_{K_R}\mathbf{j}_c$

By transforming  ${}^c\mathbf{V}_{tr}$ , one gets:

$${}^c\mathbf{V}_{tr} = \omega \begin{bmatrix} -y_{K_R} \\ s_1(\phi) - x_{K_R} \end{bmatrix} \quad (21)$$

Substituting Equations (19) and (21) into Equation (18), it is possible to write:

$$f(\phi, \phi_i) = y'_{K_R}(\phi)y_{K_R}(\phi) + x'_{K_R}(\phi)(s_1(\phi) - x_{K_R}(\phi)) = 0 \quad (22)$$

By solving Equation (22), the relationship between  $\phi_i$  and  $\phi$  of the gear  $i$  with the rack cutter.

#### 4. 2. 1. The Profile Equation of the Driving Gear

Because the driving gear is the eccentric circle gear, the parameters of the shaping movements are given by:

$$s_1(\phi_1) = \int_0^{\phi_1} \sqrt{r_1(\phi_1)^2 + \left(\frac{dr_1(\phi_1)}{d\phi_1}\right)^2} d\phi_1 \quad (23)$$

$$s_2(\phi_1) = s_1(\phi_1) + r_1(\phi_1)\sin(\psi_1 - \phi_1) \quad (24)$$

$$s_3(\phi_1) = r_1(\phi_1)\cos(\psi_1 - \phi_1) \quad (25)$$

$$\Delta s_3(\phi_1) = s_{f1} - s_3(\phi_1) \quad (26)$$

wherein:  $s_{f1} = R + e$ , and by substituting equations from Equation (23) to Equation (26) into Equation (17), the profile equation of the driving eccentric circular gear is expressed as follows:

$$\mathbf{r}_{K1} = \begin{bmatrix} (s_3(\phi_1) + y_{K_R})\cos\psi_1 + (s_2(\phi_1) - x_{K_R})\sin\psi_1 \\ (s_3(\phi_1) + y_{K_R})\sin\psi_1 - (s_2(\phi_1) - x_{K_R})\cos\psi_1 \\ 0 \end{bmatrix} \quad (27)$$

#### 4. 2. 2. The Profile Equation of the Driven Gear

The non-circular driven gear has a polar radius  $r_2(\phi_2(\phi_1)) = A_{12} - r_1(\phi_1)$  determined by Equation (15). The parameters of the shaping movements of this driven gear are given by the following equations:

$$s_1(\phi_2(\phi_1)) = \int_0^{\phi_2} \sqrt{r_1(\phi_2(\phi_1))^2 + \left(\frac{dr_1(\phi_2(\phi_1))}{d\phi_2(\phi_1)}\right)^2} d\phi_2(\phi_1) \quad (28)$$

$$s_2(\phi_2(\phi_1)) = s_1(\phi_2(\phi_1)) + r_2(\phi_2(\phi_1)) \sin(\psi_2 - \phi_2(\phi_1)) \quad (29)$$

$$s_3(\phi_2(\phi_1)) = r_2(\phi_2(\phi_1)) \cos(\psi_2 - \phi_2(\phi_1)) \quad (30)$$

$$\Delta s_3(\phi_2(\phi_1)) = s_{f2} - s_3(\phi_2(\phi_1)) \quad (31)$$

where  $s_{f1} = A_{12} - R + e$ , and by substituting equations from Equation (28) to Equation (31) into Equation (17), the equation of the NCGs profile is obtained as follows:

$$\mathbf{r}_{K_2} = \begin{bmatrix} (s_3(\phi_2(\phi_1)) + y_{K_R}) \cos \psi_2 + (s_2(\phi_2(\phi_1)) - x_{K_R}) \sin \psi_2 \\ (s_3(\phi_2(\phi_1)) + y_{K_R}) \sin \psi_2 - (s_2(\phi_2(\phi_1)) - x_{K_R}) \cos \psi_2 \\ 0 \end{bmatrix} \quad (32)$$

### 5. TOOTH UNDERCUTTING AND THE LINE OF MESHING

**5.1. Tooth Undercutting** From literature [28, 29], to avoid undercutting during the profile shaping process, the equation of the tooth profile needs to satisfy:

$$\Delta_1^2 + \Delta_2^2 = 0 \quad (33)$$

wherein:

$$\Delta_1 = \begin{vmatrix} dx_{K_R} & -{}^cV_{trx} \\ d\phi & \partial f(\phi_i) \frac{d\phi_i}{dt} \end{vmatrix}; \Delta_2 = \begin{vmatrix} dy_{K_R} & -{}^cV_{try} \\ d\phi & \partial f(\phi_i) \frac{d\phi_i}{dt} \end{vmatrix}$$

With  ${}^cV_{trx}$ ,  ${}^cV_{try}$  are the components of the sliding velocity of the shaping point  $K_R$  on the profile of the rack cutter  $\Gamma_R$ . By further developing of  $\Delta_1$ ,  $\Delta_2$  one obtains:

$$\begin{cases} \Delta_1 = A_1 - B_1 C_1 \\ \Delta_2 = A_2 - B_2 C_2 \end{cases} \quad (34)$$

wherein:

$$\begin{aligned} A_1 &= \rho_i(C_1 - EH - GFI + J); B_1 = -NGF \\ A_2 &= \rho_i(-EF - GHI + J(1 + I)); B_2 = M - s_1(\phi) \\ C_1 = C_2 &= (G^2 + E^2)^{0.5}; E = \frac{a\varepsilon^2 \sin 2\phi(\varepsilon^2 - 1)^{0.5}}{2(\varepsilon^2 \cos^2 \phi - 1)^{1/5}} \\ F &= \frac{\cos \phi(1 - \varepsilon^2)}{(1 - 2\varepsilon^2 \cos^2 \phi + \varepsilon^4 \cos^4 \phi)^{0.5}}; G = a \left( \frac{1 - \varepsilon^2}{1 - \varepsilon^2 \cos^2 \phi} \right)^{0.5} \\ H &= \frac{\sin \phi}{(1 - 2\varepsilon^2 \cos^2 \phi + \varepsilon^4 \cos^4 \phi)^{0.5}}; I = \frac{a^2 b^2}{a^4 - (a^4 - b^4) \cos^2 \phi} \end{aligned}$$

$$\begin{aligned} J &= \frac{a\varepsilon^2}{(1 - 2\varepsilon^2 \cos^2 \phi + \varepsilon^4 \cos^4 \phi)^{0.5}} \\ M &= a \frac{(1 - \varepsilon^2)^{0.5} - \varepsilon^2 \cos \phi \sin \phi(1 - \varepsilon^2 \cos^2 \phi)}{((1 - \varepsilon^2 \cos^2 \phi)(1 - 2\varepsilon^2 \cos^2 \phi + \varepsilon^4 \cos^4 \phi))^{0.5}} \\ N &= a \left( \frac{\sin^2 \phi - \cos^2 \phi(1 - \varepsilon^2)}{(1 - 2\varepsilon^2 \cos^2 \phi + \varepsilon^4 \cos^4 \phi)^{0.5}} \right) \end{aligned}$$

**5.1.1. For the Driving Gear** Because  $\Sigma_1(O_1, R)$  is the eccentric circle, the curvature radius at each point on  $\Sigma_1$  is constant and equal to  $R$ :

$$\rho_1(\phi_1) = R \quad (35)$$

**5.1.2. For the Driven Gear** From literature [1, 23], the curvature radius  $\rho_2(\phi_2)$  of  $\Sigma_2$  is determined as follows:

$$\rho_2(\phi_2) = \frac{\sqrt{\left( r_2(\phi_2)^2 + \left( \frac{dr_2(\phi_2)}{d\phi_2} \right)^2 \right)^3}}{r_2(\phi_2)^2 + 2 \left( \frac{dr_2(\phi_2)}{d\phi_2} \right)^2 - r_2(\phi_2) \frac{d^2 r_2(\phi_2)}{d\phi_2^2}} \quad (36)$$

wherein:  $r_2(\phi_2)$  is obtained from Equation (15).

**5.2. The Line of Meshing** The curve  $\zeta_K$  is a locus of the contact point  $K$  of the conjugated profiles ( $\Gamma_1, \Gamma_2$ ), with  $\Gamma_1$  belongs to the driving gear, and  $\Gamma_2$  is the driven one, as shown in Figure 8. This curve  $\zeta_K$  can also be called the line of meshing, with the point  $K$  is the mating point. At the mating moment  $K \equiv K_1 \equiv K_2$ , with  $K_1 \in \Gamma_1, K_2 \in \Gamma_2$ . On the same time when  $K_1 \in \Gamma_1$  there is a corresponding point  $I_1 \in \Sigma_1$ , and similarly, with  $K_2 \in \Gamma_2$  there is  $I_2 \in \Sigma_2 (I_1 \equiv I_2 \equiv I)$ . Therefore, when the driving gear rotates around  $O_1$  an angle  $\phi_1 = \angle(O_1 I_1, O_1 I)$  to place  $I_1$  on  $\Sigma_1$  to the position of the pitch point  $I$  on  $O_1 O_2$ , the driven gear correspondingly rotates around  $O_2$  an angle  $\phi_2(\phi_1) = i_{21}(\phi_1) \phi_1 = \angle(O_2 I_2, O_2 I)$  to move  $I_2$  on  $\Sigma_2$  to the pitch point  $I$  following gear ratio function  $i_{12}(\phi_1)$ .

The equation of the line of meshing  $\zeta_K$  can be expressed as follows:

$$\mathbf{r}_{\zeta_K} = {}^f M_1 \mathbf{r}_{K_1} \quad (37)$$

wherein:  ${}^f M_1 = \begin{bmatrix} \cos \phi_1 & -\sin \phi_1 & 0 \\ \sin \phi_1 & \cos \phi_1 & 0 \\ 0 & 0 & 1 \end{bmatrix}$

And  $\phi_1$  is the rotation angle of the driving gear around  $O_1$ .

6. CASE STUDIES

In the previous sections, the mathematical model of the novel curve has been built in order to generate the NCGs tooth profile. Where: (i) Equation (6) is established for the profile of the rack cutter based on the novel curve; (ii) Equation (14) is the condition of curve convexity for the tooth profile; (iii) Equations (17), (27) and (32) expressed the mathematical model of the NCGs profiles; (iv) Equations (34), (35) and (36) provided condition for avoiding undercutting when applying the novel curve in the generation of the NCGs tooth profile; (v) Equation (37) expressed the mathematical model of the line of meshing of the NCGs pair. Based on those results, a software program has been developed to calculate, examine and design the NCGs pair. The following case studies will illustrate steps in the NCGs design process using the novel curve. The input data for the design process are provided in Tables 1 and 2.

**Example 1** Design the external NCGs pair with profile generated from the rack cutter, of which the design parameters are taken from Tables 1 and 2:  $\beta = 0^\circ$ ;  $\lambda = 1.29$ ;  $a = 1.75$  mm;  $b = 1.36$  mm; the pitch of the rack  $p_c = 19.6$  mm; the tooth height  $h = 7$  mm with addendum  $h_a = 3.5$  mm and dedendum  $h_f = 3.5$  mm.

The gear ratio function in Figure 9 is established by the set of kinematic parameters of the NCGs pair (given in Table 3). Wherein:  $R = z_1 p_c / 2\pi$ , the number of teeth of the driving gear  $z_1 = 8$ .

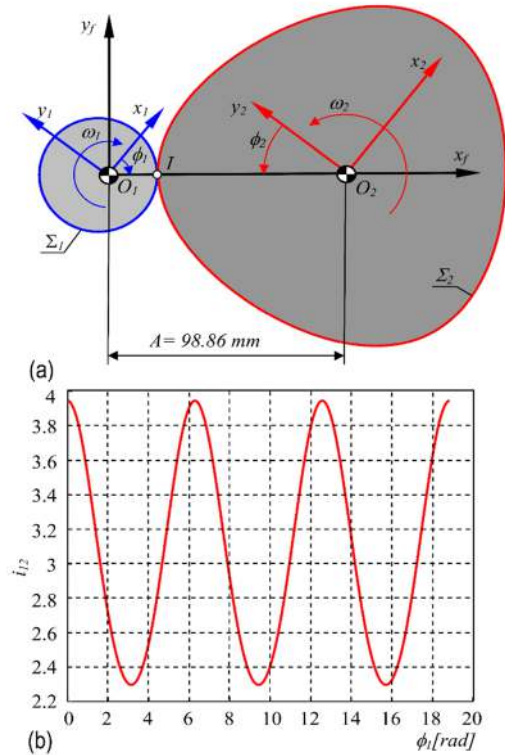


Figure 9. The NCGs pair with (a) conjugated centred and (b) gear ratio function

From the design parameters of the rack cutter and from the kinematic parameters of the NCGs pair, it is noticeable that for correct meshing, both of the gears need to be fabricated by the same rack cutter and  $t_1 = w_1 = t_2 = w_2$  can be determined by Equation (7).

It is also necessary to verify Equations (34), (35) and (36) to check condition for avoiding undercutting phenomenon (Figure 10). The design parameters of the NCG pair are calculated and presented in Table 4. Figure 11 shows the NCGs pair as well as the line of meshing.

Figure 10 shows that the novel profile avoids undercutting since there is no singularity.

From Figure 11, one obtains: (1) All of the teeth of the NCGs are identical in shape. Even in position (II) (see Figure 11a), where the curvature radius of the centre  $\rho_{II} = 48.03$  mm has a smaller value than the curvature radius in position (I) with  $\rho_I = 155.52$  mm, the teeth in both positions have identical shape and equal parameters. Same as standard cylindrical gears with the constant gear ratio, so this is an advantage of the novel profile; (2) The line of meshing of the NCGs pair is a smooth closed curve (see Figure 11b), which is entirely different from the straight line when the tooth profile of the NCGs pair is involute of a circle or arcs [7, 10, 12, 22].

**Example 2** This case aims to examine the influence of position of the point  $K_R$ , which lays on  $\Sigma_E$ , on the tooth

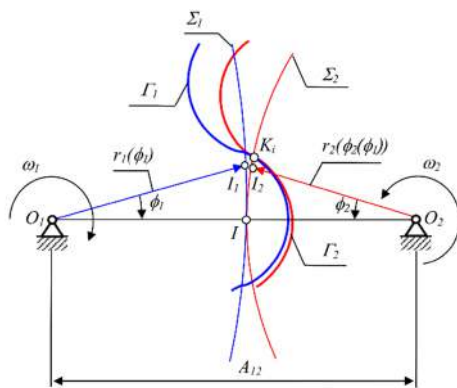


Figure 8. The line of meshing of the external NCGs pair

TABLE 3. The set of kinematic parameters of the NCGs

Parameter	Notation	Value
Center distance (mm)	$A_{12}$	98.86
Pitch radius $\Sigma_1$ (mm)	$R$	25.00
Eccentric driving gear (mm)	$e$	5.00
Cycle coefficient	$n$	3.00

height. Chosen from Tables 1 and 2 are those values  $\lambda = 0.78$ ,  $\beta = 90^\circ$ ,  $h = 5.4$  mm, the other parameters of the rack cutter and kinematic parameters of the NCGs, as well as the design steps, are selected similarly as in Example 1

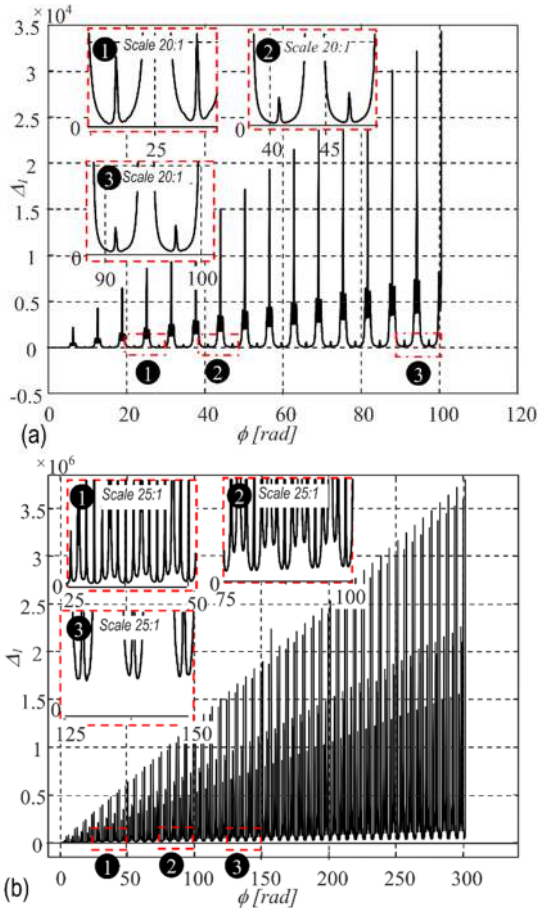


Figure 10. Condition for non-undercutting with (a) eccentric gear 1 and (b) NCGs 2

TABLE 4. Machining parameters of the NCGs pair

Parameter	Notation	Value	
		Gear1	Gear2
Center distance (mm)	$A_{12}$	98.9	
Number of teeth	$z$	8.0	24.0
Eccentric of gear1 (mm)	$e$	5.0	5.0
Pitch of $\Sigma_i$ (mm)	$p_c$	19.6	19.6
Tooth thickness (mm)	$t$	9.8	9.8
Width of space (mm)	$w$	9.8	9.8
Tooth addendum (mm)	$h_a$	3.5	3.5
Tooth dedendum (mm)	$h_f$	3.5	3.5

After ensuring that the condition of non-undercutting Equations (34), (35) and (36) satisfied, the design parameters of the NCGs pair is given by Table 5. Also, Figure 12 shows the design of the gear pair.

From Figure 12 and Table 4 one obtains: (1) If the point  $K_R$  lies on the minor semi-axis of  $\Sigma_E$ , the generated tooth will have a shorter height, the tooth tip will be sharpened, the tooth dedendum grow larger (see Figure 12b), while the number of teeth, the pitch  $p_c$ , the tooth thickness  $t$ , and space width  $w$  remain unchanged. It also means that all the teeth still have identical shape; (2) Therefore, locating  $K_R$  on the minor semi-axis of  $\Sigma_E$  will increase the load capacity of the gear pair.

**Example 3** This case aims to examine the influence of the position of the point  $K_R$  on the tit angle of teeth. From Table 1,  $\lambda$  and  $\beta$  can be selected as  $\lambda = 1.29$ ,  $\beta = 22.5^\circ$  and  $\beta = 45^\circ$ . The other parameters of the rack cutter and kinematic parameters of the NCGs are selected similarly as in the previous examples. The condition of non-undercutting Equations (34), (35) and (36) also needs to be verified. Table 5 shows the design parameters of the driven NCGs, and Figure 13 shows the final product of numerical calculation process.

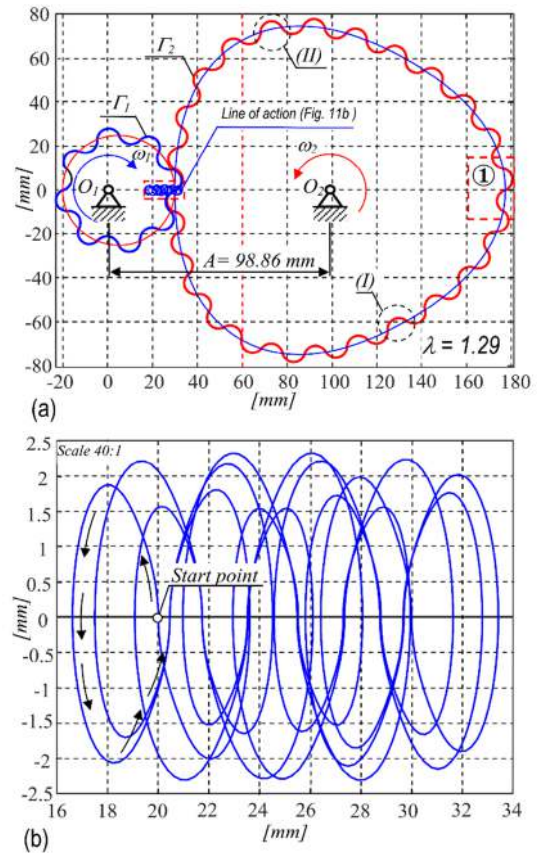
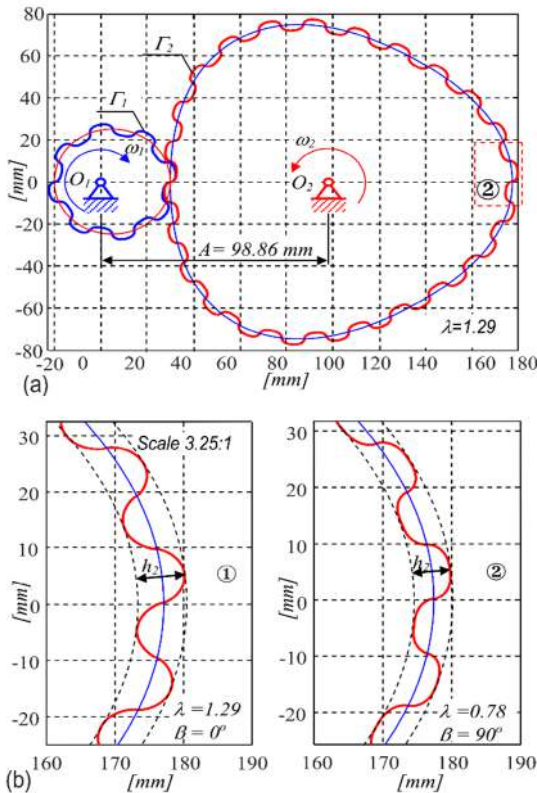


Figure 11. The external NCGs pair with  $\lambda = 1.29$  (a) the tooth profile and (b) the line of meshing

From Table 5 and Figure 13 one obtains: (1) The inclination angle of the tooth decreases when  $\beta$  increases from  $0^\circ$  and the tooth height decreases. Meanwhile, the matching parameter as the pitch  $p_c$ , tooth thickness  $t$ , space width  $w$  stay unchanged; (2) Figure 13 clearly shows the tooth with steeper addendum than dedendum can help to increase the force transmission capacity from the driving to driven gear. However, this case can only be applied in the gear pair with rotation direction determined in advance and stay unchanged during working time.



**Figure 12.** Examination of the generating process of NCGs profile in relationship with  $\lambda$ : (a) the NCGs pair and (b) comparison of profiles

**TABLE 5.** Design parameters of the NCGs

Parameter	Notation	Value	
		$\beta=22.5^\circ$	$\beta=45^\circ$
Number of teeth	$z_i$	24.00	24.00
Pitch of $\Sigma_i$ (mm)	$p_{ci}$	19.60	19.60
Tooth thickness (mm)	$t$	9.80	9.80
Width of space (mm)	$w$	9.80	9.80
Tooth addendum (mm)	$h_a$	3.4	3.2
Tooth dedendum (mm)	$h_f$	3.4	3.2

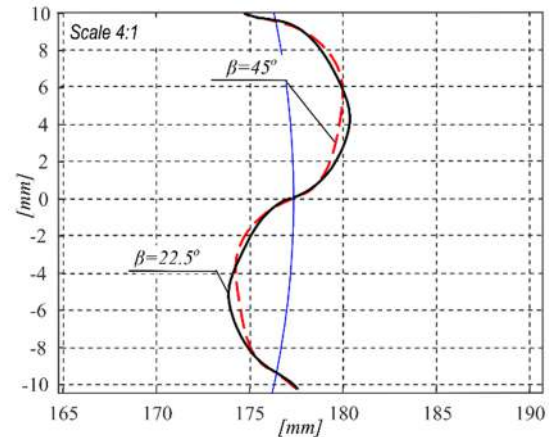


**Figure 13.** Profiles of the NCGs corresponding to the values of  $\beta$

## 7. EXPERIMENTAL MANUFACTURE AND MEASUREMENT

### 7. 1. Experimental Manufacture of the NCGs Pair

From the above theoretical research results, a design plan with: Generating ellipse  $\Sigma_E$  has a semi-major axis  $a = 1.8$  mm, a semi-minor axis  $b = 1.4$  mm; Eccentric gear has parameters: eccentricity  $e = 5$  mm, the centre  $\Sigma_1$  has a radius  $R = 25$  mm, module  $m = 6.2$  mm, Number of teeth  $z_1 = 8$ , Pitch of the centre  $p_c = 19.6$  mm, Tooth addendum  $h_a = 3.5$  mm, Tooth dedendum  $h_f = 3.5$  mm; Non-circular gears have the following parameters: Cycle coefficient  $n = 3$ , Number of teeth  $z_2 = 24$ , Pitch of the centre  $p_c = 19.6$  mm, Tooth addendum  $h_a = 3.5$  mm, Tooth dedendum  $h_f = 3.5$  mm; Center distance of gears pair  $A_{12} = 99$  mm. Figure 14 shown below is a picture of a gears pair after manufacturing with the above design parameters.

The processing machine is the wire electric discharge machine ST3240VM (Taiwan, China) with manufacturing parameters: Wire diameter is 0.18 mm, maximum cutting speed is 200 mm/min; The electrical pulse frequency is 15.625 Hz. The dielectric is Buhm woo- BW EDM -100. The work piece gears are steel 40X.

### 7. 2. Experimental Measurement of Gear Ratio for the NCGs Pair

#### 7. 2. 1. The Hardware Structure of the Experimental System

The experimental system consists of an NCG pair and hardware devices, is shown in Figure 15. The rotation speed of the gear shafts 1 and 2 are determined independently by encoders with a resolution of 600 pulses. The counter of the PLC collects measurement data from the two encoders. Data from

PLC is sent to the industrial computer for processing through software. The speed from the motor shaft is transmitted to the gear shaft 1 by a belt drive with a 1:1 speed ratio to avoid overload. The computer controls motor speed through PLC to Delta inverter.

**7. 2. 2. Experimental Measurement of Gear Ratio**

*Setting parameters:* the sampling interval  $T = 0.1$  s, motor speed 45 rpm, lubricated for NCG pair by shell grease Gadus s2 v2020-2.

After processing the data and set the standard point "0" of the graph, we have a comparison graph between theory and experimental measurement from the meshing process of the NCG pair as described in Figure 16.

From the measurement results, the measured values of the gear ratio for the gear pair are basically in agreement with the theoretical values. Some deviations were due to machining accuracy, assembly accuracy,



**Figure 14.** The prototypes of the NCGs pair after manufacture

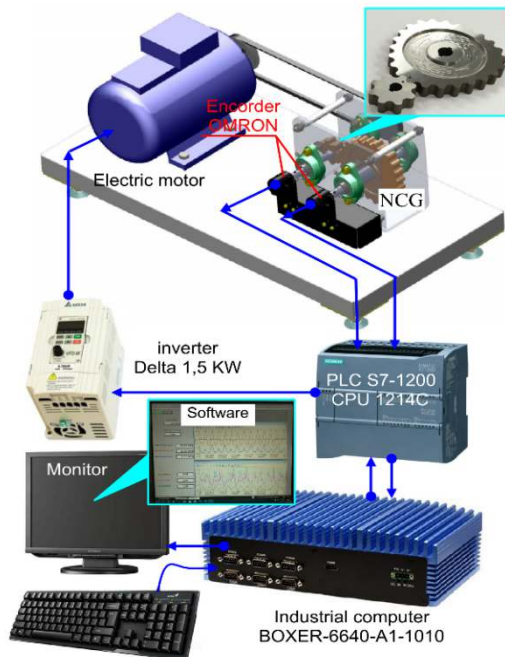


**Figure 15.** Experimental setup

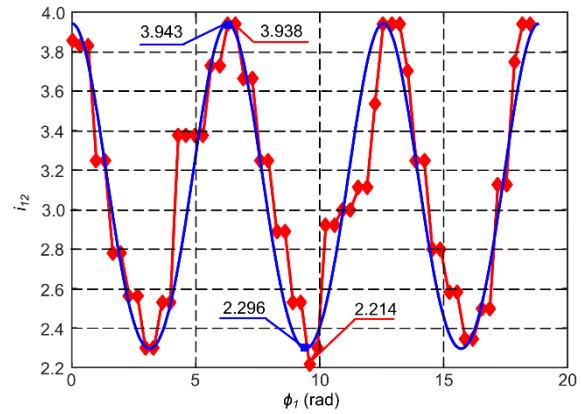


**Figure 16.** Gear ratio measured experimentally from the meshing of NCG pair

measurement accuracy, and other factors. The deviations were all within the range of 0.1 to 3.57% are reasonable. Thereby verified the feasibility and rationality of the new profile proposed by this study in the geometric design of NCG pairs.

The above results show the difference between this study versus previous studies. Therefore, this study provides a novel profile reference in the NCG design for the theory of gearing. Also, with high load capacity, can apply the novel profile proposed by this study to design non-circular gear drives for high torque equipment such as trailing edge flap system of wind turbine rotor blade or helicopter blade [30], bowling machines [31] or steering controller of tracked vehicles [32].

**8. CONCLUSIONS**

This paper proposes a novel profile and provides conditions to avoid the tooth addendum concave when applied to design tooth profiles of the NCGs. Examples to illustrate the design method of the NCGs with novel profiles have been presented. Also, a gear drive was designed, manufactured and experimentally measured to verify the applicability of the novel profiles in the tooth design of the NCGs. From there, conduct evaluation and discussion to come up with some main results as follows:

- i) Proposed the novel curve applied in the design of NCGs with the following advantages: (a) All the teeth at different positions of the gear are of a similar shape. Thus, this is the advantage of the proposed novel profile. It is verified via illustrative examples and experimental measurement on the manufactured NCG pair prototype and (b) Tooth thickness and width of space on the centre of all teeth are equal.
- (ii) Determined the condition of the parameters  $a, b$  of the generating ellipse  $\Sigma_E$  for avoiding concave addendum and dedendum of the gear. Therefore, it is possible to

apply these conditions to write a program module that automates the design of NCGs on a computer.

- (iii) With tooth profile of NCGs is the novel profile proposed by this study. The meshing line is a smooth closed curve. Unlike other profiles such as the involute of a circle or circular-arc commonly used in NCG design research, the meshing line is a straight line.

However, the limitation of this study has not mentioned the contact ratio, power transmission and gear performance. Thus, it will be considered part of our future research goals.

## 9. ACKNOWLEDGEMENTS

This work was supported by Project of Ministry of Education and Training, Vietnam, under grant Number: B2019 - BKA – 09.

## 10. REFERENCES

- Litvin, F.L., Gonzalez-Perez, I., Fuentes, A. and Hayasaka, K., "Design and investigation of gear drives with non-circular gears applied for speed variation and generation of functions", *Computer Methods in Applied Mechanics Engineering*, Vol. 197, No. 45-48, (2008), 3783-3802, doi: 10.1016/j.cma.2008.03.001.
- Guo, L. and Zhang, W., "Kinematic analysis of a rice transplanting mechanism with eccentric planetary gear trains", *Mechanism Machine Theory*, Vol. 36, No. 11-12, (2001), 1175-1188, doi: 10.1016/S0094-114X(01)00052-0.
- Zhao, X., Chu, M., Ma, X., Dai, L., Ye, B. and Chen, J., "Research on design method of non-circular planetary gear train transplanting mechanism based on precise poses and trajectory optimization", *Advances in Mechanical Engineering*, Vol. 10, No. 12, (2018), 1687814018814368, doi: 10.1177/1687814018814368.
- Zhao, X., Ye, J., Chu, M., Dai, L. and Chen, J., "Automatic scallion seedling feeding mechanism with an asymmetrical high-order transmission gear train", *Chinese Journal of Mechanical Engineering*, Vol. 33, No. 1, (2020), 1-14, doi: 10.1186/s10033-020-0432-9.
- Ottaviano, E., Mundo, D., Danieli, G.A. and Ceccarelli, M., "Numerical and experimental analysis of non-circular gears and cam-follower systems as function generators", *Mechanism Machine Theory*, Vol. 43, No. 8, (2008), 996-1008, doi: 10.1016/j.mechmachtheory.2007.07.004.
- Xu, G., Hua, D., Dai, W. and Zhang, X., "Design and performance analysis of a coal bed gas drainage machine based on incomplete non-circular gears", *Energies*, Vol. 10, No. 12, (2017), 1933, doi: 10.3390/en10121933.
- Li, J., Wu, X. and Mao, S., "Numerical computing method of noncircular gear tooth profiles generated by shaper cutters", *The International Journal of Advanced Manufacturing Technology*, Vol. 33, No. 11, (2007), 1098-1105, doi: 10.1007/s00170-006-0560-0.
- Emura, T. and Arakawa, A., "A new steering mechanism using noncircular gears", *JSME International Journal. Ser. 3, Vibration, Control Engineering, Engineering for Industry*, Vol. 35, No. 4, (1992), 604-610, doi: 10.1299/kikaic.57.154.
- Danieli, G. and Mundo, D., "New developments in variable radius gears using constant pressure angle teeth", *Mechanism Machine Theory*, Vol. 40, No. 2, (2005), 203-217, doi: 10.1016/j.mechmachtheory.2004.06.005.
- Bair, B.-W., "Computerized tooth profile generation of elliptical gears manufactured by shaper cutters", *Journal of Materials Processing Technology*, Vol. 122, No. 2-3, (2002), 139-147, doi: 10.1016/S0924-0136(01)01242-0.
- Thai, N.H., Ly, T.T.K. and Trung, N.T., "Research design and experimental manufacturing of compound non-circular gear train with an improved cycloid profile of the ellipse", in International Conference on Engineering Research and Applications, Springer. (2021), 813-825.
- Bair, B., "Computer aided design of non-standard elliptical gear drives", *Proceedings of the Institution of Mechanical Engineers, Part C: Journal of Mechanical Engineering Science*, Vol. 216, No. 4, (2001), 473-482, doi: 10.1243/0954406021525250.
- Bair, B.-W., Sung, M.-H., Wang, J.-S. and Chen, C.-F., "Tooth profile generation and analysis of oval gears with circular-arc teeth", *Mechanism Machine Theory*, Vol. 44, No. 6, (2009), 1306-1317, doi: 10.1016/j.mechmachtheory.2008.07.003.
- Litvin, F.L., Gonzalez-Perez, I., Yukishima, K., Fuentes, A. and Hayasaka, K., "Generation of planar and helical elliptical gears by application of rack-cutter, hob, and shaper", *Computer Methods in Applied Mechanics Engineering*, Vol. 196, No. 41-44, (2007), 4321-4336, doi: 10.1016/j.cma.2007.05.003.
- Mundo, D., "Geometric design of a planetary gear train with non-circular gears", *Mechanism Machine Theory*, Vol. 41, No. 4, (2006), 456-472, doi: 10.1016/j.mechmachtheory.2005.06.003.
- Zheng, F., Hua, L., Han, X., Li, B. and Chen, D., "Synthesis of indexing mechanisms with non-circular gears", *Mechanism Machine Theory*, Vol. 105, (2016), 108-128, doi: 10.1016/j.mechmachtheory.2016.06.019.
- Changbin, D., Yongping, L. and Yongqiao, W., "Dynamic meshing characteristics of elliptic cylinder gear based on tooth contact analysis", *International Journal of Engineering, Transaction A: Basics*, Vol. 33, No. 4, (2020), 676-685, doi: 10.5829/ije.2020.33.04a.19.
- Xu, H., Fu, T., Song, P., Zhou, M., Fu, C.W. and Mitra, N.J., "Computational design and optimization of non-circular gears", in Computer Graphics Forum, Wiley Online Library. Vol. 39, No. 2, (2020), 399-409.
- García Hernández, C., Kyratsis, P., Gella-Marín, R., Efkolidis, N. and Huertas-Talón, J., *Wedm manufacturing method for noncircular gears, using cad/cam software*. 2016.
- Liu, Y., Han, J., Xia, L. and Tian, X., "Hobbing strategy and performance analyses of linkage models for non-circular helical gears based on four-axis linkage", *Strojniški Vestnik-Journal of Mechanical Engineering*, Vol. 58, No. 12, (2012), 701-708, doi: 10.5545/sv-jme.2012.524.
- Liu, Y. and Diao, J., "Six-axis linkage strategy and its models for non-circular helical gears based on diagonal hobbing/strategija in modeli sestosnega diagonalnega odvalnega rezkanja neokroglih zobnikov s posevnim ozobjem", *Strojniški Vestnik-Journal of Mechanical Engineering*, Vol. 61, No. 5, (2015), 330-342, doi: 10.5545/sv-jme.2014.2371.
- Thai, N.H., Thom, P.V. and Trung, N.T., "Influence of centrodes coefficient on the characteristic of gear ratio function of the compound non-circular gear train with improved cycloid tooth profile", in IFToMM Asian conference on Mechanism and Machine Science, Springer. (2021), 204-214.

23. Zheng, F., Hua, L., Han, X., Li, B. and Chen, D., "Linkage model and manufacturing process of shaping non-circular gears", *Mechanism Machine Theory*, Vol. 96, (2016), 192-212, doi: 10.1016/j.mechmachtheory.2015.09.010.
24. Chen, C.-F. and Tsay, C.-B., "Computerized tooth profile generation and analysis of characteristics of elliptical gears with circular-arc teeth", *Journal of Materials Processing Technology*, Vol. 148, No. 2, (2004), 226-234, doi: 10.1016/j.jmatprotec.2003.07.011.
25. Changbin, D., Yongping, L. and Yongqiao, W., "Meshing error of elliptic cylinder gear based on tooth contact analysis", *International Journal of Engineering, Transaction A: Basics*, Vol. 33, No. 7, (2020), 1364-1374, doi: 10.5829/ije.2020.33.07a.24.
26. Khodadadi, M., Khalili, K. and Ashrafi, A., "Studying the effective parameters on teeth height in internal gear flowforming process", *International Journal of Engineering, Transaction C: Aspects*, Vol. 33, No. 12, (2020), 2563-2571, doi: 10.5829/ije.2020.33.12c.18.
27. Bigdeli, M. and Monfared, V., "The prediction of stress and strain behaviors in composite gears using fem", *International Journal of Engineering, Transaction B: Applications*, Vol. 34, No. 2, (2021), 556-563, doi: 10.5829/ije.2021.34.02b.29.
28. Litvin, F.L., Gonzalez-Perez, I. and Fuentes-Aznar, A., "Noncircular gears, Cambridge University Press, (2009).
29. Litvin, F.L. and Fuentes, A., "Gear geometry and applied theory, Cambridge university press, (2004).
30. Ha, K., "Innovative blade trailing edge flap design concept using flexible torsion bar and worm drive", *HighTech Innovation Journal*, Vol. 1, No. 3, (2020), 101-106, doi: 10.28991/HIJ-2020-01-03-01.
31. Furch, J. and Nguyen, Q.H., "Lifetime test of tracked vehicle torsion bars using monte carlo method", *Emerging Science Journal*, Vol. 4, No. 5, (2020), 376-389, doi.
32. Bickramdass, R., Persad, P. and Loutan Jr, K., "Evaluation of an anthropometric fast bowling machine", *HighTech Innovation Journal*, Vol. 2, No. 2, (2021), 108-119, doi: 10.28991/HIJ-2021-02-02-04.

---

### Persian Abstract

---

#### چکیده

این مقاله یک منحنی جدید را ارائه می‌کند که توسط یک نقطه متصل به یک بیضی در حالی که بدون لغزش در امتداد خط مبدأ قفسه برش می‌چرخند، ایجاد می‌شود. یک مدل ریاضی از مشخصات دنده غیر دایره ای بر اساس تئوری چرخ دنده توسعه داده شده است. اثر یک نسبت محوری  $\lambda$  (نسبت طول محورهای اصلی و فرعی بیضی) و موقعیت نقطه KR که در آن منحنی جدید شروع به ایجاد می‌کند بر روی شکل دندان و زیر بریدگی دندان غیر جفت دنده دایره ای نیز در نظر گرفته شده است. یک برنامه عددی توسعه یافته از مدل ریاضی برای محاسبه و طراحی چرخ دنده های غیر دایره ای (NCGs) پیشنهاد شده است. مطالعات موردی برای نشان دادن مراحل طراحی شکل دندان و بررسی مشخصات هندسی NCGs در رابطه با پارامترهای طراحی رک کاتر و غیره ارائه شد. را می توان برای هر مورد خاص به منظور طراحی پروفایل های مناسب NCG ها انتخاب کرد. بر این اساس، آزمایشی برای تعیین نسبت دنده جفت NCGs بر اساس مش بندی بین چرخ دنده ها ساخته شده است.

---



## Distributed Production Assembly Scheduling with Hybrid Flowshop in Assembly Stage

M. Torkashvand, F. Ahmadizar\*, H. Farughi

Department of Industrial Engineering, University of Kurdistan, Sanandaj, Iran

### PAPER INFO

#### Paper history:

Received 07 January 2022

Received in revised form 15 February 2022

Accepted 18 February 2022

#### Keywords:

Production-assembly

Basic Scheduling

Longest Processing Time

Hybrid Genetic Algorithm

Flowshop Scheduling

### ABSTRACT

A new three stage production-assembly problem is considered in this paper. To the best of our knowledge, considering parallel machines in the third stage, identical parallel factories including the three stage production-assembly system and identical parallel factories with parallel machines in the third stage of the production-assembly system, has been specifically investigated in this paper. To minimize the maximum completion time (Makespan) of all jobs in the all factories, jobs assignment to factories and their processing sequence should be done properly. A Mixed Integer Linear Programming (MILP) model is presented to solve small size problem by using cplex solver. According to the problem computational complexity, large size of problem is not possible to solve using the cplex, so to solve it and to control the computational complexity, a new improved genetic algorithm (GA) is proposed by combining GA and Longest Processing Time (LPT) method that is called Hybrid Genetic Algorithm Longest Processing Time (HGALPT). The problem parameters values are determined using one-way analysis of variance (ANOVA). Finally, in order to evaluate the efficiency and effectiveness of the proposed algorithm, and to specify each parameter impact on the objective function, sensitivity analysis is performed on the problem parameters.

doi: 10.5829/ije.2022.35.05.19

## 1. INTRODUCTION

Study the relationship between mental ideas and reality is one of the most important issues that management should pay attention to it. Implementing any plan requires strong managerial insight. Before starting any activity, searching and gathering information about the market situation, examining the past trend of the business under study and predicting the trend of short-term and long-term changes in the future, is a necessary condition for the starting a successful business. The result of this study determines whether there is a demand for a service or a product in the market or not.

To create a plan, all of the effective parameters must be specified. Reviewing and deciding to implement the plan, requires information about the current market situation, estimating the future situation and considering related budget issues. It is clear that, if the establishment

of a factory is justified to produce a product and the feasibility study is acceptable taking into account all economic, social and environmental factors; management makes the final decision to implement it. The production planning and scheduling phase occurs in the operation stage of a project, and it is at this stage that all the actions taken so far are effective with a proper planning.

A distributed production-assembly scheduling with hybrid flowshop in assembly stage is considered in this paper. In the production-assembly system, production and assembly operations are performed in two separate but consecutive stages. This system is known as the production-assembly flow shop scheduling. In this case, each job is produced in two separate stages: in the first stage, different parts of the final job are produced and in the second stage, these parts are assembled together. Often in the production stage, different operations are

\*Corresponding Author Institutional Email: [fahmadizar@uok.ac.ir](mailto:fahmadizar@uok.ac.ir)  
(F. Ahmadizar)

performed independently and in parallel to produce different components, which eventually become the final product in the assembly stage. In the field of production and preventive maintenance to increase the equipment life, production scheduling and preventive maintenance is used [1].

The main motivation for presenting this paper is to solve some of the problems in production and service environments through planning and scheduling of jobs and services. Delivery time of customer requests, using of equipment and tools optimality, increase producer and consumer satisfaction, provide products in accordance with the delivery time, variety and customers requested volume, retain their customers, reduce production costs and ultimately earn more revenue, are the result of production planning and scheduling.

Achieving to the specified goals is not easily in the mentioned systems and requires appropriate treatment against of existing challenges. There are challenges in the production-assembly scheduling field, some of them are:

- Increasing the products variety by increasing the production companies of a product with a specific function.
- Trying to increase market share by customizing customer requests and produce a product according to customer requests.
- Increasing demand diversity instead of mass production.
- Forced changes in production systems of manufacturers due to the product short life cycle.
- Dynamic and uncertain global market that has caused the creation of new technologies in the production and services sectors and the manufacturer needs to update its equipment and tools daily.

In response to the mentioned challenges, by combinations of produced components in the production stage, a high variety of the final product is created in the assembly stage, therefore, production-assembly problems are used in different production systems to increase the product flexibility and variety [2]. The production-assembly scheduling problem applies to Make-To-Order environments in which production operations begin after receiving a customer order. Each order includes a combination of product types that must be delivered to the customer in a single shipment and the manufacturer schedule unscheduled and cumulative orders, periodically [3].

The three of most important reasons for presenting this paper are as follows:

- The first is the three-stage production-assembly problem.
- The second is the same parallel machines in the third stage.
- The third is to consider identical parallel factories.

According to the first reason, the identical parallel machines in the third stage in single factory and three stage production-assembly scheduling problem in multi-factory not reviewed, as it will be mentioned in the literature review section, researchers in most papers have presented two-stage production-assembly problem; while, it is more realistic that the number of stages would be more than two. According to the second reason, in order to prevent customer dissatisfaction of product delivery delay, to reduce completion time of product and accelerate the production of the final product, considering the identical parallel machines in the third stage makes the system more efficient.

According to the third reason, it is assumed that the jobs are created in a single factory in classical production-assembly flow shop problems, while in order to reduce production costs (transportation costs) and production period, many manufacturers changed a single factory production system to a distributed production system (identical parallel factories). The distributed scheduling problem involves two main decisions: assigning jobs to factories and sequencing jobs in each factory.

By considering the three importance reasons and to the best of our knowledge it seems necessary to study, presented problem in this paper; thus, the distributed production-assembly scheduling with hybrid flowshop in assembly stage is considered. In order to adjust the jobs completion times or final products and maximize the machines capacity in all three stages, we have considered minimizing the maximum completion time as a suitable criterion for evaluation.

To the best of our knowledge, two cases of problem contributions are: the mathematical model and the solution method. Two solution methods have been used, an exact method which is the problem model and an approximate method which is the Hybrid Genetic Algorithm Longest Processing Time (HGALPT), in order to solve the problem. To solve the proposed problem, we proposed a new Mixed Integer Linear Programming (MILP) model. This model is position based and it has been used to check the results accuracy in small sizes. This model does not have the ability to solve large size problems.

The scheduling problem for single-machine, stage and factory modes have been extensively investigated in literature. The proposed models for each mode have computational complexity and the problems in this mode have been proven to be Non-deterministic Polynomial-time hard (NP-Hard) Lee et al. [4] have been proven that for the single-factory mode, the production-assembly problem of three machines (two machine in first stage and single machine in second stage) with the makespan objective function is strongly NP-hard, while our proposed problem is more complex than discussed case.

Garey et al. [5] examined the complexity of flowshop and jobshop scheduling problems and showed that for flowshop scheduling problems for more than two machines and the makespan objective function, the problem is NP-complete.

Therefore, in order to manage the computational complexity, a new meta-heuristic algorithm by combining the genetic algorithm (GA) and the longest processing time method is proposed. Here we have also used the GA, with this difference that in order to improve the results. We have combined it with an longest processing time (LPT) heuristic method and presented a modified GA. The experiments results showed the proper performance of the HGALPT algorithm. The GA has been used in many papers to solve various problems. Deng et al. [6] proposed the GA algorithm with variable neighborhood search (VNS) to minimize the total completion time and maximum completion time simultaneously.

At the end of the paper, experiments and numerical calculations have been performed, in order to evaluate the effectiveness and efficiency of the HGALPT. To investigate and evaluate the proposed mathematical model performance, the model results in the optimal solution are checked and after ensuring of the model results accuracy, the results have been compared with meta-heuristic in small size. To evaluate the meta-heuristic algorithm, the results accuracy and the problem solving speed of the meta-heuristic algorithm is investigated compared to the proposed exact model. Due to the fact that the mathematical model is not able to solve the large size of the problem, we tried to solve the problem using the classical GA and improved GA.

After performing numerical experiments, eventually, it was found that the presented algorithm has a high ability to achieve the optimal solution in less time than MILP in small sizes and provides the optimal or near-optimal solution in large sizes. Also, in order to investigate the effect of each parameter on the objective function, sensitivity analysis was performed at the end.

According to the mentioned cases, the innovations of the problem are:

1. Three stage production-assembly problem with the identical parallel machines in the third stage.
2. Identical parallel machines in the third stage of the distributed production-assembly problem.
3. Parallel factories including three stage production-assembly problem.
4. New position based mathematical model for the production-assembly problem.
5. Hybrid metaheuristic algorithm with a combination of GA and sorting algorithm based on the longest processing time.

The main framework of the paper is formed as follows: section 2 describes literature review related to distributed production-assembly scheduling with hybrid

flowshop in assembly stage. The mathematical model of the problem is presented in section 3 completely, which this section aim is to minimize the maximum completion time the all jobs. Section 4 presents the used solution method for the problem and a complete description of the algorithm with details. Section 5 shows the comparisons of solution methods in small and large sizes, the computational results of each algorithm and parameters sensitivity analysis. An overview of the actions taken and suggestions for future works is provided in section 6.

## 2. LITERATURE REVIEW

In this section, the presented papers in the production-assembly systems were reviewed. As mentioned, the problem is n job scheduling (customer order), which are a combination of product types. Various papers have considered different production modes for this problem and have presented the applications of the real world, which are referred to these papers in the following.

Hatami et al. [7] studied the distributed unrelated parallel machines, establishing a set of parallel factories with parallel machines in production stage. The job must be assigned to factories and machines and there is a single machine assembly stage. The objective function is to minimize makespan in the assembly stage.

Framinan and Perez-Gonzalez [8] considered the order scheduling problem to minimize total tardiness so that each machine is capable of producing one (and only one) specific type of product (in fact, machines are dedicated). Xiong et al. [9] assumed the distributed two stage assembly flow shop scheduling problem. The aim is to assign job to multiple factories and schedule job in each factory so that the total completion time is minimized. N jobs are available so that they can be processed by the same factory f, and each factory has the same number of m dedicated machines in the first stage and one assembly machine in the second stage.

The minimization of the makespan in the 3-machine assembly-type flowshop scheduling problem with two machines in first and a machine in second stage was considered [4]. Lee et al. [4] presented a branch and bound algorithm and three heuristic algorithms to solve the problem. Allahverdi and Al-Anzi [10] considered the two-stage assembly scheduling problem to minimize makespan with setup times. In the first stage, there are m production machine and in the second stage, an assembly machine. The three-stage production-assembly flowshop with parallel machines in the last two stages was considered by Zhang et al. [11]. The objective function is to minimize the maximum completion time of all orders.

Xiong et al. [12] considered a flexible assembly-differentiation flow shop scheduling problem to minimize total completion time with three stages of component production, assembly, and separation. All the

components of a job are processed by different machines in the first stage, then in the second stage these components are assembled together by one machine. In the third stage, each job of a specific type is processed by a dedicated machine. They propose a mixed integer programming (MIP) model, two heuristic algorithms and three meta-heuristic algorithms to solve the problem.

Liu et al. [13] proposed the distributed assembly permutation flowshop scheduling problem. The objective function is to minimize the maximum completion time. The problem is formed by two stages, the processing stage and the assembly stage. Sung and Kim [14] considered minimizing the total completion times at the multi-machine production-assembly scheduling problem. The first stage consists of two independent machines and the second stage consists of two identical machines that are located in parallel.

Maboudian and Shafaei [15] proposed the two stage assembly flow shop scheduling problem with sequence-dependent setup times and minimizing the maximum completion time and maximum tardiness objective functions. In this problem,  $n$  products must be produced, each product having  $m$  unequal parts, which in the first stage are processed simultaneously by  $m$  machines, and each part has a dedicated machine. In the second stage, the final product is created by assembling  $m$  parts using a machine. Fattahi et al. [16] presented a hybrid flow shop scheduling problem with setup and assembly operations. The parts are produced in a two-stage flexible flow shop (including one machine in the first stage and  $m$  machine in the second stage) and then convert to the final product in the assembly stage.

Xiong et al. [17] considered a distributed production-assembly flow shop scheduling problem to minimize the total weight of the maximum completion time and the average completion time. The factories are located in parallel and in each factory the jobs are first processed by  $m$  dedicated parallel machine and then sent to the assembly stage, which performs on an assembly machine. Mahdavi et al. [18] also considered hybrid flowshop scheduling with assembly operations. The parts are processed in the flexible flow shop stage and then sent to the assembly stage to produce the final product. The aim is to find a schedule that minimizes the completion time of the last product. They presented an integer programming model and two heuristic algorithms and simulated annealing algorithm to solve the problem.

Pan et al. [19] demonstrated a distributed assembly permutation flowshop scheduling problem. There are some of identical factories that a flowshop for part-processing and assembly line for product-processing there is in each factory is presented. The objective function is makespan that to be minimize. Huang and Gu [20] presented a biogeography-based optimization (NBBO) algorithm to solve the distributed assembly permutation flow-shop scheduling problem with

sequence-dependent set-up times. The objective function of this problem is minimizing the makespan. Each factory consists of  $M$  machines  $\{1, 2, \dots, M\}$ . The second stage is the assembly stage, which has only one assembly machine  $MA$  in the factory.

Lei et al. [21] distributed unrelated parallel machine scheduling with minimizing makespan and total tardiness simultaneously so that  $n$  jobs distributed among  $F$  factories located in different sites is considered. Each factory  $f$  is composed of  $m_f$  unrelated parallel machines. Fathollahi-Fard et al. [22] presented the new concept of production scheduling at sustainable Distributed Permutation Flow Shop Scheduling Problem (DPFSP). The aim is minimize the total energy consumption related to production and maximize, the social factors linked to job opportunities and lost working days. To solve the problem, they proposed novel multi-objective learning-based heuristic is established, as an extension of the Social Engineering Optimizer (SEO).

Wang and Fathollahi-Fard [23] proposed a multi-objective low-carbon hybrid flow shop scheduling problem (MLHFSP) with the consideration of machines with varied energy usage ratios. The objective function is minimizing total carbon emission (TCE) and makespan ( $C_{max}$ ). An improved multi-objective teaching-learning-based optimization (ITLBO) algorithm proposed to solve their problem and to avoid local optimum, sequential neighbourhood search (SNS) method also adopted.

Hosseini [24] presented a distributed assembly permutation flow-shop scheduling problem. The first stage of the considered production system is composed of several non-identical factories with different technology levels and so the factories' performance is different in terms of processing time and cost. The second stage is an assembly stage where in there are some parallel jon stations to assemble the ready parts into the products. The objective function is to minimize the makespan.

Jabbari et al. [25] proposed the scheduling problem for a customized production system consisting of a flow shop production line with a parallel assembly stage that produces various products in two stages. In the first stage of the production line, parts are produced using a flow shop production line, and in the second stage, products are assembled on one of the parallel assembly lines. The objective is to minimize makespan.

In the literature, the most complex studied mood in the single-factory production-assembly system is the three stage production-assembly flow shop presented by Xiong et al. [12], which is related to the case where the dedicated parallel machines in the production stage and a two-stage flexible flow shop (one machine for assembly operations and dedicated parallel machines for post-assembly operations) are established in the assembly stage. Each job in the third stage can only be processed by one dedicated machine. For the multi-factory mode.

Xiong and Xing [17] investigated two stage production-assembly flow shop scheduling problem, that the first stage is dedicated parallel machines and the second stage is single machine.

The summary of the mentioned papers in production-assembly problem is presented in Table 1, that are separated to one factory and multi factory. In order to compare the here presented problem with the papers in the literature, four criteria: objective function,

**TABLE 1.** Summary of the literature review for production-assembly problem

Author	Solution algorithm/ Objective	Machines Position	Factory Number
[8]	Constructive Heuristic and Matheuristic/total tardiness	<b>first stage:</b> dedicated parallel machines	
[25]	GA Particle Swarm Optimization (PSO) hybrid algorithm(GA & PSO)/Makespan	<b>first stage:</b> Flowshop <b>second stage:</b> parallel machine	
[18]	simulated annealing (SA)/Makespan	<b>first stage:</b> Hybrid Flowshop <b>second stage:</b> parallel machines	
[4]	branch and bound and three heuristics/Makespan	<b>first stage:</b> two unrelated parallel machines <b>second stage:</b> single machine	
[10]	Particle Swarm Optimization and Tabu search/Makespan	<b>first stage:</b> unrelated parallel machines <b>second stage:</b> single machine	Single factory
[15]	mathematical model/Makespan and maximum tardiness	<b>first stage:</b> unrelated parallel machines <b>second stage:</b> single machine	
[9]	heuristics and three hybrid meta-heuristics(HVNS, HGA-RVNS, andHDDE-RVNS)/total completion time	<b>first stage:</b> unrelated parallel machines <b>second stage:</b> single machine	
[14]	branch and bound/sum of completion times	<b>first stage:</b> two unrelated parallel machines <b>second stage:</b> two parallel machines	
[11]	hybrid geneticalgorithm(HGA) /Makespan	<b>first stage:</b> unrelated parallel machines <b>second stage:</b> parallel machines	
[16]	GA, simulated annealing (SA), NEH and Johnson’s algorithm /Makespan	<b>first stage:</b> single machine <b>second stage:</b> unrelated parallel machines <b>third stage:</b> single machine	
[12]	SPT-based heuristic, NEH-based heuristic, HGA-VNS, HDDE-VNS and HEDA-VNS/total flow time (TFT).	<b>first stage:</b> unrelated parallel machines <b>second stage:</b> single machine <b>third stage:</b> Differentiation parallel machines	
[7]	heuristic methods (Heuristics PJ1 and PJ2)/Makespan	<b>first stage:</b> Distributed unrelated parallel machines <b>second stage:</b> single machine	
[26]	Variable Neighborhood based Memetic Algorithm/Makespan	<b>first stage:</b> Distributed unrelated parallel machines <b>second stage:</b> single machine	Distributed factories in first stage
[20]	Biogeography-based optimization (BBO)/Makespan	<b>first stage:</b> Distributed Flowshop <b>second stage:</b> single machine	
[24]	Two-level self-adaptive variable neighborhood search (TL SAVNS) algorithm/Makespan	<b>first stage:</b> Distributed Flowshop <b>second stage:</b> parallel machine	
[22]	Social Engineering Optimizer (SEO)/Makespan,total energy, social factors linked to job opportunities and lost working days	<b>first stage:</b> flow-shop	
[21]	artificial bee colony/makespan and total tardiness	<b>first stage:</b> unrelated parallel machines	Distributed factories
[19]	heuristics, variable neighborhood search algorithms, and meta-heuristics/Makespan	<b>first stage:</b> Flowshop <b>second stage:</b> single machines	
[17]	GA-RVNS and VNS/makespan and mean completion time	<b>first stage:</b> unrelated parallel machines <b>second stage:</b> single machine	
current paper	Hybrid Genetic Algorithm Longest Proseccing Time/Makespan	<b>first stage:</b> unrelated parallel machines <b>second stage:</b> single machine <b>third stage:</b> parallel machines	Distributed factories

solution algorithm, position of machines and number of factories have been used which is shown in Table 1.

The papers are divided into three categories: single-factory, first stage distributed factories and distributed factories. In the one-factory mode, papers are divided into three modes: one-stage (one paper), two-stage (eight papers) and three-stage (two papers). In the three-stage mode, the first paper considers a prerequisite stage before the production stage and the second paper considers an additional stage after the assembly stage with different parallel machines.

In the first stage distributed factories, the papers are reviewed in three modes: parallel machines in the first stage and one machine in the second stage (two papers), flowshop in the first stage and one machine in the second stage (one paper) and flowshop in the first stage and parallel machines in the second stage (one paper). For distributed factories mode, papers are reviewed in two mode: one-stage (two papers) and two-stage (two papers).

According to the papers classification in Table 1 as well as real world problems, the following research gaps can be mentioned:

- Only one paper in the single-factory mode addresses the three-stage production-assembly problem where there are no identical parallel machines in stage three.
- In the distributed factories mode, no paper considers three stage while this happens in the real world.
- In the distributed factories mode, no three-stage study with parallel machines in the third stage is presented.
- None of the papers have used a hybrid GA with LPT.

To the best of our knowledge, according to the presented cases and in order to cover the four mentioned gaps, three stages production-assembly flow shop scheduling problem with parallel machines in the assembly stage and parallel factories is presented. Regarding the first gap: the three stages production-assembly problem with parallel machines in the third stage is presented in parallel factories, which includes single factory too. For the second gap: the three stage production-assembly problem in several factories is considered. For the third gap: for parallel machines in the third stage of production-assembly is considered. For the fourth gap: we present a new improved GA in this paper. Regarding the objective function, the objective function has been used in other papers but has not been used with other criteria of this paper.

### 3. MATHEMATICAL MODEL

In this section the mathematical model of the problem is presented. In flowshop scheduling problem a set of  $N$  products are produced on a set of  $m$  machines [27]. As

mentioned earlier, the distributed production-assembly scheduling problem with the hybrid flow shop in the assembly stages can be defined as following: There is the set of  $n$  jobs that are performed in three stages. Each job is processed on  $m + 2$  machines: on  $m_1$  dedicated parallel machine in the first stage, one machine in the second stage and one machine in the third stage. In the third stage, there are the number of  $m_3$  same parallel machines, where each job is processed on one machine without interruption. In the second and third stages there is a hybrid flow shop. hybrid flow shop environment is similar to flow shop, but at least in one stage the number of machines is more than one.

The aim is assignment of jobs to factories and determining the processing sequence of jobs in each factory so that the maximum completion time of jobs is minimized. The assumptions of the problem are:

- Machines are available constantly.
- Each machine processes only one job at a time.
- The first stage machines are dedicated and the processing times for each part on the machine can be different.
- All jobs components are available in zero time and their processing times are specified.
- jobs pre-emption it is not permissible.
- Each job can be processed by one machine at a time.
- The assembly of a job begins when all its components have been completed in the first stage.

The mathematical model of the problem is defined as following.

Parameters and Indices	
$n$	The number of jobs
$F$	The number of factories
$m_1$	The number of machines in the first stage
$m_3$	The number of machines in the third stage
$k$	The machines indice in the first stage $\{1, 2, \dots, m_1\}$
$i, j, r$	The jobs indices $\{1, 2, \dots, n\}$
$l, s$	The machines indice in the third stage $\{1, 2, \dots, m_3\}$
$f, q$	The factories indice $\{1, 2, \dots, F\}$
$p_{j,k}$	the processing time of job $j$ on machine $k$ at the first stage
$tt_j$	the processing time of job $j$ at the second stage
$pt_j$	the processing time of job $j$ at the third stage
$M$	A large positive number

Decision variables	
$X_{i,w,f}$	1 If job $i$ is processed in position $w$ in the production stage and the first assembly stage in factory $f$ , 0 otherwise
$Y_{i,w,l,f}$	1 If job $i$ is processed in position $w$ on machine $l$ in the second assembly stage at factory $f$ , 0 otherwise
$C_{w,k,f}$	Completion time of job in position $w$ on machine $k$ at production stage in factory $f$
$CA_{w,f}$	Completion time of the job in position $w$ in the first assembly stage in factory $f$
$CT_{w,l,f}$	Completion time of the job in position $w$ on the machine $l$ in the second assembly stage in te factory $f$

**Model**

$$\text{Minimise } C_{max} \quad (1)$$

$$\sum_{f=1}^F \sum_{w=1}^n X_{i,w,f} = 1 \quad \forall i = 1, 2, \dots, n \quad (2)$$

$$\sum_{i=1}^n X_{i,w,f} \leq 1 \quad \forall f = 1, \dots, F; \quad w = 1, \dots, n \quad (3)$$

$$\sum_{i=1}^n X_{i,w-1,f} \geq \sum_{j=1}^n X_{j,w,f} \quad \forall f = 1, \dots, F; \quad w = 2, \dots, n \quad (4)$$

$$\sum_{f=1}^F \sum_{w=1}^n \sum_{l=1}^{m_3} Y_{i,w,l,f} = 1 \quad \forall i = 1, 2, \dots, n \quad (5)$$

$$\sum_{i=1}^n Y_{i,w,l,f} \leq 1 \quad \forall f = 1, \dots, F; \quad w = 1, \dots, n; \quad l = 1, 2, \dots, m_3 \quad (6)$$

$$\sum_{i=1}^n Y_{i,w-1,l,f} \geq \sum_{j=1}^n Y_{j,w,l,f} \quad \forall w = 2, \dots, n; \quad l = 1, 2, \dots, m_3; \quad f = 1, \dots, F \quad (7)$$

$$\sum_{r=1}^n \sum_{l=1}^{m_3} Y_{i,r,l,f} = \sum_{w=1}^n X_{i,w,f} \quad \forall i = 1, 2, \dots, n; \quad f = 1, \dots, F \quad (8)$$

$$C_{w,k,f} \geq C_{w-1,k,f} + \sum_{i=1}^n p_{i,k} * X_{i,w,f} \quad \forall w = 2, \dots, n; \quad k = 1, 2, \dots, m_1; \quad f = 1, \dots, F \quad (9)$$

$$C_{1,k,f} \geq \sum_{i=1}^n p_{i,k} * X_{i,1,f} \quad \forall k = 1, 2, \dots, m_1; \quad f = 1, \dots, F \quad (10)$$

$$CA_{1,f} \geq \sum_{i=1}^n t_i * X_{i,1,f} \quad \forall f = 1, \dots, F \quad (11)$$

$$CA_{w,f} \geq CA_{w-1,f} + \sum_{i=1}^n t_i * X_{i,w,f} \quad \forall w = 2, \dots, n; \quad f = 1, \dots, F \quad (12)$$

$$CA_{w,f} \geq C_{w,k,f} + \sum_{i=1}^n t_i * X_{i,w,f} \quad \forall w = 1, \dots, n; \quad k = 1, 2, \dots, m_1; \quad f = 1, 2, \dots, F \quad (13)$$

$$CT_{w,l,f} \geq CT_{w-1,l,f} + \sum_{i=1}^n p t_i * Y_{i,w,l,f} - M * (1 - \sum_{i=1}^n Y_{i,w,l,f}) \quad \forall l = 1, 2, \dots, m_3; \quad w = 2, \dots, n; \quad f = 1, \dots, F \quad (14)$$

$$CT_{w,l,f} \geq CA_{r,f} + p t_i * Y_{i,w,l,f} - M * (2 - Y_{i,w,l,f} - X_{i,r,f}) \quad \forall i = 1, 2, \dots, n; \quad w, r = 1, 2, \dots, n; \quad l = 1, 2, \dots, m_3; \quad (15)$$

$$f = 1, \dots, F$$

$$\forall w = 1, 2, \dots, n;$$

$$C_{max} \geq CT_{w,l,f} \quad l = 1, 2, \dots, m_3; \quad (16)$$

$$f = 1, \dots, F$$

$$\forall i = 1 \dots n;$$

$$w = 1, \dots, n;$$

$$X_{i,w,f} \in \{0,1\}, Y_{i,w,l,f} \in \{0,1\} \quad l = 1, \dots, m_3; \quad (17)$$

$$f = 1, \dots, F$$

$$\forall w = 1, \dots, n;$$

$$C_{w,k,f}, CA_{w,f}, CT_{w,l,f} \geq 0 \quad k = 1, 2, \dots, m_1; \quad (18)$$

$$f = 1, \dots, F$$

Constraint (1) represents the objective function of the problem, ie the maximum completion time.

**Set of the production stage and first assembly stage constraints:** Constraint (2) means that each job must be assigned to one position. Constraint (3) indicates that one job is assigned to each position in each factory extremely. Constraint (4) indicates that a position is filled if the previous position be filled.

**Set of second assembly stage constraints:** Constraint (5) specifies that each job is assigned to only one position of a machine. Constraint (6) specifies that one job is assigned to each position of each machine, extremely. Constraint (7) indicates that a position of a machine is filled if the previous position be filled.

**Common constraints:** Constraint (8) forces that if a job is assigned to a factory for the first stages of production and assembly, it must be assigned to the same factory for the third stage. Constraint (9) specifies that completion time a job in one position at the production stage cannot be less than completion time another job in the previous position. Constraint (10) indicates that if a job is placed in the first position in the production stage, its completion time will not be less than its processing time. Constraint (11) indicates that if a job is placed in the first position in the first assembly stage, its completion time will not be less than its processing time. Constraint (12) specifies that the completion time of any job in a certain position in the first assembly stage can not be less than the its completion time in the previous position of same stage.

Constraint (13) specifies that the completion time of each job in a certain position in the first assembly stage can not be less than completion time of the same job in the production stage. Constraint (14) shows that completion time of each job in a specific position in the second assembly stage can not be less than the completion time of job in the previous position in the same stage. Constraint (15) specifies that the completion time of each job in a specific position in the second

assembly stage can not be less than the completion time of the same job in the first assembly stage. Constraint (16) specifies that the maximum completion time of jobs is greater than the completion time each job. Constraints (17) and (18) show the range of decision variables values.

**4. SOLUTION METHOD**

As previously proven in the introduction section, the distributed production-assembly scheduling problem with hybrid flowshop in assembly stage is NP-Hard and solving large sizes is not possible using the model. Abtahi and Sahraeian [28] presented two-machine flow shop scheduling problem that is NP-Hard, too. Different methods are proposed to solve the distributed scheduling problem.

To solve the distributed permutation flow-shop scheduling problem, Fathollahi-Fard et al. [22] presented a meta-heuristic algorithm called Social Engineering Optimizer (SEO). Fathollahi-Fard et al. [29] gave a full explanation of how this algorithm works. A simple, intelligent and new single-solution algorithm that has just four main steps and three simple parameters to tune. Social Engineering Optimizer starts with two initial solutions divided into attacker and defender. The attacker obtains the rules of Social Engineering techniques to reach its desired goals [29].

Garey et al. [5] investigated the behavior of Scottish red deer in order to develop a new nature-inspired algorithm. The main inspiration of this meta-heuristic algorithm is to originate from an unusual mating behavior of Scottish red deer in a breeding season. the red deer algorithm (RDA) is a population-based meta-heuristics, that starts with an initial population called red deers (RDs). Individuals in this population are separated into two types: hinds and male RDs. Besides, a harem is a group of female RDs. The general steps of this evolutionary algorithm are considered by the competition of male RDs to get the harem with more hinds via roaring and fighting behaviors.

In order to solve the mentioned scheduling problem, a GA is presented in this section. The GA is one of the most well-known evolutionary algorithms. Many papers have used this algorithm to solve the problem. Gholizadeh et al. [30] proposed a novel scenario-based GA for flexible flowshop scheduling. Li et al. [31] developed a GA for the flow shop scheduling problem. Noroozi and Mokhtari [32], Jia et al. [33, 34], Chang et al. [35], Tavakoli and Mahdizadeh [36] have used GA to solve scheduling problems. Maghzi et al. [37] used GA for multi objective scheduling problem. The GA algorithm has many applications in other fields. Abbasi and Rafiee [38] presented a parallel GA on the traveling salesman problem with Multi-core and Many-core Systems.

Eiben and Smith [39] summarized the main framework of the GA in 5 sections:

1. Representation
2. Recombination
3. Mutation
4. Parent selection
5. Survival selection

In this paper, we combine a classical GA with a local search algorithm to present a hybrid algorithm that is called a HGALPT. An heuristic algorithm that is called the Longest Processing Time (LPT) is used in order to improve the results in each iteration of the algorithm. The main steps of the improved GA in this paper are: providing the structure of the solution representation and creating the initial population, improving the solution using local search, parent selection, cross over, mutation, generation selection.

**4. 1. Chromosome Representation and Initial Population**

Each problem solution is called a chromosome in the GA. Each chromosome contains components that are as the problem inputs. An solution consists of two parts. The first part is related to jobs processing order in the first and second stages of each factory, which is shown in Figure 1, and the second part is related to determining the jobs processing sequence on third stage machines of each factory that is done by the decoding process. In Figure 1, the processing sequence of 7 jobs in 3 factories on the first and second stage machines are shown. The number zero is known as the factory separator. The number of zeros in the solution representation is equal to f-1 because the first factory does not need a separator, jobs 1 and 2 are processed in the same sequence on the first and second stage machines of the first factory, jobs 5, 4 and 6 in the second factory, and jobs 3 and 7 in the third factory.

After assigning the jobs to the factories and sequencing them in the first and second stages, according to Figure 2, the jobs are assigned to the third stage machines using decoding process. Each job is assigned to a

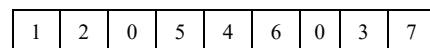


Figure 1. Chromosome representation

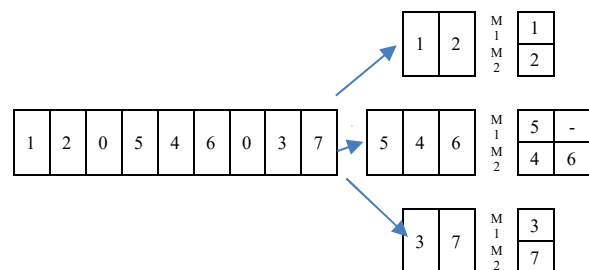


Figure 2. Decoding process

machine that has the least completion time. Figure 2 assumes that there are 2 machines in the third stage. In factory 2, job 5 is assigned to the first machine, job 4 to the second machine, and job 6 after job 4 to the second machine, which is supposed to have the shortest completion time. In order to produce the initial population, as a population size, jobs sequence with f-1 zeros is generated randomly.

**4. 2. Local Search Based on the Longest Processing Time**

In order to improve the solutions, we have used of a heuristic method based on longest processing time. In this method, a local search is performed on some of the best solutions with  $P_{lpt}$  rate of the entire population. In the LPT method, jobs are arranged in descending order of processing times. For our problem, there are three stages of operations, different modes are considered for processing time. Each job is processed simultaneously on  $m_1$  machine in the first stage, so in order to use the LPT algorithm, we considered the maximum processing time of each job as its processing time in the first stage. In the second and third stages, there is only one processing time for each job in each step. There are 6 modes for selection and arranging processing times as following:

- 1)  $JS_1 = \max_K \{p_{j,k}\}$
- 2)  $JS_2 = tt_j$
- 3)  $JS_3 = pt_j$
- 4)  $JS_4 = \max_K \{p_{j,k}\} + tt_j$
- 5)  $JS_5 = tt_j + pt_j$
- 6)  $JS_6 = \max_K \{p_{j,k}\} + tt_j + pt_j$

After determining the solutions at the end of each iteration of the algorithm, to perform the LPT, the assigned jobs to each factory are processed in descending of mode 1 ( $JS_1$ ). This operations is performed in 6 modes  $JS_1$  to  $JS_6$  on a solution separately and the best solution is selected as an alternative to the current solution. The LPT heuristic algorithm accelerate reaching of better solutions in the main algorithm.

**4. 3. SELECTION**

In the GA, the selection operator is the parents selection to perform the crossover, mutation, and create next generation. Some of solutions are transferred to the next generation with  $P_e$  rate, unchanged. In order to select the parents, the rank-based roulette wheel selection has been used [40]. In this mechanism, for each population solution, a rank based on its fitness value (the objective function value of each solution) is assigned, firstly. If PN indicates population size, the best solution rank is PN and the worst solution is 1. In order to better selection, the new rank of the parents is determined based on the linear relation (19):

$$NewRank(or) = 2 - SP + (2 * (SP - 1) * \frac{(or-1)}{(PN-1)}) \quad (19)$$

In the above statement, “or” is old rank, “NewRank (or)” is the new rank and SP is the selection pressure, the SP value is in the range [1.0, 2.0]. The parent selection probability is determined by rank or according to Equation (20).

$$Pr(or) = \frac{NewRank(or)}{\sum_{i=1}^{PN} NewRank(i)} \quad (20)$$

“Pr (or)” is the probability of selecting a individual with the rank of “or”.

**4. 4. Crossover**

There are different types of crossovers to use in the algorithm according to the problem type. Various methods are presented for implementation of crossover in sequence-based representation. Xiong et al. [9] have used different crossover types. Deng et al. [6] used of sequential crossover to combine two parents and create new individual in the production-assembly problem, also, we have used this crossover type with  $P_c$  rate. In this method, two points are randomly selected on the parents. The contents between the two points in the first parent are passed directly to the first child. In order to fill blanks in the first child, start from the second point of the second parent and select the job that do not exist in the first child, respectively, and completing start from the second point of the first child. The same steps are done to produce second child. An example of an crossover is shown in Figure 3.

**4. 5. Mutation**

After generating offspring by performing the crossover operator, a mutation operation with the  $P_m$  possibility is performed on each child. There are different types of mutation operator that one of them is swap. In this mutation type, two genes are selected and mutated. Figure 4 shows an example of this mutation type.

**4. 6. Generation Selection**

The previous population and the new population are combined and the

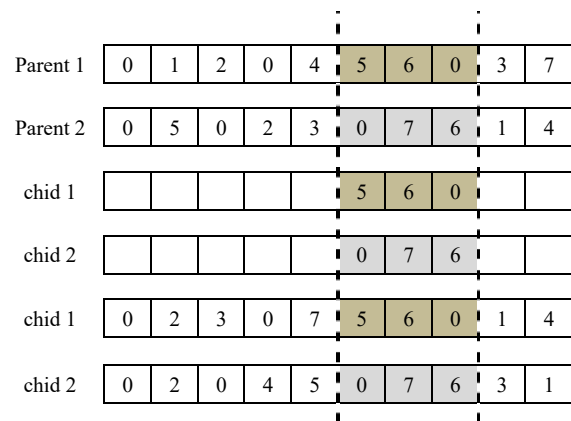


Figure 3. Crossover operator

Parent	0	2	0	4	5	0	7	6	3	1
Child	0	2	0	3	5	0	7	6	4	1

Figure 4. Mutation operator

next generation is selected among of this population individuals. To do this, the number of individuals who have the best fitness will be passed on to the next generation unchanged and with  $P_{ef}$  rate. For the rest of the next generation population, the roulette wheel mechanism is used. Here, in order to calculate the individual selection probability, the fitness function of each solution is used [40]. Equation (21) shows how to calculate each individual selection probability.

$$PrS(i) = \frac{Fitness(i)}{\sum_{j=1}^{PN} Fitness(j)} \quad \forall i = 1,2, \dots, PN \quad (21)$$

where  $PrS(i)$  and  $Fitness(i)$  indicate the selection probability and fitness function value of individual  $i$ , respectively.

5. COMPARISONS AND CALCULATION RESULTS

The calculations results are presented in different cases, in this section. Given that there are no similar papers to our problem and the presented papers are different in the literature, we used of provided values by Xiong et al. [12, 17] to determine the problem parameter ranges, which are simpler but closer to the our problem. Table 2 summarizes the problem parameters values. The parameters  $p$ ,  $tt$  and  $pt$  show the processing times of jobs in all stages and have a discrete uniform distribution in the interval [1.0, 100.0].

In order to evaluate the efficiency of the proposed algorithm, the results of the algorithm in small size have been compared with results of MILP model and the results have been extended to large size. The proposed GA is coded in Java IntelliJ IDEA 2020.1.2 software and IBM ILOG CPLEX solver Concert technology and

TABLE 2. Parameter values to create problem instance

Parameter	Parameter values ranges	
	Small size	Large size
$f$	{2,3,4}	{4,6,8}
$n$	{5,6,7,8,10}	{20,30,40,60,80,100}
$m_1$	{2,3,4}	{2,4,6,8}
$m_3$	{2,3}	{3,4,5}
$p$	U(1,100)	U(1,100)
$tt$	U(1,100)	U(1,100)
$pt$	U(1,100)	U(1,100)

problem model in GAMS 28.2.0 software and CPLEX solver. All calculations are performed on the computer with Intel (R) Core (Tm) i5-323M CPU @ 2.60 GHz 6.0 GB specifications.

Potts et al. [26] showed that two-stage assembly scheduling problem is NP-Hard and Single machine scheduling problem with considering the sequence dependent set-up times are classified in NP-Hard problems [41-43], then given that the our problem is three-stage and multi-factory mode, so, is more complex than [26]. Therefore, according to our problem complexity, it proves to be NP-Hard.

Optimal solution for small sizes can be achieved using the Mixed Integer Linear Programming (MILP) model, but for large sizes, optimal or near-optimal solutions can be achieved by a HGALPT. Due to the mentioned cases and high complexity of the problem, solving the problem using the Cplex has a memory error for large sizes, but this issue does not exist in the proposed GA. For small sizes the time limit is 3600 seconds in Cplex and  $0.5 \cdot n \cdot f$  seconds limit in HGALPT. For large sizes the 1200 seconds limit is considered as algorithm stop criterion.

In order to evaluate the performance of the algorithm, three parts are presented: the first part is related to parameters setting for small and large sizes of the problem, the second part is related to comparing the results of mathematical model and improved GA and shows the superiority of the proposed algorithm. After proving the superiority of the improved GA over the mathematical model, The third part compares the results of the GA and the HGALPT that the HGALPT results are better.

5. 1. Parameter Setting

In order to determine the parameters of the problem, more accurately, Analysis Of Variance (ANOVA) of Taguchi method for small and large sizes has been used. Seven parameters affect on the algorithm results that three levels are defined for each parameter. Problem parameters include initial population (PS), next generation elite rate ( $P_e$ ), local search rate ( $P_{lpt}$ ), crossover rate ( $P_c$ ), mutation rate ( $P_m$ ), next generation transmission rate ( $P_{ef}$ ), selection pressure (SP). Their levels values are shown in Table 3. The value of crossover rate parameter is considered equal to the complement of the mutation rate parameter, so it is not in the parameter setting calculations.

We have used Minitab software, in order to determine each parameter level. an instance of small size with values of  $n = 8$ ,  $f = 3$ ,  $m_1 = 4$ ,  $m_3 = 2$  and an instance of large size with values of  $n = 40$ ,  $f = 4$ ,  $m_1 = 4$ ,  $m_3 = 3$  is examined. For small size, using orthogonal matrix  $L_{27} = (3^6)$ , 27 different combinations of parameter levels are specified in Table 4. Relative Error (RE) and Average Relative Error (ARE) have been used to compare the results of the algorithms, that are presented

**TABLE 3.** Parameter levels

Parameter	Level	Value	Parameter	Level	Value
PS	1	30	P <sub>m</sub>	1	0.07
	2	50		2	0.09
	3	80		3	0.11
P <sub>e</sub>	1	0.02	P <sub>ef</sub>	1	0.01
	2	0.04		2	0.03
	3	0.06		3	0.06
P <sub>lpt</sub>	1	0.02	SP	1	1.3
	2	0.05		2	1.5
	3	0.07			
P <sub>c</sub>	1	0.93	3	1.7	
	2	0.91			
	3	0.89			

**TABLE 4.** ARE value according to the orthogonal array L<sub>27</sub> = (3<sup>6</sup>) for small size

Experiment number	Parameters level						ARE
	PS	P <sub>e</sub>	P <sub>lpt</sub>	P <sub>m</sub>	P <sub>ef</sub>	SP	
1	1	1	1	1	1	1	0.0159
2	1	1	1	1	2	2	0.0019
3	1	1	1	1	3	3	0.0070
4	1	2	2	2	1	1	0.0165
5	1	2	2	2	2	2	0.0037
6	1	2	2	2	3	3	0.0014
7	1	3	3	3	1	1	0.0122
8	1	3	3	3	2	2	0.0072
9	1	3	3	3	3	3	0.0000
10	2	1	2	3	1	2	0.0113
11	2	1	2	3	2	3	0.0019
12	2	1	2	3	3	1	0.0043
13	2	2	3	1	1	2	0.0000
14	2	2	3	1	2	3	0.0000
15	2	2	3	1	3	1	0.0041
16	2	3	1	2	1	2	0.0027
17	2	3	1	2	2	3	0.0000
18	2	3	1	2	3	1	0.0014
19	3	1	3	2	1	3	0.0000
20	3	1	3	2	2	1	0.0029
21	3	1	3	2	3	2	0.0019
22	3	2	1	3	1	3	0.0048
23	3	2	1	3	2	1	0.0027
24	3	2	1	3	3	2	0.0023
25	3	3	2	1	1	3	0.0048
26	3	3	2	1	2	1	0.0000
27	3	3	2	1	3	2	0.0033

by Xiong and Xing [17]. The value of RE is calculated using Equation (22).

$$RE = \frac{(Z - BEST)}{BEST} * 100 \tag{22}$$

where BEST is the best value obtained from each of the algorithms and Z is the value obtained from the execution of an instance of the problem. Each parameters combination is executed 20 times independently, the obtained ARE is given in Table 4. Table 5 summarizes the mean and standard deviation (StDev) results based on the 95% confidence level for different parameters levels in small size.

According to Table 5, PS for small size, the mean of ARE value decreases with increasing population size. The the mean of ARE difference between levels 2 and 3 is not significant, but due to the fact that the scatter in level 3 is less, this level with a value of PS = 80 is selected as the best level. For the P<sub>ef</sub>, the scattering around the mean is significant also according to Table 5 with increasing the elite rate value, the response value improves to level two but at level three, the results are not better than at level two and intensification increases, therefore, P<sub>ef</sub> = 0.03 is considered.

According to the results in Table 5 for the SP, the results of the algorithm are improved by changing and increasing the parameter value. In fact, increasing the selection pressure is appropriate for small sizes and

**TABLE 5.** Individual 95% CIs For Mean Based on Pooled StDev for small size

Parameter	Level	N	Mean	StDev
PS	1	9	0.0073	0.0063
	2	9	0.0029	0.0036
	3	9	0.0025	0.0017
P <sub>e</sub>	1	9	0.0052	0.0053
	2	9	0.0039	0.0050
	3	9	0.0035	0.0041
P <sub>lpt</sub>	1	9	0.0043	0.0048
	2	9	0.0052	0.0053
	3	9	0.0031	0.0042
P <sub>m</sub>	1	9	0.0041	0.0051
	2	9	0.0034	0.0051
	3	9	0.0052	0.0042
P <sub>ef</sub>	1	9	0.0076	0.0065
	2	9	0.0023	0.0023
	3	9	0.0029	0.0021
SP	1	9	0.0067	0.0064
	2	9	0.0038	0.0034
	3	9	0.0022	0.0027

improves the algorithm performance. The appropriate value of this parameter is  $SP = 1.7$ . For  $P_e$ ,  $P_{pt}$  and  $P_m$ , the mean of ARE results at Table 5 show no significant effect on the algorithm results and the mean of ARE value by changing the parameter level does not change significantly. According to the mean and standard deviation in Table 5, For small sizes, the parameters values in response to the best values of the levels are:  $PS=80$ ,  $P_e=0.06$ ,  $P_{pt}=0.07$ ,  $P_m=0.09$ ,  $P_c=0.91$ ,  $P_{ef}= 0.03$  and  $SP=1.7$ .

For large size, An instance of the general problem with the values  $n = 40$ ,  $f = 4$ ,  $m_1 = 4$ ,  $m_3 = 3$  is used to set the parameters. Like small size, the different combinations of parameters is adjusted according to Table 6 in 27 rows by using the orthogonal matrix of the Taguchi method. Each row is run 15 times and the obtained results ARE is calculated. According to the mean of ARE in Table 7, different levels for  $SP$ ,  $P_e$ ,  $P_{ef}$  and  $PS$  parameters have a significant effect on the algorithm results. With increasing the  $PS$  parameter value, the mean of ARE values have improved. Due to the increase in the size of the problem, the increase in population has led to the investigate more solution areas and the results are improved, so the value of the parameter  $PS$  is considered equal to  $PS = 80$ .

According to Table 7, for the  $P_e$  parameter and transferring some of the best solutions without crossover and mutation to the next generation, the best value of this parameter is equal to  $P_e = 0.02$ . For the  $P_{ef}$  parameter, which indicates the elite rate for unchanged transmission to the next generation, as shown in Table 7, the mean of ARE of the obtained results has improved with increasing rate value. This rate is related to the intensification in the problem, directly, which means that by increasing this parameter value, the amount of algorithm intensification also increases. The appropriate value of this parameter according to the Table 7 is equal to  $P_{ef} = 0.06$ .

The next parameter that its different values affects to the problem results is  $SP$ , which its low or high value indicates an increase in diversification or intensification. In this parameter, by increasing of the parameter value, the mean of ARE of the obtained results increases according to Table 7 and the results become worse. Therefore, its appropriate value is equal to  $SP = 1.3$ . Finally, according to the mean and standard deviation ARE Table 7, The parameters values based on the best levels value are:  $PS=80$ ,  $P_e=0.02$ ,  $P_{pt}=0.05$ ,  $P_m=0.11$ ,  $P_c=0.89$ ,  $P_{ef}=0.06$  and  $SP=1.3$ .

**5. 2. CPLEX and HGALPT Results Comparison for Small Size**

In order to evaluate the algorithm efficiency, its results are compared with the Cplex exact solver in 20 different sizes. The results of the calculations are shown in Table 8. where the solution quality is equal to the difference percentage from the best obtained solution. Cplex calculations are performed with 3600

**TABLE 6.** Average response value according to the orthogonal array  $L_{27} = (3^6)$  for large size

Experiment number	Parameters level						ARE
	PS	$P_e$	$P_{pt}$	$P_m$	$P_{ef}$	SP	
1	1	1	1	1	1	1	0.0631
2	1	1	1	1	2	2	0.0463
3	1	1	1	1	3	3	0.0395
4	1	2	2	2	1	1	0.0561
5	1	2	2	2	2	2	0.0672
6	1	2	2	2	3	3	0.0484
7	1	3	3	3	1	1	0.0753
8	1	3	3	3	2	2	0.0391
9	1	3	3	3	3	3	0.0622
10	2	1	2	3	1	2	0.0405
11	2	1	2	3	2	3	0.0341
12	2	1	2	3	3	1	0.0288
13	2	2	3	1	1	2	0.0519
14	2	2	3	1	2	3	0.0656
15	2	2	3	1	3	1	0.0403
16	2	3	1	2	1	2	0.0631
17	2	3	1	2	2	3	0.0563
18	2	3	1	2	3	1	0.0362
19	3	1	3	2	1	3	0.0647
20	3	1	3	2	2	1	0.0299
21	3	1	3	2	3	2	0.0407
22	3	2	1	3	1	3	0.0350
23	3	2	1	3	2	1	0.0294
24	3	2	1	3	3	2	0.0524
25	3	3	2	1	1	3	0.0451
26	3	3	2	1	2	1	0.0532
27	3	3	2	1	3	2	0.0344

seconds time limit. If the value in the column “Time” (column 7) is 3600, the value in the column “Quality” is the deviation percentage of best feasible solution that obtain from Cplex, Otherwise, the column “Quality” value is the deviation percentage of optimal solution.

For HGALPT algorithm, each instance is run 20 times. The column “Min” shows the minimum relative error, the column “ARE” shows the average relative error, the column “Max” shows the maximum relative error for the each instance, the column “STD” shows the standard deviation for the relative errors and the column “Time” shows the time limit of  $0.5 * n * f$  seconds.

From 20 instances, in 14 instance optimal solution are calculated by CPLEX, 3 instances are out of memory

**TABLE 7.** Individual 95% CIs For Mean Based on Pooled StDev for large size

Parameter	Level	N	Mean	StDev
PS	1	9	0.0553	0.0127
	2	9	0.0463	0.0133
	3	9	0.0428	0.0121
Pe	1	9	0.0431	0.0130
	2	9	0.0496	0.0129
	3	9	0.0517	0.0140
Plpt	1	9	0.0468	0.0126
	2	9	0.0453	0.0123
	3	9	0.0522	0.0155
Pm	1	9	0.0488	0.0106
	2	9	0.0514	0.0134
	3	9	0.0441	0.0160
Pef	1	9	0.0550	0.0130
	2	9	0.0468	0.0146
	3	9	0.0426	0.0102

SP	1	9	0.0458	0.0168
	2	9	0.0484	0.0112
	3	9	0.0501	0.0126

error (as indicated by OM) and 3 instances provided the best solution according to time limit of 3600 seconds, according to Table 8. from the 14 optimal solution instance obtained by CPLEX, 12 instance of the HGALPT algorithm have reached the optimal solution in a much shorter time which indicates the efficiency of the algorithm. Also, since the optimal solution has been reached, the effectiveness of the algorithm is also guaranteed.

The average of columns values for Table 8 are calculated for the total instances at the Table bottom. For comparing the solution time of the two algorithms, the average of CPLEX solution time is 1419.3005 seconds while the average of HGALPT solution time is much less and is equal to 11.225. As the instance size increases, the solution time increases and the CPLEX needs more time to reach the optimal solution or CPLEX can not provide

**TABLE 8.** Comparison of CPLEX results and HGALPT algorithm for small sizes

Instance	n	f	m <sub>1</sub>	m <sub>3</sub>	CPLEX		HGALPT				
					Quality	Time (s)	Min	ARE	Max	STD	Time (s)
1	5	2	2	3	0.000	4.87	0.000	0.000	0.000	0.000	5
2	5	3	4	2	0.000	5.84	0.000	0.000	0.000	0.000	7.5
3	6	2	2	3	0.000	31	0.000	0.000	0.000	0.000	6
4	6	3	3	2	0.000	18	0.000	0.000	0.000	0.000	9
5	6	4	4	2	0.000	44	0.000	0.000	0.000	0.000	12
6	7	2	2	3	0.000	381	0.000	0.000	0.000	0.000	7
7	7	2	3	3	0.000	398	0.000	0.001	0.011	0.002	7
8	7	3	3	2	0.000	235	0.000	0.000	0.000	0.000	10.5
9	7	3	4	2	0.000	149	0.000	0.000	0.000	0.000	10.5
10	7	4	4	2	0.000	509	0.000	0.000	0.000	0.000	14
11	8	2	2	3	0.000	2379	0.000	0.007	0.025	0.008	8
12	8	2	4	3	0.000	1340	0.000	0.010	0.043	0.012	8
13	8	3	3	2	0.000	1667	0.000	0.000	0.000	0.000	12
14	8	3	4	2	0.000	3487	0.000	0.003	0.029	0.009	12
15	8	4	2	2	0.000	3600	0.000	0.000	0.000	0.000	16
16	10	2	3	3	0.012 (OM)	3107	0.000	0.012	0.031	0.011	10
17	10	3	2	3	0.000	3600	0.000	0.010	0.027	0.008	15
18	10	3	4	2	0.000	3600	0.000	0.014	0.057	0.015	15
19	10	4	2	2	0.016 (OM)	2411	0.000	0.001	0.016	0.004	20
20	10	4	3	2	0.037 (OM)	1593	0.000	0.017	0.066	0.020	20
Average					0.0033	1427.9855	0.0000	0.0037	0.0152	0.0044	11.2250

the optimal solution and faces a time limit or out of memory error while the HGALPT algorithm is reached to solution in much less time. In view of the above, the HGALPT algorithm is more efficient than CPLEX.

### 5. 3. GA and HGALPT Results Comparison for Large Size

Given the efficiency and effectiveness for small size problems, to prove the effectiveness of the HGALPT algorithm, the results for large size are calculated and the GA and HGALPT algorithms are

compared. To prove the algorithm effectiveness, comparison of GA algorithm without LPT and using it has been done. 30 instances of problem parameters combining have been created to compare algorithms. Each algorithm is executed 5 times with a time limit of 1200 seconds and the results are recorded. The minimum relative error (Min), average relative error (ARE), maximum relative error (Max) and standard deviation for the relative error (STD) for each instance are listed in Table 9.

TABLE 9. Comparison of GA and HGALPT algorithms for large sizes

Instance	n	f	$m_1$	$m_3$	GA				HGALPT			
					Min	ARE	Max	STD	Min	ARE	Max	STD
1	20	4	2	3	0.067	0.110	0.147	0.035	0	0.031	0.086	0.034
2	20	4	4	4	0.015	0.064	0.121	0.038	0	0.033	0.051	0.021
3	20	4	6	5	0.011	0.060	0.091	0.032	0	0.024	0.057	0.023
4	20	6	2	4	0.000	0.041	0.068	0.029	0.019	0.035	0.080	0.025
5	20	6	4	3	0.076	0.104	0.132	0.027	0	0.017	0.052	0.020
6	20	6	8	3	0.054	0.088	0.120	0.030	0	0.033	0.094	0.037
7	20	8	8	3	0.026	0.125	0.168	0.057	0	0.011	0.033	0.013
8	30	4	2	3	0.033	0.053	0.077	0.016	0	0.007	0.018	0.007
9	30	4	4	4	0.04	0.079	0.130	0.044	0	0.015	0.036	0.017
10	30	4	6	5	0.043	0.100	0.161	0.043	0	0.020	0.039	0.019
11	30	6	8	3	0.032	0.089	0.174	0.059	0	0.025	0.051	0.021
12	30	8	6	3	0.056	0.111	0.147	0.037	0	0.022	0.038	0.015
13	40	4	2	3	0.052	0.086	0.115	0.024	0	0.015	0.026	0.011
14	40	4	4	4	0.099	0.110	0.120	0.010	0	0.013	0.035	0.014
15	40	4	6	5	0.076	0.106	0.129	0.020	0	0.013	0.024	0.009
16	40	6	8	3	0.115	0.185	0.241	0.046	0	0.017	0.036	0.014
17	40	8	6	3	0.074	0.113	0.143	0.027	0	0.008	0.021	0.009
18	60	4	2	3	0.111	0.141	0.185	0.027	0	0.020	0.042	0.019
19	60	4	4	4	0.087	0.122	0.142	0.022	0	0.010	0.025	0.009
20	60	6	2	4	0.128	0.147	0.183	0.024	0	0.013	0.032	0.012
21	60	6	8	3	0.130	0.157	0.175	0.019	0	0.037	0.110	0.044
22	60	8	4	3	0.076	0.144	0.187	0.046	0	0.017	0.040	0.016
23	80	4	2	3	0.027	0.074	0.104	0.028	0	0.012	0.028	0.010
24	80	4	6	5	0.079	0.088	0.109	0.012	0	0.012	0.030	0.012
25	80	6	8	3	0.093	0.154	0.212	0.044	0	0.010	0.019	0.008
26	80	6	4	5	0.111	0.133	0.167	0.022	0	0.011	0.017	0.007
27	80	8	6	3	0.137	0.187	0.226	0.040	0	0.013	0.024	0.009
28	100	4	2	3	0.066	0.094	0.134	0.027	0	0.011	0.017	0.007
29	100	4	4	4	0.048	0.079	0.114	0.031	0	0.013	0.035	0.015
30	100	6	2	5	0.073	0.164	0.308	0.102	0	0.028	0.052	0.021
<b>Average</b>					0.068	0.110	0.151	0.034	0.001	0.018	0.042	0.017

According to Table 9, from 30 instances, 29 instances of the minimum relative error, 30 instances of the ARE value, 29 instances of the maximum relative error and 27 instances of the standard deviation relative error, HGALPT values are less than GA, therefore, the effectiveness of HGALPT algorithm is determined against GA. The overall average is calculated for all columns in Table 9. The average of minimum relative error, ARE, maximum relative error and standard deviation for all instances for GA and HGALPT is {0.068, 0.110, 0.151, 0.034} and {0.001, 0.018, 0.042, 0.017}, respectively.

Therefore, for all four modes of minimum, average, maximum and standard deviation, the HGALPT algorithm has lower values than GA, indicating that the scatter of solutions around the best solution in HGALPT is less, and given that in most instances the results of HGALPT are better than those of GA, as a result, the HGALPT algorithm is more effectiveness.

**5. 3. Sensitivity Analyses** Sensitivity analysis is performed in two ways:

- 1- Investigating the effect of different values of the parameters on the makespan objective function.
- 2- Performance analysis of HGALPT and GA for different values of problem parameters.

The effective parameters in the makespan objective function are:  $n$ ,  $f$ ,  $m_1$  and  $m_3$ , which, by keeping constant the other parameters, their effect on the objective function value can be examined. For the first sensitivity analysis, to examine the effect of each parameter, four different scenarios are considered.  $S(n)$ ,  $S(f)$ ,  $S(m_1)$  and  $S(m_3)$  are the scenarios related to the parameters  $n$ ,  $f$ ,  $m_1$  and  $m_3$ , respectively, which are summarized in Table 10. In this table, for each scenario, assuming the other parameters are constant, the effect of different values of a parameter on the makespan objective function is specified.

As it can be seen in Figure 5, for the parameter of  $n$ , for different scenarios, by increasing the value of  $n$ , the value of the makespan increases in the second scenario, but in the third and fourth scenarios remains constant. The objective function is fixed for the values 6, 7 and 8 and can take any of  $n$  different values. In fact, with fixed equipment and costs, more jobs can be processed. For parameter  $f$ , as shown in Figure 6, by increasing the value of this parameter, the value of the objective function is decreases in 2 and 3 scenarios then fixed for the fourth scenarios (makespan value 242). This means that in order to reduce costs, the number of factories can be reduced, assuming that other parameters are constant.

For parameter  $m_1$ , As be seen in Figure 7, the first and second scenarios have the same objective function values, and decision-makers can choose any of these scenarios as needed. For the third scenario, the value of

**TABLE 10.** Sensitivity Analyses on the parameters

Parameter scenario	Parameters				Objective
	$n$	$f$	$m_1$	$m_3$	$C_{max}$
$S(n)$	5	2	2	2	260
	6	2	2	2	278
	7	2	2	2	278
	8	2	2	2	278
$S(f)$	8	1	2	2	455
	8	2	2	2	278
	8	3	2	2	242
	8	4	2	2	242
$S(m_1)$	8	2	1	2	278
	8	2	2	2	278
	8	2	3	2	281
	8	2	4	2	281
$S(m_3)$	8	2	2	1	307
	8	2	2	2	278
	8	2	2	3	278
	8	2	2	4	278

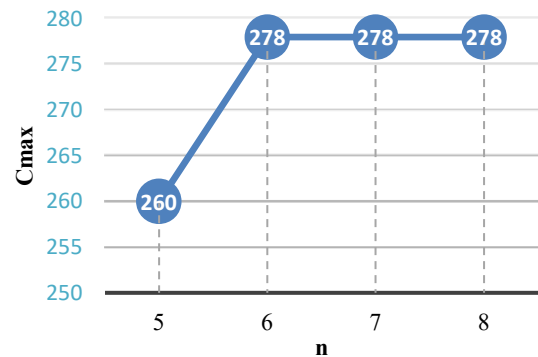


**Figure 5.** Cmax overlap vs. n

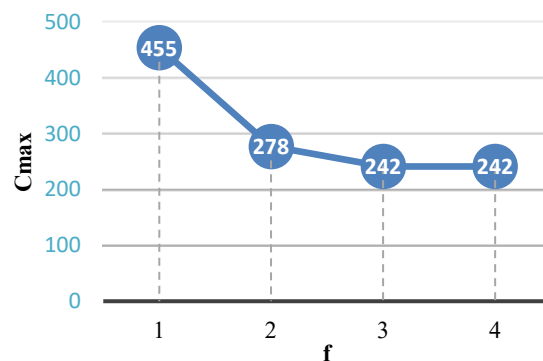


**Figure 6.** Cmax overlap vs. f

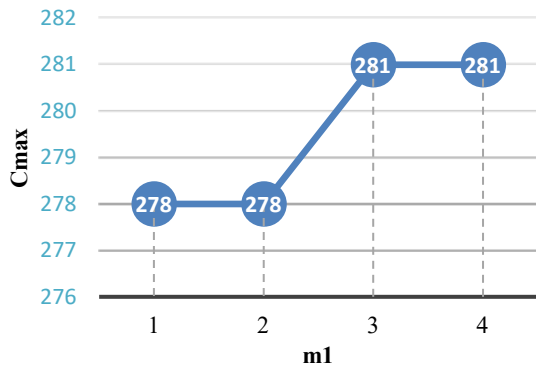


Figure 7. Cmax overlap vs. m1

the objective function changes and its value is equal to the fourth scenario, so either of these two scenarios can be used. The last parameter is m3, According to Figure 8, in which the value of the objective function remains constant from the second scenario onwards, ie increasing the number of machines in the third stage has no effect on the value of the objective function, and fewer machines are needed for the constant values of other parameters.

For the second sensitivity analysis, in order to evaluate the HGALPT algorithm and compare the degree of deviation of the solutions of the two algorithms GA and HGALPT, some possible sensitivity analyzes have been performed in this section. For this purpose, for each parameter, the percentage of relative deviation is calculated for different values of that parameter. Figure 9 shows the performance of the two algorithms based on the ARE for different values of jobs. In all sizes, the ARE value in HGALPT algorithm is less than GA and the superiority of HGALPT algorithm is obvious. Figure 10 shows a performance comparison of the two algorithms based on the ARE for factories different values. As the number of factories increases, the ARE in the GA increases.

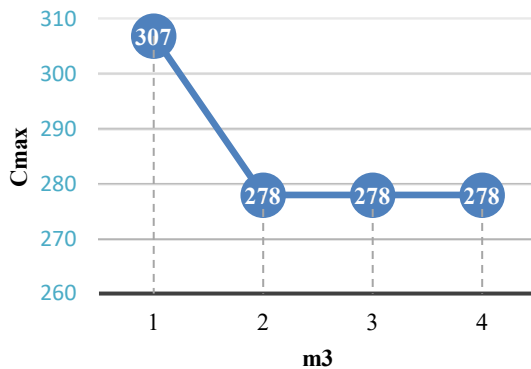


Figure 8. Cmax overlap vs. m3

Figures 11 and 12 show change rate of the ARE per number of machines in the first and third stages. In these figures, the relative error rate of HGALPT algorithm is less than GA. Assuming the values of the parameters f, m1 and m3 are constant, the ARE for different values of n in two proposed algorithms is as shown in Figure 13. Four different scenarios SC1 to SC4 are as follows:

- SC1: f=4, m1 = 2, m3 = 3
- SC2: f=4, m1 = 4, m3 = 4
- SC3: f=4, m1 = 6, m3 = 5
- SC4: f=6, m1 = 8, m3 = 3

According to Figure 13, the HGALPT algorithm performs better than the GA for different values of n in

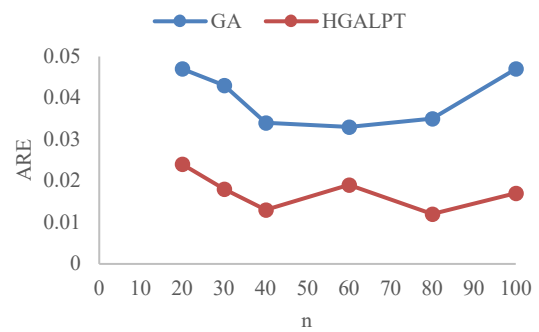


Figure 9. ARE overlap vs. n

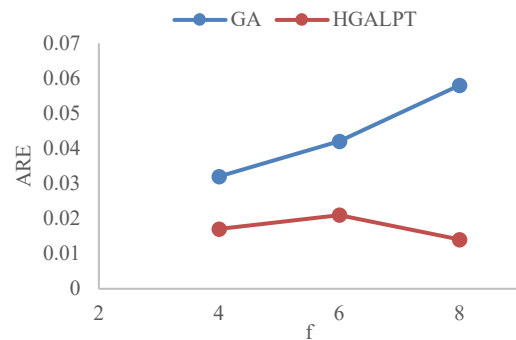


Figure 10. ARE overlap vs. f

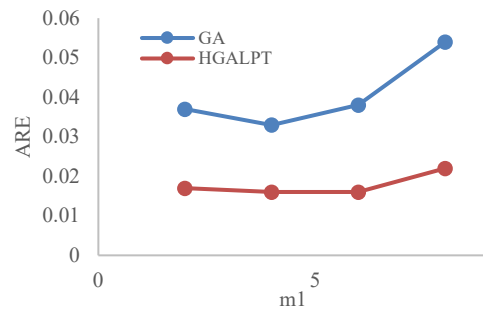


Figure 11. ARE overlap vs. m1

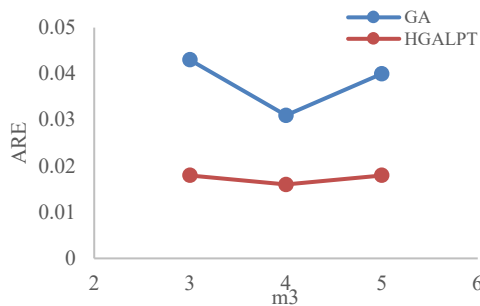


Figure 12. ARE overlap vs.  $m_3$

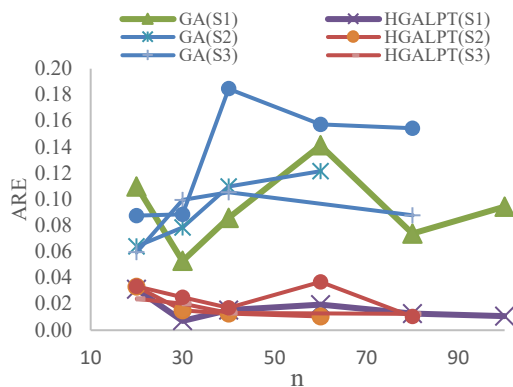


Figure 13. ARE overlap vs.  $S_1, S_2, S_3, S_4$

the four defined scenarios. According to the mentioned cases, the superiority of HGALPT algorithm over GA is determined. Also, the superiority of HGALPT algorithm over Cplex for small sizes was investigated due to less solution time. Therefore, the efficiency of the algorithm in order to solve the problem is proved in this paper.

## 6. CONCLUSION

In the classical production-assembly problems, one step is often considered for production and one step for assembly, while in the real world, the number of steps can be more (transportation, packaging, etc.). Here we have three steps. However, in order to take advantage of cheap labor or available space, it is possible to build factories in several geographical locations, so the issue is considered as a multi-factory. In order to reduce the downtime in the third stage, parallel machines are assumed in this stage.

In order to fill the gaps raised, this research is the first study in the distributed field, that investigates distributed production-assembly scheduling with hybrid flowshop in assembly stage. In order to solve the problem, a mathematical model is presented with minimizing the maximum completion time. Due to the high complexity of the proposed mathematical model, it was proved that

this problem is Non-deterministic Polynomial-time hard (NP-hard). Therefore, the mathematical model can not to solve it in large scale.

Due to the problem is NP-hard, a GA has been proposed. GAs have been used in many papers. An improved mode of this algorithm is called Hybrid Genetic Algorithm Longest Processing Time (HGALPT) algorithm is used to solve the problem in large scale. Using analysis of variance (ANOVA), the values of all parameters for small and large sizes is determined. The results of HGALPT algorithm compared with the results of mixed integer linear programming model (MILP) in small size and the results of genetic algorithm (GA) is compared with its improved algorithm HGALPT for large size which shows the efficiency of the proposed algorithm.

This research findings are: examining the possibility of several machines in the third stage of production-assembly problem, using the three stage in production-assembly problem, considering parallel factories in the three stage production-assembly problem with parallel machines in the third stage, new mathematical model to solve the problem, adjust the parameters and select the best values to run the algorithm, provide a suitable algorithm to solve the problem in large sizes and check the accuracy of the results by comparing the results of the mathematical model and finally, provide sensitivity analyses Table and graphs of the relative error percentage for different values of the problem parameters and sensitivity analyses of objective function.

Some of the limitations that we encountered in this paper, as follows: the lack of easy access to some of the papers in the problem literature, the impossibility of referring to some production environments due to the distance and the limitations of the disease outbreak. Based on the results of the research, some recommendations include the following: The first issue is to provide market research reports to management about presentation a service or product to prevent of failure. The next issue in the production is the possibility of factories building, purchasing equipment and budget control by management.

Given the above, the next issue is to consider the cost items in the proposed model and costs control. Better results are obtained if the results of the presented problem are combined with cost items and managerial insights. Finally, although the presented problem in this study has not been studied so far and is highly complex, some suggestions for future work include:

- Improving the proposed solution method by combining it with other crossover and mutation methods.
- Applying other objective functions including jobs tardiness or earliness as used.
- considering different parallel machines in the second assembly stage.

- Using other meta-heuristic algorithms such as Social Engineering Optimizer (SEO), Red Deer Algorithm (RDA) and Biogeography-Based Optimization. (BBO) to solve the problem and compare the results with the algorithm in this paper.

## 6. REFERENCES

1. Babaeimorad, S., Fatthi, P., Fazlollahtabar, H. "A Joint Optimization Model for Production Scheduling and Preventive Maintenance Interval." *International Journal of Engineering, Transactions B: Applications*, Vol. 34, No. 11 (2021), 2508-2516, DOI: 10.5829/IJE.2021.34.11B.13.
2. Shoaardebili, N., Fattahi, P. "Multi-objective meta-heuristics to solve three-stage assembly flow shop scheduling problem with machine availability constraints." *International Journal of Production Research*, Vol. 53, No. 3, (2015), 944-968. DOI: <https://doi.org/10.1080/00207543.2014.948575>.
3. Ahmadi, R., Bagchi, U., Roemer, T. A. "Coordinated scheduling of customer orders for quick response." *Naval Research Logistics (NRL)*, Vol. 52, No. 6 (2005), 493-512. DOI: <https://doi.org/10.1002/nav.20092>.
4. Lee, C. Y., Cheng, T. C. E., Lin, B. M. T. "Minimizing the makespan in the 3-machine assembly-type flowshop scheduling problem." *Management Science*, Vol. 39, No. 5, (1993), 616-625. DOI: <https://doi.org/10.1287/mnsc.39.5.616>.
5. Garey, M. R., Johnson, D. S., Sethi, R. "The complexity of flowshop and jobshop scheduling." *Mathematics of Operations Research*, Vol. 1, No. 2 (1976), 117-129. DOI: <https://doi.org/10.1287/moor.1.2.117>
6. Deng, J., Wang, L., Wang, S. Y., Zheng, X. L. "A competitive memetic algorithm for the distributed two-stage assembly flowshop scheduling problem." *International Journal of Production Research*, Vol. 54, No. 12 (2016), 3561-3577. DOI: <https://doi.org/10.1080/00207543.2015.1084063>.
7. Hatami, S., García, R. R., Romano, C. A. "The Distributed Assembly Parallel Machine Scheduling Problem with eligibility constraints." *International Journal of Production Management and Engineering*, Vol. 3, No. 1, (2015), 13-23. DOI: <https://doi.org/10.4995/ijpme.2015.3345>
8. Framinan, J. M., Perez-Gonzalez, P. "Order scheduling with tardiness objective: Improved approximate solutions." *European Journal of Operational Research*, Vol. 66, No. 3 (2018), 840-850, DOI: <https://doi.org/10.1016/j.ejor.2017.10.064>.
9. Xiong, F., Xing, K., Wang, F., Lei, H., Han, L. "Minimizing the total completion time in a distributed two stage assembly system with setup times." *Computers & Operations Research*, Vol. 47, (2014), 92-105. DOI: <https://doi.org/10.1016/j.cor.2014.02.005>.
10. Allahverdi, A., Al-Anzi, F. S. "Evolutionary heuristics and an algorithm for the two-stage assembly scheduling problem to minimize makespan with setup times." *International Journal of Production Research*, Vol. 44, No. 22, (2006), 4713-4735. DOI: <https://doi.org/10.1080/00207540600621029>.
11. Zhang, Y., Zhou, Z., Liu, J. "The production scheduling problem in a multi-page invoice printing system." *Computers & Operations Research*, Vol. 37, No. 10, (2010), 1814-1821. DOI: <https://doi.org/10.1016/j.cor.2010.01.014>.
12. Xiong, F., Xing, K., Wang, F. "Scheduling a hybrid assembly-differentiation flowshop to minimize total flow time". *European Journal of Operational Research*, Vol. 240, No. 2, (2015), 338-354. DOI: <https://doi.org/10.1016/j.ejor.2014.07.004>.
13. Liu, B., Wang, K., Zhang, R. (2016, July). "Variable neighborhood based memetic algorithm for distributed assembly permutation flowshop." In Congress on Evolutionary Computation, (2016), 1682-1686. DOI: 10.1109/CEC.2016.7743990.
14. Sung, C. S., Kim, H. A. "A two-stage multiple-machine assembly scheduling problem for minimizing sum of completion times." *International Journal of Production Economics*, Vol. 113, No. 2, (2008), 1038-1048. DOI: <https://doi.org/10.1016/j.ijpe.2007.12.007>.
15. Maboudian, Y., Shafaei, R. "Modeling a bi-criteria two stage assembly flow shop scheduling problem with sequence dependent setup times." In International Conference on Industrial Engineering and Engineering Management, (2009), 1748-1752, DOI: 10.1109/IEEM.2009.5373156.
16. Fattahi, P., Hosseini, S., Jolai, F. "Some heuristics for the hybrid flow shop scheduling problem with setup and assembly operations." *International Journal of Industrial Engineering Computations*, Vol. 4, No. 3 (2013), 393-416. DOI: 10.5267/j.ijiec.2013.03.004.
17. Xiong, F., Xing, K. "Meta-heuristics for the distributed two-stage assembly scheduling problem with bi-criteria of makespan and mean completion time." *International Journal of Production Research*, Vol. 52, No. 9 (2014), 2743-2766. DOI: <https://doi.org/10.1080/00207543.2014.884290>.
18. Mahdavi, I., Komaki, G. M., Kayvanfar, V. "Aggregate hybrid flowshop scheduling with assembly operations." In *18th International Conference on Industrial Engineering and Engineering Management*, (2011), 663-667. DOI: 10.1109/ICIEEM.2011.6035244.
19. Pan, Q. K., Gao, L., Xin-Yu, L., Jose, F. M. "Effective constructive and meta-heuristics for the distributed assembly permutation flowshop scheduling problem." *Applied Soft Computing*, Vol. 81, (2019), 105492. DOI: <https://doi.org/10.1016/j.asoc.2019.105492>.
20. Huang, J., Gu, X. "Distributed assembly permutation flow-shop scheduling problem with sequence-dependent set-up times using a novel biogeography-based optimization algorithm." *Engineering Optimization*, (2021), 1-21. DOI: <https://doi.org/10.1080/0305215X.2021.1886289>.
21. Lei, D., Yuan, Y., Cai, J. "An improved artificial bee colony for multi-objective distributed unrelated parallel machine scheduling." *International Journal of Production Research*, Vol. 59, No. 17, (2021), 5259-5271. DOI: <https://doi.org/10.1080/00207543.2020.1775911>.
22. Fathollahi-Fard, A. M., Woodward, L., Akhrif, O. Sustainable distributed permutation flow-shop scheduling model based on a triple bottom line concept. *Journal of Industrial Information Integration*, Vol. 24, 100233. (2021). <https://doi.org/10.1016/j.jii.2021.100233>
23. Wang, W., Fathollahi-Fard, A. M. "Multi-objective low-carbon hybrid flow shop scheduling via an improved teaching-learning-based optimization algorithm." *Scientia Iranica*, (2022), DOI: 10.24200/SCI.2022.58317.5665
24. Hosseini, S. M. H. "Distributed assembly permutation flow-shop scheduling problem with non-identical factories and considering budget constraints." *Kybernetes*, (2022). DOI: <https://doi.org/10.1108/K-11-2021-1112>
25. Jabbari, M., Tavana, M., Fattahi, P., Daneshamooz, F. "A parameter tuned hybrid algorithm for solving flow shop scheduling problems with parallel assembly stages." *Sustainable Operations and Computers*, Vol. 3, (2022), 22-32. DOI: <https://doi.org/10.1016/j.susoc.2021.09.002>
26. Potts, C. N., Sevast'Janov, S. V., Strusevich, V. A., Van Wassenhove, L. N., Zwaneveld, C. M. "The two-stage assembly scheduling problem: complexity and approximation." *Operations*

- Research*, Vol. 43, No. 2, (1995), 346-355. DOI: <http://dx.doi.org/10.1287/opre.43.2.346>.
27. Jabbari, M., Azizi, V. "Lot streaming in no-wait multi product flowshop considering sequence dependent setup times and position based learning factors." *International Journal of Engineering, Transactions A: Basics*, Vol. 28, No. 7, (2015), 1031-1039. DOI: 10.5829/idosi.ije.2015.28.07a.09
  28. Abtahi, Z., Sahraeian, R. (2021). "Robust and Stable Flow Shop Scheduling Problem Under Uncertain Processing Times and Machines Disruption." *International Journal of Engineering Transactions A: Basics*, Vol. 34, No. 4, (2022). DOI: 10.5829/ije.2021.34.04a.20
  29. Fathollahi-Fard, A. M., Hajiaghaci-Keshteli, M., Tavakkoli-Moghaddam, R. "The social engineering optimizer (SEO)." *Engineering Applications of Artificial Intelligence*, Vol. 72, (2018), 267-293. DOI: <https://doi.org/10.1016/j.engappai.2018.04.009>
  30. Gholizadeh, H., Fazlollahtabar, H., Fathollahi-Fard, A. M., Dulebenets, M. A. Preventive maintenance for the flexible flowshop scheduling under uncertainty: a waste-to-energy system. *Environmental Science and Pollution Research*, (2021), 1-20. DOI: <https://doi.org/10.1007/s11356-021-16234-x>
  31. Li, X., Zhang, X., Yin, M., Wang, J. "A genetic algorithm for the distributed assembly permutation flowshop scheduling problem." In Congress on Evolutionary Computation, (2015), 3096-3101. DOI: 10.1109/CEC.2015.7257275.
  32. Noroozi, A., Mokhtari, H. "Scheduling of printed circuit board (PCB) assembly systems with heterogeneous processors using simulation-based intelligent optimization methods." *Neural Computing and Applications*, Vol. 26, No. 4, (2015), 857-873, DOI: 10.1007/s00521-014-1765-z.
  33. Jia, H. Z., Fuh, J. Y., Nee, A. Y., Zhang, Y. F. "Web-based multi-functional scheduling system for a distributed manufacturing environment." *Concurrent Engineering*, Vol. 10, No. 1, (2002), 27-39. DOI: <https://doi.org/10.1177/1063293X02010001054>.
  34. Jia, H. Z., Nee, A. Y., Fuh, J. Y., Zhang, Y. F. "A modified genetic algorithm for distributed scheduling problems." *Journal of Intelligent Manufacturing*, Vol. 14, No. 3, (2003), 351-362, DOI: <https://doi.org/10.1023/A:1024653810491>.
  35. Chang, P. C., Huang, W. H., Wu, J. L., Cheng, T. C. E. "A block mining and re-combination enhanced genetic algorithm for the permutation flowshop scheduling problem." *International Journal of Production Economics*, Vol. 141, No. 1, (2013), 45-55. DOI: <https://doi.org/10.1016/j.ijpe.2012.06.007>.
  36. Tavakoli, M. R., Mahdizadeh, E. "A new ILP model for identical parallel-machine scheduling with family setup times minimizing the total weighted flow time by a genetic algorithm." *International Journal of Engineering, Transactions A: Basics*, (2007), 183-194. [https://www.ije.ir/article\\_71659\\_16ca2c1872353424a108cbcd1308c9e3.pdf](https://www.ije.ir/article_71659_16ca2c1872353424a108cbcd1308c9e3.pdf)
  37. Maghzi, P., Mohammadi, M., Pasandideh, S. H. R., Naderi, B. "Operating Room Scheduling Optimization Based on a Fuzzy Uncertainty Approach and Metaheuristic Algorithms." *International Journal of Engineering, Transactions B: Applications*, Vol. 35, No. 2, (2022), 258-275, DOI: 10.5829/IJE.2022.35.02B.01
  38. Abbasi, M., Rafiee, M. "Efficient Parallelization of a Genetic Algorithm Solution on the Traveling Salesman Problem with Multi-core and Many-core Systems." *International Journal of Engineering, Transactions A: Basics*, Vol. 33, No. 7, (2020). 1257-1265. DOI: 10.5829/IJE.2020.33.07A.12
  39. Eiben, A. E., Smith, J. E. "Introduction to evolutionary computing," *Berlin: Springer*, Vol. 53, (2003), DOI: <https://link.springer.com/book/10.1007%2F978-3-662-44874-8>
  40. Pillai, A. S., Singh, K., Saravanan, V., Anpalagan, A., Woungang, I., Barolli, L. "A genetic algorithm-based method for optimizing the energy consumption and performance of multiprocessor systems." *Soft Computing*, Vol. 22, No. 10, (2018), 3271-3285. DOI: <https://doi.org/10.1007/s00500-017-2789-y>.
  41. Bahalke, U., Yolmeh, A. M., Hajizade, A. N., Bahalke, A., "Genetic and tabu search algorithms for the single machine scheduling problem with sequence-dependent set-up times and deteriorating jobs." *International Journal of Engineering, Transactions A: Basics*, Vol. 23, No. 3, (2010), 227-234. [https://www.ije.ir/article\\_71863\\_722b2d35a63e36bcd4a13526b9d5525.pdf](https://www.ije.ir/article_71863_722b2d35a63e36bcd4a13526b9d5525.pdf)
  42. Yazdani, M., Kabirifar, K., Fathollahi-Fard, A. M., Mojtahedi, M. "Production scheduling of off-site prefabricated construction components considering sequence dependent due dates." *Environmental Science and Pollution Research*, (2021), 1-17. DOI: <https://doi.org/10.1007/s11356-021-16285-0>
  43. Fathollahi-Fard, A. M., Hajiaghaci-Keshteli, M., Tavakkoli-Moghaddam, R. Red deer algorithm (RDA): a new nature-inspired meta-heuristic. *Soft Computing*, Vol. 24, No. 19 (2020), 14637-14665. DOI: <https://doi.org/10.1007/s00500-020-04812-z>

---

### Persian Abstract

#### چکیده

در این مقاله یک مسئله تولید مونتاژ سه مرحله‌ای در نظر گرفته شده است. با توجه دانش بدست آمده ما از مسئله، فرض ماشین‌های موازی در مرحله سوم، سیستم تولید مونتاژ سه مرحله‌ای با کارخانه‌های موازی و ماشین‌های موازی در مرحله سوم سیستم تولید-مونتاژ با کارخانه‌های موازی فقط در این مقاله بررسی شده است. به منظور کمینه کردن بیشینه زمان تکمیل کارها در تمام کارخانه‌ها (Makespan)، تخصیص کارها به کارخانه‌ها و تعیین توالی آنها بایستی به صورت مناسب انجام گردد. به منظور حل مسئله در ابعاد کوچک، یک مدل برنامه‌ریزی عدد صحیح آمیخته ارائه شده است که توسط حل کننده سیپلکس (CPLEX) اجرا شده است. با توجه به پیچیدگی محاسباتی، حل مسئله در ابعاد بزرگ توسط سیپلکس امکان‌پذیر نیست، بنابراین به منظور حل آن و کنترل پیچیدگی محاسباتی، یک الگوریتم ژنتیک بهبود یافته از ترکیب الگوریتم ژنتیک و روش طولانی‌ترین زمان پردازش (LPT) ارائه شده است که الگوریتم ژنتیک ترکیبی با طولانی‌ترین زمان پردازش (HGALPT) نامیده می‌شود. پارامترهای مسئله با استفاده از تحلیل واریانس یک طرفه (ANOVA) تنظیم شده‌اند. در پایان به منظور ارزیابی کارایی و اثربخشی الگوریتم ارائه‌شده و تعیین تاثیر هر پارامتر روی تابع هدف، تحلیل حساسیت روی پارامترهای مسئله انجام شده است.

---



## The Effect of Heat on the Settlement Properties of Cement-stabilized Clay Soil

M. Hashemi\*, S. M. Marandi, M. Vahidi

Department of Civil Engineering, Shahid Bahonar University of Kerman, Kerman, Iran

### PAPER INFO

#### Paper history:

Received 06 January 2022

Received in revised form 25 February 2022

Accepted 25 February 2022

#### Keywords:

Heat

Kaolinite

Cement

Consolidation

Stabilized Clay Soil

### ABSTRACT

Clay soil may be subjected to heat in various applications, such as nuclear waste burial sites and high voltage transmission lines. The impact of heat on clay soil's physical and mechanical properties has been explored in previous studies. However, previous studies have mainly focused on the mechanical properties of clay soil without stabilizers, and the effect of heat on the properties of the stabilized clay soil is scarcely studied. The present paper has analyzed and studied the combined effects of heat and cement on the settlement properties of kaolinite clay soil. To conduct the study, kaolinite clay mixed with various degrees of cement was exposed to a range of 25 to 600 degrees Celcius. The results showed that the coefficient of consolidation gradually decreased by increasing heat up to the dehydroxylation point. An increase in heat up to 200 degrees Celcius resulted in increasing the coefficient of consolidation in the specimens containing cement. In specimens containing 10 percent of the cement at temperatures higher than 200 degrees Celcius, the coefficient of consolidation in room temperature decreased by 73 percent compared to kaolinite. Moreover, the void ratio increased in kaolinite specimens without cement when subjected to heat up to 400 degrees Celcius. By increasing the heat, the void ratio decreased in specimens containing 10 percent cement.

doi: 10.5829/ije.2022.35.05.20

## 1. INTRODUCTION

The ever-increasing expansion of construction and building, and lack of access to suitable sites have led humans to utilize sites with inappropriate engineering properties. Generally, the soil in most construction sites is not entirely capable of bearing the weight of the structure [1, 2]. The mechanical properties of soil are determined by various factors, including soil texture, moisture, volumetric density, grain distribution, shape and mineralogy, interlocking of grains, grain adhesion and chemical weathering, grain cohesion mechanisms, and presence of vegetation. Fine-grain soil is not exclusively applicable to wet environments. Due to the incompressibility of fine-grain soil, it is not suitable to be loaded in wet environments [3]. Soil stabilization is the process of changing soil properties to increase its bearing capacity and resistance to physical and chemical tension in various environments [4-6].

Various stabilization methods can be used to change soil properties such as strength, stiffness,

compressibility, swelling sensitivity to water, and volume change behavior. Thermal and electrokinetic methods may also be combined with additives to change soil grain and density [7-11].

To summarize, the process of soil stabilization results in a change of bonds between its particles. The bond change results in a new structure that is more adhesive than before. In some methods, the previous grain structure is broken, but other methods increase soil resistance through the injection of additives [12].

Soil may be subjected to heat for various reasons, which changes soil's physical and mechanical properties (especially in clayey soils). Moreover, these changes may be reversible or irreversible [13-15].

Improvement of soil properties through heat has been used in the past, and the effect of heat on soil's engineering properties such as the compressive strength has been observed empirically. These improvements have been used in construction of roads and construction materials [15].

\*Corresponding Author Institutional Email: [m.hashemi@eng.uk.ac.ir](mailto:m.hashemi@eng.uk.ac.ir)  
(M. Hashemi)

The effect of heat on clay soil's engineering properties is essential in various applications such as soil stabilization, application of heat to the clay soil surrounding nuclear waste burial sites and high voltage transmission lines, remediation of polluted soil, and construction materials.

Many scholars have studied soil remediation contaminated by crude oil, heavy metals, and radioactive material [16, 17]. Recent studies have primarily focused on the burial of high-level radioactive waste and the result of heat on the properties and function of the surrounding soil [18, 19]. The application of heat can significantly improve the geotechnical engineering properties and is useful in the remediation of polluted soil [20].

With an increase in number of nuclear power plants, many developed countries bury their nuclear waste deep into the earth. The development of uranium revival technology, the establishment of new nuclear plants, and an increase in radioactive waste call for more burial sites. Radioactive waste produces heat for a long time after its burial. The low void ratio of clay soil has made it the best choice for the burial of high-level nuclear waste, which is done hundreds of meters underground. The soil surrounding nuclear waste is subjected to heat for extended periods. The heat of nuclear waste is absorbed by the clay soil, which significantly affects its physical and chemical properties.

**Dehydration** – Clay soil dehydration is the first event that occurs after exposure to increased temperatures. In this process, the water between silicate layers of clay soil is evaporated [21]. Dehydration results in the elimination of pore water and absorbed water. Pore water is eliminated after the increase of temperature up to 100C, whereas absorbed and interlayer water is eliminated as the temperature goes up to 300C [11]. Dehydration also changes plasticity, the porosity of fine-grained and coarse grain soil, and reduced cation-exchange capacity (CEC). Moreover, dehydration decreases the distance between soil layers, hence reducing its mass [22]. Dehydration is a relatively reversible reaction, and the soil may retain its ability to absorb water with a decrease in temperature.

**Dehydroxilation** – Dehydroxilation is the process through which the hydroxyl ion is released from crystallized clay minerals by forming a water molecule [21]. This process increases temperature, and a reaction between two hydroxyl groups in the octahedral layer happens (Equation (1)) [23].



Dehydroxylation is an endothermic reaction that occurs between 400°C and 1000°C and results in the elimination of water from clay soil's crystallized structure and the destruction of soil minerals. Destruction of clay mineral structure subsequently creates amorphous shapes

[24]. Figure 1 shows the effect of hydroxyl elimination on Silica (Si) and Alumina (Al) frameworks.

Dehydroxylation in most clay soils occurs in a particular thermal range. For instance, the thermal range for dehydroxylation in kaolinite is 300 to 600 °C which destroys crystallized structures and the creation of metakaolin. Metakaolin is the amorphous leftover created after the hydroxyl group's release. Dehydroxylation of illite starts in the thermal range of 350 to 600 degrees Celcius, and its crystallized structure is destroyed in temperatures ranging from 700 to 850 degrees Celcius. Smectite clays – such as Montmorillonite – are dehydroxylated in temperatures of 500 to 2000 degrees Celcius. Similar to illite, smectite clays initially form a stable phase where parts of the crystallized structure remain intact. This structure is then entirely destroyed at 800 degrees Celcius [15, 25].

Heat causes dehydroxylation and destroys kaolinite. However, Mica and Chlorite remain intact, which means higher temperatures are needed for their dehydroxylation. Finally, heat has only reduced the distance between layers in the smectite [24].

The present paper conducts a series of macrostructure examinations on clay containing various degrees of cement under heat to study the effect of heat on the consolidation features of cement-stabilized clay soil.

## 2. MATERIAL AND METHODOLOGY

**2. 1. Kaolinite** The kaolinite used in the present paper obtained from a mine in Zarand (Kerman), located in southeast of Iran. The technical properties of soil determined using ASTM standards, and the soil was classified as CL using the united soil classification system [26, 27]. The physical properties of the soil used in this study are presented in Table 1.

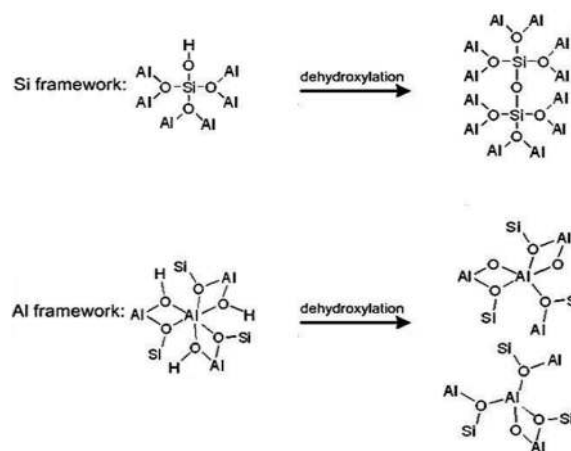


**Figure 1.** The effect of dehydroxylation on Silica and Alumina frameworks [24]

**TABLE 1.** Physical properties of kaolinite used in the present paper

Properties	Amount
Liquid limit (%)	30.3
Plastic Limit (%)	19
Plasticity index (%)	11.3
Sand	36.6
Slit	44.4
Clay	19
Unified Classification	CL
Color	Brown

**2. 2. Cement** Type 2 Portland cement was used to prepare specimens and was obtained from the Kerman Cement Plant. The properties of cement used in this study are presented in Table 2.

### 2. 3. Specimen Preparation and Experiments

More than 99% of the soil used in the present study was sifted through a size 10 sieve. Due to the adhesive nature of clay particles and their tendency to form clods, the soils were initially sifted through a size 10 sieve (to increase soil homogeneity). Afterward, 20% of moisture (plastic limit levels) was added to the soil, and it was kept for 24 hours in seal-top storage bags. Kaolinite specimens were mixed with 0, 5, 10, and 20 percent of cement (dry mixing of cement with kaolinite clay in the plastic limit) according to the standard methods, and the mix was consolidated using Teflon mallets. The surface area between each layer was scraped and scuffed to create sufficient integration. The specimens were then placed in a seal-top storage bag for protection against moisture and

**TABLE 2.** Physical and chemical properties of the used cement (obtained from Kerman Cement Plant)

Physical properties	Initial setting time (min)	170
	Final setting time (min)	220
	7-day compressive strength (MPa)	35.30
	Specific surface area (cm <sup>2</sup> /g)	3900
Chemical compounds	Calcium Oxide (CaO)	62.88%
	Silicon Dioxide (SiO <sub>2</sub> )	21.30%
	Aluminum Oxide (Al <sub>2</sub> O <sub>3</sub> )	5.17%
	Sulphur Trioxide (SO <sub>3</sub> )	2.16%
	Ferric Oxide (Fe <sub>2</sub> O <sub>3</sub> )	4.37%
	Magnesium Oxide (MgO)	1.57%
	Sodium Oxide (Na <sub>2</sub> O)	0.15%
	Potassium Oxide (K <sub>2</sub> O)	0.33%

were cured for 7 days. In the next step, the specimens were put in the oven for 24 hours at a temperature of 110 degrees Celcius. This was done to prevent the specimens from cracking in the higher temperatures of the furnace. Then, the specimens were put into the ELE furnace. Given the aim of studying the effects of heat on clay soil properties, the specimens were examined under temperatures of 25, 110, 200, 400, and 600 degrees Celcius. Except for the specimens exposed to 25 (no thermal history) and 110 degrees Celcius, the rest were put in the furnace at temperatures of 200, 400, and 600 degrees Celcius. Figure 2 shows two kaolinite specimens containing 5% of cement after 7 days of curing in zipper plastic bags and experiencing 110 degrees Celcius.

The temperature in the furnace was automatically increased at a rate of 12 degrees Celcius per minute, and the specimens were left in the furnace for 2 hours after reaching the determined temperature. After the furnace was shut down, the specimens were cooled down in the closed furnace. A consolidation test was used to measure the settlement features of the specimens. This test was conducted based on ASTM D-2435 standard [28]. Moreover, the specimens' weight was measured in each level and under each thermal condition, and the changes were calculated.

## 3. RESULTS ANALYSIS

### 3. 1. Weight Change In Kaolinite Specimens

Sudden weight change is a suitable parameter for determining dehydroxylation temperatures [15]. Dehydroxylation happens due to the release of hydroxyl ions from the crystalized structures of clay minerals by forming water molecules. The soil's weight abruptly decreases when reaching the dehydroxylation temperature. Therefore, weight changes in the specimens were monitored at various temperatures, and the results are presented in this paper. Figure 3 shows the weight changes in kaolinite specimens containing cement under various temperatures. According to Figure 3, it can be concluded that an increase in temperature has resulted in a decrease in kaolinite specimens' weight. The decrease in specimens' weight has happened with a slow, steady pace up to 200 degrees Celcius. However, the kaolinite

**Figure 2.** Kaolinite specimens containing 5% of cement

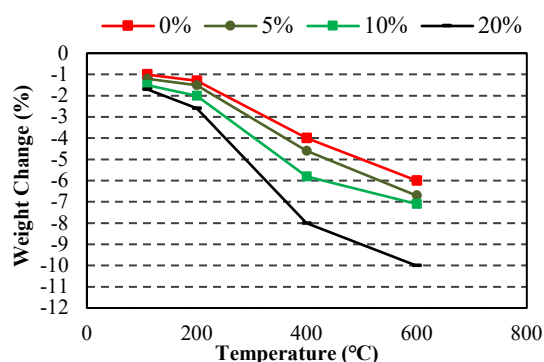


**Figure 3.** Weight change in kaolinite specimens containing cement under various temperatures

specimens' weight has decreased by 4 to 5 percent when reaching 400 degrees Celcius. This sudden change shows the start of kaolinite dehydroxylation and the destruction of clay mineral structure. The specimen's weight continues to decrease as the temperature increases up to 600 degrees Celcius. Similarly, the weight of specimens containing cement has steadily and slowly decreased as the temperature rises to 200 degrees Celcius. However, the specimens' weight changes abruptly in higher temperatures. Figure 3 shows that the weight change in specimens containing cement is more dramatic compared with the untreated specimen. At 600 degrees Celcius, the specimen containing 20 percent cement has had a 10 percent weight loss compared to the specimen containing no cement at 25 degrees Celcius.

As it can be seen, an increase in the temperature results in decreasing the weight of Kaolinite specimens. This decrease can be due to the removal of hydroxyl ions from the crystal structure of clay minerals, degradation of the structure of clay minerals, and the beginning of the dehydroxylation process [15, 29]. The size of clay particles increases by enforcing the heat on the specimens, which increases the volume of cavities. Therefore, The void ratio is very likely to increase by increasing the temperature [30, 31].

### 3. 2. Consolidation Coefficient

According to Figure 4, the consolidation coefficient of specimens containing no cement has decreased with an increase in temperature. The decrease of consolidation coefficient in 200 degrees Celcius may result in from dehydration and a decrease of interlayer distance between clay platelets. An increase in temperature from 200 to 400 degrees Celcius has no significant impact on the consolidation coefficient. However, an increase in temperature up to 600 degrees Celcius has resulted in a sudden decrease in consolidation coefficient. This may be due to the formation of bigger particles, a decrease in activity in clay's surface particles, and a lack of particles' tendency to absorb molecules of water. The decrease in consolidation coefficient coincides with weight changes,

which shows that a sudden decrease in consolidation coefficient occurs after reaching dehydroxylation temperatures.

According to Figure 4, the consolidation coefficient decreased in the specimen containing 5 percent cement as the temperature increases up to 600 degrees Celcius. A decrease in consolidation coefficient at temperatures up to 200 degrees Celcius has probably occurred due to dehydration and a decrease in interlayer distance between clay particles. The decrease in consolidation coefficient from 400 to 600 degrees Celcius in the specimen containing cement has a lower ratio compared to the one containing no cement. This may be due to the effect of high temperature on cement particles. The consolidation coefficient of the specimen in 400 degrees Celcius has decreased by 31 percent, compared to the specimen in 25 degrees Celcius. The consolidation coefficient of the specimen in 600 degrees Celcius has decreased by 14 percent compared to the specimen in 400 degrees Celcius.

According to Figure 4, the consolidation coefficient of specimens containing 10 percent cement has decreased up to 400 degrees Celcius, similar to those containing 5 percent cement. Therefore, the decrease of consolidation coefficient in 400 degrees Celcius can be attributed to dehydration and a decrease in interlayer distance between clay platelets. An increase in consolidation coefficient between 400 and 600 degrees Celcius may be attributed to the breakage of the hydration bond between cement and kaolinite. It can be concluded that 200 degrees Celcius is the optimal temperature for thermal stabilization of kaolinite soil containing 10 percent of cement. The consolidation coefficient of the specimen in 400 degrees Celcius has decreased by 40 percent compared to the one in 25 degrees Celcius. However, the consolidation coefficient of the specimen in 600 degrees Celcius has increased by 57 percent compared to the one in 400 degrees Celcius. These significant changes show the sensitivity of the kaolinite-cement bond to the heat.

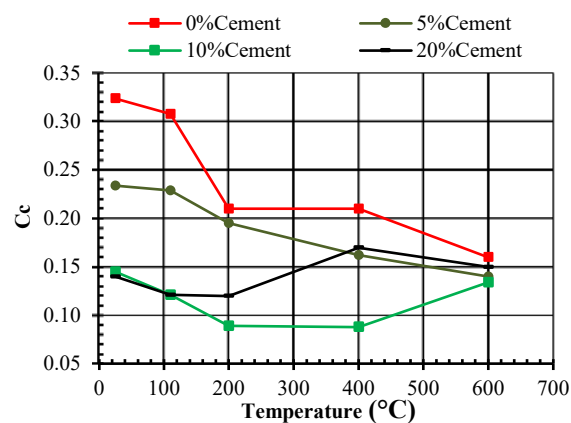


**Figure 4.** Changes of consolidation coefficient under heat in kaolinite specimens

According to Figure 4, the consolidation coefficient of specimens containing 20 percent cement has decreased at temperatures rising to 200 degrees, and then increased in temperatures between 200 and 400 degrees Celcius. However, the consolidation coefficient decreases as the temperature rise to 600 degrees Celcius. An increase in consolidation coefficient at temperatures from 200 to 400 degrees Celcius can be attributed to the breakage of the bond between kaolinite and cement. The repeated increase in consolidation coefficient can result in from dehydroxylation overshadowing the breakage of the bond between cement and kaolinite. The consolidation coefficient of the specimen at 200 degrees Celcius has decreased by 14 percent compared to the one in 25 degrees Celcius. Then, the coefficient increases by 41 percent and reaches 0.17 as the temperature rises from 200 to 400 degrees. Finally, the consolidation coefficient decreases by 11 percent as the temperature rises from 400 to 600 Celcius.

**3. 3. Coefficient of Permeability (k)** Figure 5 shows the changes in the permeability of kaolinite specimens with no cement against the void ratio. The results show an increase in permeability as the temperature rises. Permeability increases as the temperature rises to 400 degrees Celcius. It can be deduced that temperatures as high as 400 degrees Celcius result in the elimination of interlayer water, an increase in macroscopic voids within the structure, and the formation of clods in the soil. However, permeability suddenly decreases as the temperature rises from 400 to 600 degrees Celcius. The significant change in permeability can be attributed to dehydroxylation and the destruction of clay mineral structure.

Figure 6 shows the changes in the permeability of kaolinite specimens stabilized with 5 percent of cement against changes in void ratio and heat. The results show that permeability decreases as the heat rise to 600 degrees Celcius. The decrease in permeability can be due to the

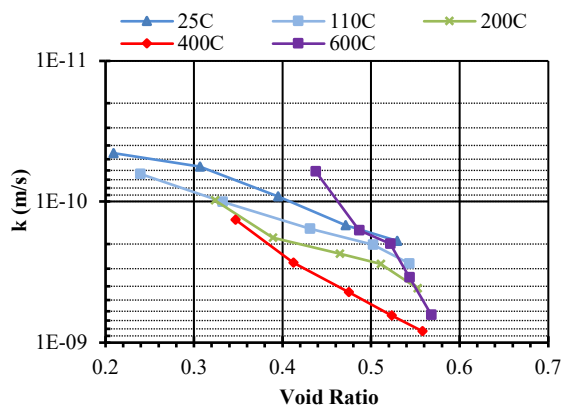


**Figure 5.** Changes in kaolinite specimens' permeability under heat – containing no cement

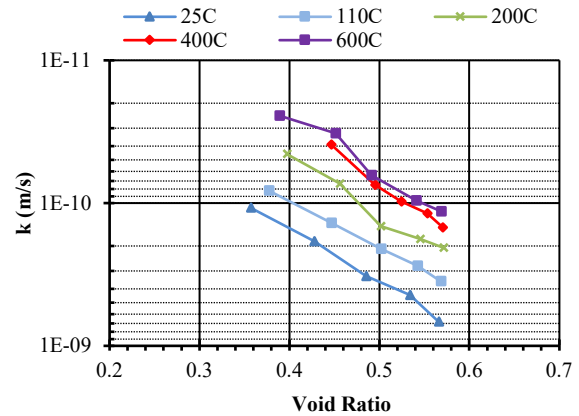


**Figure 6.** Changes in permeability of kaolinite specimens against heat and void ratio stabilized with 5 percent of cement

effect of heat on the hydration reaction of cement and kaolinite. The permeability of the specimen at 600 degrees Celcius has decreased by 83 percent compared to the permeability of the specimen at 25 degrees Celcius.

Figure 7 shows the changes in the permeability of kaolinite specimens stabilized with 10 percent of cement. The results show that as the heat rises to 600 degrees Celcius, the permeability of these specimens dramatically decreased. This significant change in permeability can be attributed to the effect of heat on the reaction of cement and kaolinite. The most significant changes in permeability occur at temperatures between 25 to 200, and 400 to 600 degrees Celcius. According to Figure 7, an increase in heat from 200 to 400 degrees does not significantly impact the permeability of the specimen. The permeability coefficient of the specimen at 200 degrees Celcius was decreased by 50 percent compared to that of the specimen at 25 degrees Celcius. At 600 degrees Celcius, the permeability coefficient of the specimen was decreased by 60 percent compared to the specimen at 400 degrees Celcius.

Figure 8 demonstrates the permeability of kaolinite specimens with 20 percent of cement under heat. The results show that at temperature of 400 degrees Celcius, the permeability of specimens containing 20 percent of cement significantly decreased. However, the permeability coefficient suddenly increases as the temperature rises from 400 to 600 degrees Celcius. This change is a result of the clay particles being replaced by cement. Therefore, it can be concluded that the optimal amount of cement for improving clay soil's permeability against heat is 10 percent.

The sudden changes in the specimens' weight reveal the dehydroxylation temperature of kaolinite to be about 400 degrees. Joshi et al. [15] found that the temperature range of 300 to 600 degrees Celcius is kaolinite's dehydroxylation point, which occurs as hydroxyl ions exit clay mineral structure. Mitchell and Soga [24]

demonstrated that the application of 550 degrees Celcius on kaolinite, mica, chlorite, and smectite clay minerals result in dehydroxylation and destruction of kaolinite's structure. The findings of the present study correspond with the literature mentioned earlier.

The present study shows that the permeability of unmixed kaolinite specimens increases against heat. Ouhadi et al. [19] found that permeability of soil decreases at 200 degrees Celcius as interlayer water is eliminated and the number of macroscopic voids is increased (see Figure 9). However, the present study showed that the permeability of kaolinite specimens decreases against heat by adding various amounts of cement. Therefore, the behavior of mixed kaolinite specimens follows an opposite trend compared to that of the unmixed specimens.

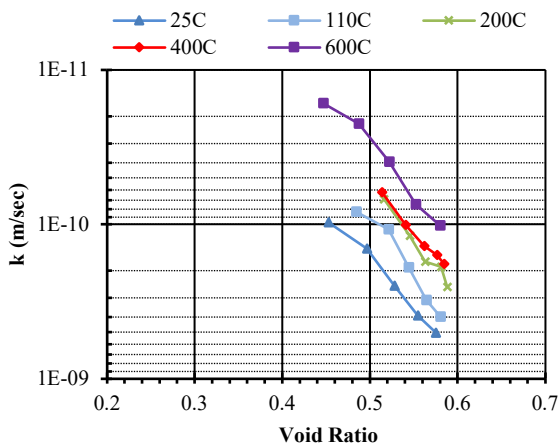


Figure 7. Changes in permeability of kaolinite specimens against heat and void ratio stabilized with 10 percent of cement

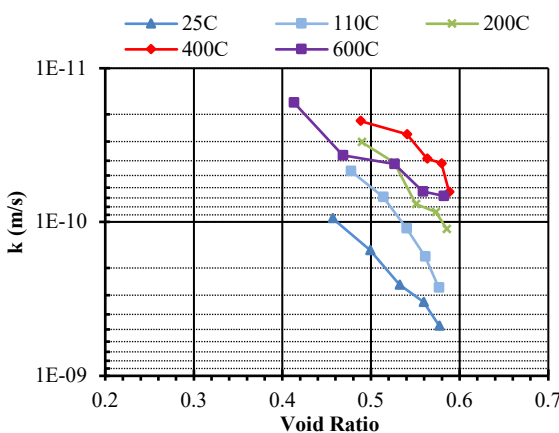


Figure 8. Changes in permeability of kaolinite specimens against heat and void ratio stabilized with 20 percent of cement

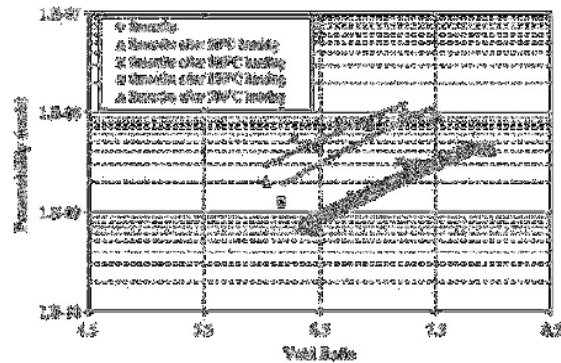


Figure 9. Changes in clay's permeability against heat

#### 4. CONCLUSION

The clayey soil may be exposed to very high temperatures in some sites like nuclear waste burial sites which can change settlement properties of the soil and threaten the environment. The present study investigated the effect of heat on the settlement properties of cement-stabilized kaolinite clay. Kaolinite clay specimens with different percentages of cement were prepared and cured at different temperatures (25, 110, 200, 400, and 600 degrees Celcius). Then, the performance of the specimens was evaluated using specimens' weight change, consolidation coefficient, and permeability coefficient. Based on the experiments, the following conclusions can be drawn.

1. The consolidation coefficient gradually decreased as the temperature rose to the dehydroxylation point. The consolidation coefficient decreased dramatically as the clay mineral structure was destroyed in dehydroxylation. At 600 degrees Celcius, the consolidation coefficient of the specimen decreased by 52 percent compared to the specimen at room temperature.
2. The consolidation coefficient decreased in specimens containing cement as the temperature rose to 200 degrees Celcius. However, applying temperatures more than 200 degrees Celcius on the same specimens yielded opposite results. This showed cement's sensitivity to high temperatures. Therefore, 200 degrees Celcius was the optimal temperature for thermal stabilization of specimens containing 10 percent cement. The consolidation coefficient of the kaolinite specimen containing 10 percent cement at 200 degrees Celcius decreased by 73 percent compared to that of the specimen at room temperature.
3. The permeability coefficient of kaolinite specimens containing no cement increased as the temperature rose to 400 degrees Celcius. The permeability coefficient of specimens containing 10 percent of cement decreased as the temperature rose. Thus, addition of 10 percent of cement can reduce the harmful environmental challenges of nuclear waste burial.

## 5. REFERENCES

1. Sheikhhosseini Lori, I., Toufigh, M.M. and Toufigh, V., "Improvement of poorly graded sandy soil by using copper mine tailing dam sediments-based geopolymer and silica fume", *Construction and Building Materials*, Vol. 281, (2021), 122591. doi.org/10.1016/j.conbuildmat.2021.122591
2. Manimaran, A., Seenu, S. and Ravichandran, P.T., "Stimulation behaviour study on clay treated with ground granulated blast slag and groundnutshell ash", *International Journal of Engineering, Transactions B: Applications*, Vol. 32, No. 5, (2019), 673-678. doi: 10.5829/ije.2019.32.05b.08
3. Wang, D.-y., Ma, W., Niu, Y.-h., Chang, X.-x. and Wen, Z., "Effects of cyclic freezing and thawing on mechanical properties of qinghai-tibet clay", *Cold Regions Science and Technology*, Vol. 48, No. 1, (2007), 34-43. doi:10.1016/j.coldregions.2006.09.008
4. Winterkorn, H.F. and Pamukcu, S., Soil stabilization and grouting, in *Foundation engineering handbook*. 1991, Springer. 317-378. doi: 10.1007/978-1-4615-3928-5\_9
5. Mir, B.A. and Reddy, S.H., "Mechanical behaviour of nano-material (al<sub>2</sub>o<sub>3</sub>) stabilized soft soil", *International Journal of Engineering, Transactions C: Aspects*, Vol. 34, No. 3, (2021), 636-643. doi: 10.5829/IJE.2021.34.03C.07
6. Bahrami, M. and Marandi, S.M., "Large-scale experimental study on collapsible soil improvement using encased stone columns", *International Journal of Engineering, Transactions C: Aspects*, Vol. 34, No. 5, (2021), 1145-1155. doi: 10.5829/ije.2021.34.03c.07
7. Nguyen, D.T. and Phan, V.T.A., "Engineering properties of soil stabilized with cement and fly ash for sustainable road construction", *International Journal of Engineering, Transactions C: Aspects*, Vol. 34, No. 12, (2021), 2665-2671. doi:10.5829/IJE.2021.34.12C.12
8. Rahmannejad, M. and Toufigh, V., "Influence of curing time and water content on unconfined compressive strength of sand stabilized using epoxy resin", *International Journal of Engineering, Transactions B: Applications*, Vol. 31, No. 8, (2018), 1187-1195. doi: 10.5829/ije.2018.31.08b.05
9. Javdanian, H., "The effect of geopolymerization on the unconfined compressive strength of stabilized fine-grained soils", *International Journal of Engineering, Transactions B: Applications*, Vol. 30, No. 11, (2017), 1673-1680. doi: 10.5829/ije.2017.30.11b.10
10. Arjomand, M.A., Abedi, M., Gharib, M. and Damghani, M., "An experimental study on geogrid with geotextile effects aimed to improve clayey soil", *International Journal of Engineering, Transactions B: Applications*, Vol. 32, No. 5, (2019), 685-692. doi: 10.5829/ije.2019.32.05b.10
11. Gharib, M., Arjomand, M.A., Abdi, M.R. and Arefnia, A., "Influence of chitin nanofiber and rice husk ash on properties and bearing resistance of soft clay soils", *International Journal of Engineering, Transactions C: Aspects*, Vol. 32, No. 3, (2019), 373-380. doi: 10.5829/ije.2019.32.03c.04
12. Evstatiev, D., "Loess improvement methods", *Engineering Geology*, Vol. 25, No. 2-4, (1988), 341-366. doi.org/10.1016/0013-7952(88)90036-1
13. Wang, M., Benway, J.M. and Arayssi, A.M., The effect of heating on engineering properties of clays, in *Physico-chemical aspects of soil and related materials*. 1990, ASTM International.
14. Jefferson, I., "Temperature effects on clay soils", Loughborough University, (1994).
15. Joshi, R., Achari, G., Horsfield, D. and Nagaraj, T., "Effect of heat treatment on strength of clays", *Journal of Geotechnical Engineering*, Vol. 120, No. 6, (1994), 1080-1088.
16. Alcocer, C. and Chowdhury, H., "Experimental study of an environmental remediation of gulf coast crude-oil-contaminated soil using low-temperature thermal treatment", in *SPE Western Regional Meeting, OnePetro.*, (1993).
17. Varlakov, A., Sobolev, I., Barinov, A., Dmitriev, S., Karlin, S. and Flit, V., "Method of treatment of radioactive silts and soils", *MRS Online Proceedings Library*, Vol. 465, (1996).
18. Gu, B., Wang, L., Minc, L. and Ewing, R., "Temperature effects on the radiation stability and ion exchange capacity of smectites", *Journal of Nuclear Materials*, Vol. 297, No. 3, (2001), 345-354.
19. Ouhadi, V., Yong, R., Goodarzi, A. and Safari-Zanjani, M., "Effect of temperature on the re-structuring of the microstructure and geo-environmental behaviour of smectite", *Applied Clay Science*, Vol. 47, No. 1-2, (2010), 2-9.
20. Morris, P.H. and Wong, L., "Modification of dredged sediments to produce useful product by heating to high temperatures", *Sustainable Tourism CRC*, (2005).
21. Brindley, G., "Thermal transformations of clays and layer silicates", in *Proceedings of the international clay conference*, Applied Publishers Wilmette, IL., (1975), 119-129.
22. Heller-Kallai, L., Thermally modified clay minerals, in *Developments in clay science*. Elsevier. (2013), 411-433. doi.org/10.1016/B978-0-08-098258-8.00014-6
23. Emmerich, K., Madsen, F.T. and Kahr, G., "Dehydroxylation behavior of heat-treated and steam-treated homoionic cis-vacant montmorillonites", *Clays and Clay Minerals*, Vol. 47, No. 5, (1999), 591-604. doi:10.1346/CCMN.1999.0470506
24. Mitchell, J.K. and Soga, K., "Fundamentals of soil behavior, John Wiley & Sons New York, Vol. 3, (2005).
25. McConville, C.J. and Lee, W.E., "Microstructural development on firing illite and smectite clays compared with that in kaolinite", *Journal of the American Ceramic Society*, Vol. 88, No. 8, (2005), 2267-2276. doi.org/10.1111/j.1551-2916.2005.00390.x
26. International, A., ASTM D422 standard test method for particle-size analysis of soils. (2007).
27. International, A., ASTM D4318-00 standard test methods for liquid limit, plastic limit, and plasticity index of soils. (2017).
28. International, A., ASTM D2435 standard test methods for one-dimensional consolidation properties of soils using incremental loading. (2011).
29. Habert, G., Choupay, N., Escadeillas, G., Guillaume, D. and Montel, J.M., "Clay content of argillites: Influence on cement based mortars", *Applied Clay Science*, Vol. 43, No. 3, (2009), 322-330. doi:10.1016/j.clay.2008.09.009
30. Yilmaz, G., "The effects of temperature on the characteristics of kaolinite and bentonite", *Scientific Research and Essays*, Vol. 6, No. 9, (2011), 1928-1939. doi: 10.5897/SRE10.727
31. Wang, M., Jao, M. and Ghazal, M., "Heating effect on swelling behaviour of expansive soils", *Geomechanics and Geoengineering: An International Journal*, Vol. 3, No. 2, (2008), 121-127. doi: 10.21275/28121602

---

**Persian Abstract**

---

**چکیده**

خاک های رسی به دلایل مختلف، از جمله اعمال حرارت در مراکز دفن زباله های هسته ای، در مناطق دفن کابل های برق فشار قوی، ممکن است در معرض حرارت قرار بگیرند. بررسی تحقیقات گذشته نشان دهنده تاثیر حرارت بر خصوصیات فیزیکی و مکانیکی خاک های رسی است. با این وجود مطالعات گذشته عمدتاً بر رفتار مکانیکی خاک رس بدون تثبیت کننده بوده است و مطالعات مربوط به تاثیر حرارت بر رفتار خاک رس تثبیت شده محدود میباشد. در این مقاله تاثیر توامان حرارت و سیمان بر خصوصیات نشست پذیری خاک رس کائولینیت مورد مطالعه و تجزیه و تحلیل قرار گرفته است. بدین منظور خاک رس کائولینیت ترکیب شده با درصد های مختلف سیمان در معرض سطوح حرارتی متفاوت شامل دماهای ۲۵ تا ۶۰۰ درجه سانتیگراد قرار داده شده اند. نتایج نشان داد که با افزایش حرارت تا پیش از دمای دی هیدروکسیلاسیون، ضریب تحکیم بتدریج کاهش یافته است. افزایش حرارت تا ۲۰۰ درجه سانتیگراد، باعث کاهش ضریب تحکیم در نمونه های حاوی سیمان شده است. لیکن در نمونه های حاوی ۱۰ درصد سیمان و افزایش حرارت به بیش از ۲۰۰ درجه سانتیگراد نتیجه عکس داشته و ۷۳ درصد نسبت به نمونه کائولینیت در دمای محیط کاهش داشته است. همچنین ضریب نفوذ پذیری در نمونه های خاک کائولینیت بدون سیمان با افزایش حرارت تا دمای ۴۰۰ درجه سانتیگراد افزایش پیدا کرده است. با اضافه نمودن سیمان تا ۱۰ درصد، با افزایش درجه حرارت ضریب نفوذ پذیری کاهش پیدا کرده است.

---



## Stabilization of Voltage and Current in the Distribution Networks using APF and TSC

H. Zare<sup>a</sup>, M. Khanalizadeh Eini<sup>\*b</sup>, A. Esmaeili<sup>c</sup>

<sup>a</sup> Department of Electricity, Mahmudabad Branch, Technical and Vocational University, Mahmudabad, Iran

<sup>b</sup> Department of Electricity, Mulla-Sadra Ramsar Branch, Technical and Vocational University, Ramsar, Iran

<sup>c</sup> Nuclear Science and Technology Research Institute, Tehran, Iran

### PAPER INFO

#### Paper history:

Received 02 November 2021

Received in revised form 28 February 2022

Accepted 01 March 2022

#### Keywords:

Thyristor Switch Capacitor

Active Filter

Distribution System

Harmonic

### ABSTRACT

Instability of voltage is a problem that has been occurring in recent years due to excessive exploitation from equipment and an increase in demand for load across the distribution system. Shortage of the reactive power in the power networks, especially distribution networks, pushes the system toward voltage instability and leads to voltage drop as well as voltage fluctuations in the feeder. One of the potential solutions for compensation is to install thyristor switched capacitor (TSC). Although TSC can reduce the total costs of compensation, the static error will reduce compensation. For this purpose, an active power filter (APF) can be applied to resolve errors resulting from TSC due to features of continuous compensation and quick dynamic response. In this research, the combined method was presented, including TSC and APF of a controllable active power injection and with appropriate switching based on the study of voltage drop in the radial distribution networks and improvement of power quality. The suggested model was executed by MATLAB software, whereby results of improvement and provision of the stability conditions (dynamic and static) of voltage and current were observed.

doi: 10.5829/ije.2022.35.05.21

## 1. INTRODUCTION

Inappropriate quality of electricity means existence of change, sinuosity, or disturbance in the quantities of voltage, current, and frequency. All lead to breakdown or malfunction of the subscribers' equipment. The term 'electricity quality' has found plentiful applications in industrial countries and electricity industry. The topic of electricity quality covers a large number of available sinuosity and disturbances in the network [1]. In other words, a new look at the sinuosity and disturbances present in the power systems shows itself as a new topic deliberation over which is counted as one of the most important cases studies of power systems.

Problems related to the quality of power have been discussed and studied for a while by researchers in the electricity industry [2]. On the other hand, today, the attention of electricity companies and their subscribers has been increasingly directed to the electricity quality. The above point covers many disturbances that exist in

the electricity company. The subjects which are placed under the topic of discussion of electricity quality are not new concepts necessarily. On the other hand, considering the existence of numerous problems resulting from the undesirable quality of electricity, usage of appropriate ways to improve it appears necessary [3]. One of the most appropriate methods is to install thyristor switched capacitor (TSC). The application of TSC can reduce total costs of compensation, but the static error will reduce the compensation. For this purpose, we can apply an active power filter (APF) to resolve the error resulting from TSC because of continuous compensation features and quick dynamic response. APF is used extensively in the compensation of the active and harmonic power of distribution networks; but it is considerably expensive and its design is difficult.

Mobashsher et al. [4] introduced an Optimal Voltage Control (OVC) framework for island microgrids (MGs) as an integrated hierarchical control scheme. They started with the optimization of the bus voltage adjustment

\*Corresponding Author Email: [moj.khanalizadeh@gmail.com](mailto:moj.khanalizadeh@gmail.com)  
(M. Khanalizadeh Eini)

points in the third level, which were then effectively followed by a secondary control that controls the distributed energy sources. Regarding their primary level controllers, the control structure distributed here is proposed for both the third and secondary levels to benefit from higher reliability, avoidance of a breakpoint, and a relatively simple communication system. At the third level, a new distributed voltage protocol, based on Lyapunov's theory, is proposed to optimize power losses and voltage profile deviations in MG. To use such a multilevel controller in a real distribution system, further study is required. New power systems do not elevate abnormal voltages even for a short time as well. Voltage reduction commonly occurs as a result of excessive load leads to undesirable behavior and operation of the load, particularly induction engines. In the systems which are under heavy load, a decrease of voltage may suggest that the load approaches the durable stability limit (dynamic and heating), and or sudden voltage reduction may be established in response the connection of very large loads [5].

The excessive load has several origins. Decrease of load in specified parts of the daily load cycle leads to gradual voltage increase. If this excessive voltage is not controlled, it results in diminished useful lifespan of insulators. Sudden excessive voltage usually originates from the disconnection of load or other equipment of the system. In this research, through the study of voltage drop in the radial distribution networks and improvement of power quality as well as stabilization of voltage range of distribution networks within the limits of permitted changes, a combined method, including TSC and APF, was presented locally and diffusely through injecting controllable reactive power or proper switching.

This article uses TSC and APF, in a way that can reduce the total compensation costs as well as voltage and current fluctuations and harmonics. One of the most important options for compensation is to install thyristor switched capacitor (TSC) banks. Use of TSC can reduce total compensation costs, but static error lowers compensation. As such, Active Power Filter (APF) can be applied to eliminate TSC errors due to continuous compensation features and fast dynamic response. In this paper, first the influence of capacitor is examined on reduction of losses, parallel capacitor controlled by thyristor (TSC) and harmonic compensator of active power filters (APF). Then, in the fifth section, the proposed model is presented.

## 2. INFLUENCE OF CAPACITOR ON REDUCTION OF LOSSES

To examine how the capacitor influences the decline of losses, a feeder has been taken into consideration according to Figure 1.

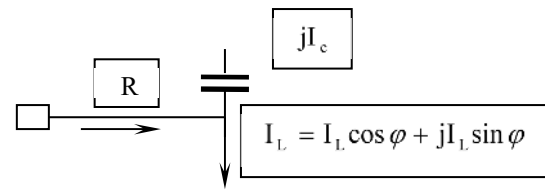


Figure 1. The effect of capacitors on loss reduction

In this figure, losses of active power of the feeder before installation of the capacitor are expressed as follows [1]:

$$P_{L_0} = I_0^2 R = (I_L \cos \varphi)^2 R + (I_L \sin \varphi)^2 R \quad (1)$$

where, R is the resistance of feeder path, the amplitude of current load, and the difference between current and voltage. After installation of the capacitor, we have:

$$P_L = I^2 R = (I_L \cos \varphi)^2 R + (I_L \sin \varphi - I_c)^2 R \quad (2)$$

Thus, the rate of change in losses could be obtained from the following relation upon installation of the capacitor:

$$\Delta P_L = P_{L_0} - P_L = 2(I_L \sin \varphi)I_c R - I_c^2 R \quad (3)$$

It is noted from Equation (3) that the change in rate of losses is a function of the reactive current in load ( $I_L \sin$ ) while active current in load ( $I_L \cos$ ) does not play a role in reduction of the losses. Thus, it can be concluded that installation of capacitor does not influence the losses resulting from active current of feeder and only affects the losses arising from reactive current of the feeder. Accordingly, in the problem capacitor placement, minimization of losses of feeder corresponds with minimization of losses of the reactive feeder.

## 3. PARALLEL CAPACITOR CONTROLLED BY THYRISTOR

Parallel capacitor controlled by thyristor (TSC) includes thyristor parallel and pair capacitors which connect and disconnect the capacitors. Figure 2 displays the façade of a TSC along with the number of the installed branches depends on the accuracy required by the compensator of active power. Considering numerous advantages of TSC, including simple designation and installation, TSC is preferred in many applications.

TSC can be used as support of feeding resource voltage, as well as for compensation of reactive power, harmonic filtering, etc. Typically, TSC is used for the compensation of reactive power. TSC injects capacitor reactive power into the system; thus, the power coefficient grows and voltage is controlled.

One of other objectives in using these tools is to improve transient stability. After examining the

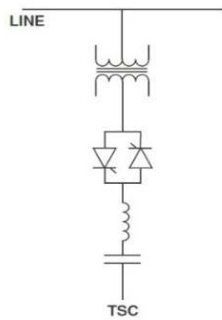


Figure 2. The main structure of TSC

advantages of TSC, several studies have been carried out on how to improve transient response of capacitors switching. Many methods have been presented in order to control TSC switching appropriately for improving transient operation and controlling the reactive power. In order to eliminate series reactor and express a reactor-free model, some researchers have used GTO pair [6]. Yet, costs will increase and control will become more complex upon (installation of GTO. Some other control techniques have been presented to improve transient stability and control reactive power as well. TSC can be configured and framed as various topologies, including triangular connection of capacitors, star connection of TSC, thyristor pair, and diode connection. Triangular connection of the capacitor bank with various semiconductor switches of power has been explored in several studies [7, 8]. These topologies can be compared in terms of structure and decomposition of voltage as well as current components [9]. The performance of these topologies is almost equal. TSC is used for different systems, including distribution systems. With time sequence of switches, they can be used to regulate voltage and compensate reactive power [10-12]. When a capacitor is connected by a sinuous voltage source, the current of capacitor will undergo severe fluctuation in case the initial voltage of the capacitor's two ends is higher than feed quantity. As a result, these changes in the current must be limited. Therefore, a series reactor with capacitor is used in TSC. The moment voltage of feeding the capacity ( $U_m$ ) is in the following form:

$$u(t) = \sqrt{2}V \sin(\omega_0 t + \alpha) \tag{4}$$

At time  $t=0$ , the switch with the initial value of the voltage current in zero capacitor is off. The value of moment current of the capacitor over time is obtained from the following equation:

$$i(t) = \sqrt{2}I_{ac} \cos(\omega_0 t + \alpha) - nB_c \left[ V_{co} - \frac{n^2}{n^2 - 1} \sqrt{2}V \sin \alpha \right] \sin \omega_n t - \sqrt{2}I_{ac} \cos \alpha \cos \omega_n t \tag{5}$$

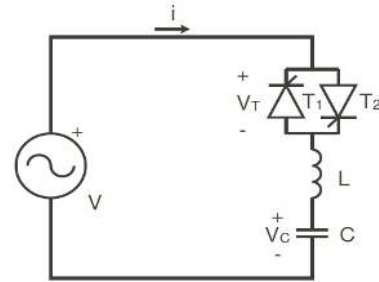


Figure 3. TSC Model with Seri Reactor

$$\begin{aligned} \omega_n &= \omega \sqrt{1 - \frac{L}{Z_c^2}} = \sqrt{\frac{L}{Z_c^2}} \cdot \omega = \frac{\omega}{X_c} \\ X_{c,app} &= \frac{V_{co} \sin \alpha}{\omega_n} = \frac{V_{co} \sin \alpha}{\frac{\omega}{X_c}} = \frac{V_{co} \sin \alpha X_c}{\omega} \end{aligned} \tag{6}$$

The quantity of reactor is selected in such a way that  $n > 3$  in the above equation. Note that resistance of the circuit in this equation has been considered to be negligible. If switching occurs in the 90-degree fire angle, we will have the following:

$$\begin{aligned} \cos \alpha = 0 &\Rightarrow \sin \alpha = \pm 1 \\ V_{co} &= \pm \sqrt{2} \frac{V n^2}{n^2 - 1} = \pm \sqrt{2} X_c I_{ac} \end{aligned} \tag{7}$$

TSC can be applied as a very useful element in the distribution system.

#### 4. HARMONIC COMPENSATOR OF ACTIVE POWER FILTERS

Recently, extensive usage of power of electronic equipment has caused harmonic disturbances in the power distribution system to increase. Arched furnaces, computer feeding sources, drives for speed regulation, etc are non-linear loads generating these disturbances. In three-phase systems, they can lead to imbalance of voltage and current as well as higher passing current. Reactive load, lack of balance and harmonic injection are as examples of problems related to power systems. There are several controlling methods to control APF. Theory of moment reactive power is one of the controlling methods as an example which has been extensively used [13]. Another method is based on recognition of harmonics [4]. Many studies have been conducted on the harmonic detection via closed-ring method as well [14-16]. Two samples of the harmonic compensation circuits with parallel APF are shown in Figure 4.  $Z_M$  shows impedance of line,  $Z_L$  indicates nonlinear load, and  $e_M(t)$  is source of system voltage. Figure 4(a) lacks feedback while Figure 4(b) is with feedback.

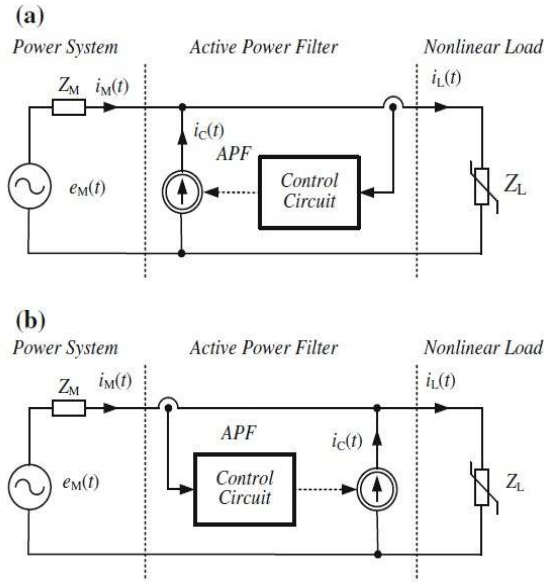


**Figure 4.** Harmonic compensation circuit with parallel APF (a) with feedback (b) without feedback

$$i_M(t) = i_L(t) - i_C(t) \tag{8}$$

In order to eliminate the harmonics, parallel APF injects current into the system. The current of line ( $i_M(t)$ ) can be achieved from the following equation: Three-phase parallel APF is one of the best systems for harmonic compensation, reactive power, imbalance, voltage drop, and voltage bulge. Indeed, APF control algorithms are very expansive [1, 5, 17].

**4. 1. Active Power Filter** Analog circuits were used in the past [18] extensively, while digital circuits are used considerably nowadays in order to control accurately. Today, application of digital active filter has been substantially expanded. Usage of digital control systems enables usage of more complicated algorithms and process digital signals [19]. Considering dynamism of APF, dynamic problems must thus be studied. As expressed earlier, active filters are applied in series, parallel, and mixed forms. Figure 5 depicts a parallel APF circuit. The circuit of Figure 4 relates to ‘with feedback’ active compensator circuit. Parallel APF injects current into the network for harmonic compensation and will lead to elimination of the harmonics as well as compensation of reactive power. This current is obtained from the following equation:

$$i_C(t) = i_L(t) - I_{H1} \sin(2\pi f_M t) \tag{9}$$

where,  $I_{H1}$  is the first harmonic amplitude and  $F_M$  is the first harmonic frequency. In the complete harmonic compensation, current of line  $I_M(t)$  will include the first harmonic of the line current:

$$i_M(t) = I_{H1} \sin(2\pi f_M t) \tag{10}$$

When the angle of phase between voltage of line  $u_1(t)$  and current of line ( $I_M(t)$ ) is zero, whereby the reactive power has been compensated well. In APF (Figure 5), three load currents of  $I_{L1}(t)$ ,  $I_{L2}(t)$  and  $I_{L3}(t)$  are measured and, then, used to determine the quantity of compensation currents of  $I_{C1}(t)$ ,  $I_{C2}(t)$ .

Three-phase inverter has consisted of a DC energy plus two  $C_1$  and  $C_2$  capacitors. The parallel APF control circuit is shown in Figure 6.

P-Q block diagram and parallel APF compensator for a three-phase system plus three balanced wires are shown in Figure 7.

Three-phase input signals of  $I_{L1}(t)$ ,  $I_{L2}(t)$ , and  $I_{L3}(t)$  are used as reference signals. The input signals of system (A-B) are calculated, using Clarke conversion, by the following method:

$$\begin{bmatrix} i_{La}(t) \\ i_{Lb}(t) \end{bmatrix} = \sqrt{\frac{2}{3}} \begin{bmatrix} 1 & -\frac{1}{2} & -\frac{1}{2} \\ 0 & \frac{\sqrt{3}}{2} & -\frac{\sqrt{3}}{2} \end{bmatrix} \begin{bmatrix} i_{L1}(t) \\ i_{L2}(t) \\ i_{L3}(t) \end{bmatrix} \tag{11}$$

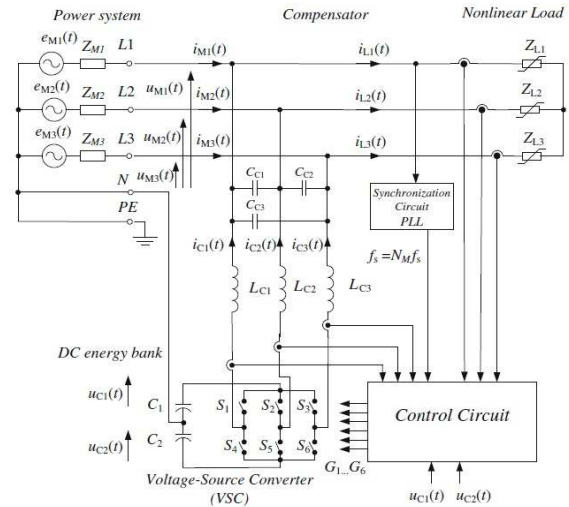


**Figure 5.** APF parallel three-phase compensator

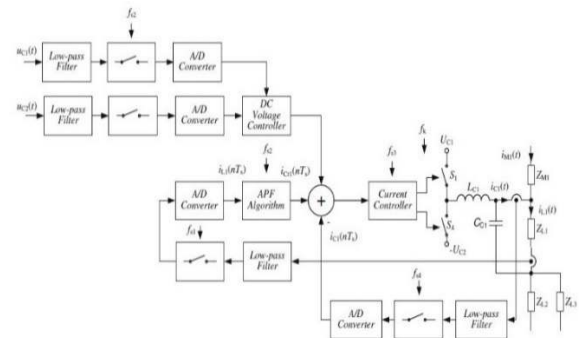


**Figure 6.** Parallel APF control circuit

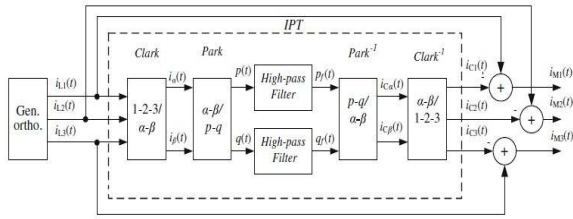


**Figure 7.** Block diagram of PQ and parallel to a three-phase three-wire APF compensation balance

After the conversion of P-Q park system:

$$\begin{bmatrix} p(t) \\ q(t) \end{bmatrix} = \begin{bmatrix} \cos(2\pi.f.t) & -\sin(2\pi.f.t) \\ \sin(2\pi.f.t) & \cos(2\pi.f.t) \end{bmatrix} \cdot \begin{bmatrix} i_{L\alpha}(t) \\ i_{L\beta}(t) \end{bmatrix} \quad (12)$$

From this change of system, 50 hertz component turns into DC components. Next, the DC component will be removed by a first rank upper-passing filter. Intensification frequency of the filter is equal to 10 hertz. Then, the achieved compensated signals of  $I_{C1}(t)$ ,  $I_{C2}(t)$ , and  $I_{C3}(t)$  are converted into a three-phase system without 50HZ component, using Park reverse conversion (Figure 8):

$$\begin{bmatrix} i_{c\alpha}(t) \\ i_{c\beta}(t) \end{bmatrix} = \begin{bmatrix} \cos(2\pi.f.t) & \sin(2\pi.f.t) \\ -\sin(2\pi.f.t) & \cos(2\pi.f.t) \end{bmatrix} \cdot \begin{bmatrix} p_f(t) \\ q_f(t) \end{bmatrix} \quad (13)$$

And conversion of reverse Clarke:

$$\begin{bmatrix} i_{c1}(t) \\ i_{c2}(t) \\ i_{c3}(t) \end{bmatrix} = \sqrt{\frac{2}{3}} \begin{bmatrix} 1 & 0 \\ -\frac{1}{2} & \frac{\sqrt{3}}{2} \\ -\frac{1}{2} & -\frac{\sqrt{3}}{2} \end{bmatrix} \cdot \begin{bmatrix} i_{c\alpha}(t) \\ i_{c\beta}(t) \end{bmatrix} \quad (14)$$

**5. SUGGESTED MODEL**

The model presented in this work is a combination of TSC and APF application. APF as a filter, is harmonic which can, by itself, eliminate not only a specific harmonic but also a harmonic with each frequency. The basis of exploitation from APF is decomposition of

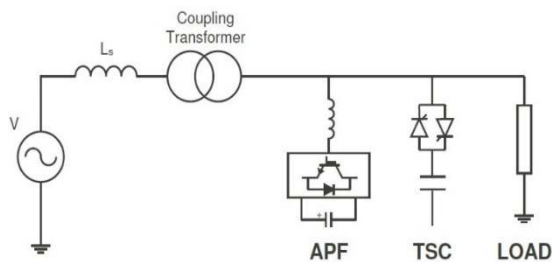


**Figure 8.** Single line diagram parallel with TSC and APF

components of the current fluctuation from the main current generating the load in a harmonic form and then obviating them. Using APF, the total reactive power cannot be compensated practically as the rate of power and costs of such compensation will grow considerably. TSC can be used as the main compensator of reactive power. Through combining these two elements, we will have an appropriate control. Figure 8 shows single-linear diagram of TSC and APF plus its connection to the power system. To feed the DC voltage, parallel capacitors have been connected to the converter. Note that if power system includes harmonic of voltage as well as harmonic of source, the tools must be used in the combined form to eliminate harmonic and reactive power control so that the best efficiency would be obtained. In this paper, combination of TSC and APF has been used to achieve the best performance optimally.

Based on requirements, thyristors of each step must be stimulated appropriately. In this state, TSC includes six thyristors in each stair, in response to which the controlling system must be able to stimulate these six thyristors. The control system of these six thyristors has been displayed in Figure 9.

By combining TSCs and their triangular connection, the control system will be as Figure 10. In this controlling system, three blocks of Figure 9 are combined, where the stimulation pulse of all TSC thyristors of TSC is generated in three-phase triangle. Productive controlling system of each TSC, via the control system, is capable of controlling the reactive power required by the system. Figure 11 compares the input voltage firstly with the reference voltage and then productive signal generated for each TSC. Also, the productive signal for each TSC includes six signals in order to stimulate every single thyristor.

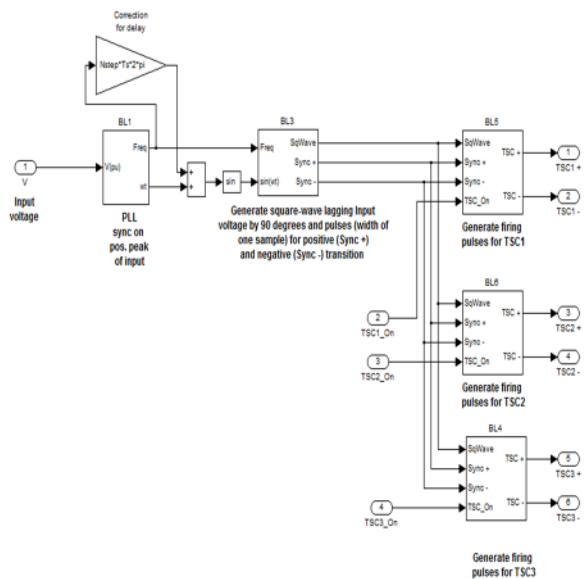


**Figure 9.** The control of any TSC unit

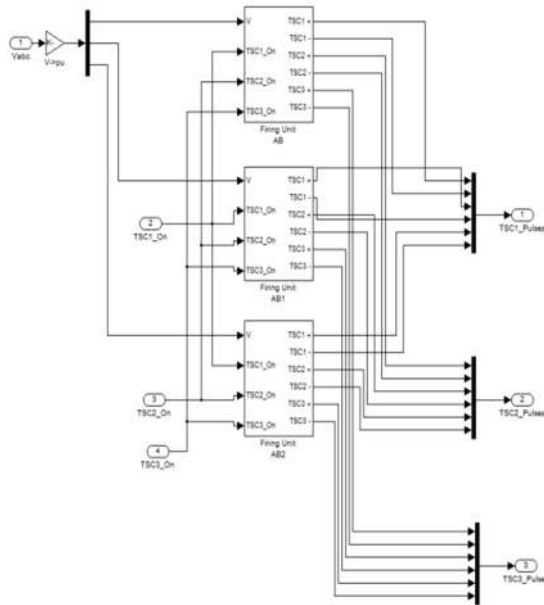


Figure 10. TSC model, control three-phase system

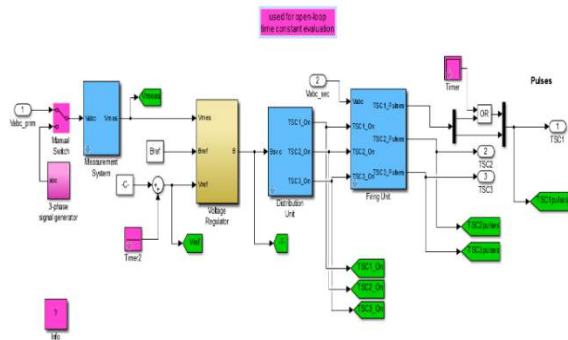


Figure 11. TSC model, control three-phase system with triangular connection

Figures 12 and 13 reveals the controlling system model of the active filter. As expressed, the active filter will change the input voltage in a desirable shape being proportional to the reference voltage.

Using this controlling model, the voltage harmonics and system current can be eliminated. Controlling model controls the pulse required by the inverter connected to capacitor and generates a pulse which is in proportion to the harmonic of voltage and current. Thus, line harmonic can be controlled. In Figure 14, capacitor and inverter along with a self and series resistances are connected. Series passive element leads to damping of harmonic and its elimination. Note that the capacity of capacitor is variable, which is used to control voltage while current harmonics is considered to be 2 milli farad. Higher filter selective capacity is tantamount to greater capability and power of the filter to eliminate the harmonics.

As expressed, the presented model is a combination of APF and TSC in order to obviate harmonic and

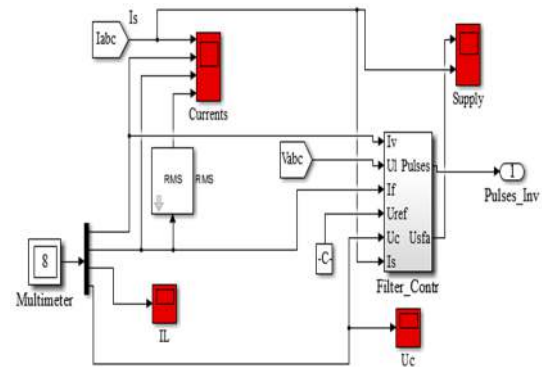


Figure 12. APF model control three-phase system

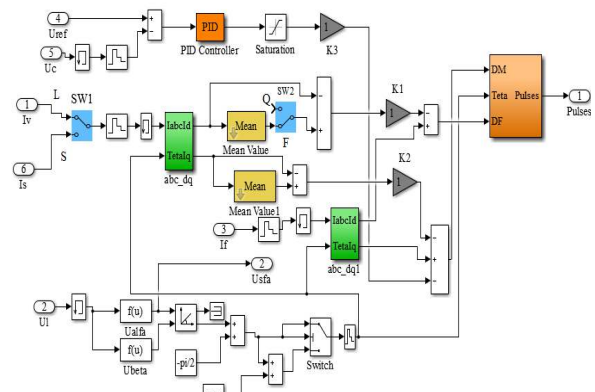


Figure 13. APF version control system in MATLAB

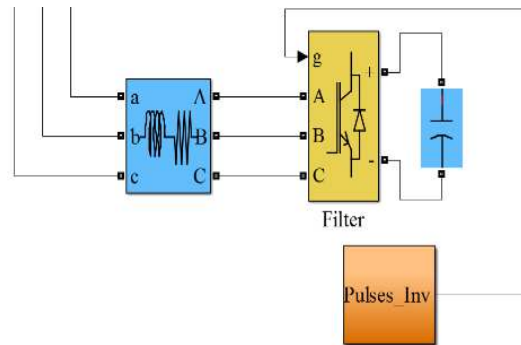


Figure 14. APF in MATLAB

compensation of the reactive power. Indeed, the presented system includes a radial system. In order to express the performance better, the suggested method of loads is in linear and non-linear forms. The distribution system consists of a 20 to 0.4kW transformer plus three linear loads and one non-linear load. The power of three linear loads is 100, 60, and 90 kW, respectively while that of the one non-linear load is 50kW. The power of each TSC has been considered to be 30 kW. If required, the power generated by each TSC can be selected as a desired value. The model presented in Figure 15 is represented in the MATLAB software.

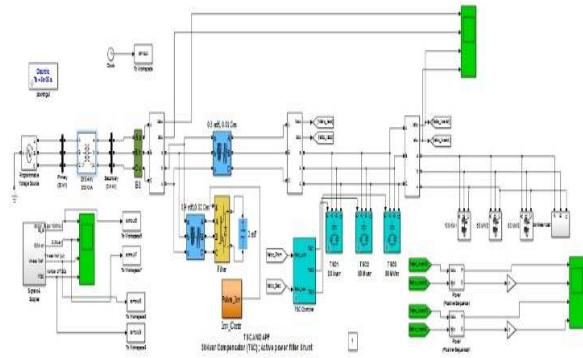


Figure 15. APF&TSC version control system in MATLAB

6. RESULTS OF SIMULATION

The presented model has been run in the Simulink environment using MATLAB software. Initially, this model is executed without using the suggested method and its results are compared with the results obtained from the model. The time required to express the optimum performance of such a structure has been selected for 3 seconds. In this state, the required TSC stairs are added to or subtracted from the system, and active filter always connects to the system and will lead to reduction of harmonics. As expressed, the power of each TSC is 30kW while the power of three linear loads is 100, 60, and 90 kW, respectively with the power of non-linear load being 50kW. Non-linear load leads to establishment of the voltage and current harmonic, whereby the voltage and current harmonic can be controlled well with a proper and combined performance. Figures 16, 17, and 18 display the quantity of voltage before compensation.

The harmonic sinuosity established in the voltage before compensation, in lieu of 20 cycles and at time of voltage durability, is equal to 8.06%. This produced harmonic shown in Figure 18 will lead to establishment of a high sinuosity in the shape of voltage wave. The effect of the harmonics established on the line voltage can be clearly seen in Figure 19.

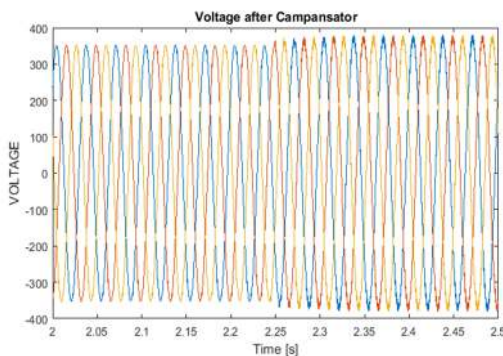


Figure 16. Line voltage after compensation

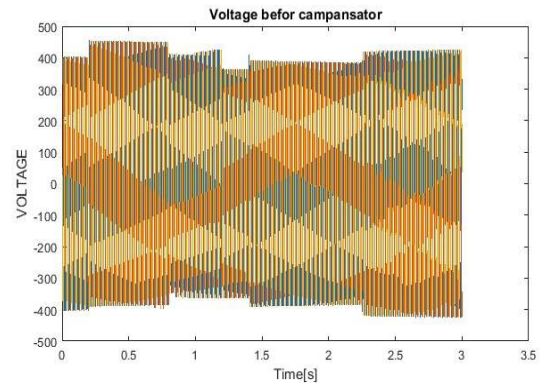


Figure 17. Vo Line voltage before compensation

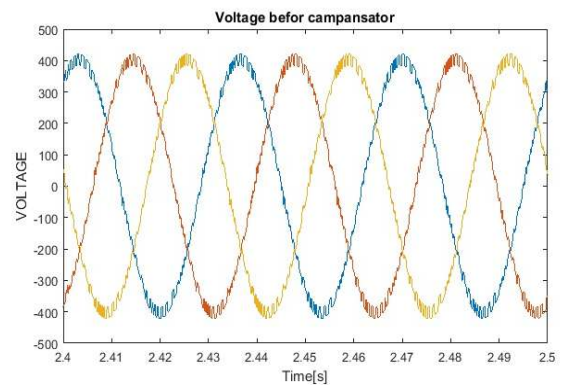


Figure 18. Line voltage before compensation

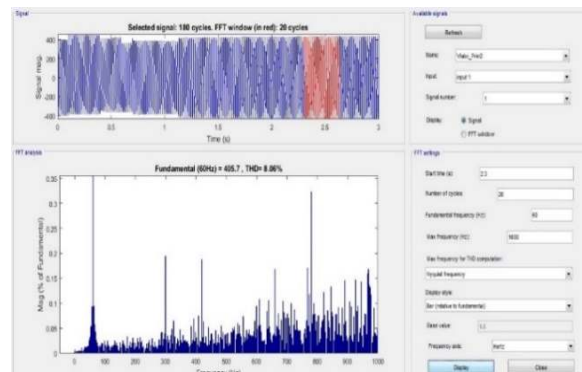


Figure 19. High-voltage harmonic distortion of the line voltage before compensation

Meanwhile, the current will also have the wave shape with a high harmonic in these conditions. Non-linear load will lead to sinuosity of the wave shape. Figures 20, 21 and 22 reveal the shape of the current waves before compensation. Sinuosity of the shape of current wave has been measured, similar to voltage, in 20 cycles in stable state as shown in Figure 23. Within this time range, the measured harmonic sinuosity (Total harmonic Distortion) had 1.83%. Harmonic sinuosity of the current has been expressed in Figure 22.

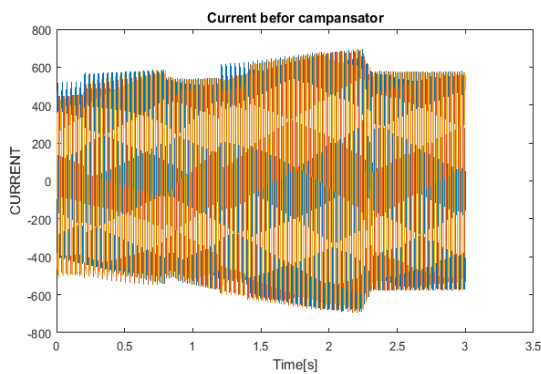


Figure 20. High-voltage line current to compensate THD

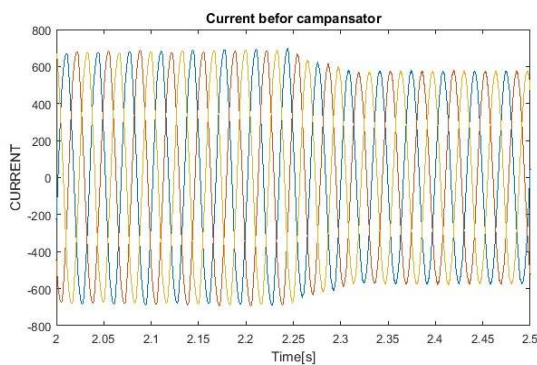


Figure 21. High-voltage line current to compensate THD

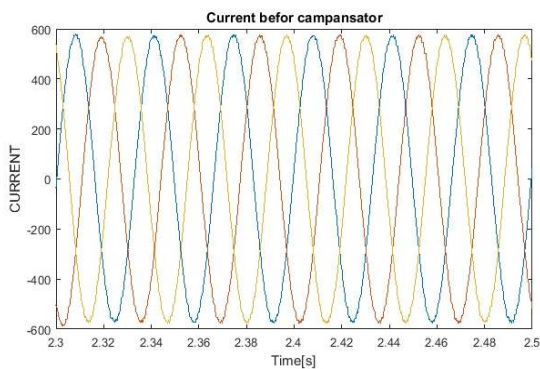


Figure 22. line voltage to compensate for the harmonic currents

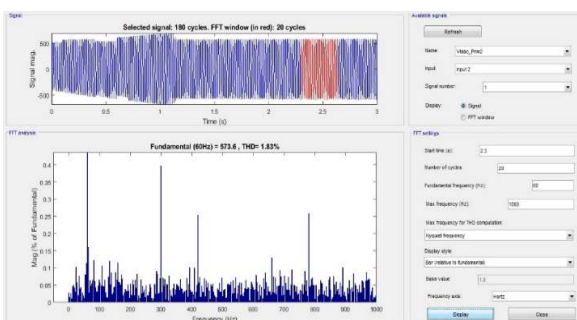


Figure 23. The line current before distortion compensation

As stated earlier, the presented model includes three steps of compensation of the parallel capacitor controlled by thyristor and as set of active filter. Steps of capacitor will lead to compensation of the required reactive power, and active filter will result in elimination and reduction of the system harmonics. In these conditions, capacitor steps determine voltage level, where the voltage level and line current can be controlled by increasing and decreasing the capacitor bank. Stairs of capacitor bank are shown in this model in Figure 24.

As displayed in Figure 25, in addition to that shape of voltage wave approaching the desirable voltage level of network, its harmonic sinuosity has decreased from 8.06 to 4.35. In other words, the established harmonic sinuosity became half, as shown in Figure 26.

After compensation, the current will have a wave shape with less harmonic sinuosity and lower current level. In this state, the line current more than 100 A has compensated less than the former state. This means that reactive power compensation along with active filter has led to improvement and reduction of level of line current. Considering this compensation, load voltage and current will become desirable as well. This reduction of current is shown in Figures 27, 28, and 29. In this state, harmonic sinuosity has dropped from 1.83 to 0.41 in Figure 30. Sinuosity of the line current in this state is one fourth before the compensation.

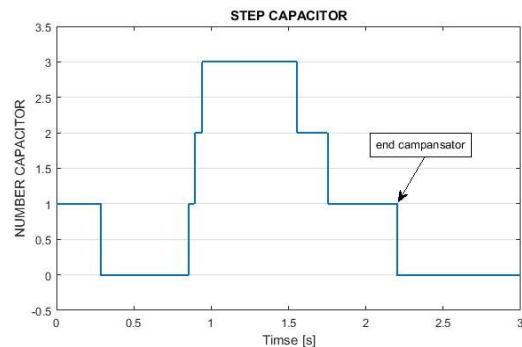


Figure 24. The added or subtracted capacitor steps for reactive power compensation

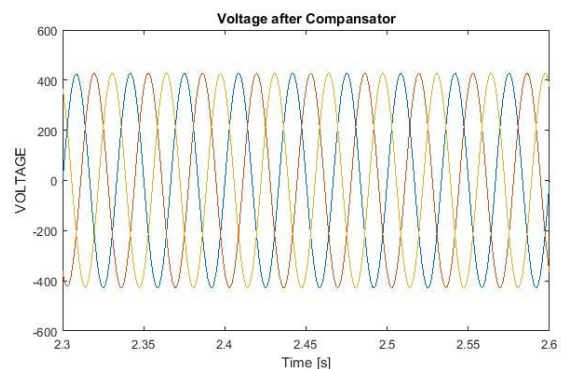


Figure 25. After line voltage compensation

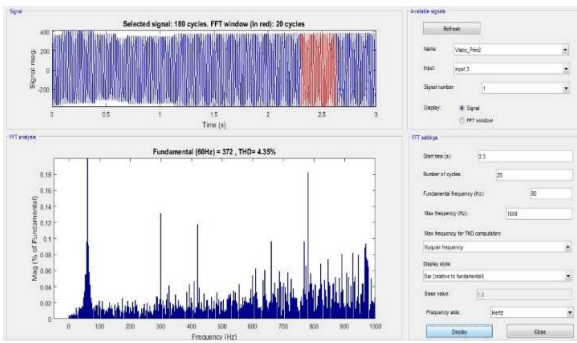


Figure 26. Line voltage distortion after compensation

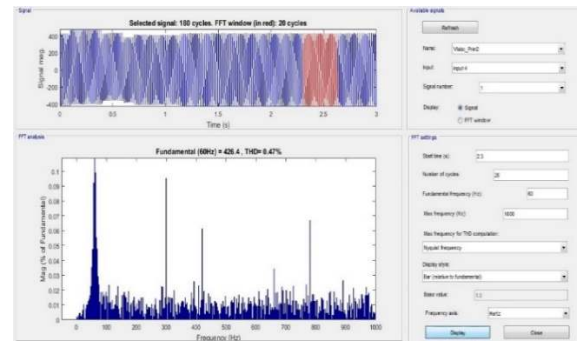


Figure 30. The line current after distortion compensation

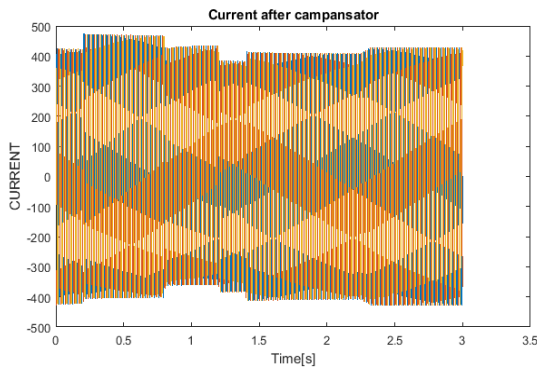


Figure 27. The current line after compensation

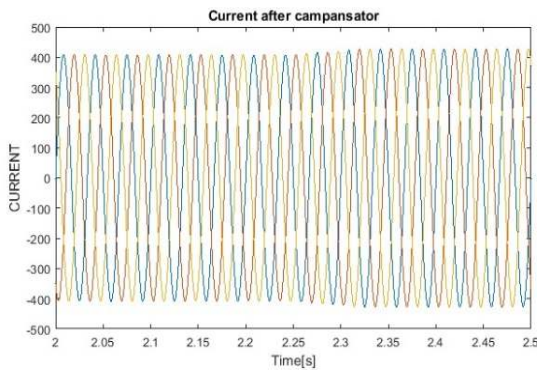


Figure 28. The current line after compensation

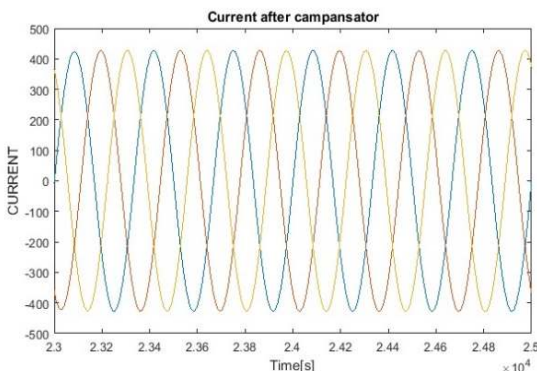


Figure 29. The current line after compensation

### 7. CONCLUSION

Exploitation of electric equipment of the power system is always encountered with new challenges. In the distribution networks, in response to increase of demand for reactive power, the system is pushed towards instability of voltage drop and voltage fluctuations in the feeder. Usage of thyristor switched capacitor (TSC) can reduce total costs of compensation. We can apply this APF in order to eliminate error resulting from (TSC) due to continuous compensation features and dynamic swift response. APF is used extensively in the compensation of the reactive and harmonic power of distribution systems, but it is expensive heavily and its design is difficult. In this paper, a combined method, including TSC and APF, was presented locally and diffusely through injecting controllable reactive power and appropriate switching based on study of voltage drop in radial distribution networks to improve the power quality and stabilize the voltage range of distribution networks within the limits of allowed changes. The suggested model was implemented by MATLAB software, where results of improvement and provision of the stability conditions (dynamic and static) of the voltage and current were observed.

### 8. REFERENCES

1. Duarte, S.N., de Souza, B.C., de Almeida, P.M., de Araújo, L.R. and Barbosa, P.G., "A compensation strategy based on consumer's voltage unbalance assessment for a distribution static synchronous compensator", *IEEE Latin America Transactions*, Vol. 18, No. 01, (2020), 156-164, doi: <https://doi.org/10.1109/TLA.2020.9049473>
2. Shahane, R.T., Borghate, V.B., Krishnan, R.R. and Nachankar, P.P., "Load compensation for non-stiff source system using mirp theory for unbalance and non-linear load using dstatcom", in 2018 International Conference on Power, Instrumentation, Control and Computing (PICC), IEEE. (2018), 1-5.
3. Feng, G., Cheng, X. and Zong, X., "Compensation point configuration method of static var generator based on clustering algorithm", in 2020 IEEE 4th Information Technology, Networking, Electronic and Automation Control Conference (ITNEC), IEEE. Vol. 1, (2020), 2055-2058.

4. Mobashsher, M.M., Keypour, R. and Savaghebi, M., "Distributed optimal voltage control in islanded microgrids", *International Transactions on Electrical Energy Systems*, Vol. 31, No. 11, (2021), e13045, doi: <https://doi.org/10.1109/PVSC43889.2021.9518943>
5. Liberado, E.V., Souza, W.A.d., Pomílio, J.A., Paredes, H.K. and Marafão, F.P., "Design of static var compensator using a general reactive energy definition", in International School on Nonsinusoidal Currents and Compensation 2013 (ISNCC 2013), IEEE. (2013), 1-6.
6. Rastogi, M. and Bhat, A.H., "Reactive power compensation using static synchronous compensator (statcom) with conventional control connected with 33kv grid", in 2015 2nd International Conference on Recent Advances in Engineering & Computational Sciences (RAECS), IEEE. (2015), 1-5.
7. Wang, M., Wang, X., Qiao, J., Wang, L. and Jin, D., "Advance coordinative control for the pcc voltage fluctuations of the asynchronous wind generator based on the statcom with tsc", in 2019 22nd International Conference on Electrical Machines and Systems (ICEMS), IEEE. (2019), 1-6.
8. Nandi, S., Biswas, P., Nandakumar, V. and Hedge, R., "Two novel schemes suitable for static switching of three-phase delta-connected capacitor banks with minimum surge current", *IEEE Transactions on Industry Applications*, Vol. 33, No. 5, (1997), 1348-1354, doi: <https://doi.org/10.1109/28.633816>
9. Ghosh, S. and Ali, M.H., "Augmentation of power quality of grid-connected wind generator by fuzzy logic controlled tsc", in 2018 IEEE/PES Transmission and Distribution Conference and Exposition (T&D), IEEE. (2018), 1-9.
10. Pathak, M.Y. and Jamnani, J., "Design and hardware implementation of svc using thyristorised control for improving power factor and voltage profile of inductive loads", in 2016 IEEE 6th International Conference on Power Systems (ICPS), IEEE. (2016), 1-6.
11. Yuqin, X., Zengping, W. and Hai, Z., "The automatic following control of arc suppression coil with thyristor switched capacitors", in 2006 1ST IEEE Conference on Industrial Electronics and Applications, IEEE. (2006), 1-5.
12. Kallaste, A., Kutt, L., Bolgov, V. and Janson, K., "Reactive power compensation for spot welding machine using thyristor switched capacitor", in 2008 Power Quality and Supply Reliability Conference, IEEE. (2008), 241-245.
13. Czarniecki, L.S. and Haley, P.M., "Unbalanced power in four-wire systems and its reactive compensation", *IEEE Transactions on Power Delivery*, Vol. 30, No. 1, (2014), 53-63, doi: <https://doi.org/10.1109/TPWRD.2014.2314599>
14. Kanno, Y., Toba, T., Shimamura, K. and Kanekawa, N., "Design method for online totally self-checking comparators implementable on fpgas", *IEEE Transactions on Very Large Scale Integration (VLSI) Systems*, Vol. 28, No. 3, (2020), 726-735, doi: <https://doi.org/10.1109/TVLSI.2019.2946180>
15. Hosseini, S., Ledwich, G. and Shannon, G., "Transient minimization within static var compensated distribution systems", in proceedings of the conference EECON91. (1991), 90-94.
16. Zhang, Z., Liu, Y. and Guan, H., "Unbalance loads compensation with statcom based on pr controller and notch filter", in 2018 10th International Conference on Modelling, Identification and Control (ICMIC), IEEE. (2018), 1-6.
17. Ai-jun, H., Fei, S. and Wen-jin, C., "Zero-cross triggering technology of series scrs with optical fiber at medium voltage: Application for thyristor switched capacitor", in 2005 IEEE/PES Transmission & Distribution Conference & Exposition: Asia and Pacific, IEEE. (2005), 1-5.
18. Ko, W.-H. and Gu, J.-C., "Design and application of a thyristor switched capacitor bank for a high harmonic distortion and fast changing single-phase electric welding machine", *IET Power Electronics*, Vol. 9, No. 15, (2016), 2751-2759, doi: <https://doi.org/10.1049/iet-pel.2016.0310>
19. Candy, J.C. and Temes, G.C., "Multitbit oversampled a/d convertor with digital error correction", (1992), doi: <https://doi.org/10.1109/9780470545461.ch24>

---

### Persian Abstract

---

#### چکیده

ناپایداری ولتاژ یکی از مشکلاتی است که در سال های اخیر و به دلیل بهره برداری بیش از حد از تجهیزات و افزایش تقاضا برای بار در سیستم توزیع رخ داده است. کمبود توان راکتیو در شبکه های قدرت به ویژه شبکه توزیع، سیستم را به سمت ناپایداری ولتاژ سوق می دهد و منجر به ایجاد افت ولتاژ و نوسانات ولتاژ در فیدر فشار ضعیف می-شود. یکی از مهم ترین گزینه های پیشنهادی برای جبران سازی، نصب بانک های خازن سوئیچ شونده با استفاده از تریستور (TSC) است. استفاده از TSC می تواند کل هزینه های جبران سازی را کاهش دهد اما خطای استاتیکی باعث کاهش جبران خسارت می شود. برای این منظور فیلتر توان فعال (APF) را می توان برای از بین بردن خطاهای حاصل از TSC به دلیل ویژگی های جبران پیوسته و پاسخ دینامیکی سریع اعمال کرد. در این تحقیق روش ترکیبی شامل TSC و APF تزریق توان اکتیو قابل کنترل و با سوئیچینگ مناسب با مطالعه افت ولتاژ در شبکه های توزیع شعاعی و بهبود کیفیت توان ارائه شد. مدل پیشنهادی توسط نرم افزار MATLAB اجرا شد و نتایج بهبود و تامین شرایط پایداری (دینامیک و استاتیکی) ولتاژ و جریان مشاهده گردید.

---



## Fouling Performance of A Horizontal Corrugated Tube due to Air Injection

H. Sharifi<sup>a</sup>, P. Ahmadi Moghaddam<sup>\*a</sup>, S. Jafarmadar<sup>b</sup>, A. M. Nikbakht<sup>a</sup>, A. Hosainpour<sup>a</sup>

<sup>a</sup> Department of Bio Systems Engineering, Faculty of Agriculture, Urmia University, Urmia, Iran

<sup>b</sup> Department of Mechanical Engineering, Urmia University, P.O.Box 165, Urmia, Iran

### PAPER INFO

#### Paper history:

Received 23 October 2021

Received in revised form 3 February 2022

Accepted 21 February 2022

#### Keywords:

Fouling

Air Injection

Molasses of Sugar Beet

Heat Transfer Coefficient

### ABSTRACT

In the present study, the fouling performance of a circumferentially corrugated tube was probed due to the air injection. The molasses of sugar beet was considered as the working fluid. The tube was considered to be under constant heat flux. Also, the flow rate of the molasses of sugar beet was considered to be constant. Five different flow rates of the airstream were considered to check the effect of airflow rate. The flow rate of working fluid was kept at the constant flow rate of 2 L/min. The tests were conducted for 5000s (84 minutes). For a better understanding of the nature of the flow, the structure of two-phase steam was recorded via a Canon SX540 Camera. The results presented that the air injection in the corrugated tube will completely change the structure of the working fluid which will bring a very turbulent structure for the working fluid. The thermal results presented that during the testing time, the air injection will keep the heat transfer coefficient about 120% higher than a single-phase stream. The mass evaluation results revealed that the air injection could decrease the weight of fouled substance up to 75%.

doi: 10.5829/ije.2022.35.05b.22

## 1. INTRODUCTION

The fouling phenomenon is known as the most important problem in industrial systems and the production processes [1, 2]. The fouling phenomenon in thermal systems not only brings up many maintenance costs but also, reduces the thermal efficiency of the systems which leads to a reduction of the efficiency of the whole system [3]. In recent decades, corrugated tubes are proposed as the ultimate solution to be used in thermal systems since they have better thermal performance and their anti-fouling nature in comparison with the smooth tubes [3, 4]. The ejection phenomena and the throttling effect of the corrugations lead to more stability of the small pieces of the fouling substances and weaken the effect of gravity on these parcels. On the other hand, the corrugations interrupt the development of the boundary layer and increase the turbulence intensity of the mainstream which leads to the improvement of heat transfer and increases the stability of the parcels within the flow stream [5-7]. Furthermore, in recent years, the application of air injection is proposed as a very effective method for heat

transfer improvement within thermal systems [8, 9]. However, very rare studies have probed the simultaneous effect of air injection and corrugation on the fouling and thermal performance of a thermal system. In the following, a summary of the studies on using both corrugated tubes, air injection, and the fouling phenomenon is provided.

Li et al. [10] investigated the effect of H-type fins on the thermo-hydraulic and fouling performance of a tube heat exchanger. Their results presented that H-type fins with three pairs of grooves could reduce the fouling rate up to 23.7%. Trafczynski et al. [11] evaluated the fouling performance of a heat exchanger and proposed applicable suggestions to better schedule the operation of the heat exchanger. The effect of Sodium carboxymethyl cellulose (SCMC) on the fouling performance of a heat transfer surface was investigated by Xu et al. [12]. Through their study; they probed the effect of different parameters of solution mass flow rate, solution inlet temperature, and solution viscosity. Chapela et al. [13] probed a transient model of thermal performance and fouling phenomena of a biomass shell boiler. Tang et al.

\*Corresponding Author Institutional Email: [P.ahmadi@urmia.ac.ir](mailto:P.ahmadi@urmia.ac.ir)  
(P. Ahmadi Moghaddam)

[14] proposed the honeycomb circular tube bundles as a new design for the fouling reduction within a shell and multitude heat exchanger. Furthermore, they developed new correlations for Nusselt number, friction factor, and fouling thermal resistance. Their results revealed that the predicted results from the correlations had only a 4% deviation from the results of numerical simulations. Zhao et al. [15] investigated the thermal performance and fouling properties of an evaporating falling film through a vertical tube. Through their study, they compared the effect of the porous surface with a plain tube. Their results revealed that although the thermal performance of a tube with a porous surface was a little worse than the plain tube the fouling rate of the tube with a porous surface was one-tenth of the that associated with the plain tube. Wang et al. [16] investigated the fouling properties of a finned tube heat exchanger. Through their study, the effect of different tubes and arrangements were evaluated. Their finding presented that double H-type fins could slightly reduce fouling. The fouling performance of an enhanced tube utilized in a cooling tower was probed by Shen et al. [17]. They developed a model for predicting the fouling residence which presented a maximum error of 0.0645. In another study, Wang et al. [18] compared the thermal and fouling performance of a plain tube with a helically ribbed tubes. They investigated Reynolds number was considered to be 16000. Their results presented a better fouling performance for ribbed tubes when compared to plain tube. Son et al. [19] used the air injection as an anti-fouling method for a plate type microfiltration membrane. Through their study, they investigated the effect of continues and periodic air injection algorithms. Their results revealed a very effective influence of periodic air injection on the reduction of fouling through the considered membrane. Sinaga et al. [20] conducted an experimental investigation and probed the effect of air injection on the thermal performance of a double tube heat exchanger. They mentioned that the air injection increases the turbulence intensity of the overall stream which would lead in better thermal and fouling performance of the heat exchangers.

In the present study, the simultaneous effect of using circumferential corrugation and air injection on the thermal and fouling performance of a straight heat exchanger are evaluated and compared with a plain tube heat exchanger. From the above-provided literature and based on the authors' knowledge, almost no investigation had considered the effect of the two aforementioned factors. Indeed, the available papers in literature are divided into two main groups. The first group examines, only the THERMAL performance of corrugated tubes in the presence of NONE-boiling gas liquid two phase flow and there was almost **NO** investigation on the Fouling performance of the corrugated tube together with NONE-boiling two phase flow. Besides, the second group

reported the effect of boiling gas liquid two phase flow on the thermal and fouling performance of the corrugated tube in the presence of boiling two-phase flow. Indeed, the nature and application of boiling two phase flow and None-boiling two phase flow is completely different. This makes the necessity of investigation on the fouling performance of none-boiling two phase flow inside the corrugated tubes. Furthermore, the available papers on thermal performance of none-boiling two phase flow inside the corrugated tubes have focused on steady flow, whereas the nature of streams that deal with fouling phenomena is unsteady which should be addressed even in more future papers. Thus, it would be of great importance for thermal engineers to probe the effect of both air injection and circumferential corrugation on the fouling performance of a straight tube.

## 2. EXPERIMENTAL METHODOLOGY AND PROCEDURE

Figure 1 presents the schematic of the test rig provided for carrying out the considered tests. The air injection method utilized in this study was previously used by different researchers [5, 21, 22]. The advantage of this injection method is that since it is located outside the heat exchange unit, it could be utilized for the existing thermal systems in industrial applications. From Figure 1, it could be realized that the test rig has consisted of two main parts. The first one was the air supply part which was consisted of a compressor, two valves, and one air flow rate measuring Rotameter. The second one is the working fluid supply system which was comprised of a lotion tank (which was used for storing the molasses of sugar beet), two control valves, and one lotion flow rate measuring Rotameter.

The air was injected into the lotion stream through the mixing well. Then the two-phase stream had been passed through the test section. Passing through the test section, the lotion gained thermal energy from the heated walls of the corrugated tube. The thermal energy was produced via heater wires that were wrapped around the tube at the whole length of the test section. At the final stage and after passing the test section, the two-phase lotion was directed into a heat exchanger to lose its thermal energy and to find the initial temperature. Then, this two-phase stream was again directed into the lotion tanks. Through the lotion tank, the air was divided from the molasses of sugar beet due to the buoyancy effect.

For the data recording, two evaluation methods were conducted. First weight variation analyses and second heat transfer coefficient evaluation. The heat transfer coefficient evaluation is an indirect method for understanding the thermal resistance variation due to the fouling phenomena. For measuring the heat transfer coefficient, the surface temperatures of the corrugated

and helical tubes were measured. Also, the inlet and outlet temperature of the lotion was measured too. It is worth mentioning that the inlet temperatures of the air stream and working fluid (molasses of sugar beet) were kept almost constant and were about  $12^{\circ}\text{C} \pm 0.5$  and  $14^{\circ}\text{C} \pm 0.5$ , respectively. Also, the mass weighting evaluation was performed by a scale (Model: Bama 111) which had an accuracy of  $\pm 0.1$  g. the temperature recording system was a 12 Channel digital data logger (Model: Lutron 4208SD) which had coupled with K type thermocouples. The aforementioned system provides an accuracy of  $\pm 0.5^{\circ}\text{C}$  for measuring the temperature. It is worth mentioning that the running test time was considered to be 5000s (about 84minute). Indeed, there was no clear concept or restriction on defining testing time through the literature. However the authors followed the published research work by Peyghambarzadeh et al. [23] and tried to determine the testing time in the range of what they have considered.

Table 1 present the different cases considered in the present study simultaneous with the geometrical properties of both plain and corrugated tube.

It is noteworthy that the uncertainty analysis was performed based on the method proposed by Moffat [24]. This method was previously used by numerous researchers [5, 7, 20, 25, 26]. The uncertainty for heat transfer coefficient and weight were found to be a maximum of 8.65% and 5%, respectively.

### 3. PARAMETER DEFINITION

The time-dependent heat transfer coefficient was defined as follows:

The total thermal energy gained by the working fluid could be measured via the following equation. At which the  $\dot{m}$ ,  $C_p$ ,  $T_{out}$  and  $T_{in}$  denote the mass flow rate, specific heat capacity, the outlet temperature of the working fluid, and the inlet temperature of the working fluid respectively.

To define the properties of multiphase flows, different theories were developed, however, each of these could provide the proper results in a certain range of air and gas flow rates. In lower values of gas flow rate, the two-phase stream properties associated with thermal behavior could be assumed to be equal to the liquid phase. This is since the mass flow rate and the Cp of the

air flow rate are significantly less than the water flow rate. It should be noted that many experts [27–30] have stated that this effect is negligible. Through the present investigation, the maximum fraction between the air mass flow rate and water mass flow rates was 0.0053 which denotes that the total energy gained by the air stream is so less than that of the water stream. Consequently, the effect of the definition type of Cp of the gas stream could be neglected [30-33].

$$Q(t) = \dot{m}(t)C_p(T_{out}(t) - T_{in}(t)) \quad (1)$$

For finding the convective heat transfer coefficient, the above calculated thermal energy should be equal to that gained via the convective method. Which results in a calculation of the heat transfer coefficient in the following type.

$$h(t) = \frac{Q(t)}{A(\bar{T}_w(t) - T_b(t))} \quad (2)$$

As mentioned before mass analyses were performed in this study. For the better presentation of results, the following parameters were defined in this study.

In this study, the difference in the initial weight of the tube and the weight of the tube at the end of each test is defined as  $\beta$  and is defined as follows:

$$\beta = W_{t=5000}(t) - W_i \quad (3)$$

At the above equation the  $W_{t=5000}(t)$  is the weight of tubes at the end of run time and the  $W_i$  is the initial weight of the tube. In the results section the  $\beta_p$  and  $\beta_c$  are defined as the weight difference of plain tube and corrugated tube, respectively.

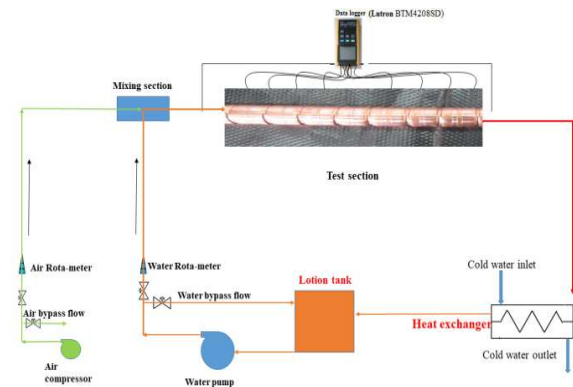


Figure 1. Presentation of a schematic view of the test rig

TABLE 1. Various cases are considered in the present study

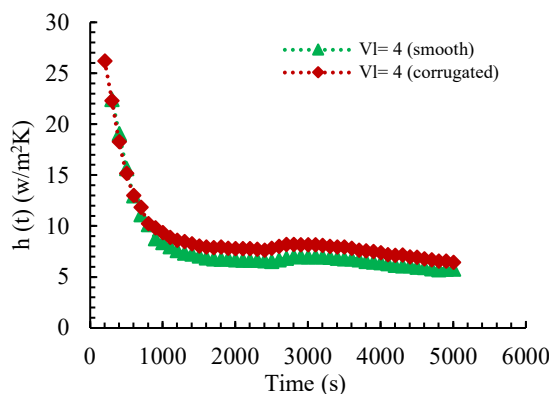
Tube type	Water flow rate (L/min)	Airflow rate (L/min)	Thermal energy (W)	Airflow inlet temperature ( $^{\circ}\text{C}$ )	Liquid flow inlet temperature ( $^{\circ}\text{C}$ )
Plain	2	0,1,2,3,4,5	1000	12	14
Corrugated	2	0,1,2,3,4,5	1000	12	14

Also, the weight difference percentage is defined as follows:

$$\alpha = \frac{W_{t=5000}(t) - W_i}{W_i} \times 100 \tag{4}$$

#### 4. RESULTS AND DISCUSSIONS

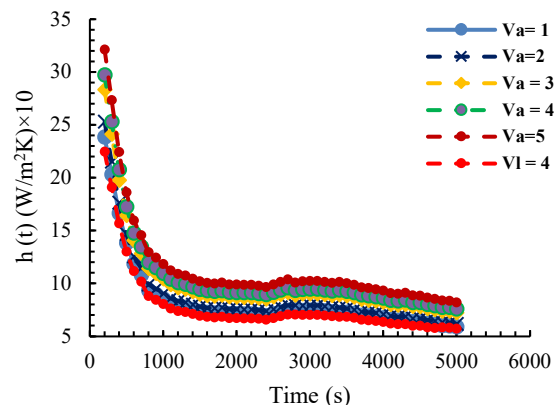
**4. 1. Thermal Analysis** In this section, the time-dependent heat transfer coefficient of the both plain tube and corrugated tube are provided in case of both air injection and single-phase flow. In Figure 2, the time-dependent heat transfer coefficient of the plain tube and corrugated tube in the case of single-phase flow is presented. The flow rate of the liquid phase ( $V_L$ ) was kept constant and it was equal to 4 L/min. From Figure 2, it could be realized that through the corrugated tube, the heat transfer coefficient is more than that related to the smooth tube through the run time. Since all the parameters were equal between the smooth and corrugated tubes, the difference in the heat transfer coefficient is related to the fouling resistance of the two tubes which was due to higher turbulence intensity of flow inside the corrugated tube. Actually, the smooth tubes gain more fouled substance on their walls and this causes to increment of the fouling resistance of the tube which leads to a reduction of heat transfer coefficient. However, for the corrugated tube, the corrugated walls increases the turbulence intensity of the liquid stream which results in longer remaining of the fouling parcels through the liquid stream and prevent the fouling of the parcels through the working fluid. In fact, the corrugations provide two throttling and ejection effects at the entrance and existence of the corrugated regions. This causes a fluctuation in the pressure drop and changes the directions of the movement of the parcels through the working fluid. All these together prevent the creation of a fouling layer through the tube and reduce its' thickness which leads to the increment of heat transfer coefficient.



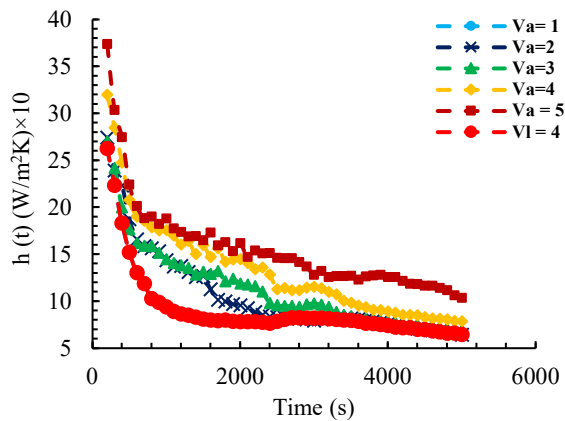
**Figure 2.** Variation of heat transfer coefficient vs time for single-phase stream

Figure 3 presents the variation of the time-dependent heat transfer coefficient in the case of air injection. As mentioned before the liquid flow rate was kept constant and was equal to 4 L /min; however, five different airflow rates ( $V_a$ ) of 1, 2, 3, 4, and 5 L /min were considered to check the effect of air injection flow rate. As could be realized from Figure 3, the air injection has increased the heat transfer coefficient through the running time. Also, by the increment of air injection rate, the increment of the airflow rate has significantly increased. Indeed, the air injection causes the creation of air bubbles/ slugs within the liquid phase. The coincidence between the air bubbles and liquid phase causes to increment of the turbulence intensity of the flow stream and results in more stability of the fouling parcels within the flow stream. Consequently, the fouling layer develops at a more slow rate and the heat transfer coefficient remains at high values. By the increment of air injection flow rate, the air bubbles get bigger resulting in a more powerful coincidence with the solid body of the tube walls and the working fluid parcels. By the increment of the reaction between the air bubbles and working fluid parcels the stability of the fouling parcels within the working fluid increases. On the other hand, the movement of the air slugs on the top of the tube (horizontal orientation of tube is considered in this paper) sweeps the fouling layer and prevents it from getting developed. Consequently, the heat transfer coefficient achieves higher values.

Figure 4 presents the variation of heat transfer coefficient for the cases with air injection through the corrugated tube. From Figure 4, it could be realized that the influence of air injection of the performance enhancement through the corrugated tube is more than that in the smooth tube. Indeed, through the corrugated tube, the coincidences of the bubbles with grooved walls cause the creation of vortexes within the liquid phase. These vortexes prevent the accumulation of parcels on the heated walls of the tube which enhances the fouling performance and increases the heat transfer coefficient.



**Figure 3.** Variation of heat transfer coefficient vs time for two-phase and single phase flows within smooth tube



**Figure 4.** Variation of heat transfer coefficient vs time for two-phase and single phase flows within corrugated tube

By comparing Figures 3 and 4, it could be realized that the curves associated with Figure 3 are more smooth than those related to Figure 4 (corrugated tube). It is due to the very turbulent nature of the flow inside the corrugated tube. To understand this, the flow structure of the gas/liquid two-phase flow through the corrugated tube was probed within a glass-made corrugated tube. Through the glass-made corrugated tube, all the hydraulic properties of the flow stream were identical to that in the real heated test section. Figure 5 presents the flow structure of the gas/liquid two-phase flow within the corrugated tube. It is worth mentioning that for capturing the presented flow structures, a Canon SX 540 camera was used which had a shutter speed of 1/2000s. Also, it should be noted that for investigating the flow structure, water was used instead of molasses of sugar beet. It is because due to the darkness of the molasses of sugar beet, capturing the appropriate photos was impossible. However, it should be noted that due to the appropriate viscosity of molasses of sugar beet in comparison with water, the flow structures of these two combinations of gas and liquid could be assumed to be almost identical [34, 35].

From Figure 5, it could be seen that as the air gets injected into the corrugated tube, the air slugs and air bubbles together become created. The interface of air slugs with the water phase is very wavy within the corrugated tube. However, the interface of air slugs with the water phase within the smooth tube has consisted of a very smooth line. It is seen that by the increment of air injection flow rate, numerous tiny bubbles are created in the flow. It could be seen that by the increment of the number of the tiny bubble the dispersion form of the bubbles also changes. Indeed, in the low air injection flow rates, the bubbles move at the upper half of the tube whereas in the higher flow rates the bubble disperse at the whole cross-section of the tube. This way of dispersion significantly affects the accumulation of the fouling parcels and prevents the creation of a fouling

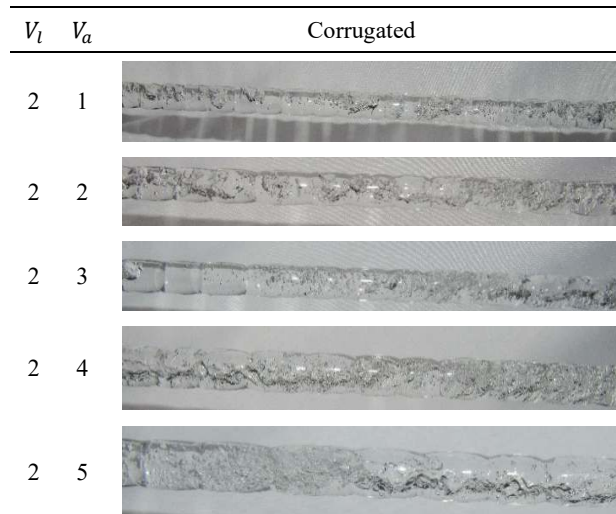


**Figure 5.** Flow structures due to air injection through the corrugated tube

layer. Consequently, the fouling resistance remains in minor values and the heat transfer coefficient becomes in higher values than that in single-phase flow.

**4. 2. Weight Variation Analysis**

Figure 6 A and B, presents the mass variation results for the plain tube and corrugated tube, respectively. It could be seen that the maximum accumulated mass of fouling substance was related to the cases without air injection at both the plain tube and corrugated tube. It could be easily found

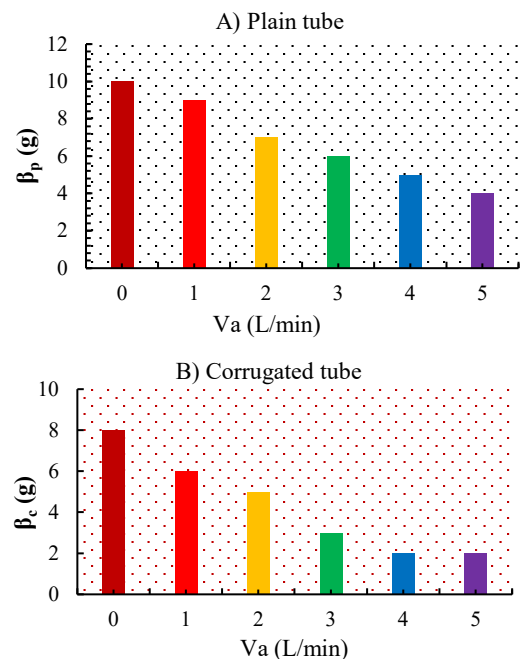


**Figure 6.** Mass variation results, A) plain tube, B) corrugated tube

that by the increment of air injection flow rate, the mass variation results diminish, denoting this point that the augmentation of the air injection flow rate reduces the accumulated weight of the fouling substances. The maximum mass variation was about 10 g and was related to the plain tube at a single-phase stream. Also, the minimum mass variation results are related to corrugated tube and values of 2g which was related to the two-phase flow with an airflow rate of L /min.

Figure 7 A and B, presents the percentage variation of the mass weight results associated with a plain tube and corrugated tube, respectively. It could be easily understood that the maximum percentage variation of weight variation results is associated with corrugated tubes and presents an about 75% enhancement in the accumulation of fouled particles in comparison to the single-phase flow. A very important point that should be mentioned is that the mass variation results associated with an airflow rate of 4 and 5 L /min are almost identical in the corrugated tube. Indeed, by the increment of air injection flow rate through the corrugated tube, the flow structure totally changes and a fully bubbly flow could be seen in the airflow rates of 4 and 5 L /min. In these airflow rates, the dispersion of air bubbles is placed through all the cross-sections of the corrugated tube. This type of dispersion, significantly increases the turbulence intensity of the flow stream and causes the fouling particles to remain through the flow and prevents them from getting accumulated on the walls of the corrugated tube. The same value of percentage variation of weight

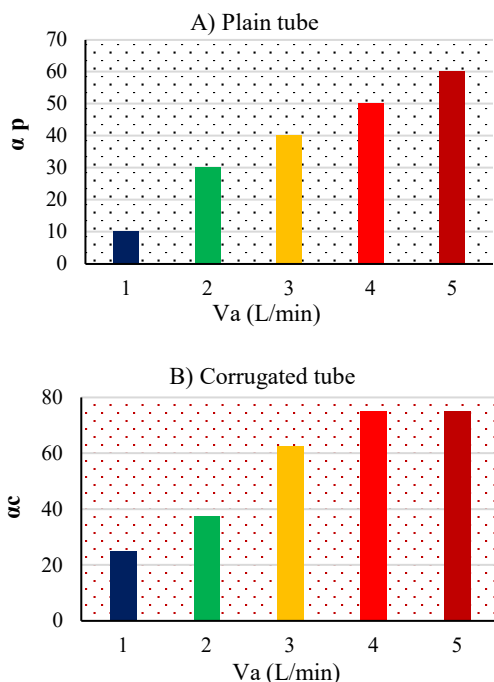


Figure 7. Percentage variation results, A) plain tube, B) corrugated tube

variation results indicates that through the corrugated tube, the airflow rate of 4 L /min could be assumed as an optimized value for the enhancement of fouling performance of the corrugated tubes.

## 5. CONCLUSIONS

Through this investigation, the thermal and fouling performance of plain tubes and the corrugated tube is compared and evaluated. The tubes were under constant heat flux and the molasses of sugar beet was considered as the working fluid. The tests were implemented for 5000s (84minute). For a better understanding of the nature of the flow, the structure of the two-phase stream was recorded via a Canon SX540 Camera within a glass-made tube. The main findings of the present paper were as following:

- The corrugated tube has more heat transfer coefficient over time compared to the plain tube.
- The flow structure within the corrugated tube is more complex than that in the plain tube.
- The dispersion of the bubbles in the corrugated tube is more even than that in a plain tube.
- The corrugated tube has significantly better fouling performance than the plain tube.
- It was found that the increment of air injection flow rate leads to a reduction of fouling accumulation on the walls of the tube.
- The maximum reduction in the fouling accumulation for the corrugated tube was found to be 75%.

## 6. REFERENCES

1. Patel, J. S., Bansal, B., Jones, M. I., Hyland, M. "Fouling behaviour of milk and whey protein isolate solution on doped diamond-like carbon modified surfaces." *Journal of Food Engineering*, Vol. 116, No. 2, (2013), 413-421. DOI: 10.1016/j.jfoodeng.2012.12.014
2. Barish, J. A., Goddard, J. M. "Anti-fouling surface modified stainless steel for food processing." *Food and Bioprocess Processing*, Vol. 91, No. 4, (2013), 352-361. DOI: 10.1016/j.fbp.2013.01.003
3. Zakrzewska-Trznadel, G., Harasimowicz, M., Miśkiewicz, A., Jaworska, A., Dłuska, E. Wroński, S. "Reducing fouling and boundary-layer by application of helical flow in ultrafiltration module employed for radioactive wastes processing." *Desalination*, Vol. 240, No. 1-3, (2009), 108-116. DOI: 10.1016/j.desal.2007.10.091
4. Sun, M.; Zeng, M. "Investigation on turbulent flow and heat transfer characteristics and technical economy of corrugated tube." *Applied Thermal Engineering*, Vol. 129, No. 1, (2018), 1-11. DOI: 10.1016/j.applthermaleng.2017.09.136
5. Khorasani, S., Davvand, A. "Effect of air bubble injection on the performance of a horizontal helical shell and coiled tube heat exchanger: An experimental study." *Applied Thermal Engineering*, Vol. 111, No. 1, (2017), 676-683. DOI: 10.1016/j.applthermaleng.2016.09.101

6. Sadighi Dizaji, H., Jafarmadar, S., Abbasalizadeh, M. Khorasani, S. "Experiments on air bubbles injection into a vertical shell and coiled tube heat exchanger; exergy and NTU analysis." *Energy Conversion and Management*, Vol. 103, No. 1, (2015), 973-980. DOI: 10.1016/j.enconman.2015.07.044
7. Cao, Y., Nguyen, P. T., Jermisittiparsert, K., Belmabrouk, H., Alharbi, S. O., khorasani, M. S. "Thermal characteristics of air-water two-phase flow in a vertical annularly corrugated tube." *Journal of Energy Storage*, Vol. 31, No. 1, (2020), 101605. DOI: 10.1016/j.est.2020.101605
8. Peyghambarzadeh, S. M., Vatani, A., Jamialahmadi, M. "Influences of bubble formation on different types of heat exchanger fouling." *Applied Thermal Engineering*, Vol. 50, No. 1, (2013), 848-856. DOI: 10.1016/j.applthermaleng.2012.07.015
9. Liu, L., Gao, B. Liu., J. Yang., F. "Rotating a helical membrane for turbulence enhancement and fouling reduction." *Chemical Engineering Journal*, Vol. 181-182, No. 1, (2012), 486-493. DOI: 10.1016/j.cej.2011.12.007
10. Li, X. L., Wang, S. Q., Yang, D. L., Tang, G. H., Wang, Y. C. "Thermal-hydraulic and fouling performances of enhanced double H-type finned tubes for residual heat recovery." *Applied Thermal Engineering*, Vol. 189, (2021), DOI: 10.1016/j.applthermaleng.2021.116724
11. Trafczynski, M., Markowski, M., Urbaniec, K., Trzcinski, P., Alabrudzinski, S.; Suchecki, W. "Estimation of thermal effects of fouling growth for application in the scheduling of heat exchangers cleaning." *Applied Thermal Engineering*, Vol. 182, (2021), 116103. DOI: 10.1016/j.applthermaleng.2020.116103
12. Xu, Z., Zhao, Y., He, J., Qu, H., Wang, Y., Wang, B. "Fouling characterization of calcium carbonate on heat transfer surfaces with sodium carboxymethyl cellulose as an inhibitor". *International Journal of Thermal Sciences*, Vol. 162, (2021), 106790. <https://doi.org/10.1016/j.ijthermalsci.2020.106790>
13. Chapela, S., Cid, N., Porteiro, J., Míguez, J. L. "Numerical transient modeling of the fouling phenomena and its influence on thermal performance in a low-scale biomass shell boiler." *Renewable Energy*, Vol. 161, (2020), 309-318. DOI: 10.1016/j.renene.2020.07.068
14. Tang, S.-Z., Li, M.-J., Wang, F.-L., Liu, Z.-B. "Fouling and thermal-hydraulic characteristics of aligned elliptical tube and honeycomb circular tube in flue gas heat exchangers". *Fuel*, Vol. 251, (2019), 316-327. <https://doi.org/10.1016/j.fuel.2019.04.045>
15. Zhao, L., Tang, W., Wang, L., Li, W., Minkowycz, W. J. "Heat transfer and fouling characteristics during falling film evaporation in a vertical sintered tube." *International Communications in Heat and Mass Transfer*, Vol. 109, (2019), 104388. DOI: 10.1016/j.icheatmasstransfer.2019.104388
16. Wang, F.-L., Tang, S.-Z., He, Y.-L., Kulacki, F. A., Yu, Y. "Heat transfer and fouling performance of finned tube heat exchangers: Experimentation via on line monitoring." *Fuel*, Vol. 236, (2019), 949-959. <https://doi.org/10.1016/j.fuel.2018.09.081>
17. Shen, C., Gao, R., Wang, X., Yao, Y. "Investigation on fouling of enhanced tubes used in a cooling tower water system based on a long-term test." *International Journal of Refrigeration*, Vol. 104, (2019), 9-18. DOI:10.1016/j.ijrefrig.2019.05.003
18. Wang, Z., Li, G., Xu, J., Wei, J., Zeng, J., Lou, D., Li, W. "Analysis of fouling characteristic in enhanced tubes using multiple heat and mass transfer analogies." *Chinese Journal of Chemical Engineering*, Vol. 23, No. 11, (2015), 1881-1887. <https://doi.org/10.1016/j.cjche.2015.07.011>
19. Son, D.-J., Kim, D.-G., Kim, W.-Y., Hong, K.-H. "Anti-fouling effect by internal air injection in plate-type ceramic membrane fabricated for the treatment of agro-industrial wastewater." *Journal of Water Process Engineering*, Vol. 41, (2021), 102021. <https://doi.org/10.1016/j.jpwe.2021.102021>
20. Sinaga, N., khorasani, S., Sooppy Nisar, K., Kaood, A. "Second law efficiency analysis of air injection into inner tube of double tube heat exchanger." *Alexandria Engineering Journal*, Vol. 60, No. 1, (2021), 1465-1476. DOI: 10.1016/j.aej.2020.10.064
21. Khorasani, S., Moosavi, A., Dadvand, A., Hashemian, M. "A comprehensive second law analysis of coil side air injection in the shell and coiled tube heat exchanger: An experimental study." *Applied Thermal Engineering*, Vol. 150, (2019), 80-87. DOI: 10.1016/j.applthermaleng.2018.12.163
22. Rostami, S., Ahmadi, N., Khorasani, S. "Experimental investigations of thermo-exergitic behavior of a four-start helically corrugated heat exchanger with air/water two-phase flow." *International Journal of Thermal Sciences*, Vol. 145, (2019), 106030. DOI: 10.1016/j.ijthermalsci.2019.106030
23. Peyghambarzadeh, S. M., Vatani, A., Jamialahmadi, M. "Influences of bubble formation on different types of heat exchanger fouling." *Applied Thermal Engineering*, Vol. 50, (2013), 848-856. <https://www.sciencedirect.com/science/article/pii/S1359431112004875>
24. Moffat, R. J. "Describing the uncertainties in experimental results". *Experimental Thermal and Fluid Science*, Vol. 1, No. 1, (1988), 3-17. [https://doi.org/10.1016/0894-1777\(88\)90043-X](https://doi.org/10.1016/0894-1777(88)90043-X)
25. Rezaei, R. A., Jafarmadar, S., Khorasani, S. "Presentation of frictional behavior of micro helical tubes with various geometries and related empirical correlation; an experimental study." *International Journal of Thermal Sciences*, Vol. 140, No. 1, (2019), 377-387. DOI:10.1016/j.ijthermalsci.2019.03.011
26. Tian, M. W., Khorasani, S., Moria, H., Pourhedayat, S., Dizaji, H. S. "Profit and efficiency boost of triangular vortex-generators by novel techniques." *International Journal of Heat and Mass Transfer*, Vol. 156, (2020), 119842. DOI: 10.1016/j.ijheatmasstransfer.2020.119842
27. Cao, Y., Nguyen, P.T., Jermisittiparsert K., Belmabrouk H., Alharbi S.O., khorasani M.S. "Thermal characteristics of air-water two-phase flow in a vertical annularly corrugated tube." *Journal of Energy Storage*, Vol. 31, (2020), 101605.
28. Sinaga, N, Khorasani, S., Sooppy Nisar, K., Kaood, A. "Second law efficiency analysis of air injection into inner tube of double tube heat exchanger." *Alexandria Engineering Journal*, Vol. 60, (2021), 1465-1476.
29. Khorasani, S, Moosavi, A, Dadvand, A, Hashemian, M. "A comprehensive second law analysis of coil side air injection in the shell and coiled tube heat exchanger: An experimental study." *Applied Thermal Engineering*, Vol. 150, (2019), 80-87. <https://linkinghub.elsevier.com/retrieve/pii/S1359431118352591>
30. Rostami, S., Ahmadi N., Khorasani S. "Experimental investigations of thermo-exergitic behavior of a four-start helically corrugated heat exchanger with air/water two-phase flow." *International Journal of Thermal Science*, Vol. 145, (2019), 106030. <https://linkinghub.elsevier.com/retrieve/pii/S1290072919303126>
31. Bhagwat, S. M., Ghajar, A. J. "Experimental investigation of non-boiling gas-liquid two phase flow in downward inclined pipes." *Experimental Thermal Fluid Science*, Vol. 89, (2017), 219-237. <http://www.sciencedirect.com/science/article/pii/S089417717302522>
32. Bhagwat, S. M., Ghajar, A. J. "Experimental investigation of non-boiling gas-liquid two phase flow in upward inclined pipes." *Experimental Thermal Fluid Science*, Vol. 79, (2016), 301-318. <http://www.sciencedirect.com/science/article/pii/S089417716302096>
33. Kim D., Ghajar A. J. "Heat transfer measurements and correlations for air–water flow of different flow patterns in a horizontal pipe." *Experimental Thermal Fluid Science*, Vol. 25, (2002), 659-676.

34. Bhagwat, S. M.; Ghajar, A. J. "Experimental investigation of non-boiling gas-liquid two phase flow in upward inclined pipes". *Experimental Thermal and Fluid Science*, Vol. 79, (2016), 301-318. DOI: 10.1016/j.expthermflusci.2016.08.004
35. Bhagwat, S. M.; Ghajar, A. J. "Similarities and differences in the flow patterns and void fraction in vertical upward and downward two phase flow." *Experimental Thermal and Fluid Science*, Vol. 39, (2012), 213-227. DOI: 10.1016/j.expthermflusci.2012.01.026

---

#### Persian Abstract

---

#### چکیده

در مطالعه حاضر، عملکرد رسوب گذاری یک لوله ماریپیج تحت تزریق هوا مورد بررسی قرار گرفت. ملاس چغندر قند به عنوان مایع کارکردی در نظر گرفته شد. لوله تحت شار حرارتی ثابت در نظر گرفته شد. همچنین میزان جریان ملاس چغندر قند بصورت ثابت در نظر گرفته شد. پنج نرخ جریان مختلف جریان هوا برای بررسی تأثیر سرعت جریان هوا در نظر گرفته شد. میزان جریان سیال کارکردی بر روی سرعت ثابت ۲ لیتر در دقیقه ثابت گردید. آزمایشها به مدت زمان ۵۰۰۰ ثانیه (۸۴ دقیقه) انجام شدند. برای درک بهتر ماهیت جریان، ساختار بخار دو فاز از طریق دوربین Canon SX540 ثبت گردید. نتایج ارائه شده نشان می دهد که تزریق هوا در لوله ماریپیج ساختار سیال کارکردی را کاملاً تغییر می دهد که ساختاری بسیار آشفته برای سیال کارکردی نتیجه می دهد. نتایج حرارتی نشان داد که در طول زمان آزمایش، تزریق هوا ضریب انتقال حرارت را در حدود ۱۲۰ درصد بیشتر از جریان تک فاز نگه می دارد. نتایج ارزیابی توده نشان داد که تزریق هوا می تواند وزن ماده رسوب شده را تا ۷۵ درصد کاهش دهد.

---



## Analysis of Role of Cloud Computing in Providing Internet Banking Services: Case Study Bank Melli Iran

H. Hamidi\*<sup>a</sup>, S. H. Seyed Lotfali<sup>b</sup>

<sup>a</sup> Department of Industrial, K. N. Toosi University of Technology, Tehran, Iran, Tehran, Iran

<sup>b</sup> Department of Information Technology, Islamic Azad University E-Campus, Tehran, Iran

### PAPER INFO

#### Paper history:

Received 05 November 2021

Received in revised form 22 December 2021

Accepted 23 December 2021

#### Keywords:

Efficiency Factor

Cloud Computing

Banking Services

Factor Analysis

### ABSTRACT

In this paper, the cloud-computing model proposed by Davis has been used to explain the main parameters of cloud computing by the use of information systems. This paper investigates influential factors in decision to use cloud computing among employees of the national bank information technology organization based on the cloud-computing model. To analyze and investigate the use of cloud computing in national bank services, the designed questionnaire was distributed among 230 experts and acquainted with the information technology industry in the national bank information technology organization; which resulted in the questionnaire's Cronbach's alpha 0.84. After conducting exploratory and confirmatory factor analysis with regard to analytical coefficients, utility factors were proved to have the most critical influence on the decision of using cloud computing in the electronic banking system. The findings of this research can be considered as guidelines used by national bank managers to employ cloud computing technology.

doi: 10.5829/ije.2022.35.05b.23

## 1. INTRODUCTION

Information and communications technology (ICT) is an integral part of business processes that affect the delivery and performance of business operations [1]. Therefore, companies and banks spend a large amount of their budget on purchasing and maintaining ICT infrastructure. Business needs never stay there; they tend to shrink and grow [2]. But ICT infrastructure is usually designed to be able to respond to demand in peak hours of consumption. Therefore, considerable investments have been made in the launch of ICT hardware and software [3-5]. Frequent improvements in technology have introduced the trend to build existing hardware and software. Companies spend a lot of money on the ICT infrastructure, which is not particularly practical for small businesses. ICT departments need to focus more on the daily activities related to ICT rather than focusing on core activities. On the other hand, banks also need to minimize the costs of electronic banking and financial services. The primary purpose of this study is examining the reasons for the use of cloud services in electronic

banking in the context of National Bank of Iran, one of the largest banks in Iran. The results can be used by senior managers of the Bank for making decision about the use of cloud computing technologies. Cloud computing refers to the delivery of information technology (IT) resources as services via the internet, contrary to hosting and operating these resources locally based on subscription or payments [6]. John McCarthy in 1961 stated that "calculations may someday be organized as an auxiliary tool" [7]. His prediction was realized with an increase in the network speed and reliability of the Internet. Cloud computing allows people to use it to compute, store and network in exchange for payment, which is similar to the method used in electric and telephone services used in the everyday world. Many other technologies such as distributed computation, virtualization, grid computing, and auxiliary computation have also been developed to evolve cloud computing. According to the National Institute of Standards and Technology (NIST), cloud computing is a model for enabling the network to be able to provide a common repository of configured computational resources (such

\*Corresponding Author Institutional Email: [h\\_hamidi@kntu.ac.ir](mailto:h_hamidi@kntu.ac.ir)  
(H. Hamidi)

as networks, servers, storage, applications, and services) that can be quick and have the minimum management or service provider effort [8].

Cloud computing is developed according to the structure, platform, and application as service-based services in a model as cost payments for users [9, 10]. In the industry, these services exist as Infrastructure as a Service (IaaS), Platform as Service (PaaS), and Software as a Service (SaaS), respectively [11, 12]. In e-banking, it is also the structure of providing different services and services based on various services in electronic banking, which can be significantly enhanced using cloud technology infrastructure.

The main objective of this paper is to explore the problems that are the main root of the lack of a cloud-focused banking system. The remaining of the paper are organized as the following parts. In the second part, the frameworks for using cloud computing are introduced.

## 2. THE USE OF CLOUD COMPUTING

Today, information technology is a crucial tool in promoting countries' economic competitiveness. Currently, its usage has significant implications on the productivity of organizations. These effects can only be realized if IT capabilities are widely used; therefore, several theoretical models are proposed at the individual and organizational level for the use of cloud computing [13, 14].

**2.1. UCCTAM Model of Cloud Computing** The UCCTAM model introduced in 2015 is a widely used theory for individual acceptance of an information system and information management [15]. Most studies focus on users' reception positions in choosing or not using freedom technology [16]. This study is successfully used to predict the use of cloud computing technology by new systems [17]. In addition, research aimed to investigate the effect of customers' trust on Internet banking acceptance based on the UCCTAM model [18]. Based on this model, the utility factor and ease of use are the key factors determining the efficiency of technology.

**2.2. Experimental History of Research** Many pieces of research have been developed to identify the main parameters of cloud computing. Kamankesh and Hamidi [19] have suggested that the adoption and use of cloud computing have been studied among almost 750 students of local colleges enrolled in basic arithmetic courses. This study investigated factors such as software access, ease of traffic, personal creativity, concern of technology, teacher support, and reliability as main parameters on utility factor, ease of use, actual use, and future profitability. The results of path analysis indicate that two elements, including profitability and ease of use,

have a positive effect on the decision-making use of cloud computing. In contrast, the ease of use factor is more effective due to the negative effect of factors such as concern of technology, access to software, and convenience of traffic on factor. It has no significant impact on the use of cloud computing.

Alvanchi et al. [20] investigated the adoption of cloud computing applications among 209 librarians of the Central Libraries of Tunisia. In this study, which was survey type and data collection method during 11 months, the author emphasizes the effect of four factors of usefulness, ease of use, attitude towards the use and decision making of cloud computing applications. Due to the results of this study, there is a significant relationship between productivity factor and attitude factor toward the use of librarians as well as the factor of attitude toward the use of cloud computing applications, and there is only a significant relationship between the factor of ease of use with profitability factor and attitude toward usage.

Research studies are based on a conceptual model. The conceptual model indicates the desired variables in an investigation and the relationship between them. In this research, a cloud computing model is used as a model for various research fields. In this model, four factors, namely, utility, ease of use, attitude towards use, and decision using cloud computing technology, are considered. Figure 1 shows the conceptual model used in this study.

Thus, the present study is conducted based on three hypotheses as follows:

The first hypothesis: the decision element to use cloud computing is influenced by attitude towards the use of cloud computing, ease of use, and utility factors.

The second hypothesis: attitude factor towards the use of cloud computing is affected by ease of use and usefulness factors.

The third hypothesis: the effect of usefulness is affected by ease of use.

## 3. RESEARCH METHODOLOGY

The purpose of this paper is to investigate individual factors associated with cloud computing among IT

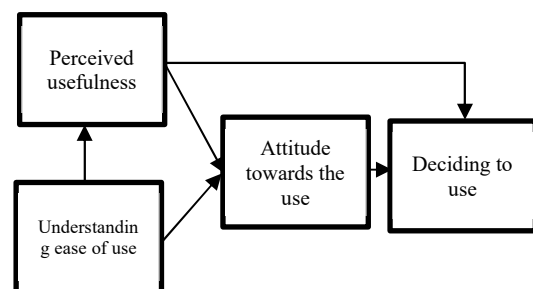


Figure 1. Conceptual model of research

professionals in the field of electronic banking at the National Bank of Iran. Hence, this study can be classified as a descriptive survey. We provided a questionnaire for collecting data. In order to validate the questionnaire, an initial version of it was presented to academic researchers, cloud computing professionals working at the national bank of Iran's technology organization (SADAD) and top level executives of SADAD. After applying necessary reforms to the questionnaire, the sectors in the questionnaire were designed and the questions related to each section are based on elements of the "cloud computing model" used in this study. The questions of this questionnaire include 17 closed questions, apart from questions related to general specifications. To determine the reliability of the measurement instrument, the final questionnaire was distributed randomly between 10 individuals from the research population, and the alpha coefficient of the questionnaire was calculated using the SPSS software, and a Cronbach's value of 0.84 was obtained. Considering that the reliability of this survey exceeds 70 %, it can be inferred that the questionnaire has a relatively high reliability. The research population of this study consists of 230 employees and managers working in the IT sector of the National Bank of Iran. Hence, 230 questionnaires were prepared and distributed among the demographic society, a well-known target society associated with cloud computing technology. Among 230 questionnaires, 209 questionnaires were returned and analyzed. In this study, descriptive and inferential statistical methods have been used. In order to understand the existence of meaningful relationships between the independent and dependent variables, the correlation analysis method is operated using the "spearman" statistic. For statistical analysis, exploratory factor analysis methods, confirmatory factor analysis, and path analysis were used. Statistical analysis of the research data was carried out using SPSS software and Amos software.

**3. 1. Reliability and Validity** After data collection, the validity and reliability of the collected data must be inspected.

Validity: the validity of a research method refers to how accurately it is able to measure what it is intended to measure.

Reliability: The ability to replicate the method or instrument of measurement. If there is no reliability method, the Collecting data will not have validity as well [21].

### 3. 2. Validity and Reliability of Research Tools

**3. 2. 1. Validity** Content validity is the validation method commonly used to examine the components of a measurement instrument. The content validity of a

measurement tool depends on its constituent questions. The test has content validity if the instrument's questions define specific traits and skills that the researcher intends to measure.

**3. 2. 2. Reliability** Reliability or credit is one of the technical characteristics of measurement. The concept has to deal with this when the measuring instrument in the same condition achieves the same results. The objective of reliability is that if the measuring process is carried out several times in a short interval of time and with a single group of people, the results are expected to be close to each other. We use an index called "reliability coefficient" to measure the reliability, and its size usually varies between Zero and One. "Zero" reliability factor defines the reliability, and the reliability factor "One" is representative of the validity [22, 23]. There are several ways to determine the reliability of the measurement instrument, such as the repeat method, the Tasnif method, Kord Richardson method, and Cronbach "s alpha.

$$r_{\alpha} = \frac{j}{(j-1)} \left[ 1 - \frac{\sum_{j=1}^k S_j^2}{S^2} \right] \quad (1)$$

Relationship 1: Cronbach "s alpha calculation formula  
In which the number of questions of questionnaires: j

The variance of the scores on each subset:  $S_j^2$   
Total variance:  $S^2$

Typically, a Cronbach "s alpha value between 0.6 and 0.8 is acceptable, and a value higher than 0.8 indicates high reliability. It is evident that the closer the number is to one, the better. In this study, Cronbach "s alpha technique is used to determine the reliability of the questionnaire.

Most of the research is based on the questionnaire in humanities and behavioral sciences. The quality control issue of the results of a questionnaire includes a wide range of topics. If we assume the questionnaire as a test, a good test should have good qualities such as objectivity, ease of implementation, feasibility, interpretation, and image to achieve good results. Among these features, validity and reliability are more important [24]. Given below is the Cronbach's alpha that is more prevalent than other methods:

The method of using Cronbach's alpha coefficient to determine the reliability of a questionnaire or test by emphasizing internal correlation can be used. In this method, one or more parts of the questionnaire are used to measure the reliability coefficient of the test. If the questions are expressed in two cases, True =one or False = zero. The Alpha coefficient is calculated from Relationship (2):

$$\alpha = \frac{k}{(K-1)} \left[ 1 - \frac{\sum_{i=1}^k pq}{S^2} \right] \quad (2)$$

Relationship 2: Cronbach "s alpha coefficient

where “K” is the number of questions, “p” is the number of correct responses, “q” is the number of wrong answers and the total variance of the questions (and if the questions are worth the value), each question has its own value (Cronbach “s alpha from the following equation calculates the reliability of the test:

$$\alpha = \frac{k}{(K-1)} \left[ 1 - \frac{\sum_{i=1}^k S_i^2}{S^2} \right] \quad (3)$$

Relationship 3: The reliability of the test

where “k” is the number of questions, the variance of each question, and “S<sup>2</sup>” is the variance of the whole question. Reliability of the questionnaire: Since a questionnaire is a questionnaire with several questions (such as a five-point Likert scale) such as a test, the high correlation can be calculated by Cronbach’s alpha [24, 25]. Cronbach “s alpha method can be used not only for two zero and one value options but also for multi-value options (such as a five-point Likert scale). If the test parts or the tests that are made out of the total of them are individually, then the Alpha factor does not require that individual questions be correctly and incorrectly [22]. To further explain how to use the alpha coefficient, suppose a questionnaire is designed to test the three hypotheses that the questions pertaining to each hypothesis are considered a little test.

Suppose the variance of three little tests is equal to:

$S_3^2 = 7$  and  $S_2^2 = 4$  and  $S_1^2 = 6$ , and the total variance of the test is equal to 33 due to  $k = 3$ , the Cronbach “s alpha coefficient is calculated as Formula 4.

$$\alpha = \frac{k}{(K-1)} \left[ 1 - \frac{\sum_{i=1}^k S_i^2}{S^2} \right] = \frac{3}{(3-1)} \left[ 1 - \frac{6+4+7}{32} \right] = 0.7 \quad (4)$$

Relationship 4: Calculation of Cronbach “s alpha coefficient

It is said that if the alpha coefficient is more than 0.7, the test has acceptable validity. As a result, the above test has acceptable validity.

## 4. RESEARCH FINDINGS

The data obtained from the research questionnaires were presented in the following three subsections:

### 4. 1. The Description of the Research Community

From the analysis of 209 questionnaires in this study, it was found that men (56%) had more participation than women (44%). In terms of the job situation, information technology industry experts have the highest number of respondents (79%). In terms of the work area, most respondents were active in the hardware and network domains (37%). The highest rate of work between 5 and 10 years (35%) and the highest level of education was related to the expert group (57%). Most of the

participants were in the computer engineering survey (52%), and others had other documents [13].

### 4. 2. Exploratory Factor Analysis of the Research Variables

Since four factors are introduced as influential factors of cloud computing in this research, separate factor analysis has been done for each of these factors, and the results are shown in Table 1. The first row is the number of variables related to each factor. The second row defines the “KMO” test value, which is one of the prerequisites for first conducting an exploratory factor analysis. Since the “KMO” value is for all factors above 0.5, the variables are suitable for factor analysis. The third row represents a significant number of the Bartlett test, which is another prerequisite for exploratory analysis. The fourth row “Share number” show commonalities. It examines suitability of questions in each exploratory factor. If the Share number is at least 0.5, the indicators are accepted [14]. In this part, after removing inappropriate questions, the number of factors was larger than 0.5. Thus, the above questions have appropriate validity for factor analysis. Having a higher quality and special value above 0.5, stated in the fifth and sixth lines, the appropriateness of questions is a confirmation factor analysis.

### 4. 3. Confirmatory Factor Analysis of the Research Variables

In order to perform a confirmatory factor analysis, Imos software was used. The fit indices of the model are shown in Table 2. The results from Table 2 indicate that all fit indices are acceptable. In this paper, the proposed model is used to model the fitness indices of the model concerning all vegetation indices of the model. In other words, the observed data were primarily based on the conceptual model of the research.

## 5. DISCUSSION

The correlation matrix is the basis of the analysis of causal models. In this study, the correlation matrix has

**TABLE 1.** Results from the exploratory factor analysis of the research variables

Variable	Factor of use	Ease of use	Attitude towards the use	Deciding to use
Variable number	4	5	2	3
KMO Test	0.745	0.657	0.500	0.677
Bartlett Test	0.000	0.000	0.000	0.000
Share number	0.986	0.980	0.991	0.996
Operating loads	0.711- 0.784	0.621 – 0.736	0.794	0.770 - 0.846
Special values	2.327	1.842	1.261	2.011

**TABLE 2.** Performance indices of the model

Index	Estimation	Acceptable fitness criterion
Squared K	3.345--- P=0.067	<1-----P>0.05
Index of Comparative elegance	0.946	0.90>
smooth index of excellence	0.933	0.90>
Root mean residual	0.014	<0.05
Squared Root variance of approximation error	0.106	<0.10
Necessary index of fit	0.992	>0.90
Adjustable index of fit	0.920	>0.85

been used to analyze the meaningful relationship between the research variables, and the results are presented in Table 3.

According to the result obtained from Table 3, we can say that there is a positive relationship between all research variables with a confidence of 99 percent. This result matches the results of the survey in literature [25]. Analyzing the results in terms of model path coefficients, this section of the research variables using Imos software was tested using the statistical method analysis technique using the general least squares method. Path analysis is one of the multivariate analysis methods, which, in addition to investigating the direct effects of independent and dependent variables, considers their indirect effects.

The researcher conducted by Naghsh Nilchia and, Vafaei [16] believed that the path coefficients between each of the questions and factors, if meaningful, are the reason for initial convergence in the research tool. Due to the positive effect of all the path coefficients obtained in Figure 2, we can conclude that there is an increasing relationship between all research variables. The contribution of the usefulness factor in attitude towards the use is much higher than the contribution of ease of use. Table 4 shows the direct, indirect effect, and the total effect of independent variables on the dependent variable

**TABLE 3.** correlation matrix of the research variables

Variable	Operating factor	Ease of use	Attitude towards the use	Deciding to use
Operating factor	1			
Ease of use	0.227**	1		
Attitude towards the use	0.336**	0.202**	1	
Deciding to use	0.396**	0.231**	0.260**	1

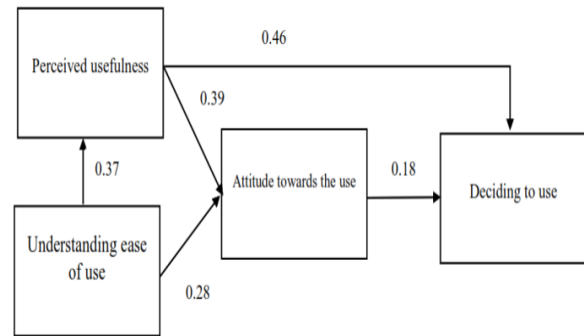


**Figure 2.** Path coefficients of the conceptual research model

**TABLE 4.** Direct and indirect effect and the total effect of variables on the decision variable

Variables	Straight effect	The effect is not straight	Whole effect
Operating factor	0.46	0.70	0.53
Ease of use	-	0.011	0.050
Attitude towards using	0.18	-	0.18

(the decision to use cloud computing). Due to the direct and indirect effect and the total effect of research variables on the decision to use cloud-computing technology, the variable factor has the most significant impact on the decision variable. Attitude variables are used for use and ease of use in the next rankings; therefore, the decision variable using cloud computing is influenced by the variable factor variables, ease of use, and attitude towards the use of cloud computing. However, the first hypothesis is confirmed.

The second hypothesis examines the effect of two utility factors and ease of use on the attitude variable.

According to the results of the total effect of productivity factor and ease of use in Table 5 on the attitude variable relative to the use, the second hypothesis is confirmed. It can be concluded that the variable effect is more effective than the variable of ease of use. The third hypothesis examines the ease of use on the usefulness factor. Due to the positive correlation between the two variable factors and ease of use, the third hypothesis is confirmed.

**TABLE 5.** Direct and indirect effect and the total effect of variables on the attitude variable

Variables	Straight effect	The effect is not straight	Whole effect
Operating factor	2.33	-	2.33
Ease of use	2.26	2.54	2.54

## 6. CONCLUSION

Cloud computing has many advantages, this paper investigates influential factors in the decision to use cloud computing among employees of the national bank information technology organization based on the cloud-computing model. As the results of this study show, there is a significant relationship between utility factors and attitude toward usage. While the relationship between agents is the ease of use and attitude towards the use of other relationships, the result is consistent with the results of the studies in literature. The results of the analysis show that the utility factor has the most significant impact on the decision-making use of cloud computing technology. After the utility factor, attitude factors are used to make use and ease of use in order to influence the decision to use in the next rankings. Due to the novelty of cloud computing technology in Iran, the results of this study are completely consistent with the predictions. Senior managers of the National Bank have to promote the level of knowledge of users about familiarity with cloud computing and deployment. The level of knowledge of users about information systems can affect users' ease of use and thus influences attitude factors toward using cloud computing technology. This study shows a correlation between ease of use and attitude towards other relationships. Another factor affecting this result is employees' resistance in applying new technologies and adjusting them to traditional methods; therefore, before launching new technologies such as cloud computing, employee culture is used in using these technologies, to which managers need to pay attention. Cloud computing requires training and, more importantly, continuous support to remove barriers and problems. In other words, support mechanisms are decisive factors in the application of this technology. The findings of this study can be effective on the application of cloud computing in the national bank for the managers of the national bank. For future research, in addition to individual factors, other main factors such as environmental factors, technical factors, organizational factors should be considered in the use of cloud computing in e-banking.

## 7. REFERENCES

- Langmead, B. and Nellore, A., "Cloud computing for genomic data analysis and collaboration", *Nature Reviews Genetics*, Vol. 19, No. 4, (2018), 208-219, doi: 10.1038/nrg.2017.113.
- Huang, D. and Wu, H., "Mobile cloud computing: Foundations and service models, Morgan Kaufmann, (2017).
- Wang, Y., Li, J. and Wang, H.H., "Cluster and cloud computing framework for scientific metrology in flow control", *Cluster Computing*, Vol. 22, No. 1, (2019), 1189-1198, doi: 10.1007/s10586-017-1199-3.
- Yu, Y., Miyaji, A., Au, M.H. and Susilo, W., *Cloud computing security and privacy: Standards and regulations*. 2017, Elsevier.1-2.
- Zhang, Y., Chen, X., Li, J., Wong, D.S., Li, H. and You, I., "Ensuring attribute privacy protection and fast decryption for outsourced data security in mobile cloud computing", *Information Sciences*, Vol. 379, (2017), 42-61, doi: 10.1016/j.ins.2016.04.015.
- Timothy, D.P. and Santra, A.K., "A hybrid cryptography algorithm for cloud computing security", in 2017 International conference on microelectronic devices, circuits and systems (ICMDCS), IEEE. (2017), 1-5.
- Arunkumar, R.J. and Anbuselvi, R., "Enhancement of cloud computing security in health care sector", *International Journal of Computer Science and Mobile Computing*, Vol. 6, No. 8, (2017), 23-31.
- Pham, V.V.H., Liu, X., Zheng, X., Fu, M., Deshpande, S.V., Xia, W., Zhou, R. and Abdelrazek, M., "Paas-black or white: An investigation into software development model for building retail industry saas", in 2017 IEEE/ACM 39th International Conference on Software Engineering Companion (ICSE-C), IEEE. (2017), 285-287.
- Aljawarneh, S., Cloud security engineering concept and vision: Concept and vision, in Cyber security and threats: Concepts, methodologies, tools, and applications. 2018, IGI Global.93-101.
- Hamidi, H., Vafaei, A. and Monadjemi, A., "Algorithm based fault tolerant and check pointing for high performance computing systems", *Journal of Applied Sciences*, Vol. 9, No. 22, (2009), 3947-3956, doi: 10.3923/jas.2009.3947.3956.
- Khan, N. and Al-Yasiri, A., Cloud security threats and techniques to strengthen cloud computing adoption framework, in Cyber security and threats: Concepts, methodologies, tools, and applications. 2018, IGI Global.268-285.
- Hamidi, H. and Mohammadi, K., "Modeling fault tolerant and secure mobile agent execution in distributed systems", *International Journal of Intelligent Information Technologies*, Vol. 2, No. 1, (2006), 21-36, doi: 10.4018/jiit.2006010102.
- Khalil, I.M., Khreishah, A. and Azeem, M., "Cloud computing security: A survey", *Computers*, Vol. 3, No. 1, (2014), 1-35, doi: 10.3390/computers3010001.
- Bahrami, L., Safaie, N., "Effect of motivation, opportunity and ability on human resources information security management considering the roles of attitudinal, behavioral and organizational factors", *International Journal of Engineering, Transactions C: Aspects*, Vol. 34, No. 12, (2021), 2624-2635., doi: 10.5829/ije.2021.34.12c.07.
- Subashini, S. and Kavitha, V., "A survey on security issues in service delivery models of cloud computing", *Journal of Network and Computer Applications*, Vol. 34, No. 1, (2011), 1-11, doi: 10.1016/j.jnca.2010.07.006.
- Nilchi, A.N., Vafaei, A. and Hamidi, H., "Evaluation of security and fault tolerance in mobile agents", in 2008 5th IFIP International Conference on Wireless and Optical Communications Networks (WOCN'08), IEEE. (2008), 1-5.
- Kandukuri, B.R. and Rakshit, A., "Cloud security issues", in 2009 IEEE International Conference on Services Computing, IEEE. (2009), 517-520.
- Jensen, M., Schwenk, J., Gruschka, N. and Iacono, L.L., "On technical security issues in cloud computing", in 2009 IEEE international conference on cloud computing, IEEE. (2009), 109-116.
- Hamidi, H. and Kamankesh, A., "An approach to intelligent traffic management system using a multi-agent system", *International Journal of Intelligent Transportation Systems*

- Research*, Vol. 16, No. 2, (2018), 112-124, doi: 10.1007/s13177-017-0142-6.
20. Alvanchi, A., Didehvar, N., Jalilehvand, M., Adami, P. and Shahmir, S., "Semi-augmented reality, a novel approach to improve customer safety in the pre-sale process of under construction buildings", *International Journal of Engineering, Transactions C: Aspects*, Vol. 34, No. 10, (2021), doi: 10.5829/ije.2021.34.10a.01.
  21. Torabi, A., Hamidi, H. and Safaie, N., "Effect of sensory experience on customer word-of-mouth intention, considering the roles of customer emotions, satisfaction, and loyalty", *International Journal of Engineering, Transactions C: Aspects*, Vol. 34, No. 3, (2021), 682-699, doi: 10.5829/ije.2021.34.03c.13.
  22. Daraei, A. and Hamidi, H., "An efficient predictive model for myocardial infarction using cost-sensitive j48 model", *Iranian Journal of Public Health*, Vol. 46, No. 5, (2017), 682, doi: <http://ijph.tums.ac.ir/index.php/ijph/article/view/9918>
  23. Armbrust, M., Fox, A., Griffith, R., Joseph, A.D., Konwinski, A., Lee, G., Rabkin, A., Stoica, I. and Zaharia, M., "A view of cloud computing, communications of the acm", *Vol*, Vol. 53, No., (2010), 5058, doi: 10.1145/1721654.1721672.
  24. Jansen, W.A., "Cloud hooks: Security and privacy issues in cloud computing", in 2011 44th Hawaii International Conference on System Sciences, IEEE. (2011), 1-10.
  25. Mohammadi, S. and Jahanshahi, H., "A study of major mobile payment systems' functionality in europe", in 2008 11th International Conference on Computer and Information Technology, IEEE. (2008), 605-610.

---

### Persian Abstract

---

#### چکیده

با توجه به گسترش روزافزون استفاده از رایانش ابری به عنوان الگوی جدید ارتباطی در سازمان‌ها، تحلیل رفتار کاربران در مواجهه با این فناوری در هر یک از سازمان‌های استفاده کننده ضروری است. در این مقاله، مدل استفاده رایانش ابری که توسط دیویس ارائه شده است، برای تبیین پارامترهای اصلی براستفاده رایانش ابری توسط کاربران سیستم‌های اطلاعاتی مورد استفاده قرار گرفته است. هدف اصلی این مقاله بررسی مشکلاتی است که ریشه در عدم استقرار سیستم بانکداری متمرکز ابری دارد. نتایج حاصل از تحلیل‌ها نشان می‌دهد که عامل سودمندی بیشترین تأثیر را بر تصمیم به استفاده از فناوری رایانش ابری دارد. پس از عامل سودمندی، عوامل نگرش نسبت به استفاده و سهولت استفاده به ترتیب اهمیت اثرگذارتری دارند. یافته‌های این پژوهش می‌تواند به عنوان راهنمایی کاربردی مورد استفاده مدیران بانک ملی در جهت تصمیم‌گیری در استفاده از فناوری رایانش ابری قرار گیرد.

---



## Unconfined Compressive Strength Characteristics of Treated Peat Soil with Cement and Basalt Fibre

P. Ghasem Ghanbari<sup>a</sup>, M. Momeni<sup>a</sup>, M. Mousivand<sup>b</sup>, M. Bayat<sup>\*a</sup>

<sup>a</sup> Department of Civil Engineering, Najafabad Branch, Islamic Azad University, Najafabad, Iran

<sup>b</sup> Department of Civil Engineering, Gonbad Kavoos Branch, Islamic Azad University, Gonbad Kavoos, Iran

### PAPER INFO

#### Paper history:

Received 02 January 2022

Received in revised form 23 February 2022

Accepted 25 February 2022

#### Keywords:

Basalt fibre

Cement

Unconfined Compressive Strength

Peat

### ABSTRACT

So far many studies have focused on the mechanical behavior of fibre reinforced soils and stabilized soils with conventional chemical stabilizers such as cement and lime; however, very limited researches were conducted on the unconfined compressive strength characteristics of fibre reinforced cement stabilized peat soils. Fibre-reinforcement of a stabilized soil resulted in a significant improvement in the ductility and strength characteristics of weak or soft soils. The main objective of the current study is considering the effects of cement content, fibre content, fibre length and curing time on the unconfined compressive strength (UCS) of peat soil. The study finds that adding basalt fibre or cement causes a remarkable increase in the UCS values of peat soil. The UCS value of the cement-stabilized sample is observed significantly more than basalt fibre-reinforced ones. However, the sample reinforced with basalt fibers showed more ductile behavior compared to the stabilized sample with cement. The results showed that the increase in UCS values of combined basalt fibre and cement inclusions was more than the increase caused by each of them, individually.

doi: 10.5829/ije.2022.35.05b.24

## 1. INTRODUCTION

The geotechnical properties of soils can be improved through material modification in civil projects. However, design and the construction of civil projects over soft and weak soil such as peat deposits have remained a major challenge. The replacement of such soil is expensive and not economically feasible; therefore, it has been necessary to improve soil properties. Peat soils are considered as extremely soft, wet, unconsolidated materials which are generally composed of fibrous organic matters. These soils are an extreme form of soft soils which are generally associated with high compressibility, medium to low permeability, low strength and large settlements and hold serious problems in civil engineering constructions [1-3]. Previous researchers investigate on any possible techniques or practices to enhance strength properties of peat soils. Various soil improvement techniques such as utilize

mechanical energy and/or man-made materials have been used to improve the mechanical characteristics of weak or soft soils in practice for many years [4-6]. The problems of structures situated on weak or soft deposits are represented by significant settlement, low shear and compressive strength parameters [7-11]. Similar to conventional additive such as cement or lime, natural or synthetic fibres such as cotton, coir, sisal, polypropylene, basalt and polyester may be used to enhance the mechanical characteristics of weak or soft soils [12-15]. The effectiveness of soil improvement method is mainly dependent on the soil characteristics. Cement or lime stabilization have been used for many years which has been reported in the literature as a popular soil improvement technique. Previous studies indicated that cementation bonds among soil particles become stronger and pore spaces between soil particles could be occupied by cementing materials when various cementing materials were mixed with weak soils which could be

\*Corresponding Author Institutional Email: [bayat.m@pci.iaun.ac.ir](mailto:bayat.m@pci.iaun.ac.ir)  
(M. Bayat)

resulted in an increase in the strength [16-19]. In previous studies reported in the literature, cement stabilization have been suggested as an effective method to improve the mechanical characteristics of weak soils [20-22]. Kalantari et al. [23] studied the mechanical behavior of silica fume and cement stabilized peat soils using unconfined compressive strength (UCS) and California bearing ratio (CBR) under soaked and unsoaked conditions. The results showed that the strength of peat soil layer increased when cement and silica fume have been used to stabilize and improve the mechanical properties of the peat soil.

Boobathiraja et al. [24] investigated the mechanical behavior of stabilized peat soil. They reported that the addition of lime and cement improved the mechanical characteristics of soil. A comparison of the results of cement and lime stabilized the specimens indicated that cement appeared to perform better than the lime. On the other hand, a lot of studies proved the beneficial effects of various types of fibres on the mechanical characteristics of reinforced soils [25-32]. Among various types of fibres, Basalt fibre (BF) is a new kind of inorganic, biologically inactive, environmentally friendly fibre which has better physical and mechanical characteristics with more cost-effective than other fibres [9, 33]. BF has been a popular material in civil engineering constructions such as soil reinforcement, concrete and asphalt [33-41]. Ndepete and Sert [42] indicated that the shear strength parameters of soil under undrained condition have been improved with the inclusion of BF with an optimum fibre content of 1.5%, when compared to the natural soil. Wang et al. [38] investigated the mechanical behavior and microstructure of BF reinforced cemented kaolinite. They found that the inclusion of BF resulted in enhancement of strength and ductility of specimens. Saberian and Rahgozar [43] studied the mechanical behavior of stabilized sand with gypsum, lime or cement along with waste tyre chips. The results showed that cement stabilized specimens exhibited the greatest improvement in UCS as well as improvements in the shear strength parameters ( $c$  and  $\phi$ ). Kalantari et al. [2] investigated the CBR and UCS values of treated peat soil with cement, polypropylene and steel fibres. The results showed that the UCS and CBR values of specimens containing 5% of cement, 0.15% of polypropylene fibres and 2% of steel fibres increased by as high as 748.8% and 122.7%, respectively.

Even though, many studies have been conducted to investigate the mechanical behavior of treated soils with various materials such as cementation materials and fibres, limited studies have been performed to study mechanical behavior of treated peat soils. Due to the low strength of peat soils, in the current study, the BF and cement were used to enhance the UCS value of peat soil specimens.

## 2. TEST APPARATUS, MATERIALS AND TESTING PROCEDURE

The unconfined compression test is widely used to determine the compressive strength value of cohesive or treated soils because of simple experimental process, and low requirement for the equipment. In this study, a series of UCS tests was carried out on treated peat soil specimens with cement and BF under a constant strain rate of 1% per minute according to ASTM D2166.

First stage of present study is collection of the peat soil from the south of Isfahan. The physical and chemical properties of peat soil are presented in Table 1. Field visits show that this soil is weak and needs to be improved for construction purposes.

The peat samples were brown in color and they were hemic (37 % fibre), high ash (22 %) and moderately acidic condition (pH 5.5) according to ASTM 4427-92.

In this work, basalt fibre was used for the reinforcement of peat samples, as shown in Figure 1. As shown in this figure, the effects of fibre lengths of 6, 12 and 18 mm were studied. The effect of fibre content varied from 0% to 5% and cement content varied from 0% to 5% has been investigated. Table 2 shows the physical and mechanical properties of basalt fibre. Type II Portland cement was used to stabilize peat samples. The physical and chemical characteristics of cement are shown in Table 3. The compressive and tensile strength values of cured cement samples in 28-day were equal to 44 and 2.8 MPa, respectively. The compressive and tensile strength tests were conducted according to ASTM 109 and ASTM 190, respectively.

**TABLE 1.** Physical and chemical properties of Chaghakhor peat

Characteristics	Values and descriptions
Fibre content (%)	37
Organic content (%)	55
Liquid limit (%)	307
Density of solids ( $\text{g}/\text{cm}^3$ )	1.66
Dry density ( $\text{Mg}/\text{m}^3$ )	0.31

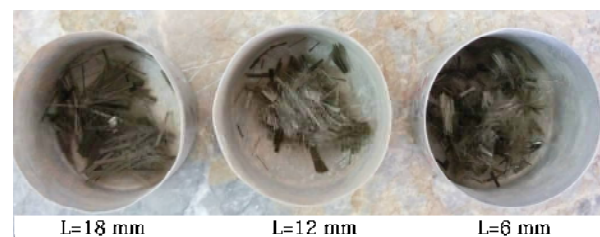


**Figure 1.** Photograph showing the discrete short basalt fibre

**TABLE 2.** Physical and mechanical properties of basalt fibers

Property	Value
Cut length (mm)	12
Filament diameter ( $\mu\text{m}$ )	17
Density ( $\text{g}/\text{cm}^3$ )	2.61
Elastic modulus (GPa)	95
Tensile strength (MPa)	3000

**TABLE 3.** Physical and chemical properties of cement

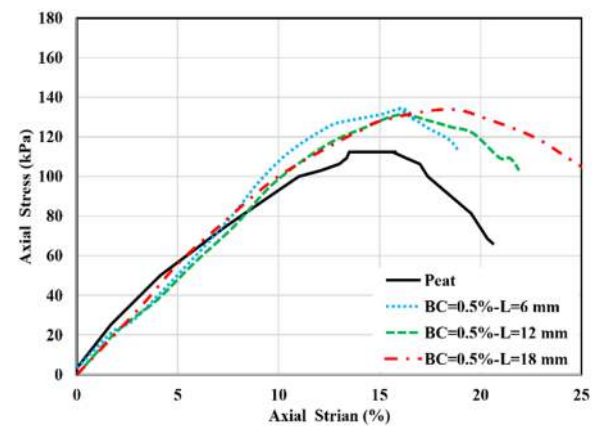
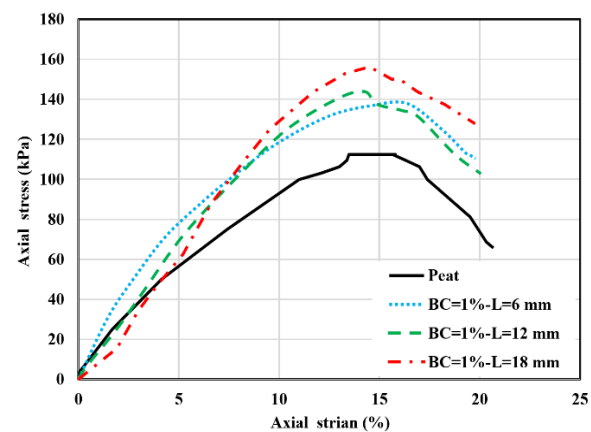
Property/composition	Value
Specific gravity	3.14
Specific surface area ( $\text{m}^2/\text{kg}$ )	320
CaO (%)	60.4
SiO <sub>2</sub> (%)	15.9
Al <sub>2</sub> O <sub>3</sub> (%)	9.5
SO <sub>3</sub> (%)	6.4
Fe <sub>2</sub> O <sub>3</sub> (%)	4.1
MgO (%)	0.9
K <sub>2</sub> O (%)	0.7
TiO <sub>2</sub> (%)	0.1

The peat was first oven dried for at least 24 h at 110°C, and then additives (i.e. basalt fiber or cement, if any) were mixed in dry state with dry peat. The required amount of distilled water was sprayed onto the mixture and the constituents were mixed until a homogeneous mixture was obtained. The treated samples with a natural moisture content were placed in three layers in a mold with height and diameter of 100 mm and 50 mm, respectively. Each layer of samples was given 25 blows by using the tamping. After sample preparation, the samples were then taken out of the mold and wrapped with a plastic film. Afterwards, the samples were stored in the humidity controlled chamber (temperature= 20°C, and relative humidity= 95%) until testing at 14, 28 or 60 days of curing. Finally, after all the tests, all the stress-strain diagrams in Excel were plotted and compared to find a suitable combination selection for improvement.

### 3. TESTS RESULTS AND DISCUSSION

The effects of fibre length on the stress-strain curve of the reinforced samples at basalt contents (BC) of 0.5% and 1% are shown in Figures 2 and 3, respectively. As shown from the results, the UCS values of reinforced samples are always greater than that of peat sample regardless of fibre content and fiber length (L). The reinforced samples exhibited a more ductile behavior

with a larger strain corresponding to the peak stress than that of peat sample which is good agreement with the reported data in the literature [9, 47-49]. The UCS value of reinforced samples with basalt content of 0.5% is almost independent of fibre length; however, the UCS value of reinforced samples with basalt content of 1% increases slightly with an increase in fibre length. In general, the sample containing longest fibres (18 mm) showed the highest UCS value. A comparison of Figures 2 and 3 shows that the UCS values of reinforced samples increases about 10% with an increase in fibre content from 0.5% to 1% which also reported in previous studies [41, 42, 48, 50]. Figure 4 shows the effect of fibre content on the stress-strain curve of the reinforced samples for a given fibre length of 18 mm. The results reveal the improvement of the UCS for reinforced samples with an increase in fibre content. An increase in the fibre content from 0.5% to 2% results in an increase in the UCS value from 133 kPa to 205 kPa. The basalt fibre-reinforced samples indicate a more ductile behavior than the peat sample.

**Figure 2.** Stress–strain curves of the basalt fibre-reinforced samples with BC=0.5% and varied fibre length**Figure 3.** Stress–strain curves of the basalt fibre-reinforced samples with BC=1% and varied fibre length

The effects of cement content on the stress-strain curve of the stabilized samples at cement contents (CC) of 2% and 5% at various curing times are shown in Figures 5 and 6, respectively. Addition of cement has important effect on the behaviors of peat samples and increases the UCS values and decreases the strain corresponding to the peak stress. The cement-stabilized peat samples with cement exhibits brittle behavior and the most improvement in UCS value is observed within the first 7 days. The UCS increases gradually with an increase in curing time which good agreement with previous studies [10, 51-54]. Comparison of the fibre-reinforced samples with cement-stabilized samples showed that for a given additive content, the cement stabilized samples exhibited higher UCS values than those reinforced with fibre. As shown, the UCS increases with increasing the curing time from 7 to 60 days. From Figure 5, it could be seen that by an increase in the curing time from 7 to 60 days the UCS value of cement-stabilized samples containing 2% cement increased from 220 kPa to 415 kPa. As shown from Figure 6, for the samples containing 5% cement, the UCS value increased from 520 kPa to 880 kPa with an increase in the curing

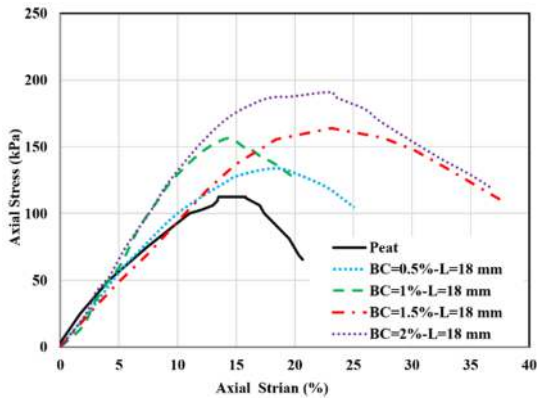


Figure 4. Stress-strain curves of the basalt fibre-reinforced samples with varied fibre content and fibre length of 18 mm

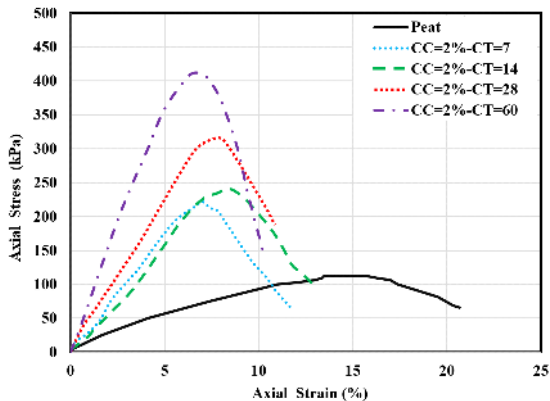


Figure 5. Stress-strain curves of the cement-stabilized samples with cement content of 2% at various curing times

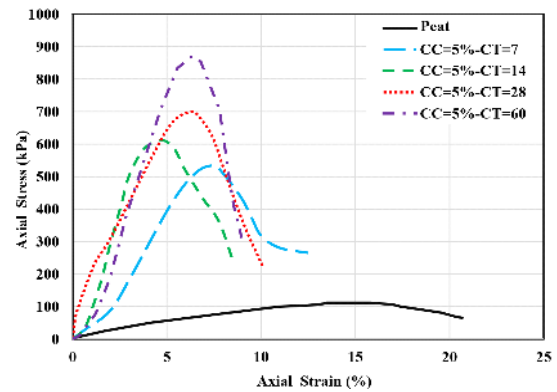


Figure 6. Stress-strain curves of the cement-stabilized samples with cement content of 5% at various curing times

time from 7 to 60 days. Figures 7 and 8 show the stress-strain curve of the fibre-reinforced cement-stabilized samples at various curing times with fibre content of 1% and cement contents of 2% and 5%, respectively. The results indicate the treated samples behaved as a brittle material with higher axial stress values than that of peat sample regardless of cement content and curing time. There is a general slightly increase in UCS value for treated samples as curing time increased. The axial strain corresponding to the peak stress for treated samples decreased with increasing curing time. A comparison of Figures 7 and 8 indicate that the UCS values of treated samples increases about 10% with the increase about two times as cement content increases from 2% to 5% for a given curing time. A comparison between cement-stabilized samples and treated samples with basalt fibre and cement shows that the addition of 1% of basalt fibre in the stabilized samples with 2% cement content resulted in an increase of 15% to 40% of UCS values depending on curing time. On the other hand, curing time has less influence on the UCS values of the treated samples with basalt fibre and cement than in treated samples without basalt fibre.

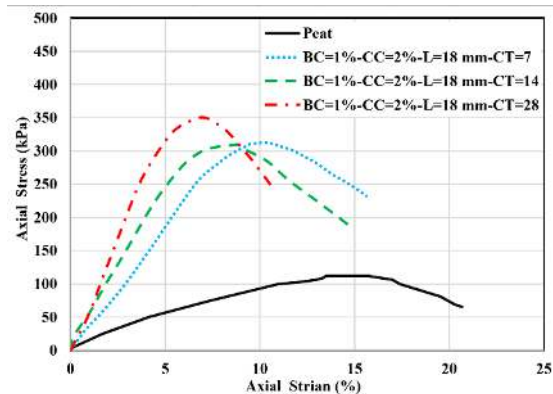
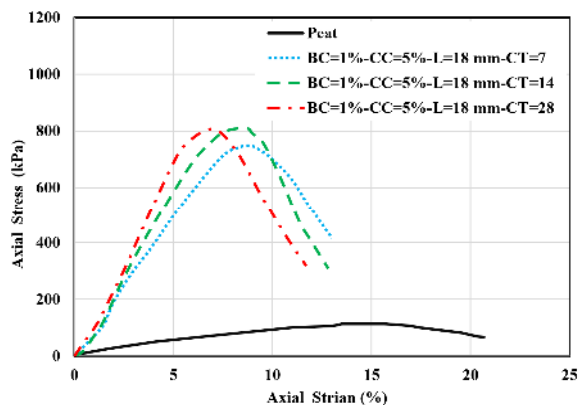


Figure 7. Stress-strain curves of the treated samples with fibre content of 1% and cement content of 2% at various curing times



**Figure 8.** Stress–strain curves of the treated samples with fibre content of 1% and cement content of 5% at various curing times

#### 4. CONCLUSIONS

Peats are an extreme form of soft soils which are generally associated with high compressibility, medium to low permeability, low strength and large settlements and hold serious problems in civil engineering constructions. In the current study, a series of UCS tests were conducted on the peat samples to study the influences of basalt fibre content, fiber length, cement content and curing time. Based on the results, the following conclusions are reached.

The addition of basalt fiber or cement significantly enhanced the UCS values of peat soil. Increasing basalt fiber content or cement content leads to a significant increase of UCS values. The UCS value was more with the addition of cement than the same content of basalt fibre especially for high curing time. For example, the UCS value of stabilized sample with 2% cement content at curing time 60 days was almost twice that of reinforced sample with 2% basalt fibre. In other words, the strength of cement-stabilized samples was very much greater than that of the fibre-reinforced samples for long-term performance. However, the sample reinforced with basalt fibers showed more ductile behavior compared to the stabilized sample with cement. Furthermore, the axial strain at failure for cement-stabilized sample decreased with increasing cement content or curing time. In general, the results show that a combination of fiber and cement could be suitable for peat improvement.

#### 5. REFERENCES

1. A. P. Pinheiro, "Architectural Rehabilitation and Sustainability of Green Buildings in Historic Preservation," *HighTech and Innovation Journal*, Vol. 1, No. 4, (2020), 172-178. doi: 10.28991/hij-2020-01-04-04.
2. B. Kalantari, A. Prasad, and B. B. K. Huat, "Peat stabilization using cement, polypropylene and steel fibres," *Geomechanics and Engineering*, Vol. 2, No. 4, (2010), 321-335. doi: 10.12989/gae.2010.2.4.321.
3. M. A. Rahgozar and M. Saberian, "Physical and chemical properties of two Iranian peat types," *Mires and Peat*, Vol. 16, (2015), 1-17. [http://mires-and-peat.net/media/map16/map\\_16\\_07.pdf](http://mires-and-peat.net/media/map16/map_16_07.pdf)
4. M. H. Hoseini, A. Noorzad, and M. Zamanian, "Physical modelling of a strip footing on a geosynthetic reinforced soil wall containing tire shred subjected to monotonic and cyclic loading," *International Journal of Engineering, Transactions B: Applications*, Vol. 34, No. 10, (2021), 2266-2279, doi: 10.5829/IJE.2021.34.10A.08.
5. D. T. Nguyen and V. T. A. Phan, "Engineering properties of soil stabilized with cement and fly ash for sustainable road construction," *International Journal of Engineering, Transactions B: Applications*, Vol. 34, No. 12, (2021), 2665-2671, doi: 10.5829/IJE.2021.34.12C.12.
6. S. D. Turkane and S. K. Chouksey, "Partial Replacement of Conventional Material with Stabilized Soil in Flexible Pavement Design," *International Journal of Engineering, Transactions B: Applications*, Vol. 35, No. 05, (2022), 908-916, doi: 10.5829/ije.2022.35.05b.07.
7. G. Russo, G. Marone, and L. Di Girolamo, "Hybrid Energy Piles as a Smart and Sustainable Foundation," *Journal of Human, Earth, and Future*, Vol. 2, No. 3, (2021), 306-322, doi: 10.28991/hef-2021-02-03-010.
8. R. Vali, "Water Table Effects on the Behaviors of the Reinforced Marine Soil-footing System," *Journal of Human, Earth, and Future*, Vol. 2, No. 3, (2021), 296-305, doi: 10.28991/hef-2021-02-03-09.
9. S. Hadi Sahlabadi, M. Bayat, M. Mousivand, and M. Saadat, "Freeze–Thaw Durability of Cement-Stabilized Soil Reinforced with Polypropylene/Basalt Fibers," *Journal of Materials in Civil Engineering*, Vol. 33, No. 9, (2021), 04021232, doi: 10.1061/(asce)mt.1943-5533.0003905.
10. M. Salehi, M. Bayat, M. Saadat, and M. Nasri, "Experimental Study on Mechanical Properties of Cement-Stabilized Soil Blended with Crushed Stone Waste," *Korean Journal of Civil Engineering*, Vol. 25, No. 6, (2021), 1974-1984, doi: 10.1007/s12205-021-0953-5.
11. M. R. ShahriarKian, S. Kabiri, and M. Bayat, "Utilization of Zeolite to Improve the Behavior of Cement-Stabilized Soil," *International Journal of Geosynthetics and Ground Engineering*, Vol. 7, No. 2, (2021), 35, doi: 10.1007/s40891-021-00284-9.
12. M. Salehi, M. Bayat, M. Saadat, and M. Nasri, "Prediction of unconfined compressive strength and California bearing capacity of cement- or lime- pozzolan-stabilized soil admixed with crushed stone waste," *Geomechanics and Geoengineering*, In Press, (2022), doi: 10.1080/17486025.2022.2040606.
13. J. S. Yadav and S. K. Tiwari, "A study on the potential utilization of crumb rubber in cement treated soft clay," *Journal of Building Engineering*, Vol. 9, (2017), 177-191, doi: 10.1016/j.jobbe.2017.01.001.
14. N. M. Al-Akhras, M. F. Attom, K. M. Al-Akhras, and A. I. H. Malkawi, "Influence of fibers on swelling properties of clayey soil," *Geosynthetics International*, Vol. 15, No. 4, (2008), 304-309, doi: 10.1680/gein.2008.15.4.304.
15. M. Syed, A. GuhaRay, S. Agarwal, and A. Kar, "Stabilization of Expansive Clays by Combined Effects of Geopolymerization and Fiber Reinforcement," *Journal of The Institution of Engineers (India): Series A*, Vol. 101, No. 1, (2020), 163-178, doi: 10.1007/s40030-019-00418-3.
16. P. Ghadir and N. Ranjbar, "Clayey soil stabilization using geopolymer and Portland cement," *Construction and Building Materials*, Vol. 188, (2018), 361-371, doi:

- 10.1016/j.conbuildmat.2018.07.207.
17. Y. Liu *et al.*, "Stabilization of expansive soil using cementing material from rice husk ash and calcium carbide residue," *Construction and Building Materials*, Vol. 221, (2019), 1-11, doi: 10.1016/j.conbuildmat.2019.05.157.
  18. P. Sukmak, K. Kunchariyakun, G. Sukmak, S. Horpibulsuk, S. Kassawat, and A. Arulrajah, "Strength and Microstructure of Palm Oil Fuel Ash–Fly Ash–Soft Soil Geopolymer Masonry Units," *Journal of Materials in Civil Engineering*, Vol. 31, No. 8, (2019), 04019164, doi: 10.1061/(asce)mt.1943-5533.0002809.
  19. S. Aryal and P. K. Kolay, "Long-Term Durability of Ordinary Portland Cement and Polypropylene Fibre Stabilized Kaolin Soil Using Wetting–Drying and Freezing–Thawing Test," *International Journal of Geosynthetics and Ground Engineering*, Vol. 6, No. 1, (2020), 1-15, doi: 10.1007/s40891-020-0191-9.
  20. S. Horpibulsuk, R. Rachan, A. Chinkulkijniwat, Y. Raksachon, and A. Suddeepong, "Analysis of strength development in cement-stabilized silty clay from microstructural considerations," *Construction and Building Materials*, Vol. 24, No. 10, (2010), 2011-2021, doi: 10.1016/j.conbuildmat.2010.03.011.
  21. ASTM, "Standard Test Method for Consolidated Undrained Triaxial Compression Test for Cohesive Soils (D 4767 – 95)," ASTM, 2003. <https://compass.astm.org/download/D4767.15423.pdf%0Awww.astm.org> (accessed May 22, 2017).
  22. L. You, Y. Yue, K. Yan, and Y. Zhou, "Characteristics of cement-stabilized macadam containing surface-treated recycled aggregates," *Road Materials and Pavement Design*, Vol. 22, No. 9, (2020), 1-15, doi: 10.1080/14680629.2020.1740771.
  23. B. Kalantari, A. Prasad, and B. B. K. Huat, "Stabilizing peat soil with cement and silica fume," *Proceedings of the Institution of Civil Engineers: Geotechnical Engineering*, Vol. 164, No. 1, (2011), 33-39, doi: 10.1680/geng.900044.
  24. S. Boobathiraja, P. Balamurugan, M. Dhansheer, and A. Adhikari, "Study on Strength of Peat Soil Stabilized with Cement and Other Pozzolanic Materials," *International Journal of Civil Engineering Research*, Vol. 5, No. 4 (2014): 431-438. Available: <http://www.ripublication.com/ijcer.htm>
  25. C. Liu, Y. Lv, X. Yu, and X. Wu, "Effects of freeze-thaw cycles on the unconfined compressive strength of straw fiber-reinforced soil," *Geotextiles and Geomembranes*, Vol. 48, No. 4, (2020), 581-590, doi: 10.1016/j.geotextmem.2020.03.004.
  26. X. Bao, Z. Jin, H. Cui, G. Ye, and W. Tang, "Static liquefaction behavior of short discrete carbon fiber reinforced silty sand," *Geosynthetics International*, Vol. 27, No. 6, (2020), 606-619, doi: 10.1680/jgein.20.00021.
  27. M. D. Toé Casagrande, M. R. Coop, and N. C. Consoli, "Behavior of a Fiber-Reinforced Bentonite at Large Shear Displacements," *Journal of Geotechnical and Geoenvironmental Engineering*, Vol. 132, No. 11, (2006), 1505-1508, doi: 10.1061/(asce)1090-0241(2006)132:11(1505).
  28. M. Mirzababaei, A. Arulrajah, A. Haque, S. Nimbalkar, and A. Mohajerani, "Effect of fiber reinforcement on shear strength and void ratio of soft clay," *Geosynthetics International*, Vol. 25, No. 4, (2018), 471-480, doi: 10.1680/jgein.18.00023.
  29. Y. Yilmaz, "Experimental investigation of the strength properties of sand-clay mixtures reinforced with randomly distributed discrete polypropylene fibers," *Geosynthetics International*, Vol. 16, No. 5, (2009), 354-363, doi: 10.1680/gein.2009.16.5.354.
  30. A. P. S. Dos Santos, N. C. Consoli, and B. A. Baudet, "The mechanics of fibre-reinforced sand," *Geotechnique*, Vol. 60, No. 10, (2010), 791-799, doi: 10.1680/geot.8.P.159.
  31. A. S. Zaimoglu, "Freezing-thawing behavior of fine-grained soils reinforced with polypropylene fibers," *Cold Regions Science and Technology*, Vol. 60, No. 1, (2010), 63-65, doi: 10.1016/j.coldregions.2009.07.001.
  32. D. R. Freitag, "Soil randomly reinforced with fibers," *Journal of Geotechnical Engineering*, Vol. 112, No. 8, (1986), 823-826, doi: 10.1061/(ASCE)0733-9410(1986)112:8(823).
  33. X. Lv, H. Zhou, X. Liu, and Y. Song, "Experimental study on the effect of basalt fiber on the shear behavior of cemented sand," *Environmental Earth Sciences*, Vol. 78, No. 24, (2019), 1-13, doi: 10.1007/s12665-019-8737-7.
  34. X. Zhang, X. Gu, J. Lü, and Z. Zhu, "Experiment and simulation of creep performance of basalt fibre asphalt mortar under uniaxial compressive loadings," *Journal of Southeast University (English Edition)*, Vol. 32, No. 4, (2016), 472-478, doi: 10.3969/j.issn.1003-7985.2016.04.013.
  35. F. Elgabbas, E. A. Ahmed, and B. Benmokrane, "Flexural Behavior of Concrete Beams Reinforced with Ribbed Basalt-FRP Bars under Static Loads," *Journal of Composites for Construction*, Vol. 21, No. 3, (2017), 04016098, doi: 10.1061/(asce)cc.1943-5614.0000752.
  36. R. Tanzadeh, J. Tanzadeh, M. honarmand, and S. A. Tahami, "Experimental study on the effect of basalt and glass fibers on behavior of open-graded friction course asphalt modified with nano-silica," *Construction and Building Materials*, Vol. 212, (2019), 467-475, doi: 10.1016/j.conbuildmat.2019.04.010.
  37. V. Dhand, G. Mittal, K. Y. Rhee, S. J. Park, and D. Hui, "A short review on basalt fiber reinforced polymer composites," *Composites Part B: Engineering*, Vol. 73, (2015), 166-180, doi: 10.1016/j.compositesb.2014.12.011.
  38. D. Wang, H. Wang, S. Larsson, M. Benzerzour, W. Maherzi, and M. Amar, "Effect of basalt fiber inclusion on the mechanical properties and microstructure of cement-solidified kaolinite," *Construction and Building Materials*, Vol. 241, (2020), 118085, doi: 10.1016/j.conbuildmat.2020.118085.
  39. V. Fiore, T. Scalici, G. Di Bella, and A. Valenza, "A review on basalt fibre and its composites," *Composites Part B: Engineering*, Vol. 74, (2015), 74-94, doi: 10.1016/j.compositesb.2014.12.034.
  40. Q. Ma and C. Gao, "Effect of Basalt Fiber on the Dynamic Mechanical Properties of Cement-Soil in SHPB Test," *Journal of Materials in Civil Engineering*, Vol. 30, No. 8, (2018), 04018185, doi: 10.1061/(asce)mt.1943-5533.0002386.
  41. S. Lin, X. Lei, Q. Meng, and J. Xu, "Properties of biocemented, basalt-fibre-reinforced calcareous sand," *Proceedings of the Institution of Civil Engineers - Ground Improvement*, Vol. 0, No. 0, (2019), 1-9, doi: 10.1680/jgrim.19.00023.
  42. C. P. Ndepete and S. Sert, "Use of basalt fibers for soil improvement," *Acta Physica Polonica A*, Vol. 130, No. 1, (2016), 355-356, doi: 10.12693/APhysPolA.130.355.
  43. M. Saberian and M. A. Rahgozar, "Geotechnical properties of peat soil stabilized with shredded waste tyre chips in combination with gypsum, lime or cement," *Mires and Peat*, Vol. 18, No. September, (2016), 1-16, doi: 10.19189/MaP.2015.OMB.211.
  44. ASTM, "Standard Test Method for Unconfined Compressive Strength of Cohesive Soil 1," ASTM International, 2013. <https://www.astm.org/Standards/D2166> (accessed Mar. 19, 2020).
  45. ASTM International, "C109/C109M-05. Standard Test Method for Compressive Strength of Hydraulic Cement Mortars," Annual Book of ASTM Standards, 2005. <https://www.astm.org/Standards/C109> (accessed Mar. 20, 2020).
  46. US Army Corps of Engineers, "CRD-C260-01 Standard Test Method for Tensile Strength of Hydraulic Cement Mortars," *COE Standards*, 2001. [https://www.wbdg.org/FFC/ARMYCOE/STANDARDS/crd\\_c260.pdf](https://www.wbdg.org/FFC/ARMYCOE/STANDARDS/crd_c260.pdf) (accessed Mar. 20, 2020).

47. B. han Yang *et al.*, "Strength characteristics of modified polypropylene fiber and cement-reinforced loess," *Journal of Central South University*, Vol. 24, No. 3, (2017), 560-568, doi: 10.1007/s11771-017-3458-0.
48. C. Tang, B. Shi, W. Gao, F. Chen, and Y. Cai, "Strength and mechanical behavior of short polypropylene fiber reinforced and cement stabilized clayey soil," *Geotextiles and Geomembranes*, Vol. 25, No. 3, (2007), 194-202, doi: 10.1016/j.geotexmem.2006.11.002.
49. Y. Yilmaz and V. Ozaydin, "Compaction and shear strength characteristics of colemanite ore waste modified active belite cement stabilized high plasticity soils," *Engineering Geology*, Vol. 155, (2013), 45-53, doi: 10.1016/j.enggeo.2013.01.003.
50. R. Sharma, "Laboratory study on sustainable use of cement-fly ash-polypropylene fiber-stabilized dredged material," *Environment, Development and Sustainability*, Vol. 20, No. 5, (2018), 2139-2159, doi: 10.1007/s10668-017-9982-0.
51. A. Kumar and D. Gupta, "Behavior of cement-stabilized fiber-reinforced pond ash, rice husk ash-soil mixtures," *Geotextiles and Geomembranes*, Vol. 44, No. 3, (2016), 466-474, doi: 10.1016/j.geotexmem.2015.07.010.
52. R. K. Sharma, "Laboratory study on stabilization of clayey soil with cement kiln dust and fiber," *Geotechnical and Geological Engineering*, Vol. 35, No. 5, (2017), 2291-2302, doi: 10.1007/s10706-017-0245-5.
53. P. Jongpradist, N. Jumlongrach, S. Youwai, and S. Chucheeprakul, "Influence of Fly Ash on Unconfined Compressive Strength of Cement-Admixed Clay at High Water Content," *Journal of Materials in Civil Engineering*, Vol. 22, No. 1, (2010), 49-58, doi: 10.1061/(asce)0899-1561(2010)22:1(49).
54. D. Eme, T. Nwofor, and S. Sule, "Correlation between the California Bearing Ratio (CBR) and Unconfined Compressive Strength (UCS) of Stabilized Sand-Cement of the Niger Delta," *International Journal of Civil Engineering*, Vol. 3, No. 3, (2016), 7-13, doi: 10.14445/23488352/ijce-v3i3p103.

---

### Persian Abstract

---

#### چکیده

تاکنون مطالعات زیادی بر روی رفتار مکانیکی خاک‌های تقویت‌شده با الیاف و خاک‌های تثبیت‌شده با تثبیت‌کننده‌های شیمیایی معمولی مانند سیمان و آهک انجام شده است، با این حال تحقیقات بسیار محدودی بر روی ویژگی‌های مقاومت فشاری محصور نشده خاک‌های peat تثبیت‌شده با سیمان به همراه الیاف انجام شده است. اضافه شدن الیاف به خاک تثبیت شده با سیمان منجر به بهبود قابل توجهی در ویژگی‌های رفتاری همچون شکل پذیری و مقاومت خاک‌های ضعیف یا نرم می‌شود. هدف اصلی مطالعه حاضر در نظر گرفتن اثرات مقدار سیمان، مقدار الیاف، طول الیاف و زمان عمل‌آوری بر روی مقاومت فشاری محصور نشده خاک peat است. این مطالعه نشان می‌دهد که افزودن الیاف بازالت یا سیمان باعث افزایش قابل توجهی در مقادیر UCS می‌شود. مقدار UCS نمونه تثبیت شده با سیمان به طور قابل توجهی بیشتر از نمونه‌های تقویت شده با الیاف بازالت است. با این حال، نمونه تقویت‌شده با الیاف بازالت، رفتار نرمتری نسبت به نمونه تثبیت شده با سیمان نشان دادند. نتایج نشان داد که افزایش مقادیر UCS در ترکیبی از الیاف بازالت و سیمان بیشتر از افزایش ایجاد شده توسط هر یک از آنها به صورت جداگانه است.

---

## AIMS AND SCOPE

The objective of the International Journal of Engineering is to provide a forum for communication of information among the world's scientific and technological community and Iranian scientists and engineers. This journal intends to be of interest and utility to researchers and practitioners in the academic, industrial and governmental sectors. All original research contributions of significant value focused on basics, applications and aspects areas of engineering discipline are welcome.

This journal is published in three quarterly transactions: Transactions A (Basics) deal with the engineering fundamentals, Transactions B (Applications) are concerned with the application of the engineering knowledge in the daily life of the human being and Transactions C (Aspects) - starting from January 2012 - emphasize on the main engineering aspects whose elaboration can yield knowledge and expertise that can equally serve all branches of engineering discipline.

This journal will publish authoritative papers on theoretical and experimental researches and advanced applications embodying the results of extensive field, plant, laboratory or theoretical investigation or new interpretations of existing problems. It may also feature - when appropriate - research notes, technical notes, state-of-the-art survey type papers, short communications, letters to the editor, meeting schedules and conference announcements. The language of publication is English. Each paper should contain an abstract both in English and in Persian. However, for the authors who are not familiar with Persian, the publisher will prepare the latter. The abstracts should not exceed 250 words.

All manuscripts will be peer-reviewed by qualified reviewers. The material should be presented clearly and concisely:

- *Full papers* must be based on completed original works of significant novelty. The papers are not strictly limited in length. However, lengthy contributions may be delayed due to limited space. It is advised to keep papers limited to 7500 words.
- *Research notes* are considered as short items that include theoretical or experimental results of immediate current interest.
- *Technical notes* are also considered as short items of enough technical acceptability with more rapid publication appeal. The length of a research or technical note is recommended not to exceed 2500 words or 4 journal pages (including figures and tables).

*Review papers* are only considered from highly qualified well-known authors generally assigned by the editorial board or editor in chief. Short communications and letters to the editor should contain a text of about 1000 words and whatever figures and tables that may be required to support the text. They include discussion of full papers and short items and should contribute to the original article by providing confirmation or additional interpretation. Discussion of papers will be referred to author(s) for reply and will concurrently be published with reply of author(s).

## INSTRUCTIONS FOR AUTHORS

Submission of a manuscript represents that it has neither been published nor submitted for publication elsewhere and is result of research carried out by author(s). Presentation in a conference and appearance in a symposium proceeding is not considered prior publication.

Authors are required to include a list describing all the symbols and abbreviations in the paper. Use of the international system of measurement units is mandatory.

- On-line submission of manuscripts results in faster publication process and is recommended. Instructions are given in the IJE web sites: [www.ije.ir](http://www.ije.ir)-[www.ijeir.info](http://www.ijeir.info)
- Hardcopy submissions must include MS Word and jpg files.
- Manuscripts should be typewritten on one side of A4 paper, double-spaced, with adequate margins.
- References should be numbered in brackets and appear in sequence through the text. List of references should be given at the end of the paper.
- Figure captions are to be indicated under the illustrations. They should sufficiently explain the figures.
- Illustrations should appear in their appropriate places in the text.
- Tables and diagrams should be submitted in a form suitable for reproduction.
- Photographs should be of high quality saved as jpg files.
- Tables, Illustrations, Figures and Diagrams will be normally printed in single column width (8cm). Exceptionally large ones may be printed across two columns (17cm).

## PAGE CHARGES AND REPRINTS

The papers are strictly limited in length, maximum 6 journal pages (including figures and tables). For the additional to 6 journal pages, there will be page charges. It is advised to keep papers limited to 3500 words.

### **Page Charges for Papers More Than 6 Pages (Including Abstract)**

For International Author ***	<b>\$55 / per page</b>
For Local Author	<b>100,000 Toman / per page</b>

## AUTHOR CHECKLIST

- Author(s), bio-data including affiliation(s) and mail and e-mail addresses).
- Manuscript including abstracts, key words, illustrations, tables, figures with figure captions and list of references.
- MS Word files of the paper.



THOMSON REUTERS  
WEB OF SCIENCE



Scopus®



CAS®  
A DIVISION OF THE  
AMERICAN CHEMICAL SOCIETY



 Crossref



Scientific Indexing Services

Google  
Scholar